Book of Proceedings

The Ninth International Congress
of the Serbian Society of Mechanics
July 5-7, 2023, Vrnjačka Banja, Serbia

The Ninth International Congress of the Serbian Society of Mechanics, July 5-7, 2023, Vrnjačka Banja, Serbia – Book of Proceedings

Editor
Professor Nenad Filipović
Professor Miloš Kojić

Technical Editor
Đorđe Dimitrijević

Proofreaders
Neda Vidanović Miletić
Milena Đorđević
Marijana Dimović

Year of publication
2023

ISBN-978-86-909973-9-8

TABLE OF CONTENTS

Dear colleagues,

The Serbian Society of Mechanics organized the 9th International Congress of the Serbian Society of Mechanics from 5th to 7th July 2023 in Vrnjačka Banja, Serbia. The aims of the congress were to bring together leading academic scientists, researchers and research scholars to exchange and share experiences and research results on various aspects of Theoretical and Applied Mechanics. The congress brought an interdisciplinary platform for researchers, practitioners and educators to present and discuss the most recent innovations, theories, algorithms, as well as practical challenges encountered and solutions adopted in the fields of Classical Mechanics, Solid and Fluid Mechanics, Computational Mechanics, Biomechanics, Applied Mathematics and Physics, Structural Mechanics and Engineering. More information on the Conference can be found on the webpage: http://www.ssm.kg.ac.rs/congress_2023/.
Co-organizers of the conference were:
Faculty of Engineering, University of Kragujevac
Faculty of Mechanical Engineering, University of Belgrade
Faculty of Technical Science, University of Novi Sad
Faculty of Mechanical Engineering, University of Niš
Institute for Information Technology, University of Kragujevac
University of Kragujevac
Mathematical Institute of the Serbian Academy of Sciences and Arts
Serbian Academy of Sciences and Arts
Serbian Society of Computational Mechanics.

Financial support was provided by the Ministry of Science, Technological Development and Innovation of the Republic of Serbia.

Plenary speakers were:

1. Assoc. Prof. Dr Miha Brojan – *University of Ljubljana, Slovenia*
   Title: From symmetry breaking to functionality: Examples from nonlinear mechanics of beams, plates and shells
2. Prof. Dr. Dimitri V. Georgievskii – *Institute of Mechanics, Lomonosov Moscow State University, Russia*
   Title: Elements of the Theory of Constitutive Relations and Formulations of the Linearized Problems on Stability
3. Prof. Dr. Stefano Lenci – *Department of Civil and Building Engineering, and Architecture, Polytechnic University of Marche, Ancona, Italy*
   Title: Nonlinear Wave Propagation in Cables and Beams Resting on a Bilinear Foundation
4. Prof. Dr. Parviz Moin – *Center for Turbulence Research, Stanford University, California, USA*
   Title: Large Eddy Simulation at Affordable Cost: Application to a Full Aircraft Configuration
5. Prof. Dr Rafal Rusinek – *Lublin University of Technology, Lublin, Poland*
   Title: Bio-electro-mechanical System of the Human Middle Ear
6. Assoc. Prof. Dr. Jelena M. Svorcan – *Department of Aerospace Engineering, Faculty of Mechanical Engineering, University of Belgrade, Serbia*
   Title: Numerical Investigation of Flows Around Small-Scale Propellers: Possibilities and Challenges

There were also presentations within four Mini-symposia:

- MS1: Mechanical Metamaterials
  Organizers: Milan Cajić, *Mathematical Institute SANU, Serbia*; Danilo Karličić, *Mathematical Institute SANU, Serbia*
- MS2: Turbulence
  Organizer: Đorđe Čantrak, *University of Belgrade, Serbia*
  Plenary speakers:
  1. Prof. Dr. Parviz Moin – *Center for Turbulence Research, Stanford University, California, USA*
  Title: Probing Turbulence Physics Using Numerical Simulation Databases – A Case Study in Predictive Science
  2. Prof. Dr. Nikolay Nikitin – *General Aerodynamics Laboratory, Institute of Mechanics, Lomonosov Moscow State University, Russia*
  Title: Secondary Flows of Prandtl's Second Kind. Mechanism of Formation and Method of Prediction
  3. Prof. Dr. Ji Pei – *National Research Center of Pumps, Jiangsu University, China*
  Title: Research on High Efficiency and High Reliability Pumps in Jiangsu University
- MS3: Biomechanics and Mathematical Biology
  Organizers: Andjelka Hedrih, *Mathematical Institute of the Serbian Academy of Sciences and Arts, Serbia*; Marat Dosaev, *Lomonosov Moscow State University, Moskva, Russian Federation*
  Plenary Speakers:
  1. Prof. Dr. Su Fong-Chin – *Department of Biomedical Engineering, College of Engineering, National Cheng Kung University, Tainan, Taiwan; Medical Device Innovation Center, National Cheng Kung University, Tainan, Taiwan*
  Title: An Exergame-Integrated IoT-Based Ergometer System for Personalized Training of the Elderly
  2. Prof. Dr. Marco Amabili – *Department of Mechanical Engineering, McGill University, Montreal, Canada*
  Title: Effect of Smooth Muscle Activation in the Static and Dynamic Mechanical Characterization of Human Aortas
- MS4: Nonlinear Dynamics
  Organizer: Julijana Simonović, *Faculty of Mechanical Engineering University of Niš, Serbia*

We have received more than 130 high-quality research papers. As a result of the strict review process and evaluation, the committee selected 91 papers for publishing in this Book of proceedings.
Special gratitude goes to the members of the program and scientific review committee as well as to all chairs, organizers and committee members for their dedication and support.

On behalf of the Organizing Committee

Prof. Dr Nenad Filipović
Chair of ICSSM2023

Book of Proceedings

UPGRADED TWO-STEP-SCALING APPROACH TO THE DTB CHARACTERIZATION OF FERRITIC STEELS

Sreten Mastilovic[1,*], Branislav Djordjevic[2] and Aleksandar Sedmak[3]

[1] Institute for Multidisciplinary Research, University of Belgrade, Kneza Viseslava 1a, Belgrade
e-mail: misko.mastilovic@imsi.bg.ac.rs
[2] Innovation Center of Faculty of Mechanical Engineering, Kraljice Marije 16, Belgrade, Serbia
e-mail: brdjordjevic@mas.bg.ac.rs
[3] Faculty of Mechanical Engineering, University of Belgrade, Kraljice Marije 16, Belgrade, Serbia
e-mail: asedmak@mas.bg.ac.rs
[*] *Corresponding author*

Abstract

The fracture toughness of ferritic steels in the DTB (ductile-to-brittle) transition temperature region is a stochastic *extrinsic* property known for pronounced experimental data scatter that necessitates statistical approach in the DTB characterization. The novel two-step-scaling (2SS) method, proposed recently for the size effect-modeling across the DTB transition region, is developed based on the weakest-link statistics and the two-parametric Weibull distribution. Specifically, the size sensitivity of the Weibull parameters of scale and shape are built into the appropriate framework. This approach is upgraded in this article to render the comparison with the existing models more transparent. Specifically, the original 2SS method is enhanced by adding a lower limit on fracture toughness, resulting in the translated (three-parameter) Weibull cumulative distribution function. This third Weibull parameter, often dubbed the location parameter, defines a threshold value that limits the accessible fracture toughness domain. The upgraded 2SS approach is compared to two established methods of the DTB fracture toughness assessment, which favorably reflected upon its generality and application flexibility.

Keywords: scaling, fracture toughness, size effect, Weibull distribution, location parameter.

1. Introduction

The brittle fracture at low temperatures is characterized by pronounced variations of fracture toughness (especially for small specimen) as well as others fracture properties and a statistical approach is a necessity. The Weibull theory is one of the first size-effect theories of the strength of materials that is developed on purely statistical arguments [1, 2]. The Weibull statistics is based on the weakest-link theory that is considered appropriate for modeling of the cleavage fracture of ferritic steels in the DTB (ductile-to-brittle) transition region, addressed in the present study. The plasticity mechanisms and stress redistribution are largely suppressed, which results in catastrophic failure, and, consequently, an inherently statistical nature of the size effect – the kind traditionally described by the Weibull distribution. Landes et al. (e.g., [4]) based their statistical

approach on the premise that the cleavage fracture toughness is controlled by the weakest link at the crack front. They used the two-parameter Weibull distribution, $\mathsf{W}(\beta, \eta)$, which is a frequent choice for the DTB characterization to this day (e.g., [3, 5]). A succinct historical survey of some of the most influential statistical studies of the cleavage fracture toughness of ferritic steels that make use of the Weibull statistics is, as an example, recently compiled in [6].

The novel two-step-scaling (2SS) approach has been developed [3, 7] with a focus on the DTB assessment of the fracture toughness size effect. The present study upgrades that original 2SS approach by introducing a lower limit on fracture toughness in the Weibull CDF (cumulative distribution function), resulting in a three-parameter Weibull distribution, $\mathsf{W}(\beta, \eta, \gamma)$. This third Weibull parameter, called the location parameter, defines a threshold value that limits the accessible fracture toughness domain [8].

2. The 2SS procedure revisited

The starting point in the present analysis is the translated Weibull CDF:

$$F\left(K \mid \beta, \eta, \gamma\right) = 1 - \exp\left[-\left(\frac{K-\gamma}{\eta}\right)^{\beta}\right]; \qquad (K-\gamma) \geq 0; \beta, \eta, \gamma \in \Re^{+} \tag{1}$$

where β, η (= K_0-$K_{\min}$) and γ (=$K_{\min}$=const.) are the Weibull shape, scale and location parameters [9], respectively. In Eq. (1), the symbol K is used for the generic critical value of the stress intensity, while K_0 and $K_{\min}$ stand for the normalization and the threshold values, respectively.

The scaling procedure involves also the $\mathsf{W}(\beta, \eta, \gamma)$ probability density function (PDF)

$$f\left(K \mid \beta, \eta, \gamma\right) = \frac{\beta}{\eta}\left(\frac{K-\gamma}{\eta}\right)^{\beta-1} \exp\left[-\left(\frac{K-\gamma}{\eta}\right)^{\beta}\right] = \frac{dF\left(K\right)}{dK} \tag{2}$$

that represents slope in the F vs. $(K\text{-}\gamma)$ space. Hereinafter, $dK = d(K\text{-}\gamma)$ is used for brevity.

Furthermore, it is of interest to derive the maximum CDF slope, which corresponds to the inflection point (Π) defined by:

$$\left.\frac{d^2F}{dK^2}\right|_{K=K_{\Pi}} = \left(\frac{\beta}{\eta}\right)^2\left(\frac{K_{\Pi}-\gamma}{\eta}\right)^{\beta-2} \exp\left[-\left(\frac{K_{\Pi}-\gamma}{\eta}\right)^{\beta}\right]\left[1-\frac{1}{\beta}-\left(\frac{K_{\Pi}-\gamma}{\eta}\right)^{\beta}\right] = 0 \tag{3}$$

The inflection point definition (3) determines its coordinate in the F vs. $(K\text{-}\gamma)$ space

$$K_{\Pi} - \gamma = \eta \cdot \left(1-\frac{1}{\beta}\right)^{1/\beta} \tag{4}$$

that corresponds to $f_{\max}$ (5) and represents the mode of the Weibull distribution (1) by definition.

After a straightforward derivation, the Weibull CDF slope (2) at the inflection point (4) that corresponds to the PDF maximum is obtained in the following form:

$$S = \left.\frac{dF(K)}{dK}\right|_{K=K_{\Pi}} = \frac{1}{\eta}\,\Xi(\beta) = f(K)\big|_{K=K_{\Pi}} = f_{\max} \tag{5}$$

where

$$\Xi(\beta) = \beta\left(1-\frac{1}{\beta}\right)^{1-1/\beta} \exp\left[-\left(1-\frac{1}{\beta}\right)\right]; \quad \beta > \beta_{\times} \approx 1.35 \tag{6}$$

designates the shape function (as introduced in [3]). The domain definition $(6)_2$ ensures that the

Weibull CDF assumes the characteristic sigmoid shape [3, 10].

2.2 The two-step scaling scheme for the three-parameter Weibull CDF

The same basic relationships derived in the preceding section are revisited herein in the scaled space: $F{\cdot}W^{\xi}$ vs. $(K\text{-}\gamma){\cdot}W^{\kappa}$ illustrated in Fig. 1e. The motivation is that the gist of present approach to investigating the fracture toughness size effect rests upon the two scaling premises [3]:

(i) The scaling condition along the CDF abscissa (driven by the scaling parameter κ):

$$\eta_* = \eta \cdot W^{\kappa} = \left(K_0 - K_{\min}\right) \cdot W^{\kappa} = const. \tag{7}$$

defining the size-independent Weibull scale parameter η_* in *the scaled space* (Fig. 1c), and

(ii) The scaling condition along the CDF ordinate (driven by the scaling parameter ξ):

$$S_* = S \cdot W^{\xi} = const. \tag{8}$$

defining the common CDF slope S_* in the scaled space (Fig. 1e) that represents the common PDF maximum (Fig. 1f), related to the PDF maxima in the same space (Fig. 1b) by the formula

$$f_{\max} = W^{\kappa-\xi}\, S_* \tag{9}$$

Thus, it is required to re-derive the CDF slope (5), this time in the $F\text{–}(K\text{-}\gamma)$ space, which yields

$$S_* = \left.\frac{dy}{dx}\right|_{x=x_{\Pi}} = \frac{1}{\eta_*}\,\Xi(\beta)\,W^{\xi} \tag{10}$$

In the preceding derivation, it is convenient to use the change of variables $y = F{\cdot}W^{\xi}$ and $x = (K\text{-}\gamma){\cdot}W^{\kappa}$, which results in the functional dependence of the inflection point coordinate in the scaled space upon the Weibull shape parameter

$$\frac{\left(K_{\Pi} - \gamma\right) \cdot W^{\kappa}}{\eta_*} = \left(1 - \frac{1}{\beta}\right)^{1/\beta} \tag{11}$$

that is unchanged compared to Eq. $(4)_1$ (by virtue of the first constancy condition (7)).

A couple of observations could be made based on Eq. (10). First, the Weibull scale parameter in the scaled space is size-independent (Fig. 1c) by virtue of the K-scaling condition, $\eta_* = const.$ (7). Second, the CDF slope in the scaled space $F{\cdot}W^{\xi}$ vs. $(K\text{-}\gamma){\cdot}W^{\kappa}$ is also size-independent (Fig. 1c) by virtue of the second step scaling condition, $S_* = const.$ (8). Consequently, Eq. (10) implies that

$$\Xi(\beta)\,W^{\xi} = const. \tag{12}$$

The value of shape function Ξ

$$\Xi\left(\beta \,|\, W, \xi\right) = S_*\, \eta_*\, W^{-\xi} \tag{13}$$

can be calculated for each particular specimen size once ξ and S_* are determined.

The pair of scaling parameters (κ, ξ) that govern the two scaling steps (illustrated in Fig. 1) is defined by the constancy conditions (7) and (12):

$$\kappa = \log_{\left(\frac{W_j}{W_i}\right)}\left(\frac{\eta_i}{\eta_j}\right), \quad \xi = \log_{\left(\frac{W_j}{W_i}\right)}\left[\frac{\Xi\left(\beta_i\right)}{\Xi\left(\beta_j\right)}\right] \tag{14}$$

where indices i, j (=1,2,..) mark the input experimental data sets (e.g., W_1, W_2,...= 25, 50,...).

The shape parameter $\beta(W, \xi)$ can be determined based on Eq. (6) once the value of $\Xi\,(\beta|W, \xi)$

is known.

Finally, the Weibull CDF can now be written in the following form

$$F\left(K \mid \beta, \eta_*, \gamma\right) = 1 - \exp\left\{-\left(\frac{(K-\gamma)\cdot W^{\kappa}}{\eta_*}\right)^{\beta(W,\xi)}\right\}; \qquad (K-\gamma) \geq 0;\ \beta, \eta_*, \gamma \in \Re^{+} \tag{15}$$

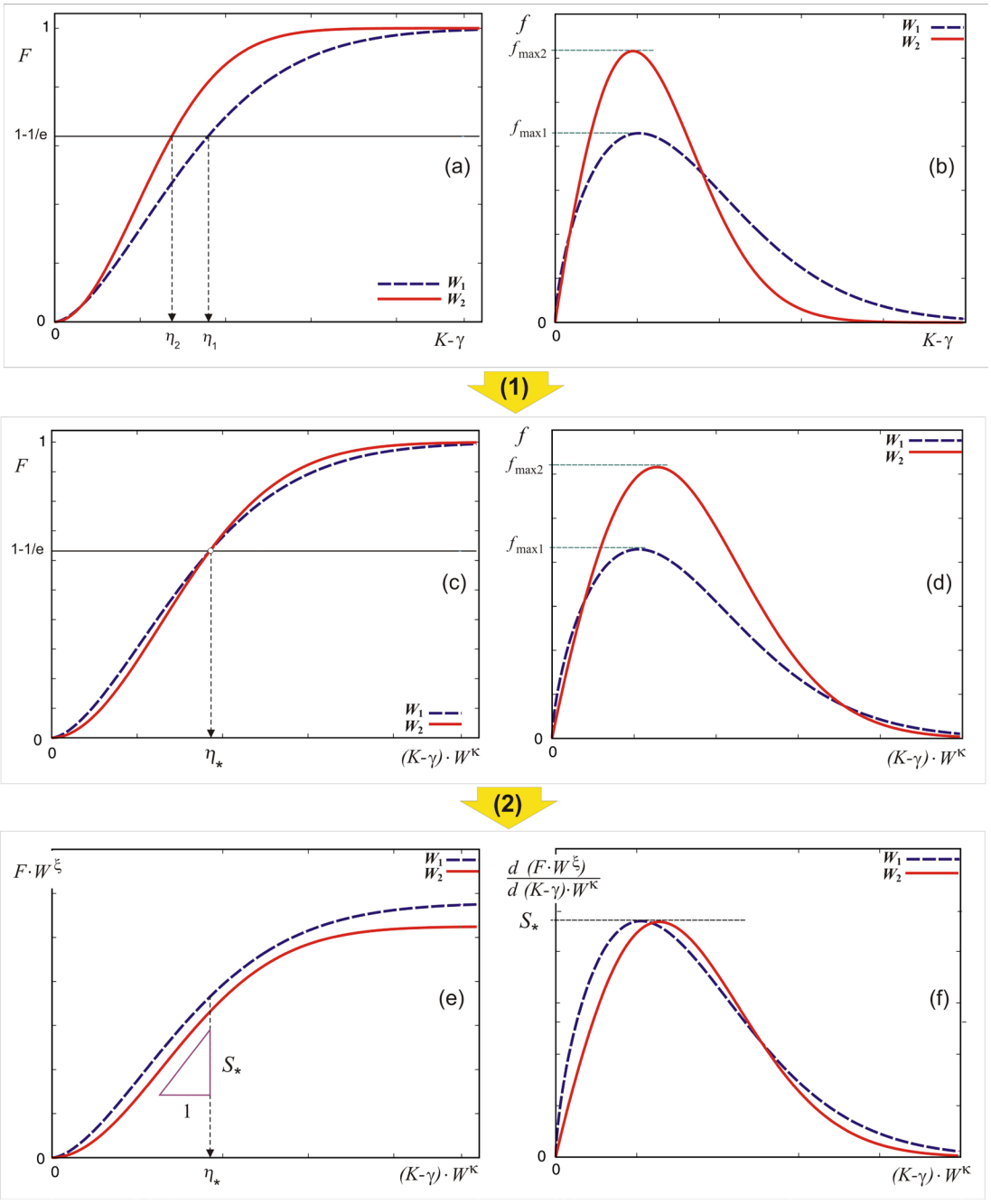

Fig. 1. Schematics of the two scaling steps in the upgraded 2SS procedure (W_1 and W_2 mark sizes of two experimental data sets)

3. Relationship between the novel 2SS method and two established methods for DTB characterization of fracture toughness

The scaling along the abscissa is defined by the parameter κ which ensures that the constancy condition (7) is met. Therefore, in the novel 2SS procedure, κ is an independent fitting parameter determined by the input experimental data sets. Application of the 2SS method requires as an input at least two experimental data sets corresponding to two C(T) specimen size (e.g., W_1 and W_2 shown in Fig. 1). If that is the case, the constancy condition governing the first scaling step (along the abscissa) can be written in the form:

$$\eta_* = \eta_1 \cdot W_1^{\kappa} = \eta_2 \cdot W_2^{\kappa} \quad \Rightarrow \quad \left(K_{01} - K_{\min}\right) \cdot W_1^{\kappa} = \left(K_{02} - K_{\min}\right) \cdot W_2^{\kappa} \tag{16}$$

The constancy condition written in the form of Eq. (16) will serve for comparison of the 2SS method with two established methods for DTB fracture toughness assessment.

First, it is obvious from Eq. $(16)_1$ that if the Weibull scale parameter (η_2) for the specimen of effective width W_2 is unknown, it can be calculated from the corresponding values of the first specimen as follows:

$$\eta_2 = \eta_1 \cdot \left(\frac{W_1}{W_2}\right)^{\kappa} \tag{17}$$

The relation (17) is identical to the corresponding expression from the 1-point method [5, 6]

$$K_{B_2} = K_{B_1} \cdot \left(\frac{B_1}{B_2}\right)^{1/\beta}, \quad K_{\min} = 0, \ \beta = const. \tag{18}$$

for the special case $\kappa = 1/\beta$ (bearing in mind that the geometric similarity implies $B_1/B_2 = W_1/W_2$). (Importantly, the 2SS procedure can use any characteristic linear dimension of the C(T) specimen, not necessarily the effective width, W. Assuming the geometrical similarity, $B \propto W$, the specimen thickness can replace the width in Eq. (16) without loss of generality.)

Similarly, based on the three-parameter Weibull CDF of cleavage fracture with constant shape parameter ($\beta = 4$), Wallin [8] proposed the following expression

$$K_{B_2} = K_{\min} + (K_{B_1} - K_{\min}) \left(\frac{B_1}{B_2}\right)^{1/4} \tag{19}$$

It is obvious that Eq. $(16)_2$ reduces Eq. (19) if the scaling parameter $\kappa = 1/\beta = 1/4$ (since K_B and K_0 depict the the same physical property). It should be emphasized that the assumption of the size-insensitivity of the Weibull shape parameter ($\beta = \text{const.}$) makes the second scaling in the 2SS method unnecessary (i.e., $\xi \equiv 0$ in Eq. (8) and Fig. 1) since the first scaling would result in the overlap of the Weibull CDF in Fig. 1c. This indicates that the 2SS method is both more general and more flexible then both above mentioned methods.

4. Numerical example: Prediction of CDF (K_{Jc}) of 22NiMoCr37 reactor steel at T=-91ºC

The following numerical example is performed using C(T) sample thickness B as the sample size parameter instead of the effective width W to demonstrate that their use is interchangeable in the presence of geometric similarity. The application of the 2SS approach starts with the data fitting of the two input experimental data sets (B = 12.5, 25) mm with the 3-parameter Weibull CDF.

Assuming the threshold $\gamma = K_{\min} = 40$ MPa$\sqrt{\text{m}}$ based on the two available experimental data sets [10], the fitting results in the Weibull scale and shape parameters (η and β, respectively) given in Table 1. The Ξ values are calculated by using Eq. (6), once β values are known.

B	β	η_0	γ	$\eta=\eta_0-\gamma$	Ξ
12.5	2.70	119.	40.	79.0	1.075
50	4.25	92.0	40.	52.0	1.611
100	**5.25**	**82.2**	40.	**42.2**	**1.973**

Table 1. The Weibull parameters and the corresponding shape function. The values corresponding to B = 12.5, 50 mm are the inputs used to calculate the extrapolated estimate for B = 100 mm (the bold font)

The pair of the scaling parameters (κ, ξ) is calculated from Eq. (14)

$$\kappa = \log_{\left(\frac{50}{12.5}\right)}\left(\frac{79.0}{52.0}\right) = 0.302\,, \quad \xi = \log_{\left(\frac{50}{12.5}\right)}\left(\frac{1.075}{1.611}\right) = -0.292 \tag{20}$$

The size-independent Weibull scale parameter η_{B*} in the scaled space, $P(K_{Jc}\cdot B^{\kappa})$ vs. $K_{Jc}\cdot B^{\kappa}$, is calculated by using the B-related form of the constancy condition (7) and the Weibull parameters from Table 1:

$$\eta_{B*} = 79.0\cdot 12.5^{0.302} = 52.0\cdot 50^{0.302} = 169.4 = const. \tag{21}$$

Similarly, the common *CDF* slope (S_{B*}) in the scaled space can be calculated based on Eq. (10) for each particular specimen dimension B

$$S_{B*} = \frac{1}{\eta_*}\Xi\left(\beta\,|\,B\right)\cdot B^{\xi} = \frac{1}{169.4}\cdot 1.075\cdot 12.5^{-0.292} = \frac{1}{169.4}\cdot 1.611\cdot 50.0^{-0.292} = 0.003035 = const. \tag{22}$$

The value of the shape function for the C(T) sample dimension B=100 mm, calculated by using Eq. (13), determines the corresponding Weibull shape parameter based on Fig. 2:

$$\Xi\left(\beta\,|\,B=100, \xi=-0.292\right) = 0.003035\cdot 169.4\cdot 100^{-(-0.292)} = 1.973 \quad \Rightarrow \quad \beta = 5.25 \tag{23}$$

The red solid line in Fig. 1 illustrated the Weibull CDF extrapolation for B = 100 mm and offers the comparison with the experimental data reported in [11].

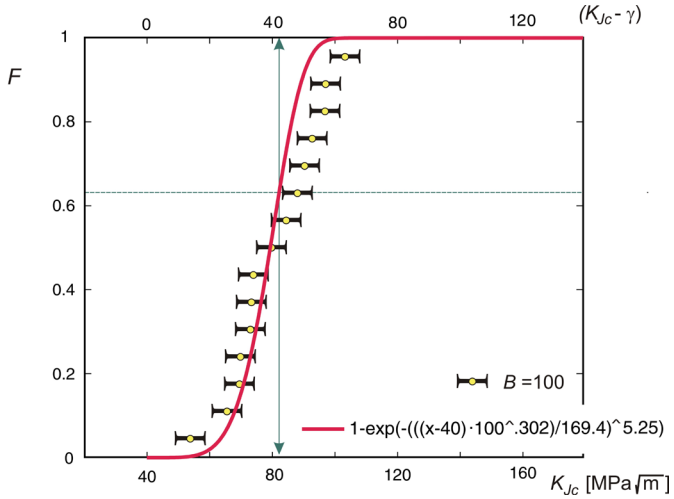

Fig. 2. The output of the 2SS procedure at T = -91ºC obtained based on the inputs presented in Table 1. The estimated K_{Jc} CDF for the C(T) sample sizes B = 100 mm represents an extrapolation of the input data. The symbols of width ±5 MPa√m are centered at the actual experimental data points. The solid line corresponds to 3-parameter Weibull predictions with the assumed fracture-toughness thresholds $\gamma = K_{min}$ = 40 MPa√m.

Finally, the Weibull CDF can now be written in the following form

$$F(K) = 1 - \exp\left\{-\left(\frac{(K-40)\cdot B^{0.302}}{169.}\right)^{\beta(B,\xi=-0.292)}\right\}; \qquad (K-40) \geq 0;\ \beta \in \Re^{+} \tag{15}$$

The extrapolation results in Fig. 2 are considered satisfactory considering the evident irregularity of the experimental data sets [10] reflecting the inherent stochasticity of fracture toughness in the DTB temperature transition region.

5. Summary

This article is devoted to an upgrade of the novel 2SS approach proposed recently to account for the size effect in the two-parameter Weibull ($\mathsf{W}(\beta, \eta)$) CDF of fracture toughness in the DTB transition temperature region. A model modification consists in the addition of a fracture-toughness threshold value (i.e. the Weibull location parameter) which constitutes the transition to the three-parameter Weibull distribution, $\mathsf{W}(\beta, \eta, \gamma)$ used extensively by Wallin and coworkers and many other researchers over the last few decades.

The aforementioned upgrade of the 2SS method highlights its relationship with two established models. In comparison, although the 2SS method requires experimental datasets of at least two C(T) sizes while the other two methods need only one, it obviously offers greater analytical flexibility in return. Importantly, it is shown that 2SS method reduces to the above mentioned methods if $\kappa = 1/\beta$ = const. Although these relations deserve further study, it can be affirmed without hesitation that the assumption β = const. is restrictive and its physical justification is somewhat elusive at present. From the standpoint of the 2SS procedure, the size-insensitivity of the Weibull shape parameter makes the second scaling (along the CDF ordinate) unnecessary since CDF curves would overlap into a single curve after the first scaling. Based on the experimental data analysis performed so far, the 2SS approach provides more realistic predictions than the above mentioned methods that are admittedly simpler and require smaller experimental data sets; the latter being a circumstance that should not be taken lightly.

Finally, the upgraded 2SS procedure is applied to an experimental data set available for 22NiMoCr37 ferritic steel extensively utilized as a pressure vessel material in nuclear industry. This experimental data, taken from the EURO fracture toughness data set, correspond to temperature -91ºC that belongs to the DTB transition region. The extrapolation results are considered satisfactory considering the irregularity of the measurement data compiled from two different laboratories, which reflect the inherent stochasticity of fracture toughness.

References:

[1] Weibull W., *A Statistical Theory of the Strength of Materials*. Generalstabens Litografiska Anstalts Förlag, Stockholm, 1939.

[2] Weibull W., *A Statistical Distribution Function of Wide Applicability*, Journal of Applied Mechanics, 18(3): 293-297, 1951.

[3] Mastilovic S., Djordjevic B., Sedmak A. *A scaling approach to size effect modeling of J_c CDF for 20MnMoNi55 reactor steel in transition temperature region*. Engineering Failure Analysis 131: 105838, 2022.

[4] Landes J., Zerbst U., Heerens J., Petrovski B., Schwalbe K., *Single-Specimen Test Analysis to Determine Lower-Bound Toughness in the Transition*, in Fracture Mechanics: Twenty-Fourth Volume, ed. J. Landes, D. McCabe, and J. Boulet (West Conshohocken, PA: ASTM International), 171-185, 1994.

[5] Djordjevic B., Sedmak A., Petrovski B., Dimic A., *Probability Distribution on Cleavage Fracture in Function of J_c for Reactor Ferritic Steel in Transition Temperature Region*, Engineering Failure Analysis, 125, 105392, 2021.

[6] Djordjevic B., Sedmak A., Mastilovic S., Popovic O., Kirin S. *History of ductile-to-brittle transition problem of ferritic steels.* Procedia Structural Integrity 42: 88–95, 2022.

[7] Mastilovic S., Djordjevic B., Sedmak A., *Corrigendum to "A scaling approach to size effect modeling of J_c CDF for 20MnMoNi55 reactor steel in transition temperature region"* [Eng. Fail. Anal. 131 (2022) 105838] Engineering Failure Analysis 142: 106751, 2022.

[8] Wallin K., *The Size Effect in K_{Ic} Results*, Enginnering Fracture Mechanics 22: 149-163, 1985.

[9] Mastilovic S., *Some Sigmoid and Reverse-Sigmoid Response Patterns Emerging from High-Power Loading of Solids*. Theoretical and Applied Mechanics 45: 95-119, 2018.

[10] Lucon E., Scibetta M., Application of Advanced Master Curve Approaches to the EURO Fracture Toughness Data Set. Open Report of the Belgian Nuclear Research Centre SCK•CEN-BLG-1036. Mol, Belgium, 2007.

REALIZATION OF THE BRACHISTOCHRONIC MOTION OF CHAPLYGIN SLEIGH IN A VERTICAL PLANE WITH UNILATERAL NONHOLONOMIC CONSTRAINT

Aleksandar M. Obradović [1], Oleg Yu. Cherkasov[2], Luka N. Miličić[1] and Slaviša Šalinić[3]

[1] Faculty of Mechanical Engineering, University of Belgrade, KraljiceMarije 16, 11120 Belgrade 35, Serbia
e-mail: aobradovic@mas.bg.ac.rs, lmilicic@mas.bg.ac.rs
[2] Lomonosov Moscow State University, Faculty of Mechanics and Mathematics, GSP-1, 1 Leninskye Gory, 119991, Moscow, Russia
e-mail:OYuChe@yandex.ru
[3] Faculty of Mechanical and Civil Engineering in Kraljevo, University of Kragujevac, Dositejeva 19, 36000 Kraljevo, Serbia
e-mail: salinic.s@mfkv.kg.ac.rs

Abstract

The paper considers the procedure for determining the brachistochronic motion of the Chaplygin sleigh in a vertical plane, where the blade is such that it prevents the motion of the contact point in one direction only. The position of the sleigh mass center and orientation at the final positions is specified, as well as the initial value of mechanical energy. The simplest formulation of a corresponding optimal control problem is given and it is solved by applying Pontryagin's maximum principle. For some cases, analytical solutions of differential equations of the two-point boundary value problem (TPBVP) of the maximum principle, were found. Numerical integration was carried out for other cases using the shooting method, where the assessment of missing terminal conditions was given and it was shown that the solution obtained represents the global minimum time for the brachistochronic motion. The method of the brachistochronic motion by means of a single holonomic and a single unilateral nonholonomic mechanical constraint is presented.

Keywords: Chaplygin sleigh, maximum principle, unilateral nonholonomic constraint, analytical solutions.

1. Introduction

Classical Bernoulli's problem of determining the brachistochrone for the particle in a vertical plane [1] has experienced many attempts at this problem generalizations for different, more complex, mechanical systems. A more detailed review of literature devoted to these generalizations can be found in the PhD dissertation [2], as well as in papers [3-14]. Our paper will deal with determining the brachistochronic motion of Chaplygin sleigh in a vertical plane, which was also the research subject in [15]. However, our paper differs basically from the mentioned paper by a unilateral nonholonomic constraint, unlike classical bilateral constraint of the blade type, that is present in [15]. Details about this type of constraint can be found in the paper [16], which presents an appropriate blade profile that corresponds to a unilateral constraint. Note that the results published so far for the Chaplygin sleigh motion are based on the assumption that Chaplygin sleigh moves on a horizontal plane (see e.g. [8, 17-25]), or on an inclined one [20].

Let us consider a Chaplygin sleigh of mass m and the radius of inertia i with respect to the central axis moving in a vertical plane as it is shown in Fig. 1. The sleigh position is defined by coordinates X and Y of the mass center C and angle φ between axis O_x and blade at point C. The sleigh position is specified at the initial and final instant but the initial value of mechanical energy is also known, $E = mgL$, which is large enough for the sleigh to reach the final position, where g is acceleration of gravity. Let U and V be the projections of the velocity of point C onto a blade and perpendicular to a blade, respectively. If the constraint is bilateral [15], then $V = 0$, this paper will also consider the cases of unilateral constraints, when $V \geq 0$ or $V \leq 0$, depending on two possible cases, related to the side to which the constraint restrains. The same figure also shows profiles of the corresponding blades for all mentioned cases.

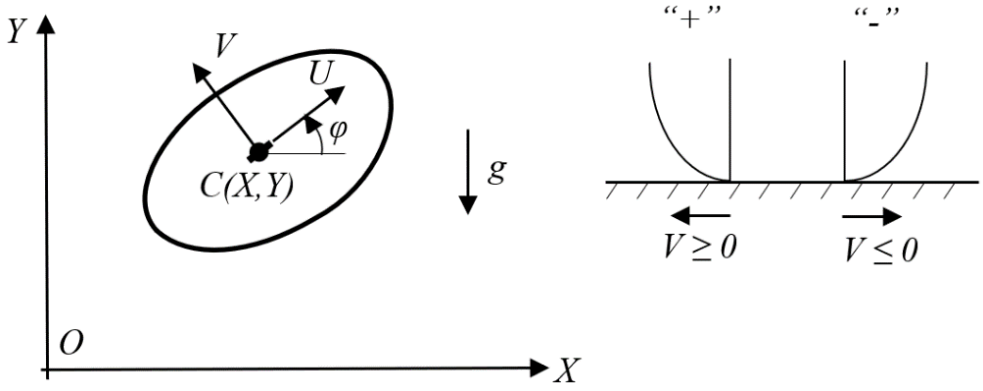

Fig. 1. A Chaplygin sleigh in a vertical plane

During brachistochronic motion, which in the original understanding of this problem is realized by ideal mechanical constraints, without action of the active forces, the mechanical energy remains unchanged:

$$\frac{1}{2}m\left(U^2 + V^2 + i^2\Omega^2\right) + mgY = mgL \tag{1}$$

where L is a given constant, which has the dimension of length.
In this paper, the brachistochronic motion will be determined only using kinematic differential equations:

$$\begin{aligned} \dot{X} &= U\cos\varphi - V\sin\varphi \\ \dot{Y} &= U\sin\varphi + V\cos\varphi \\ \dot{\varphi} &= \Omega \end{aligned} \tag{2}$$

which significantly simplifies this problem, considering the determination of the brachistochronic motion itself. The variable Ω represents the angular velocity of the body. It is only remarked herein that when the reaction *Rc* is defined from dynamic equations, it must be checked whether its direction corresponds to the unilateral constraint orientation.
To determine the brachistochronic motion, which corresponds to a minimum time between two specified positions, Pontryagin's maximum principle will be applied [26, 27]. Chapter 2 will present the simplest possible formulation of the optimal control problem. Chapter 3 will describe the procedure of solving this optimization task with special reference to the possibility of obtaining analytical solutions. Illustration of the procedure given by using concrete numerical examples will be reported in Chapter 4. Realization of the motion by means of ideal mechanical constraints will be shown in Chapter 5.
This paper is an expansion of paper [28], with a numerical example added on which we have merging of subintervals, where $V = 0$ or $V \neq 0$, as well as the possibility of analyzing realization of the brachistochronic motion by the help of a single holonomic and a single unilateral nonholonomic constraint.

Formulation of the optimal control problem

Introducing dimensionless quantities:

$$X = ix,\quad Y = iy,\quad \Omega = \omega\sqrt{\frac{g}{i}},\quad V = \pm v^2\sqrt{gi},\quad U = u\sqrt{gi},\quad t = \tau\sqrt{\frac{i}{g}},\quad L = il \tag{3}$$

the equations of state are obtained:

$$\begin{aligned} x' &= u\cos\varphi \mp v^2\sin\varphi \\ y' &= u\sin\varphi \pm v^2\cos\varphi \\ \varphi' &= \omega \end{aligned} \tag{4}$$

where the appropriate sign, "**+**" or "**–**", corresponds to the direction for the case of a corresponding blade. The notation $(...)'$ represents differentiation with respect to dimensionless time τ. The principle of conservation of mechanical energy for the considered problem in dimensionless variables reads:

$$u^2 + v^4 + \omega^2 + 2y - 2l = 0 \tag{5}$$

The initial conditions of motion are:

$$\tau_0 = 0 \quad x(\tau_0) = 0 \quad y(\tau_0) = 0 \quad \varphi(\tau_0) = 0 \tag{6}$$

whereas the final position is defined according to:

$$\tau_1 = ? \quad x(\tau_1) = x_1 \quad y(\tau_1) = y_1 \quad \varphi(\tau_1) = \varphi_1 \tag{7}$$

The problem of determining the brachistochronic motion consists of determining the optimal controls:

$$u = u(\tau) \quad v = v(\tau) \quad \omega = \omega(\tau) \tag{8}$$

and their corresponding final equations of motion of this system so that the system is converted from the initial state (6) in a minimum time τ_1 into the state (7) with the constraint (5). The functional being minimized in this problem has the form:

$$J = \int_0^{\tau_1} d\tau = \tau_1 \tag{9}$$

Solving the optimal control problem

In order to solve this problem, let us write the appropriate Pontryagin's function H for the case of time minimization [26, 27]:

$$H = -1 + \lambda_x(u\cos\varphi \mp v^2 \sin\varphi) + \lambda_y(u\sin\varphi \pm v^2\cos\varphi) + \lambda_\varphi \omega - \mu(u^2 + v^4 + \omega^2 + 2y - 2l) \tag{10}$$

where μ is the multiplier corresponding to the constraint of mechanical energy (5) and $\lambda_x, \lambda_y, \lambda_\varphi$ are co-state variables. The co-state system of differential equations [26, 27] reads:

$$\lambda_x' = 0 \quad \lambda_y' = 2\mu \quad \lambda_\varphi' = -\left(\lambda_x\left(-u\sin\varphi \mp v^2\cos\varphi\right) + \lambda_y\left(u\cos\varphi \mp v^2\sin\varphi\right)\right) \tag{11}$$

Optimality conditions of the maximum principle [26, 27]:

$$\frac{\partial H}{\partial u} = 0, \quad \frac{\partial H}{\partial v} = 0, \quad \frac{\partial H}{\partial \omega} = 0 \tag{12}$$

yield expressions for optimal controls:

$$\begin{aligned} u &= \frac{1}{2\mu}(\lambda_x\cos\varphi + \lambda_y\sin\varphi) \\ v^2 &= 0 \ \vee \ v^2 = \frac{\pm 1}{2\mu}(-\lambda_x\sin\varphi + \lambda_y\cos\varphi) \\ \omega &= \frac{1}{2\mu}\lambda_\varphi \end{aligned} \tag{13}$$

where the multiplier μ, in cases when independent variable τ at the end of motion is not specified, is defined from the condition:

$$H(\tau) = 0 \tag{14}$$

and it has the value:

$$\mu(\tau) = \frac{1}{4(l - y(\tau))} > 0 \tag{15}$$

which is positive over the considered interval of motion.
In order that it would be the maximum of Pontryagin's function, the corresponding second-order derivatives must be negative:

$$\frac{\partial^2 H}{\partial u^2} < 0, \quad \frac{\partial^2 H}{\partial v^2} < 0, \quad \frac{\partial^2 H}{\partial \omega^2} < 0 \tag{16}$$

wherefrom the criterion is finally obtained for the choice of an appropriate control:

$$\begin{aligned} u &= 2(l-y)(\lambda_x \cos\varphi + \lambda_y \sin\varphi) \\ v^2 &= \begin{cases} 0, & \pm(-\lambda_x \sin\varphi + \lambda_y \cos\varphi) \le 0 \\ \pm 2(l-y)(-\lambda_x \sin\varphi + \lambda_y \cos\varphi), & \pm(-\lambda_x \sin\varphi + \lambda_y \cos\varphi) > 0 \end{cases} \\ \omega &= 2(l-y)\lambda_\varphi \end{aligned} \tag{17}$$

It can be seen that in choosing the solution of (17) the function $S = (-\lambda_x \sin\varphi + \lambda_y \cos\varphi)$ has the major role, whose sign is the basis for distinguishing segments of motion over which $V = 0$ or $V \neq 0$

Differential equations of the two-point boundary value problem (TPBVP) are obtained by substituting (17) in (4) and (11). It is necessary to supplement boundary conditions (6) and (7) with condition (5) at the beginning or end of the interval of motion in order to, also, define unknown dimensionless time of motion τ_1.

Here, it should be noted that, in a general case, different solutions of (17) can be combined over different intervals of motion depending on the sign of a corresponding expression. In a general case, there are not analytical solutions of differential equations of the TPBVP if $v^2 = 0$ over the entire interval of motion or over some subintervals of motion. In those cases, the problem must be solved numerically. If the shooting method is applied and backward numerical integration is done, by the choice of three parameters, λ_x , λ_{y1} , τ_1**,** three initial conditions are guessed **(**6**),** where it is, based on (5), (14) and (17):

$$\lambda_\varphi(\tau_1) = \pm\sqrt{\frac{1}{2(l-y_1)} - (\lambda_x \cos\varphi_1 + \lambda_{y1} \sin\varphi_1)^2} \tag{18}$$

and it should be checked which sign corresponds to the task concrete parameters.

Assessment of the interval of parameters' values is also obtained from (5):

$$\begin{aligned} &\left|\lambda_x \cos\varphi_1 + \lambda_{y1} \sin\varphi_1\right| \le \frac{1}{\sqrt{2(l-y_1)}} \\ &\left|\lambda_x\right| \le \frac{1}{\sqrt{2l}} \\ &\left|\lambda_{y1}\right| < \frac{1}{\sqrt{2(l-y_1)}} \end{aligned} \tag{19}$$

and it significantly assists in shooting as well as in seeking the global minimum if there are multiple solutions for TPBVP.

If the constraint is side-oriented so that the extremal solution over the entire interval is on an open set, differential equations of TPBVP have a simpler form:

$$\begin{aligned} x' &= 2(l-y)\lambda_x \qquad \lambda_x{}' = 0 \\ y' &= 2(l-y)\lambda_y \qquad \lambda_y{}' = \frac{1}{2(l-y)} \\ \varphi' &= 2(l-y)\lambda_\varphi \qquad \lambda_\varphi{}' = 0 \end{aligned} \tag{20}$$

and have general solutions in the analytical form:

$$\begin{aligned} y &= l - \frac{1+\cos(pt+\alpha)}{p^2} \\ x &= \frac{2\lambda_x}{p^2}(t+\frac{1}{p}\sin(pt+\alpha)) + C_1 \\ \varphi &= \frac{2\lambda_\varphi}{p^2}(t+\frac{1}{p}\sin(pt+\alpha)) + C_2 \end{aligned} \tag{21}$$

where $(p, \alpha, \lambda_x, \lambda_\varphi, C_1, C_2)$ are determined together with unknown moment τ_1 from (5), (6) and (7). It should be noted that these solutions also correspond to the case when the blade does not exist at all, consequently for the general case of the brachistochronic plane-parallel motion of a rigid body.

Form and structure of optimal controls will depend on whether the constraint is bilateral, unilateral and whether it exists at all, if unilateral it will also depend on corresponding direction, but on initial conditions (6), final conditions (7) and quantity l, as well.

Numerical examples

Let us show for the concrete parameters of the task:

$$l = 2,\ x_1 = \varphi_1 = \frac{\pi+2}{2\sqrt{2}},\ y_1 = 1 \tag{22}$$

the procedure described in previous section, particularly for the constraints $V \geq 0$ (Case "+") and $V \leq 0$ (Case "-").

In the case "-", it is shown that, over the entire interval of motion, the solution is on an open set and that there are analytical solutions of the corresponding TPBVP:

$$\begin{aligned} x &= \frac{(\tau+\sin\tau)}{\sqrt{2}}, \quad y = 1-\cos\tau, \quad \varphi = \frac{(\tau+\sin\tau)}{\sqrt{2}} \\ \lambda_x &= \frac{1}{2\sqrt{2}}, \quad \lambda_y = \frac{\sin\tau}{2(1+\cos\tau)}, \quad \lambda_\varphi = \frac{1}{2\sqrt{2}}, \quad \tau_1{}^- = \frac{\pi}{2} \end{aligned} \tag{23}$$

It can be also noticed that the mass center trajectory is a deformed cycloid with the coefficient $\frac{1}{\sqrt{2}}$.

In the case "+", it is shown that over the entire interval of motion the extremal solution is on the boundary $V = 0$. Based on the assessments (19) of all possible values of the missing parameters, considering their positive signs, graphical representation can be given of the surfaces that correspond to obtaining the appropriate initial conditions. Figure 2 shows three surfaces of different colors, each of which corresponds to the fulfillment of one of the initial conditions (6).

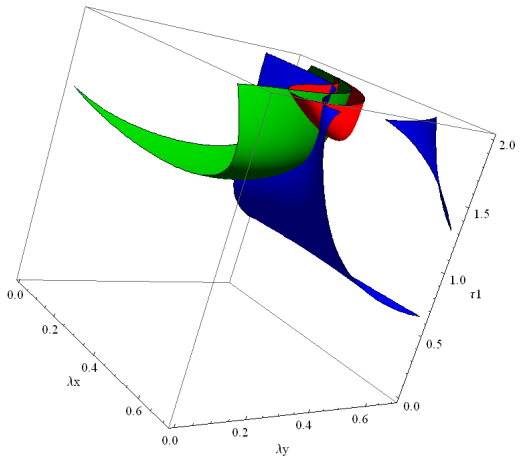

Fig. 2. Representation of the global minimum time of motion.

These surfaces have been obtained based on numerical calculations of the corresponding TPBVP in the program Wolfram Mathematica [29] using commands NDSolve[...], ContourPlot3D[...] and they represent numerical dependencies:

$$x_0(\lambda_x,\lambda_{y1},\tau_1)=0,\quad y_0(\lambda_x,\lambda_{y1},\tau_1)=0,\quad \varphi_0(\lambda_x,\lambda_{y1},\tau_1)=0 \tag{24}$$

The parametric values sought are at their intersection:

$$\lambda_x=0.499037,\quad \lambda_{y1}=0.369326,\quad \tau_1^{+}=1.76731 \tag{25}$$

and it can be also seen that the point of intersection is at the lowest position along the axis of dimensionless moment τ_1, whereby it is numerically shown that the obtained solution represents the global minimum time of motion. This method of graphical representation for any three-parameter shooting is very useful when TPBVP has multiple solutions, out of which the one with the lowest time should be chosen [8].

Numerical solutions correspond to parametric values (25), as shown in Fig. 3, together with analytical solutions (23), which correspond to opposite orientation of a unilateral constraint.

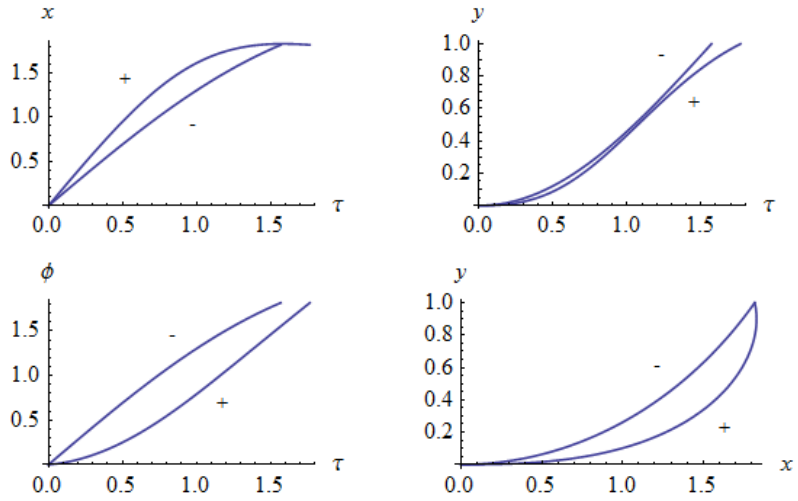

Fig. 3. Final equations of motion and mass center trajectory of the Chaplygin sleigh.

It can be noticed that the time of motion in Case "-", τ_1^-, is lower compared to τ_1^+ in Case "+". The first case corresponds to the brachistochronic plane-parallel motion of a rigid body in the vertical plane, while the second case corresponds completely to the case of a classical double-sided blade, as analyzed in [15]. The same figure depicts the trajectory of the mass center for both cases. In addition, based on the numerical and analytical solution, it can be shown that the function $S = -\lambda_x sin\varphi + \lambda_y cos\varphi$ is negative over the entire interval of motion and that conditions (17) of the maximum principle are fully satisfied.

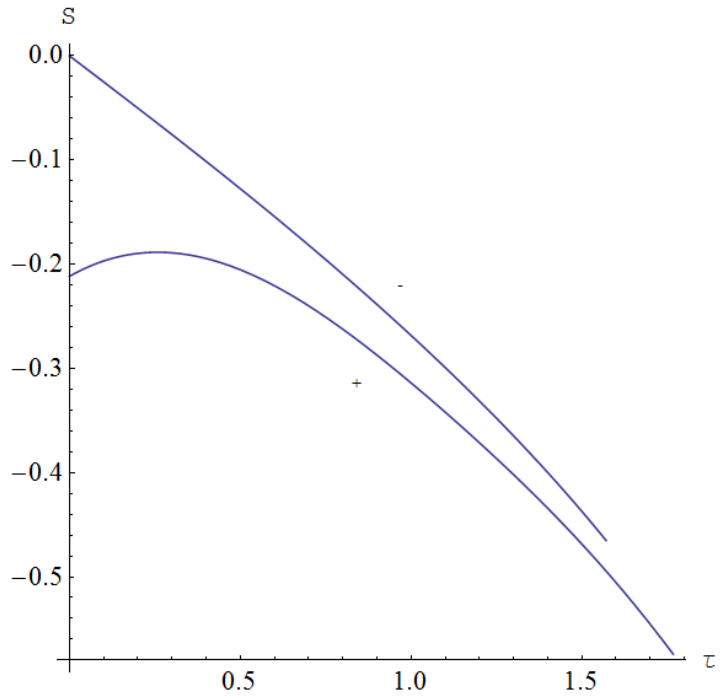

Fig. 4. Function $S = -\lambda_x sin\varphi + \lambda_y cos\varphi$.

Such task parameters can be defined, contour conditions and initial mechanical energy, so that the brachistochronic motion contains segments where optimal solution is from an open set and segments on which $V = 0$. Let the numerical parameters (22) be slightly modified

$$l = 2,\ x_1 = \varphi_1 = 1.25\ \ y_1 = 1 \tag{26}$$

where only Case "+" will be considered. Solving the TPBVP defined by (4-7), (11) and (17) yields values of the parameters (25):

$$\lambda_x = 0.378358,\quad \lambda_{y1} = 0.475233,\quad \tau_1 = 1.18207 \tag{27}$$

for which Fig. 25 shows the diagram of changes in dimensionless velocities and angular velocity, where it is seen that there are segments on which $V = 0$ or $V > 0$. The same figure gives the function $= -\lambda_x sin\varphi + \lambda_y cos\varphi$, whose sign conditions the optimal change of velocity (17).

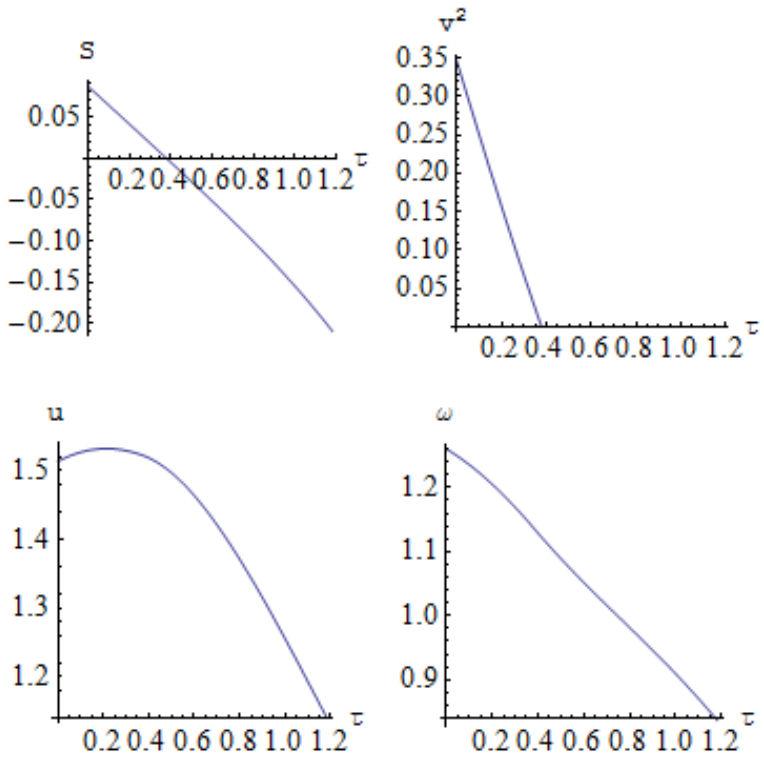

Fig. 5. Diagrams of dimensionless velocities, angular velocity and function S

Realization of motion by means of ideal mechanical constraints

Also, it would be necessary to show the method of realization by the help of ideal constraints, which would be also generalization of the paper [22], for the case of guides, or the paper [7], if motion is realized by rolling of the moving centroid along the stationary one. This additional research would require using of dynamical differential equations of the Chaplygin sleigh motion.

The brachistochronic motion (23) in case "-" can be fully realized like in the paper [7].

In this Chapter we will opt for realizing the brachistochronic motion using an additional holonomic constraint of the guide type. Two cases will be considered, when the guide is at point A or at point B, where $AC = BC = i$ (see Fig. 6).

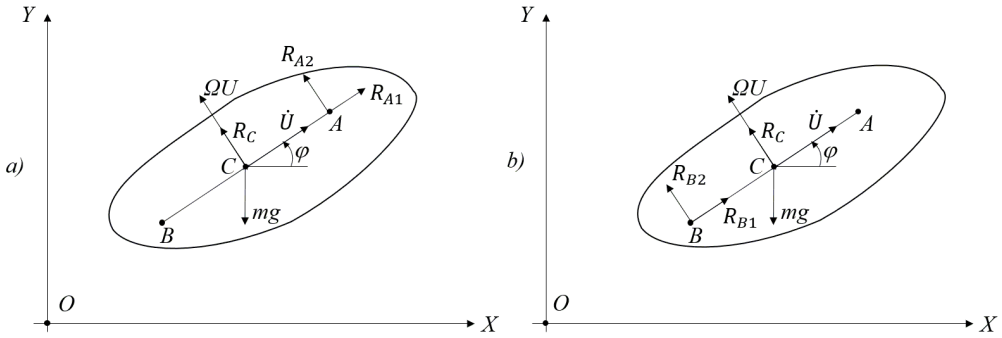

Fig.6.

Let's limit ourselves to the case "+" where the solutions of earlier considered TPBVP with parameters (25) are known now. On this solution, for the entire time of motion $V = 0$. If the guide is at point A, dynamical equations have dimensionless form ($R_C = mg\,r_C$, $R_A = m\,g\,r_A$, $R_B = mgr_B$):

$$u' = r_{A1} - \sin\varphi \;,\; \omega u = r_{A2} + r_C - \cos\varphi \;,\; \omega' = r_{A2} \tag{28}$$

whereas the same equations for the case of guides at point B are:

$$u' = r_{B1} - \sin\varphi \;,\; \omega u = r_{B2} + r_C - \cos\varphi \;,\; \omega' = -r_{B2} \tag{29}$$

where u' and ωu are dimensionless projections of point C acceleration onto corresponding directions and a ω' is body's dimensionless angular acceleration.
From above mentioned equations all reactions of constraints can be also defined, but for further analysis it is needed to determine the laws of change in reaction *Rc* in both cases:

$$r_C = \omega u + \cos\varphi - \omega' \tag{30}$$

$$r_C = \omega u + \cos\varphi + \omega' \tag{31}$$

and check its sign *(Rc>0)*.

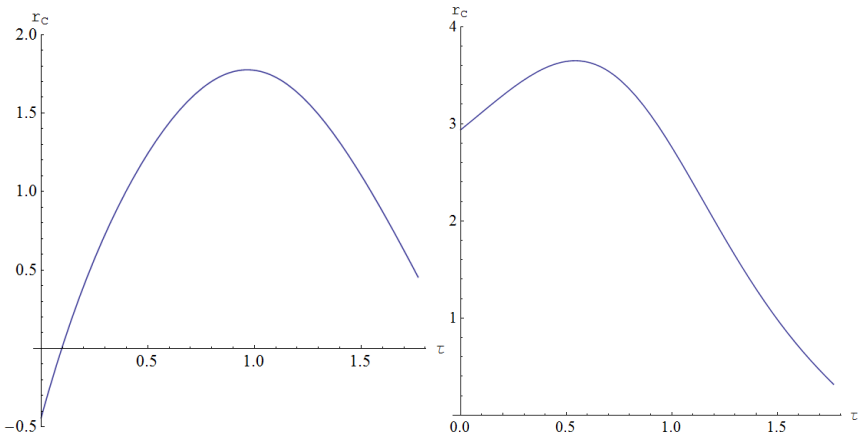

Fig.7. Dimensionless reaction of constraint for the case of guides at points A and B

Figure 7 presents the laws of change (30) and (31), which indicate that the brachistochronic motion is impossible to realize if the guide is at point A. At the initiation of motion it is necessary that *Rc<0* , which this constraint is unable to realize. In contrast, it is possible to position the guide at point B, because then it is *Rc>0* over the entire interval of motion.
This is the essential difference compared to the case of a classical blade considered in work [15], where both methods of realization are possible because the nonholonomic constraint is bilaterally restraining. Also, note that in mentioned work [15] one of the two additionally imposed holonomic constraints is redundant. The brachistochronic planar motion of the body is possible to achieve only by means of two ideal mechanical constraints, the third one is unnecessary. In a unilateral restricting nonholonomic constraint of the blade type [16] the position of another constraint, the guide, must be chosen in such way that necessary force at the contact point must correspond to condition

Rc>0 over the entire time interval.
In the third case from Section 4, on different segments of brachistochronic motion, it is possible to combine guides at different points on the segment where $V = 0$, depending on the check of conditions *Rc>0.* On the segments where $V > 0$, *Rc=0* the brachistochronic motion can be realized by the help of centroids [7] or guides at two different points, where the considered points A and B can be used.

Conclusions

The paper contributes to the unexplored area of optimal control of the motion of nonholonomic mechanical systems with unilateral restricted constraint reaction. The simplification of the optimal control task is also the originality of our work, based only on kinematic equations. A special contribution represents the analytical solution of differential equations for individual cases of unilateral constraints, when the solution is on an open set. It also entirely corresponds to the case of brachistochronic plane-parallel motion of a rigid body in the vertical plane, when the blade does not exist. The mass center trajectory is a deformed cycloid, unlike ordinary cycloid, in the case of a classical brachistochrone. It is shown that in the concrete case, with numerical solution of TPBVP, the obtained solution represents, for specified task parameters, the global minimum time of motion.
A special contribution of this work is a detailed analysis of the possibility of realizing planar motion of the rigid body by means of two ideal mechanical constraints, of which one is a unilateral restricting nonholonomic constraint.
Continuing research can take place in several directions. It is also possible, as indicated in a classical paper by Caratheodory [18], to impose maximum possible value of the unilateral constraint reaction of the blade. In that regard, the results of [22], which considered constrained classical nonholonomic bilateral constraint of the blade type, could be generalized to the motion in the vertical plane with unilateral constraint.

Acknowledgment: This research was supported by the Ministry of Science, Technological Development, and Innovation of the Republic of Serbia (Grants No. 451-03-47/2023-01/200105 and No. 451-03-47/2023-01/200108). This support is gratefully acknowledged.

References:

[1] J. Bernoulli, *Problema novum ad cuius solutionem Mathematici invitantur (A new problem that mathematicians are invited to solve),* Acta Eruditorum 15 (1696), 264–269.
[2] A.V. Zarodnyuk, *Optimization of controlled descent and generalized brachistochrone problems (in Russian)*, PhD, Moscow State University, Faculty of Mechanics and Mathematics, 2018.
[3] S. Šalinić, *Contribution to the brachistochrone problem with Coulomb friction*, Acta Mechanica 208 (2009), 97-115.
[4] O. Jeremić, S. Šalinić, A. Obradović, Z. Mitrović, *On the brachistochrone of a variable mass particle in general force fields*, Mathematical and Computer Modelling 54(11-12) (2011), 2900-2912.
[5] S. Šalinić, A. Obradović, Z. Mitrović, *On the brachistochronic motion of mechanical systems with unilateral constraints*, Mechanics Research Communications 45 (2012), 1-6.

[6] S. Šalinić, A. Obradović, Z. Mitrović, S. Rusov, *Brachistochrone with limited reaction of constraint in an arbitrary force field*, Nonlinear Dynamics 69(1-2) (2012), 211-222.
[7] A. Obradović, S. Šalinić, O. Jeremić, Z. Mitrović, *On the brachistochronic motion of a variable-mass mechanical system in general force fields*, Mathematics and Mechanics of Solids 19(4) (2014), 398-410.
[8] R. Radulović, S. Šalinić, A. Obradović, S. Rusov, *A new approach for the determination of the global minimum time for the Chaplygin sleigh brachistochrone problem*, Mathematics and Mechanics of Solids 22(6) (2017), 1462-1482.
[9] A. Obradović, S. Šalinić, R. Radulović, *The brachistochronic motion of a vertical disk rolling on a horizontal plane without slip*, Theoretical and Applied Mechanics 44(2) (2017), 237-254.
[10] A.S. Sumbatov, *Brachistochrone with Coulomb friction as the solution of an isoperimetrical variational problem*, International Journal of Non-Linear Mechanics 88 (2017), 135-141.
[11] A.S. Sumbatov, *Problem on the brachistochronic motion of a heavy disk with dry friction*, International Journal of Non-Linear Mechanics 99 (2018), 295-301.
[12] O.Y. Cherkasov, E.V. Malykh, N.V. Smirnova, *Brachistochrone problem and two-dimensional Goddard problem*, Nonlinear Dynamics 111(1) (2023), 243-254.
[13] O.Y. Cherkasov, N.V. Smirnova, *On the Brachistochrone problem with state constraints on the slope angle*, International Journal of Non-Linear Mechanics 139 (2022), 103871.
[14] N.V. Smirnova, O.Y. Cherkasov, *Range maximization problem with a penalty on fuel consumption in the modified Brachistochrone problem*, Applied Mathematical Modelling 91 (2021), 581-589.
[15] Y.F. Golubev, *Brachistochrone for a rigid body sliding down a curve*, J. Comput. Syst. Sci. Int. 52 (2013), 571–587.
[16] V.V. Kozlov, *On the dynamics of systems with one-sided non-integrable constraints*, Theoretical and Applied Mechanics 46(1) (2019), 1–14.
[17] S.A.Chaplygin, *On the theory of motion of nonholonomic systems*. *The reducing-multiplier theorem*, Math. Collect. 28 (1) (1911), 303-314, [English Translation by A. V. Getling, Regular and Chaotic Dynamics 13(4) (2008), 369-376].
[18] C. Carathéodory, *Der Schlitten*, ZAMM - Journal of Applied Mathematics and Mechanics / Zeitschrift für Angewandte Mathematik und Mechanik, 13 (2) (1933), 71-76.
[19] J.G. Papastavridis, *Time-integral theorems for nonholonomic systems*, International Journal of Engineering Science 25 (7) (1987), 833-854.
[20] A.V. Borisov, I.S. Mamayev, *The dynamics of a Chaplygin sleigh*, Journal of Applied Mathematics and Mechanics 73 (2) (2009), 156-161.
[21] Y.N. Fedorov, L.C. García-Naranjo, *The hydrodynamic Chaplygin sleigh*, Journal of Physics A: Mathematical and Theoretical 43 (43) (2010), 434013.
[22] S. Šalinić, A. Obradović, Z. Mitrović, S Rusov, *On the brachistochronic motion of the Chaplygin sleigh*, Acta Mechanica 224 (2013), 2127-2141.
[23] A.V. Karapetyan, A.Y. Shamin, *On the movement of the Chaplygin sleigh on a horizontal plane with dry friction*, Acta Astronautica 176 (2020), 733 – 740.
[24] I.A. Bizyaev, A.V. Borisov, I.S. Mamaev, *Dynamics of a Chaplygin sleigh with an unbalanced rotor: regular and chaotic motions*, Nonlinear Dynamics 98(3) (2019), 2277 – 22911.
[25] I.A. Bizyaev, A.V. Borisov, S.P. Kuznetsov, *The Chaplygin sleigh with friction moving due to periodic oscillations of an internal mass*, Nonlinear Dynamics 95(1) (2019), 699-714.
[26] L.S. Pontryagin, V.G. Boltyansky, R.V. Gamkrelidze, E.F. Mishchenko, *The Mathematical Theory of Optimal Processes*, Interscience Publishers, John Wiley and Sons, New Jersey, 1962.
[27] A.E. Bryson, Y.C. Ho, *Applied Optimal Control*, Hemisphere, New York, 1975.

[28] A. Obradović, O.Y. Cherkasov, L. Miličić, *The brachistochronic motion of Chaplygin sleigh in a vertical plane with unilateral nonholonomic constraint*, T.4.3, 9th International Congress of Serbian Society of Mechanics Vrnjačka Banja, Serbia, July 5-7, 2023.
[29] S. Wolfram, *The Mathematica Book*, 5th ed. Champaign, IL: Wolfram Media, 2003.

PARALLELIZED SOFTWARE FOR FAST VIRTUAL STENTING SIMULATION OF PATIENT-SPECIFIC CORONARY ARTERY

Tijana Djukic[1,2], Igor Saveljic[1,2] and Nenad Filipovic[3]

[1] Institute for Information Technologies, University of Kragujevac, Jovana Cvijica bb, 34000 Kragujevac, Serbia
e-mail: tijana@kg.ac.rs
[2] Bioengineering Research and Development Center, BioIRC, 6 Prvoslava Stojanovica Street, 34000 Kragujevac, Serbia
e-mail: isaveljic@kg.ac.rs
[3] Faculty of Engineering, University of Kragujevac, 6 Sestre Janjica Street, 34000 Kragujevac
e-mail: fica@kg.ac.rs

Abstract

One of the clinical treatments of stenotic arteries is the stent deployment. In this study, a numerical model that simulates mechanical behavior of both stent and arterial wall, as well as their interaction was used. This model was implemented in a software that is able to simulate the stent deployment process within patient specific artery in real time, using the resources of the graphics card of the computer and GPU (Graphics Processing Unit) programming principles. An important focus of this study is the improvement of performance of the stent deployment application using several optimization techniques. Three different computer configurations were used to test the performance of the application. The computation time is effectively reduced, due to the applied parallelization and optimization techniques. On the best configuration used, the maximum of around 88-fold speedup was obtained compared to the single-core CPU implementation. The obtained results show that using GPUs it is possible to run demanding and precise simulations of stent deployment on a common personal computer. This software can help clinicians to quickly perform patient-specific virtual interventions and analyze the outcomes of the stent deployment procedure before the actual intervention.

Keywords: numerical simulation, fast virtual intervention, stent deployment, GPU programming, performance optimization.

1. Introduction

Atherosclerosis is one of the most common diseases of the cardiovascular system that occur as a result of inflammation within arterial walls and further formation of plaques and constrictions within blood vessels. These constrictions further induce changes in the blood flow that affect the blood supply of organs and tissues. One of the clinical treatments for these patients is the implantation of an endovascular prosthesis called a stent. Stent is a small cylindrical device, made of metal alloys that is inserted in the stenotic artery and expanded, to widen the artery and to restore its original shape and blood flow. Stent deployment is a process that involves large

displacements and deformations and it would be very useful for clinicians to have the possibility of analyzing several scenarios, for example the deployment of stents with different sizes and initial positions and the effects of these choices on the outcome prior to the intervention, to ensure highest possible effectiveness of the treatment and prevent complications.

Numerical simulations have been also used to study the behavior of the stent during deployment in stenotic arteries [1,2]. In this study, a numerical model that was presented and validated in the literature [3] is used to simulate the process of stent deployment. It was demonstrated in [4] that this model can be used to predict the shape of the arterial wall after stent implantation. This model was further improved in [3] to model the process more realistically by including a more complex material model that represents the arterial wall. Also, the model was extensively tested against clinical patient-specific data. This successful validation demonstrated that this model can be used in clinical practice to predict the outcome of a virtual stenting intervention prior to the actual one. However, in order for this model to be useful for clinicians, it is essential that various simulations can be executed quickly. This is why the focus of this study is on the parallelization of the mentioned numerical model. Using the presented parallelization approach and included optimization techniques, the developed software can provide fast and reliable predictions to the clinicians. The developed software is able to simulate stent deployment process within patient-specific artery in real time, using the resources of the graphics card of the computer and programming principles.

In this study, the numerical model was implemented such that the entire computation was performed on the GPU, while only the coordinates of nodes of the stent and arterial wall are transferred back to the CPU, in order to visualize the results. The coordinates were rendered in each time step in the main window of the application, using OpenGL. The performance of the application is additionally improved, by applying certain optimization techniques that will be discussed in this study. Three different configurations were used to test the performance of the application. The obtained speedup shows that by using GPUs it is possible to monitor the entire simulation process in real time, on a personal computer.

The paper is organized as follows. Section 2 briefly presents the numerical model and lists details about the parallelization. In Section 3 additional improvements and applied optimizations are described. Section 4 presents the results of the speedup obtained with parallelization. Section 5 discusses other approaches to model stent deployment process and concludes the paper.

2. Materials and methods

In this Section, the numerical model is explained in detail. The preparation of geometrical data that is used in the simulations is described in Section 2.2. Finally, details about the parallelization procedure are discussed in Section 2.3.

2.1 Numerical model

The numerical model consists of three parts: modeling of the stent expansion, modeling the deformation of the arterial wall and modeling the interaction of the stent and the arterial wall. Details of the numerical model are described in literature [3] and here it will only be briefly introduced.

The stent is modeled as a mesh of nodes. Nodes are separated along the length of the stent and grouped in so-called rings. The motion of stent node in time is governed by the expansion force, like it is proposed in literature [5], while the force with which the arterial wall opposes further stent expansion is also considered.

The interaction of the stent and arterial wall is modeled by interpolating the forces on the contact surface. The meshes representing the stent and arterial wall do not overlap precisely, and hence these forces cannot be transferred directly from one node to the other. These forces have to

be interpolated over the surrounding nodes of each mesh. The interpolation of the forces over the surrounding nodes of each mesh is performed using the Dirac delta function [6].

The motion of nodes of the arterial wall in time is modeled using the same approach that is used for stent nodes, only the forces are calculated differently. The external force that causes the motion of the nodes of the arterial wall is interpolated from the surrounding stent nodes and the internal force is calculated using the finite element method [7]. The deformation caused by the stent in the previous time step causes an internal force, with which the arterial wall opposes the deformation. In order to calculate the stress tensor required for the calculation of internal force, it is necessary to define the relation between internal stress and deformation. This relation is defined using the hyperelastic Mooney-Rivlin model. Material coefficients and equations used for this material model can be found in [3], where the entire representation of the arterial wall for a stenotic artery is discussed in detail.

All the equations of the numerical model are solved in iterations, until the convergence criterion is satisfied. In numerical simulations performed in this study and in literature [3,4], it is considered that the convergence is reached when the maximum absolute change in the non-dimensional displacement in a time step is less than 10^{-3}.

2.2 Geometrical data for numerical simulations

Numerical simulations presented in this study are performed using clinical data for a particular patient. Data is obtained from the EVINICI database that was accessed within the European project – SMARTool that is funded under the European Programme Horizon 2020. Within this study, clinical data consisted of 0.3 mm DICOM images from CT scan examinations. The automatic segmentation algorithm available within the commercial software Mimics was used to extract the patient-specific 3D geometry of the vessel in stereolithography (STL) format, as surface triangulation. These data are then further used to generate tetrahedral meshes of the particular segment of the coronary artery. Several mesh resolutions were used, the number of nodes of the stent mesh varied from 4907 to 29452, while the number of elements in the tetrahedral mesh of the arterial wall varied from 1277 to 61272.

2.3 Parallelization of software for stent deployment using CUDA architecture

In the numerical implementation of the numerical model presented in Section 2.1, the entire procedure is divided in 7 phases:

1) Calculation of stent rings
2) Calculation of elements of arterial wall in contact with stent nodes
3) Expansion of the stent
4) Distribution of forces from stent nodes to nodes of the arterial wall
5) Deformation of the artery
6) Calculation of internal forces in the arterial wall
7) Distribution of forces from the nodes of the arterial wall to the stent nodes.

All data necessary for the simulation are allocated on the GPU device and initialized from the CPU only during the initialization of the program. All data reside in the GPU memory and are not restored to the CPU memory, to avoid unnecessary and time consuming transfers of data. Only the coordinates of nodes representing the stent and arterial wall are transferred back to the CPU after each iteration, in order to visualize the results in real time.

In each of the above listed phases, only the data about the particular node of the stent or arterial wall and data about the nodes connected to the particular node are used, and hence all the calculations can be performed for each node independently. This makes the presented numerical model suitable for execution on a GPU device. CUDA architecture (Compute Unified Device Architecture) developed by NVIDIA was used for the implementation of the numerical model.

This architecture provides a software tool that extends the programming language C/C++ and that enables the execution of the computational part of the computer program on the GPU device. For each of the listed phases a specific CUDA function called kernel is developed. These kernel functions are called from the main program run on the CPU and the code of the functions is executed in parallel, using a grid of threads. Since the calculations are independent for each node of the mesh, each node is assigned to one thread during execution of kernel functions. The 7 kernel functions are repeated in iterations, until the convergence criterion is satisfied.

3. Improvements of performance

In this Section, details about the improvement techniques are provided. These techniques were applied during implementation of the numerical model to improve the performance of the developed software.

3.1 Calculation of element in contact

In order to calculate the external force acting on the stent, it is necessary to calculate the distance between a stent node and the arterial wall. To calculate the distance, first, the element of the mesh representing the arterial wall that could be in contact with the stent node should be determined. The element in contact is determined for each stent node, using a loop over all elements of the arterial wall.

This procedure should be repeated in each iteration. But, since the time step is very small, the displacements of nodes in one iteration are relatively small and it can be considered that if the stent node is no longer in contact with the element calculated in previous time step, then the particular node is in contact with one of the neighboring elements. Elements that share an edge with the particular element are considered its neighboring elements. Using this approximation, the elements in contact are calculated for each stent node using a loop over all elements only once, during the simulation setup and initialization. During the simulation, in the iteration loop, only the current element in contact and its neighboring elements are considered.

3.2 Calculation of close nodes

The interaction between stent and arterial wall is performed using the interpolation of the forces on the contact surface. This practically means that in each iteration, for each node of the stent, all nodes of the arterial wall should be checked, to determine whether the distance between these two nodes is less than the predefined value and if it is, the force should be distributed. The same should be done for each node of the arterial wall. This approach is very time-consuming, so it was additionally optimized. The force that is causing the motion of stent nodes is the internal expanding force and it acts along the normal vector in the particular stent node. The external force that could potentially cause the stent node to move away from the direction of the normal vector is lower in magnitude than the forces acting along this direction, so it can considered that the deviation of the motion of the stent node from its path along the normal vector is small (less than 5%). Using this assumption, for each stent node it is possible to determine the nodes of the arterial wall that could potentially be close to the stent node during its motion. The minimal distance between the arterial node and stent node during its motion is calculated as the normal distance of the arterial node from the direction of motion of stent node. If this distance is smaller than the predefined value (with an additional tolerance that is included to consider the deviation of the motion of nodes from its assumed paths), then this arterial node is considered a close node to the particular stent node. Two new arrays are introduced that save the ID numbers of close nodes for both artery and stent. Then, in the appropriate kernel function, instead of always performing a loop over all nodes, only the nodes marked as potentially close and saved in the

mentioned arrays are considered.

3.3 Data management

One of the main problems that should be addressed during parallelization is the memory bandwidth. In other words, it can occur that the access to the data from GPU memory can require more time than the actual computations. An important aspect of optimization should be to increase memory bandwidth by reducing the accesses to global memory and by ensuring that access to data is as coalesced as possible. Access to data in GPU memory is coalesced if, during kernel execution, threads in blocks access consecutive memory locations. If this is the case, CUDA architecture ensures that this access is done using a single request and this makes the access more efficient.

For the software discussed in this study, in all kernel functions, it is necessary to read data (coordinates, forces, data about elements etc.) from the global GPU memory. In order to ensure coalesced data access, special attention was dedicated to the storage of data. Most of the quantities have 3 components and the data is grouped using the CUDA structure "float4". Although in some arrays the fourth component is not used, the data access is significantly improved due to mentioned data coalescence. The speedup that is obtained using this approach of data storage is around 52 percent.

Also, in order to ensure faster rendering of geometries of the stent and arterial wall in each iteration, instead of drawing each element separately, all elements are drawn using the "primitive restart" option of OpenGL and the coordinates of all nodes are stored in vertex buffer objects. This enables faster communication between the CPU and GPU memory and this optimization provided an additional speedup of around 22 percent.

4. Results

In this Section, the results of the parallelization are presented. During the testing of the speedup, the following software components were used: NVIDIA CUDA version 4.0 and OpenGL version 4.3. These versions were chosen (rather old, not the newest ones) to ensure that even computers with older configurations can be used to run the developed software. The software enables the user to manipulate the objects on the screen (the artery and the stent), to position the stent using the mouse pointer and finally, to monitor the simulation process in real time. An option is also provided to visualize either just the geometry of the arterial wall, or to show the distribution of force with which the stent is acting on the arterial wall, or to show the distribution of the internal stress in the arterial wall caused by the deformation. A screenshot of the software, during simulation, with shown distribution of force is shown in Figure 1.

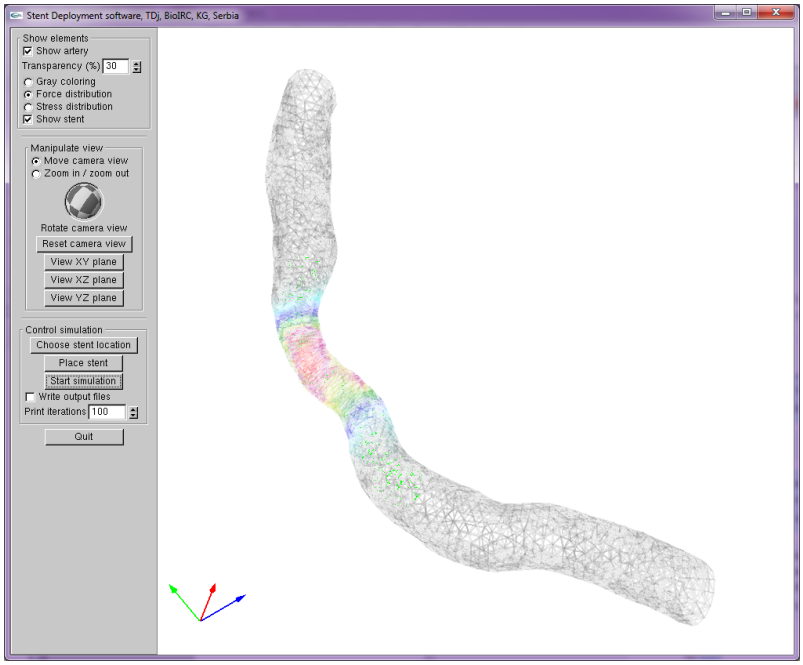

Fig. 1. Screenshot of the software for stent deployment during simulation, the geometry of the artery is colored based on the magnitude of the force with which stent acts on the arterial wall

First, the accuracy of the parallelized version is compared with the sequential version. The deviation of results for the final values of internal stress was less than 1.5% and the deviation of final coordinates of stent nodes was less than 1.2%, which demonstrates that the parallelization did not affect the accuracy of the software. The small differences arise due to the different compilers and architectures on which each version is executed.

The performance improvement using the optimization techniques described in Section 3 is shown in Figure 2. The execution time of the software for overall 2000 iterations is measured, for each kernel function listed in Section 2.3. In these simulations the stent mesh contained 14726 nodes and the mesh representing arterial wall contained 12765 elements with 4263 nodes. As it can be observed from Figure 2, the most time-consuming kernel function before optimization was function 2 that calculates the contact elements. This is the case because in this function, each thread that represents each stent node has a loop over all elements of the arterial wall, to find the contact element. After optimization described in Section 3.1, this function is performed much faster as the loop is completely excluded. Similarly, execution time of the kernel functions 4 and 7 is significantly reduced after optimization described in Section 2.2, because the loops over all nodes in search of close nodes are excluded. Since the number of nodes of the stent mesh was greater than the number of nodes of the arterial wall in the performed simulations, the effect of the exclusion of the loop is more evident for function 4, where the loop over stent nodes is excluded. The execution time of other functions is also reduced, due to the different data storage and more coalesced data access.

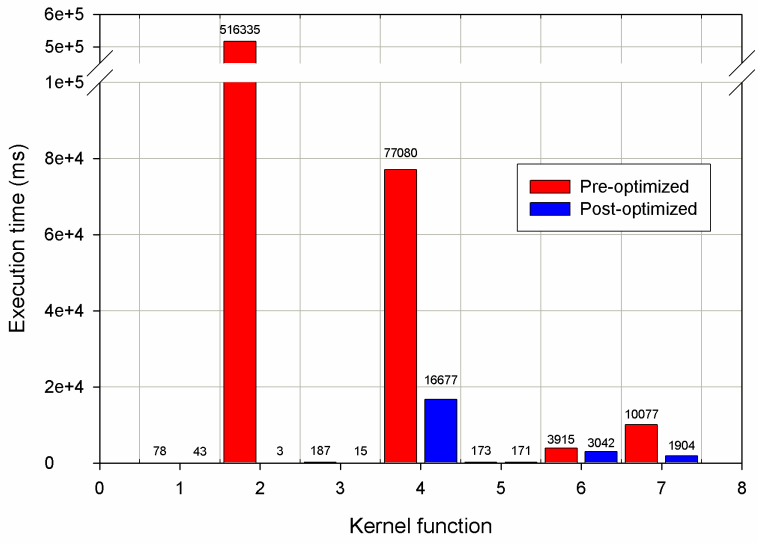

Fig. 2. Comparison of execution times of individual kernel functions, before and after applying optimization techniques

In this study, three different configurations were used, with three different graphics cards. Details about these configurations are given in Table 1.

Processor	Configuration 1	Configuration 2	Configuration 3
RAM memory	Pentium DualCore, 2.80 GHz	Intel Core i5, 3.20 GHz	Intel Core i5, 2.59 GHz
Graphics card	4 GB	8 GB	16 GB
Operating system	NVIDIA GeForce GT 630	NVIDIA GeForce GTX 650	GeForce RTX 2070
Processor	Windows 7, 64-bit	Windows 10, 64-bit	Windows 10, 64-bit

Table 1. Details about the configurations used for testing of software performance

The speedup of the software is calculated to show the efficiency of the proposed parallelization approach. The execution time was measured for the version using one CPU core and the version using the GPU device and the speedup between these versions was calculated. The scalability of the software is analyzed, since the speedup varies when the mesh size varies. Figure 3a shows the variation of speedup for different number of nodes of the mesh representing the stent, while always using the same mesh representing the arterial wall (with 12765 elements and 4263 nodes). Figure 3b shows the variation of speedup for different meshes representing the arterial wall, while always using the same mesh representing the stent (with 14726 nodes). Different meshes of the arterial wall cause greater variation of the speedup, because there are more loops over both elements and nodes of the arterial wall in the implementation of the kernel functions and these parts of the program are more time-consuming than the ones dealing with stent nodes. As the number of nodes of both meshes rises, the speedup is greater. This is in accordance with the assumption that the efficiency of the parallelization using GPU devices becomes more evident with larger amount of data that is being processed.

Overall, when using the configuration 1, the maximum of around 10-fold speedup compared to the single-core CPU implementation was obtained. With configuration 2, this maximum speedup was around 19 times and with configuration 3, this maximum speedup was around 88

times. This difference in the overall speedup can be explained by the different configurations, i.e. different processors, but mostly due to the different graphics cards. The graphics card of the configuration 3 is the one with highest performance and hence the greatest speedup is obtained using this card as the GPU device.

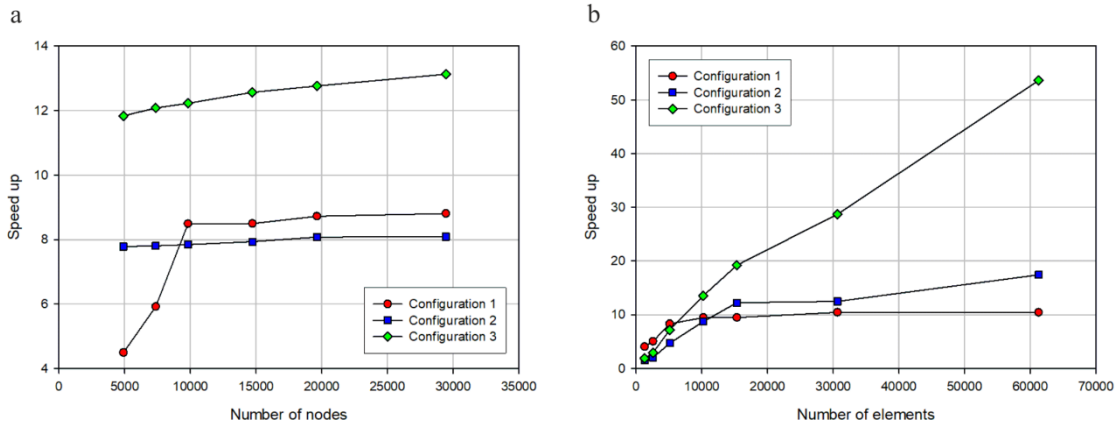

Fig. 3. Speedup of stent deployment software on three considered configurations. (a) with varying number of stent nodes. (b) with varying number of elements of arterial wall

Results for a specific patient are presented in Figure 4. The considered patient is 75 years old male, with an initial stenosis of 96% in the mid segment of the right coronary artery. The simulation was performed in around 1600 iterations and lasted approximately 34 seconds. Figure 4a shows the initial geometry that was obtained using the procedure described in Section 2.2. The results of stent deployment simulation are shown in Figures 4b and 4c, where the model is colored based on obtained distributions of internal stress and stent forces acting on the arterial wall, respectively.

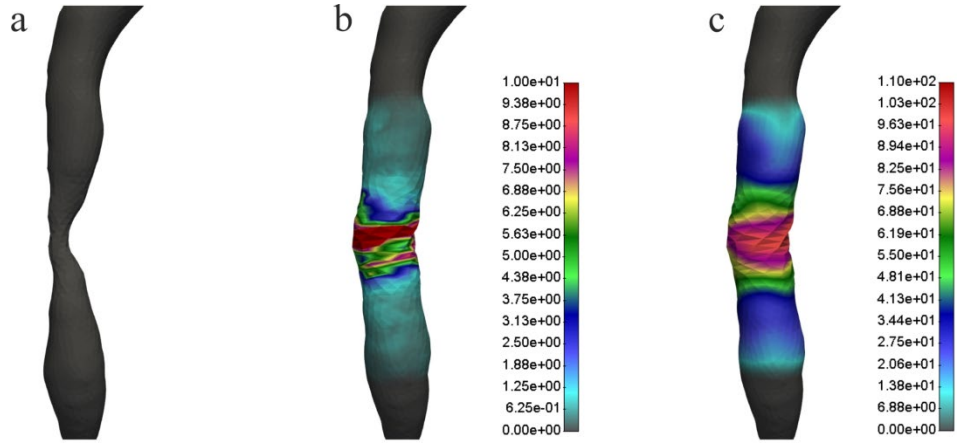

Fig. 4. Results of the stent deployment simulation for a patient-specific coronary artery. (a) Initial shape of the artery before stent deployment. (b) Final shape of the artery after stent deployment, with plotted distribution of internal stress of the arterial wall, scale bar is shown on the right, units are kPa. (c) Final shape of the artery after stent deployment, with plotted distribution of stent forces acting on the arterial wall, scale bar is shown on the right, units are mN

5. Discussion and conclusion

Stent behavior was analyzed by many authors in literature. Several numerical modeling techniques dealt with the deployment of the stent within realistic geometry of atherosclerotic

human coronary arteries [2,8,9]. A simplified model of the stenotic artery was used to investigate the effects of different stent materials and design on the mechanical behavior of stents during deployment process [10]. Patient-specific coronary bifurcation models are used in [11] to simulate the deployment of three different stent models and analyze the obtained stress distributions. The stenting procedure in the carotid artery was simulated in an endovascular simulator developed by Gosling et al. [12]. This software was used to train clinicians and to estimate the importance of such a tool in the learning process.

However, most numerical simulations cited above use simplified geometry of the artery and/or use commercially available software for the simulations. The numerical model presented in this paper enables more realistic simulations, because the geometry of the artery is extracted from clinical patient-specific data. Commercially available programs require a lot of time for the execution of the simulation and the results cannot be monitored in real time. This is an important aspect in clinical practice, where the results of the simulation should be obtained as quickly as possible, in order to provide clinicians a fast tool that they can use to analyze different treatment options. The numerical model presented in this paper is implemented using C++ programming language, completely parallelized and uses the available resources of the GPU device to enable the tracking of the simulation results in real time.

This study presents an approach to perform computational-based modeling of a process in biomechanics, namely, stent deployment within patient-specific coronary arteries. Such large-scale and demanding simulations were previously performed only on supercomputing architectures. The method presented in this study enables to run demanding and precise simulations of in silico stent deployment on a common computer, since the computation time is effectively reduced, due to the applied parallelization and optimization techniques. The presented software enables virtual testing of different stent sizes and positions and this could help clinicians to analyze possible outcomes of diverse alternative stent deployments in a small amount of time, thus lowering possible complications for the patient and ensuring better patient-specific treatment.

Acknowledgments: This research was funded by Ministry of Science, Technological Development and Innovation of the Republic of Serbia, contract number [451-03-47/2023-01/200378 (Institute for Information Technologies, University of Kragujevac) and 451-03-47/2023-01/200107 (Faculty of Engineering, University of Kragujevac)]. The research presented in this study was part of the project that has received funding from the European Union's Horizon 2020 research and innovation programme under grant agreement No. 952603 – SGABU. This article reflects only the author's view. The Commission is not responsible for any use that may be made of the information it contains. We acknowledge that part of the results of this research have been achieved using the DECI resource KAY based in Ireland at ICHEC (Irish Centre for High-End Computing) with support from the PRACE aisbl.

References:

[1] Auricchio F., Di Loreto M., Sacco E., *Finite element analysis of a stenotic artery revascularization through stent insertion*, Comp Meth Biomech Biomed Eng, Vol. 4, 249-263, 2001.

[2] Gijsen F. J.H., Migliavacca F., Schievano S., Socci L., Petrini L., Thury A., Wentzel J. J., van der Steen A. F.W., Serruys P. W.S., Dubini G., *Simulation of stent deployment in a realistic human coronary artery*, BioMedical Engineering OnLine, Vol. 7, 23, 2008.

[3] Djukic T., Saveljic I., Pelosi G., Parodi O., Filipovic N., *A study on the accuracy and efficiency of the improved numerical model for stent implantation using clinical data*, Computer Methods and Programs in Biomedicine, Vol. 207, 106196, 2021.

[4] Djukic T., Saveljic I., Pelosi G., Parodi O., Filipovic N., *Numerical simulation of stent deployment within patient-specific artery and its validation against clinical data*, Computer Methods and Programs in Biomedicine, Vol. 175, 121-127, 2019.

[5] Larrabide I., Kim M., Augsburger L., Villa-Uriol M.C., Rüfenacht D., Frangi A.F., *Fast virtual deployment of self-expandable stents: Method and in vitro evaluation for intracranial aneurysmal stenting*, Med Image Anal., Vol. 16, 721-30, 2012.

[6] Peskin C. S., *Numerical analysis of blood flow in the heart*, Journal of Computational Physics, Vol. 25, 220-252, 1977.

[7] Kojic, M., Filipovic, N., Stojanovic, B., Kojic, N., *Computer modeling in bioengineering: Theoretical Background, Examples and Software*, John Wiley and Sons, Chichester, England, 2008.

[8] Auricchio F., Conti M., De Beule M., De Santis G., Verhegghe B., *Carotid artery stenting simulation: From patient-specific images to finite element analysis*, Medical Engineering & Physics, Vol. 33, 281-289, 2011.

[9] Zahedmanesh H., Kelly D. J., Lally C., *Simulation of a balloon expandable stent in a realistic coronary artery - Determination of the optimum modelling strategy*, Journal of Biomechanics, Vol. 43, 2126-2132, 2010.

[10] Schiavone A., Zhao L. G., Abdel-Wahab A. A., *Effects of material, coating, design and plaque composition on stent deployment inside a stenotic artery — Finite element simulation*, Materials Science and Engineering: C, Vol. 42, 479-488, 2014.

[11] Mortier P., Holzapfel G. A., De Beule M., Van Loo D., Taeymans Y., Segers P., Verdonck P., Verhegghe B., *A Novel Simulation Strategy for Stent Insertion and Deployment in Curved Coronary Bifurcations: Comparison of Three Drug-Eluting Stents*, Annals of Biomedical Engineering, Vol. 38, 88–99, 2010.

[12] Gosling A. F., Kendrick D. E., Kim A. H., Nagavalli A., Kimball E. S., Liu N. T., Kashyap V. S., Wang J. C., *Simulation of carotid artery stenting reduces training procedure and fluoroscopy times*, J Vasc Surg, Vol. 66, 298-306, 2017.

LEADING EDGE SHAPE OPTIMIZATION OF A NOVEL FAMILY OF HYBRID DOLPHIN AIRFOILS

Zorana Z. Dančuo[1], Ivan A. Kostić[2], Olivera P. Kostić[2], Aleksandar Č. Bengin[2] and Goran S. Vorotović[2]

[1] Innovation Center, Faculty of Mechanical Engineering, University of Belgrade, Kraljice Marije 16, 11120 Belgrade 35
e-mail: zdancuo@mas.bg.ac.rs
[2] Faculty of Mechanical Engineering, University of Belgrade, Kraljice Marije 16, 11120 Belgrade 35
e-mail: ikostic@mas.bg.ac.rs, okostic@mas.bg.ac.rs, abengin@mas.bg.ac.rs, gvorotovic@mas.bg.ac.rs

Abstract

A new mathematical concept of an airfoil was proposed by the Romanian scientist and mathematician Iosif Taposu. The concept introduces a family of new airfoils named "The Dolphin Airfoils". This paper presents an effort to enhance the aerodynamic characteristics of this particular family by modifying their leading edge domains, applying two methods: the "semielliptical" and the "NA-DEL" method. Numerical calculations were performed using RANS equations with the k-ω SST turbulent model in ANSYS FLUENT, and initially obtained numerical results were verified by comparisons with NACA experiments. Then the original Dolphin airfoils were computationally analyzed together with the NACA's geometrically adequate counterparts. Calculations and flow visualizations showed that the sharp nose domain of the Dolphin had to be modified, due to extensive flow separation in this area, even at small angles of attack. This way the original Dolphin-like nose shape was lost. It led to the development of a novel family of Hybrid Dolphin Airfoils, where authors have achieved aerodynamic enhancements over all considered original Dolphins, while seven hybrid airfoils had better aerodynamic characteristics than the compatible NACA four digit family wing sections. This way an innovative approach to the Dolphin's leading edge shape optimization has been proposed. The new hybrid airfoil series is primarily aimed at the general aviation applications.

Keywords: aerodynamics, hybrid dolphin airfoils, CFD analysis, leading edge domain optimization**,** semielliptical approach**,** NA-DEL**,** general aviation.

1. Introduction

Aquatic mammals capture the attention of aerospace engineers more and more since their motion through the water fluid is flawless and highly efficient for their living needs. This paper narrows the research down to specific water animals - dolphins. The reason is very simple and easy to explain, even to non-professionals. The similarity of the dolphin's body shape to standard NACA airfoils is undeniable. Although dolphins have more pointed noses than subsonic airfoils, fair amounts of geometrical characteristics remain similar. This fact provides a solid basis for research and investigation in bionic airfoil design.

Among previous research in this field, which is very wide and not fully explored yet, some fundamental findings provide insight into this phenomenon. One of them is certainly known as the Gray paradox [1, 2].

James Gray was a zoologist who, back in the 1930s, made investigations on the morphology of dolphins. He was very skeptical about the muscle mass of dolphins and the fact that they could swim that fast. He concluded that with such low muscle mass, there must be a hidden mechanism that allows dolphins to swim fast and with low drag. He hypothesized that the flow over the dolphin's body remains laminar [1, 2]. Gray's paradox provided a solid foundation for further research on the boundary layer formed on the skin surface of swimming dolphins and paved the way, eventually, for new bionic airfoils.

Pavlov [3] presented his hypothesis on the reasons for the low resistance that dolphins create while swimming. His assumption is consistent with Gray's assumption, that there must be a ″secret mechanism″. In his paper [3], after a simulation of the flow over the dorsal fins, he confirmed that there is a correlation between the structure of the dolphin's skin and low drag produced while swimming. He stated that the skin behaves like an anisotropic permeable wall and enables a smooth flow pattern over the body surface.

Another researcher was interested in the skin structure of a humpback whale, a marine mammal similar to dolphins. Hansen [4] dealt with protrusions on the skin and their influence on the aerodynamic performance of airfoils on the leading edge. The study was presented in detail in her doctoral thesis. The emphasis is on protrusions - tubercles as a mechanism of indirect flow control [4].

Nowadays, many smart materials are used even for coatings of the aircraft fuselage to reduce drag during flight. Airliners always tend to minimize fuel consumption to achieve more economic flights. Shark skin riblet-like materials are found to be very effective in drag reduction in turbulent flow conditions. A study performed by Dean et al. [5] shows that riblets, which are in line with the direction of flow, can reduce friction/viscous drag up to 10% percent.

Among a wide variety of researches, dolphins served as an inspiration for hybrid design of airfoils. Chinese scientists, Huang et al. [6] proposed a bionic airfoil obtained by modifying the symmetrical NACA 0018 airfoil. Huang cut the leading edge of the airfoil to certain points on the upper and lower camber where it was merged tangentially with another profile. The other profile was the contour of a real dolphin's head. As a result, a new hybrid profile was formed. With further adaptations, two more Dolphin- type bionic airfoils were designed, and five subgroups [6].

Another example of a modified airfoil with a bio-inspired nose, i.e. leading edge, is presented in paper [7]. A modification of the leading edge of the NACA 2412 airfoil was bio-inspired by the nose of a porpoise, a dolphin-like marine animal. The aim of the work is better passive control of the boundary layer.

The shape of the dolphins was also inspiring to robotics engineers. The design of so-called bio-robots is very complex. Prior knowledge of the mechanisms of nature, robot kinematics, and dynamics, fluid mechanics - more and a wide field of knowledge is a premise for bionic design. Wang et al. [8] presented a dynamic model of a dolphin-like bio-robot. He proposed a propulsive model of a dolphin. Wang defined the hydrodynamics around the dolphin's tail. After an extensive investigation of all necessary parameters, a virtual model was created and the simulation was performed.

Dogangil et al. [9] developed another Dolphin robot prototype. Prototypes were named RODO-1 and RODO-2. RODO-1 is a robot with three joints, while RODO-2 represents a biomimetic robot of a dolphin's body. The author claims that the propulsive thrust in dolphins is generated in the area behind the dorsal fin, but also claims that the entire body has propulsive functions in different ways. RODO-2 does not have a propeller, which avoids the creation of a large vortex wake and noise.

Zhang et al. [10] was fascinated with bio-inspired airfoils and their possible application in the prevention of noise pollution caused by aircraft. Given that in earlier research it was established that the leading edge with protrusions increases lift and reduces drag, the idea arose to apply the same methodology in aeroacoustics in order to reduce noise. The paper highlights the need to delay the transition from laminar to turbulent regime and proposes the introduction of noise regulation structures inspired by dolphin-like mechanisms.

However, an interesting new approach in aerodynamics was proposed by a Romanian mathematician Iosif Taposu [11]. He found his inspiration in nature, i.e. dolphins, but his work is not essentially bionic. He formulated a set of equations for the design of special airfoils that apparently mimic the shape of dolphins. Taposu's model served as the foundation for a new family of airfoils developed by the authors of this paper.

2. Geometry, methods and mathematical model

2.1 Taposu's mathematical model of the Dolphin airfoil

As stated above, the mathematical model of the Dolphin airfoil is a fairly new concept and was introduced by I. Taposu [11]. In Figures 1, 2, and 3, the basic geometric parameters of this airfoil family are given. A wide range of profiles can be designed by changing and varying these parameters, depending on the actual design requirements. Recommended values of parameters are suggested by the author [11]. Taposu's original designations of certain constructive parameters are the same as standard aerodynamic nomenclature, such as α, and in that sense they should be interpreted with caution, according to the context.

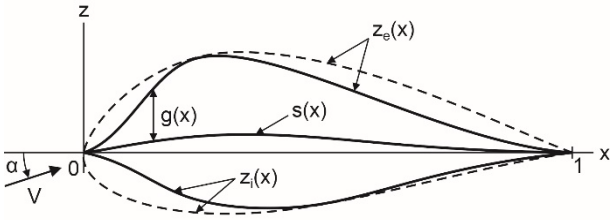

Fig. 1. Taposu's Dolphin airfoil [11]

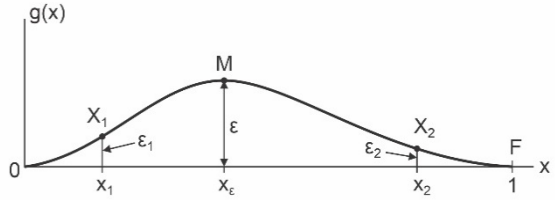

Fig. 2. Half- thickness distribution along unit chord [11]

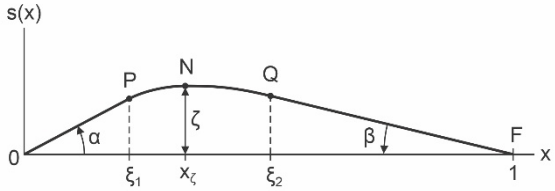

Fig. 3. Skeleton line distribution along unit chord [11]

Equations from which a Dolphin airfoil can be designed are piecewise functions of the half- thickness distribution and the skeleton line. Equations (1), (2) define thickness distribution:

$$g(x) = \varepsilon \begin{cases} F_1(x), & 0 \le x \le x_1 \\ F_2(x), & x_1 < x \le x_\varepsilon \\ F_3(x), & x_\varepsilon < x \le x_2 \\ F_4(x), & x_2 < x \le 1 \end{cases} \quad (1)$$

where in (1):

$$F_1(x) = \frac{x^2}{x_1 x_\varepsilon},\ F_2(x) = 1 - \frac{(x-x_\varepsilon)^2}{x_\varepsilon(x_\varepsilon - x_1)},\ F_3(x) = 1 - \frac{(x-x_\varepsilon)^2}{(x_\varepsilon - x_2)(x_\varepsilon - 1)},\ F_4(x) = \frac{(x-1)^2}{(x_2-1)(x_\varepsilon-1)} \quad (2)$$

The piecewise function of the skeleton line is given by:

$$s(x) = \begin{cases} \Phi_1(x), & 0 \le x \le \xi_1 \\ \Phi_2(x), & \xi_1 < x \le x_\zeta \\ \Phi_3(x), & x_\zeta < x \le \xi_2 \\ \Phi_4(x), & \xi_2 < x \le 1 \end{cases} \quad (3)$$

where in (3):

$$\Phi_1(x)=x\tan\alpha, \quad \Phi_2(x)=\zeta-\frac{(x-x_\zeta)^2\tan\alpha}{2(x_\zeta-\xi_1)}, \quad \Phi_3(x)=\zeta-\frac{(x-x_\zeta)^2\tan\beta}{2(\xi_2-x_\zeta)}, \quad \Phi_4(x)=(1-x)\tan\beta \qquad (4)$$

2.2 Turbulent model and numerical calculation

Numerical analyses were performed using the Reynolds-averaged Navier-Stokes equations (RANS). This model is based on the time-averaged equations of fluid motion. A two-equation *k-ω* SST turbulent model was used in ANSYS FLUENT [12]. The governing equations (5, 6) of this model are:

$$\frac{D(\rho k)}{Dt}=\tau_{ij}\frac{\partial u_i}{\partial u_j}-\beta^*\rho\omega k+\frac{\partial}{\partial x_j}\left[\left(\mu+\sigma_k\mu_t\right)\frac{\partial k}{\partial x_j}\right] \qquad (5)$$

$$\frac{D(\rho\omega)}{Dt}=\frac{\gamma}{v_t}\tau_{ij}\frac{\partial u_i}{\partial x_j}-\beta\rho\omega^2+\frac{\partial}{\partial x_j}\left[\left(\mu+\sigma_\omega\mu_t\right)\frac{\partial\omega}{\partial x_j}\right]+2\rho\left(1-F_1\right)\sigma_{\omega 2}\frac{1}{\omega}\frac{\partial k}{\partial x_j}\frac{\partial\omega}{\partial x_j} \qquad (6)$$

The SST model uses a blending function F_1 and differs from the standard *k-ω* model. The blending function gives advantages over the standard model in a way that the standard *k-ω* model is used near the surface and the *k-ε* model is applied in free shear domains. It is less sensitive to the mesh structure, and in comparison to higher order RANS models with four or five equations it is completely satisfactory [12, 13, 14, 15].

A 2D density-based model was adopted for all calculations. Air was set to the ideal gas, and Sutherland's three-coefficient method was used for the viscosity. The outlet was set to *pressure outlet*, inlet to *pressure-far-field*, with operating pressure p = 101325 Pa, temperature T = 288.15 K, and the free-stream Mach number M = 0.2564 (for MRe = 6). The airfoil has unit chord length. The length and height of the control volume are equal to 25 airfoil chord lengths. A structured C-mesh with 115600 elements proved to be optimal for the analyses. More detailed explanations of the applied numerical settings and conditions are given in [16]. Before comparisons between the NACA and here presented modified hybrid airfoils were done, the computational results obtained for the NACA 00xx and NACA 24xx airfoils were validated by comparisons with the existing experimental data from the NACA Report No. 824 [17]. In this paper only "standard roughness" cases [17] were analyzed, which imply an early transition of the laminar to the turbulent boundary layer. Namely, in the general aviation category, for which these hybrid airfoils are primarily aimed, many manufacturers still prefer metal wing design. In order to keep manufacturing costs low, some wings are made using round head instead of flush rivets, overlapping instead of facing skins, etc., which make early boundary layer transition inevitable.

Airfoils that were used as reference in this study are standard "four-digit" NACA 00xx and NACA 24xx series. The ″Dolphin concept″ took two main directions or two ways of shape modifications. The initially implemented semielliptical method, presented in [16], was a good starting point for the development of a family of hybrid Dolphin airfoils. Terms ″original Dolphin″, ″Dolphin M4″ (the fourth semielliptical modification of Taposu's airfoil [16]), were expanded to another concept of modification introduced in this paper, named the ″NA-DEL″. Airfoils NACA 2410, NACA 2412, NACA 2415, and NACA 0006 have been modified by this method, and analyzed. Comparisons were made between the standard NACA, Taposu's Dolphin airfoils with the same basic geometrical characteristics as the NACA airfoils, and the modified versions denoted as Dolphin M4 and NA-DEL.

3. New geometry definitions and comparative results

In [16] a detailed explanation of the modification of the Dolphin 2415 airfoil is given. In this paper, the authors will explain the principles of the semielliptical and NA-DEL modification in a similar fashion, using Dolphin 2412 M4 and NA-DEL 2412 as examples. First, in Figure 4 the standard NACA 2412 and

the original Dolphin 2412 airfoil with unit chord are presented. Their basic geometric characteristics - maximum thickness, camber and their positions are the same.

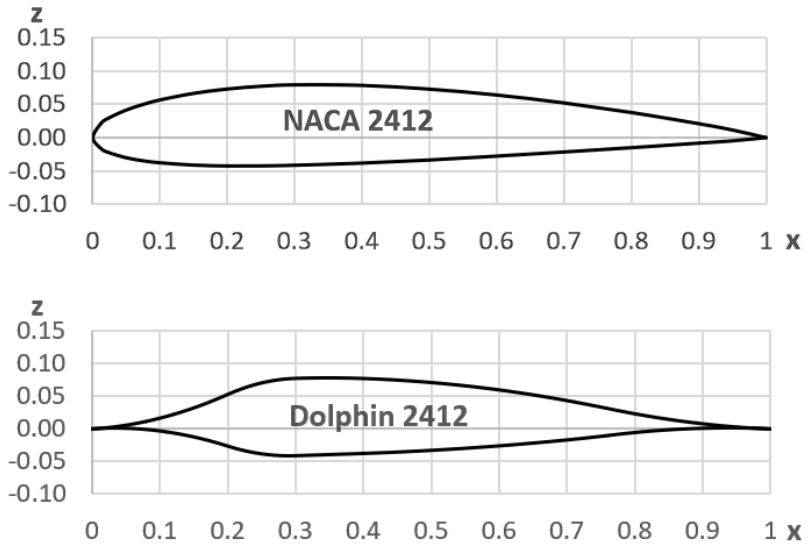

Fig. 4. The NACA 2412 and the original Dolphin 2412 airfoils

The airfoils differ significantly, especially in the leading edge zone. Particularly in this area, aerodynamic performances drastically change, but not in favor of the original Dolphin 2412. Therefore, modifications were performed. The first method that was applied was the semielliptical method described in [16]. First, the modification M1 was performed, and then respectively M2, M3, and M4 [16]. The NA-DEL modification method arose as a new idea to get even better aerodynamic performances. This method proved to be the most efficient in the case of Dolphin NA-DEL 2412. The average aerodynamic efficiency given in Table 1, shows the improvement in comparison to the NACA 2412 (which has its default efficiency of 100%), and the Dolphin 2412 M4 is 3.97% more efficient than the NACA 2412. This result is significant in terms of aerodynamic efficiency.

For better understanding, the semielliptical principle will be presented at short notice in this paper. Modification M1, denoted as Dolphin 2412 M1, was inspired by the air-flow separation which occurs in the vicinity of the leading edge. The sharp nose was modified by assigning a leading edge radius. The radius amounts 1/3 of the standard NACA four digit airfoil series nose radius, merged by tangents with the original airfoil. The second modification of the semielliptical Dolphin 2412 M2 was inspired by a white vortex created on the leading edge of the original Dolphin leading edge at AoA +4°. In this case, the aerodynamic forces have performed a “natural optimization” at a certain AoA. As in M1, a new leading edge radius was assigned, but only for the upper camber of the airfoil. The new leading edge radius on M2 amounts 2/3 of the standard NACA 4-digit airfoil series radius. It was merged with the upper camber of the original airfoil by its tangent to points on the upper camber. The lower camber of M2 remained the same as in M1. As the modifications progressed, step by step the original sharp leading edge was slowly vanishing until it was lost. With modification M3 a geometry of an upper quarter elliptical Dolphin airfoil was obtained. The M3 geometry was created by focusing on the increase of the maximum lift coefficient. Flow patterns that were obtained after each numerical analysis and flow simulation in FLUENT gave the authors new perspectives on the possible most efficient airfoil geometry. After quantitative and qualitative analyses of the M2 results, the decision was to apply an elliptic arc on the upper camber from the leading edge up to the maximum point of the upper camber of the original Dolphin airfoil. The lower camber geometry was preserved from modification M1. Finally, after numerical analyses of the M3 modification, a new idea emerged. The elliptic contour on the upper airfoil camber has solved the early drag divergence problems that occurred in versions M1 and M2. The suitable solution was to preserve the upper camber from modification M3, while the lower

camber, i.e. airfoil surface has been replaced by a lower elliptic arc tangentially joined with the original Dolphin airfoil. This modification proved to be most efficient for thickness ratios from 12- 15% of the NACA 24xx series.

After the semielliptical approach, the NA-DEL method arose. NA-DEL stands as an abbreviation for NACA – "NA", and DOLPHIN (in Serbian - *Delfin*) – "DEL". As the name suggests, the algorithm of this method is to employ the leading edge domain of the standard NACA airfoil and merge it with the original Dolphin at maximum thickness points at its lower and upper camber. The appropriate NACA and the original Dolphin have to be of the same basic geometry. In the case of NA-DEL 2412, the NACA 2412 and the original Dolphin 2412 were merged at points x =0.35, z = 0.0791241, on the upper camber. These are the points of the maximum thickness on the upper camber of the original Dolphin, and at points x = 0.29, z = -0.0418166 on the lower camber, which are the points of the maximum thickness on the original Dolphin's lower camber. The NACA 2412 airfoil was geometrically perfectly blended with the original Taposu's Dolphin.

This way, the most successful hybrid configuration was formed. NA-DEL 2412 proved to be better than the original NACA and Taposu's Dolphin airfoil, but also better than the Dolphin 2412 M4 configuration. A C-mesh was created for numerical calculations for Dolphin 2412 M4 and NA-DEL 2412. There is a slight difference in shape and geometry between the two airfoils. Table 1 shows the average aerodynamic efficiency of NACA 24xx and 00xx airfoils. NACA 24xx airfoils are given the value, for all columns 100%. Other profiles are compared with them. In the maximum lift coefficient and lift-to-drag ratio columns, a result above 100% represents an improvement, whereas in the drag coefficient column, only a result under 100% represents an improvement, i.e. drag reduction.

Airfoil	$c_{L\,max}$ [%]	$c_{D\,min}$ [%]	$\left(\frac{c_L}{c_D}\right)$ max [%]	Mean values [%]
NACA 2410	***100***	***100***	***100***	***100***
Dolphin 2410 M4	82.08	103.67	167.68	**115.36**
NA-DEL 2410	84.67	104.79	159.53	**113.13**
NACA 2412	***100***	***100***	***100***	***100***
Dolphin 2412 M4	102.52	96.33	108.04	**104.74**
NA-DEL 2412	112.56	93.74	107.33	**108.72**
NACA 2415	***100***	***100***	***100***	***100***
Dolphin 2415 M4	100	97.37	106.51	**103.04**
NA-DEL 2415	107.5	95.35	109.88	**107.34**
NACA 0006	***100***	***100***	***100***	***100***
Dolphin 0006 M4	127.68	99.27	92.51	**106.97**
NA-DEL 0006	86.74	101.05	88.8	91.5

Table 1. Comparison of aerodynamic characteristics of the NACA, Dolphin M4 and NA-DEL airfoils

Drag reduction and lift increase were achieved for all hybrid airfoils, except the Dolphin 2410 M4 and NA-DEL 2410. But, the 2410 shows a significant increase in maximum lift-to-drag ratio, which is +67.68%. This makes this hybrid also advanced in comparison to its NACA counterpart. All three columns are averaged for each section: NACA, M4, and NA-DEL. If the obtained result (denoted as ″mean values″ in Table 1.) is above 100%, the airfoil is considered to have higher aerodynamic efficiency, and the objective is achieved. For some airfoils such as the NACA 2412 and NACA 2415, the NA-DEL method turned out to give better results than the semielliptical modification. Both methods are efficient in this case. The decision lies in the hands of the designer about which airfoil to choose.

Results given in Table 1 show that the NA-DEL 2412 has an overall aerodynamic efficiency 3.97% higher than the Dolphin 2412 M4, and 8.72% higher than the NACA 2412. This percentage and increase in aerodynamic efficiency represents a significant improvement. The following new airfoils have average aerodynamic efficiency higher than the four digit NACA 24xx sections: 2410 M4 by 15.36%, NA-DEL by 13.13%; 2412 M4 by 4.74%, NA-DEL by 8.72%; 2415 M4 by 3.04%, NA-DEL 7.34%, and considering NACA 0006 category, only for the semielliptical modification 0006 M4 by 6.97%.

The NA-DEL method proved to be effective modification for the 24xx series, with only a slight decrease in comparison to the semielliptical method in case of NA-DEL 2410 by -2.22%, but is still better than NACA 2410 by 13.13%. In case of NACA 0006, the semielliptical method gave good results. The NA-DEL method for the symmetrical 0006 series shows a drawback of -8.5% in comparison to NACA 0006, and quite significant -15.47% compared with the Dolphin 0006 M4.

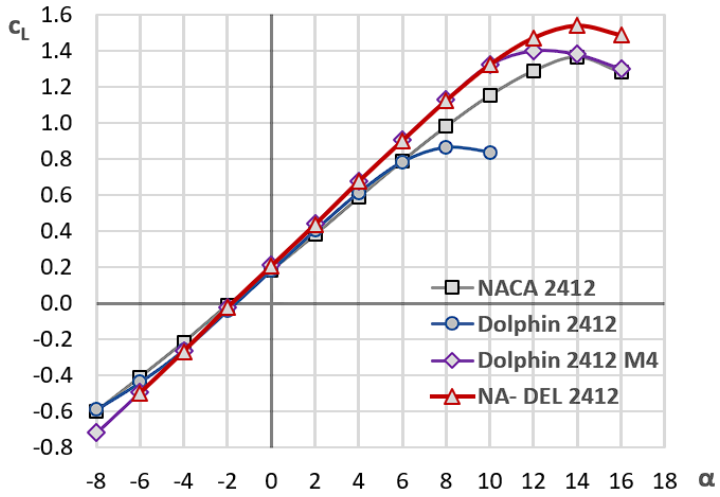

Fig. 5. Lift curves (standard roughness)

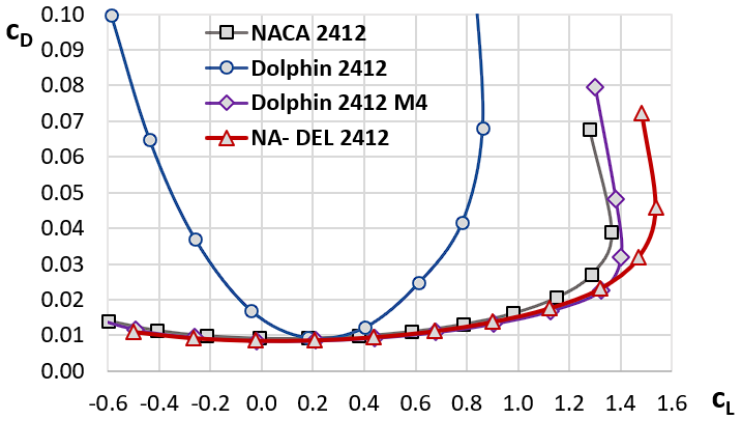

Fig. 6. Drag polar curves (standard roughness)

Airfoil comparisons are generally very complex, and should be based on multiple relevant parameters. As shown in Table 1, they can be averaged by assigning the same (or different) "specific weights" of their influence. In that sense, no general algorithm can be proposed, since their significance will very much depend on the actual aircraft project, the 3D wing geometry for which they should be applied, and various design and performance requirements. Because of that, the next relevant step is to analyze their aerodynamic characteristics in a wider range of angles of attack, using both lift curves and drag polars.

Lift curves (Fig. 5) indicate that both M4 and specially NA-DEL modifications achieve higher maximum lift coefficients than NACA 2412, while the original Dolphin's $c_{L\,max}$ is only about the half of these values. This is one of clear indicators why the original Dolphin airfoils with sharp leading edge could

not have been used efficiently in general aviation so far. In [16] it was shown that here applied calculation model tends to slightly overestimate the $c_{L\ max}$. Since exactly the same calculation model and grid generation algorithm were applied for all calculations presented both in [16] and here, lift curves in Figure 5 can readily be used for mutual airfoil comparisons, while authors expect to obtain more accurate $c_{L\ max}$ estimates for the new airfoils from the wind tunnel tests, which are in the final phase of preparation.

Drag polar curves (Fig. 6) provide another indication of why the original Dolphin is inappropriate for general aviation implementations. Its drag coefficient matches the values of other airfoils only in a very narrow $c_L \approx 0.3$ domain, while slightly above and below it the drag very rapidly diverges to the values that other three airfoils could not achieve even at the post-stall regimes. At $c_L > 1.0$, both NA-DEL 2412 and Dolphin 2412 M4 generate lower drag than NACA 2412. This means that during the take-off and landing, airplanes with NA-DEL or M4 modifications would produce less drag for the same amount of generated lift, than aircraft with the NACA 2412 (it is applied on one of the best-selling and most popular general aviation airplanes - Cessna 172). Also, both NA-DEL 2412 and Dolphin 2412 M4 have larger maximum lift-to-drag ratios (at which piston-engined airplanes are the most fuel-efficient in cruising flight) by 7 – 8 % than NACA 2412 (Table 1), some new potential Cessna 172 with NA-DEL or M4 replacements would generate less wing profile drag, approximately by the same amount during the cruising regime. Drag reduction is of vital importance in aerodynamics for a large number of reasons. The most obvious are economic reasons, environmental control, and ecological sustainability due to the reduction in fuel consumption and thus reduced pollution.

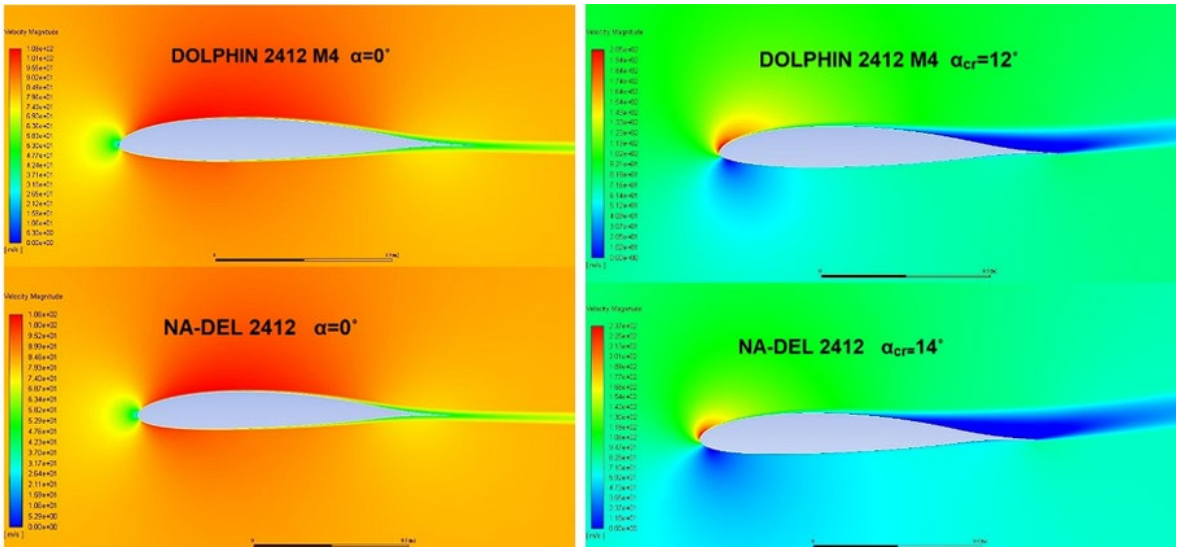

Fig. 7. Velocity contours for the Dolphin 2412 M4 and NA-DEL 2412 at $\alpha = 0^{\circ}$ (left), and at their critical angles of attack (right).

Qualitative analyses can also provide very useful insights and conclusions, and they can be performed by analyzing pressure, temperature, density, velocity, Mach number, etc. distributions around an airfoil. In Figure 7 the velocity magnitudes around the Dolphin 2412 M4 airfoil and the NA-DEL 2412 at zero and critical angles of attack are presented. The airfoils show similar, smooth flow patterns. The front stagnation point, surrounded by the sphere shaped bubbles in leading edge domains, adopts its natural positions over the rounded noses on both airfoils through the whole range of AoA. The same analyses for the original Dolphin [16] have shown that the restricted front stagnation point movements due to its sharp nose generate massive separation bubbles in leading edge domain and produce the mentioned immense drag divergence problem.

Here presented investigations have shown that approximately 70% of the original Dolphin's rear contour can produce more favorable flow patterns than of the NACA's 24xx series, and combined with appropriately rounded nose domains, they can provide better aerodynamic characteristics. From Table 1 it

is obvious that the Dolphin 2412 M4 shows +4.74%, and with NA-DEL 2412 +8.72% increase in the overall aerodynamic efficiency, compared to the NACA 2412.

4. Conclusions

This research has introduced two new methods for the original Dolphin airfoil leading edge domain optimizations. The first has been named the semielliptical method, in which the natural flow patterns were visualized and used to modify the zones of the original Dolphin where flow separations were immanent, and modification denoted as M4, with two quarter-ellipses at new nose proved to be the most efficient. The second method ″NA-DEL″ is a geometrical method based on merging partial contours of the four digit NACA and the original Dolphin airfoils into one new hybrid airfoil. Here presented investigations have shown that the thickness ratios can influence the quality and efficiency of these modifications. An example of computational analyses has been presented, where modified Dolphin 2412 M4 and NA-DEL 2412 airfoils proved to have better aerodynamic characteristics in comparison to both the original Dolphin 2412 airfoil and the classical NACA 2412. The Dolphin 2412 M4 and NA-DEL 2412 hybrids should be suitable for applications in general aviation industry, where lowering of production costs sometimes leads to the metal wing designs with round head rivets and overlapping skins. Such surfaces provoke early transition of laminar to turbulent boundary layer. In such cases application of classical airfoils, like the NACA four digit series is a better choice than low drag airfoils, which are very sensitive to surface roughness. In this sense, the M4 and NA-DEL modifications can be appropriate substitutes for the NACA four digit wing sections. Wind tunnel test will be performed in the nearest future to validate the above mentioned findings.

Acknowledgment: This paper is part of research supported by the Ministry of Science, Technological Development and Innovation of the RS under Contract 451-03-47/2023-01/ 200213 dated 02/03/2023.

References:

[1] Fish, F.E., *The myth and reality of Gray's paradox: implication of dolphin drag reduction for technology.* Bioinspiration & biomimetics, Vol. 1, No. 2, R17, 2006.
[2] Carpenter P.W, Davies C, Lucey AD*. Hydrodynamics and compliant walls: Does the dolphin have a secret?*, Current Science, 758-65, 2000.
[3] Pavlov, V. V., *Dolphin skin as a natural anisotropic compliant wall*, Bioinspiration & biomimetics, Vol. 1, No. 2, 2006.
[4] Hansen, K.L., Effect of Leading Edge tubercles on airfoil performance, PhD Thesis, University of Adelaide, School of Mechanical Engineering, 2012.
[5] Dean, B., Bhushan., B., *Shark-skin surfaces for fluid-drag reduction in turbulent flow: a review*, Philosphical Transactions of the Royal Society, Vol. 368, 4775– 4806, 2010.
[6] Huang, S., Hu, Y., Wang, Y., *Research on aerodynamic performance of a novel dolphin headshaped bionic airfoil,* Vol. 214, Energy, 2021.
[7] Raj Mohamed, M.A., Guven, U., Yadav, R., *Flow separation control of NACA-2412 airfoil with bio-inspired nose,* Aircraft Engineering and Aerospace Technology, Vol. 91 No. 7, 1058-1066, 2019.
[8] Wang, Y., Yu, J., Zhang, J., *Modeling and simulation of porpoising for a multilink dolphin robot, IEEE International Conference on Robotics and Biomimetics*, 2131-2136, 2011.
[9] Dogangil, G., Ozcicek, E., Kuzucu, A., *Modeling, Simulation, and Development of a Robotic Dolphin Prototype*, Proceedings of the IEEE International Conference on Mechatronics & Automation, 952-957, 2005.
[10] Zhang, M., Frendi, K., *Bioinspired Passive Control of Airfoil Radiated Noise*, 22nd AIAA/CEAS Aeroacoustics Conference, 2016.
[11] Taposu, I., *Profilele delfin. Un nou concept în aerodinamică (The Dolphin Profiles. A new Concept in Aerodynamics, in Romanian)*, S.C. Editura Technica S.A., Bucharest, Romania, 2002.

[12] Menter, F. R., *Two-Equation Eddy-Viscosity Turbulence Models for Engineering Applications*, AIAA Journal, Vol. 32, No. 8, 1994.
[13] Kostić, O., Stefanović, Z., Kostić, I., *CFD Modeling of Supersonic Airflow Generated by 2D Nozzle With and Without an Obstacle at the Exit Section*, FME Transactions, Vol. 43, No. 2, 107- 113, 2015.
[14] Jemcov, A., Gonzales, J. P., Maruszewski, J.P., Kelly, R. T., *Non-Iterative Wall Model Formula for Non-Equilibrium Boundary Layer Flows*, FME Transactions, Vol. 50, No. 2, 223-237, 2022.
[15] Kostić, O., Computational Simulation of Air-flow in Supersonic Nozzle with Obstacle at Exit, (in Serbian), PhD Thesis, University of Belgrade, Faculty of Mechanical Engineering, Belgrade, Serbia, 2016.
[16] Dančuo, Z., Kostić, I., Kostić, O., Bengin, A., Vorotović, G., *Initial Development of the hybrid semielliptical Dolphin airfoil*, Thermal Science, Vol. 26, No. 3, 2199-2210, 2022.
[17] Abbott, I. H., Doenhoff, A.E., Stivers, L.S. Summary of Airfoil Data Report NACA Report No. 824, National Advisory Committee for Aeronautics, USA, 1945

NOMENCLATURE AND ABBERVIATIONS

g(x)	half-thickness distribution
s(x)	skeleton line distribution
$z_e(x)$	upper camber function (suction surface)
$z_i(x)$	lower camber function (pressure surface)
x_1	point at x-coordinate for local half-thickness
x_2	point at x-coordinate for local half-thickness
c_L	lift coefficient
c_D	drag coefficient
c_L/c_D	lift-to-drag ratio
MRe	Mega Reynolds number, Re x 10^6
AoA	angle of attack

Greek symbols

x_ζ	position of the maximum camber
x_ε	position of the maximum thickness
ζ	camber
ξ_1	camber at point x_1
ξ_2	camber at point x_2
ε	half- thickness of the airfoil
ε_1	half-thickness at point x_1
ε_2	half-thickness at point x_2
β_1	the slope of the tangent to the x-axis which is equal to the derivative of the function $g(x)$ at point x_1
β_2	the slope of the tangent to the x-axis which is equal to the derivative of the function $g(x)$ at point x_2
α	Taposu's construction parameter in Equation (4)
α	angle of attack, AoA
α_{cr}	stall angle, critical AoA

MODELLING OF LANDSLIDE DYNAMICS: ROLE OF DISPLACEMENT DELAY AND NATURAL BACKGROUND NOISE

Srđan D. Kostić[1,2]

[1] Jaroslav Černi Water Institute, 80 Jaroslava Černog Street, 11226 Belgrade, Serbia
[2] Faculty of Technical Sciences, University of Novi Sad, 6 Trg Dositeja Obradovića, Novi Sad, Serbia
e-mail: srdjan.kostic@jcerni.rs, srdjan.kostic@uns.ac.rs

Abstract

Novel stochastic landslide model is suggested and analyzed within this paper. The effect of delay in displacements of the neighboring blocks and the influence of random background noise is included, for the first time, in the explicit mathematical model and examined. Such setup of landslide model is considered as close to natural conditions since delayed displacement among different parts of the unstable slope occurs due to changes in friction, while ambiental seismic noise represents continuous background factor affecting the landslide dynamics. Type of noise as linear stationary stochastic process with Gaussian inputs (random noise) is determined by surrogate testing of the recordings of ambiental noise before and after the small seismic event at the location of Zavoj dam in Serbia. Two explicit mathematical models are suggested for landslide dynamics: two-block model with time delay in displacement of the neighboring blocks and model of n all-to-all coupled blocks with included delay and random background noise. Both models exhibit small displacements of constant velocity in equilibrium state, which mimics well the dynamics of creeping landslides. Dynamical analysis of both models is conducted numerically using Runge-Kutta 4th order numerical method. Results obtained indicate that landslide dynamics is not affected by the introduced time delay for certain friction conditions, while background random noise has surprisingly positive stabilizing effect. In particular, it appears that the increase of time delay in a two-block deterministic landslide model for certain friction conditions does not lead to onset of instability. On the other hand, the increase in intensity of random background noise in a landslide model near the bifurcation point composed of n globally coupled blocks "pushes" the bifurcation curve further thus making the examined dynamical system stable. These findings, although provided on a theoretical level of the mechanism behind the landslide dynamics, could have important implications in further research on landslide dynamics.

Keywords: landslide, noise, time delay, bifurcation.

1. Introduction

Inspection of slope stability and identification of its main controlling factors represents an obligatory task in any design work. Commonly, landslide stability and conditions for triggering instability are examined by invoking the limit equilibrium methods [1] or finite element method [2]. In recent years, smooth particle hydrodynamics also found its place in the contemporary slope

stability analysis, primarily due to the fact it enables the analysis of the post-failure behavior [3]. Although all these methods provide satisfying results, the dynamics of the land sliding itself remains relatively uninvestigated, which further prevents proper identification of the (de)stabilizing factors. One attempt in this direction is the representation of landslide dynamics as dynamics of the spring-block model on an inclined slope.

The idea of representation of landslide dynamics as a dynamics of spring-block model is not new and it originally comes from Davis [4], who proposed a model for an accumulation slide in a form of connected two block on an inclined slope (Fig.1). In this original model, motion of the two-block system was accurately described by three ordinary differential equations, where connection between feeder (lower) and accumulation (upper) slope is assumed to be both elastic and viscous (through differences in velocities and acceleration). Frictional strength was represented by conventional effective stress model, where friction is assumed to be the function of piezometric elevation, slope angle and angle of internal friction.

Apart from the original setup and a new model of a landslide dynamics, Davis [4] also pointed out the existence of time delay in displacement between the feeder and accumulation part of the slope (Fig. 2).

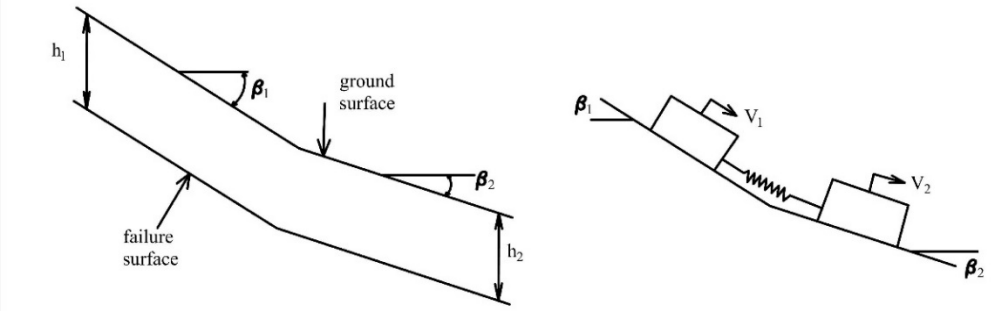

Fig. 1. Spring-block model of landslide dynamics, originally proposed by Davis [4]

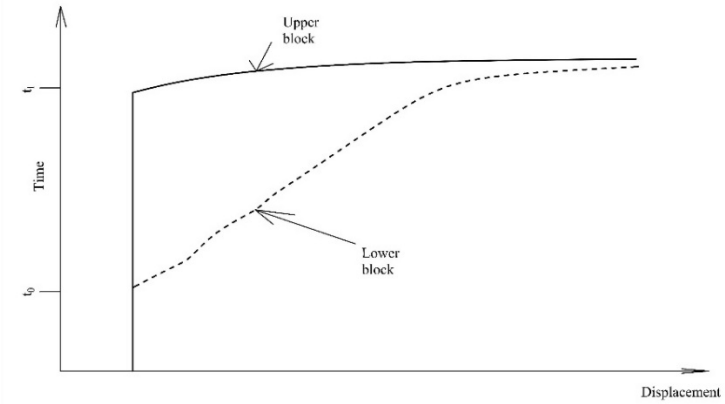

Fig. 2. Time delay between the movement of the lower (feeder) and upper (accumulation) part of the slope, as proposed by Davis [4]

From this point of view, such finding could be considered as avant-garde, since it is well known that existence of delay increases dimensionality of the analyzed system, which further sets a path for the onset of rich dynamical behavior. Although such finding was significant, it has not been investigated since then, mostly because dynamical systems with time delay are not easy to solve, and numerical computation in that time was not strong enough to perform computationally demanding calculations.

In 1997, Cartwright et al. analyzed spring-block (Burringe-Knopoff) model as a convenient model of frictional sliding, and, for the first time, included rate dependent friction in the analysis

of landslide dynamics (Fig.3). One should note that idea of rate dependent friction came from the analysis of earthquake fault nucleation process [8].

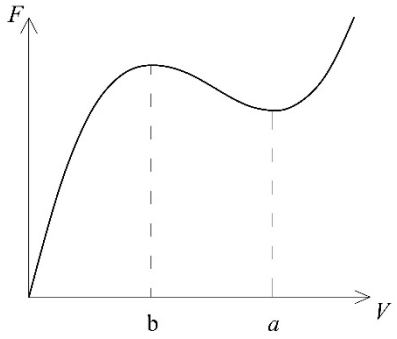

Fig. 3. Rate dependent friction assumed in examined landslide models.

In that time (1997), friction law associate with landslides was still on the level of Coulomb-Mohr assumptions, and scientific and engineering community was not ready to accept rate-dependent friction law as a valid assumption for friction along the sliding surface. This idea came to life again in 2012, when Viesca and Rice examined the conditions for nucleation of slip-weakening rupture instability in landslides by localized increase of pore pressure. This was further explored by Lucas et al. [7], who declared frictional velocity-weakening mechanism as applicable to small and large landslides. This paper could be considered as a starting one for a whole new direction of research of the role of velocity weakening friction law in landslide dynamics [9, 11, 12, 13].

As for the effect of noise on landslide dynamics, there are no previously conducted studies. Recordings of ambiental noise are generally used as a method to predict (estimate) landslide dynamics [14], but not as a significant landslide triggering factor. However, it has been previously suggested that significant changes of dynamics could be induced by the effect of noise [15].

Based on the aforementioned, the following is assumed in the present paper:

- Rate dependent friction law
- Time delay in displacement of neighboring blocks
- Existence of permanent background noise.

Under these assumptions, landslide dynamics is analyzed and the effect of time delay and noise is qualitatively and quantitatively evaluated.

2. Model setup

Model for landslide dynamics is developed starting from the model proposed by Davis [4]:

$$\begin{aligned} m_1\dot{V}_1 &= W_1 sin\beta_1 - S_1 - F \\ m_2\dot{V}_2 &= W_2 sin\beta_2 - S_2 + F \\ \dot{F} &= k(V_1 - V_2) + c\left(\dot{V}_1 - \dot{V}_2\right) \end{aligned} \tag{1}$$

where W is the block weight, g is acceleration of gravity, S denotes the sliding resistance on failure surface, F represents combined elastic and viscous forces, k and c are the spring and dash pot constant, and β_i is the slope angle. Starting from model (1), a new two-block model is proposed with the included effect of time delay:

$$\begin{aligned} \frac{dU_1(t)}{dt} &= V_1(t) \\ \frac{dV_1(t)}{dt} &= \frac{1}{m}\left[k\left(U_2(t-\tau) - U_1(t)\right) - F\left(V_0 + V_1(t)\right) + F(V_0)\right] \end{aligned} \tag{2}$$

$$\frac{dU_2(t)}{dt} = V_2(t)$$
$$\frac{dV_2(t)}{dt} = \left[k\left(U_1(t-\tau) - U_2(t)\right) - F\left(V_0 + V_2(t)\right) + F(V_0)\right]$$

where U_i is the displacement of the i-th block, V_i is the velocity of the i-th block, F is the rate-dependent friction force, V_0 is the constant background velocity and τ is the delay in the position of the blocks.

Effect of noise is examined in the model of n interconnected blocks:

$$dx_i(t) = y_i(t)dt$$
$$dy_i(t) = -\left[a\left(V + y_i(t)\right)^3 - b\left(V + y_i(t)\right)^2 + c\left(V + y_i(t)\right)\right]dt + \quad (3)$$
$$(aV^3 - bV^2 + cV)dt + \sum_{j=1}^{N} k_1\left(x_j(t-\tau) - x_i(t)\right)dt + \sqrt{2D}dW_i$$

where x_i and y_i are displacement and velocity of the i-th block, respectively, and a, b and c are parameters of the cubic friction force, which according to Morales et al. [10] has the following form: $Fc(V) = 3.2V^3 - 7.2V^2 + 4.8V$. Background noise was previously investigated as a significant contributing factor for earthquake nucleation dynamics [16, 17]. In these previous studies, both random and colored nature of noise was found in the real observed recordings. In particular, nonlinear time series analysis of GPS recordings of the ground movement along the San Andreas fault in California revealed the random nature of these displacements. On the other hand, analysis of the recordings of the movement along the fault in Driny cave (Male´Karpaty mts in Slovakia) and the noise before and after the earthquake on 8th September 2015 at the BKS station (Byerly Seismogrpahic Vault, Berkley), indicated the existence of the colored background noise. In the present paper, we analyze the ambiental noise before and after the small seismic event recorded at accelerograph station ETNA located at Zavoj dam, which is considered to be a landslide-prone area.

Next we introduce deviations from the mean field $\langle x(t)\rangle = \lim_{N\to\infty}\frac{1}{N}\sum_{i=1}^{N} x_i(t)$ and $\langle y(t)\rangle = \lim_{N\to\infty}\frac{1}{N}\sum_{i=1}^{N} y_i(t)$, for each element: $n_x(t) = \langle x(t)\rangle - x_i(t), n_y(t) = \langle y(t)\rangle - y_i(t)$. We assume these fluctuations are Gaussian and statistically independent in different elements. A set of moments known as cumulants or Thiele semi-invariants has an important property that all of them vanish in the Gaussian case. Therefore, we introduce the following notation for the first and second order cumulants: (a) the means $m_x(t) = \langle x(t)\rangle, m_x(t-\tau) = \langle x(t-\tau)\rangle, m_y(t) = \langle y(t)\rangle$, (b) the mean square deviations $s_x(t) = \langle n_x^2(t)\rangle, s_y(t) = \langle n_y^2(t)\rangle$ and (c) the cross-cumulant $U(t) = \langle n_x n_y\rangle$.

From cumulant analysis one can find that $\langle y^3\rangle = \frac{1}{N}\sum_{i=1}^{N} y_i^3 = m_y^3 + 3m_y s_y$

$\langle y^4\rangle = \frac{1}{N}\sum_{i=1}^{N} y_i^4 = m_y^4 + 6m_y^2 s_y + 3s_y^2,\ \langle xy\rangle = \frac{1}{N}\sum_{i=1}^{N} x_i y_i = U + m_x m_y$

$\langle xy^2\rangle = \frac{1}{N}\sum_{i=1}^{N} x_i y_i^2 = m_x s_y + m_x m_y^2 + 2m_y,\ \langle xy^3\rangle = \frac{1}{N}\sum_{i=1}^{N} x_i^3 y_i = 3s_y\ U + 3m_y^2 U + m_x m_y^3 + 3m_y m_x s_y$

From cumulant analysis and by considering Ito's chain rule the following mean-field approximated model is obtained:

$$\dot{m}_x(t) = m_y(t)$$
$$\dot{m}_y(t) = (-3aV^2 + 2bV - c)m_y(t) + (b - 3aV)\left(s_y(t) + m_y^2(t)\right)$$
$$- a\left(m_y^3(t) + 3m_y(t)s_y(t)\right)$$

$$\frac{1}{2}\dot{s}_x(t) = U(t)$$
$$\frac{1}{2}\dot{s}_y(t) = s_y(t)\left[(2bV - 3aV^2 - c) + 2(b - 3aV)m_y(t) - 3a\left(m_y^2(t) + s_y(t)\right)\right] - kU(t) + D \quad (4)$$
$$\dot{U}(t) = U(t)\left[(2bV - 3aV^2 - c) + 2(b - 3aV)m_y(t) - 3a(s_y(t) + m_y^2(t))\right] + s_y(t) - ks_x(t)$$

It could be easily shown that both starting stochastic (3) and mean-field approximated model (4) exhibit qualitatively the same dynamics.

One should note that both models exhibit constant background velocity which is the characteristic property of the long-lasting creeping landslides. Such examples are frequent in engineering practice, one is them is landslide "Plavinac" in Smederevo, whose displacements are being observed for over a decade (Fig. 4).

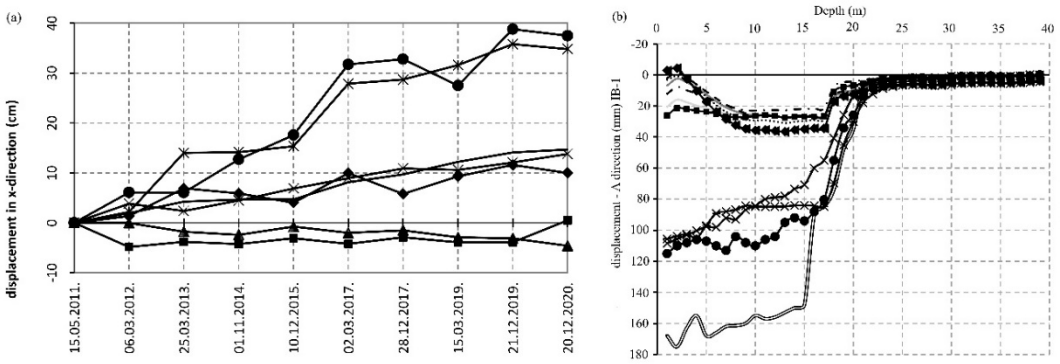

Fig. 4. Recorded continuous displacements of creeping landslide; example of "Plavinac" landslide in Smederevo (Serbia): (a) superficial displacements recorded at geodetic benches; (b) displacements along the depth in the installed inclinometer IB-1 (period 2016-2021).

3. Results

3.1 Effect of time delay

Results of the numerical computation of model (3) are shown in Fig. 5. As one can see a supercritical Hopf bifurcation occurs for rather strong spring stiffness k (>6) and high values of time delay τ (>1). Regarding the effect of spring stiffness, one needs to assume high spring stiffness, i.e. system under study (conditionally stable slope) needs to be observed as a system of strongly coupled accumulation and feeder slope, in order for instability to occur. As for the effect of the introduced time delay, occurrence of instability for high values of τ shows the high resilience of the conditionally stable slope to occurrence of time delay between the motion of feeder and accumulation slope. This may indicate that the time delay indicated originally by Davis [4], as shown in Fig. 6, maybe does not have significant influence on the system dynamics, for the chosen values of friction parameters.

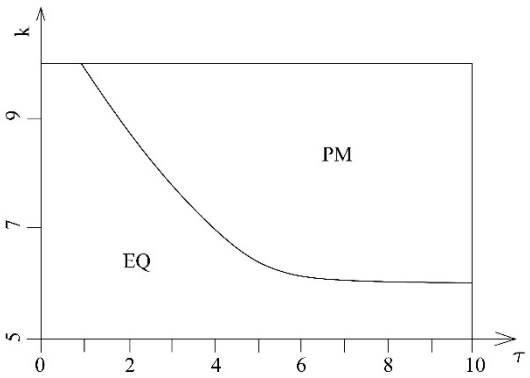

Fig. 5. Hopf bifurcation curve k(τ), for the fixed values of parameters V_0 = 0.1, *a*=3.2, *b*=-7.2 and *c*=4.8. EQ stands for the equilibrium creep regime, while PM denotes unstable periodic oscillations.

If we want to examine further the effect of time delay, let us analyze the influence of the frictional parameters on the effect of τ. If one holds value of time delay and spring constant above the bifurcation curve, increase of parameters a, b and c suppress the effect of the introduced time delay (Fig. 6). This indicates that sliding surfaces with low friction parameters are more susceptible to the onset of instability.

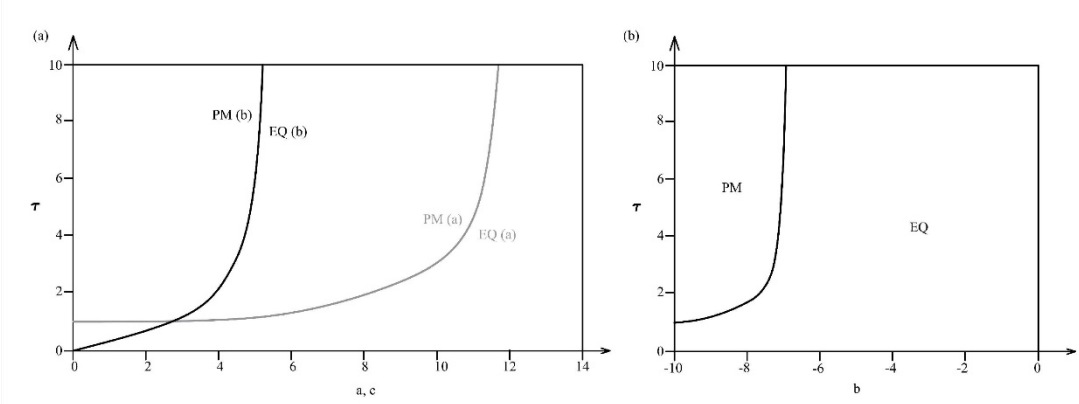

Fig. 6. Bifurcation diagrams regarding the effect of frictional parameters on the onset of instability: (a) τ=f(a), (b) τ=f(b), (c), τ=f(c) for fixed parameters values: V_0 = 0.1, K=7, a=3.2, b=-7.2 and c=4.8. EQ stands for the equilibrium state, while PM denote periodic (oscillatory) regime.

3.2 Effect of noise

In order to determine the adequate type of background noise, we firstly analyze the real recordings of the ambiental noise before and after the small seismic event recorded at accelerograph station ETNA located at Zavoj dam (Fig. 7), which is considered to be a landslide-prone area. For this purpose, we invoke the method of surrogate data testing. We constructed 20 surrogate time series, and calculated the zeroth-order prediction error, which were tested against a null hypothesis that data represent a linear stationary stochastic process with Gaussian inputs. For this purpose, 20 surrogate datasets were formed by randomizing the Fourier surrogates of the original data, and then by computing the inverse transform to obtain randomized time series.

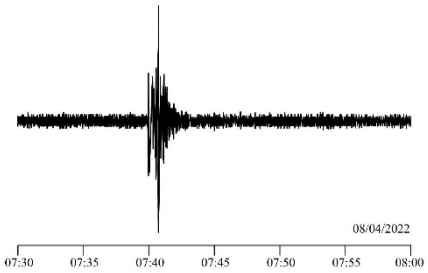

Fig. 7. Ambiental noise before and after the small seismic event on 08/04/2022 recorded at ETNA accelerograph station at location of Zavoj dam.

The results of the analysis indicated that background noise belongs to the linear stationary stochastic process with Gaussian inputs, since zeroth-order prediction error ε_0 is within ε for all the tested surrogates (Fig. 8).

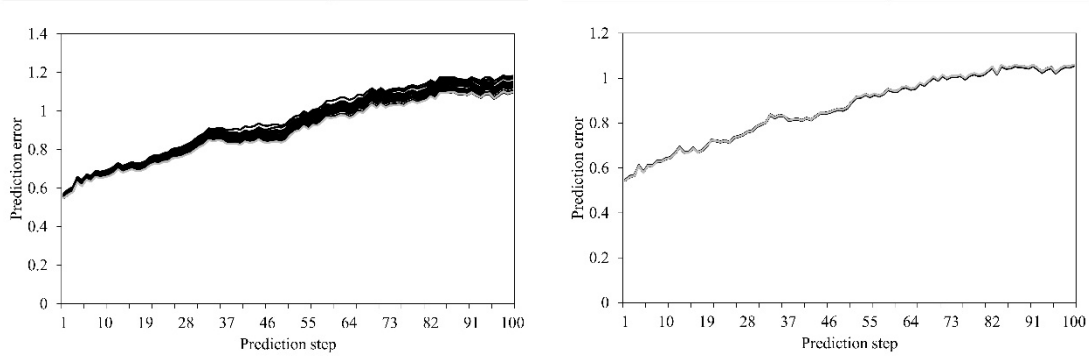

Fig. 8. Results of surrogate data testing that background noise belongs to the linear stationary stochastic process with Gaussian inputs: temporal distribution of the zeroth-order prediction error for the original dataset (gray) and for the surrogate datasets (black). It is clear that ε_0 is well within ε for all the tested surrogates.

The analysis of the influence of background random noise on dynamics of landslide model (4) is conducted numerically, using 4th order Runge-Kutta numerical method, under the effect of the introduced time delay τ and spring stiffness k. Results of the conducted analysis indicate the occurrence of the direct supercritical Hopf bifurcation, with the increase of time delay and/or spring stiffness (Fig. 9). Particularly, the observed dynamical system goes from equilibrium state to regular periodic oscillations, which are considered as the unstable dynamical regime.

Regarding the effect of noise, there is a positive effect of background random noise on the landslide stability. This effect could be clearly seen both for the low and high values of time delay and spring stiffness, as shown in Fig. 9. Such effect for high values of time delay and relatively low values of spring stiffness is shown in Fig. 10(a). Such conditions are expected in strongly weathered rock masses, with the loose connections between the actually moving parts of the unstable slope, where higher values of delayed displacements are expected. On the other and, effect of noise for low values of time delay and high values of spring stiffness is shown in Fig. 10(b). Such regime corresponds to the slope built of rock mass which is just slightly weathered and with low deformability, where low values of delayed displacements are expected. One could see that increase of D for constant k and τ leads to stabilization of landslide dynamics.

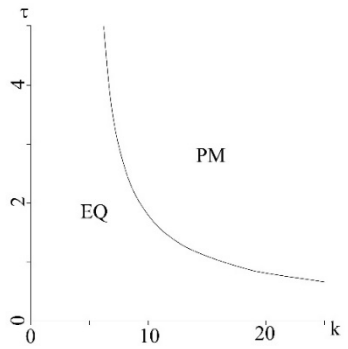

Fig. 9. Bifurcation diagrams τ-k for model (4). While τ and k are varied, other parameters are being held constant: ε=10-4, p=1, V_0=0.2, a=4.8, b=-7.2, c=3.2, initial conditions: m_x=0.001, m_y=0.0001; s_x=s_y=0.05, D=0.0001.

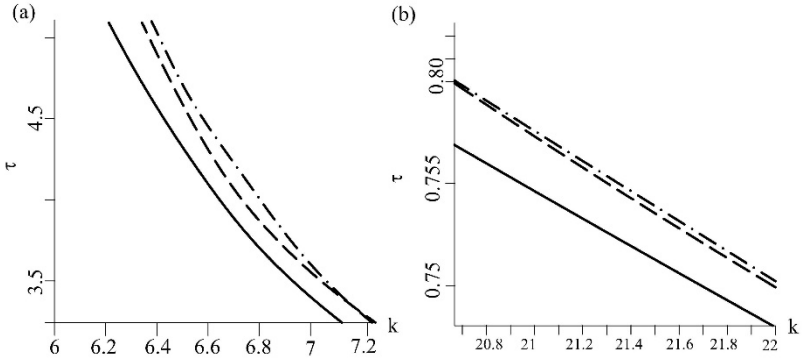

Fig. 10. Effect of noise intensity on dynamics of the observed system (4): (a) for high values of time delay τ and low values of spring stiffness k, (b) for low values of time delay τ and high values of spring stiffness k. Constant values of other parameters are the same as for Fig. 9. Continuous curve stands for D=10^{-4}, dashed curve for D=10^{-3} and dashed-dot curve for 10^{-2}.

3. Conclusions

The effect of delayed displacement and random background noise is examined in the present paper. Displacement delay is assumed following the initial suggestion made by Davis [4]. New models for landslide dynamics are proposed and investigated. The influence of time delay is examined in the suggested two-block model, with the assumed rate-dependent friction law. Impact of noise, on the other hand, is analyzed in a model of n globally coupled blocks. Background noise is introduced in the model as random, considering the results of ambiental noise testing recorded before and after the small seismic event on 08/04/2022 at ETNA accelerograph station installed at the location of Zavoj dam (landslide prone area). Surrogate data testing indicates that recorded time series belong to the linear stationary stochastic process with Gaussian inputs.

Modelling of landslide dynamics is conducted under the following assumptions: (a) friction law is rate dependent; (b) time delay exists in displacement of neighboring blocks; (c) there is a permanent effect of background seismic noise. Both models exhibit small constant displacements in equilibrium state, which is considered to correspond to the continuous movements of creep landslides. Examples of recorded superficial displacements of geodetic benches and movements along the depth in the installed inclinometer at the location of "Plavinac" landslide (Smederevo, Serbia) are presented.

Dynamics of the two-block model is represented through a system of deterministic delay differential equations, which is solved numerically. On the other hand, dynamics of n all-to-all

coupled blocks is assumed to be governed by a set of stochastic delay differential equations, which are solved firstly by applying the mean-field approximation and, then, by analysis the approximated deterministic system. One can easily show that both the stochastic and deterministic system exhibit qualitatively the same dynamics before and after the bifurcation point.

The results obtained indicate that in the model of two coupled blocks sliding on an inclined slope, increase of time delay for certain friction conditions between the upper and lower part of the slope does not have effect on stability of landslide dynamics. It seems that in such setup friction plays a crucial role, and it suppresses the destabilizing effect of time delay, leading the dynamics of the observed delay model to equilibrium state for the constant value of the introduced time delay. On the other hand, fine analysis of the effect of the random background noise indicates the stabilizing effect of noise, i.e. the increase of noise intensity leads to stabilization of landslide dynamics.

Considering the significant effect of noise on landslide dynamics, further analysis should explore the possible occurrence of more bifurcation curves (more complex behavior). Also, further analysis in this direction could include possible significant effect of the artificially generated colored noise on the landslide dynamics. Regarding the effect of time delay, one could examine the possible effect of time delay in the velocities of the neighboring blocks.

References:

[1] Tozato K., Dolojan N.L.J, Touge Y., Kure S. et al., *Limit equilibrium method-based 3D slope stability analysis for wide area considering influence of rainfall,* Engineering Geology, Vol. 308, 106808, 2022.

[2] Kostić S., Guranov I., Vasović N., Kuzmanović D. *Mechanics of weathered clay-marl rock masses along the rupture surface in homogeneous dry slopes*, Theoretical and Applied Mechanics, Vol. 43, 85-98, 2016.

[3] Mahallem A., Roudane M., Krimi A. et al. *Smoothed Particle Hydrodynamics for modelling landslide–water interaction problems*. Landslides, Vol. 19, 1249–1263, 2022.

[4] Davis R.O., *Modelling stability and surging in accumulation slides,* Engineering Geology, Vol. 33, 1-9, 1992.

[5] Cartwright J.H.E., Hernandez-Garcia E., Piro O., *Burridge-Knopoff models as elastic excitable media*, Physical Review Letters, Vo. 79, 527–530, 1997.

[6] Viesca R.C., Rice J.R.,*Nucleation of slip-weakening rupture instability in landslides by localized increase of pore pressure*, Journal of Geophysical Research, 117, B03104, 2012.

[7] Lucas A., Mangeney A., Ampuero J., *Frictional velocity-weakening in landslides on Earth and on other planetary bodies*, Nature Communications, Vol. 5, 3417, 2014.

[8] Kostić S., Franović I., Todorović K., Vasović N. *Friction memory effect in complex dynamics of earthquake model*, Nonlinear Dynamics, Vol. 73, 1933–1943, 2013.

[9] Handwerger A.L., Rempel A.W., Skarbek R.M., Roering J.J., Hilley G.E., *Rate-weakening friction characterizes both slow sliding and catastrophic failure of landslides*, Proc. Natl. Acad. Sci. USA. Vol. 113, 10281-10286, 2016.

[10] Morales J.E.M., James G., Tonnelier A., *Travelling waves in a spring-block chain sliding down a slope*, Physical Review E, Vol. 96, 012227, 2017.

[11] Liu W., He S., Li X. et al., *Two-dimensional landslide dynamic simulation based on a velocity-weakening friction law*, Landslides, Vol. 13, 957–965, 2016.

[12] Yamada M., Mangeney A., Matsushi Y. et al. *Estimation of dynamic friction and movement history of large landslides*, Landslides, Vol. 15, 1963–1974, 2018.

[13] Finnegan N.J., Brodsky E.E., Savage H.M. Nereson A.L., Murphy, C.R. *Seasonal slow landslide displacement is accommodated by mm-scale stick-slip events*, Geophysical Research Letters, 49, e2022GL099548, 2022.

[14] Breton M., Bontemps N., Guillemot A., Baillet L., Larose, E. *Landslide monitoring using seismic ambient noise correlation: challenges and applications*, Earth-Science Review, Vol. 216, 03518, 2021.
[15] Bashkirtseva I., Nasyrova V., Ryashko L. *Noise-induced bursting and chaos in the two-dimensional Rulkov model*. Chaos Solitons and Fractals, Vol 110, 76-81., 2018.
[16] Vasović N., Kostić S., Franović I., Todorović K. *Earthquake nucleation in a stochastic fault model of globally coupled units with interaction delays,* Communications in Nonlinear Science and Numerical Simulation, Vol. 38, 117-129, 2016.
[17] Kostić S., Vasović N., Todorović K., Franović I. *Effect of colored noise on the generation of seismic fault movement: Analogy with spring-block model dynamics*, Chaos, Solitons & Fractals, Vol. 135, 109726, 2020.

A BRIEF REVIEW OF THE RESULTS OF FORCED VIBRATIONS OF ELASTICALLY COUPLED NANO-STRUCTURES

Marija Stamenković Atanasov and Ivan R. Pavlović

[1] Department of Theoretical and Applied Mechanics, Faculty of Mechanical Engineering, University of Niš, 14 A. Medvedeva Street, 18000 Niš, Serbia
e-mail: marija.stamenkovic.atanasov@masfak.ni.ac.rs, pivan@masfak.ni.ac.rs

Abstract

This paper studies the oscillatory behavior of different types of elastically coupled nano-structures comprising two carbon nano-tubes modelled as two nano-beams, two graphene nano-sheets modelled as two nano-plates and a combination of nano-plates and double-curved shallow nano-shells. Different parameters that influence the dynamic responses of the upper and lower elements of the presented elastically coupled nano-structures are analysed in detail. These are: nonlocal parameter, magnetic field, radius of curvature of a doubly curved shallow nano-shell and different values of external loads. The objective of the study of these nano-systems is to show that such systems have a damping effect on both amplitudes of vibrations of the nano-system transverse displacements for all observed external loads due to the increase in the intensity of the magnetic field and the increase in the non-local parameter. Also, the application of the mentioned coupled nano-structures in nano-sensors is discussed.

Keywords: nano-sensor, forced vibrations, coupled nano-structures, nano-beam, nano-plate, shallow nano-shell.

1. Introduction

Year by year, the finish line of researchers is to improve the characteristics of nano-sensors. Designing new nano-systems that are made of coupled nano-beams, nano-plates and nano-shells can provide the ability to improve the characteristics of nano-sensors. Nanotechnology offers the possibility of sensors to be specific and detect multiple analytes and monitor their presence in real time. The new nano-sensors can employ a sensing technique that can increase the diagnostic signals by more than one million times. Nano-systems are made of graphene materials which received much attention in nano-engineering theory and practice. Due to widespread applications of nano-electro-mechanical-systems (NEMS) such as nano-sensors, nano-electro-chemical nano-sensors, nanoactuators, there are a lot of various higher-order continuum theories involving material length scale parameters. In order to perform mathematical modelling of a nano-system, one of applied theories is nonlocal theory of Eringen [1-2]. Nonlocal elastic theory has attracted a lot of attention because of the necessity of modelling and analysis of very small-sized mechanical structures in the development of nanotechnologies. A brief review reporting the recent advances on the carbon nanostructured materials-based sensors covering recently published studies is

presented in paper [3]. Also, in paper [4], the recent studies of carbon nanomaterials-based nano-force and nano-mass sensors using mechanical analysis of vibration behaviour are presented.

In this paper, the nano-systems which can be used as nano-mechanical sensors and electro-chemical nano-sensors based on vibration analysis were discussed numerically. Influences of different parameters on dynamic responses of the upper and lower nano-elements of the elastically coupled nano-structures are analysed in detail.

2. Considered nano-systems

In this paper, elastically coupled nano-structures comprising two carbon nano-tubes modelled as two nano-beams [5], two graphene nano-sheets modelled as two nano-plates [6] and a combination of nano-plates and double-curved shallow nano-shells [7] are analysed. By applying Eringen's non-local stress theory, Euler-Bernoulli's beam theory, Kirchhoff-Love's plate theory, and Novozhilov's linear theory of shallow shells, differential equations are derived from papers [5,6,7] to describe the vibrations (movements) of elastically coupled nano-structures. The connection between nano-structures is carried out with Winkler-s elastic layer. All the orthotropic double systems are simply supported. It is assumed that the material and geometric characteristics for upper and lower nano-elements of nano-systems are the same except for the nano-system of coupled nano-plate and nano-shell, where radii of curvature exist at shell. Solving procedure and solutions of all three nano-systems are discussed in detail in papers [5,6,7].

Fig. 1 shows several coupled nano-structures that were analysed in this paper, as well as their application in nano-sensors. Figure 1a shows a biosensor, while Figure 1b shows an electro-chemical nano-sensor whose transducer is based on graphene, and which can be made of nano-beams, nano-plates or nano-shells shown in Figure 1c. A single nano-strip shown in Figure 1b can be made from the coupled nano-structures shown in Figure 1c. All considered nano-structures in Figure 1c, which are under the influence of various external loads (various nano-particles spread along the upper nano-element), are considered in the continuation of this paper. Also, different parameters that influence the dynamic responses of the upper and lower nano-elements of the presented elastically coupled nano-structures are analysed in detail.

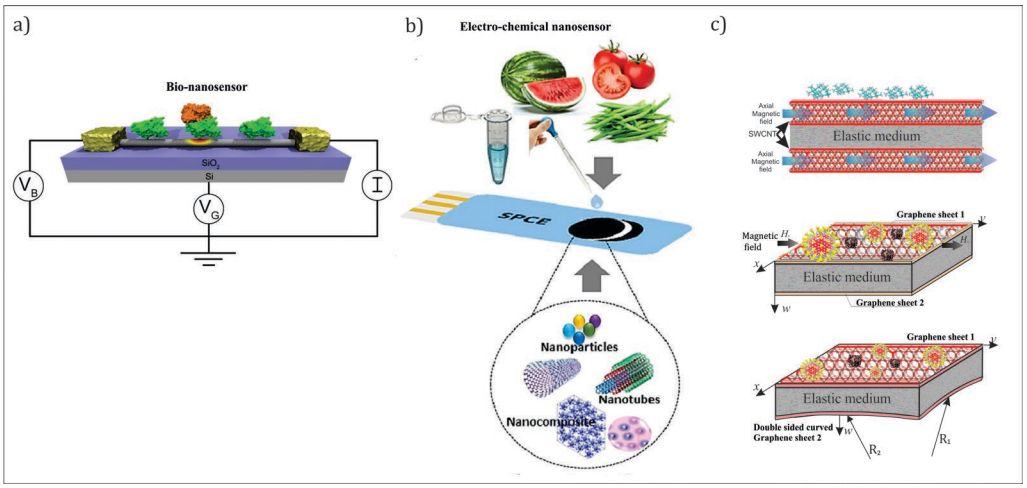

Fig. 1. Application of coupled nano-structures to a) bio-nanosensor and b) electro-chemical nanosensor, c) considered coupled nano-structures

2.1 Numerical results

Different parameters that influence the dynamic responses of the upper and lower elements of the presented elastically coupled nano-structures are analysed in detail through numerical results.

These are: non-local parameter, magnetic field, stiffness of elastic layer, radius of curvature of a doubly curved shallow nano-shell and different values of external loads. All material and geometric parameters are used from papers [5,6,7].

Forced vibration responses at the nano-beams mid-points are analysed for the case of external excitation under the influence of the magnetic field and nonlocal parameter. We consider that the uniform harmonic load (Fig. 2a) acts on the upper nano-beam in the nano-system composed of elastically coupled two nano-beams. Also, we assume that both nano-beams have the same geometrics and materials characteristics and are subjected to the axial compressive loads $\overline{F_1}$ and $\overline{F_2}$. Using the analytical solution for transversal displacements obtained from paper [5], we plot $\overline{w}_1(\xi,\tau)=\overline{w}_1(0.5,\tau)$ and $\overline{w}_2(\xi,\tau)=\overline{w}_2(0.5,\tau)$ as time function for different nonlocal and magnetic field parameters, as shown in Fig. 2. Fig. 2 shows how the coupled double nano-beam system responds to changes in the nonlocal and magnetic field parameter. It can be noticed that the nonlocal parameter (Figs. 2b, 2c) and magnetic field parameter (Figs. 2d, 2e) have a dampening effect on both response vibration amplitudes of the nano-system. By selecting the intensity of the magnetic field, we can set the response vibration amplitude in a certain range without changing any other material and geometric characteristics of the systems.

Forced vibration responses at the nano-plates system are analysed for two cases of external excitation: uniformly distributed continuous harmonic load and concentrated harmonic force. We consider that the uniformly distributed continuous harmonic load (Fig. 3a) acts on the upper nano-plate in the nano-system composed from elastically coupled two nano-plates. Also, we consider that the concentrated harmonic force (Fig. 4a) acts on the upper nano-plate in the nano-system composed of elastically coupled two nano-plates. Two cases of the nano-systems are under the influence of the magnetic field within the framework of the nonlocal elasticity theory. Using the analytical solutions for transversal displacements obtained from [6], we plot displacements in the mid points $\overline{w}_1$ and $\overline{w}_2$ as time function for different nonlocal and magnetic field parameters, as shown in Figs. 3 and 4.

In order to observe the nonlocal and magnetic field parameters for the uniformly distributed continuous harmonic load case, Fig. 3 shows its effect on the dynamic response of nano-plate one (3b) and nanoplate two (3c) of the nano-system. Also, it can be seen that without effects of nonlocal and magnetic field parameters, the dynamic response for both plates has a much higher value, than with its effects. From Fig. 3(c) the dynamic response of nano-plate two is almost imperceptible with effects of nonlocal and magnetic field parameters as compared to without these effects. For this reason, the dynamic response with mentioned effects is enlarged in Fig. 3(c). Because of that, we have concluded that nonlocal and magnetic field parameters greatly reduced dynamical response of nano-plates one and two. The increase of the magnetic field parameter leads to the reduction of forced vibration responses of nano-plates one and two.

The same observations can be concluded for the case of the concentrated harmonic force, showed in Figs. 4b and 4c, respectively.

The effects of external excitation of uniformly distributed continuous harmonic load is showed in Figs. 3d and 3e. Dynamic response of nano-plate one, and dynamic response of nano-plate two are presented in Figs. 3d and 3e, respectively. It can be noticed that with increases of amplitude of uniformly distributed continuous harmonic load, the dynamic response of nano-plate one and two are increased.

The effect of external excitation of concentrated harmonic force is showed in Figs. 4d and 4e. It can be noticed that with increases of amplitude of concentrated harmonic force, the dynamic response of nano-plate one and two are increased.

Forced vibration responses at the nano-system composed of elastically coupled nano-plate with nano-shell are analysed for uniformly distributed harmonic load. We consider that the

uniformly distributed harmonic load (Fig. 5a) acts on the upper nano-plate in the system. Using the analytical solutions for transversal displacements obtained from paper [7], we plot displacements in the mid points w_1 and w_2 as time function for different nonlocal parameters in Figs. 5b and 5c and different parameters of radii curvatures in Figs. 5d and 5e.

The effect of the nonlocal parameter of the nano-system composed from elastically coupled nano-plate with nano-shell at the dynamic response of upper nano-plate in Fig. 5b, and the nano-shell in Fig. 5c are presented. The dynamic response for upper nano-plate has decreasing value with an increasing nonlocal parameter (see Fig. 5b). From Fig. 5c the dynamic response for nano-shell has increasing value for an increasing nonlocal parameter. The same observation is presented in paper [8].

The effects of the external excitation on the dynamic response of upper nano-plate on Fig. 5d, and the nano-shell on Fig. 5e, are presented. It can be noticed that with an increase in external excitation the dynamic response of nano-plate and nano-shell are increases.

The effect of the radii of curvatures R_2 when $R_1 \to \infty$ on the transversal displacements of the nano-system composed of elastically coupled nano-plate with nano-shell are presented in Figs. 5f and 5g. It can be noticed that with an increase of radii of curvature, the dynamic response of upper nano-plate and lower nano-shell of nano-system also increases.

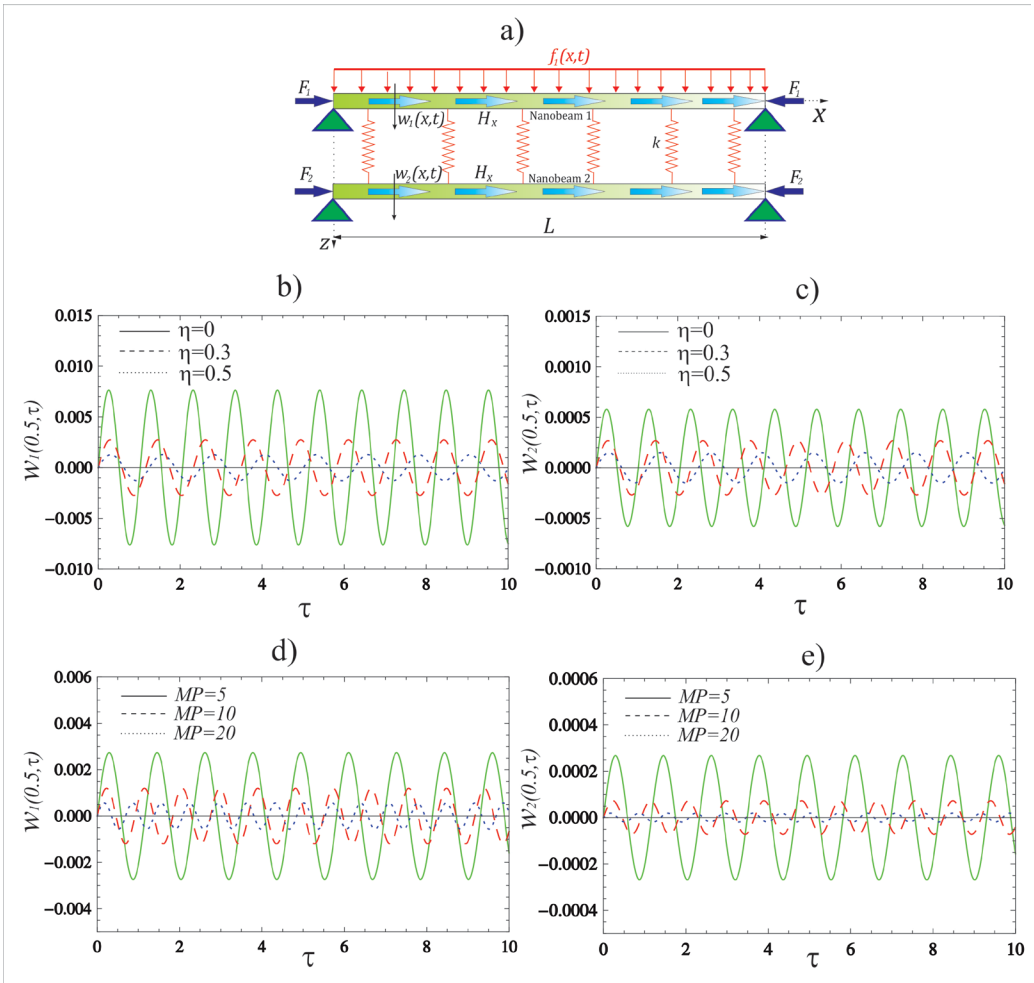

Fig. 2. Dynamic responses of forced vibration of nano-system composed of elastically coupled two nano-beams a) caused by uniform harmonic load; b) effect of nonlocal parameter at the upper nano-beam; c) effect of nonlocal parameter at the lower nano-beam; d) effect of magnetic field parameter at the upper nano-beam; e) effect of magnetic field parameter at the lower nano-beam.

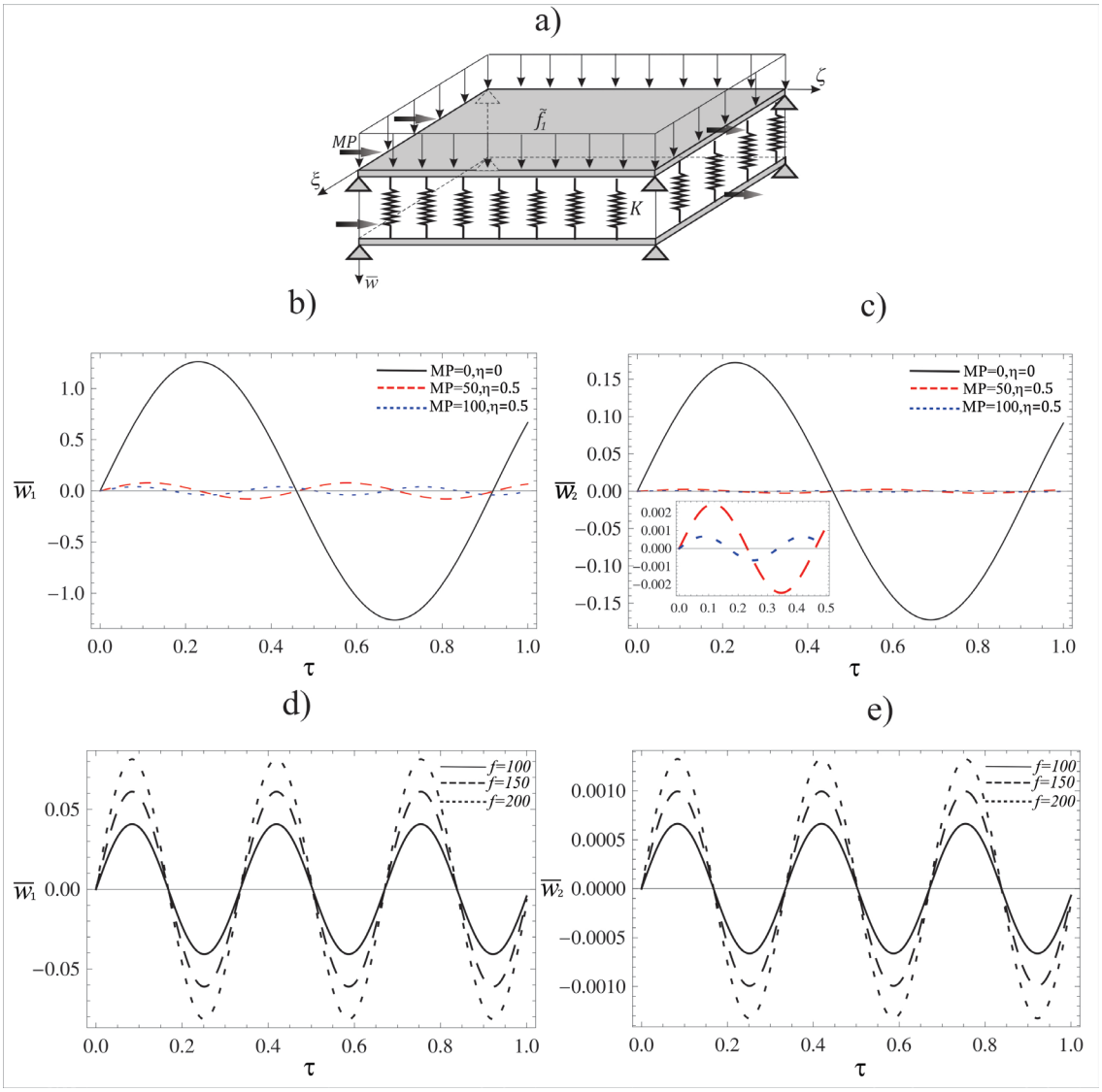

Fig. 3. Dynamic responses of forced vibration of nano-system composed of elastically coupled two nano-plates a) caused by uniformly distributed continuous harmonic load; b) effect of nonlocal and magnetic field parameters at the upper nano-plate; c) effect of nonlocal and magnetic field parameters at the lower nano-plate; d) effect of amplitude of uniformly harmonic load at the upper nano-plate; e) effect of amplitude of uniformly harmonic load at the lower nano-plate.

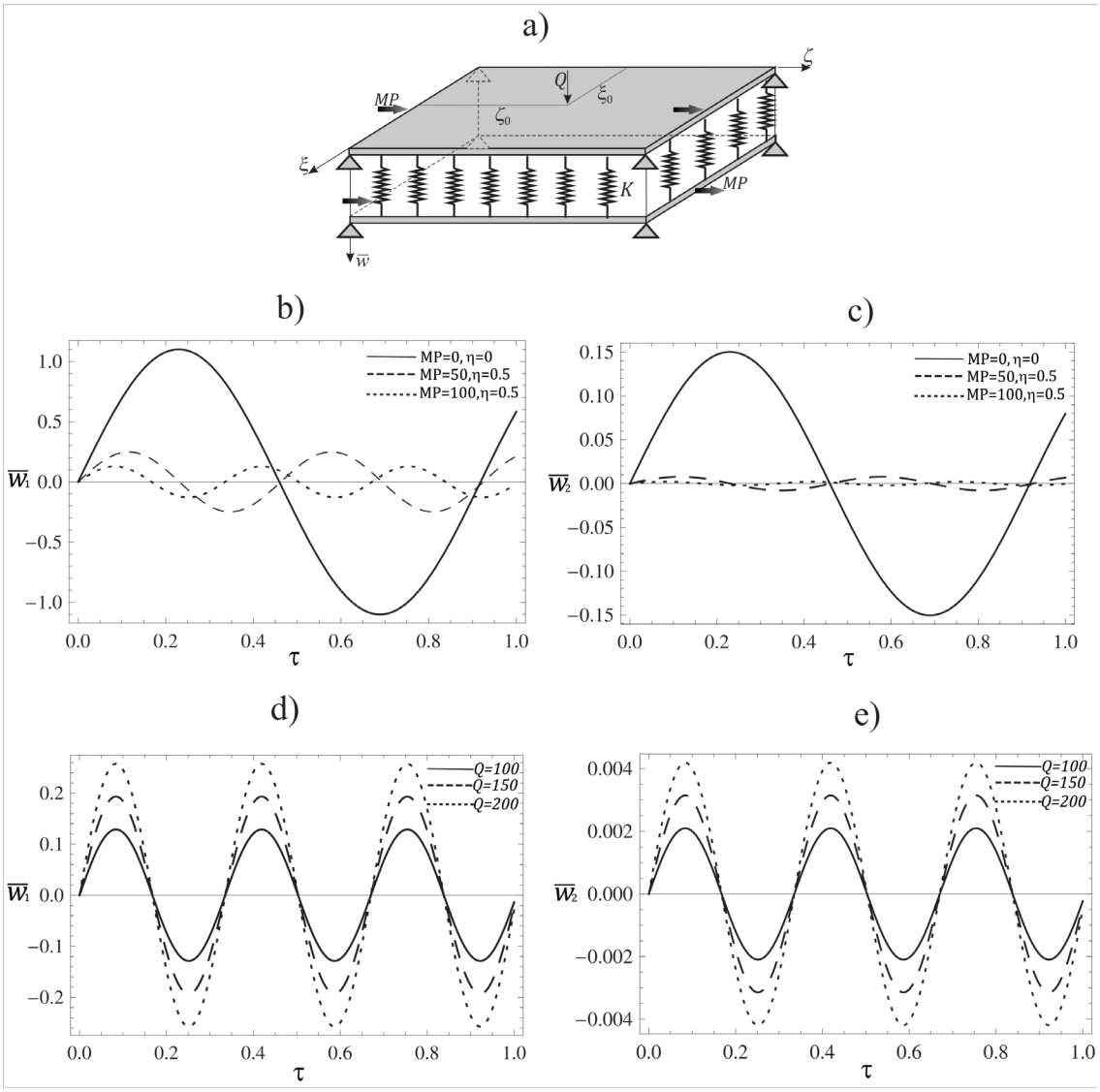

Fig. 4. Dynamic responses of forced vibration of nano-system composed of elastically coupled two nano-plates a) caused by concentrated harmonic force; b) effect of nonlocal and magnetic field parameters at the upper nano-plate; c) effect of nonlocal and magnetic field parameters at the lower nano-plate; d) effect of amplitude of concentrated harmonic force at the upper nano-plate; e) effect of amplitude of concentrated harmonic force at the lower nano-plate.

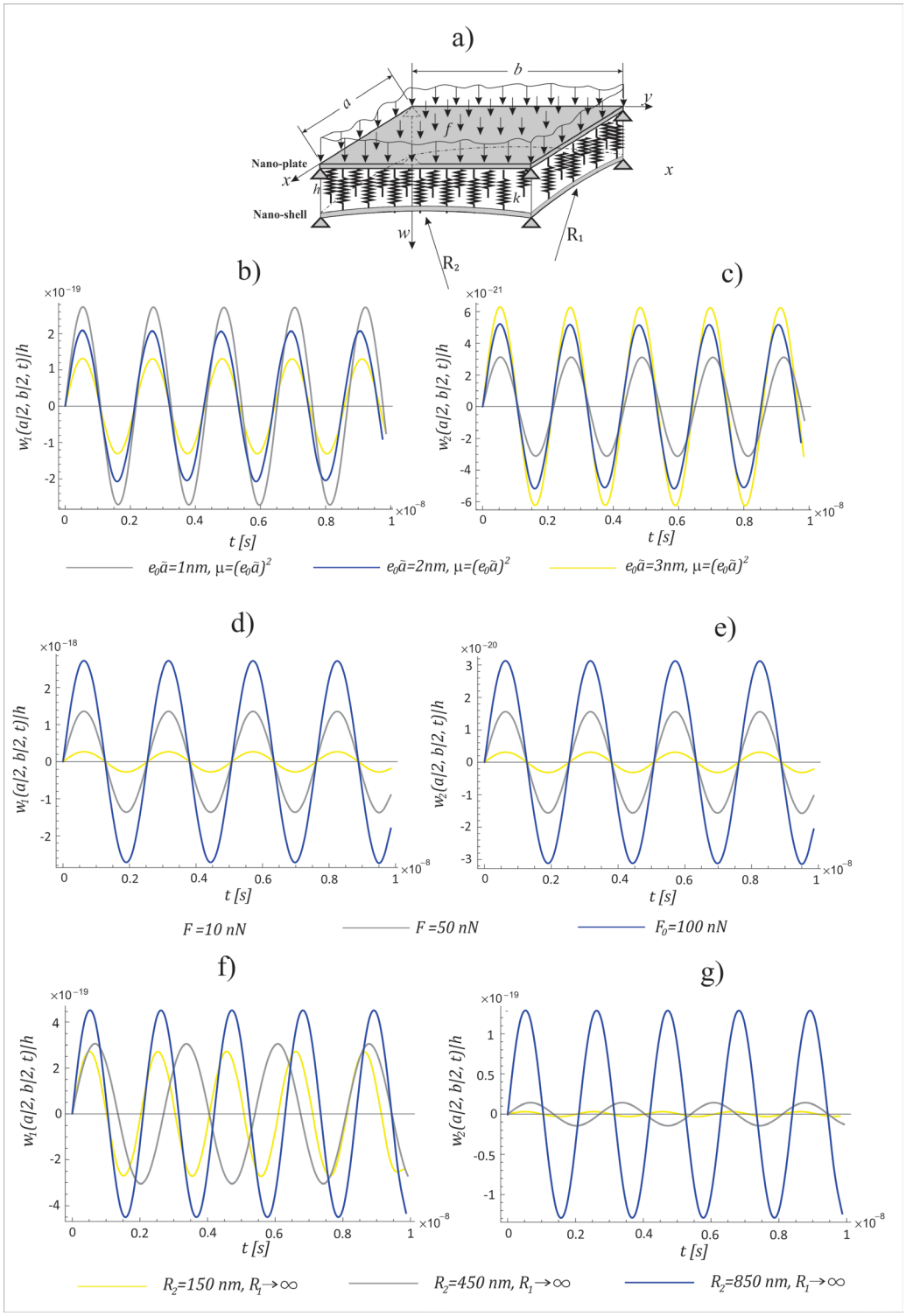

Fig. 5. Dynamic responses of forced vibration of the nano-system composed of elastically coupled nano-plate with nano-shell a) caused by uniformly distributed harmonic load; b) effect of nonlocal parameter at the upper nano-plate; c) effect of nonlocal parameter at the lower nano-shell; d) effect of amplitude of uniformly distributed harmonic load at the upper nano-plate; e) effect of amplitude of uniformly distributed harmonic load at the lower nano-shell; f) effect of radii of curvature at the upper nano-plate; g) effect of radii of curvature at the lower nano-shell.

3. Conclusions

New models of nano-sensors should be well projected to reduce the measurement uncertainty and increase testing accuracy. The present paper can provide an insight into the application of carbon nanomaterials-based nano-mechanical sensors with conclusions as follows.

We have concluded that the influence of nonlocal and magnetic field parameters greatly reduced dynamical response of upper and lower nanostructures of the nano-systems. The only place where the influence of nonlocal parameter caused an increase in value of the dynamic response is in lower nano-shell in a nano-system composed of elastically coupled nano-plate with nano-shell. Similar observations were found in the literature.

By examining the effects of external excitation in double nano-systems it can be noticed that with an increase of external excitation, the dynamic response of upper and lower nano-structures of nano-systems is increased.

By examining the effects of radii of curvatures at the nano-system composed of elastically coupled nano-plate with nano-shell, it can be noticed that with an increase of radii of curvatures, the dynamic response of upper and lower nano-structure is increased.

Acknowledgments: This research was financially supported by the Ministry of Science, Technological Development and Innovation of the Republic of Serbia (Contract No. 451-03-47/2023-01/200109).

References:

[1] Eringen, A. C., Edelen, D. G. B., *On nonlocal elasticity,* International Journal of Engineering Science, Vol. 10(3), 233-248, 1972.
[2] Eringen, A. C., *Nonlocal continuum field theories,* Springer Science & Business Media, 2002.
[3] Bezzon, V. D., Montanheiro, T. L., de Menezes, B. R., Ribas, R. G., Righetti, V. A., Rodrigues, K. F., Thim, G. P., *Carbon nanostructure-based sensors: a brief review on recent advances*. Advances in Materials Science and Engineering, Article ID 4293073, 2019.
[4] Shi, J.X., Lei, X.W. and Natsuki, T., *Review on carbon nanomaterials-based nano-mass and nano-force sensors by theoretical analysis of vibration behavior*. Sensors, 21(5), p.1907, 2021.
[5] Stamenković, M., Karličić, D., Goran, J., Kozić, P., *Nonlocal forced vibration of a double single-walled carbon nanotube system under the influence of an axial magnetic field*. Journal of Mechanics of Materials and Structures, 11(3), 279-307, 2016.
[6] Atanasov, M. S., Karličić, D., Kozić, P., *Forced transverse vibrations of an elastically connected nonlocal orthotropic double-nanoplate system subjected to an in-plane magnetic field*. Acta Mechanica, 228(6), 2165-2185, 2017.
[7] Atanasov, M. S., Pavlović, I. Jovanović B. D., *Forced vibration of the nano-system composed from elastically connected nano-plate and nano-shell with influence of different parameters*. 8 th International Congress of Serbian Society of Mechanics Kragujevac, Serbia, 28-30. June, 624-633, 2021.
[8] Arefi, M., *Analysis of a doubly curved piezoelectric nano shell: nonlocal electro-elastic bending solution*. European Journal of Mechanics-A/Solids, 70, 226-237, 2018.

DYNAMIC BEHAVIOR OF A NANO-SYSTEM UNDER THE INFLUENCE OF MOVING EXTERNAL NANOPARTICLE

Marija Stamenković Atanasov[1], Danilo Karličić[2] and Ivan R. Pavlović[3]

[1] Department of Theoretical and Applied Mechanics, Faculty of Mechanical Engineering, University of Niš, A. Medvedeva 14, 18000 Niš, Serbia
e-mail: marija.stamenkovic.atanasov@masfak.ni.ac.rs
[2] Mathematical Institute of the Serbian Academy of Sciences and Arts, Kneza Mihaila 36, Belgrade, Serbia
e-mail: danilok@mi.sanu.ac.rs
[3] Department of Theoretical and Applied Mechanics, Faculty of Mechanical Engineering, University of Niš, A. Medvedeva 14, 18000 Niš, Serbia
e-mail: ivan.pavlovic@masfak.ni.ac.rs

Abstract

This paper deals with analysis of the dynamic response due to influence of externally moving force to the nano-beams system, including magnetic field. Based on the Eringen nonlocal elasticity theory and Euler-Bernoulli beam theory, the system of two coupled non-homogeneous partial differential equations of motion is presented. The dynamic responses of the nano-system for moving external nanoparticle are considered. The effects of the axial magnetic field, ratio axial external forces, amplitude and velocity of moving external nanoparticle and stiffness coefficient of the elastic medium on the forced dynamic behaviour of nano-system are considered through numerical examples. From numerical results we can conclude that the dynamical behaviour of nano-system is greatly influenced by the magnetic field, stiffness coefficient of the elastic medium, ratio axial external forces and amplitude and velocity of moving external nanoparticle. It is shown that by selecting the intensity of the axial magnetic field, it is possible to adjust the stiffness of the system without changing the material and geometric parameters.

Keywords: forced vibrations, moving external load, coupled nano-structures, nano-beam.

1. Introduction

One of the most important elements in nano-systems are carbon nanotubes (CNTs). Because of their low weight, they have drawn considerable attention from scientists and engineers in the field of nanotechnology, see [1,2,3]. A brief review reporting the recent advances on the carbon nanostructured materials-based sensors covering recently published paper is presented in paper [4]. Nonlocal elastic theory has attracted a lot of attention because of the necessity of modelling and analysis of very small-sized mechanical structures in the development of nanotechnologies. According to Eringen [5,6], the nonlocal theory gives great approximation for a large class of problems in nano-systems where the influence of length-scales is very pronounced. It is known that the dynamic deflections predicted by the classical local theory are always smaller than those

predicted by the nonlocal theory due to the nonlocal effects. This is proven in many papers [7,8,9]. The influences of the nonlocal parameter, velocity of the moving nanoparticle and the coefficient of elastic layer between the two nanotubes on the dynamic responses are discussed and analysed in paper [10]. The effects of compressive axial load on the forced vibrations of the double-beam system in local domain are discussed in paper [11]. The effects of compressive axial load on the forced vibrations of the double-beam system in nonlocal domain are discussed in paper [12].

Elastically connected two nano-beams under the influence of an axial external forces, axial magnetic field and external transverse load are considered in this paper. The study shows that the dynamic behaviour of the nano-system is greatly influenced by the stiffness coefficient of the elastic medium, ratio axial external forces and the amplitude and velocity of moving external nanoparticle.

2. Formulation of a nano-system

The system of elastically connected two nano-beams which is under the influence of an axial external forces, axial magnetic field and external transverse load is shown in Fig.1a. The presented nano-system is assumed to be modelled as a system composed of two parallel nano-beams, which have the same length and are continuously joined by a Winkler elastic layer. The stiffness modulus of the Winkler elastic layer is denoted with k. The transversal displacement of the two nano-beams is denoted by $w_1(x,t)$ and $w_2(x,t)$, respectively, Fig. 1b. For the sake of simplicity, we will consider only the case of identical nano-beams, where geometric and physical properties are the same for both nano-beams and defined as: A is the cross-sectional area, E is the Young's modulus, ρ is the mass density, I is the moment of inertia and L is the length of the nano-beam. We assume that both nano-beams are subjected to axial compressions F_1 and F_2, that are positive in compression. Also, we assume that upper nano-beam is subjected to moving constant load $f(x,t)$ that is positive when acts downward. The influence of the Lorentz magnetic force on the double nano-beam system is caused by the axial magnetic field which acts in the x direction, as shown in Fig. 1.

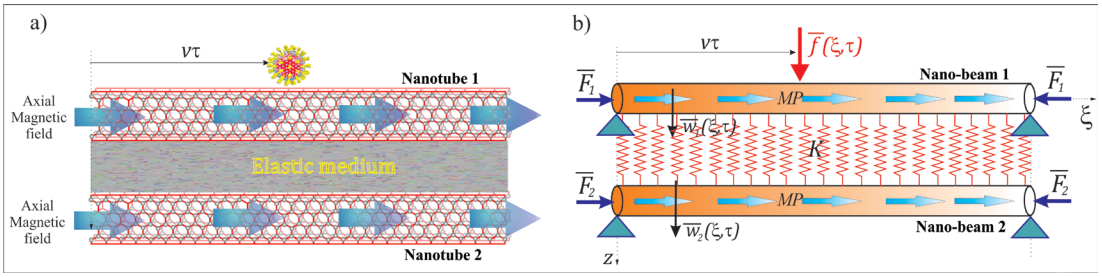

Fig.1. The system of elastically connected nano-beams affected by an axial magnetic field and external moving constant load, a) Physical model b) Mechanical model.

Using the Euler-Bernoulli beam theory [13] and Eringen nonlocal elasticity [5,6], the governing equations of motion of the nonlocal double nano-beam system can be given as in paper [12]:

$$\frac{\partial^2 \overline{w}_1}{\partial \tau^2}+\frac{\partial^4 \overline{w}_1}{\partial \xi^4}+K\left(\overline{w}_1-\overline{w}_2\right)+\left(\overline{F}_1-MP\right)\frac{\partial^2 \overline{w}_1}{\partial \xi^2}-\eta^2\frac{\partial^2}{\partial \xi^2}\left[\frac{\partial^2 \overline{w}_1}{\partial \tau^2}+K\left(\overline{w}_1-\overline{w}_2\right)+\left(\overline{F}_1-MP\right)\frac{\partial^2 \overline{w}_1}{\partial \xi^2}\right]=\overline{f}-\eta^2\frac{\partial^2 \overline{f}}{\partial \xi^2}, \quad (1)$$

$$\frac{\partial^2 \overline{w}_2}{\partial \tau^2}+\frac{\partial^4 \overline{w}_2}{\partial \xi^4}-K\left(\overline{w}_1-\overline{w}_2\right)+\left(\overline{F}_2-MP\right)\frac{\partial^2 \overline{w}_2}{\partial \xi^2}-\eta^2\frac{\partial^2}{\partial \xi^2}\left[\frac{\partial^2 \overline{w}_2}{\partial \tau^2}-K\left(\overline{w}_1-\overline{w}_2\right)+\left(\overline{F}_2-MP\right)\frac{\partial^2 \overline{w}_2}{\partial \xi^2}\right]=0. \quad (2)$$

3. Solution methodology

In order to simplify the solving of Eqs. (1) and (2), dimensionless parameters were introduced, shown in paper [12]. Solving the procedure of dynamic responses is shown in the mentioned paper.

Assuming that the boundary conditions of the nano-system are simply supported, and using Bernoulli-Fourier method, the solutions of nano-system are obtained in the forms:

$$\overline{w_1}(\xi,\tau)=\sum_{n=1}^{\infty}\sin(n\pi\xi)\sum_{i=I}^{II}\frac{1}{\omega_{ni}}\int_0^{\tau}R_{ni}(s)\sin\left[\omega_{ni}\left(\tau-s\right)\right]ds, \tag{3}$$

$$\overline{w_2}(\xi,\tau)=\sum_{n=1}^{\infty}\sin(n\pi\xi)\sum_{i=I}^{II}\alpha_{ni}\frac{1}{\omega_{ni}}\int_0^{\tau}R_{ni}(s)\sin\left[\omega_{ni}\left(\tau-s\right)\right]ds, \tag{4}$$

where are

$$R_{nI}=2M\frac{\alpha_{nII}}{\alpha_{nII}-\alpha_{nI}}\int_0^1\left(\overline{f}-\eta^2\frac{\partial^2\overline{f}}{\partial\xi^2}\right)\sin(n\pi\xi)d\xi, \tag{5}$$

$$R_{nII}=2M\frac{\alpha_{nI}}{\alpha_{nI}-\alpha_{nII}}\int_0^1\left(\overline{f}-\eta^2\frac{\partial^2\overline{f}}{\partial\xi^2}\right)\sin(n\pi\xi)d\xi. \tag{6}$$

The amplitude of vibration of the nano-system is:

$$\alpha_{ni}=\frac{K-\left(\overline{F_1}-MP\right)k_n^2+\dfrac{k_n^4}{1+\eta^2k_n^2}-\omega_{ni}^2}{K},\quad k_n=n\pi,\quad n=1,3,5...\quad i=I,II. \tag{7}$$

Natural frequency of the nano-system is in the form:

$$\omega_{ni}^2=\frac{1}{2}\left[b\mp\sqrt{b^2-4c}\right],\qquad i=I,II \tag{8}$$

where are

$$b=2K-\left(\overline{F_1}+\overline{F_2}-2MP\right)k_n^2+2\frac{k_n^4}{1+\eta^2k_n^2}, \tag{9}$$

$$c=\left[K-\left(\overline{F_1}-MP\right)k_n^2+\frac{k_n^4}{1+\eta^2k_n^2}\right]\left[K-\left(\overline{F_2}-MP\right)k_n^2+\frac{k_n^4}{1+\eta^2k_n^2}\right]-K^2. \tag{10}$$

When the first nano-beam is subjected to action of moving constant load

$$\overline{f}(\xi,\tau)=F\delta\left(\xi-v\tau\right), \tag{11}$$

where F is the amplitude of an external moving constant force and $\delta(\xi)$ is the Dirac delta function.

By replacing (11) into equations (5) and (6), we obtain:

$$R_{nI}=2MF\frac{\alpha_{nII}}{\alpha_{nII}-\alpha_{nI}}\sin(n\pi v\tau)\left[1+\eta^2k_n^2\right],\quad M=\left(1+\eta^2k_n^2\right)^{-1}, \tag{12}$$

$$R_{nII}=2MF\frac{\alpha_{nI}}{\alpha_{nI}-\alpha_{nII}}\sin(n\pi v\tau)\left[1+\eta^2k_n^2\right],\quad n=1,3,5.... \tag{13}$$

By replacing (12) and (13) with (3) and (4) and assuming that only the steady-state response has practical significance, the displacement of the upper and lower nano-beam of nano-system are:

$$\overline{w_1}(\xi,\tau)=\sin\left(\Omega_n\tau\right)\sum_{n=1}^{\infty}A_{nI}\sin(n\pi\xi), \tag{14}$$

$$\overline{w_2}(\xi,\tau)=\sin\left(\Omega_n\tau\right)\sum_{n=1}^{\infty}A_{nII}\sin(n\pi\xi), \tag{15}$$

where are

$$A_{nI}=\lambda_3\left[\frac{\alpha_{nII}}{\omega_{nI}^2-\Omega_n^2}-\frac{\alpha_{nI}}{\omega_{nII}^2-\Omega_n^2}\right], \tag{16}$$

$$A_{nII}=\lambda_3\alpha_{nI}\alpha_{nII}\left[\frac{1}{\omega_{nI}^2-\Omega_n^2}-\frac{1}{\omega_{nII}^2-\Omega_n^2}\right], \tag{17}$$

$$\lambda_3=\frac{2MF\left(1+\eta^2k_n^2\right)}{\alpha_{nII}-\alpha_{nI}}=\frac{2F}{\alpha_{nII}-\alpha_{nI}}, \tag{18}$$

$$\Omega_n=k_nv,\quad n=1,3,5... \tag{19}$$

4. Numerical results and discussion

In this section, forced vibration responses at the nanobeams mid-points *(0.5, τ)* are analysed under the external moving constant force. Also, the system is subjected to action of the axial magnetic field within the framework of the nonlocal elasticity theory. It is assumed that both nanobeams in the system have the same geometric and material characteristics and are subjected to the axial compressive loads $\overline{F_1}$ and $\overline{F_2}$. To analyse forced vibrations, we use smaller values for the dimensionless stiffness modulus and magnetic fields, because using larger values leads to obtaining smaller values for the vibration amplitude of transversal displacements $\overline{w}_1(\xi,\tau)=\overline{w}_1(0.5,\tau)$ and $\overline{w}_2(\xi,\tau)=\overline{w}_2(0.5,\tau)$. The velocity of a moving particle is ν=0,3. Material and geometrical values for material characteristics are used from paper [12]. The novelty of this research in relation to the mentioned paper [12] lies in the analysis of the impact of the amplitude and velocity of moving constant load, stiffness of elastic layer, and ratio of axial forces on the dynamic response of presented nano-system.

The effect of the amplitude of moving load on the dynamic response of the nano-beam 1 and nano-beam 2 of the nano-system is presented in Fig. 2. It can be noticed that with an increase in the amplitude of moving load, dynamic response of nano-beam 1 and nano-beam 2 increases. During that analysis, dimensionless parameter was used of the coupled nano-beam system: nonlocal parameter is *η=0,3*; ratio of axial forces is $\chi=\overline{F}_2/\overline{F}_1=0.5$; stiffness modulus *K=5;* magnetic field *MP=5;* vibration mode shape is *n=1.*

The effect of the velocity of moving load on the dynamic response of the nano-beam 1 and nano-beam 2 of the nano-system is presented in Fig. 3. It can be noticed that with an increase in the velocity of moving load, dynamic response of nano-beam 1 and nano-beam 2 increases. Also, it can be observed that the period of oscillation is shorter at higher velocity of moving external load. During that analysis, they were used dimensionless parameter of the coupled nano-beam system: nonlocal parameter is *η=0,3*; ratio of axial forces is χ=0,5; stiffness modulus *K=5;* magnetic field *MP=5;* amplitude of moving load is *F=0,2*; vibration mode shape is *n=1.*

The effect of ratio axial forces on the dynamic response of the nano-beam 1 and nano-beam 2 of the nano-system is presented in Fig. 4. It can be noticed that with an increase of ratio axial

forces, dynamic response of nano-beam 2 increases (see Fig. 4b). Effect of ratio axial force on the dynamic response of nano-beam 1, there is no impact (see Fig. 4a). During that analysis, dimensionless parameter were used of the coupled nano-beam system: nonlocal parameter is $\eta=0,3$; amplitude of moving load is $F=0,2$; magnetic field $MP=5;$ stiffness modulus $K=5;$ vibration mode shape is $n=1$.

The effect of the stiffness modulus of the Winkler elastic layer on the dynamic response of the nano-beam 1 and nano-beam 2 of the nano-system is presented in Fig. 5. It can be noticed that with an increased stiffness of the Winkler elastic layer, dynamic response of nano-beam 1 decreases (see Fig. 5a). Dynamic response of nano-beam 2 is increased with increased stiffness of the Winkler elastic layer. During that analysis, dimensionless parameter of the coupled nano-beam system was used: nonlocal parameter is $\eta=0,3$; amplitude of moving load is $F=0,2$; magnetic field $MP=5;$ ratio of axial forces is χ=0,5; vibration mode shape is $n=1$.

The effect of the magnetic field on the dynamic response of the nano-beam 1 and nano-beam 2 of the nano-system is presented in Fig. 6. It can be noticed that with an increased magnetic field, dynamic response of nano-beam 1 and nano-beam 2 decreases. During that analysis, dimensionless parameter was used of the coupled nano-beam system: nonlocal parameter is $\eta=0,3$; amplitude of moving load is $F=0,2$; stiffness modulus is $K=5;$ ratio of axial forces is χ=0,5 vibration mode shape is $n=1$.

The presented papers shows the possibility to control vibration amplitudes in a certain range by changing only the axial magnetic field parameter without changing any other physical parameter of the nano-system. Also, this ability provides us with a great practical application of such systems in dynamic absorbers, nano-resonators and nano-actuator devices.

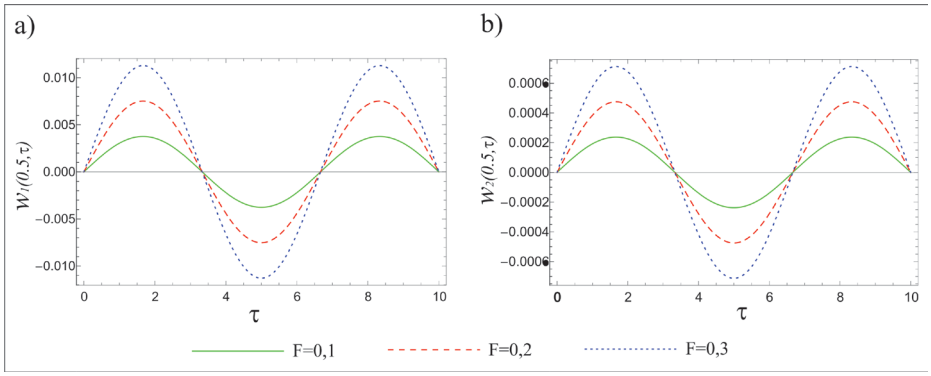

Fig.2. The effect of the amplitude of moving load on the dynamic response a) displacement of nano-beam 1 b) displacement of nano-beam 2

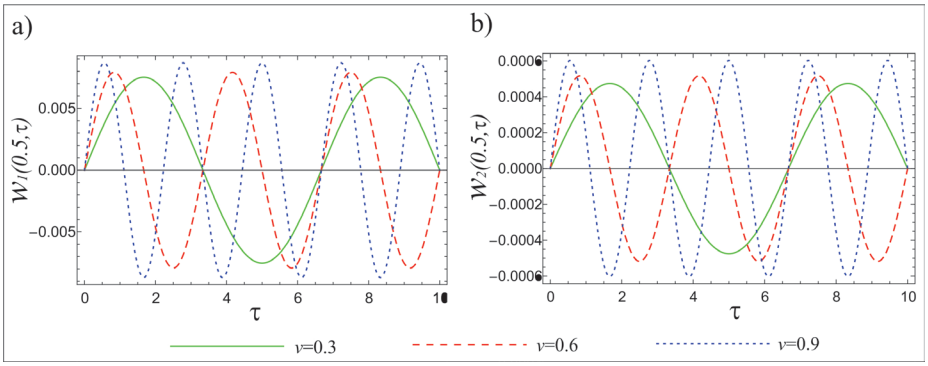

Fig. 3. The effect of the velocity of moving load on the dynamic response a) displacement of nano-beam 1 b) displacement of nano-beam 2

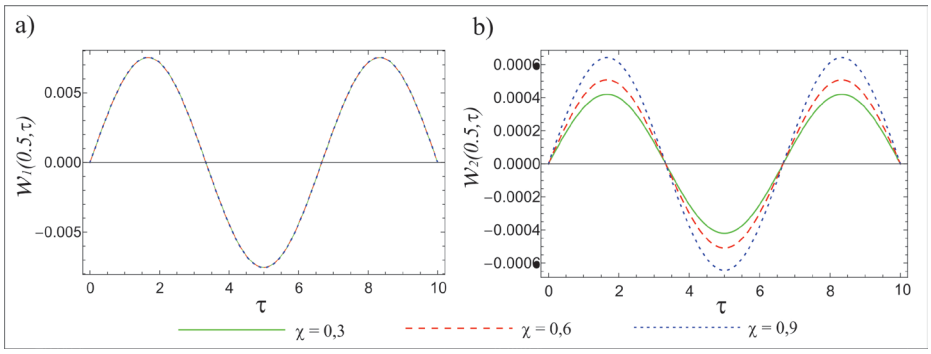

Fig.4. The effect of the ratio axial forces on the dynamic response a) displacement of nano-beam 1 b) displacement of nano-beam 2

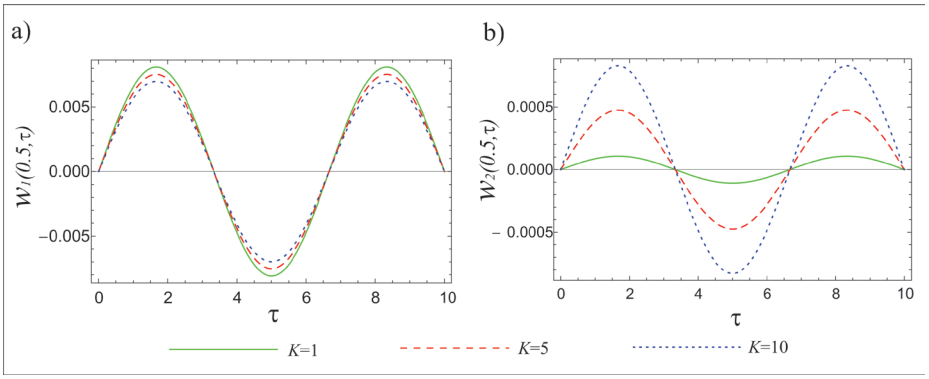

Fig.5. The effect of the stiffness of elastic layer on the dynamic response a) displacement of nano-beam 1 b) displacement of nano-beam 2

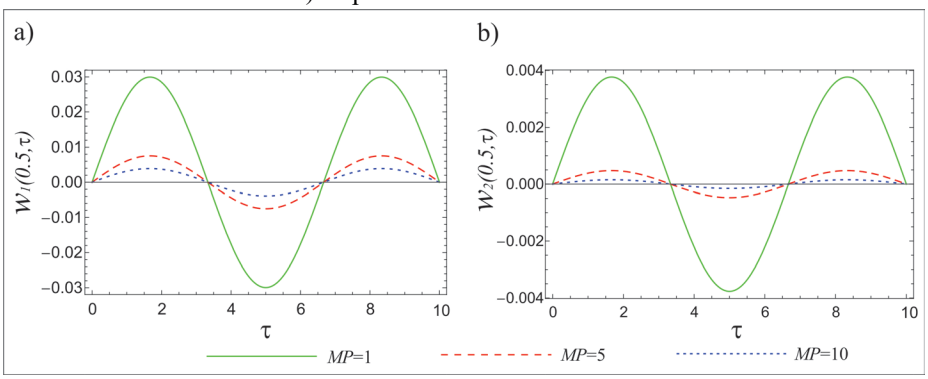

Fig.6. The effect of the magnetic field on the dynamic response a) displacement of nano-beam 1 b) displacement of nano-beam 2

5. Conclusions

This paper aimed to investigate the damped forced vibration of presented nano-system (elastically connected two nano-beams) subjected to external moving load, and axial compressive load and axial magnetic field. The influences of nano-scale were evaluated by the help of Eringen nonlocal theory. Euler-Bernoulli beam theory was used combining with Eringen nonlocal theory to derive the governing equations of motion.

Effects of the axial magnetic field, ratio axial external forces, amplitude, and velocity of moving external nanoparticle and stiffness coefficient of the elastic medium on the forced dynamic behaviour of nano-system are discussed in this paper. According to the numerical results of the present paper, some notable points could be expressed as follows:

- Increasing amplitude and velocity of moving load leads to the increase of transverse response of forced vibration nano-beam 1 and nano beam 2.
- Increasing velocity of moving load the period of oscillation is shorter.
- Increasing ratio axial compressive load leads to the increase of transverse response of forced vibration nano beam 2. No influence was observed on the transverse response of nano-beam 1.
- Increasing stiffness of the Winkler elastic layer leads to the decrease in transverse response of nano beam 1 and the increase in transverse response of forced vibration of nano beam 2.
- Increasing axial magnetic field leads to decrease transverse response of forced vibration of nano beam 1 and nano-beam 2.

The results obtained in this paper can be used for the development of nano-electromechanical devices, where engineers have a better insight into the behaviour of here presented nano-system, under the influence of the considered parameters.

Acknowledgments: This research was financially supported by the Ministry of Science, Technological Development and Innovation of the Republic of Serbia (Contract No. 451-03-47/2023-01/200109).

References:

[1] Reich, S., Thomsen, C., Maultzsch, J., *Carbon nanotubes: basic concepts and physical properties*. John Wiley & Sons, 2008.
[2] Roy, S., Gao, Z., *Nanostructure-based electrical biosensors*, Nano Today, Vol. 4(4), 318-334. 2009.
[3] Garg, A., H. D. Chalak, M. O. Belarbi, A. M. Zenkour, R. Sahoo., *Estimation of carbon nanotubes and their applications as reinforcing composite materials–an engineering review.* Composite Structures 272, 114234, 2021.
[4] Bezzon, V. D., Montanheiro, T. L., de Menezes, B. R., Ribas, R. G., Righetti, V. A., Rodrigues, K. F., Thim, G. P., *Carbon nanostructure-based sensors: a brief review on recent advances*. Advances in Materials Science and Engineering, Article ID 4293073, *2019*.
[5] Eringen, A. C., Edelen, D. G. B., *On nonlocal elasticity,* International Journal of Engineering Science, Vol. 10(3), 233-248, 1972.
[6] Eringen, A. C., *Nonlocal continuum field theories,* Springer Science & Business Media, 2002.
[7] Malikan M, Nguyen VB, Tornabene F., *Damped forced vibration analysis of single-walled carbon nanotubes resting on viscoelastic foundation in thermal environment using nonlocal strain gradient theory*. Engineering Science and Technology, an International Journal, 21(4):778-86, 2018.
[8] Karličić, D., Murmu T., Cajić M., Kozić P., Adhikari S., *Dynamics of multiple viscoelastic carbon nanotube based nanocomposites with axial magnetic field*. Journal of Applied Physics, 115(23), 234303, 2014.
[9] Murmu, T., McCarthy, M. A., Adhikari, S., *Nonlocal elasticity based magnetic field affected vibration response of double single-walled carbon nanotube systems*. Journal of Applied Physics, 111(11), 113511, 2012.
[10] Şimşek, M., *Nonlocal effects in the forced vibration of an elastically connected double-carbon nanotube system under a moving nanoparticle*. Computational Materials Science, 50(7), 2112-2123, 2011.
[11] Zhang, Y. Q., Lu, Y., & Ma, G. W., *Effect of compressive axial load on forced transverse vibrations of a double-beam system*. International Journal of Mechanical Sciences, 50(2), 299-305., 2008.

[12] Stamenković, M., Karličić, D., Goran, J., Kozić, P., *Nonlocal forced vibration of a double single-walled carbon nanotube system under the influence of an axial magnetic field*. Journal of Mechanics of Materials and Structures, 11(3), 279-307, 2016.
[13] Reddy, J. N., *Energy principles and variational methods in applied mechanics*. John Wiley & Sons, 2002.

FREE VIBRATION ANALYSIS OF FGM PLATES BY USING LAYER WISE DISPLACEMENT MODEL

M. Cetkovic[1]

[1] Department of Engineering Mechanics and Theory of Structures, Faculty of Civil Engineering, University of Belgrade, Bul. Kralja Aleksandra 73, 11000 Belgrade, Serbia
e–mail: cetkovicm@grf.bg.ac.rs

Abstract

In this paper, the free vibration analysis of simply supported functionally graded material (FGM) plate is analyzed. The displacement model based on Generalized Laminate Plate Theory (GLPT) assumes layer wise (LW) linear variation of in–plane displacements, constant transverse displacement, linear strain–displacement relations and linear material properties. The effective material properties of FGMs are assumed to be given by the Voigt's rule of mixture (ROM). The Power law distribution of volume fraction is assumed through the plate thickness. The mathematical model includes the quadratic variation of transverse shear stresses within each mathematical layer of the plate. The principle of virtual displacements (PVD) is used to derive Euler–Lagrange differential equations of motions for free vibration problem. The Closed form solution is derived following the Navier's technique and solving the eigenvalue problem. An original MATLAB computer program is coded for the numerical solution. The results reveal that the effects of side–to–thickness ratio, power–low index and material properties have significant effect on free vibration frequencies of FGM plates.

Keywords: Free vibration, FGM plate, LW Theory, Navier solution, MATLAB program.

1. Introduction

Functionally graded materials (FGM) were initially developed in Japan in the 1980s for thermal insulation purposes during the space plane project [1]. After that, the improvement of the material properties of FGM have extended their applications towards the biomedical, aerospace and automotive, bullet–proof and defence industries [2]. The initially assumed concept of FGM was the mixing of two materials, usually metal (ductile phase) and ceramic (brittle phase), in order to obtain the gradual variation of material properties. These material properties, often called the effective material properties, despite of their complex heterogeneous microstructure, are mathematically defined by specific homogenization scheme. The homogenization scheme includes different material models, such as Power law model (P─FGM), Exponential model (E─FGM), Sigmoid law model (S─FGM), Mori–Tanaka scheme etc. When the appropriate homogenization scheme is adopted, the mathematical formulation, numerical solution, and finally the behaviour of FGM structural components under various loading conditions may be found.

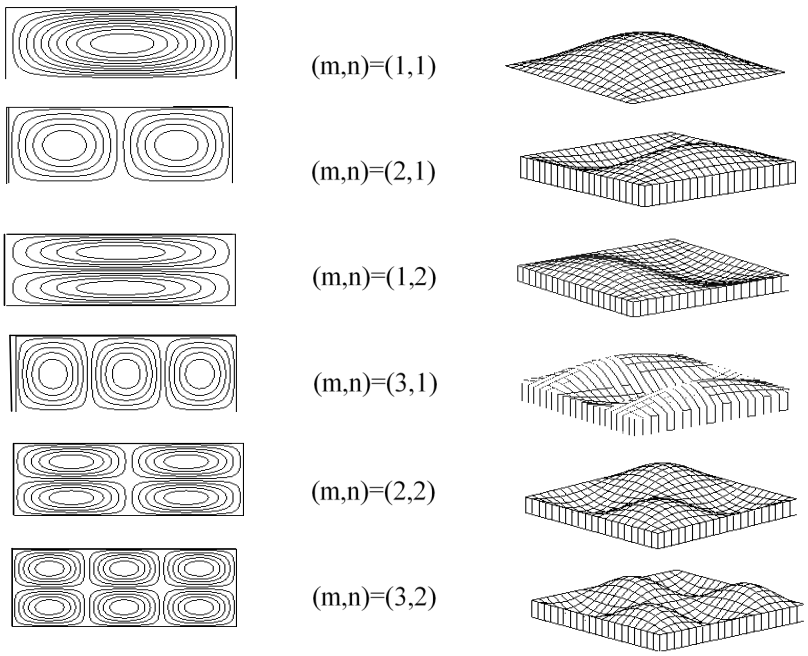

Fig. 1. The contour lines and mode shapes for simply supported rectangular plate

Among the critical loading conditions, important for the safe design of FGM structures is the failure due to vibrations. The vibrations may be initiated from the external source, or by initial disturbance, when no external force is applied. The first one are the forced vibrations, and the second one are the free vibrations. Both vibrations may be damped or undamped, linear or nonlinear [3]. In this paper linear free vibrations of P─FGM plates are analysed.

Mathematical models for free vibration analysis of FGM plates are formulated using either 3D theory of elasticity, Equivalent Single Layer Theories (ESL), and more recently Carrera's Unified Formulation (CUF). Since there are limited number of 3D elasticity solutions, the most literature regarding free vibrations of FGM plates are based on ESL theories, which are Classical Plate Theory (CPT), First–order Shear Deformation Theory (FSDT) and Higher–order Shear Deformation Theory (HSDT).

Batra and Vel presented 3D elasticity solution for free and forced vibration analysis of simply supported P─FGM sandwich plates [4]. The three displacement componenets are expanded by a series of Chebyshev polynomials multiplied by appropriate functions to satisfy the essential boundary conditions. The governing steady state coupled ordinary differential equations are solved by employing the power series method. The parametric study including the volume faction index, layer thickness ratio and aspect ratio is performed. It is observed that for thick FGM plates, there are significant differences between the exact solution and results obtained from CPT theory, even when the transverse shear and the transverse normal stresses are computed by integrating the 3D elasticity equations. However, the results from FSDT and HSDT are shown the good agreement with exact solution.

Since there are limited number of 3D elasticity solutions for FGM plates, and considerable computational cost is needed, an ESL theories are used. Abrate [6] used CPT to analyze free vibrations of P─FGM plates. He showed that by selecting an appropriate reference plane, the uncoupled governing equations may be obtained. As a consequence, the FGM plate will behave like homogeneous isotropic plate. Chen et al. [7] studied linear and nonlinear free vibrations frequencies of an initially stressed P─FGM plate with initial stresses and initial geometrical imperfections. The perturbation technique is used to derive the nonlinear governing equations using the Galerkin method. The governing equations are solved by the Runge–Kutta method. It is shown that linear and nonlinear vibration frequency of the FGM plate increases with the volume fraction

of ceramic. Since, CLPT neglects transverse shear deformation it becomes inadequate for the analysis of moderately thick to thick plates. In these cases, FSDT which assumes constant transverse shear strains, should be adopted. Zhao et al. [8] presented free vibration analysis of P─FGM plates using FSDT and the element–free kp–Ritz method. It is found that significant influence on the frequency has volume fraction exponent that ranges between 0 and 5. Natarajan et al. [9] used FSDT to study static bending, free vibration, and mechanical and thermal buckling behaviour of FGM plates. The effective properties of the FGM plates are computed using the rule of mixtures or employing the Mori–Tanaka homogenization scheme. The cell–based smoothed finite element method with discrete shear gap technique is employed to find the numerical solution of governing equations. The effects of material gradient index n, skewness of the plate ψ, the plate aspect ratio a/b, the plate thickness a/h, and boundary conditions on the global response, are numerically presented. In FSDT the shear correction factor is not easy to accurately define and HSDT should be adopted. Matsunaga [10] studied natural frequencies and buckling stresses of P─FGM plates using HSDT with power series expansions of displacement components, subjected to in–plane stresses. The fundamental set of equations are derived through Hamilton's principle. The governing equations are solved using closed form Navier solution. It is noticed that the critical buckling stresses for thick plates occur at higher displacement modes as in the isotropic case. Jha et al. [11] presented free vibration response of P─FGM and E─FGM rectangular simply supported plates based on HSDT. The equations of motion are derived using Hamilton's principle, while numerical solutions are obtained using Navier technique and are incorporated into a MATLAB computer program. It is shown that natural frequency decreases with increase of the metal percentage of FGM. This is due to the fact that the Young's modulus of ceramic is higher than metal. For the same value of power low index, the natural frequency increases for the higher modes. Also as a/h is increased, the plates become thin, more flexible thus giving the decrease of the natural frequencies. Gupta et al. [12] used HSDT for free vibration of geometrically imperfect P─FGM plates. Mori–Tanaka and Voigt micromechanics models are employed to determine the effective material properties of the plate. It is found that the proposed theory can accurately predict the free vibration responses of functionally graded ceramic–metal plates. In wish to obtain generalized expression, Carrera proposed so called Carrera's Unified Formulation (CUF). The CUF enables the formulation of a large variety of 2D and quasi–3D hierarchical models using unified approach. The unified approach assumes that the variational statement and governing differential equations are given in terms of fundamental nuclei, which are mathematically and formally independent from the expansion orders used in the displacement field and from the kinematic description used such as ESL or LW theories. Cinefra et al. [13] used Carrera's Unified Formulation to study free vibration analysis of P─FGM plate. PVD is used to derive governing differential equation and are solved using the Navier's closed form technique. The obtained results are in good agreement with the reference solutions. Also, the analysis is showen that HSDT are necessary to provide an adequate accuracy for thick plates, while CPT gives erroneous results, especially for high wave numbers and high–order frequencies.

In order to fulfill the lack of free vibration solutions based on LW plate theories in the literature, in this paper an analytical solution for free vibrations of P─FGM plates using Reddy's LW theory [14] is formulated. After establishing the accuracy of the present LW model for linear and geometrically nonlinear bending, vibration and buckling analysis of perfect and imperfect laminated composite and sandwich plates subjected to thermo–mechanical load in the authors previous papers [15–20], in this paper free vibration analysis of FGM plates is further investigated. The mathematical model assumes layer wise variation of in–plane displacements and constant transverse displacement through the plate thickness, linear strain–displacement relations and linear mechanical material properties. The material properties of FGM plates are assumed to be constant in xy–plane and vary through the thickness by a power law function in terms of the volume fraction of the constituents. The effective materials properties are given by the rule of mixture. The governing Euler–Lagrange differential equations of free vibration problem are derived using

Principle of virtual displacements (PVD). Euler–Lagrange differential equations of motions are solved using Navier's technique. The original MATLAB program is coded and used to study the effects of side to thickness ratio, power law index and material properties on free vibration frequencies. The accuracy of the numerical model is verified by comparison with the available results from the literature.

2. Theoretical Formulation

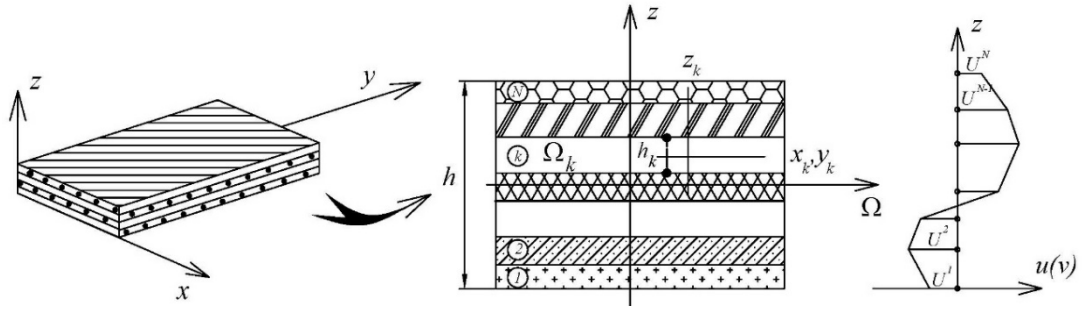

Fig. 2. Plate geometry and LW in–plane displacement field

A LW plate model is composed of n layers. It is assumed that 1) layers are perfectly bonded together, 2) material of each layer is linearly elastic, 3) strains are small, 4) each layer is of uniform thickness, 5) inextensibility of normal is imposed, Figure 2.

2.1 Displacement field

The displacements components (u_1, u_2, u_3) at a point (x, y, z) of plate are expressed as [14]:

$$\begin{aligned} u_1(x,y,z) &= u(x,y) + \sum_{I=1}^{N} U^I(x,y)\cdot\Phi^I(z) \\ u_2(x,y,z) &= v(x,y) + \sum_{I=1}^{N} V^I(x,y)\cdot\Phi^I(z) \\ u_3(x,y,z) &= w(x,y) \end{aligned} \tag{1}$$

where (u, v, w) are displacements of a point $(x, y, 0)$ on the reference plane, functions $\Phi^I(z)$ are 1D linear Lagrange interpolation functions of thickness coordinates, while (U^I, V^I) are the values of (u_1, u_2) at the I–th plane, Fig. 2.

2.2 Strain–displacement relations

The strains associated with the displacement field (1) are given using linear strain–displacement relations:

$$\begin{aligned} \varepsilon_{xx} &= \frac{\partial u}{\partial x} + \sum_{I=1}^{N} \frac{\partial U^I}{\partial x}\Phi^I \\ \varepsilon_{yy} &= \frac{\partial v}{\partial y} + \sum_{I=1}^{N} \frac{\partial V^I}{\partial y}\Phi^I \\ \gamma_{xy} &= \frac{\partial u}{\partial y} + \frac{\partial v}{\partial x} + \sum_{I=1}^{N} \left(\frac{\partial U^I}{\partial y} + \frac{\partial V^I}{\partial x} \right)\Phi^I \end{aligned}$$

$$\gamma_{xz} = \sum_{I=1}^{N} U^I \frac{d\Phi^I}{dz} + \frac{\partial w}{\partial x} \qquad (2)$$
$$\gamma_{yz} = \sum_{I=1}^{N} V^I \frac{d\Phi^I}{dz} + \frac{\partial w}{\partial y}$$

2.3 Constitutive equations

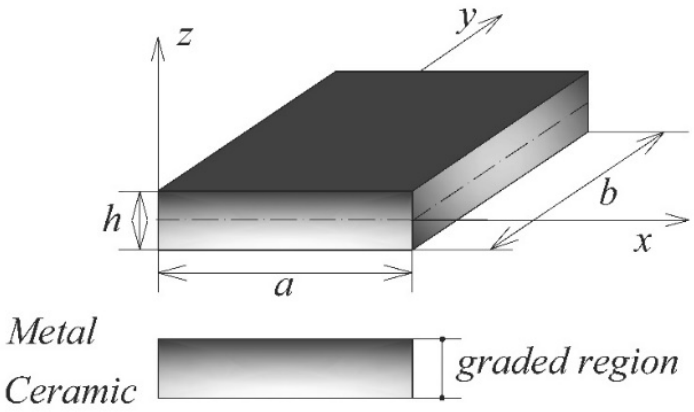

Fig. 3. Geometry and material gladiation of FGM plate

The plate is made from a mixture of ceramic and metal Figure 3, where the rule of mixture is defined as:

$$P_e = V_m + (P_c - P_m) V_c(z) \qquad (3)$$

The P_e denotes the effective material properties of FGM plate, such as Young's modulus E and mass density ρ, while Poisson's coefficient ν is assumed to be constant. The subscripts c and m denote the ceramic and metal, corresponding the material property of the lower and upper surface of the plate, respectively. The V_c is volume fraction of ceramic. The volume fraction is given by the power low distribution, Figure 4 in the thickness direction as:

$$V_c(z) = \left(\frac{z}{h} + \frac{1}{2}\right)^n \qquad (4)$$

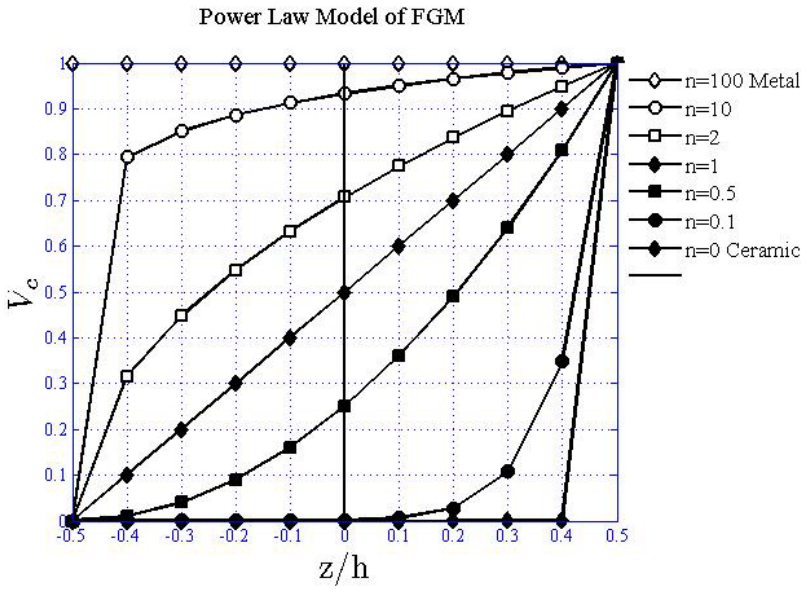

Fig. 4. Volume fraction V_c distribution along the plate thickness for different values of the volume fraction index n

Where n denotes the power low index by which the gradation of the constituents are controlled and may take the values $[0,\infty]$. When the volume fraction exponent is 0 plate is fully made of ceramic, and when the volume fraction exponent is 1 the variation of the volume fraction is linear.

A linear elastic material behavior is considered. The stress–strain relations are given by the generalized Hook's law as:

$$\begin{Bmatrix}\sigma_{xx}\\ \sigma_{yy}\\ \tau_{xy}\\ \tau_{xz}\\ \tau_{yz}\end{Bmatrix}^{(k)} = \begin{bmatrix}Q_{11} & Q_{12} & Q_{13} & 0 & 0\\ Q_{12} & Q_{22} & Q_{23} & 0 & 0\\ Q_{13} & Q_{23} & Q_{33} & 0 & 0\\ 0 & 0 & 0 & Q_{44} & 0\\ 0 & 0 & 0 & 0 & Q_{55}\end{bmatrix}^{(k)} \times \left(\begin{Bmatrix}\varepsilon_{xx}\\ \varepsilon_{yy}\\ \gamma_{xy}\\ \gamma_{xz}\\ \gamma_{yz}\end{Bmatrix}^{(k)}\right) \tag{5}$$

where Q_{ij} are elastic stiffness of FGM plate, given as:

$$Q_{11} = Q_{11} = \frac{(1-\nu)}{(1-2\nu)(1+\nu)}E(z), Q_{12} = Q_{13} = Q_{23} = \frac{1}{(1-2\nu)(1+\nu)}E(z)$$

$$Q_{33} = Q_{44} = Q_{55} = \frac{1}{2(1+\nu)}E(z) \tag{6}$$

2.4 Governing equations and boundary conditions

The governing Euler–Lagrange equations of motion, defining free vibration of FGM plates are given in the following form:

$$
\begin{aligned}
N_{xx,x} + N_{xy,y} &= I_0 \ddot{u} + \sum_{J=1}^{N} I^J \ddot{U}^J \\
N_{xy,x} + N_{yy,y} &= I_0 \ddot{v} + \sum_{J=1}^{N} I^J \ddot{V}^J \\
Q_{x,x} + Q_{y,y} &= I_0 \ddot{w} \\
N^I_{xx,x} + N^I_{xy,y} - Q^I_{xz} &= I^I \ddot{u} + \sum_{J=1}^{N} I^{IJ} \ddot{U}^J \\
N^I_{xy,x} + N^I_{yy,y} - Q^I_{yz} &= I^I \ddot{v} + \sum_{J=1}^{N} I^{IJ} \ddot{V}^J
\end{aligned}
\tag{7}
$$

Where $I_0 = \int_{-h/2}^{h/2} \rho(z)\, dz, \quad I^I = \int_{-h/2}^{h/2} \rho(z)\, \Phi^I dz, \quad I^{IJ} = \int_{-h/2}^{h/2} \rho(z)\, \Phi^I \Phi^J dz$, and ρ is mass density, while appropriate force and displacement boundary conditions are:

$$
\left\{N_{nn}\ N_{ns}\ Q_n\ N^I_{nn}\ N^I_{ns}\right\} = \left\{N^*{}_{nn}\ N^*{}_{ns}\ Q^*{}_n\ N^{*I}_{nn}\ N^{*I}_{ns}\right\}, \left\{u_n\ u_s\ w\ U^I_n\ V^I_n\right\} = \left\{u^*{}_n\ u^*{}_s\ w^*\ U^{*I}_n\ V^{*I}_n\right\} \tag{8}
$$

3. Analytical solution

Navier's solution of Euler–Lagrange equilibrium equations is derived for rectangular plates *axb* with the following simply supported boundary conditions:

$$
\begin{aligned}
v = w = V^I = N_{xx} = N^I_{xx} = 0 \quad &\text{at} \quad x = 0, a \\
u = w = U^I = N_{yy} = N^I_{yy} = 0 \quad &\text{at} \quad y = 0, b
\end{aligned}
\tag{9}
$$

The displacement field which satisfies the boundary conditions (9) and Euler–Lagrange equations of motions (7), is assumed in the form:

$$
\begin{aligned}
\left(u(x,y); U^I(x,y)\right) &= \sum_{m=1}^{\infty}\sum_{n=1}^{\infty} \left(u_{mn}; U^I{}_{mn}\right) \cdot e^{i\omega_{mn}t} \cdot \cos\frac{m\pi}{a}x \cdot \sin\frac{n\pi}{b}y \\
\left(v(x,y); V^I(x,y)\right) &= \sum_{m=1}^{\infty}\sum_{n=1}^{\infty} \left(v_{mn}; V^I{}_{mn}\right) \cdot e^{i\omega_{mn}t} \cdot \sin\frac{m\pi}{a}x \cdot \cos\frac{n\pi}{b}y \\
w(x,y) &= \sum_{m=1}^{\infty}\sum_{n=1}^{\infty} W_{mn} \cdot e^{i\omega_{mn}t} \cdot \sin\frac{m\pi}{a}x \cdot \sin\frac{n\pi}{b}y
\end{aligned}
\tag{10}
$$

Substituting displacement field (10) into the governing equations of motions (7) the governing free vibration equations of FGM plates are obtained:

$$
\left([\mathbf{K}] - \omega^2_{mn} [\mathbf{M}] \right) \{ \Delta \} = \{\mathbf{0}\} \tag{11}
$$

For each choice of (m,n) the free vibration frequency or eigenvalues ω_{mn} is obtained. The smallest of all ω_{mn} not equal to zero is the fundamental frequency ω^{cr}_{mn}. The vector of free vibration mode shapes is then $\{\Delta\}^T = \left\{X_{mn}, Y_{mn}, W_{mn}, U^I_{mn}, V^I_{mn}\right\}$, while $[\mathbf{K}]$ and $[\mathbf{M}]$ are given in [16].

4. Numerical results and discussion

Using previously derived analytical solutions, an original computer program was coded using MATLAB programming language, for free vibration of simply supported FGM plates. The parametric effect of side to thickness ratio b/h, power law index n and material properties on fundamental frequency are analyzed.

Example 1: The first example is the FGM ($Ti-6Al-4V\ /\ Al_2O_3$) simply supported plate made of following material properties:

Metal ($Ti-6Al-4V$): $E_m = 70\ GPa, \quad \nu = 0.3, \quad \rho_m = 4429\ kg/m^3$

Ceramic (Al_2O_3): $E_c = 380\ GPa, \quad \nu = 0.3 \quad \rho_c = 2370\ kg/m$

The fundamental frequency is presented in nondimensional form:

$$\overline{\omega} = \omega_{cr}\sqrt{\frac{12(1-\nu^2)\rho_c a^2 b^2}{\pi^4 E_c h^2}}$$

		b/h					
Theory	n	5	10	20	30	50	100
HSDT [12]	0	1.6999	1.9391	2.0053	2.0202	2.0295	2.0343
Present LW		1.6230	2.2801	2.3342	2.3458	2.3528	2.3565
HSDT [12]	1	1.2592	1.4248	1.4706	1.4809	1.4873	1.4906
Present LW		1.3524	1.4801	1.5146	1.5221	1.5266	1.5289
HSDT [12]	2	1.1370	1.2935	1.3375	1.3474	1.3536	1.3567
Present LW		1.2104	1.3131	1.3446	1.3514	1.3555	1.3576
HSDT [12]	5	1.0312	1.1922	1.2387	1.2491	1.2557	1.2591
Present LW		1.0919	1.1897	1.2200	1.2266	1.2305	1.2326
HSDT [12]	10	0.9760	1.1306	1.1752	1.1852	1.1916	1.1949
Present LW		1.0276	1.1207	1.1497	1.1559	1.1597	1.1617
HSDT [12]	100	0.8577	0.9708	1.0151	1.0229	1.0277	1.0302
Present LW		0.9117	0.9869	1.0101	1.0151	1.0182	1.0197

Table 1. Comparison of nondimensional fundamental frequency $\overline{\omega}$ of simply supported $Ti-6Al-4V\ /\ Al_2O_3$ plate for various power low index n and side to thickness ratio b/h

Table 1 shows that the present LW solution is in close agreement with HSDT [12] solution, for all thickness ratios. It is shown that frequency parameter decreases with the increase of volume fraction index, or power low index. This is due to the fact that the larger power low index means the smaller the ceramic phase and the reduced stiffness. Also, as noticed by Gupta et al. [12] the considerable rise in the frequency parameter is up to b/h=30, after that no significant change may be observed.

Example 2: The second example is the FGM ($Al\ /\ Al_2O_3$) simply supported plate made of following material properties:

The FGM (Al / Al_2O_3) plate is made of following material properties:

Metal (Al): $E_m = 70\ GPa, \quad \nu = 0.3, \quad \rho_m = 2707\ kg/m^3$

Ceramic (Al_2O_3): $E_c = 327.27\ GPa, \quad \nu = 0.3, \quad \rho_c = 2370\ kg/m^3$

In Figure 5 the close agreement of present LW solution with HSDT [12] solution for all power low indexes and side to thickness ratios a/h. As observed from the previous example, the fundamental frequency parameter decreases with the increase of power low index and side to thickness ratio a/h.

The fundamental frequency is presented in nondimensional form: $\bar{\bar{\omega}} = \omega_{cr} h \sqrt{\frac{\rho_c}{E_c}}$

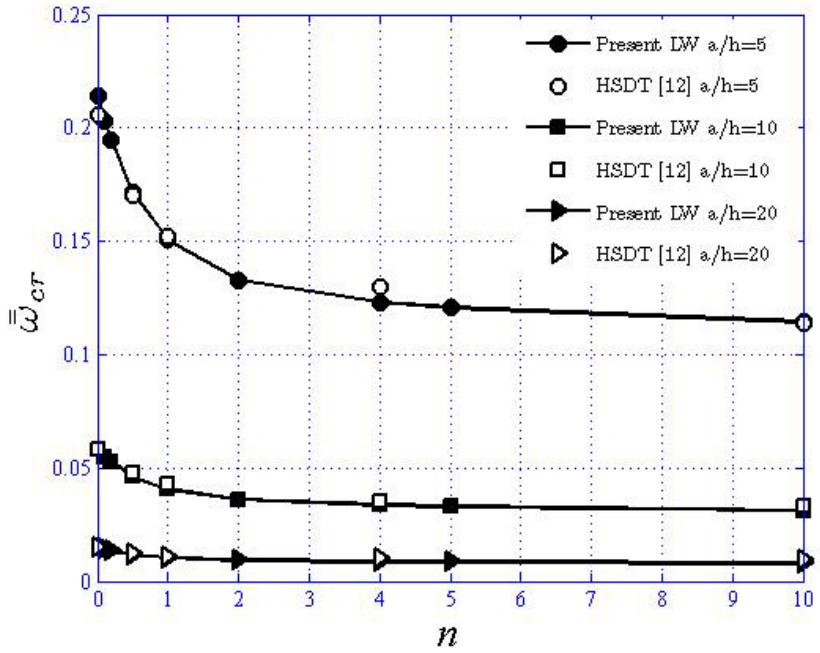

Fig. 5. Comparison the effects of power low index n and side to thickness ratio a/h on fundamental frequency $\bar{\bar{\omega}}$ for simply supported Al / Al_2O_3 plate

5. Conclusion

In this paper, the free vibration analysis of FGM plates is formulated using LW displacement model [14]. The principle of virtual displacement (PVD) is used to derive Euler–Lagrange differential equation of motion. The governing differential equations are solved following the Navier's technique and solving the eigen value problem. An original MATLAB program is coded for numerical solution and used to analyze the effects of side to thickness ratio, power low index and material properties on free vibration frequency of simply supported FGM plate. The results have shown that the proposed model gives acceptable results when compared to HSDT [12] solutions from the literature and may serve to verify other numerical solutions, such as finite element one.

Acknowledgment: The author is thankful for the financial support received by the Ministry for Education, Science and Technology, Republic of Serbia, grant number 200092.

References:

[1] Knoppers G. E, Gunnienk J. W, Hout J, Vliet W. *The Reality of Functionally Graded Material Products* (In Intelligent Production Machines and Systems–First I PROMS Virtual Conference: Proceedings and CD–ROM set), (Elsevier), 467, 2005.

[2] Suresh S, Mortensen A. *Fundamentals of functionally graded materials* (Materials Today). London: IOM Communications Ltd. ISBN: 1–86125–063–0, 1998.

[3] Chakraverty S, Pradhan K.K. *Vibration of functionally graded beams and plates*. Elsevier, ISBN: 978–0–12–804228–1, 2016.

[4] Vel S. S, Batra R.C. *Three–vDimensional Exact Solution for the Vibration of Functionally Graded Rectangular Plates.* Journal of Sound and Vibration, Vol. 272(3–5), 703–730, 2004.

[5] Li Q, Iu V. P, Kou K.P. T*hree–dimensional vibration analysis of functionally graded material sandwich plates*. Journal of Sound and Vibration. Vol. 311, 498–515, 2008.

[6] Abrate S. *Functionally graded plates behave like homogeneous plates*. Composites: Part B, Vol (39), 151–158, 2008.

[7] Chen C. S, Tan A. H. *Imperfection sensitivity in the nonlinear vibration of initially stresses functionally graded plates*. Composite Structures. Vol. 78, 529–536, 2007.

[8] Zhao X, Lee Y.Y, Liew K.M. *Free vibration analysis of functionally graded plates using the element–free kp–Ritz method*. Journal of Sound and Vibration. Vol. 319, 918–939, 2009.

[9] Natarajan S, Ferreira A. J. M, Bordas S, Carrera E, Cinefra M, Zenkour A.M. *Analysis of Functionally Graded Material Plates Using Triangular Elements with Cell–Based Smoothed Discrete Shear Gap Method*. Mathematical Problems in Engineering. Vol. 2014, ID 247932, 1–13, 2014.

[10] Matsunaga H. *Free vibration and stability of functionally graded plates according to a 2D higher–order deformation theory*. Composite Structures. Vol. 82, 499–512, 2008.

[11] Jha D.K, Kant T, Singh R.K. *Free vibration response of functionally graded thick plates with shear and normal deformations effects*. Composite Structures. Vol. 96, 799–823, 2013.

[12] Gupta A, Talha M. *An assessment of a non–polynomial based higher order shear and normal deformation theory for vibration response of gradient plates with initial geometric imperfections*. Composites Part B. Vol. 107, 141–161, 2016.

[13] Cinefra M, Soave M. *Accurate Vibration Analysis of Multilayered Plates Made of Functionally Graded Materials*. Mechanics of Advanced Materials and Structures. Vol. 18, 3–13, 2011.

[14] Reddy J.N., Barbero E.J., Teply J.L., *A plate bending element based on a generalized laminated plate theory,* International Journal for Numerical Methods in Engineering, Vol. 28, 2275–2292, 1989.

[15] Cetkovic M. Vuksanovic Đ. *Bending, Free Vibrations and Buckling of Laminated Composite and Sandwich Plates Using a Layerwise Displacement Model*. Composite Structures. Vol. 88(2), 219–227, 2009.

[16] Cetkovic M. *Nonlinear Behavior of Laminated Composite Plates*. In: PhD Thesis (in Serbian), Faculty of Civil Engineering in Belgrade, Serbia, 2011.

[17] Cetkovic M. Vuksanovic Đ. *Large Deflection Analysis of Laminated Composite Plates using Layerwise Displacement Model*. Structural Engineering and Mechanics. Vol. 40(2), 257–277, 2011.

[18] Cetkovic M. *Thermo–Mechanical Bending of Laminated Composite and Sandwich Plates Using Layerwise Displacement Model*. Composite Structures. Vol. 125, 388–399, 2015.

[19] Cetkovic M. *Thermal Buckling of Laminated Plates Using Layerwise Displacement Model*. Composite Structures. Vol. 142, 238–253, 2016.

[20] Cetkovic M. *Influence of initial geometrical imperfections on thermal stability of laminated composite plates using layer wise finite element*. Composite Structures, Vol. 291, 115547, 2022.

STABILITY ANALYSIS OF FGM PLATES USING LAYER WISE DISPLACEMENT MODEL

M. Cetkovic

Department of Engineering Mechanics and Theory of Structures University of Belgrade, Bul. Kralja Aleksandra 73, 11000 Belgrade, Serbia
e–mail: cetkovicm@grf.bg.ac.rs

Abstract

In this paper, the stability analysis of simply supported functionally graded material (FGM) plate under mechanical in–plane compressive loads is analyzed. The displacement model based on Generalized Laminate Plate Theory (GLPT) assumes piece–wise linear variation of in–plane displacements, constant transverse displacement, non–linear strain–displacement relations (in von Karman sense) and linear material properties. The properties of FGMs are assumed to be constant in xy–plane and vary through thickness by a power law function in terms of volume fraction of the constituents. The mathematical model includes the quadratic variation of transverse shear stresses within each layer of the plate. The principle of virtual displacements (PVD) is used to derive Euler–Lagrange differential equations of linearized buckling problem. Closed form solution is derived following the Navier's technique and solving the eigenvalue problem. The original MATLAB computer program is coded for the numerical solution. The results reveal that the effects of side–to–thickness ratio, power–low index and modulus ratio have significant effect on critical buckling loads of FGM plates.

Keywords: elastic stability, FGM plate, LW Theory, Navier solution, MATLAB program.

1. Introduction

For the present time, different types of composite materials like fibre reinforced composite, particulate composites, and metal matrix composites (MMC) have been used in different applications, from automotive, aerospace, and biomedical to civil engineering structures. A particulate type of MMC are FGM composites, in which the volume fraction of two constituents varies along either of three spatial direction [1, 2]. The two constituent materials are generally metal and ceramic, where metal provides high toughness, while ceramic gives high thermal resistance [3]. The gradation of material properties in FGMs are usually evaluated using specific rule of mixture, giving the continuous change of material properties at microscopic level, and overcoming the disadvantages of traditional composite materials, such as the mismatch of material properties across the layers interfaces [4].

The advanced material properties of FGM components made them suitable for high temperature and high–speed applications. In these applications, severe localized stresses may develop, which at certain level may lead to the buckling failure of structural components [5].

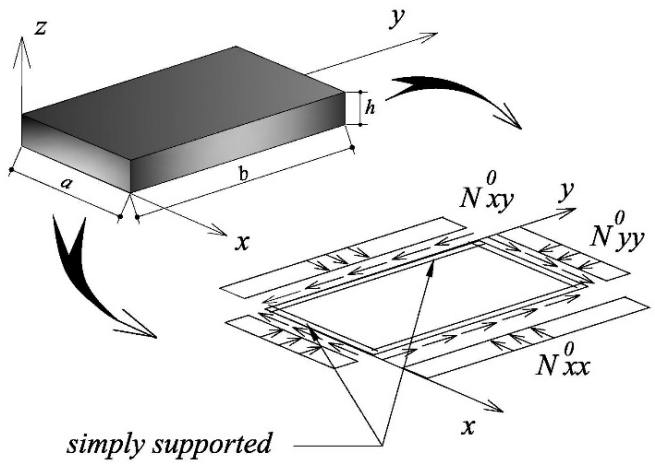

Fig. 1. Buckling of rectangular plate under action of in–plane compressive and shearing loads

Up to date, the buckling failure of structural components is mostly related to laminated composite plates [6–11] using different plate theories (classical plate theories (CPT), first–order shear deformation theories (FSDT) and higher order shear deformation theories (HSDT)), as well as different solution methods: analytical and numerical such as: finite difference method (FDM), finite element method (FEM), boundary element method (BEM), extended finite element method (XFEM), differential quadrature method (DQM) and radial point interpolation method (RPIM). In addition, many studies include buckling with different types of boundary and edge loading conditions [12–14].

Over the last decades, due to the advance properties of functionally graded material over the laminated composite, the demand for buckling analysis of FGM plates subjected to in-plane loads is increased (Figure 1). The mathematical models, as mentioned for laminated composites, are based on either on 3D elasticity theory, Equivalent single layer (ESL) plate theories, or local–global Layer wise (LW) or Zig–Zag theories.

Uymaz et al. [15] presented shear buckling problem of FG plates using the Ritz method based on the 3D linear elasticity plate theory. The effect of material composition, aspect ratio a/b and side to thickness ratio a/h on critical buckling load with different boundary conditions is presented. Hoang et al. [16] used CLPT to analyse buckling and post–buckling behaviors of thin functionally graded plates with and without imperfections, subjected to in–plane compressive, thermal, and combined loads. The Galerkin procedure is used to solve closed form expressions of post–buckling equilibrium path. Song et al. [17] analyzed the buckling and post–buckling analysis of FGM plates under biaxial compression using two–step perturbation technique. The material properties of plates are assumed to be graded along the thickness direction. The equilibrium and compatibility equations are derived by using FSDT and taking into account both geometrical nonlinearity in von Kármán sense and initial geometrical imperfection. Auad et al. [18] also used FSDT to analyze buckling and post–buckling behavior of FGM plates under uniaxial loading using a NURBS–based isogeometric formulation. The geometrically nonlinear effects are considered using the von Kármán theory. The buckling loads decrease with the volume fraction exponent. The nonlinear equilibrium paths confirmed that FGM plates with simply supported boundary conditions do not present bifurcation buckling and display a stable nonlinear behavior similar to imperfect homogeneous and laminated plates. On the other hand, in clamped FGM plates, bifurcation buckling is present, with a slight imperfection sensitivity, which increases with the volume fraction exponent. Kulkarni et al. [19] and Reddy et al. [20] analyzed static and buckling analysis of FGM plate using recently developed non–polynomial HSDT. The solution of the governing differential equations is obtained by adopting Navier–type analytical technique. The parametric study indicated

that the power index plays a vital role in the structural analyses of FGP along with other geometric properties such as aspect ratio and span to thickness ratio.

To fulfil the lack of buckling solutions based on LW plate theories in the literature, in this paper an analytical solution for mechanical buckling of FGM plates using LW theory of Reddy's [21] is formulated. After establishing the accuracy of the present LW model for linear and geometrically nonlinear bending, vibration and buckling analysis of perfect and imperfect laminated composite and sandwich plates subjected to thermo–mechanical load in authors' previous papers [22–27], in this paper mechanical buckling analysis of FGM plates is further investigated. The mathematical model assumes layer wise variation of in–plane displacements and constant transverse displacement through the plate thickness, non–linear strain–displacement relations (in von Karman sense) and linear mechanical material properties. The material properties of FGM plates are assumed to be constant in xy–plane and vary through the thickness by a power law function in terms of volume fraction of the constituents. The effective materials properties are given by the rule of mixture. The governing Euler–Lagrange differential equations of linearized buckling problem are derived using Principle of virtual displacements (PVD). An Euler–Lagrange differential equations are solved using Navier's analytical solution. The original MATLAB program is coded and used to study the effects of side to thickness ratio, modulus ratio and power low index on critical buckling load. The accuracy of the numerical model is verified by comparison with the available results from the literature.

2. Theoretical formulation

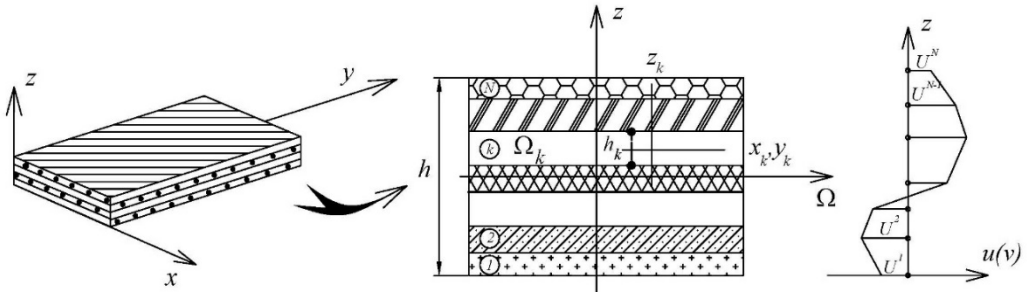

Fig. 2. Plate geometry and LW in–plane displacement field

A LW plate model is composed of n layers. It is assumed that 1) layers are perfectly bonded together, 2) material of each layer is linearly elastic, 3) strains are small, 4) each layer is of uniform thickness and 5) inextensibility of normal is imposed (Figure 2).

2.1 Displacement field

The displacements components (u_1, u_2, u_3) at a point (x, y, z) of plate are expressed as [21]:

$$\begin{aligned} u_1(x,y,z) &= u(x,y) + \sum_{I=1}^{N} U^I(x,y) \cdot \Phi^I(z) \\ u_2(x,y,z) &= v(x,y) + \sum_{I=1}^{N} V^I(x,y) \cdot \Phi^I(z) \\ u_3(x,y,z) &= w(x,y) \end{aligned} \tag{1}$$

where (u, v, w) are displacements of a point $(x, y, 0)$ on the reference plane, functions $\Phi^I(z)$ are 1D linear Lagrange interpolation functions of thickness coordinates, while (U^I, V^I) are the values of (u_1, u_2) at the I–th plane (Fig. 2).

2.2 Strain–displacement relations

The strains associated with the displacement field (1) are given using von Karman's non–linear strain–displacement relations:

$$\begin{aligned}
\varepsilon_{xx} &= \frac{\partial u}{\partial x} + \sum_{I=1}^{N} \frac{\partial U^I}{\partial x} \Phi^I + \frac{1}{2}\left(\frac{\partial w}{\partial x}\right)^2 \\
\varepsilon_{yy} &= \frac{\partial v}{\partial y} + \sum_{I=1}^{N} \frac{\partial V^I}{\partial y} \Phi^I + \frac{1}{2}\left(\frac{\partial w}{\partial y}\right)^2 \\
\gamma_{xy} &= \frac{\partial u}{\partial y} + \frac{\partial v}{\partial x} + \sum_{I=1}^{N} \left(\frac{\partial U^I}{\partial y} + \frac{\partial V^I}{\partial x}\right) \Phi^I + \frac{\partial w}{\partial x}\frac{\partial w}{\partial y} \\
\gamma_{xz} &= \sum_{I=1}^{N} U^I \frac{d\Phi^I}{dz} + \frac{\partial w}{\partial x} \\
\gamma_{yz} &= \sum_{I=1}^{N} V^I \frac{d\Phi^I}{dz} + \frac{\partial w}{\partial y}
\end{aligned} \tag{2}$$

2.3 Constitutive equations

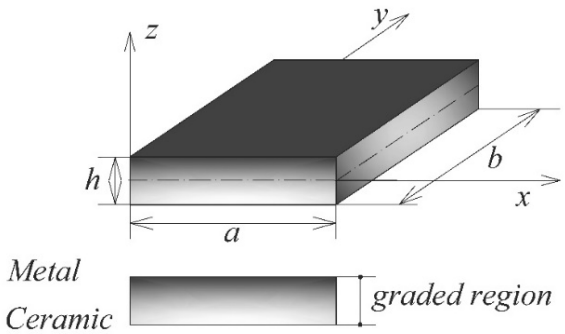

Fig. 3. Geometry and material gladiation of FGM plate

The plate is made from a mixture of ceramic and metal (Figure 3), where the rule of mixture is defined as:

$$P_e = V_m + \left(P_c - P_m\right) V_c\left(z\right) \tag{3}$$

The P_e denotes the effective material properties of FGM plate, such as Young's modulus E while Poisson's coefficient ν is assumed to be constant. The subscripts c and m denote the ceramic and metal, corresponding the material property of the lower and upper surface of the plate, respectively. The V_c is volume fraction of ceramic. The volume fraction is given by the power low distribution (Figure 4) in the thickness direction as:

$$V_c\left(z\right) = \left(\frac{z}{h} + \frac{1}{2}\right)^n \tag{4}$$

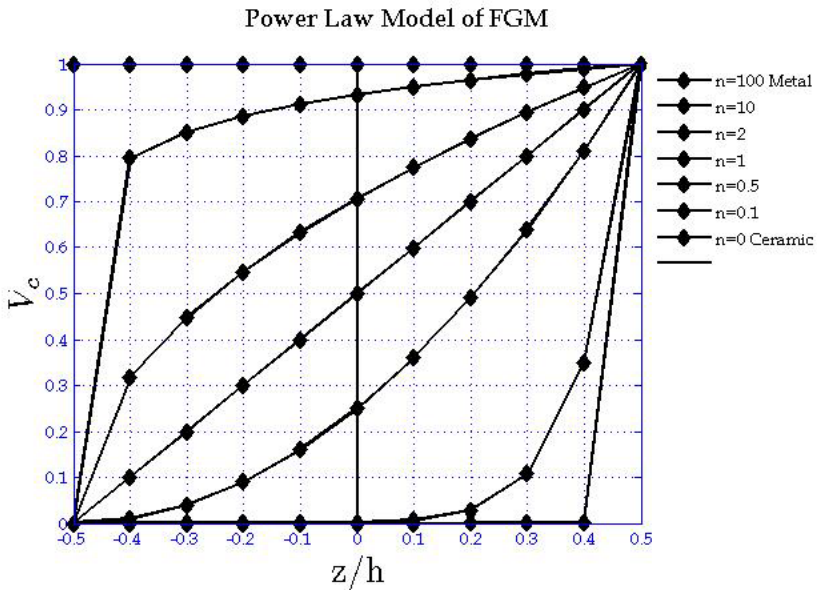

Fig. 4. Volume fraction V_c distribution along the plate thickness for different values of the volume fraction index n

where n denotes the power low index by which the gradation of the constituents is controlled and may take the values $[0, \infty]$. When the volume fraction exponent is 0 plate is fully made of ceramic, and when the volume fraction exponent is 1 the variation of the volume fraction is linear.

A linear elastic material behavior is considered. The stress–strain relations are given by the generalized Hook's law as:

$$\begin{Bmatrix} \sigma_{xx} \\ \sigma_{yy} \\ \tau_{xy} \\ \tau_{xz} \\ \tau_{yz} \end{Bmatrix}^{(k)} = \begin{bmatrix} Q_{11} & Q_{12} & Q_{13} & 0 & 0 \\ Q_{12} & Q_{22} & Q_{23} & 0 & 0 \\ Q_{13} & Q_{23} & Q_{33} & 0 & 0 \\ 0 & 0 & 0 & Q_{44} & 0 \\ 0 & 0 & 0 & 0 & Q_{55} \end{bmatrix}^{(k)} \times \left(\begin{Bmatrix} \varepsilon_{xx} \\ \varepsilon_{yy} \\ \gamma_{xy} \\ \gamma_{xz} \\ \gamma_{yz} \end{Bmatrix}^{(k)} \right) \tag{5}$$

where Q_{ij} are elastic stiffness of FGM plate, given as:

$$Q_{11} = Q_{11} = \frac{(1-\nu)}{(1-2\nu)(1+\nu)} E(z), Q_{12} = Q_{13} = Q_{23} = \frac{1}{(1-2\nu)(1+\nu)} E(z)$$

$$Q_{33} = Q_{44} = Q_{55} = \frac{1}{2(1+\nu)} E(z) \tag{6}$$

2.4 Governing equations and boundary conditions

The governing Euler–Lagrange equilibrium equations, defining thermal buckling of FGM plates are given in the following form:

$$N_{xx,x} + N_{xy,y} = 0$$

$$N_{xy,x} + N_{yy,y} = 0$$

$$Q_{xz,x} + Q_{yz,y} + \eta(w) = 0 \tag{7}$$

$$N^I_{xx,x} + N^I_{xy,y} - Q^I_{xz} = 0$$

$$N^I_{xy,x} + N^I_{yy,y} - Q^I_{yz} = 0$$

where $\eta(w) = \frac{\partial}{\partial x}\left(N^0_{xx}\frac{\partial w}{\partial x} + N^0_{xy}\frac{\partial w}{\partial y}\right) + \frac{\partial}{\partial y}\left(N^0_{yy}\frac{\partial w}{\partial y} + N^0_{xy}\frac{\partial w}{\partial x}\right)$, while appropriate force and displacement boundary conditions are:

$$\left\{N_{nn}\ N_{ns}\ Q_n\ N^I_{nn}\ N^I_{ns}\right\} = \left\{N^*_{nn}\ N^*_{ns}\ Q^*_n\ N^{*I}_{nn}\ N^{*I}_{ns}\right\}, \left\{u_n\ u_s\ w\ U^I_n\ V^I_n\right\} = \left\{u^*_n\ u^*_s\ w^*\ U^{*I}_n\ V^{*I}_n\right\} \tag{8}$$

3. Analytical solution

Navier's solution of Euler–Lagrange equilibrium equations is derived for rectangular plates *axb* with the following simply supported boundary conditions:

$$v = w = V^I = N_{xx} = N^I_{xx} = 0 \quad \text{at} \quad x = 0, a$$
$$u = w = U^I = N_{yy} = N^I_{yy} = 0 \quad \text{at} \quad y = 0, b \tag{9}$$

The displacement field which satisfies the boundary conditions (9) and Euler–Lagrange equilibrium equations (7), is assumed in the form:

$$\left(u(x,y);\, U^I(x,y)\right) = \sum_{m=1}^{\infty}\sum_{n=1}^{\infty}\left(u_{mn};U^I{}_{mn}\right)\cdot cos\frac{m\pi}{a}x\cdot sin\frac{n\pi}{b}y$$
$$\left(v(x,y);\, V^I(x,y)\right) = \sum_{m=1}^{\infty}\sum_{n=1}^{\infty}\left(v_{mn};V^I{}_{mn}\right)\cdot sin\frac{m\pi}{a}x\cdot cos\frac{n\pi}{b}y \tag{10}$$
$$w(x,y) = \sum_{m=1}^{\infty}\sum_{n=1}^{\infty} W_{mn}\cdot sin\frac{m\pi}{a}x\cdot sin\frac{n\pi}{b}y$$

Substituting displacement field (10) into the governing equations (7) the characteristic stability equations for buckling of FGM plates are obtained:

$$\left(\left[\mathbf{K}\right] - \mathrm{N}^{\mathrm{cr}}\left[\mathbf{K}_{\mathrm{G}}\right] \right)\left\{ \mathbf{\Delta} \right\} = \left\{\mathbf{0}\right\} \tag{11}$$

For each choice of (m,n) the characteristic numbers or eigenvalues N_{mn} is obtained. The smallest of all N_{mn} not equal to zero is the critical buckling load N^{cr}_{mn}. The vector of buckling mode shapes is then $\left\{\Delta\right\}^T = \left\{X_{mn}, Y_{mn}, W_{mn}, U^I_{mn}, V^I_{mn}\right\}$ while $\left[\mathbf{K}\right]$ and $\left[\mathbf{K}_{\mathrm{G}}\right]$ are given in [23].

4. Numerical results and discussion

Using previously derived analytical solutions, an original computer program was coded using MATLAB programming language, for buckling of simply supported FGM plate subjected to uniaxial compression. The parametric effect of side to thickness ratio b/h, power law index n and modulus ratio E_m / E_c on critical buckling load are analyzed. The FGM (Al / Al_2O_3) plate is made of following material properties:

Aluminium (Al): $E_m = 70\ GPa, \quad \nu = 0.3$

Alumina (Al_2O_3): $E_c = 380\ GPa, \quad \nu = 0.3$

The critical buckling load is presented in nondimensional form as $\overline{N} = N_{cr} \dfrac{a^2}{E_m h^3}$.

Theory	n	b/h				
		10	20	40	50	100
CPT [20]		17.68	17.68	17.68	17.68	17.68
FSDT [20]	0.1	17.76	17.40	17.62	17.64	17.67
HSDT [20]		16.74	17.41	17.59	17.61	17.64
Present LW		16.91	17.49	17.64	17.66	17.68
CPT [20]		9.78	9.78	9.78	9.78	9.78
FSDT [20]	1	9.33	9.66	9.75	9.76	9.77
HSDT [20]		9.29	9.64	9.73	9.74	9.75
Present LW		9.41	9.69	9.76	9.77	9.78
CPT [20]		5.87	5.87	5.87	5.87	5.87
FSDT [20]	10	5.66	5.78	5.85	5.86	5.87
HSDT [20]		5.42	5.75	5.83	5.84	5.86
Present LW		5.45	5.67	5.72	5.72	5.74

Table 1. Comparison of nondimensional buckling load $\overline{N}$ of simply supported Al / Al_2O_3 subjected to uniaxial compression

Table 1 shows that the present LW solution is in close agreement with HSDT [20] solution, while CPT [20] and FSDT [20] slightly over predicts critical buckling load for all thickness ratios. In addition, CPT is insensible to the variation of plate thickness, for given power low index n. The nondimensional buckling load decreases with increasing power law index n.

Figure 5 shows variation of nondimensional critical buckling load with metal–ceramic modulus ratio, for plates with different power low index. The present results are in good agreement with HSDT [20] results from the literature. It is shown that the nondimensional critical buckling load decreases as the metal–to–ceramic modulus ratio increases, due to the fact that higher values of metal–to–ceramic modulus ratio correspond to high portion of metal. Also, the nondimensional critical buckling load decreases as the power law index increases.

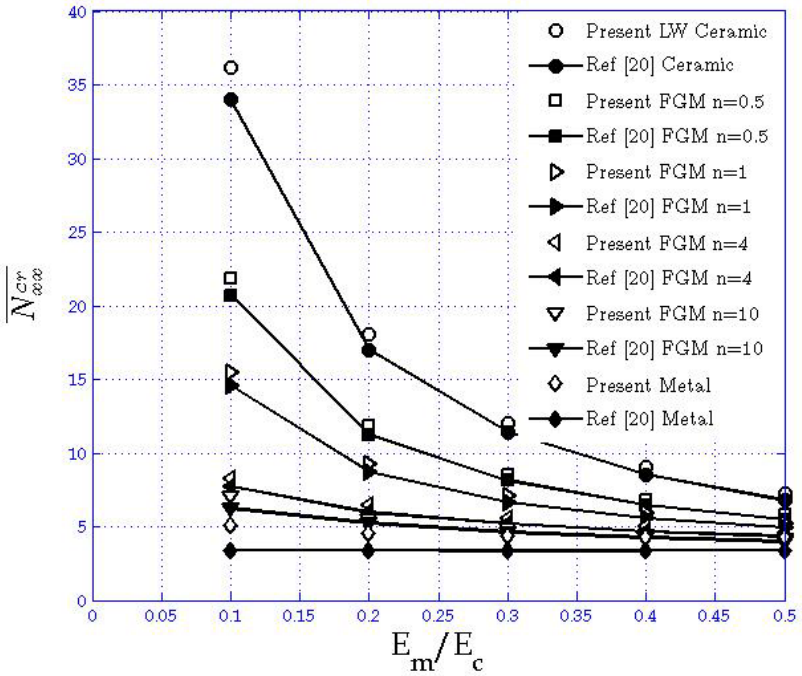

Fig. 5. Effects of modulus ratio E_m / E_c on critical buckling load $\overline{N}$ under uniaxial compression for simply supported Al / Al_2O_3 plate and various power low index n

5. Conclusion

Stability analysis of FGM plates is formulated using LW displacement model [21]. The model assumes LW variation of in–plane displacements, constant transverse displacement, nonlinear strain displacement relations and linear material properties. The effective material properties of ceramic–metal FGM plate are calculated using the rule of mixture and power low distribution of volume fraction through the plate thickness. The closed–form Navier's solution is derived for linearized buckling problem. An original MATLAB program is coded for numerical solution and used to analyze the effects of side to thickness ratio, modulus ratio and power low index on critical buckling load of simply supported FGM plate. The results have shown close agreement with the results from the literature, and may be used as a benchmark for other numerical solutions, such as finite element.

Acknowledgment: The author is thankful for the financial support received by the Ministry of Science, Technological Development and Innovation, Republic of Serbia, grant number 200092.

References:

[1] Chakraverty S, Pradhan KK. *Free vibration of exponential functionally graded rectangular plates in thermal environment with general boundary conditions*. Aerosp Sci Technology, Vol. 36.132–56, 2014.

[2] Lee YY, Zhao Xin, Reddy JN. *Post–buckling analysis of functionally graded plates subject to compressive and thermal loads*. Comput Methods Appl Mech Eng, Vol. 199 (25–28), 1645–53, 2010.

[3] Supen K.S, Anup G. *Influence of porosity distribution on free vibration and buckling analysis of multi–directional functionally graded sandwich plates.* Composite Structures, Vol. 279, 114795, 2022.
[4] Chen C.S, Lin C.Y, Chien R.D. *Thermally induced buckling of functionally graded hybrid composite plates*, International Journal of Mechanical Sciences. Vol. 53, 1–58, 2020.
[5] Balakrishna A, Padmanav D, Singh B.N. *Buckling analysis of porous FGM sandwich plates under various types nonuniform edge compression based on higher order shear deformation theory.* Composite Structures, Vol. 251, 112597, 2020.
[6] Mohammad A.T, *Buckling of the composite laminates under mechanical loads with different layups using different plate theories.* Advanced Composites Letters, Vol. 24 (1), 12–20, 2015.
[7] Reddy JN, Khdeir AA. *Buckling and vibration of laminated composite plates using various plate theories*. AIAA J, Vol. 27(12), 1808–17, 1989.
[8] Matsunaga H. *Vibration and stability of cross–ply laminated cross–ply laminated composite plates according to a global higher order plate theory*. Compos Struct, Vol. 48(4), 231–4, 2000.
[9] Timarci T, Aydogdu M. *Buckling of symmetric cross–ply plates with various boundary conditions*. Compos Struct, Vol. 68(4), 381–9, 2005.
[10] Aydogdu M. *Comparison of various shear deformation theories for bending, buckling, and vibration of rectangular symmetric cross–ply plate with simply supported edges*. J Compos Mater, Vol. 40(23), 2143–55, 2006.
[11] Xiang S, Wang K, Ai Y, Sha Y, Shi H. *Analysis of isotropic, sandwich and laminated plates by a meshless method and various shear deformation theories*. Compos Struct. Vol 91(1), 31–7, 2009.
[12] Metin A, Tolga A. *Buckling of cross–ply composite plates with linearly varying in–plane loads.* Composite Structures. Vol. 183, 221–231, 2018.
[13] Sarat K. P, Ramachandra L.S, *Buckling of rectangular plates with various boundary conditions loaded by non–uniform in–plane loads*. International Journal of Mechanical Sciences. Vol. 52, 819–828, 2010.
[14] Kumar A, Panda S.K, Kumar R. *Buckling behavior of laminated composite skew plates with various*. International Journal of Mechanical Sciences. Vol. 100, 136–144, 2015.
[15] Uymaz B, Aydogdu M, *Three dimensional shear buckling of FG plates with various boundary conditions.* Composite Structures. Vol. 96,670–682, 2013.
[16] Hoang V.T, Nguyen D. D. *Nonlinear analysis of stability for functionally graded plates under mechanical and thermal load.* Vol. 92 (5), 1184–1191, 2010.
[17] Song M, Yang J, Kitipornchai S, Weidong Z. *Buckling and post–buckling of biaxially compressed functionally graded multilayer graphene nanoplatelet–reinforced polymer composite plates.* International Journal of Mechanical Sciences. Vol. 131–132, 345–355, 2017.
[18] Auada S.P, Pracianoa J. S. C, Barrosoa E. S., Sousa J. B. M., E. Parente J. E. *Isogeometric Analysis of FGM Plates*. Materials Today: Proceedings 8, 738–746, 2019.
[19] Kulkarni K, Singh B.N, Maiti D.K. *Analytical solution for bending and buckling analysis of functionally graded plates using inverse trigonometric shear deformation theory*. Composite Structures. Vol. 134, 147–157, 2015.
[20] Reddy B.S, Kumar J.S, Reddy C. E, Reddy V. K. *Buckling Analysis of Functionally Graded Material Plates Using Higher Order Shear Deformation Theory*. Journal of Composites. Article ID 808764, 1–12, 2013.
[21] J.N. Reddy, E.J. Barbero, J.L. Teply, *A plate bending element based on a generalized laminated plate theory,* International Journal for Numerical Methods in Engineering, Vol. 28, 2275–2292, 1989.

[22] Cetkovic M. Vuksanovic Đ. *Bending, Free Vibrations and Buckling of Laminated Composite and Sandwich Plates Using a Layerwise Displacement Model*. Composite Structures. Vol. 88(2), 219–227, 2009.
[23] Cetkovic M. *Nonlinear Behavior of Laminated Composite Plates*. In: PhD Thesis (in Serbian), Faculty of Civil Engineering in Belgrade, Serbia, 2011.
[24] Cetkovic M. Vuksanovic Đ. *Large Deflection Analysis of Laminated Composite Plates using Layerwise Displacement Model*. Structural Engineering and Mechanics. Vol. 40(2), 257–277, 2011.
[25] Cetkovic M. *Thermo–Mechanical Bending of Laminated Composite and Sandwich Plates Using Layerwise Displacement Model*. Composite Structures. Vol. 125, 388–399, 2015.
[26] Cetkovic M. *Thermal Buckling of Laminated Plates Using Layerwise Displacement Model*. Composite Structures. Vol. 142, 238–253, 2016.
[27] Cetkovic M. *Influence of initial geometrical imperfections on thermal stability of laminated composite plates using layer wise finite element*. Composite Structures, Vol. 291, 115547, 2022.

VIBRATIONS OF A VISCOELASTIC ROD MODELED BY FRACTIONAL BURGERS CONSTITUTIVE EQUATIONS

Slađan Jelić[1] and Dušan Zorica[2]

[1] Department of Physics, Faculty of Sciences, University of Novi Sad, Trg D. Obradovića 4, 21000 Novi Sad, Serbia
e-mail: sladjan.jelic@df.uns.ac.rs
[2] Department of Physics, Faculty of Sciences, University of Novi Sad, Trg D. Obradovića 4, 21000 Novi Sad, Serbia
e-mail: dusan.zorica@df.uns.ac.rs

Abstract
Dynamic response of the one-dimensional viscoelastic rod of finite length, that has one end fixed and the other subject to prescribed displacement, is analyzed analytically, yielding the displacement of an arbitrary rod's point. Thermodynamically consistent Burgers models are adopted as the constitutive equations describing mechanical properties of the rod. Short-time asymptotics implies the finite wave propagation speed in the case of the second class models, contrary to the case of the first class models. Moreover, Burgers model of the first class yield quite classical shapes of displacement time profiles resulting from the boundary forcing assumed as the Heaviside function, while model of the second class yields response that resembles to the sequence of excitation and relaxation processes.

Keywords: thermodynamically consistent fractional Burgers models, fractional Burgers wave equation, initial-boundary value problem.

1. Introduction

The Cauchy initial value problem for the fractional Burgers wave equation is considered in [15] for the infinite domain, while the initial-boundary value problem on a finite spatial domain $x \in [0, L]$ during time $t > 0$, i.e., the wave propagation in a viscoelastic rod of finite length L

fixed at one of its ends and free on the other, having the displacement of a free end prescribed, is considered in [10] and the account of obtained results is presented this paper.

In order to model the wave propagation in one-dimensional deformable viscoelastic body, the equation of motion and strain ε for small local deformations

$$\frac{\partial}{\partial x}\sigma(x,t) = \rho \frac{\partial^2}{\partial t^2}u(x,t) \text{ and } \varepsilon(x,t) = \frac{\partial}{\partial x}u(x,t), \tag{1}$$

are coupled with the thermodynamically consistent fractional Burgers model either of the first class

$$\left(1 + a_{1\,0}\mathrm{D}_t^{\alpha} + a_{2\,0}\mathrm{D}_t^{\beta} + a_{3\,0}\mathrm{D}_t^{\gamma}\right)\sigma(x,t) = \left(b_{1\,0}\mathrm{D}_t^{\mu} + b_{2\,0}\mathrm{D}_t^{\mu+\eta}\right)\varepsilon(x,t) \tag{2}$$

or of the second class

$$\left(1+a_1\,{}_0\mathrm{D}_t^{\alpha}+a_2\,{}_0\mathrm{D}_t^{\beta}+a_3\,{}_0\mathrm{D}_t^{\beta+\eta}\right)\sigma(x,t)=\left(b_1\,{}_0\mathrm{D}_t^{\beta}+b_2\,{}_0\mathrm{D}_t^{\beta+\eta}\right)\varepsilon(x,t) \tag{3}$$

where ${}_0\mathrm{D}_\tau^{\xi}$ denotes the operator of Riemann-Liouville fractional differentiation of order $\xi\in[n,n+1], n\in\mathbb{N}_0$, defined by

$${}_0\mathrm{D}_t^{\xi}y(t)=\frac{\mathrm{d}^{n+1}}{\mathrm{d}t^{n+1}}\left(\frac{\mathrm{t}^{-(\xi-n)}}{\Gamma\left(1-(\xi-n)\right)}*y(t)\right),\qquad t>0$$

through the convolution in time: $f(t)*_t g(t)=\int_0^t f(t')g(t-t')\mathrm{d}t',\ t>0$, see [11].

Fractional Burgers wave equation, represented by the system of equations (1) and either (2) or (3), is subject to zero initial conditions

$$\begin{gathered}u(x,0)=0,\qquad \frac{\partial}{\partial t}u(x,0)=0,\qquad \sigma(x,0)=0,\qquad \frac{\partial}{\partial t}\sigma(x,0)=0,\\ \varepsilon(x,0)=0,\qquad \frac{\partial}{\partial t}\varepsilon(x,0)=0,\qquad x\in[0,L]\end{gathered} \tag{4}$$

as well as to the boundary conditions

$$u(0,t)=0\quad\text{and}\quad u(L,t)=Y(t),\qquad t>0 \tag{5}$$

corresponding to a rod fixed at one end and forced on the other. Wave propagation in a rod of finite length, i.e., the initial-boundary value problem (1), subject to initial and boundary conditions (4) and (5), is considered in [6,7] for the case of viscoelastic material modeled by the fractional distributed-order equation with power type constitutive function, while in [3] a fluid-like model of viscoelastic body is employed.

Thermodynamical consistency analysis of the fractional Burgers model

$$\left(1+a_1\,{}_0\mathrm{D}_t^{\alpha}+a_2\,{}_0\mathrm{D}_t^{\beta}+a_3\,{}_0\mathrm{D}_t^{\gamma}\right)\sigma(x,t)=\left(b_1\,{}_0\mathrm{D}_t^{\mu}+b_2\,{}_0\mathrm{D}_t^{\nu}\right)\varepsilon(x,t) \tag{6}$$

containing model parameters: $a_1,a_2,a_3,b_1,b_2>0$, $\alpha,\beta,\mu\in[0,1]$, with $\alpha\le\beta$, and $\gamma,\nu\in[1,2]$, performed in [13], implied two classes of thermodynamically consistent models, represented by (2) and (3). In the case of models belonging to the first class, the highest differentiation order of strain $\mu+\eta\in[1,2]$ with $\eta\in\{\alpha,\beta\}$ is greater than the highest differentiation order of stress, that is either $\gamma\in[0,1]$ in the case of Model I, in addition to $0\le\alpha\le\beta\le\gamma\le\mu\le1$ and $\eta\in\{\alpha,\beta,\gamma\}$ or $\gamma\in[1,2]$ in the case of Models II - V, in addition to $0\le\alpha\le\beta\le\mu\le1$ and $(\eta,\gamma)\in\{(\alpha,2\alpha),(\alpha,\alpha+\beta),(\beta,\alpha+\beta),(\beta,2\beta)\}$ while for models belonging to the second class differentiation orders of stress $\beta\in[0,1]$ and $\beta+\eta\in[1,2]$ coincide with the highest differentiation orders of strain in addition to $0\le\alpha\le\beta\le1$ so that $\eta=\alpha$ in the case of Model VI; $\eta=\beta$ in the case of Model VII; and $\alpha=\eta=\beta$, $\bar{a}_1=a_1+a_2$ and, $\bar{a}_2=a_3$ in the case of Model VIII. Similar forms of the fractional Burgers models are checked for the thermodynamical consistency in [2,8].

The time-evolution of stress, represented by the relaxation modulus, is obtained from the constitutive equation for the strain prescribed as the Heaviside step function, while the time-evolution of strain, represented by the creep compliance, is obtained from the constitutive

equation for stress prescribed as the Heaviside step function, and it is considered in [14] for the thermodynamically consistent Burgers models, while the proof of the dissipativity properties of the hereditary fractional wave equations, using a priori energy estimates, is presented in [17], where the constitutive equation of viscoelastic body is given in terms of relaxation modulus.

Extensive list of references regarding the properties of viscoelastic materials of fractional order including the literature of the wave propagation problems, with the emphasis on classical and fractional Burgers models can be found in [10]. The overview of fractional order models of viscoelastic materials, wave propagation problems including dispersion and attenuation processes are found in [4,5,9,12,16].

2. Solution of fractional Burgers wave equation

The system of governing equations (1) with either (2) or (3), representing the fractional Burgers wave equation, subject to initial and boundary conditions (4) and (5), transforms into

$$\frac{\partial}{\partial x}\sigma(x,t)=\frac{\partial^2}{\partial t^2}u(x,t),\qquad \varepsilon(x,t)=\frac{\partial}{\partial x}u(x,t) \tag{7}$$

with either

$$\left(1+a_1\,{}_0\mathrm{D}_t^{\alpha}+a_2\,{}_0\mathrm{D}_t^{\beta}+a_3\,{}_0\mathrm{D}_t^{\gamma}\right)\sigma(x,t)=\left(b_1\,{}_0\mathrm{D}_t^{\mu}+b_2\,{}_0\mathrm{D}_t^{\mu+\eta}\right)\varepsilon(x,t),\qquad \text{or} \tag{8}$$

$$\left(1+a_1\,{}_0\mathrm{D}_t^{\alpha}+a_2\,{}_0\mathrm{D}_t^{\beta}+a_3\,{}_0\mathrm{D}_t^{\beta+\eta}\right)\sigma(x,t)=\left(b_1\,{}_0\mathrm{D}_t^{\beta}+b_2\,{}_0\mathrm{D}_t^{\beta+\eta}\right)\varepsilon(x,t) \tag{9}$$

subject to

$$\begin{gathered}u(x,0)=0,\qquad \frac{\partial}{\partial t}u(x,0)=0,\qquad \sigma(x,0)=0,\qquad \frac{\partial}{\partial t}\sigma(x,0)=0,\\ \varepsilon(x,0)=0,\quad \frac{\partial}{\partial t}\varepsilon(x,0)=0,\qquad x\in[0,L],\end{gathered} \tag{10}$$

$$u(0,t)=0\quad\text{and}\quad u(L,t)=Y(t),\qquad t>0 \tag{11}$$

after introducing dimensionless quantities

$$\bar{x}=\frac{x}{L},\qquad \bar{t}=\frac{t}{T},\qquad \bar{u}=\frac{u}{L},\qquad \bar{Y}=\frac{Y}{L},\qquad \bar{\sigma}=\sigma\frac{T^{\xi}}{b_1},\qquad \bar{\varepsilon}=\varepsilon,\qquad \overline{a_1}=\frac{a_1}{T^{\alpha}},$$

$$\overline{a_2}=\frac{a_2}{T^{\beta}},\qquad \overline{a_3}=\frac{a_3}{T^{\zeta}},\qquad \bar{b}=\frac{b_2}{b_1T^{\eta}},\qquad \text{with}\qquad T=\left(\frac{\rho L^2}{b_1}\right)^{\frac{1}{2-\xi}},$$

where $(\xi,\zeta)=(\mu,\gamma)$ for the first and $(\xi,\zeta)=(\beta,\beta+\eta)$, $\eta\in\{\alpha,\beta,\gamma\}$ for the second class of Burgers models and after omitting bars over dimensionless quantities. By applying the Laplace transform, defined by

$$\tilde{f}(s)=\mathcal{L}[f(t)](s)=\int_0^{\infty}f(t)\mathrm{e}^{-st}\mathrm{d}t,$$

and by taking into account zero initial conditions (10), the governing equations, i.e., either (7), (8), or (7), (9), become

$$\frac{\partial}{\partial x}\tilde{\sigma}(x,s)=s^2\tilde{u}(x,s),\qquad \tilde{\varepsilon}(x,s)=\frac{\partial}{\partial x}\tilde{u}(x,s),\qquad \tilde{\sigma}(x,s)=\tilde{G}(s)\tilde{\varepsilon}(x,s), \tag{12}$$

where the complex modulus is

$$\tilde{G}(s)=\frac{\phi_{\varepsilon}(s)}{\phi_{\sigma}(s)},\qquad \text{with either} \tag{13}$$

$$\phi_{\sigma}(s)=1+a_1s^{\alpha}+a_2s^{\beta}+a_3s^{\gamma},\qquad \phi_{\varepsilon}(s)=s^{\mu}+bs^{\mu+\eta},\qquad \text{or} \tag{14}$$

$$\phi_{\sigma}(s)=1+a_1s^{\alpha}+a_2s^{\beta}+a_3s^{\beta+\eta},\qquad \phi_{\varepsilon}(s)=s^{\beta}+bs^{\beta+\eta}, \tag{15}$$

for the first, respectively second class of Burgers models, so that system of equations (12) solved with respect to $\tilde{u}$ reduce to the ordinary differential equation with constant coefficients

$$\frac{\partial^2}{\partial x^2}\tilde{u}(x,s)-s^2\tilde{u}(x,s)=0,$$

whose solution is

$$\tilde{u}(x,s)=C_1(s)\mathrm{e}^{\frac{xs}{\sqrt{\tilde{G}(s)}}}+C_2(s)\mathrm{e}^{-\frac{xs}{\sqrt{\tilde{G}(s)}}},\qquad \text{i.e.,}$$
$$\tilde{u}(x,s)=C(s)\sinh\frac{xs}{\sqrt{\tilde{G}(s)}}, \tag{16}$$

since the first boundary condition in (11), corresponding to fact that rod's end is fixed, ensures that $2C=C_1=-C_2$.

Displacement in the Laplace domain for the prescribed displacement of rod's free end, according to (16), takes the following form:

$$\tilde{u}(x,s)=\tilde{Y}(s)\frac{\sinh\frac{xs}{\sqrt{\tilde{G}(s)}}}{\sinh\frac{s}{\sqrt{\tilde{G}(s)}}}, \tag{17}$$

since the function \$C\$ is determined from the Laplace transform of displacement and boundary condition $(11)_2$ as

$$C(s)=\frac{\tilde{Y}(s)}{\sinh\frac{s}{\sqrt{\tilde{G}(s)}}}.$$

Displacement in the Laplace domain, given by $(17)_1$, can be expressed either through the solution kernel image $\tilde{P}$ in the case of Burgers models of the first class, or through the regularized solution kernel image $\tilde{P}_{\mathrm{reg}}$ in the case of models belonging to the second class, that are defined as

$$\tilde{P}(x,s)=\frac{\sinh\frac{xs}{\sqrt{\tilde{G}(s)}}}{\sinh\frac{s}{\sqrt{\tilde{G}(s)}}}\ \text{and}\ \tilde{P}_{\mathrm{reg}}(x,s)=\frac{1}{s}\tilde{P}(x,s). \tag{18}$$

Considering the asymptotics of solution kernel image $\tilde{P}$ and its regularized version $\tilde{P}_{\mathrm{reg}}$ as $s\to\infty$ one obtains

$$\tilde{P}(x,s)=\mathrm{e}^{-(1-x)\frac{s}{\sqrt{\tilde{G}(s)}}}\frac{1-\mathrm{e}^{-2\frac{xs}{\sqrt{\tilde{G}(s)}}}}{1-\mathrm{e}^{-2\frac{s}{\sqrt{\tilde{G}(s)}}}}\sim\mathrm{e}^{-\sqrt{\frac{a_3}{b}}(1-x)s^{1-\frac{\delta}{2}}}\ \text{and}\ \tilde{P}_{\mathrm{reg}}(x,s)\sim\frac{1}{s}\mathrm{e}^{-\sqrt{\frac{a_3}{b}}(1-x)s}, \tag{19}$$

because of the asymptotics of complex modulus $\tilde{G}$ given by (13), that yields

$$\tilde{G}(s)\sim\begin{cases}\dfrac{b}{a_3}s^{\delta}, & \text{for models of the first class, with } \delta=\mu+\eta-\gamma\\ \dfrac{b}{a_3}, & \text{for models of the second class,}\end{cases},\quad \text{as } s\to\infty. \tag{20}$$

Therefore, the short-time asymptotics of solution kernel P for models of the first class is obtained as

$$P(x,t)\sim\frac{1}{\pi}\int_0^{\infty}\sin\left(\sqrt{\frac{a_3}{b}}(1-x)\rho^{1-\frac{\delta}{2}}\sin\frac{\delta\pi}{2}\right)\mathrm{e}^{-\rho t+\sqrt{\frac{a_3}{b}}(1-x)\rho^{1-\frac{\delta}{2}}\cos\frac{\delta\pi}{2}}\mathrm{d}\rho,\qquad \text{as } t\to 0, \tag{21}$$

by inverting the Laplace transform of $(19)_1$ using the definition and integration in the complex plane, while the short-time asymptotics of regularized solution kernel $\tilde{P}_{\mathrm{reg}}$, corresponding to models of the second class, yields

$$P_{\mathrm{reg}}(x,t)\sim H\left(t-\sqrt{\frac{a_3}{b}}(1-x)\right),\qquad \text{as } t\to 0. \tag{22}$$

On the other hand, the asymptotics of regularized solution kernel image $\tilde{P}_{\mathrm{reg}}$ as $s\to 0$, yields

$$\tilde{P}_{\text{reg}}(x,s)=\frac{1}{s}\frac{\left(1+xs^{1-\frac{\xi}{2}}+\cdots\right)-\left(1-xs^{1-\frac{\xi}{2}}+\cdots\right)}{\left(1+s^{1-\frac{\xi}{2}}+\cdots\right)-\left(1-s^{1-\frac{\xi}{2}}+\cdots\right)}\sim\frac{1}{s}x,$$

implying

$$P_{\text{reg}}(x,t)\sim x\mathrm{H}(t)=x,\qquad \text{as } t\to\infty, \tag{23}$$

since the asymptotics of complex modulus $\tilde{G}$ given by (13), yields

$$\tilde{G}(s)\sim s^{\xi},\qquad \text{as } s\to 0,\qquad \text{with } \xi\in\{\mu,\beta\}. \tag{24}$$

Using the inverse Laplace transform of the derivative of function in $(18)_2$ one obtains

$$P(x,t)=\frac{\partial}{\partial t}P_{\text{reg}}(x,t)+P_{\text{reg}}(x,0)\,\delta(t)=\frac{\partial}{\partial t}P_{\text{reg}}(x,t), \tag{25}$$

since the asymptotics of $\tilde{P}_{\text{reg}}$ as $s\to\infty$ yields $s\tilde{P}_{\text{reg}}\sim e^{-\sqrt{\frac{a_3}{b}}(1-x)s}\to 0$, see $(19)_2$ and by the initial value Tauber theorem $P_{\text{reg}}(x,0)=\lim_{s\to\infty}s\tilde{P}_{\text{reg}}(x,s)=0$. More precisely, the solution kernel is

$$\begin{aligned}P(x,t)&=\frac{\partial}{\partial t}\left(P_{\text{reg}}(x,t)\,H\left(t-\sqrt{\frac{a_3}{b}}(1-x)\right)\right)\\&=\frac{\partial}{\partial t}P_{\text{reg}}(x,t)\,H\left(t-\sqrt{\frac{a_3}{b}}(1-x)\right)+P_{\text{reg}}(x,t)\,\delta\left(t-\sqrt{\frac{a_3}{b}}(1-x)\right),\end{aligned} \tag{26}$$

since the regularized solution kernel P_{reg} is zero up to $t=\sqrt{\frac{a_3}{b}}(1-x)$ and non-zero afterwards, according to (22).

The solution kernel P is calculated by the definition of inverse Laplace transform in [10] using the Cauchy residues theorem, since complex valued function $\tilde{P}$ has infinite number of poles, each of them of the first order, that are obtained as zeros of its denominator, i.e., as solutions of the equation

$$\sinh\frac{s}{\sqrt{\tilde{G}(s)}}=0\ \text{ implying }\ \frac{s}{\sqrt{\tilde{G}(s)}}=-\mathrm{i}k\pi,\ \text{ i.e., }\frac{s^2}{\tilde{G}(s)}+(k\pi)^2=0,\ \ k=0,\pm1,\pm2,\ldots \tag{27}$$

More precisely, there is a pair of complex conjugated poles s_k and $\bar{s}_k$ for each $k\in\mathbb{N}_0$ lying in the left complex half-plane. In addition to poles, function $\tilde{P}$ may have branch points other than $s=0$ due to the square root of function $\tilde{G}$, since its denominator ϕ_σ has either one negative real zero or a pair of complex conjugated zeros with negative real part, while in the case when function ϕ_σ does not have zeros, then function $\tilde{P}$ has no branch points other than $s=0$.

The explicit form of solution kernel P and its regularized form P_{reg} in the case when function $\tilde{P}$ either has no branch points other then $s=0$ or has one negative real branch point are given by

$$\begin{aligned}P(x,t)=&-\frac{1}{\pi}\int_0^\infty \mathrm{Im}\left(\frac{\sinh\frac{xs}{\sqrt{\tilde{G}(s)}}}{\sinh\frac{s}{\sqrt{\tilde{G}(s)}}}\right)e^{-\rho t}\mathrm{d}\rho\\&+2\sum_{k=1}^{\infty}(-1)^k\frac{\sin(k\pi x)}{k\pi}e^{-\rho_k t|\cos\varphi_k|}\,\mathrm{Re}\left(\frac{s_k}{1+(k\pi)^2\frac{\tilde{G}'(s_k)}{2s_k}}e^{\mathrm{i}\rho_k t\sin\varphi_k}\right),\end{aligned} \tag{28}$$

$$P_{\mathrm{reg}}(x,t)=x-\frac{1}{\pi}\int_0^{\infty}\mathrm{Im}\left(\frac{1}{\rho e^{i\pi}}\frac{\sinh\frac{xs}{\sqrt{\tilde{G}(s)}}}{\sinh\frac{s}{\sqrt{\tilde{G}(s)}}}\right)e^{-\rho t}d\rho$$
$$+2\sum_{k=1}^{\infty}(-1)^k\frac{\sin(k\pi x)}{k\pi}e^{-\rho_k t|\cos\varphi_k|}\,\mathrm{Re}\left(\frac{1}{1+(k\pi)^2\frac{\tilde{G}'(s_k)}{2s_k}}e^{i\rho_k t\sin\varphi_k}\right), \tag{29}$$

while the solution kernel $\mathbb{P}$ and its regularized form take the form

$$P(x,t)=-\frac{1}{\pi}\int_0^{\infty}\mathrm{Im}\left(\frac{\sinh\frac{x\rho e^{i\varphi_0}}{\sqrt{\tilde{G}(\rho e^{i\varphi_0})}}}{\sinh\frac{\rho e^{i\varphi_0}}{\sqrt{\tilde{G}(\rho e^{i\varphi_0})}}}e^{i(\varphi_0+\rho t\sin\varphi_0)}\right)e^{-\rho t|\cos\varphi_0|}d\rho$$
$$+2\sum_{k=1}^{\infty}(-1)^k\frac{\sin(k\pi x)}{k\pi}e^{-\rho_k t|\cos\varphi_k|}\,\mathrm{Re}\left(\frac{s_k}{1+(k\pi)^2\frac{\tilde{G}'(s_k)}{2s_k}}e^{i\rho_k t\sin\varphi_k}\right), \tag{30}$$

$$P_{\mathrm{reg}}(x,t)=x\frac{\varphi_0}{\pi}+\frac{1}{\pi}\int_0^{\infty}\mathrm{Im}\left(\frac{1}{\rho e^{i\varphi_0}}\frac{\sinh\frac{x\rho e^{i\varphi_0}}{\sqrt{\tilde{G}(\rho e^{i\varphi_0})}}}{\sinh\frac{\rho e^{i\varphi_0}}{\sqrt{\tilde{G}(\rho e^{i\varphi_0})}}}e^{i(\varphi_0+\rho t\sin\varphi_0)}\right)e^{-\rho t|\cos\varphi_0|}d\rho$$
$$+2\sum_{k=1}^{\infty}(-1)^k\frac{\sin(k\pi x)}{k\pi}e^{-\rho_k t|\cos\varphi_k|}\,\mathrm{Re}\left(\frac{1}{1+(k\pi)^2\frac{\tilde{G}'(s_k)}{2s_k}}e^{i\rho_k t\sin\varphi_k}\right), \tag{31}$$

in the case when function $\tilde{P}$ has a pair of complex conjugated branch points with negative real part $s_0=\rho e^{i\varphi_0}$ and $\bar{s}_0$ in addition to $s=0$. Note, the form (30) of solution kernel P is more general, since it reduces to (28) for $\varphi_0=\pi$.

The solution kernel P according to either (28) or (30), consist of two terms: the first is at most non-monotonic in both space and time and the second one is a superposition of standing waves oscillating in time with angular frequency $\omega_k=\rho_k\sin\varphi_k$ and amplitude decreasing in time. Note, values of $x\in[0,1]$ and $t>0$ are not independent in the case of the second model class, since $P_{\mathrm{reg}}(x,t)\neq 0$ for $t>\sqrt{\frac{a_s}{b}}(1-x)$, according to (22), implying the finite velocity of disturbance propagation, which is not the case for the first model class, due to the short-time asymptotics of solution kernel P, see (21).

Having the solution kernel calculated either by (28) and (30) in the case of the first model class, or by (26) in the case of the second model class, the displacement in the case of prescribed displacement of rod's free end is

$$u(x,t)=Y(t)*P(x,t), \tag{32}$$

by the inverse Laplace transform of $(17)_1$, with the solution kernel image $\tilde{P}$ defined by (18).

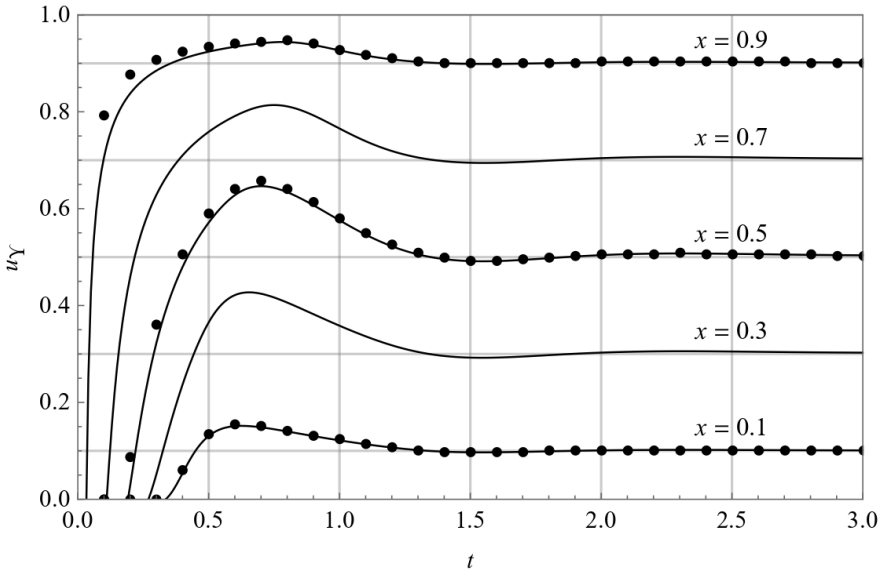

(a) Case of Model V.

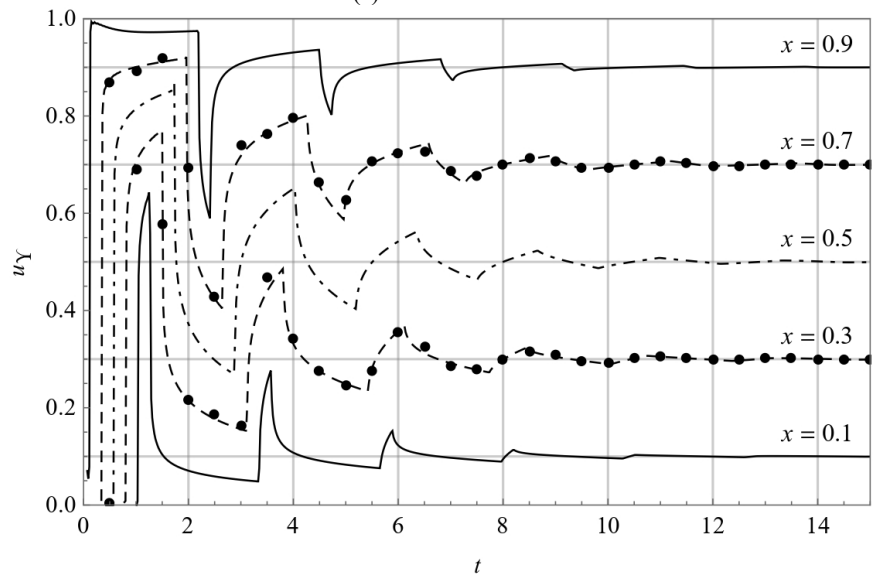

(b) Case of Model V.

Fig. 1. Displacement of a rod when the displacement of its free end is assumed as the Heaviside function, i.e., $Y = H$, obtained according to analytical expression (lines) and by numerical Laplace transform inversion (dots).

3. Numerical examples

Figures 1 and 2 present displacements of several points of the rod for displacement of rod's free end given as the Heaviside step function, i.e., for boundary condition $(11)_2$ taken as $Y = H$. The regularized solution kernel P_{reg} actually represents the step response, due to defining relation $(18)_2$ for regularized solution kernel image $\tilde{P}_{\mathrm{reg}}$ that yields

$$u_Y(x,t) = P_{\mathrm{reg}}(x,t) = H(t) * P(x,t)$$

after performing the inverse Laplace transform, see also (32).

The step response displays damped oscillatory behavior that settles at the value of point's position, i.e.

$$\lim_{t\to\infty} u_Y(x,t) = x, \tag{33}$$

as predicted by the large-time asymptotics of regularized solution kernel P_{reg} given by (23). The time profiles of step response in the case of Model V, given by

$$\left(1 + a_{1\,0}\mathrm{D}_t^{\alpha} + a_{2\,0}\mathrm{D}_t^{\beta} + a_{3\,0}\mathrm{D}_t^{2\beta}\right)\sigma(x,t) = \left(b_{1\,0}\mathrm{D}_t^{\mu} + b_{2\,0}\mathrm{D}_t^{\mu+\beta}\right)\varepsilon(x,t), \tag{34}$$

have quite classical shapes of the oscillatory behavior with pronounced damping, see Figure 1a.

On the other hand, the profiles in the case of Model VII, given by

$$\left(1 + a_{1\,0}\mathrm{D}_t^{\alpha} + a_{2\,0}\mathrm{D}_t^{\beta} + a_{3\,0}\mathrm{D}_t^{2\beta}\right)\sigma(x,t) = \left(b_{1\,0}\mathrm{D}_t^{\beta} + b_{2\,0}\mathrm{D}_t^{2\beta}\right)\varepsilon(x,t), \tag{35}$$

being also damped oscillatory, resemble to the sequence of excitation and relaxation processes, since profiles repeatedly change their convexity from concave to convex, as clearly visible from Figure 1b. Nevertheless, curves obtained by analytical expressions are consistent with curves represented by dots, which are obtained by numerical Laplace transform inversion using fixed Talbot method, see [1]. Regarding the short-time asymptotics, step response differs for Burgers models of the first and second class, since in the case of first class models time profiles continuously increase from zero, obtaining non-zero values depending on point's position, see short-time asymptotics (21) of solution kernel P and Figure 1a, while in the case of second class models time profiles jump from zero depending on point's position, since the short-time asymptotics is represented by the Heaviside function, see (22) and Figure 1b.

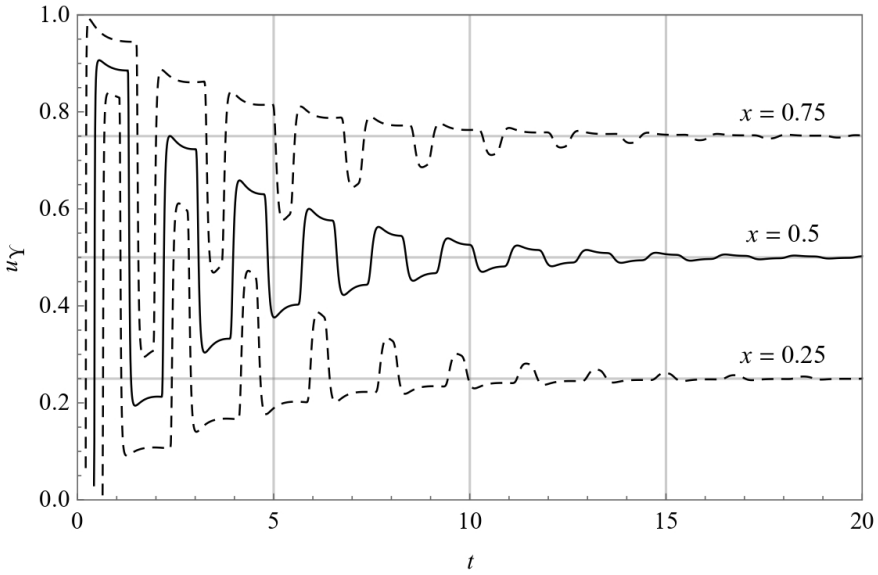

Fig. 2. Displacement of a rod when the displacement of its free end is assumed as the Heaviside function, i.e., $Y = H$, for Model V in the case of complex conjugated branch points.

Plots from Figure 1 correspond to the case when solution kernel image $\tilde{P}$ and its regularization $\tilde{P}_{\mathrm{reg}}$ have no branch points except for $s = 0$ so that the step responses are obtained using (29) with model parameters as in Table 1, while time profiles from Figure 2 correspond to the case when kernel image additionally has a pair of complex conjugated branch points with negative real part, hence the step responses are calculated by (31) using model parameters from Table 1. Although model parameters in the case of complex conjugated branch points do not satisfy narrowed thermodynamical restrictions, required in the proof that kernel image has a pair of complex conjugated poles s_k, $k \in \mathbb{N}$, this requirement is checked numerically, so as the fact that the argument of branch point is greater than the arguments of poles. Time profiles of the step response from Figure 2 are peculiarly shaped, as if two vibrations with different frequencies are superposed, since there is a relaxation process instead of peak, that is followed by another faster

relaxation process, appearing after two successive excitation processes having different speeds. Moreover, responses have an envelope, which is typical for damped oscillations.

Model	Branch points	a_1	a_2	a_3	b	α	β	γ	μ	η
Model V	$s=0$	0.005	0.8	0.115	0.376	0.6	0.61	2β	0.8	β
	$s=0, s_0, \bar{s}_0$	0.075	0.8	1.14	1.39	0.4	0.685		0.7	
Model VII	$s=0$	0.01	4.5	4	3	0.7	0.845	-	-	

Table 1. Model parameters.

4. Conclusion

The fractional Burgers wave equation, written as the system of equations consisting of the equation of motion and strain (1), that are coupled either with Burgers models of the first class (2) or with models of the second class (3), is used to model the dynamic response of the initially undisturbed one-dimensional viscoelastic rod of finite length having one end fixed and the other subject to prescribed displacement, according to boundary conditions (5). Laplace transform method is used in order to express the displacement of an arbitrary rod's point in terms of boundary condition convoluted with the solution kernel.

The short-time asymptotics of solution kernels implied that their time profiles continuously increase from zero as time increases, with the significant rise depending on the point's position in the case of Burgers models of the first class, see short-time asymptotics for solution kernel P given by (22), implying the infinite wave propagation speed. On the other hand, solution kernel P corresponding to the Burgers models of the second class, has to be regularized, so that the short-time asymptotics of P_{reg} is the Heaviside function of the argument $t-\sqrt{\frac{a_3}{b}}(1-x)$ see (22), implying the finite wave propagation speed $c=\sqrt{\frac{b}{a_3}}$, due to the sudden jump in the value of P_{reg} at $t=\frac{1-x}{c}$.

Solution kernel consist of two terms: the integral one is at most non-monotonic in both space and time and the one expressed through the sine Fourier series represents a superposition of standing waves, each of them oscillating with amplitude decreasing in time, having the damping and angular frequency determined by the pole of the solution kernel image. Moreover, the form of solution kernel also depends on occurrence of branch points of solution kernel image.

Time profiles of the displacement step response are of quite classical shape corresponding to the damped oscillatory behavior in the case of Burgers models of the first class, while in the case of the second class models, the time profiles are peculiarly shaped resembling to the sequence of excitation and relaxation processes.

References:

[1] Abate J. and Valkó P. P., *Multi-precision Laplace transform inversion*, International Journal for Numerical Methods in Engineering, 60:979-993, 2004.

[2] Atanackovic T. M., Janev M., and Pilipovic S., *On the thermodynamical in isothermal deformations of fractional Burgers model,* Philosophical Transactions of the Royal Society A, 378:20190278-1-13, 2020.

[3] Atanackovic T. M., Konjik S., Oparnica Lj., and Zorica D., *Thermodynamical restrictions and wave propagation for a class of fractional order viscoelastic rods,* Abstracts and Applied Analysis, 2011:ID975694-1-32, 2011.

[4] Atanackovic T. M., Pilipovic S., Stankovic B., and Zorica D., F*ractional Calculus with Applications in Mechanics: Vibrations and Diffusion Processes,* Wiley-ISTE, London, 2014.

[5] Atanackovic T. M., Pilipovic S., Stankovic B., and Zorica D., F*ractional Calculus with Applications in Mechanics: Wave propagation, Impact and Variational Principles,* Wiley-ISTE, London, 2014.
[6] Atanackovic T. M., Pilipovic S., and Zorica D., *Distributed-order fractional wave equation on a finite domain: creep and forced oscillations of a rod,* Continuum Mechanics and Thermodynamics, 23:305-318, 2011.
[7] Atanackovic T. M., Pilipovic S., and Zorica D., *Distributed-order fractional wave equation on a finite domain: Stress relaxation in a rod,* International Journal of Engineering Science, 49:175-190, 2011.
[8] Bazhlekova E. and Tsocheva K., F*ractional Burgers' model: thermodynamic constraints and completely monotonic relaxation function*, Comptes rendus de l'Académie bulgare des Sciences, 69:825-834, 2016.
[9] Holm S., *Waves with Power-Law Attenuation*, Springer Nature Switzerland AG, Cham, 2019.
[10] Jelić S. and Zorica D., *Fractional Burgers wave equation on a finite domain*, Chaos, Solitons, and Fractals, 154:111632-1-26,2022.
[11] Kilbas A. A., Srivastava H. M., and Trujillo J. J., *Theory and Applications of Fractional Differential Equations*, Elsevier B.V., Amsterdam, 2006.
[12] Mainardi F., *Fractional Calculus and Waves in Linear Viscoelasticity*, Imperial College Press, London 2010.
[13] Okuka A. S. and Zorica D., *Formulation of thermodynamically consistent fractional Burgers models*, Acta Mechanica, 229:3557-3570, 2018.
[14] Okuka A. S. and Zorica D., F*ractional Burgers models in creep and stress relaxation tests*, Applied Mathematical Modelling, 77:1894-1935, 2020.
[15] Oparnica Lj., Zorica D., and Okuka A. S., *Fractional Burgers wave equation*, Acta Mechanica, 230:4321-4340, 2019.
[16] Rossikhin Yu. A. and Shitikova M. V., *Application of fractional calculus for dynamic problems of solid mechanics: Novel trends and recent results*, Applied Mechanics Reviews, 63:010801-1-52, 2010.
[17] Zorica D. and Oparnica Lj., *Energy dissipation for hereditary and energy conservation for non-local fractional wave equations*, Philosophical Transactions of the Royal Society A, 378:20190295-1-24, 2020.

AN OVERVIEW: WITH THE ANĐELIĆ AND RAŠKOVIĆ TENSOR INTO TRANSFORMATIONS OF THE BASE VECTORS IN THE TANGENT SPACE OF THE POSITION VECTOR OF THE KINETIC POINT

Katica R. (Stevanović) Hedrih[1,2]

[1] Mathematical Institute of Serbian Academy of Sciences and Arts, Belgrade, Serbia
e-mail: katicah@mi.sanu.ac.rs,khedrih@sbb.rs
[2] Faculty of Mechanical Engineering, University of Niš, Niš, Serbia
e-mail: katicahedrih@gmail.com

Abstract:

The article is dedicated to the 120th anniversary of the birth of academician Tatomir Anđelić (1903-1993) and the memory of professor Danilo P. Rašković (1910-1985), heads of the Department of Mechanics of the Mathematical Institute of the Serbian Academy of Sciences.

The paper, also, presents analytical expressions of angular velocities and changes in intensity of base vectors in the tangent space of the position vector of the kinetic point during its movement in various functional orthogonal curvilinear systems.

Keywords: tensor, Andjelić, Rašković, Japanese scientists, base vectors of the tangent space, nonlinear transformation, orthogonal curvilinear coordinate systems, angular velocities.

1. Preliminaries

Academician Tatomir P. Anđelić (1903-1993) [A1, A3] was the first in Europe to introduce tensors with lectures at the Scientific Center of Mechanics in Udine in Italy and the audience of those lessons at the well-known publisher Springer, and also introduced tensor calculus [1] into the university teaching of mechanics at the faculties of natural sciences and mathematics, Also, Professor Danilo P. Rašković (1910-1985) [A2, A3] introduced tensor calculus [9, 10, 11] into the university teaching of kinematics and dynamics, as well as into the theory of elasticity at technical faculties and brought the thesaurus closer to engineering students.

Given the cooperation of Serbian mechanics and mathematicians, and among them especially the academician Tatomir P. Anđelić (1903-1993) and Mileva Prvanović (July 16, 1929 - February 12, 2016), with the Japanese scientist Akitsugi Kawaguchi (April 8, 1902 - July 30, 1984), [A4, A6] founder of the scientific society Tensor, as well as the unique Journal Tensor, as well as with Professor Tomoaki Kawaguchi (February 10, 1935) [A5, A6], the current president of the Tensor Society and the editor of the Tensor Journal [2-7] , the communication will also discuss the cooperation between Serbian and Japanese scientists.

2. Main scientific results

Starting from the notion of linear and nonlinear transformations, affine and functional-nonlinear mappings of coordinates and coordinate systems, geometrical and kinematical

invariants along linear or nonlinear transformations from one to other coordinate system are pointed out.

Analytical expressions of basic vectors of tangent space of kinetic point vector positions in generalized, as well as in series of particular cases of curvilinear coordinate systems for the cases of orthogonal and nonorthogonal curvilinear coordinate systems are derived.

Examples of expressions of basic vectors of tangent space of kinematical point vector position in polar-cylindrical, spherical, parabolic-cylindrical and three-dimensional-thee-parabolic system of curvilinear orthogonal coordinates are presented [2-8] .

Next, analytical expressions of change of basic vectors of tangent space of kinetic point vector position with time, also, are done.

Original analytical expressions of angular velocity and velocity of dilatations of basic vectors of tangent space of kinetic point vector position, in generalized curvilinear coordinate systems as well as in series of special orthogonal curvilinear coordinate system are derived by author of this paper and presented.

3. An example: Generalized orthogonal functional elliptical curvilinear coordinate system

Relation between coordinates ξ, η and φ of orthogonal generalized e**lliptical** curvilinear coordinate system and coordinated x, y and z of Descartes coordinate system which is afine space are nonlinear and transformation of the coordinates. Generalized nonlinear functional transformation from afine system coordinates to generalized el**liptical** curvilinear coordinate system which is no afine coordinate system space are in the following forms (see Reference [8] and Figure 1.a*): $x=\sqrt{\left(1-\eta^2\right)\left(\xi^2-1\right)}\cos\varphi$, $y=\sqrt{\left(1-\eta^2\right)\left(\xi^2-1\right)}\sin\varphi$ and $z=\eta\xi$.

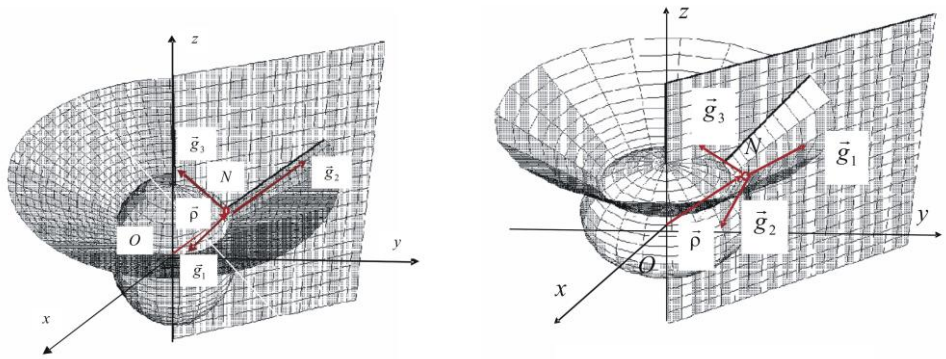

a* b*

Figure 1. Presentation of the position vector of a kinetic point in different positions in three dimensional space, with corresponding basic vectors $\vec{g}_{(\alpha)i}$ of position vector $\vec{\rho}_{(\alpha)}(q)$ tangent space (without index (α) denotation of the order of point); **a*** in elliptical coordinate system with orthogonal curvilinear coordinates; b* in three dimensional oblate spheridal coordinate system with orthogonal curvilinear coordinates [8, 4, 5].

Basic vectors of the position vector tangent space in elliptic coordinates are in the following forms:

$$\vec{g}_1=\vec{g}_\xi=\frac{\partial\vec{\rho}}{\partial\xi}=\vec{i}\,\xi\sqrt{\frac{\left(1-\eta^2\right)}{\left(\xi^2-1\right)}}\cos\varphi+\vec{j}\,\xi\sqrt{\frac{\left(1-\eta^2\right)}{\left(\xi^2-1\right)}}\sin\varphi+\eta\vec{k}$$

$$\vec{g}_2=\vec{g}_\eta=\frac{\partial\vec{\rho}}{\partial\eta}=-\vec{i}\,\eta\sqrt{\frac{\left(\xi^2-1\right)}{\left(1-\eta^2\right)}}\cos\varphi-\vec{j}\,\eta\sqrt{\frac{\left(\xi^2-1\right)}{\left(1-\eta^2\right)}}\sin\varphi+\xi\vec{k} \qquad (1)$$

$$\vec{g}_3 = \vec{g}_\varphi = \frac{\partial \vec{\rho}}{\partial \varphi} = -\vec{i}\sqrt{\left(1-\eta^2\right)\left(\xi^2-1\right)}\sin\varphi + \vec{j}\sqrt{\left(1-\eta^2\right)\left(\xi^2-1\right)}\cos\varphi$$

Then, by scalar products with units vectors of the position vector tangent space in elliptically coordinates in directions of these basic vectors, we obtain velocity of extensions of each of the basic vectors of position vector tangent space during the kinetic point motion, in the following form:

:

$$\begin{aligned}
\overset{*}{\vec{g}}_\xi &= \left\langle \dot{\xi}\xi \frac{\left(1-\eta^2\right)}{\left(\xi^2-\eta^2\right)} - \xi^3\dot{\xi}\frac{\left(1-\eta^2\right)}{\left(\xi^2-\eta^2\right)\left(\xi^2-\eta^2\right)} - \xi^2\eta\dot{\eta}\frac{1}{\left(\xi^2-\eta^2\right)} + \frac{\left(\xi^2-1\right)}{\left(\xi^2-\eta^2\right)}\dot{\eta}\eta \right\rangle \vec{g}_\xi \\
\overset{*}{\vec{g}}_\eta &= \left\langle \dot{\eta}\eta\frac{\left(\xi^2-1\right)}{\left(\xi^2-\eta^2\right)} + \eta^2\xi\dot{\xi}\frac{1}{\left(\xi^2-\eta^2\right)} - \ddot{\eta}\eta^3\frac{\left(\xi^2-1\right)}{\left(\xi^2-\eta^2\right)\left(1-\eta^2\right)} + \dot{\xi}\xi\frac{\left(1-\eta^2\right)}{\left(\xi^2-\eta^2\right)} \right\rangle \vec{g}_\eta \\
\overset{*}{\vec{g}}_\varphi &= \left(\overset{*}{\vec{g}}_\varphi, \frac{\vec{g}_\varphi}{\left|\vec{g}_\varphi\right|}\right)\frac{\vec{g}_\varphi}{\left|\vec{g}_\varphi\right|} = \frac{\left\langle -\eta\dot{\eta}\left(1-\eta^2\right) + \xi\dot{\xi}\left(1-\eta^2\right)\right\rangle}{\left(1-\eta^2\right)\left(\xi^2-1\right)}\vec{g}_\varphi
\end{aligned} \tag{2}$$

Analytical expressions of resultatants of angular velocities $\vec{\omega}_{P\xi}$, $\vec{\omega}_{P\eta}$ and $\vec{\omega}_{P\varphi}$ of the rotation of basic vectors of vector position tangent space of kinetic point during the motion, expressed in curvilinear functional elliptical coordinate system are in the following form:

$$\begin{aligned}
\vec{\omega}_{P\xi} &= \vec{\omega}_{P\xi,\eta} + \vec{\omega}_{P\xi,\varphi} \\
\vec{\omega}_{P\xi} &= \frac{1}{\left(\xi^2-\eta^2\right)}\left\langle \dot{\xi}\eta - \dot{\eta}\xi - \frac{\dot{\xi}\xi^2\eta}{\left(\xi^2-1\right)} - \frac{\xi\eta^2\dot{\eta}}{\left(1-\eta^2\right)}\right\rangle \vec{g}_\varphi - \frac{\xi\dot{\varphi}\left(1-\eta^2\right)}{\left(\xi^2-\eta^2\right)}\vec{g}_\eta \\
\vec{\omega}_{P\eta} &= \vec{\omega}_{P\eta,\varphi} + \vec{\omega}_{P\eta,\xi} \\
\vec{\omega}_{P\eta} &= \frac{1}{\left(\xi^2-\eta^2\right)}\left\langle \dot{\eta}\xi + \dot{\xi}\eta + \frac{\eta\xi^2\dot{\xi}}{\left(\xi^2-1\right)} - \frac{\dot{\eta}\eta^2\xi}{\left(1-\eta^2\right)}\right\rangle \vec{g}_\varphi - \frac{\dot{\varphi}\eta\left(\xi^2-1\right)}{\left(\xi^2-\eta^2\right)}\vec{g}_\xi \\
\vec{\omega}_{P\varphi} &= \vec{\omega}_{P\varphi,\eta} + \vec{\omega}_{P\varphi,\xi} = -\frac{\dot{\varphi}\xi\left(1-\eta^2\right)}{\left(\xi^2-\eta^2\right)}\vec{g}_\eta - \frac{\dot{\varphi}\eta\left(\xi^2-1\right)}{\left(\xi^2-\eta^2\right)}\vec{g}_\xi
\end{aligned} \tag{3}$$

4. Conclusions

In Figure 1.b* coordinate surfaces and coordinate curvilinear line of orthogonal generalized oblate spheroidal curvilinear coordinate system are presented.

Nonlinear relation between coordinates x, y and z of Descartes coordinate system which is afine space and generalized oblate spheroidal curvilinear coordinates ξ, η and φ are nonlinear and these are in the following forms:

$$\begin{aligned}
x &= aCh\xi\cos\eta\cos\varphi && \xi \geq 0, \quad h_1^2 = h_2^2 = a^2\left(Sh^2\xi + \sin^2\eta\right) \\
y &= aCh\xi\cos\eta\sin\varphi && -\frac{\pi}{2} \leq \eta \leq \frac{\pi}{2}, \; h_3^2 = a^2Ch^2\xi\cos^2\eta \\
z &= aSh\xi\sin\eta && 0 \leq \varphi \leq 2\pi
\end{aligned} \tag{4}$$

Then, by scalar products with unit vectors of the position vector tangent space in oblate spheroidal coordinates in directions of these basic vectors is not difficult to obtain analytical expression of the velocity of extension of first of the basic vectors of position vector tangent space in oblate spheroidal curvilinear orthogonal coordinates during the kinetic point motion in the following form:

$$\overset{*}{\vec{g}}_{\xi}=\frac{d\left|\vec{g}_{\xi}\right|}{dt}\frac{\vec{g}_{\xi}}{\left|\vec{g}_{\xi}\right|}=\frac{1}{\left(Sh^2\xi+\sin^2\eta\right)}\left\langle\dot{\xi}Ch\xi Sh\xi-\dot{\eta}\cos\eta\sin\eta\right\rangle\vec{g}_{\xi} \tag{5}$$

Also, using vector products $\left\lfloor\vec{\omega}_{P\xi},\vec{g}_{\xi}\right\rfloor$, $\left\lfloor\vec{\omega}_{P\eta},\vec{g}_{\eta}\right\rfloor$ and $\left\lfloor\vec{\omega}_{P\varphi},\vec{g}_{\varphi}\right\rfloor$ it is easier to separate angular velocities $\vec{\omega}_{P\xi}$, $\vec{\omega}_{P\eta}$ and $\vec{\omega}_{P\varphi}$ of the rotation of basic vectors of vector position tangent space of kinetic point during the motion, expressed in curvilinear functional oblate spheroidal coordinate system. Analytical expression of angular velocity $\vec{\omega}_{P\xi}$ of first basic vector rotation of position vector tangent space of kinetic point in functional oblate spheroidal coordinate system is in the following form:

$$\vec{\omega}_{P\xi}=\vec{\omega}_{P\xi,\eta}+\vec{\omega}_{P\xi,\varphi}=-\frac{\left\langle\dot{\varphi}Ch\xi Sh\xi\cos^2\eta\right\rangle\vec{g}_{\eta}+\left\langle\dot{\xi}\cos\eta\sin\eta-\dot{\eta}Ch\xi Sh\xi\right\rangle\vec{g}_{\varphi}}{a\sqrt{2}Ch\xi\cos\eta\left(Sh^2\xi+\sin^2\eta\right)} \tag{6}$$

References:

[1] Andjelić, T. P., Tenzori, Zavod za izdavanje udžbenika, 1965.

[2] Hedrih (Stevanović) K. , R., Visibility or appearance of nonlinearity, Tensor, N.S. Vol. 72, No. 1 (2010), pp. 14-33, #3. Tensor Society, Chigasaki, Japan, ISSN 0040-3504.

[3] Hedrih (Stevanović) K.R., The Dissipation Function of a Nonconservative System of Mass Particles, Tensor, N.S.,Vol.63, No.2(2002), pp.176-186. Tensor Society, Japan.

[4] Hedrih (Stevanović) K , Linear and non-linear transformation of coordinates and angular velocity and intensity change of basic vectors of tangent space of a position vector of a material system kinetic point, The European Physical Journal Special Topics, 230(18-20), 3673-3694. EPJS-D-21-00010R1) DOI: 10.1140/epjs/s11734-021-00226-6, ISSN 1951-6355

[5] Hedrih (Stevanović) K R., Angular velocityand intensity under change of basic vectors of position vector of tangent space of a meterial system kinetic point -Consideration of the difference betwenn linear and nonlinear transformations, To memory of academician Vladimir Metodievich Matrosov (May 8, 1932-April 17,2011) President of Academy of nonlinear Sciences. Tensor, Vol. 75, No. 1 pp. 71-93. Tensor Society (Tokyo), c/o Kawaguchi Inst. of Math. Soc. , Japan.

[6] Hedrih (Stevanović) K R.,, Rheonomic Coordinate method Applid to Nonlinear Vibration Systems with Hereditary Elements, (www-EUROMECH 3rd ENOC, Copenhagen 1999, http:// www.imm.dtu.dk/ documents/user /mps/ENOC/proceeedings/, Technical University of Denmark.4A, pp. 1-24.).

[7] Hedrih (Stevanović) K R., Tangent space extension of the position vectors of a discrete rheonomic mechanical system, Professor N. R. Sen Memorial Lecture, Bulletin of the Calcutta Mathematical Society Volume 104, No.2(2012) pp. 81-102. Bull.Cal.Math. 104 (2) 81-102 (2012).

[8] Heinbockel J.H., Introduction to Tensor Calculus and Continuum Mechanics, Department of Mathematics and Statistic Old Dominion University, Copyright c 1996 by J.H. Heinbockel. All rights reserved. Reproduction and distribution of these notes is allowable provided it is for non-profit purposes only.

[9] Rašković DP.: *Osnovi tenzorskog računa (Basic of Tensor Calculus(*, Mašinski fakultet Kragujevac, 1974.

[10] Rašković DP.: *Mehanika II- Kinematika* (Mechanics II, Kinematics), III i dalja izdanja, Zavod za izdavanje udžbenika, 1953, 1966, str.347.
file:///C:/Users/Vladimir/AppData/Local/Temp/Mehanika_II_kinematika_R.pdf

[11] Rašković DP., Teorija elastičnosti (Theory of Elasticity), Naučna knjiga, Beograd, 1985.
http://elibrary.matf.bg.ac.rs/handle/123456789/3765

APPENDIX

Tensor calculus connection: Academicina Tatomir P. Andjelić (1903-1993) , Professor Dr. Akitsugu Kawaguchi (1972-1902) and Prof. Dr. Ing. Dipl. Math. Danilo P. Rašković (1910-1985) and Professor Tomoaki Kawaguchi (February 10, 1935 -)

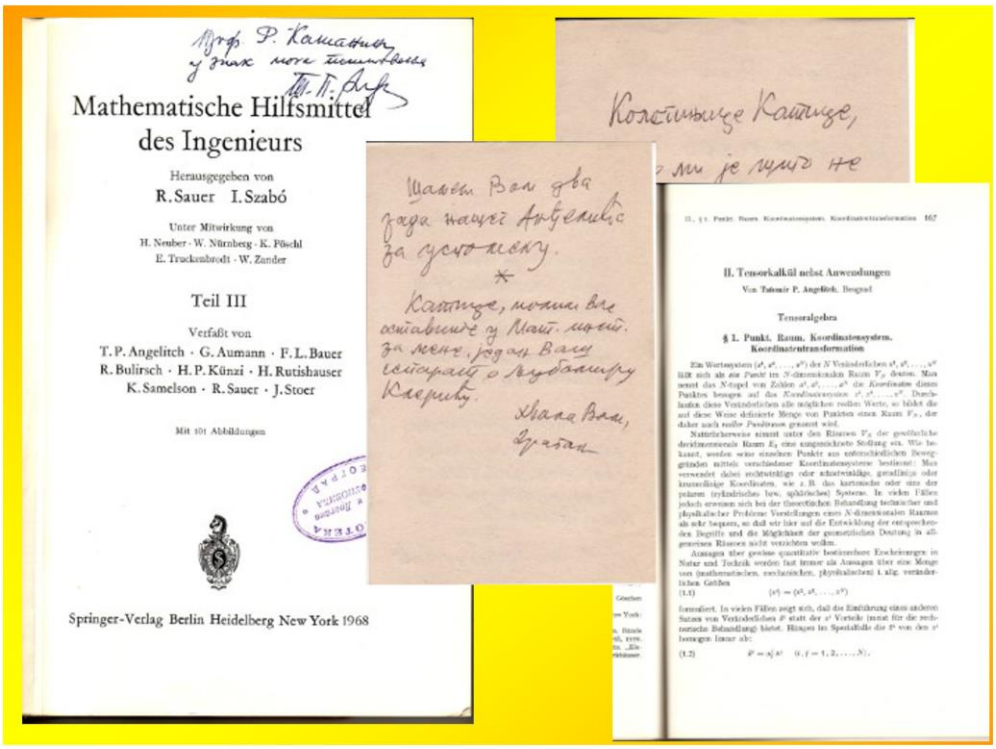

Figure 1A. Tensor publications by Academicina Tatomir P. Andjelić (1903-1993) [A1, A3]

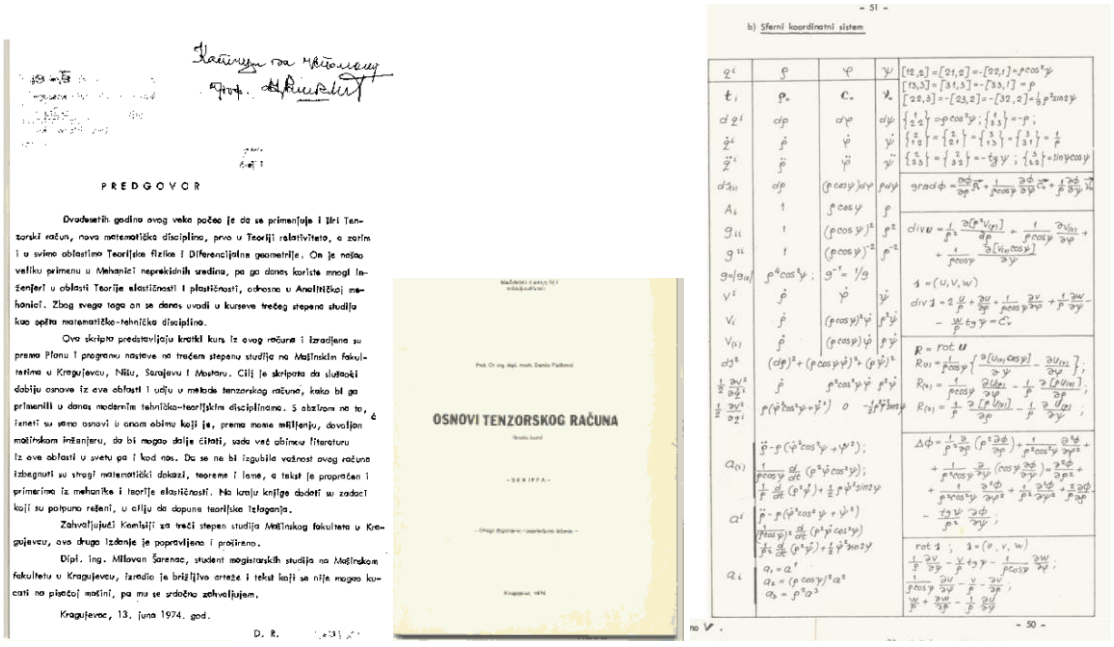

Figure 2A. Tensor publications by Prof. Dr. Ing. Dipl. Math. Danilo P. Rsšković (1910-1985) [A2. A3]

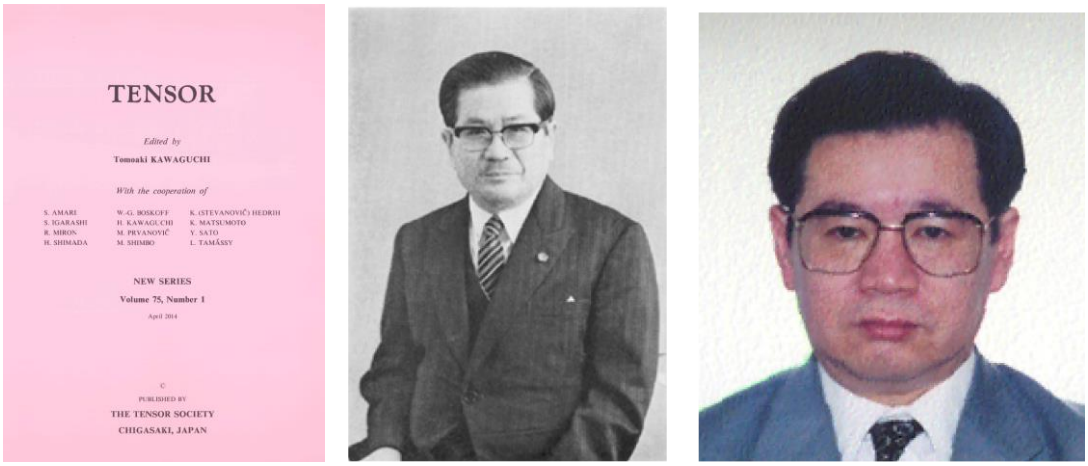

Figure 3A. Cover of Journal Tensor (left); Professor Dr. Akitsugu Kawaguchi (1972- 1902) , founder and first President of Tensor Society and founder and first Editor of Journal Tensor (middle); Professor Dr. Tomoaki Kawaguchi (1935 -) present President of Tensor Society and Editor of Journal Tensor (right) [A4, A5]

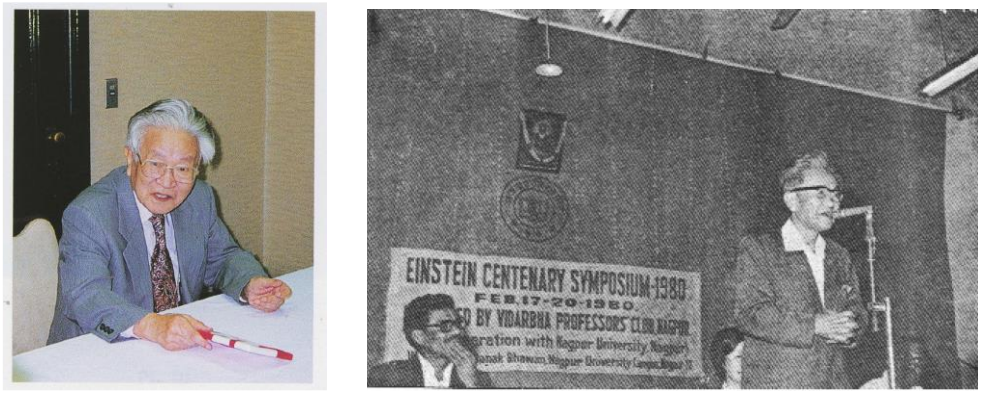

Figure 4A. Kazuo Kondo (1911-2001): Kazuo Kondo at the 80th Birthday (left); Kondo making the opening address at the Einstein Centenary Symposium Nagpur, India, 1980 (right). [A6]

Figure 5A. Gathering of members of the Tensor Society and Editorial Board of Journal Tensor at the international conferences of the Tensor Society: (left) the president of the Tensor Society Tomoaki Kawaguchi and the academician Rdu Miron at the University "Alexander Ion Cuza" in Iași, Romania 2013; (right) academic Milea Prvanović and president of Tensor Society Tomoaki Kawaguchi in Tokyo, Japan 2015 and Katica (Stevanović) Hedrih

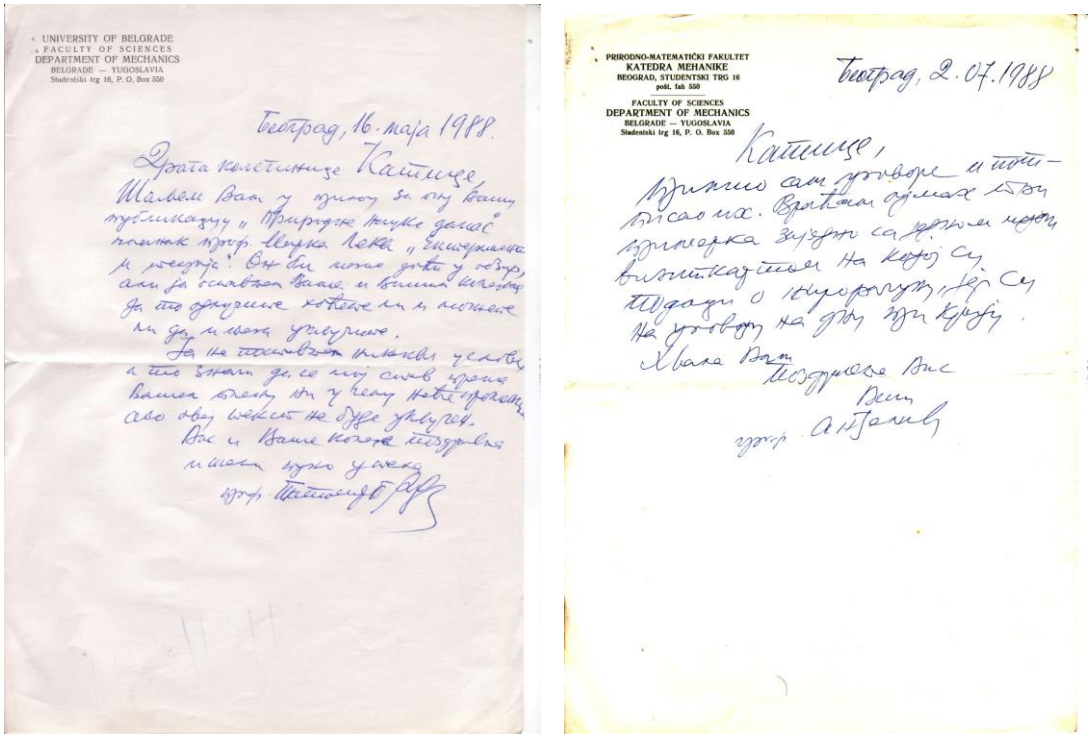

Figure 6A. Two letters written by academician Tatomir P. Andjelić (1903 -1993) [A1, A3]

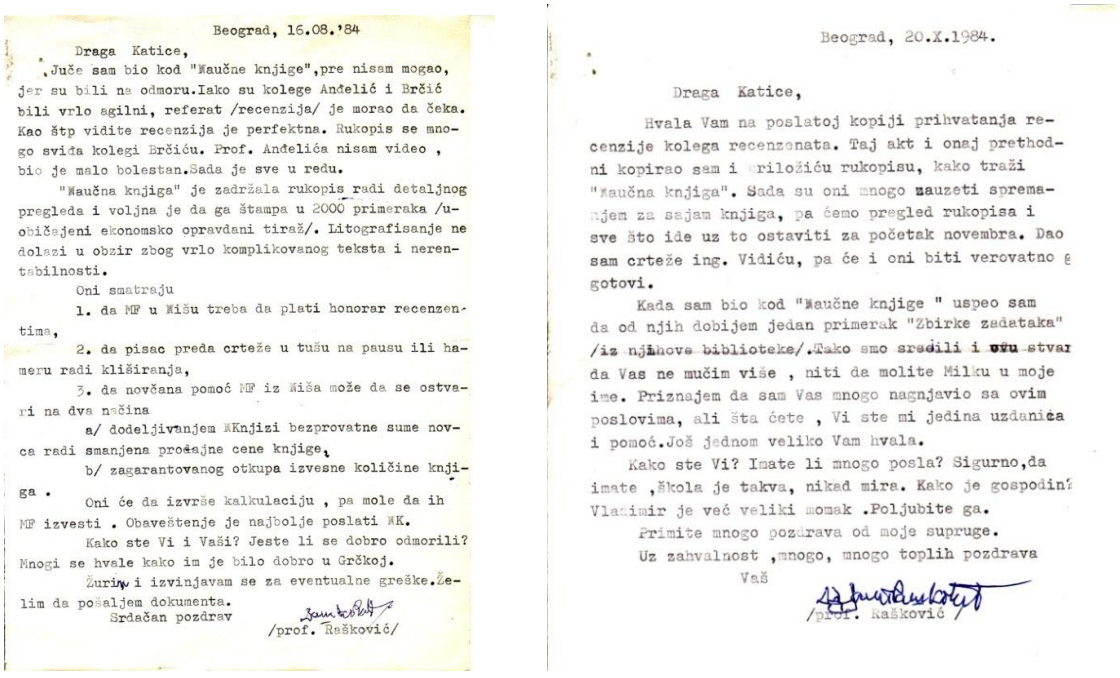

Figure 7A. Two letters written by Prof. Dr. Ing. Dipl. Math. Danilo P. Rašković (1910 -1985) [A2. A3]

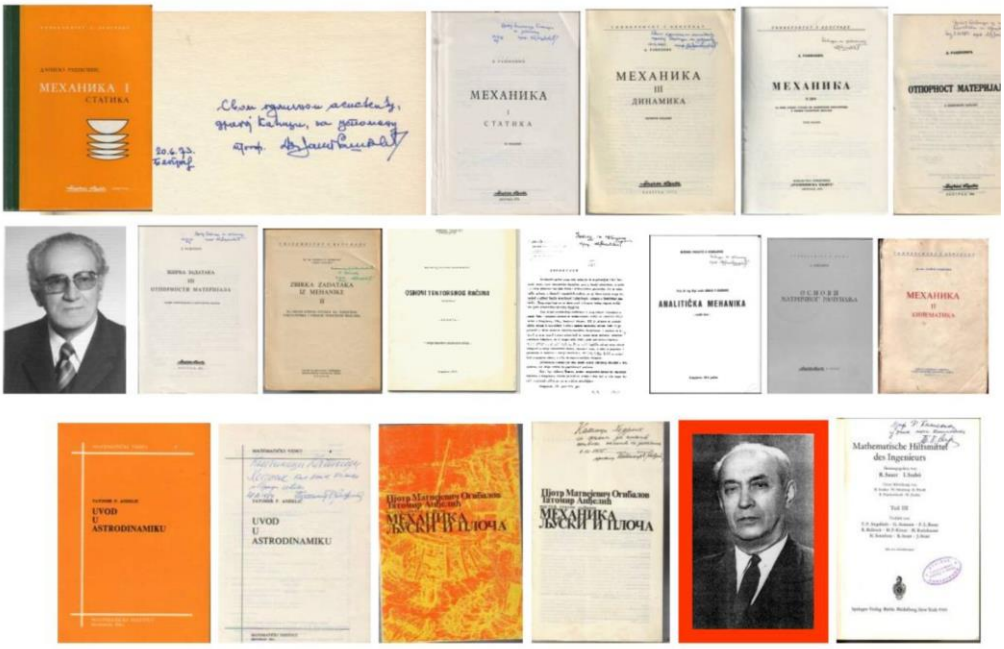

Figure 7A. Covers of References authored by Prof Dr. Ing. Dipl. Math. Danilo P. Rašković (1910 -1985) (up) [A2. A3] and by academician Tatomir P. Andjelić (1903 -1993) (daunt) [A1, A3]

References in Appendix:

A1. Hedrih (Stevanović) K R., Academician Tatomir P. Andjelić (190 3-1993), Bio-bibliography, Chapter in book: Lives and work of the Serbian Scientists, Edited by Academician Miloje Sarić, Edition of Serbian Academy of Sciences and Arts, Beograd. Biographies and Bibliographies. Committee for the Research into the lives and Work of the Scientistts of Serbian Origin. Book VI., pp. 435-485, Beograd 2000. (In Serbian with Abstract in English)).

A2. Hedrih (Stevanović) K R., Studović M., Professor Danilo P. Rašković (1910 -1985), Bio-bibliography, Chapter in book: Lives and work of the Serbian Scientists, Edited by Academician Vladan Djordjević, Edition of Serbian Academy of Sciences and Arts, Beograd. Biographies and Bibliographies. Committee for the Research into the lives and Work of the Scientistts of Serbian Origin. Book IX., pp. 239-270, Beograd 2003.-to appear, (In Serbian with Abstract in English)

A3. Saplememt Book in English: Lives and Work of the Serbian Scientists, Volume I-X, Book of Abstracts, 20 0 7p. 458, Edited by Vladan Djordjević, Dragomir Vitorovic and Dragoslav Marinkovic, Edition of Serbian Academy of Sciences and Arts, Beograd. Biographies and Bibliographies. Committee for the Research into the lives and Work of the Scientistts of Serbian Origin: Hedrih (Stevanović), K., Akademik Ljubomir Klerić (1844-1910), pp. 125-128. Hedrih (Stevanović), K. , Rektor Kosta Alković (1836-1909), pp.3-4. Katica (Stevanović) Hedrih, Akademik Tatomir P. Andjelić (190 3-1993,),pp.9-12. Katica (Stevanović) Hedrih i Milovan Studović, Profesor Danilo P. Rašković (1910 -1985), pp. 303-306.

A4. PROFESSOR AKITSUGU KAWAGUCHI- The Anniversary of Akisugu KAWAGUCHI's 100 years birth, the Founder of Tensor Society, FACTA UNIVERSITATIS Series: Mechanics, Automatic Control and Robotics Vol.3, No 13, 2003, pp. 773 – 774; Preprint: Tensor N.S. Vol. 24 (1972) - Editorial - **.** Hedrih (Stevanović) K R., file:///C:/Users/Katica/Downloads/macar200301-24%20(5).pdf

A5. PROFESSOR TOMOAKI KAWAGUCHI, Professor of Mejiro University, Present President of Tensor Society, Japan; FACTA UNIVERSITATIS Series: Mechanics, Automatic Control and Robotics Vol.3, No 13, 2003, pp. 773 – 774; Editorial - **.** Hedrih (Stevanović) K R., file:///C:/Users/Katica/Downloads/macar200301-24%20(5).pdf

A6. Grenville J. Croll Alternative, The Natural Philosophy of Kazuo Kondo, 1/23; Copyright © 2006-2020 Grenville Croll. All Rights Reserved. 1 / 23; Natural Philosophy Association grenvillecroll@gmail.com; file:///C:/Users/Katica/Downloads/0712.0641.pdf

DEVELOPMENT OF A HYBRID FIXED-WING VTOL UNMANNED AERIAL VEHICLE

Radoslav D. Radulović and Milica P. Milić

[1] Faculty of Mechanical Engineering, University of Belgrade, Kraljice Marije 16, 11120 Belgrade 35
e-mail: rradulovic@mas.bg.ac.rs, mmilic@mas.bg.ac.rs.

Abstract

As the use of unmanned aerial vehicles (UAV) has expanded worldwide, the market needs for the development of multi-role unmanned systems are increasing. These unmanned systems tend to largely find their constant and irreplaceable role in many industries. The development of such systems is a complex process, which, among other things, must include detailed structural, static and dynamic calculations and testing. The UAV presented in this paper is a hybrid powered aircraft with vertical take-off and landing (VTOL) with a composite structure and an innovative hybrid propulsion with a starter-generator system. VTOL gives an advantage in the exploitation of the aircraft itself, because it does not require special ground conditions or space for take-off and landing. The starter and generator system enables a smaller amount of fixed mass, such as batteries, while the structure made of composite materials enables a smaller mass and the desired characteristics of strength, resistance to corrosion and fatigue. This paper presents development review process of the latest technology in terms of the concept of system and subsystem operation, as well as financially favorable and high-quality construction.

Keywords: composite materials, hybrid propulsion, VTOL UAV, development.

1. Introduction

In the recent years, the development and production of unmanned aerial vehicles (UAVs) are in expansion. UAVs exist in various sizes and with wide ranges of performances, starting from micro-UAVs to the large UAVs categorized on the basis of take-off masses and overall dimensions and capability to long range flight. We can also categorize them by the type of propulsion: electric, hybrid, jet propulsion, etc. So far, the most massive application of unmanned aerial vehicles has been shown in military and recreational purposes. Prototypes are emerging for applications in other industries, such as transportation or performing operations which are potentially dangerous for humans etc. The most widespread type of UAVs is the multi-rotor, due to its simplicity of control, maneuverability and ability for vertical take-off and landing (VTOL). The main disadvantage of electric powered aircraft is energy consumption during cruise which results in a relatively short operational time. Usually, fixed-wing UAVs provide much larger energy efficiency during cruise, but they require runways for take-off and landing and they do not have the possibility of VTOL configuration. Taking into account advantages of both types, the solution is to have a hybrid configuration, with VTOL abilities like multi-rotor aircrafts and

energy efficiency during cruise like fixed-wing UAVs. This hybrid configuration can be obtained by integration of multiple rotors to the fixed-wing UAVs.

In recent years, electric propulsion of aircraft has attracted a lot of attention among researchers and innovators. Through research and testing, the main defect in the use of the electric propulsion was determined, namely specific density of batteries' energy, which applied as energy source in electric propulsion, is much lower than of kerosene, up to 60. On the other hand, main benefits of the electric propulsion are: clean energy, low noise level, low mass of electric motors, without pollution caused by engine operation [1]. According to the latest research, the electric propulsion should become a real competitor to the conventional propulsion in the next ten years. New research increasingly leads to an increase in the specific density of batteries energy, as well as the use of ultra capacitors.

This paper presents an overview of the conceptual prototype solution of a hybrid unmanned aerial vehicle. This UAV is a VTOL configuration. It further says that it takes off and lands vertically with the help of four electric motors in a quadcopter configuration. This enables the aircraft to take off and land on any terrain. After reaching a certain height, the drive switches to the fifth engine, which is a piston engine, and the aircraft continues cruising with that engine. While the piston engine is running, the batteries are charged via a generator, specially developed and adapted to this system to use the power of the piston engine as energy to charge the batteries. The transition to hybrid propulsion is a modern technology that greatly contributes to the improvement of the autonomy of unmanned systems [2].

2. Requirements for the development of an unmanned aerial vehicle

Requirements for the development of this unmanned aerial vehicle primarily included propulsion and the method of exploitation. The aircraft should have the ability to take off and land vertically, so a VTOL configuration and the ability to take off and land conventionally. The structure should be composite and ensure optimal ratio of mass and strength of the structure. Transition to a piston engine and flight autonomy of up to 5 hours, with a payload of 25 kg. Mission of UAV is offensive UAV or for target positioning and irradiation.

General characteristics are:

Payload	25 kg
Gross Weight	87 kg
Fifth Engine	Piston Engine Twin Spark
Engine Power	14.5 kW
Minimal speed	70 km/h
Cruise speed	150 km/h
Maximum speed	200 km/h
Lift to drag ratio	13
Maximal vertical speed	7 m/s
Wing area	2.2 m^2
Wingspan	4.6 m
Aspect Ratio	9.62

Table 1. General characteristics of UAV

Table 1 shows the general characteristics fulfilled by the development of this unmanned aerial vehicle. The profile of the mission that the UAV fulfills can be described in several steps:

1. Vertical take-off and vertical climbing up to 1000m height with velocity of 4 m/s to 7m/s in quad-copter mode.

2. Transition from vertical to horizontal flight. This includes the electric start of the piston engine, the descent into horizontal flight and the shutdown of the electric engine.
3. Cruise and loitering with velocity of 120 km/h.
4. Transition from horizontal flight to hovering.
5. Hovering. Duration of hovering depends on the current charge of the batteries, which are charging for the duration of the horizontal flight via a generator, specially developed and adapted to this system.
6. Transition from hovering to horizontal flight.
7. Cruise to final destination.
8. Transition from horizontal flight to vertical flight. Reverse the procedure described in procedure 2.
9. Vertical landing with velocity of 4 m/s in quad-copter mode.

All requirements were taken into account when choosing the optimal methods for the development of this UAV.

3. Dimensioning of lifting surfaces

3.1. Wing geometry

The airfoil NASA/LANGLEY LS(1)-0417 (GA(W)-1) was chosen for the wing. The airfoil data are given in Table 2. The maximum lift coefficient depending on the Reynolds number is given in Table 3. These data were obtained on the basis of experimental research.

Maximum thickness	17%
Zero lift angle	-4.4°
Lift coefficient at zero angle of attack	0.52

Table 2. Basic information about the airfoil.

MRe	$c_{L\max}$
0.37	1.35
0.51	1.39
0.67	1.43
1.9	1.65

Table 3. Maximum airfoil lift coefficient depending on the Reynolds number.

The data given in Table 3 are graphically shown in Figure 1 and approximated by the following polynomial of the third degree:

$$c_{L\max} = 0.04436\mathrm{MRe}^3 - 0.1878\mathrm{MRe}^2 + 0.425\mathrm{MRe}+1.216$$

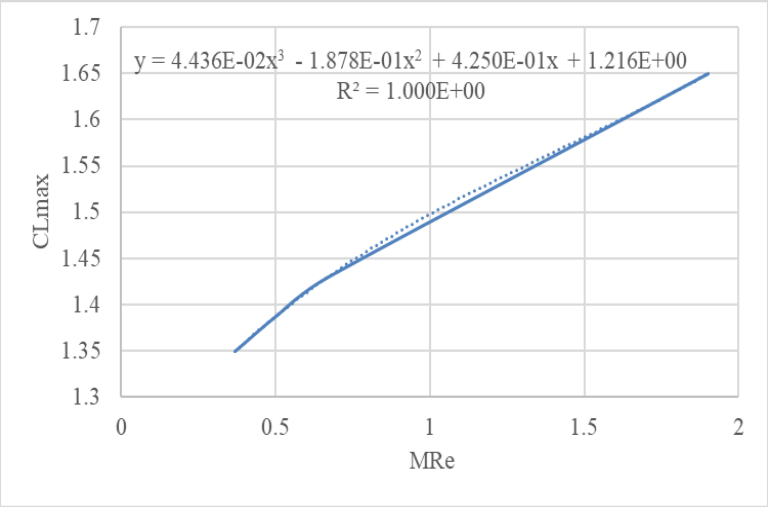

Fig. 1. Maximum drag coefficient of the airfoil depending on the Reynolds number

For the cruise mode of the aircraft, the Reynolds number 1MRe was estimated, so that the following maximum lift coefficient is obtained: $c_{L\max} = 1.5$.

The wing area is determined based on two criteria. The first criterion is cruising speed. The wing loading for cruise mode is obtained as follows:

$$\left(\frac{W}{S}\right)_{\text{cr}} = \frac{1}{2g}\rho V_{\text{cr}}^2\sqrt{\pi A e C_{\text{D0}}} = 54.078\,\text{kg/m}^2 \tag{1}$$

where A it represents the slenderness of the wing, for which the value is taken as 10, e is the Oswald factor, for which the value is taken as 0.8, while C_{D0} represents the coefficient of resistance of the aircraft at the angle of zero lift, for which the value is taken as 0.03. The second criterion is based on the speed of the overrun flight. The wing loading for this flight mode is:

$$\left(\frac{W}{S}\right)_{\text{stall}} = \frac{1}{2g}\rho V_{\min}^2 C_{L\max} = 42.194\,\text{kg/m}^2 \tag{2}$$

where $C_{L\max}$ represents the maximum lift coefficient of the wing, which is taken to be 90% of the maximum airfoil lift: $C_{L\max} = 0.9c_{L\max} = 1.35$. The authoritative value of the wing load for its dimensioning is the smaller value, which is obtained for the swept flight mode. For that mode, the following wing area is obtained: 2.062m^2.

3.2 Tail geometry

An inverted V tail is adopted. NACA0012 was taken for the airfoil of the tail surfaces. When calculating classic tail configurations, the horizontal and vertical are calculated separately, based on the geometric characteristics of the wings, the growth of the aerodynamic centers of the tails and wings, and adopted volume coefficients. For V and inverse V tails, the areas of the fictitious horizontal and vertical tails are calculated first. In theory, the area and angle of the V dihedral and the inverse V tail are obtained as follows:

$$S_{\text{Tail}} = \sqrt{S_{\text{H}}^2 + S_{\text{V}}^2}\ ,\ \Gamma_{\text{Tail}} = \arctan\frac{S_{\text{V}}}{S_{\text{H}}} \tag{3}$$

However, it is recommended that the area of these tail configurations be larger than theoretical, so the area and angle of the V dihedral and the inverse V tail are obtained as follows:

$$S_{\text{Tail}} = S_{\text{H}} + S_{\text{V}},\ \Gamma_{\text{Tail}} = \arctan\sqrt{\frac{S_{\text{V}}}{S_{\text{H}}}} \tag{4}$$

Table 4 shows the adopted parameters for sizing tail surfaces.

The distance between the aerodynamic centers of the wings and the tail	$L = 2\text{m}$
Tail constriction	$\lambda_{\text{Tail}} = \frac{2}{3}$
Volumetric coefficient of the horizontal tail	$n_{\text{H}} = 0.74$
Volumetric coefficient of the vertical tail	$n_{V} = 0.05$

Table 4. Parameters for dimensioning tail surfaces.

The horizontal and vertical tail surfaces are obtained as follows:

$$S_{\text{H}} = \frac{c_{\text{H}} c_{\text{MAC}} S}{L} = 0.3955\text{m}^2,\ S_{\text{V}} = \frac{c_{\text{V}} b S}{L} = 0.2444\text{m}^2$$

Where $c_{\text{MAC}} = \frac{c_{\text{MACi}} S_{\text{i}} + c_{\text{MACo}} S_{\text{o}}}{S} = 0.503\text{m}$ is the length of the aerodynamic chord of the wing, $b = 4.6\text{m}$ wingspan and S=2.062m^2 wing area.

So, we get the area of the inverse V tail, as well as the angle of the dihedral:

$S_{\text{Tail}} = 0.6399\text{m}^2$, $\Gamma_{\text{Tail}} = 38°$.

After dimensioning the lifting surfaces, a 3D model of the UAV was created and is shown in Fig. 2.

Fig. 2. The 3D model of the VTOL UAV.

4. Aerodynamic calculation of finesse and polar in cruise regime

One of the most important phases of development is the aerodynamic calculation, after sizing the aerodynamic surfaces. The preliminary analytical aerodynamic calculation used in this paper shows that the UAV meets the performance of existing UAVs of that category, weighing up to 90 kg. The preliminary calculation was performed in accordance with the procedures described in the literature. [3-6].

4.1. Operating flight condition

In accordance with the intended mission of this UAV. Nominal flight altitudes are on the order of 500–1000 m. This calculation is performed for 500 m of flight altitude. The data from the Standard Atmosphere at a height of 500m are: air density ρ=1.16727 kg/m^3, coefficient of kinematic viscosity ν=1.79579E-05 m^2/s. These data are necessary for the calculation of the drag profile in cruise regime.

4.2. Aerodynamic forces

The maximum finesse of the aircraft is shown by the polar

$$C_X = C_{X0} + \frac{C_Z^2}{\pi A e} = 0.04039 + 0.04297 C_Z^2 \tag{5}$$

The lift, drag and finesse coefficients for cruise regime are:

$$C_{Zcr} = \frac{2mg}{\rho V_{cr}^2 S} = 0.5371, \quad C_{Xcr} = 0.05278, \quad F_{cr} = \frac{C_{Zcr}}{C_{Xcr}} = 10.1758 \tag{6}$$

and the maximum finesse of the aircraft is shown by the polar are:

$$C_{Zcr} = \frac{2mg}{\rho V_{cr}^2 S} = 0.96943, \quad F_{cr} = \frac{C_{Zcr}}{C_{Xcr}} = 12.002 \tag{7}$$

With reference to previous relations, wing aspect ratio $\lambda = 9.876$ and Oswald factor of efficiency $e = 0.75$ the total drag coefficient on the cruise mode is $C_{Xcr} = 0.05278$ respectively, lift coefficient $C_{Zcr} = 0.5371$, cruise speed $V_{cr} = 120$km/h .

A graphical representation of the polar and finesse is in Fig. 3.

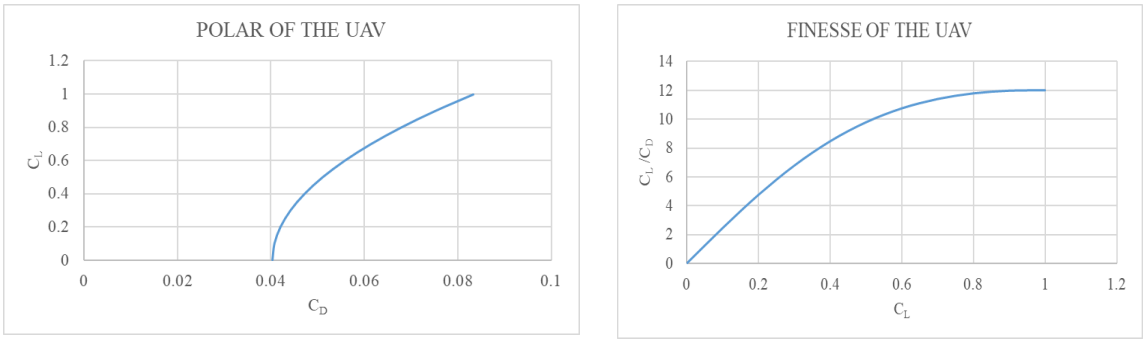

Fig. 3. Polar and Finesse of the UAV

If UAVs are categorized by weight, the expected finesse for this category of UAV and its performance is between $C_{Zcr}/C_{Xcr} = 7$ and $C_{Zcr}/C_{Xcr} = 13$. The preliminary calculation shows that the results are satisfactory.

5. Propulsion

5.1. Electric motors and batteries

Power for hovering and vertical climbing in quadcopter mode can be calculated using disc theory:

$$P_{\mathrm{h}} = \sum_{i=1}^{4} P_{\mathrm{h}i} = \sum_{i=1}^{4} T_i v_{\mathrm{h}i}, \quad P_{\mathrm{cl}} = \sum_{i=1}^{4} P_{\mathrm{cl}i} = \sum_{i=1}^{4} P_{\mathrm{h}i} \left[\frac{V_{\mathrm{cl}}}{2v_{\mathrm{h}i}} + \sqrt{\left(\frac{V_{\mathrm{cl}}}{2v_{\mathrm{h}i}} \right)^2 + 1} \right] \tag{8}$$

where T_i represents the thrust of the i-th propeller, V_{cl} is the climb speed in quadcopter mode, while $v_{\mathrm{h}i}$ represents the induced hover speed, which is calculated as follows:

$$v_{\mathrm{h}i} = \sqrt{\frac{T_i}{A_i}\frac{1}{2\rho}} = \sqrt{\frac{D_{\mathrm{L}i}}{2\rho}} \tag{9}$$

where $D_{\mathrm{L}i} = \dfrac{T_i}{A_i}$ represents the disk load of the i-th propeller. The power required for vertical descent cannot be calculated using disk theory for low speeds, so this power will be assumed to be equal to the power required for hovering. The required power of the i-th engine for hovering and vertical climbing is:

$$P_{\mathrm{eng\_h}i} = \frac{P_{\mathrm{h}i}}{\eta_{\mathrm{p}i}} = \frac{T_i v_{\mathrm{h}i}}{\eta_{\mathrm{p}i}}, \quad P_{\mathrm{eng\_cl}i} = \frac{P_{\mathrm{cl}i}}{\eta_{\mathrm{p}i}} = \frac{P_{\mathrm{h}i}}{\eta_{\mathrm{p}i}}\left[\frac{V_{\mathrm{cl}}}{2v_{\mathrm{h}i}} + \sqrt{\left(\frac{V_{\mathrm{cl}}}{2v_{\mathrm{h}i}}\right)^2 + 1}\right] \tag{10}$$

where $\eta_{\mathrm{p}i}$ represents the degree of utility of the i-th propeller.

The battery power required for hovering and vertical climbing is calculated as follows:

$$\begin{aligned} P_{\mathrm{bat\_h}} &= \sum_{i=1}^{4}\frac{P_{\mathrm{h}i}}{\eta_{\mathrm{p}i}\eta_{\mathrm{eng}i}\eta_{\mathrm{esc}i}\eta_{\mathrm{c}i}} = \sum_{i=1}^{4}\frac{T_i v_{\mathrm{h}i}}{\eta_{\mathrm{p}i}\eta_{\mathrm{eng}i}\eta_{\mathrm{esc}i}\eta_{\mathrm{c}i}}, \\ P_{\mathrm{bat\_cl}} &= \sum_{i=1}^{4}\frac{P_{\mathrm{cl}i}}{\eta_{\mathrm{p}i}\eta_{\mathrm{eng}i}\eta_{\mathrm{esc}i}\eta_{\mathrm{c}i}} = \sum_{i=1}^{4}\frac{P_{\mathrm{h}i}}{\eta_{\mathrm{p}i}\eta_{\mathrm{eng}i}\eta_{\mathrm{esc}i}\eta_{\mathrm{c}i}}\left[\frac{V_{\mathrm{cl}}}{2v_{\mathrm{h}i}} + \sqrt{\left(\frac{V_{\mathrm{cl}}}{2v_{\mathrm{h}i}}\right)^2 + 1}\right] \end{aligned} \tag{11}$$

The energy consumed by the hovering and vertical climbing battery is:

$$E_{\mathrm{bat\_h}} = P_{\mathrm{bat\_h}} t_{\mathrm{h}}, \quad E_{\mathrm{bat\_cl}} = P_{\mathrm{bat\_cl}} t_{\mathrm{cl}} \tag{12}$$

where t_{h} and t_{cl} represent the hovering and vertical climbing times, respectively [7].

Assuming that the finesse in horizontal flight is around 10, the disc loading for two-bladed propeller is $D_L = 268\mathrm{N/m}^2$, Table 5 presents the required energy from batteries for each segment of flight.

Energy from batteries	Vertical take-off and climbing	Hovering
(kW)	16	14.7

Table 5. Required energy from batteries for each segment of flight.

In accordance with the needs of the system, electric motors were chosen. With one engine, a maximum thrust of 303 N can be achieved, while the maximum power is 7.125kW. The maximum voltage that can be achieved with batteries is 53.9 V. The selected electric motors are the most efficient in this case and meet the needs of the project. The relationship between power and thrust is shown in Fig.4.

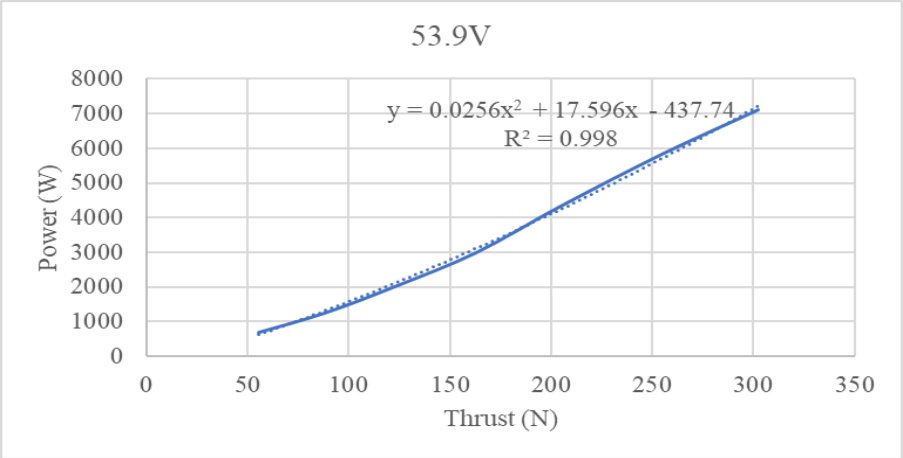

Fig. 4. The ratio of required power and thrust for vertical flight**.**

5.2. Calculation of the propulsion unit for horizontal flight

Aerodynamic drag in cruise mode is calculated as follows:

$$R_{X\text{cr}} = \frac{1}{2}\rho V_{\text{cr}}^2 S C_{X\text{cr}} \tag{13}$$

Respectively,

$$R_{X\text{cr}} = \frac{mg}{F_{\text{cr}}} \tag{14}$$

The required thrust is equal to the aerodynamic drag force:

$$T_{\text{cr}} = R_{X\text{cr}} = \frac{1}{2}\rho V_{\text{cr}}^2 S C_{X\text{cr}} = \frac{mg}{F_{\text{cr}}} = 49.4\text{N} \tag{15}$$

The power of propulsion unit required for cruise mode is:

$$P_{\text{cr}} = \frac{T_{\text{cr}} V_{\text{cr}}}{\eta_{\text{p}}} = 2.195\text{kW} \tag{16}$$

Where η_{p} represents the degree of utility of the propeller whose preliminary value is $\eta_{\text{p}} = 0.75$.

5.3. Required power and thrust at maximum speed in horizontal flight

As with cruise regime, the thrust and required power at maximum speed in horizontal flight can be determined. Thrust is:

$$T_{\max} = R_{X\max} = \frac{1}{2}\rho V_{\max}^2 S C_{X\max} = \frac{mg}{F_{\max}} = 100.98\text{N} \tag{17}$$

The power of propulsion unit required for cruise mode is:

$$P_{\max} = \frac{T_{\max} V_{\max}}{\eta_{\text{p}}} = 7.48\text{kW} \tag{18}$$

Based on the maximum speed of the aircraft, the required power of the propulsion group can be determined based on statistical parameters [4]:

$$\frac{P[\text{hp}]}{W_0[\text{lb}]} = a V_{\max}^C [\text{ml/h}] \tag{19}$$

Where the parameters a and C are determined based on the ratio of power and mass of the aircraft. In the available literature [4], parameters can be find by category.

Based on the categorization from the literature, it can be seen that there is no clear classification of the aircraft that is the subject of the calculation. Therefore, two cases will be considered: "Homebuilt-composite" and "General aviation - single engine". Converting the mass of the aircraft and the maximum speed into the appropriate units of measurement, the following powers of the propulsion unit are obtained:

- first case: $P = 7.09\text{kW}$
- second case: $P = 7.868\text{kW}$

Based on the obtained results, it can be seen that the obtained values are very close to the value obtained by analytical calculation.

5.4. Power and thrust required for climbing in airplane mode

Thrust and power required for climbing in airplane mode are obtained as follows:

$$T_{\text{cl}} = \frac{1}{2}\rho V^2 C_X S + mg\frac{v_{\text{cl}}}{V} \tag{20}$$

$$P_{\text{cl}} = \frac{\frac{1}{2}\rho V^3 C_X S + mgv_{\text{cl}}}{\eta_{\text{p}}} \tag{21}$$

Thrust and required power were analyzed for multiple aircraft speeds in airplane mode and climb speed, to establish the highest values.

Results for speed of 120 km/h are shown in Table 6.

V[km/h]	v_{cl}[m/s]	T_{cl}[N]	P_{cl}[kW]
120	1	69.704	3.098
	2	90.306	4.0136
	3	110.907	4.929
	4	131.508	5.845
	5	152.109	6.76
	6	172.71	7.676

Table 6. Power and thrust required for climbing

5.5. Thrust and required power for a proper turn

The thrust required for a proper turn is calculated as follows:

$$T_{\text{st}} = \frac{1}{2}\rho V^2 C_X S + \frac{n^2 m^2 g^2}{\frac{1}{2}\rho V^2 S\pi Ae} \tag{22}$$

where n is the load coefficient. Assuming that the load factor is 3, and that the turn is performed at cruising speed, the following thrust value is obtained:

$$T_{\text{st}} = 184.655\text{N}$$

The required power of the power unit is:

$$P_{\text{st}} = \frac{T_{\text{st}} V_{\text{cr}}}{\eta_{\text{P}}} = 8.207\text{kW}$$

Based on the previous power calculation, a piston engine with a maximum power of 13.2kW was selected. This engine was tested with several different propellers and accordingly the 28/12 propeller was chosen.

6. Conclusions

Development of fixed-wing VTOL UAV is still in rising phase. The corresponding aerodynamic configuration's improvement, design optimization of structure, flight control theory improvement and development and energy management technology still need to be improved. The research of fixed-wing VTOL UAV will become an important direction of aircraft's development.

This paper presents a preliminary calculation for the initial phases of the UAV development. As this is an early stage of the project, there remains the possibility of more detailed analysis, e.g. numerical calculation, testing and validation. Sometimes it is necessary to develop models for establishing the calculation, production and validation methodology, due to the deficiency of literature. Experience also plays an important role in such development projects. Also, this paper presents the requirements that were met during the development of this multi role system. In addition, the basic parts of the preliminary conceptual design are presented.
Future work should include the integration of all subsystems and systems. Independent testing of piston engine and starter-generator and autopilot systems.

ORCID
Radoslav D. Radulovic https://orcid.org/0000-0002-9345-919X
Milica P. Milic https://orcid.org/0000-0003-4505-6086

Acknowledgements: The authors would like to express their gratitude to EDePro company for research work on the project ALECS multirole system.

References:

[1] Hepperle M., *Electric flight-potential and limitations*, Energy Efficient Technologies and Concepts of Operation, 22-24 October 2012, Lisbon, Portugal, 2012
[2] Ozdemir U., Aktas Y., O., Vuruskan A., Dereli Y., Tarhan A., F., Demirbag K., Erdem A., Kalaycioglu G., D., Ozkol I., Inalhan G., *Design of a commercial hybrid VTOL UAV system*, Journal of Intelligent and Robotic Systems, Vol. 74, 371-393, 2014.
[3] Sadraey, M.H.: Unmanned aircraft design. A review of fundamentals, Morgan & Claypool Publishers, 2017
[4] Reymer, D., P., Aircraft Design: a ConceptualApproach, Third edition, AIAA, Reston, Virginia, USA, 1999.
[5] Roskam J., *Airplane Design, Part VI: Preliminary Calculation of Aerodynamic, Thrust and Power Characteristic,* Roskam Aviation and Engineering Corporation, Ottawa, Kansas, USA, 1987.
[6] Roskam J., *Airplane Design, Part VII: Determination of Stability, Control and Performance Characteristic: FAR and Military Requirements,* Roskam Aviation and Engineering Corporation, Ottawa, Kansas, USA, 1988.
[7] Gloudemans, J., Davis, P., Gelhausen, P.: A rapid geometry modelerfor conceptual aircraft. In: 34th Aerospace Sciences Meeting and Exhibit. AIAA, Reston,1996.

DETERMINATION OF THE OVERALL MATERIAL PARAMETERS IN THE SERIES-PARALLEL ROCK-MASS MIXTURE

Dragan M. Rakić[1], Miroslav Živković[1], and Milan Bojović[1]

[1] Faculty of Engineering,
University of Kragujevac, Sestre Janjić 6, 34000 Kragujevac
e-mail: drakic@kg.ac.rs, miroslav.zivkovic@kg.ac.rs, mbojovic@outlook.com

Abstract:

In this paper, the authors were involved in the development of relations that determine the parameters of the overall material based on the parameters of series and parallel connections of materials and their volume fractions. The criteria used to compare the mechanical behavior of the mixture model and the overall material is that uniaxial compression and tension tests give overall responses. In the analysis, it was assumed that the two materials in one part of the volume form a serial connection, while that serial connection in the other part of the volume forms a parallel connection, so a kind of composite is formed. The conducted numerical analyses show that it is possible to define relations for translating the parameters of the composite material into one overall material for the case of uniaxial tests. In the case of damage concrete constitutive model, which was used to simulate the behavior of the rock mass, the use of uniaxial tests is justified, because they are used to determine the material parameters of this model. Another reason that justifies the use of uniaxial tests is that the failure in concrete and rock mass occurs due to exceeding the normal stresses in the principal directions, which corresponds to the case of uniaxial tests. The results of the numerical analysis show the accuracy of the implementation of this approach.

Keywords: overall property, series-parallel model, constitutive modelling, finite element method

1. Introduction

The main goal of this paper is to determine the overall parameters of the rock mass material for the case of using the elastic-plastic constitutive model with damage, based on known material parameters and their volume fractions in the mixture [1]. The case of mechanical behavior of materials in series and parallel connection, as well as the arbitrary combinations of series and parallel connection of materials [2] was considered. In the literature, there are several approaches for determining the overall parameters which describe the overall behavior of a model made of two or more different materials. These approaches were mainly developed for the analysis of the mechanical behavior of composites. The two basic approaches which are most often encountered in the literature are Voigt Estimate (VE) and Reuss Estimate (RE) for two-phase components [3]. The Voigt Estimate corresponds to the case of parallel connection, where the same strain occurs in the phases exposed to uniaxial loading, while the total stress represents the sum of the stresses in each of the phases proportional to their volume fractions. The Reuss Estimate corresponds to the case of series connection of materials, where the phases exposed to uniaxial load have the same

stress values, while the total strain is equal to the sum of the strains in each of the phases proportional to their volume fractions. The disadvantage of this approach is that it determines only the limit values of the material parameters [4], while in real conditions, with arbitrary geometry, the parameter values of the overall material lie between these limit values.

The two most common approaches used to describe the mechanical behavior of composites in practice are: Mori-Tanaka Estimation (MTE) and Self Consistent Estimation (SCE) [5, 6]. However, these approaches are not easy to apply when it comes to complex constitutive models, such as damage concrete constitutive model which was used to describe the mechanical behavior of the rock mass in this analysis. For this reason, the numerical analysis of series and parallel connections of materials, as well as their arbitrary combinations, was carried out and then relations that determine the parameters of the overall material on the basis of volume fractions were defined. The condition used to determine the overall materials parameters is that the mechanical response of the models is the same, as well as the factors of safety in the numerical simulations of the uniaxial compression and uniaxial tension tests are the same. In order to identify the parameters of the constitutive model [7] for which relations need to be established, a sensitivity analysis was first conducted. Verification of the adopted relations was carried out on numerical simulations of uniaxial compression and tension tests. These tests were adopted for the verification of the developed methodology, because the parameters of damage concrete constitutive model are determined based on them. Examples were generated with a mixture of serial and parallel connection, which is the most common case in real conditions when it comes to rock mass. These tests showed that it is possible to determine the parameters of the overall material whose mechanical behavior fully corresponds to the mechanical behavior of the model with a mixture of series and parallel connection, in the case where the volume fractions of individual materials are known. The PAK program package [8, 9] was used for all numerical simulations carried out within this paper.

2. Theoretical basics

2.1 Mixture models for elastic material

The rock mass in real conditions consists of several quasi-homogeneous zones that have different mechanical behaviors [10]. These quasi-homogeneous zones often have an arbitrary geometry, that is, they occupy arbitrary orientations in the rock mass, which when discretizing the domain for numerical analysis is not always possible to model with sufficient accuracy. The reason for this is that detailed modeling of quasi-homogeneous zones of the rock mass would require a dense mesh of finite elements, which is not always possible in real conditions because this would significantly increase the number of finite elements, and thus increase the requirements for computer resources. In order to overcome this problem, the domain is discretized using finite elements of optimal size with the aim of obtaining the optimal number of finite elements. However, this method often results in a coarse mesh of finite elements, so within the same finite element, several different materials can be found. Materials arranged in this way can be in series or parallel connection, but combinations of these two connections are most common (Fig. 1). In that case, it would be optimal to determine the overall material parameters within the elements in which there are different quasi-homogeneous zones.

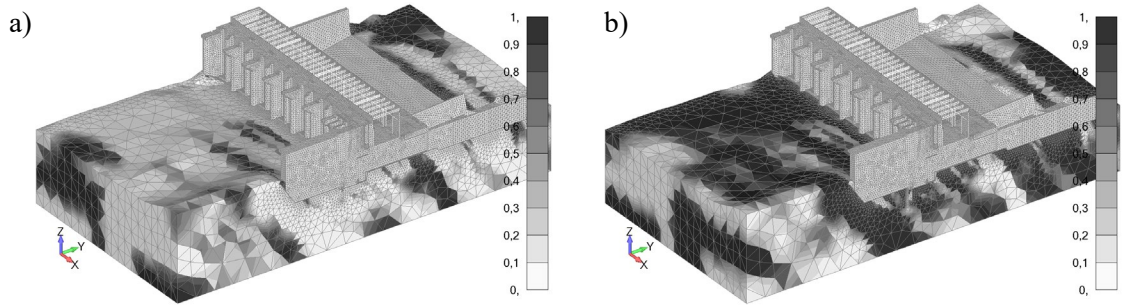

Fig. 1. The volume fraction of material 1 and material 2

Since the rock mass material is dominantly exposed to compressive load, the assumption that the analyzed models are loaded under pressure will be adopted. The parallel connection of two materials forming a kind of composite loaded with uniaxial compressive load is shown in Fig. 2a.

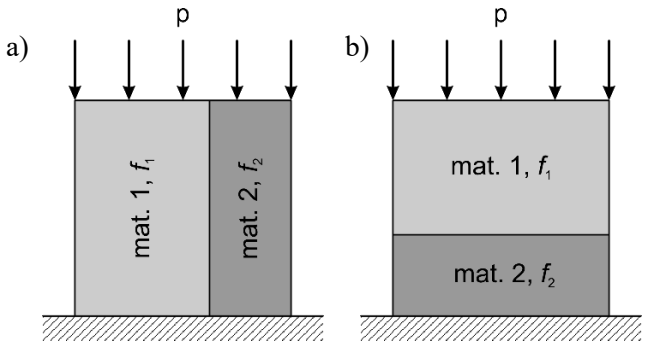

Fig. 2. Models with a) in-parallel and b) in-series connections

Based on the conditions for the parallel connection of the two materials, as stated in the introduction, the strain is the same in both phases:

$$\varepsilon = \varepsilon_1 = \varepsilon_2 \tag{1}$$

while the total stress is equal to the sum of the stresses in each of the phases but proportional to their volume fractions:

$$\sigma = \sigma_1 f_1 + \sigma_2 f_2 \tag{2}$$

Quantities σ and ε represent the overall stress and strain, σ_1 and σ_2 are the stresses in the materials 1 and 2, ε_1 and ε_2 are the strains in materials 1 and 2, while the quantities f_1 and f_2 represent the volume fractions of materials 1 and 2 (V_1 and V_2) in the total volume (V):

$$f_1 = \frac{V_1}{V}, \quad f_2 = \frac{V_2}{V}, \quad V = V_1 + V_2 \tag{3}$$

Substituting equations (1) and (2) into the equation representing Hook's law [11]:

$$E = \frac{\sigma}{\varepsilon} \tag{4}$$

Follows the expression for the equivalent modulus of elasticity of the parallel connection of two elastic materials:

$$E = E_1 f_1 + E_2 f_2 \tag{5}$$

The case of series connection of two elastic materials is shown in Fig. 2b. In this case, the total stress in the model is equal to the stress in each of the phases:

$$\sigma = \sigma_1 = \sigma_2 \tag{6}$$

while the overall strain is equal to the sum of the strains in each of the phases proportional to their volume fractions:

$$\varepsilon = \varepsilon_1 f_2 + \varepsilon_2 f_2 \tag{7}$$

By substituting equations (6) and (7) into equation (4) the expression for the overall modulus of elasticity can be written as:

$$\frac{1}{E} = \frac{f_1}{E_1} + \frac{f_2}{E_2} \tag{8}$$

By applying the relations defined in this chapter for serial and parallel connection of materials, all the parameters of the constitutive model whose theoretical basics are presented below were analyzed.

2.2 CDP constitutive model

The concrete damaged plasticity constitutive model within this paper was used to describe mechanical behavior of the rock-mass. This constitutive model defines the behavior of material using the yield function originally developed by Lubliner et al [12] and improved by Lee and Fenves [13].

According to the incremental theory of plasticity, the tensor of the total strain can be decomposed into elastic and plastic strain [14]:

$$\boldsymbol{\varepsilon} = \boldsymbol{\varepsilon}^E + \boldsymbol{\varepsilon}^P \tag{9}$$

The elastic part is defined by the following equation:

$$\boldsymbol{\varepsilon}^E = \mathbf{C}^{-1}\boldsymbol{\sigma} \tag{10}$$

where **C** represents the elastic stiffness tensor.

The plastic part is an irreversible part of the total strain which can be expressed by applying equations (9) and (10) as:

$$\boldsymbol{\varepsilon}^P = \boldsymbol{\varepsilon} - \mathbf{C}^{-1}\boldsymbol{\sigma} \tag{11}$$

The damage that occurs in the material is most often described using stiffness degradation. The following equation defines elastic stiffness using scalar stiffness degradation parameter [14]:

$$\mathbf{C} = \left(1 - d\right)\mathbf{C}_0 \tag{12}$$

where d represents the scalar degradation parameter, and $\mathbf{C}_0$ is the initial stiffness matrix.

Based on equation (12), current elasticity modulus can be defined as:

$$E = (1-d)E_0 \tag{13}$$

where E_0 denotes the initial value of elasticity modulus.

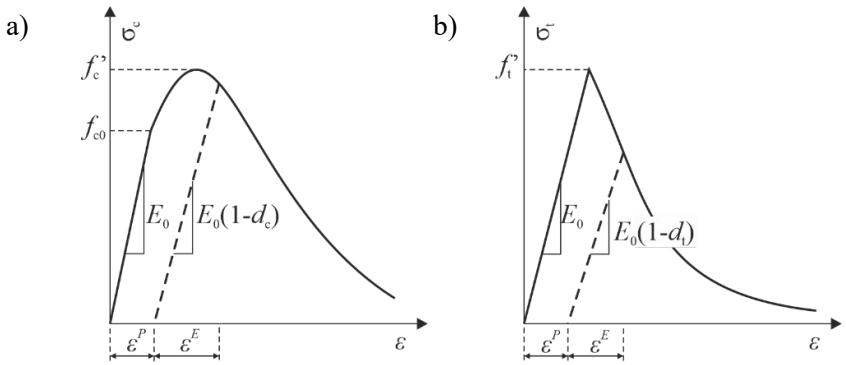

Fig. 3. Dependence of effective stress on strain for: a) compression and b) tension

Yield function of concrete damaged plasticity constitutive model [14, 15] is defined using the following equation:

$$F(\bar{\boldsymbol{\sigma}}, \boldsymbol{\kappa}) = \frac{1}{1-\alpha}\left(\alpha \bar{I}_1 + \sqrt{\frac{3}{2}}\left\|\bar{\mathbf{S}}\right\| + \beta(\boldsymbol{\kappa})\left\langle \bar{\sigma}_{\max}\right\rangle\right) - c_c(\boldsymbol{\kappa}) \le 0 \tag{14}$$

Where the following notation was used: $c_c(\boldsymbol{\kappa}) = \bar{\sigma}_c(\boldsymbol{\kappa})$ - material cohesion, $\bar{I}_1 = \mathrm{tr}\bar{\boldsymbol{\sigma}}$ - first stress tensor invariant, $\bar{\mathbf{S}} = \bar{\boldsymbol{\sigma}} - \bar{\sigma}_m \mathbf{I}$ - deviator of effective stress, $\bar{\sigma}_m = \frac{1}{3}\mathrm{tr}\bar{\boldsymbol{\sigma}}$ - mean effective stress, $\bar{\sigma}_{\max}$ - algebraic maximum of eigenvalues of effective stress tensor $\bar{\boldsymbol{\sigma}}$

The dependence of the effective stress with respect to strain for compression and tension is shown in Fig. 3.

Maximum stress (f_c', f_t') and yield stresses (f_{c0}, f_{t0}) for compression and tension are defined with following equations [14], respectively:

$$f_c^{'} = f_{cm} = f_{c0}\frac{(1+a_c)^2}{4a_c}, \qquad f_t^{'} = f_{t0} \tag{15}$$

where a_c represents compression curve parameter.

Based on the presented constitutive relations, it can be concluded that the relations between stress, strain and degradation are extremely complex [16, 17] and that it is not possible to obtain the overall material parameters in a closed form but rather the relations can be formed based on the results of numerical analysis.

3. The series-parallel model

As the connection of quasi-homogeneous zones of the real rock mass is neither series nor parallel, as elaborated in the previous chapter, the effects of different mixtures are discussed in this chapter. In the first case, a model consisting of two phases was considered, where one phase is included in the other as a cylindrical volume (particle). It was adopted that the volume fractions are 70%-30% in favor of the higher strength material (Fig. 4a).

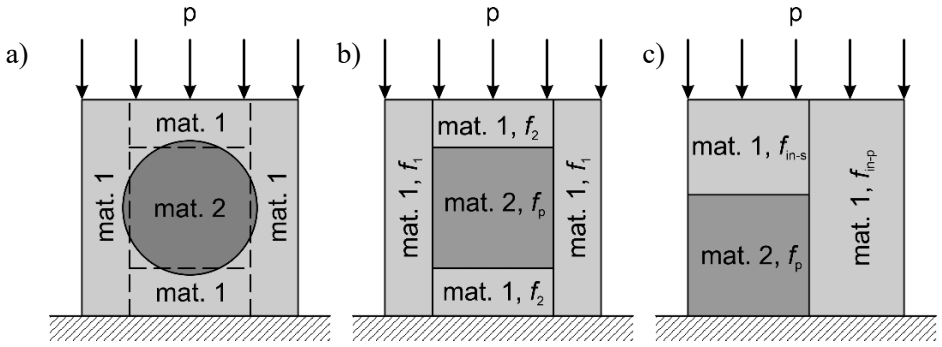

Fig. 4. The in-series and in-parallel material mixture

In this way, a mixture of series and parallel connections was formed, which is the most common case in real conditions. In the second case (serial-parallel), a model with the same volume fraction of the material was analyzed but the cylindrical shape of the inclusion was replaced by a square shape (Fig. 4b). In the third case (simple), an additional simplified model was analyzed, where the materials were regrouped to form one series and one parallel connection (Fig. 4c) while the volume fractions remained the same as in the previous two cases. Quantities $f_{in\text{-}p}$ and $f_{in\text{-}s}$ in Fig. 4 represent the volume fractions of materials that are in parallel and serial connection, respectively.

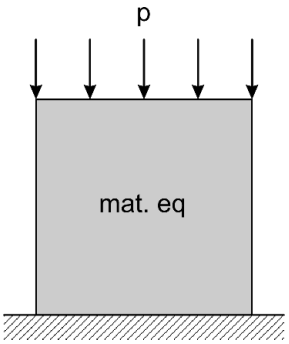

Fig. 5. One-material equivalent model

For the models formed in this way, a numerical analysis of the uniaxial compression and tension test was carried out and the dependence between stress and strains was analyzed for known volume fractions. After these models with series and parallel mixture of two materials, a model with one overall material was analyzed using the same boundary conditions and loads as in the previous cases (Fig. 5). The criteria for determining the parameters of the overall material are that the model gives the same mechanical response in uniaxial compression and tension tests, and that the numerical simulations using the applied pressure give the same factors of safety in all cases.

4. Application of the series-parallel model

For the cases described in the previous chapter, finite element models of unit dimensions were formed using hexahedral finite elements with eight nodes. Numerical simulations were carried out on the models formed in this way using the prescribed displacements. They are loaded by applying the prescribed displacements in order to ensure the convergence of the numerical solutions even after the peak strength of the material is exceeded. The displacements are applied in all nodes on the upper surface of the model, which ensures the condition from the initial assumption that the strains are the same in both phases in the case of parallel connection, that is, that the stress is the same in both phases in the case of series connection. The material parameters used in the numerical simulation were taken from the report on numerical simulations of real dam [18, 7] and are shown in the Table. 1

mat.	E (GPa)	ν	f_c' (kPa)	f_t' (kPa)	a_c	D_c	a_t	D_t	G_c (kPa)	G_t (kPa)	α_p	α_F	γ
1	5,70	0.213	88.5	6.33	6.36	0.5	0.5	0.5	3.22E-02	2.49E-03	0.174	0.210	7.44
2	1,00	0.276	35.5	2.79	8.91	0.5	0.5	0.5	1.49E-02	1.16E-03	0.116	0.110	4.95
eq.	3.19	0.230	55.0	4.91	6.96	0.5	0.5	0.5	2,00E-02	1,10E-03	0.151	0.165	6.46

Table. 1. Material parameters

In order to establish relations for obtaining overall material parameters, a sensitivity analysis of the constitutive model was conducted. The sensitivity analysis was conducted using uniaxial compression and tension tests, where the parameters were determined for the case of series and parallel connections and their influence on the stress-strain dependence was analyzed.

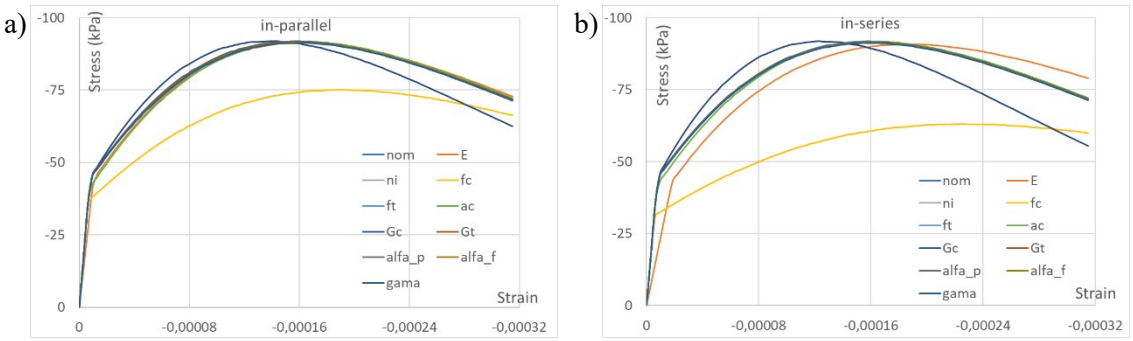

Fig. 6. Sensitivity test of uniaxial compression test a) in-parallel, b) in-series

By conducting the sensitivity analysis, the parameters of the constitutive model that have the greatest influence on the material behavior were identified, depending on the type of connection (series or parallel). These parameters were then calculated for the overall material. The results of the sensitivity analysis are shown in Fig. 6 and Fig. 7.

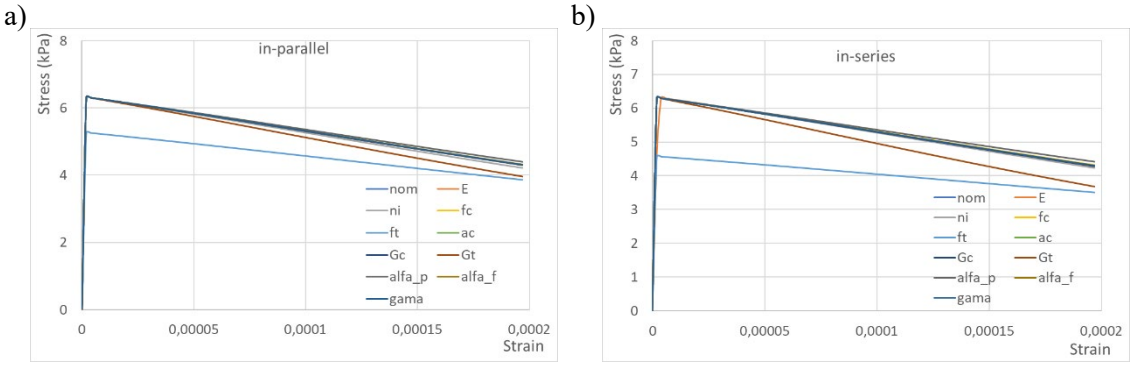

Fig. 7. Sensitivity test of uniaxial tension test a) in-parallel, b) in-series

After sensitivity analysis and establishing the relations for determining the parameters of the overall material, numerical simulations were carried out for all four cases shown in Fig. 4 and Fig. 5. The results of the conducted analyzes are shown in Fig. 8.

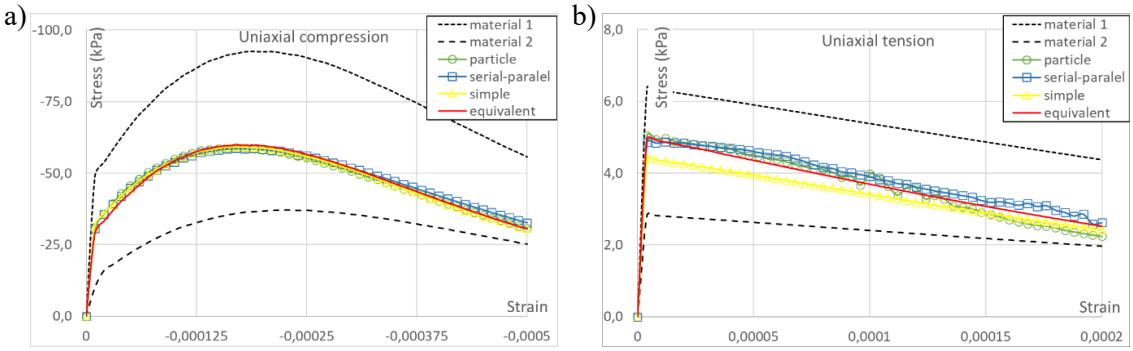

Fig. 8. In-series and in-parallel mixture: a) compression, b) tension

The result of conducted analyses show that it is possible to determine the parameters of the overall material for the case of uniaxial compression and uniaxial tension tests, so that the behavior of the overall material corresponds to the behavior of the models with the mixture of series and parallel connection of the two materials.

In addition to the stress-strain analysis, the factors of safety for the same numerical tests were also determined. The conducted analyses show that the factors of safety for compression and tension uniaxial tests have a deviation of less than 5%, which serves as an additional validation of

the procedure for determining the parameters of the overall material in the case of a series and parallel mixture.

5. Conclusions

The paper proposes the approach for determining the overall parameters of a homogeneous material for the case of series and parallel mixture of two materials. The parameters of the overall material were calculated using known relations for series and parallel connection of elastic materials. Numerical verification was carried out through the implementation of the proposed methodology on uniaxial compression and tension tests.

The use of uniaxial compression and tension tests is justified because the parameters of this constitutive model are precisely determined on the basis of these tests. Also, failure in concrete and rock mass material occurs as a result of exceeding the normal stress in the principal directions, which corresponds to the conditions prevailing in uniaxial tests. It is shown that the composite consisting of the series and parallel mixture of two materials can be replaced by an overall homogeneous material if the volume fractions of the basic materials are known. In this way, the problem of using a fine mesh to capture different materials can be solved, which significantly reduces the requirements for computer resources.

Acknowledgements: This research is partly supported by the Ministry of Education and Science, Republic of Serbia, Grant TR32036 and Grant TR37013.

References:

[1] Cho J., Ha D., *Averaging and finite-element discretization approaches in the numerical analysis of functionally graded materials*, Materials Science and Engineering: A, pp. 187-196, 2001.
[2] Tan J., Jia Y., Li L., *A series–parallel mixture model to predict the overall property of particle reinforced composites*, Composite Structures, pp. 219-225, 2016.
[3] Sadowski P., Kowalczyk-Gajewska K., Stupkiewicz S., *Classical estimates of the effective thermoelastic properties of copper–graphene composites*, Composites Part B: Engineering, pp. 278-290, 2015.
[4] Hill R., *A self-consistent mechanics of composite materials*, Journal of the Mechanics and Physics of Solids, pp. 213-222, 1965.
[5] Benveniste Y., *A new approach to the application of Mori-Tanaka's theory in composite materials*, Mechanics of Materials, pp. 147-157, 1987.
[6] Reiter T., Dvorak G., Tvergaard V., *Micromechanical models for graded composite materials*, Journal of the Mechanics and Physics of Solids, pp. 1281-1302, 1997.
[7] Rakić D., Bodić A., Milivojević N., Dunić V., Živković M., *Concrete damage plasticity material model parameters identification*, Journal of the Serbian Society for Computational Mechanics, t. 15, br. 2, pp. 111-122, 2021.
[8] Živković M., Vulović S., Rakić D., Dunić V., Grujović N., *Software for solving coupled problems - PAK Multiphysics*, University of Kragujevac, Faculty of Mechanical Engineering, Kragujevac, 2019.
[9] Kojić M., Slavković R., Živković M., Grujović N., Rakić D., *Software for geomechanics - PAK-GEO*, Faculty of Mechanical Engineering, University of Kragujevac, Kragujevac, 2010.
[10] Rakić D., Stojković M., Ivetić D., Živković M., Milivojević N., *Failure Assessment of Embankment Dam Elements: Case Study of the Pirot Reservoir System*, Applied Sciences, t. 12, br. 2, p. 558, 2022.
[11] Kojić M., Slavković R., Živković M., Grujović N., *Finite element method 1, Linear analysis (in Serbian)*, University of Kragujevac, Faculty of Mechanical Engineering: Kragujevac, 1998.
[12] Lubliner J., Oliver J., Onate E., *A plastic-damage model for concrete*, International Journal of Solids and Structures, t. Volume 25, br. 3, pp. 299-326, 1989.

[13]Lee J., Fenves G., *Plastic-Damage Model for Cyclic Loading of Concrete Structures*, Journal of Engineering Mechanics, t. 124, br. 8, 1998.
[14]Lee J., *Theory and implementation of plastic-damage model for concrete structures under cyclic and dynamic loading*, Berkeley, California: University of California, 1996.
[15]Rakić D., Dunić V., Živković M., Grujović N., Divac D., *Modeling of damaged concrete using initial degradation parameter*, Journal of the Serbian Society for Computational Mechanics, t. 13, br. 2, pp. 8-18, 2019.
[16]Karsan D., Jirsa J. O., *Behavior of Concrete Under Compressive Loadings*, Journal of the Structural Division Vol. 95, 1969.
[17]Taylor R., *FEAP: a finite element analysis program for engineering workstation. Rep. No. UCB/SEMM-92 (Draft version)*, University of California: Berkeley: Department of Civil Engineering, 1992.
[18]Water institut Jaroslav Černi, *Safety management system for HPP Djerdap 1 dam - Report of the FE model of thermal, filtration and stress-strain processes at the overflow and power section of the dam and power plant*, Water institut Jaroslav Černi, Belgrade, 2017.

CORRUGATION ELASTICITY AS A NEW PROPERTY OF NANOSTRUCTURED MATERIAL: HOLOGRAPHIC ANALYSIS OF *APATURA* BUTTERFLY WINGS

Marina Simovic Pavlovic[1], Katarina Nestorovic [2], Aleksandra Radulovic[3], and Maja Pagnacco[4]

[1] Faculty of Mechanical Engineering, University of Belgrade, Kraljice Marije 16, Belgrade, Serbia
e-mail: simovicmarina99@gmail.com
[2] Military Technical Institute, Ratka Resanovica 1, Belgrade, Serbia
e-mail: katarina.nestorovic993@gmail.com
[3] Institute of General and Physical Chemistry,University of Belgrade, Studentski trg 12/V, Belgrade, Serbia
e-mail: aradulovic@iofh.bg.ac.rs ,
[4] Institute of Chemistry, Technology and Metallurgy, University of Belgrade, Njegoseva 12, Belgrade, Serbia
e-mail: maja.pagnacco@ihtm.bg.ac.rs

Abstract

The corrugation of the structure is a special property of the material that has a great influence on almost all other characteristics of the same. The connection between materials based on the corrugation of natural structures such as *Apatura* butterfly wings and its examination (the six samples of same species) by the method of holographic interferometry (with four different wavelengths of laser radiation) is presented in this paper. The concept of material's corrugation elasticity is presented as well as the advantages of this concept. The holographic method was implemented as appropriate for monitoring the structure dynamics at the nanoscale. Finally, the important factor that impacts the elasticity of the corrugation of the material lies in the optical factors of the environment is emphasized, i.e., in the light of laser radiation that structure interferes with. A completely non-linear dependence on the wavelengths of light is shown, where for wavelengths of 532 nm and 660 nm the elasticity of the corrugation is observed, while for 450 nm and 980 nm a plastic deformation of the corrugation is observed. These preliminary studies open new possibilities in the synthesis and testing of different materials and monitoring of their dynamics in real time.

Keywords: corrugated materials, structure morphology, holographic monitoring, dynamics monitoring, *Apatura* butterfly.

1. Introduction

When talking about nanostructures, very small deviations in dimensions play a big role. The corrugation of the material - the nanostructure, has numerous advantages and the material itself has different properties due to different types of corrugation [1]. To gain a deeper understanding

of the range of complex corrugated structures, the three different types of corrugation of natural structures are presented by Scanning Electron Microscope (SEM) images in Figure 1.

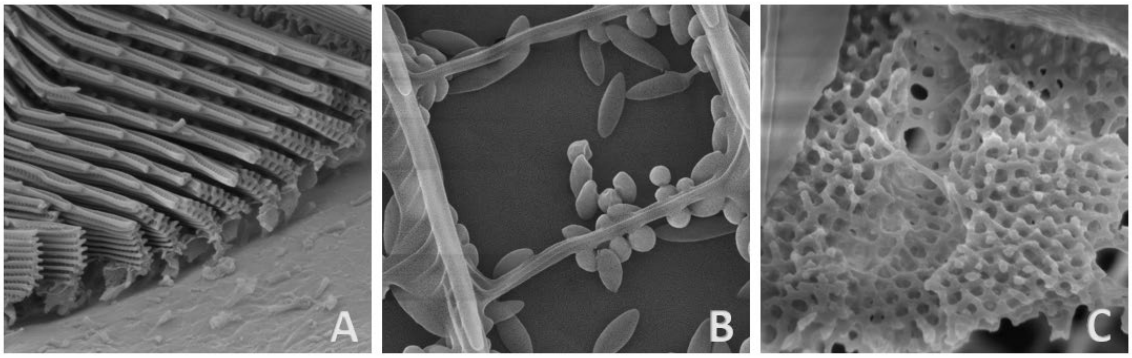

Fig. 1. SEM images of the representatives of various structures: *Morpho didius* butterfly (A), *Pieris rapae* butterfly (B), and *Calophrys rubi* butterfly (C).

In this paper we deal with the corrugation of the surface of nanomaterials of *Apatura* butterfly wings. Generally, surface corrugation can have a huge impact on the performance of the material as well as on the durability of the structure. Measurements of the corrugation could be done in a several different ways [2], such as measuring the average corrugation and the extreme values. However, determining the characteristics of the corrugation itself and its behavior under certain influences is of much greater importance.

The influence of temperature on the material, its deformation, can be examined by different methods [3, 4], easily and visually ascertained, when it comes to obvious tearing of the structure or a change in the chemical composition. [5] When dealing with a change in corrugation property that has the potential to return to its original state after some period of time, microscopic observation is not always the best method. The method itself or the conditions required for the method used can lead to error. For example, a sample holder could speed up the cooling process, more precisely it could lead to an unrealistic degree of heating. In this case, the method of holographic interferometry [6] can be an excellent choice since it has the possibility to follow the deformation over time. Hence, if there is a very small change in the moment of exposure, which changes over time or the object of exposure returns to its original state, holography will record such information. Therefore, the holographic method is ideal when talking about the dynamics of complex corrugations of nanoscale structures.

When we talk about the behavior of the corrugation itself of a nanostructure during and after deformation, more precisely about the plastic or elastic deformation [7] of that corrugation, it can be said that we are aiming for a higher level of behavior of corrugated nanomaterials. The concept of *corrugation elasticity* of the material can be introduced, which would imply the ability of the material to return its damaged corrugation property to the original form. The benefits of corrugated materials are enormous [8], so a detailed examination of their characteristics and the disclosure of their special properties are of great importance.

To test the elasticity of the corrugation the less-understand phenomena at micro-scales called thermophoretic effect was used. [9, 10] When the distance between surfaces which have different temperatures, is in order of the free path of the molecules, thermal forces occur. Due to the mentioned temperature differences, the surrounding gas causes the formation of a force, and the resulting forces are called mechanical displacement. In this specific experiment, the temperature difference is caused by radiation of lasers of different wavelengths. Finally, this mechanical displacement of the corrugation is noticed on the *Apatura* butterfly wing structure, and it is holographically monitored.

2. Materials and methods

2.1 Samples

The structure of butterfly wings proved to be a very characteristic corrugated structure. An example of the mentioned type of structure, precisely "herringbone" type, the structure of the *Apatura* butterfly's wing [11] used to examine the phenomenon presented here, is shown in Figure 2 (A and B).

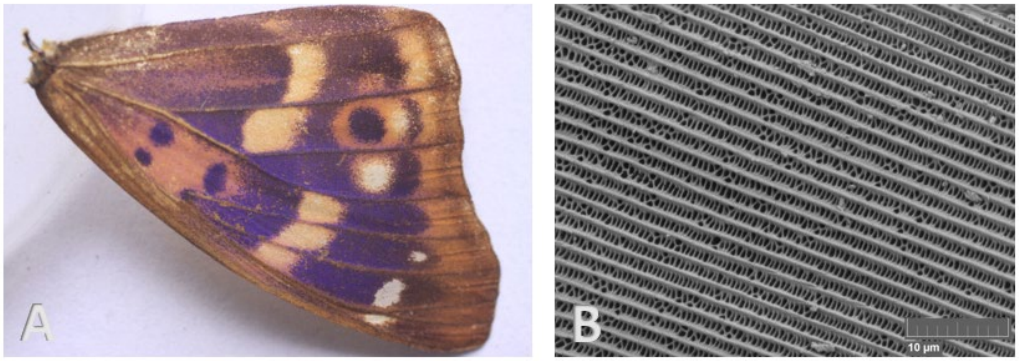

Fig. 2. Apatura butterfly wing: A photographic image (A) and SEM image (B).

2.2 Scanning Electron Microscopy (SEM)

Standard methods were used as auxiliary methods for obtaining the results of this research. Surface morphology of samples was characterized by scanning electron microscope *JEOL JSM 6610 LV (Japan).* Part of the recorded samples before the SEM procedure was not irradiated with laser light, while the other part has been irradiated and passed the holographic recording. This division is important for later analysis. The SEM image of apatura butterfly wing before laser treatment is presented in Figure 2 (B).

2.3 Holography

Holography, or holographic interferometry, is a method that records information about the deformation of an object between two moments of exposure. [12, 13] For this research, a special case of holographic interferometry was used, applied to monitor the mechanical movement of a part of the biophotonic structure that occurred as a result of external heating, that is, interaction with laser radiation. In this sense, this displacement is observed at the nanoscopic level in real time. The whole process is carried out in order to analyze the properties of the corrugated structure, which is deformed due to interaction with electromagnetic radiation. The possibility of a short exposure, i.e. the recording of complete three-dimensional information about the resulting changes, proved to be a very significant property of holographic study. Such an option of subsequent reconstruction is very important for movable objects of small and variable dimensions.

A simplified holographic setup was used in the experiment and the scheme of the here applied holographic setup is given elsewhere. [14]

2.4 Pre-characterization

Before the main part of the experiment, a small number of samples were used to determine the power range of the lasers that play the role of incident light sources. The mentioned samples were first tested for the lowest power to which they react. In the second phase, they were tested for the

power at which the samples burn and at which moment they are destroyed. An optimal power of 1mW was determined for performing the main part of the experiment. The total number of tested samples in the main part of the experiment is six.

Each of the samples was heated by external lasers with four different wavelengths of light (450 nm, 532 nm, 660 nm and 980nm). In the following segment, the influence of light of different wavelengths on the elasticity of the corrugation of the examined structure was monitored and analyzed.

3. Results and discussion

Initially several butterfly species with various wing scale types were compared to find the best design for photophoretically sensitive micro-platelets. The selected *Apatura* butterfly belongs to the structure of the herringbone type. Afterwards, these samples were tested for the intensity of photophoretic response [10] in mentioned holographic setup.

When suitable species for examination were determined, the experiments were started after obtaining the SEM images. The goal was to observe the behavior of corrugations in time. Firstly, the deformation of the corrugation would be initiated by heating with light of different wavelengths, and then the cooling process would be observed.

Different wavelength lasers were used to heat the samples (450 nm, 532 nm, 660 nm, and 980 nm). This procedure was holographically monitored. As part of analyses holographic reconstructions were made and showed the thermal imprint [14]. The sample cooling time was the critical point in the analysis (the period after the end of the laser illumination).

Forty frames are created and are arranged so that each one is compared to the first, zero frame, which represents the initial state of the sample. In this way, we checked whether the complete cooling of the sample occurs and in what period. The following panels (Figure 3 and Figure 4) present holographic reconstructions [14] of the *Apatura* wing pattern for two different wavelengths. The reconstructions of all 40 frames were not included, 15 were chosen in order to see more clearly and also not to lose the flow of cooling or non-cooling.

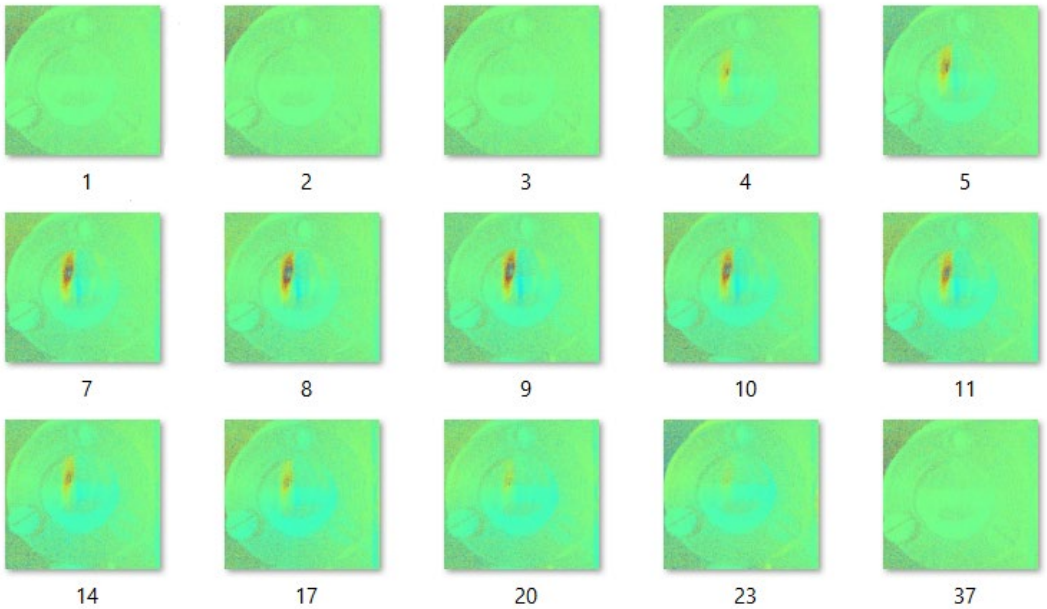

Fig. 3. Holographic reconstructions of the deformation of the corrugation of the wing structure of the *Apatura* butterfly tracked in time and caused by heating with laser light of a wavelength of 532 nm. The elastic deformation of the corrugation is observed, i.e., the return of the structure to its original state in less than 5 minutes.

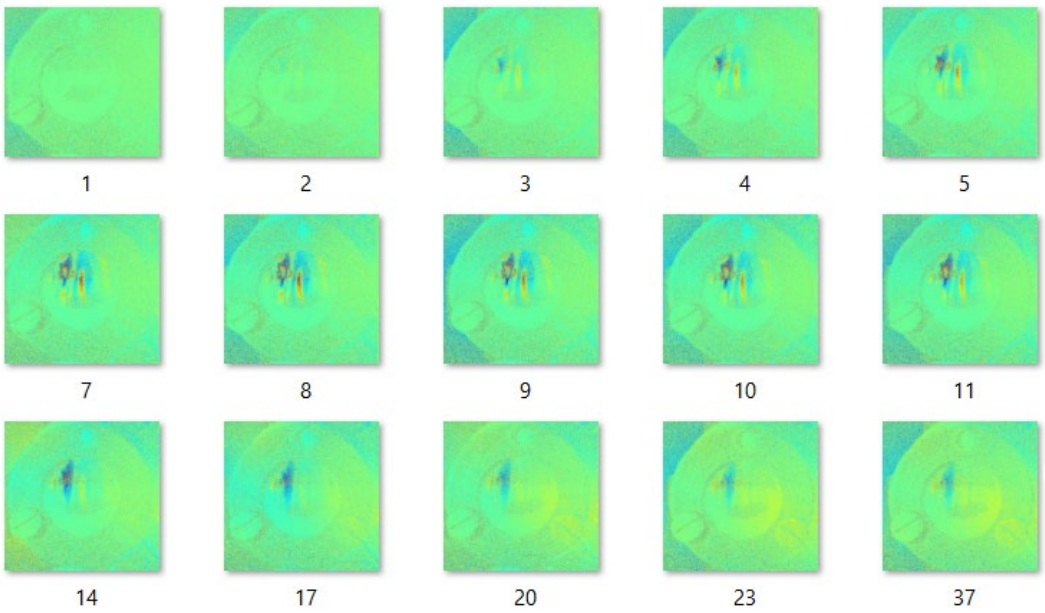

Fig. 4. Holographic reconstructions of the deformation of the corrugation of the wing structure of the *Apatura* butterfly tracked in time and caused by heating with laser light of a wavelength of 980 nm. The plastic deformation of the corrugation is observed, i.e., the structure does not return to its original state after 5 minutes of rest.

Firstly, the difference in temperature absorption due to heating with laser light of different wavelengths was measured. The highest absorption was measured when using wavelengths of 450 nm, and the lowest for the wavelength of 980 nm. This order was not followed in the direction of cooling the sample, that is returning the deformed corrugation to its previous state. For the wavelengths of 532 nm and 660 nm, a complete return to the initial state is observed (Figure 3), while for the wavelengths of 450 nm and 980 nm plastic deformation can be seen (Figure 4). This result is important because it shows the nonlinearity of the dependence on the wavelengths of the laser light used. This data indicates that every wavelength must be examined in this direction and that a linear response cannot be assumed.

As another characterization parameter, SEM images of the samples were taken. Regarding the used samples, those that holographically showed plastic deformation, the SEM image of that sample after use in the holographic setup also showed irreversible deformation of the structure and this is shown in Figure 5.

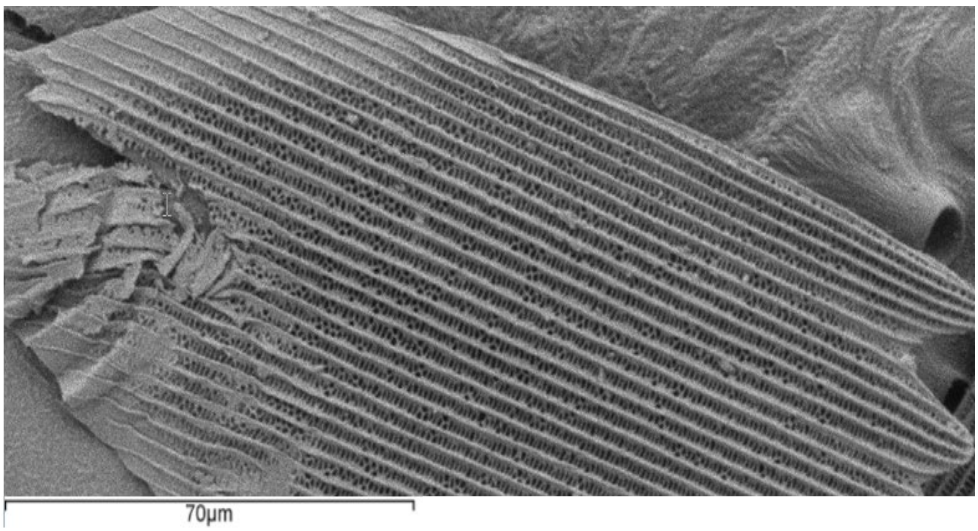

Fig. 5. SEM image of the corrugation of *Apatura* butterfly's wing after the experiment with the observed plastic deformation of the corrugation at wavelength 980 nm of laser radiation.

The elasticity of the corrugation structure is a concept subject to further extensive testing. What is important at this stage is that we have shown that this concept should be included in a separate characteristic of the material.

The property of the elasticity of the material corrugation was examined in this research for deformations caused by incident light of different wavelengths. Regarding laser power, at this moment, the only important thing is the optimal power on which the phenomenon of corrugation elasticity can be observed, because it was done on one type of butterfly wing, that is, on one type of corrugated structure. The powers of the lasers used as sources of incident light could also be an important parameter when this research is directed in the direction of different possible structures. Currently, the main effect being investigated is that of the wavelength of light that heats the structure and causes deformation. As the holographic reconstructions compare the real-time recording with the initial state, the cooling period of the samples was monitored and whether the corrugation of the sample returned to its original state.

It is important to note that the initial tests are described here, and for absolutely accurate information about this phenomenon, it is necessary to perform a very complex analysis (with more different samples representing more different types of structure, as well as for the entire spectrum of wavelengths) of the correlation between the corrugated structure and the wavelengths of the incident light, which will be the subject of further research. From these preliminary tests, it is established that the elasticity of the corrugation of the structure depends on the optical factors of the environment, which is the wavelength of light acting on the structure.

This type of examination gives the characteristics of structured materials in terms of reaction to the interference with light of different wavelengths. Specifically, it can be concluded that the corrugation of the herringbone type structure behaves elastically for two examined wavelengths from the visible spectrum, while it shows plastic deformation for another two wavelengths, in the UV and IR region.

Regarding the possibility of making artificial materials, this kind of material could be especially important for implementing in micro and nano electromechanical systems for different purposes for example as sensors/detectors of infrared radiation. [10, 15]

3. Conclusions

In this work, the innovative concept of the elasticity of the nanostructure corrugation was investigated. Wing samples of *Apatura* butterflies were used as a representative structure. Six

samples of the mentioned structure were prepared and all of them were subjected to identical testing. A holographic method was used to monitor the deformation of the corrugation caused by heating with laser light of four different wavelengths (450 nm, 532 nm, 660 nm, 980 nm), as well as the period after the heating stopped. The investigation resulted with the conclusion that the same samples react differently when exposed to different wavelengths: At wavelengths of 532 nm and 660 nm, they show the elasticity of the corrugation, while plastic deformation of the corrugation is observed at wavelengths of 450 nm and 980 nm. The possibility of affecting the physical and thermodynamic function of a material by nano corrugation is an entirely new and exciting feature that unprecedentedly merges photonics with material sciences. Understanding the behavior of the corrugation structure under the influence of the light of different wavelengths can delineate the specific application (thermal, sensory, military) of different materials in different conditions and raise the analysis of material properties to a higher level.

Acknowledgments: M.S.P. and M.P. acknowledge the support of the Office of Naval Research Global through the Research Grant N62902-22-1-2024. A.R. acknowledges support from Ministry of Science, Technological Development, and Innovation of the Republic of Serbia (Grant No. 451-03-47/2023-01/200051). M.P. acknowledges support from the Ministry of Education, Science and Technological Development of the Republic of Serbia (Grant No. 451-03-47/2023-01/200026).

References:

[1] Feraboli, P. *Development of a corrugated test specimen for composite materials energy absorption,* J. Compos. Mater. Vol. 42(3), 229-256, 2008.
[2] Klonowski W, Olejarczyk E, Pie R. *A new simple fractal method for nanomaterials science and nanosensors,* Mater. Sci.-Pol. Vol. 23(3), 606-612, 2005.
[3] Su JF, Wang XY, Dong H. *Influence of temperature on the deformation behaviours of melamine-formaldehyde microcapsules containing phase change material*, Mater. Lett. Vol. 84, 158-161, 2012.
[4] Demidov AV, Pereborova NV, Makarova AA, Chistyakova ES. *Development of a method for taking into account the influence of temperature in predicting complex deformation processes of polymeric textile materials*, Fibre Chem. Vol. 52, 279-282, 2020.
[5] Parent LR, Bakalis E, Ramirez-Hernandez A, Kammeyer JK, Park C, De Pablo J, Zerbetto F, Patterson JP, Gianneschi NC. *Directly observing micelle fusion and growth in solution by liquid-cell transmission electron microscopy,* J. Am. Chem. Soc. Vol. 139(47), 17140-17151, 2017.
[6] Ostrovsky YI, Shchepinov VP, Yakovlev VV. *Holographic Interferometry in Experimental Mechanics*, Vol. 60, Springer, 2013.
[7] Lee EH, McMeeking RM. *Concerning elastic and plastic components of deformation*, Int J Solids Struct, Vol. 16(8), 715-721, 1980.
[8] Yan Q, Li Y, Zhang T, Zhang X, Liu Y. *A Periodic corrugated metallic nanomesh for broadband light absorption enhancement,* Available at SSRN 4054450
[9] Tehranian S, Giovane F, Blum J, Xu Y, Gustafson B. *Photophoresis of micrometer-sized particles in the free-molecular regime*, Int.l J. Heat Mass Transf. Vol. 44, 1649-1657, 2001.
[10] M. Simović Pavlović, *Radiometric detector based on biological structures - MEMS / NEMS,* Doctoral dissertation, Faculty of Mechanical Engineering, University of Belgrade, 2022. (PhD thesis in Serbian)
[11] Han Z, Wu L, Qiu Z, Guan H, Ren L. *Structural colour in butterfly Apatura Ilia scales and the microstructure simulation of photonic crystal,* J. Bionic Eng., 14-19, 2008.
[12] Kreis T. *Handbook of holographic interferometry: optical and digital methods*, Weinheim: John Wiley & Sons; 2013.

[13] Pantelić D, Grujić D, Vasiljević D. *Single-beam, dual-view digital holographic interferometry for biomechanical strain measurements of biological objects*, J. Biomed. Opt. Vol. 19(12), 127005, 2014.
[14] Simovic-Pavlovic M, Pagnacco MC, Grujic D, Bokic B, Vasiljevic D, Mouchet S, Verbiest T, Kolaric B. *Uncovering hidden dynamics of natural photonics structures using holographic imaging*, J. Vis. Exp., e63676, 2022.
[15] Simovic-Pavlovic M, Bokic B, Vasiljevic D, Kolaric B. *Bioinspired NEMS - Prospective of collaboration with nature*, Appl. Sci. Vol. 12, 905, 2022.

DIFFERENT BUTTERFLY WING STRUCTURES AS AN INSPIRATION FOR MILITARY APPLICATIONS

Marina Simovic Pavlovic[1], Katarina Nestorovic [2], Darko Jankovic[3], Aleksandra Radulovic[4], and Maja Pagnacco[5]

[1] Faculty of Mechanical Engineering, University of Belgrade, Kraljice Marije 16, Belgrade, Serbia
e-mail: simovicmarina99@gmail.com
[2] Military Technical Institute, Ratka Resanovica 1, Belgrade, Serbia
e-mail: katarina.nestorovic993@gmail.com
[3] Military Academy, University of Defence, Veljka Lukića Kurjaka 33, Belgrade, Serbia
e-mail: darkoojanko@gmail.com
[4] Institute of General and Physical Chemistry, University of Belgrade, Studentski trg 12/V, Belgrade, Serbia
e-mail: aradulovic@iofh.bg.ac.rs ,
[5] Institute of Chemistry, Technology and Metallurgy, University of Belgrade, Njegoseva 12, Belgrade, Serbia
e-mail: maja.pagnacco@ihtm.bg.ac.rs

Abstract

A variety of biophotonic species structures have been identified, as well as matches of certain types. The properties of these various morphologies are acknowledged as suitable for defining some new nanomaterials with broad applications. Military materials were found to be an especially interesting field of application. Individual structures and their application directions, as well as possible manufacturing techniques and materials, are defined.

Keywords: biomaterials, corrugation morphology, biomimetic, military applications.

1. Introduction

In nature, there are countless perfect, hidden solutions for many technological problems that are waiting to be recognized. Biomimetics is a field that deals with the application of such patterns from nature in technology and everyday life. [1] Modern times have developed the need and opportunities to find new improved materials, with extremely small dimensions and specific characteristics. This study investigates the nanostructure of biological species, butterfly wings, which are an ideal model for biomimicry due to their unique morphology. [2] Butterfly wings are also fascinating due to the diversity of structures found in different species. Figure 1 shows some examples of structures of various kinds.

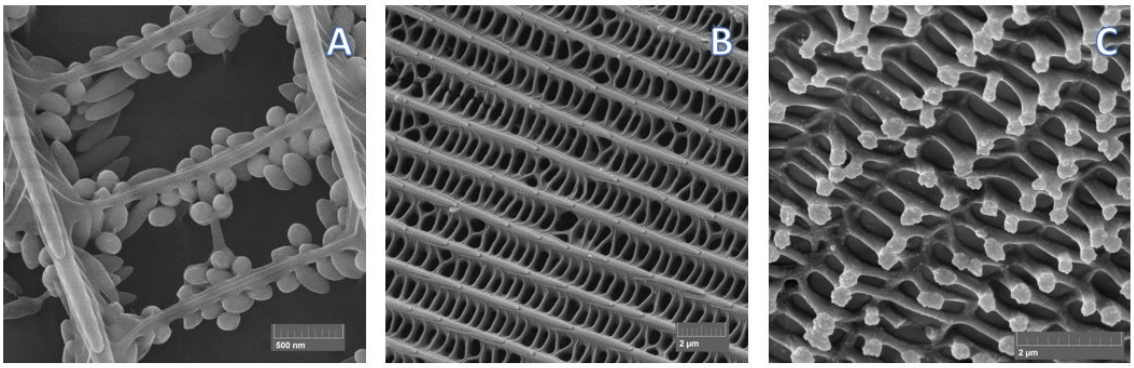

Fig. 1. SEM images of the biological structures: (A) *Pieris rapae* butterfly wing, (B) *Apatura iris* butterfly wing, and (C) *Issoria lathonia* butterfly wing.

Different types of structures were analyzed, and the technology of their production was proposed. By achieving characteristic nano dimensions within a certain material, a new type of material can be introduced. It is crucial to note that, despite their comparable chemical composition, the physical structure of butterfly wings can vary greatly. More crucially, structural differences define certain mechanical properties. Recognizing biological structures as established mechanical systems opens the door to new material development and industrial applications.

2. Materials and methods

2.1 Samples

Test samples were made by cutting different butterfly wings. The cutting was done with special tools, designed to achieve the desired size without the possibility of damaging the scales of the butterfly's wing, which consist of a large number of scales and hairs. This tool is a mold of certain diameters with a sharpened edge that rests on the sample and a kind of hammer that exerts force on the mold and in this way the sample is cut.

2.2 Scanning Electron Microscopy (SEM)

Scanning electron microscope *JEOL JSM 6610 LV (Japan)* was used for surface morphology recording. Before SEM measurements were conducted, samples were rinsed with diethyl-ether to obtain a clear surface. Rinsed samples were positioned on adhesive tape fixed to specimen tabs and then to ion sputter coated with gold.

2.3. Holography

Holography is an optical technique that registers mechanical changes at the nanoscale level by utilizing the interference of two beams. This approach is thoroughly detailed elsewhere. [3,4]

3. Results and Discussion

Among the numerous varieties of butterflies and their various structures, certain types can be distinguished. The following sections will discuss five different kinds of structures.
First and foremost, one basic structure must be presented. The butterfly *Issoria lathonia* [5] shown in Figure 2A belongs to the nanostructure usual for butterflies and shares traits with many other species. Despite their lack of specificity, natural nanostructures are always significant for the study

of various effects (thermal, optical, physicochemical, etc.) [6] applicable within a variety of micro and nano electromechanical systems (MEMS/NEMS). [7]

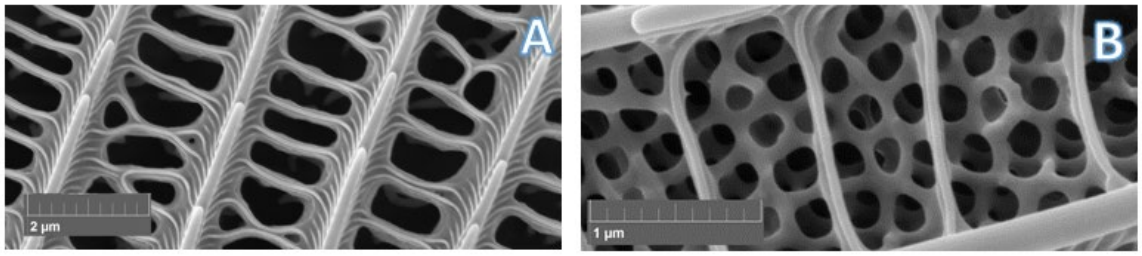

Fig. 2. SEM images: (A) *Issoria lathonia* butterfly wing and (B) *Calophrys rubi* butterfly wing.

The butterfly *Calophrys rubi* [8] is an example of a three-dimensional optical crystal structure (Figure 2B). In terms of controlling light and its interaction with various wavelengths, such optical materials have enormous potential. [9] These capabilities guarantee widespread use in a variety of light-related applications. In addition to traditional optical systems, a potential application in the military could be found in the construction of missiles in terms of fiber-optic communication needed for guidance.

The studied species of *Apatura* butterflies [10] and *Morpho* butterflies [11] belong to the herringbone type of structure (Figure 3). These structures are complex, but they also have promising material characteristics like ordering, sensitivity, and elasticity. Potential materials with this morphology would be most useful in the field of sensing, which is especially important for military uses. [12]

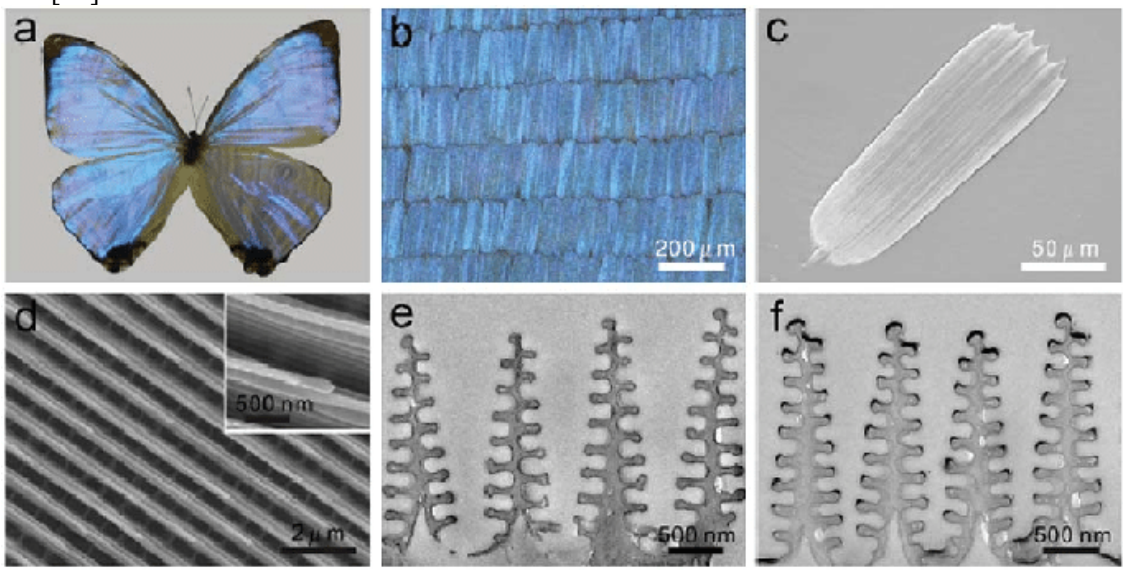

Fig. 3. Morphologies and structures of the *Morpho* butterfly wing: (a) The photo of the *Morpho sulkowskyi* butterfly; (b) Optical microscopy image of the scales on the wing surface; (c) SEM image of a single butterfly wing scale supported on a silicon substrate; (d) Top SEM view of the photonic architecture of the scale. The inset figure is a high magnification SEM showing the multilayered lamella structures; (e) TEM image of a transverse section of the scale showing ridges with lamella structures; (f) TEM image showing the selectively modified ridges. Figure 3 is taken from the ref. [11], licensed under CC BY-NC.

The butterfly *Pieris rapae* [13] is a representative of the nanogranular structure (Figure 4). Such structures are essential because they can perform the function of granular materials [14]. The idea is to take benefit of such materials' granularity while incorporating them into a consistent nanogranular material. This sort of material would offer significant benefits in terms of impact energy control and would be appropriate for armor construction [15].

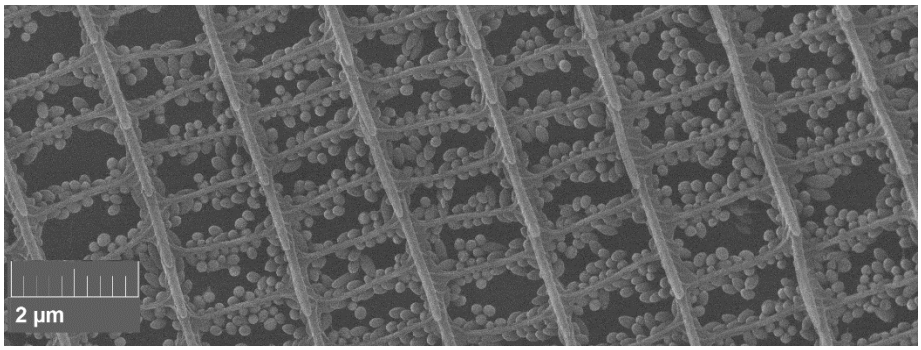

Fig. 4. SEM image of *Pieris rapae* butterfly wing.

Polyomatus [16] is a type of butterfly with a Bragg lattice type of structure (Figure 5). A changing refractive index of light characterizes a Bragg grating [17]. From a technological standpoint, these kinds of systems are most commonly used as optical components that serve as filters. The Bragg grating works by setting the filter to reflect a precisely defined range of wavelengths of emitted light while allowing others to pass through the filter unhindered. Such materials can also be used in sensing and various optical testing techniques.

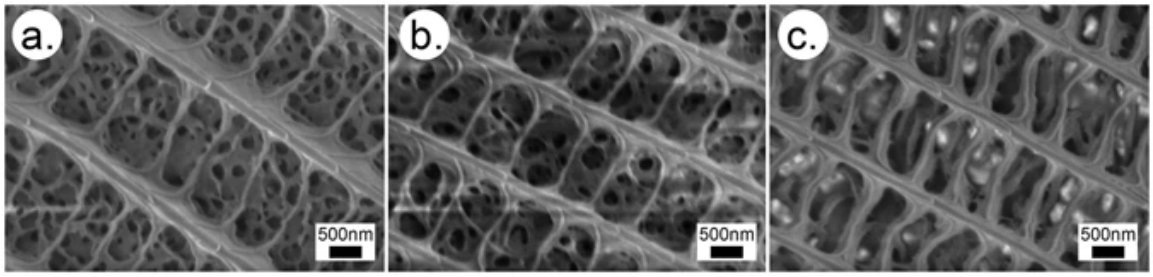

Fig. 5. SEM images of the wing scales of the female *Polyomatus*:(a) Dentate apex blue scale, (b) rounded apex blue scale, (c) brown scale. Figure 5 is taken from the ref. [16] licensed under CC BY 4.0.

For the production of certain materials, it is essential to select a material that can be processed using the chosen technology and a technology that can address the challenges presented by nanomaterials.

Silicone [18] can be considered a potential material due to properties such as temperature resistance, water resistance, and a variety of other benefits. This material can also be three-dimensionally stamped [19], which could be a perfect technology for such structures. Prior to the manufacturing process, the structure must be simplified in terms of engineering without losing its distinctive properties, and its exact dimensions must be determined. Additionally, a simplified representation of the architecture of one kind of biological structure – the structure of *Morpho* butterfly wing is provided in Figure 6.

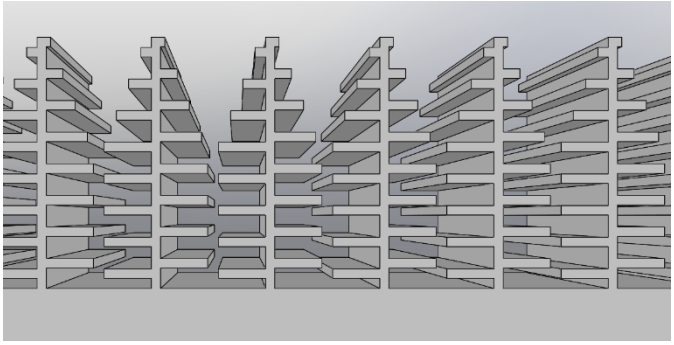

Fig. 6. simplified representation of the architecture of herringbone type of nano structure for potential application in sensor industry.

This structure was chosen after investigating the thermo-mechanical phenomenon – thermophoretic effect that occurs when electromagnetic radiation is absorbed on a piece of material, causing a temperature gradient to form on it while the mean free path of the molecules in the surrounding gas is roughly equal to the characteristic dimension of the piece of material. [20] The thermophoretic effect is based on the fact that molecules of the surrounding gas carry considerably more mechanical momentum from the warmer side of the material than the colder side, creating forces that cause the substance to move mechanically. The holographic interference method measures the conversion of the energy of invisible electromagnetic radiation into mechanical displacement of the micromechanical detecting system, so that the magnitude of the mechanical displacement is proportionate to the energy. This structure proved to be an ideal mechanical model for reproducing the effect that identifies infrared radiation, and hence an ideal structure for application in detection systems.

The main benefit of this kind of research is the possibility to raise a known material with good characteristics (e.g. silicone) to a higher level. This can be achieved by corrugating the material. In this work, for the first time, examples of different corrugations of the same biological material and the possibilities of their different applications are presented.

3. Conclusions

This work included the examination of different types of butterfly wings and the finding of representatives of certain types of structures. Each representation has a different type of structure and therefore carries different mechanical properties. In this work, for the first time, butterfly wing structure types are classified into separate types of arrangement. These types were recognized as established systems within different structures and their properties served as a parameter to select potential applications. The proposed types of structures are assumed to be biomimetic models for the production of artificial materials that would have applications in the military industry. A material, silicone, has also been proposed as ideal for testing biomimicry and for checking the properties of artificially obtained structures.

Acknowledgements: M.S.P. and M.P. acknowledge the support of the Office of Naval Research Global through the Research Grant N62902-22-1-2024. A.R. acknowledges support from Ministry of Science, Technological Development, and Innovation of the Republic of Serbia (Grant No. 451-03-47/2023-01/200051). M.P. acknowledges support from the Ministry of Education, Science and Technological Development of the Republic of Serbia (Grant No. 451-03-47/2023-01/200026).

References:

[1] Suresh Kumar N, Padma Suvarna R, Chandra Babu Naidu K, Banerjee P, Ratnamala A, Manjunatha H. *A review on biological and biomimetic materials and their applications,* Appl. Phys. A, Vol. 126(6), 445, 2020.

[2] Lee J, Jung Y, Lee M, Hwang JS, Guo J, Shin W, Min J, Pyun KR, Lee H, Lee Y, Shiomi Y, Kim YJ, Kim BW, Ko SH. *Biomimetic reconstruction of butterfly wing scale nanostructures for radiative cooling and structural coloration*, Nanoscale Horizons, Vol. 7(9), 1054-1064, 2022.

[3] Kreis T. *Handbook of holographic interferometry: optical and digital methods*, Weinheim: John Wiley & Sons; 2013.

[4] Simovic-Pavlovic M, Pagnacco MC, Grujic D, Bokic B, Vasiljevic D, Mouchet S, Verbiest T, Kolaric B. *Uncovering hidden dynamics of natural photonics structures using holographic imaging*, J. Vis. Exp., e63676, 2022.

[5] Zobar D, Genc H. *Biology of the queen of spain fritillary, Issoria lathonia (Lepidoptera: nymphalidae)*, Florida Entomologist, Vol. 91(2), 237-240, 2008.

[6] Yang CC, Mai YW. *Thermodynamics at the nanoscale: A new approach to the investigation of unique physicochemical properties of nanomaterials*, Materials Science and Engineering: R: Reports, Vol. 79, 1-40, 2014.
[7] Simovic-Pavlovic M, Bokic B, Vasiljevic D, Kolaric B. *Bioinspired NEMS - Prospective of collaboration with nature*, Appl. Sci. Vol. 12, 905, 2022.
[8] Krupitsky A, Skrylnyk Y, Pak O. *A new species of the Callophrys rubi (Linnaeus, 1758) group from Afghanistan (Lepidoptera, Lycaenidae),* Zoology in the Middle East, Vol. 68(4), 332-340, 2022.
[9] Shaltout AM, Shalaev VM, Brongersma ML. *Spatiotemporal light control with active metasurfaces*, Science, Vol. 364(6441), eaat3100, 2019.
[10] Han Z, Wu L, Qiu Z, Guan H, Ren L. *Structural colour in butterfly Apatura Ilia scales and the microstructure simulation of photonic crystal,* J. Bionic Eng., 14-19, 2008.
[11] He J, Villa NS, Luo Z, An S, Shen Q, Tao P, Song C, Wu J, Deng T, Shang W. *Integrating plasmonic nanostructures with natural photonic architectures in Pd-modified Morpho butterfly wings for sensitive hydrogen gas sensing*, RSC advances, Vol. 8(57), 32395-32400, 2018.
[12] Simovic Pavlovic M, Tomic Lj, Kolaric B, Vasiljevic D. *A new infrared radiation detection system as an inspiration for the potential construction of a radiometric detector,* 10th International Scientific Conference on Defensive Technologies OTEH 2022, 286-288, 2022.
[13] Hern A, Edwards-Jones GARETH, MCKINLAY RG. *A review of the pre-oviposition behaviour of small cabbage white butterfly, Pieris rapae (lepidoptera: Pieridae)*, Annals of Applied Biology, Vol. 128(2), 349-371, 1996.
[14] Abed Zadeh A, Barés J, Brzinski TA, Daniels KE, Dijksman J, Docquier N, Everitt HO, Kollmer JE, Lantsoght O, Wang D, Workamp M, Yhao Y, Zheng H. *Enlightening force chains: a review of photoelasticimetry in granular matter*, Granular Matter, Vol. 21, 1-12, 2019.
[15] Gilson L, Rabet L, Imad A, Coghe F, Van Roey J, Guéders C, Gallant J. *Ballistic impact response of an alumina-based granular material: Experimental and numerical analyses*, Powder Technology, Vol. 385, 273-286, 2021.
[16] Kertész K, Piszter G, Bálint Z, Biró LP. *Biogeographical patterns in the structural blue of male Polyommatus icarus butterflies*, Scientific reports, Vol. 9(1), 2338, 2019.
[17] Sahota JK, Gupta N, Dhawan D. *Fiber Bragg grating sensors for monitoring of physical parameters: A comprehensive review*, Optical Engineering, Vol. 59(6), 060901-060901, 2020.
[18] Barroso G, Li Q, Bordia RK, Motz G. *Polymeric and ceramic silicon-based coatings–a review*, Journal of materials chemistry A, Vol. 7(5), 1936-1963, 2019.
[19] Terrani K, Jolly B, Trammell M. *3D printing of high-purity silicon carbide*, Journal of the American Ceramic Society, Vol. 103(3), 1575-1581, 2020.
[20] Simović Pavlović M, Pagnacco M, Radulović A, Senćanski J, Marković M. *Thermophoresis or When Small Objects Meet Temperature Gradient: Numerous Applications,* Kem. Ind., Vol. 72, in press, 2023.

NONLINEAR SEA SURFACE WAVES

Teodor Vrećica

Mathematical Institute, Serbian Academy of Sciences and Arts, Belgrade, Serbia
e-mail: teodorv@mi.sanu.ac.rs

Abstract

A summary of my PhD dissertation, limited to the most important results and ideas, is given in this paper. The dissertation is dedicated to the investigation of surface gravity water waves, which, due to the way they are generated (wind forcing), are also often called wind waves. These waves have been studied for a long time, yet there is still a number of physical properties which are not properly understood. Two different topics regarding nonlinear three wave interactions are the main focus: nonlinear evolution of wave fields in shallower waters, and nonlinear generation of long waves by wind gusts.

Keywords: water waves, fluid mechanics, nonlinear interactions.

1. Introduction

Water waves are one of the fundamental components of the Earth's climate, regulating exchanges between the atmosphere and the oceans, generation of sea spray, and the albedo of the water surface [1]. While their properties in deep waters are relatively well understood and modeled on global scales, some wave phenomena remain an open question. In [2] (which is essentially a combination of [3, 4, 5]), we further the understanding of the water waves, with a focus on the nonlinear three wave interactions.

In the nearshore waters, waves undergo a significant nonlinear evolution, which is currently not grasped by (stochastic) global wave forecasting models. We advance both deterministic and stochastic nonlinear wave evolution modeling in nearshore waters and provide an improved understanding of how spatial and temporal inhomogeneities affect nonlinear wave evolution. One of the main achievements of this work is the establishment of the modeling basis for extending all operational wave forecasting models to the nearshore region and even the breaking zone in an appropriate manner.

Deterministic models, accounting for nonlinear triad interactions, slow time evolution, and nonlinear energy dissipation effects are derived following the mild-slope approach. The model is in a sense a hybrid one (following [6]). It uses a more accurate vertical structure of Boussinesq models but is solved in the frequency domain. Implementation of amplitude slope effects (due to dissipation, nonlinear, and shoaling effects), enabled it to also give good predictions for breaking cases, and improved accuracy over mildly sloping beaches. It was observed that individual realizations of the deterministic model can greatly deviate from an ensemble average. In general, good agreements were found between the model output, field measurements, and lab experiments.

Stochastic models of wave evolution in shallower waters are derived from the new deterministic models. The nonlinear source terms describe the magnitude of energy transfer

between different wave components. In intermediate waters, the energy is transferred back and forth between the components. One of the main achievements of this work is extracting only a mean part of the oscillating term, based on the local parameters ("localizing" the model in a way that provides net energy transfer without requiring the integration of the history of the wave propagation). This enables them to be implemented in operational wave forecasting models (such as [7]), as it significantly reduces the amount of required computational resources. Two different physical modes of behavior are identified, one in intermediate water depths, and the other in the transition area between intermediate and shallow waters (with some dependence on the slope as well). A semi-local formulation of the coefficient is also derived, which rather than precalculating interaction coefficients precalculates their change between grid points---a method that provides better accuracy but still enables overcoming of Nyquist limitation. While not as accurate as deterministic models, the stochastic models show good agreements with measurements. This leads to the conclusion that the accuracy of the operational wave forecasting models can be greatly improved in the nearshore region by implementing nonlinear source terms based on the presented formulations.

Another main focus of the thesis was on a subclass of surface waves called infragravity (IG) waves [8], which have large wavelengths and propagation speeds compared to wind-induced waves. IG waves can resonate with the ice sheets and are closely related to various physical phenomena and applications such as altimetry measurements, sediment transport, and Earth's hum [9]. As their strongest generation mechanism is nonlinear wave shoaling, their study was mostly limited to coastal areas. Recently, due to their potential influence on satellite altimetry, there is a renewed interest in IG waves in open oceans. Existing formulations of IG waves in open seas account only for generation and reflection from far beaches. By analyzing our Acoustic Doppler Current Profiler (ADCP) measurements in the Mediterranean, and previous pressure cell measurement campaigns, we found several cases where storms appear to generate IG waves in the open seas. To account for the discrepancies, a new IG wave generation mechanism based on the Bragg resonance of sub-grid oscillations of wind gusts and wind waves is found and modeled. Comparisons with measurements show very good agreements. Depending on the geographical location and season, the gust generated waves were even shown to be the main source of IG wave energy in the open ocean. The presented work fills a gap in IG wave generation theory and hopefully provides a major advancement toward a new IG wave forecasting model.

1.1 Resonance conditions

To better understand the nonlinear interactions, it is helpful to observe the problem in the frequency and wavenumber domains with respect to resonant interactions. A classical solution of wave component takes the form $a^{i(kx-\omega t)}$ where k and ω are wavenumber and frequency. Each of the wave components can be thought of as a mass spring, oscillating with different frequency and stiffness (k). If the wave field is linear, every spring is independent from the other springs. However, wave fields are inherently nonlinear. Each combination of two or more springs (waves) acts as a forcing on another spring (wave). If the phase function of the wave ($P = \omega t - kx$) does not match that of the forcing, this only results in forced non-resonant oscillations. These typically act as a simple second order corrections to the spring motion.

This property is one of the first investigated water wave phenomena. In a case where only a single free water wave harmonic exists, this leads to the famous Stokes wave solution. It states that the quadratic nonlinearity results in an additional component, which travels together with the primary wave. For this reason, it is often called a bound wave. The bound component is reversely proportional in magnitude to the phase mismatch. As the value of the mismatch reaches zero or near zero, the wave motion becomes fully coupled, and energy is exchanged between different wave components. Full nonlinear equations need to be resolved.

Due to the nature of the dispersion relation, $\omega^2 = gk\tanh(kh)$ with g representing gravity, it is impossible to close the resonance in both frequency and wavenumber space for the lowest order nonlinearity (three wave interactions). However, it was shown in [10] that the changing bathymetry can act as an additional component to close the resonance. In shallow waters where kh tends to zero, the nature of the dispersion relation changes, and groups of three waves can directly resonate. These properties are illustrated in Figure 1.

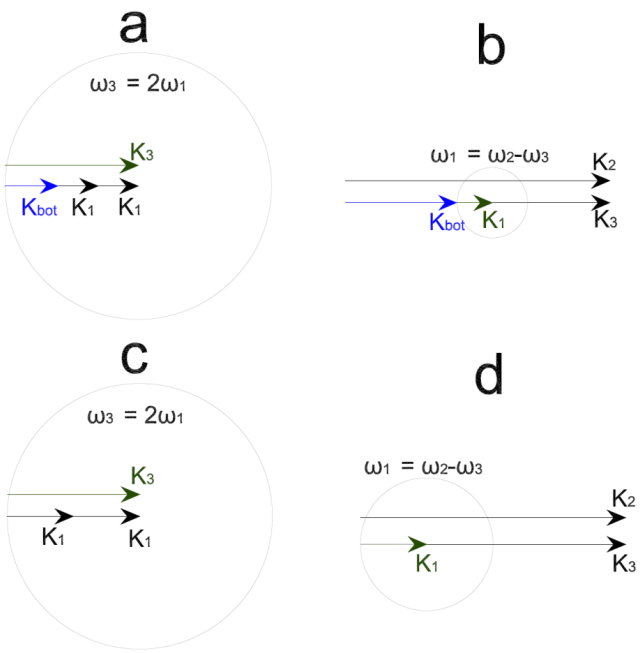

Fig. 1. Geometric construction of class III Bragg unidirectional resonance triad interactions. Panels a and c: superharmonic self-interaction (k_1+k_1) generating a second harmonic wave (k_3) in intermediate (a) and shallow water depths (c). Panels b and d: subharmonic interaction (k_2-k_3) generating a long wave (k_1) in intermediate (b) and shallow water depths (d). Black arrows represent interacting wave components and the generated wave. Blue arrows represent the bottom component (K_{bot}) where required for closing the wave resonance condition. The circles represent all wavenumber solutions that satisfy the frequency resonance closure. In contrast to intermediate water depth interactions, unidirectional shallow water interaction conditions can be satisfied without requiring a bottom component. This indicates a very different physical behavior.

2. Governing equations

The equations governing the irrotational flow of an incompressible inviscid fluid with a free surface are given as:

$$\nabla^2\phi + \phi_{zz} = 0,\ -h < z < \eta \quad (1)$$

$$\phi_z - \nabla\phi\cdot\nabla\eta - \eta_t = 0,\ z = \eta \quad (2)$$

$$\phi_t + g\eta + ((\nabla\phi)^2 + \phi_z^2)/2 = 0,\ z = \eta \quad (3)$$

$$\phi_z + h\cdot\phi = 0,\ z = -h \quad (4)$$

Eq. 1 is Laplace's equation for the velocity potential ϕ. Eq. 4 describes the free-slip bottom boundary condition and eqs. 2 and 3 are the kinematic and dynamic free surface boundary condition, respectively. The coordinate system is Cartesian, where z is zero at the undisturbed water level and points upwards, while the x and y axes are in the onshore and alongshore direction respectively. h represents the water depth, η the surface elevation, subscripts denote partial differentiation by z or t and the horizontal gradient operator is represented by ∇.

By applying the Fourier transform to the water surface and the velocity potential, combining the four equations, and significant further transformations, the following equations can be obtained:

$$\frac{1}{C_{g,p}}\frac{\partial a_p}{\partial t}+\frac{\partial a_p}{\partial x}+\frac{2C'_{g,p}}{C_{g,p}}=-\varepsilon i\sum_{s=p-N}^{N}W_{s,p-s}a_s a_{p-s}\,e^{-i\int k_s+k_{p-s}-k_p dx} \tag{5}$$

$$\frac{1}{C_{g,p}}\frac{\partial E_p}{\partial t}+\frac{\partial E_p}{\partial x}+\frac{C'_{g,p}}{C_{g,p}}=4\sum_{s=p-N}^{N}\Re\left[Q_{s,p-s}E_s E_{p-s}+Q_{s,p}E_s E_p+Q_{p,p-s}E_p E_{p-s}\right]W_{s,p-s} \tag{6}$$

where subscripts denote frequency, a is the complex amplitude of surface elevation, C_g is the velocity of energy propagation, and W and Q are the nonlinear interaction kernels.

These equations describe the evolution of the complex amplitude of the sea surface (a, eq. 5) and wave energy (E, eq. 6) for the unidirectional wave field. They take into account the variable bathymetry to enable energy transfer. For the details of the derivation procedure and values of coefficients (which are functions of wavenumbers and angular frequencies), see [3].

Due to Nyquist limitation (term Q contains an integral and is highly oscillatory), it is necessary to utilize numerical grids with resolution proportional to the shortest wavelength under consideration. This requires enormous computational power, making it impossible to model even smaller scale areas such as bays. To resolve this issue, a formulation of the coefficient based only on local parameters was derived following the approach of [11]. An example of a nonlocal coefficient and a localized one is shown in Figure 2. The localized coefficient is shown to match the mean transfer of energy quite well.

Similar to the effects of the bottom, wind gusts can act as additional components to close the resonance condition. In [5] a new model was derived which accounts for the generation of IG waves due to forcing by wind gusts. The form of the equations is similar to that of eqs. 1 and 2, albeit with different coefficients.

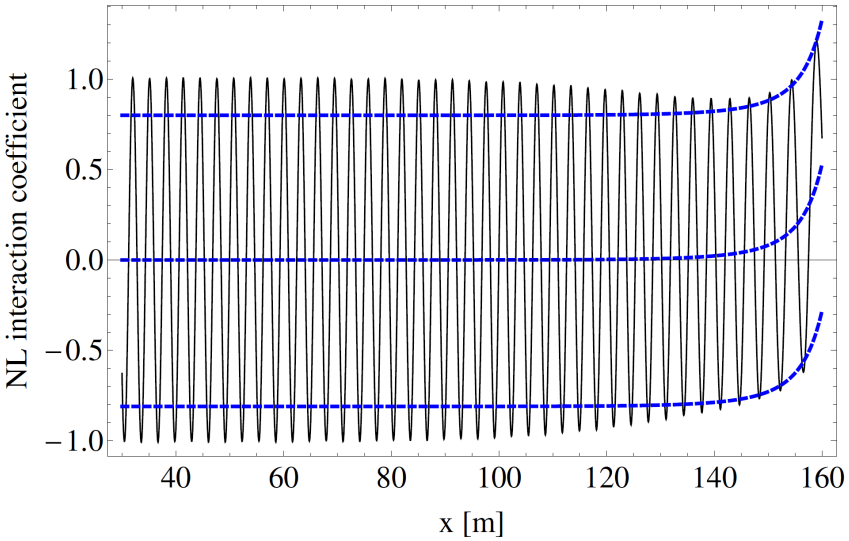

Fig. 2. The localized and nonlocal nonlinear interaction coefficients Q. The coefficients describe the transfer of energy to the second harmonic due to the self-interaction of the first harmonic over a 1/25 slope from deep to intermediate water. The localized coefficient has also been plotted with a shift to the negative and positive directions to better present how it follows the mean evolution of the nonlocal coefficient.

3. Examples

To test the validity of the nonlinear shoaling models, the evolution of wave spectra (defined as a distribution of wave energy across frequency), was simulated and compared to the field

measurements of [12]. The output of the commonly used (in large scale operational wave modeling) source terms is also presented. It can be seen in Figure 3 that the new model (full blue line) is grasping the evolution of the spectra far better across all frequencies. This shows a potential for implementation of the model into large scale operational wave models.

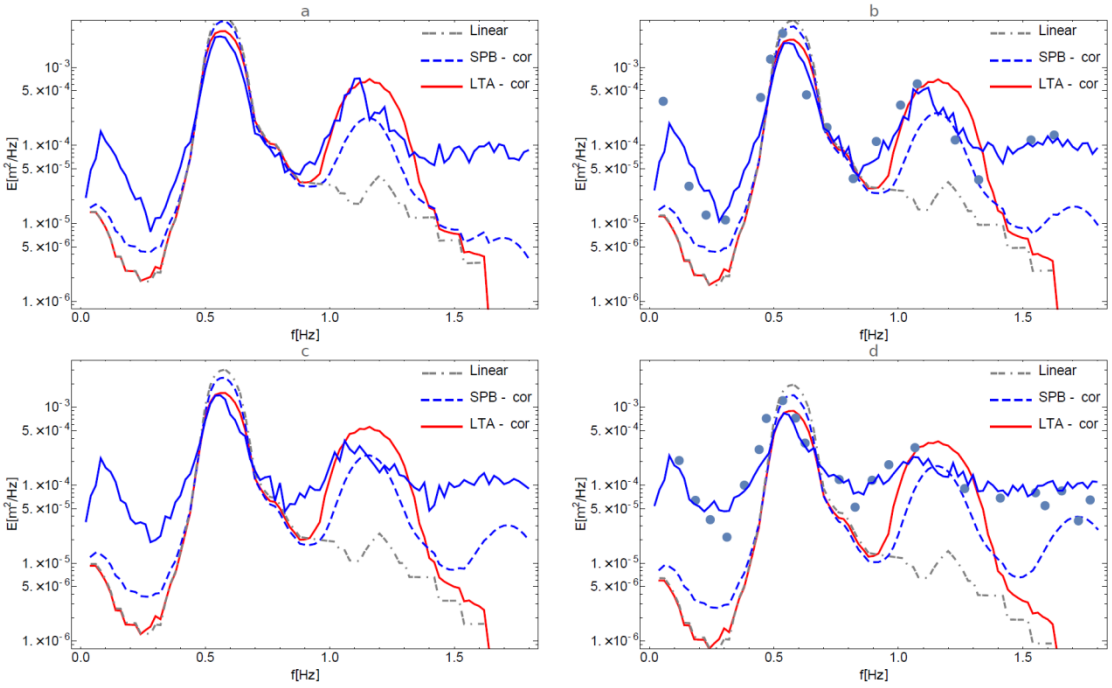

Fig. 3. (a) Comparison of nonlinear shoaling between existing stochastic models. In the figures full red line represents the LTA model, the dash-dot-dash gray line is the linear model, the full blue line is the new formulation of the deterministic model, and the dashed blue line is the corrected SPB model. The gray dots represent the measurements. The spectrum at water depths of 18m(a), 15m(b), 12m(c), and 9m(d) is shown.

Elevated levels of IG wave energy, compared to the output of the model accounting for reflection from coasts [13], were observed by the buoys of the Aogashima array during the winter months of 2015 [14]. To account for this discrepancy, the generation of IG waves due to gusts was simulated along wave ray paths originating from the center point of the array. Results are shown in Figure 4. The values of significant wave height (which is proportional to the square root of wave energy) are well described by the new model, which gives a significant contribution during the winter. Moreover, the gust based mechanism was found to describe well the shape of the observed IG wave spectra.

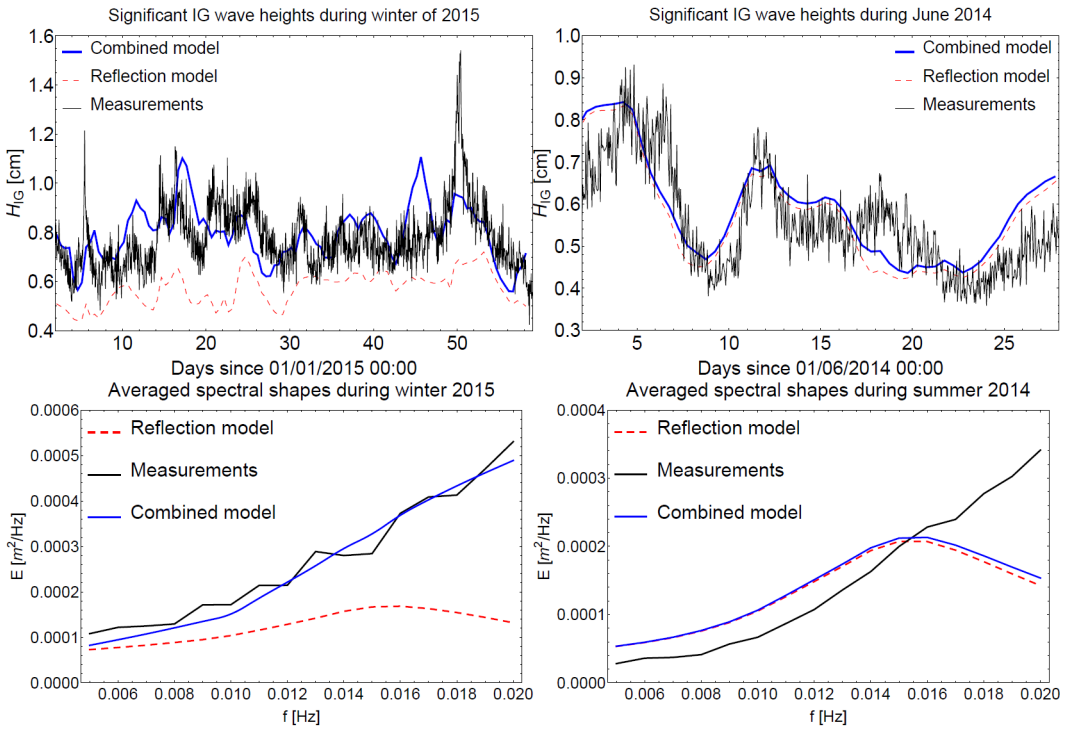

Fig. 4. Measured (black line) and modeled (red dashed line – reflection model, blue line - combined model) significant IG wave height in the 50-200 second range at Aogashima array are shown for winter (a) and summer months (b). The simulation of IG wave generation is performed along ray paths of 0.005, 0.01, 0.015, and 0.02Hz waves originating from the midpoint of the Aogashima array. Averaged spectral quantities are shown in (c) for winter and in (d) for summer.

4. Conclusions

New nonlinear models of wave evolution are derived for coastal areas and IG waves in open oceans. Their output is compared to various field measurements and lab experiments, and several new water wave physical properties are identified. The models are also further derived to a form fitting for implementation into operational forecasting models. The biggest achievement of this thesis, in my opinion, is an improved understanding of the spatiotemporal changes of the wave field. This opens new directions of research (including propagation of semi-dispersive waves, investigation of deep water bathymetry features on long waves, nonlinear effects of currents, new parameterizations of depth induced wave breaking, fully 3D wave modeling, nonlinear corrections to dispersion relation).

Acknowledgement: I have been supported by the project no. 7744592 MEGIC ”Integrability and Extremal Problems in Mechanics, Geometry and Combinatorics” of the Science Fund of Serbia.

References:

[1] Cavaleri, L., Fox-Kemper, B. and Hemer, M., 2012. Wind waves in the coupled climate system. *Bulletin of the American Meteorological Society*, *93*(11), pp.1651-1661.
[2] Vrećica, T., 2019. Nonlinear sea surface waves, *PhD dissertation,* pp. 1-157
[3] Vrećica, T. and Toledo, Y., 2016. Consistent nonlinear stochastic evolution equations for deep to shallow water wave shoaling. *Journal of Fluid Mechanics*, *794*, pp.310-342.

[4] Vrećica, T. and Toledo, Y., 2019. Consistent nonlinear deterministic and stochastic wave evolution equations from deep water to the breaking region. *Journal of Fluid Mechanics*, *877*, pp.373-404.
[5] Vrećica, T., Soffer, R. and Toledo, Y., 2019. Infragravity wave generation by wind gusts. *Geophysical Research Letters*, *46*(16), pp.9728-9738.
[6] Bredmose, H., Agnon, Y., Madsen, P.A. and Schäffer, H.A., 2005. Wave transformation models with exact second-order transfer. *European Journal of Mechanics-B/Fluids*, *24*(6), pp.659-682.
[7] Tolman, H.L., 2009. User manual and system documentation of WAVEWATCH III TM version 3.14. *Technical note, MMAB Contribution*, *276*(220).
[8] Tucker, M.J., 1950. Surf beats: Sea waves of 1 to 5 min. period. *Proceedings of the Royal Society of London. Series A. Mathematical and Physical Sciences*, *202*(1071), pp.565-573.
[9] Bertin, X., de Bakker, A., Van Dongeren, A., Coco, G., André, G., Ardhuin, F., Bonneton, P., Bouchette, F., Castelle, B., Crawford, W.C. and Davidson, M., 2018. Infragravity waves: From driving mechanisms to impacts. *Earth-Science Reviews*, *177*, pp.774-799.
[10] Liu, Y. and Yue, D.K., 1998. On generalized Bragg scattering of surface waves by bottom ripples. *Journal of Fluid Mechanics*, *356*, pp.297-326.
[11] Toledo, Y. and Agnon, Y., 2012. Stochastic evolution equations with localized nonlinear shoaling coefficients. *European Journal of Mechanics-B/Fluids*, *34*, pp.13-18.
[12] Freilich, M.H. and Guza, R.T., 1984. Nonlinear effects on shoaling surface gravity waves. *Philosophical Transactions of the Royal Society of London. Series A, Mathematical and Physical Sciences*, *311*(1515), pp.1-41.
[13] Ardhuin, F., Rawat, A. and Aucan, J., 2014. A numerical model for free infragravity waves: Definition and validation at regional and global scales. *Ocean Modelling*, *77*, pp.20-32.
[14] Tonegawa, T., Fukao, Y., Shiobara, H., Sugioka, H., Ito, A. and Yamashita, M., 2018. Excitation location and seasonal variation of transoceanic infragravity waves observed at an absolute pressure gauge array. *Journal of Geophysical Research: Oceans*, *123*(1), pp.40-52.

PHASE-FIELD MODELING OF HIGH CYCLIC FATIGUE IN BRITTLE MATERIALS

Vladimir Lj. Dunić[1], Miroslav M. Živković[1], Vladimir P. Milovanović[1] and Jelena M. Živković[1]

[1] Faculty of Engineering, University of Kragujevac, Sestre Janjić 6, 34000 Kragujevac, Serbia
e-mail: dunic@kg.ac.rs

Abstract

The engineering structures are designed to operate in an elastic domain, and the plastic deformations are not permissible. Therefore, the safety of structures can be violated if the structure is subjected to cyclic loading conditions due to the accumulation of damage in the material. The damage of the material is usually considered as the appearance of micro-cracks and dislocation. These phenomena can be modeled by the Phase-Field Damage Modeling (PFDM) approach. The PFDM in brittle materials considers the elastic strain energy the main and the only source of material damage. By introducing the fatigue degradation function, the PFDM can be extended to predict the structure's fatigue under cyclic loading-unloading conditions. The PFDM framework is implemented into Finite Element Software, and the first simulation results on one element example are presented. The results show good qualitative simulation results, which follow the phenomenology of structures' behavior under cyclic loading and fatigue conditions.

Keywords: cyclic loading, fatigue, elastic strain energy, phase-field modeling, damage.

1. Introduction

The fracture of structures subjected to cyclic loading is one of the primary failure mechanisms. So, developing the correct simulation models to predict fatigue behavior is essential. In the material, the crack is first initiated by micro-voids and micro-cracks, while in further loading, the cracks grow and propagate, leading to the structure's fracture.

In the experimental investigation of fatigue, the fatigue life is estimated as the relationship between cyclic stress or strain range and the number of cycles in the form of Wöhler diagrams or S-N curves. In high-cycle fatigue (HCF), the material is subjected to low-stress amplitude in an elastic regime, leading to many fracture cycles.

The phase-field damage model (PFDM) is based on Griffith's thermodynamic framework. The crack will increase if the released energy exceeds the material toughness Francfort and Marigo [1] and Bourdin et al. [2].

Many researchers tried implementing fatigue into PFDM [3, 4]. Therefore, a fatigue degradation function describing the fatigue history is introduced to reduce the material toughness [4-6].

This paper presents the PFDM implementation for modeling the fatigue behavior of metallic materials, and the first simulation results are shown. The application of the implementation is proposed for HCF based on Golahmar et al. [4] and Carrara et al. [5]

The theoretical background of the phase field fatigue framework is described in Section 2. Then, the obtained results and discussion are provided in Section 3. Finally, the article ends with conclusions in Section 4.

2. Methods

2.1 A phase field model for fatigue damage

By the formulation of cracks in one-dimensional solids, and the extension of the regularized crack functional to multi-dimensional problems [7,8], the crack surface is defined as follows:

$$S(d)=\int_V \gamma(d,\nabla d)dV \tag{1}$$

where γ is the crack surface density function per unit volume. The internal potential energy density ψ is considered as the sum of mechanical $\psi^M(\boldsymbol{\varepsilon},d)$ and fracture surface energy density $\varphi^S(d,\nabla d)$ [7,8]:

$$\psi = \psi^M(\boldsymbol{\varepsilon},d)+\varphi^S(d,\nabla d) \tag{2}$$

where $\boldsymbol{\varepsilon}$ is the total strain tensor and d is the damage variable. The mechanical strain energy density of virgin material $\psi_0(\boldsymbol{\varepsilon})$ is multiplied by degradation function $g(d)$ to define the mechanical strain energy density ψ^M as [7,8]:

$$\psi^M(\boldsymbol{\varepsilon},d)=g(d)\psi_0(\boldsymbol{\varepsilon})=g(d)\frac{1}{2}\boldsymbol{\varepsilon}^T:\boldsymbol{\sigma}_0 \tag{3}$$

where $\boldsymbol{\sigma}_0$ is the Cauchy stress tensor of an undamaged solid. Similarly, the "damaged" Cauchy stress $\boldsymbol{\sigma}$ is given in the following form [7,8]:

$$\boldsymbol{\sigma}=g(d)\boldsymbol{\sigma}_0=g(d)\mathbf{C}_0:\boldsymbol{\varepsilon} \tag{4}$$

where $\mathbf{C}_0$ is the fourth-order elastic constitutive matrix. The fracture surface energy Φ^S at the crack surface S is defined as [7,8]:

$$\Phi^S=\int_S G_c dS \approx \int_V G_c\gamma(d,\nabla d)dV=\int_V \varphi^S(d,\nabla d)dV \tag{5}$$

where the fracture surface energy density dissipated by the formation of the crack is:

$$\varphi^S(d,\nabla d)=G_c\gamma(d,\nabla d) \tag{6}$$

and G_c is the Griffith-type critical fracture energy release rate. For a cumulative history variable $\bar{\alpha}\geq 0$, and a fatigue degradation function $f(\bar{\alpha})$, the fracture surface energy density can be re-formulated as follows [4,5]:

$$\bar{\varphi}^S(d,\nabla d,\bar{\alpha})=f(\bar{\alpha})G_c\gamma(d,\nabla d) \tag{7}$$

The total internal potential energy W_{int} functional is defined as [6-8]

$$W_{\text{int}} = \int_V \psi dV = \int_V \left\{ g(d)\frac{1}{2}\boldsymbol{\varepsilon}^T : \boldsymbol{\sigma}_0 + f(\bar{\alpha})G_V \left[\frac{d^2}{2} + \frac{l_c^2}{2}|\nabla d|^2 \right] \right\} dV \tag{8}$$

where a critical fracture energy release rate per unit volume is $G_V = G_c / l_c$ and l_c is the characteristic length. The variation of the internal potential energy over the total strain and damage is given as [4-8]:

$$\delta W_{int} = \int_V \left\{ \boldsymbol{\sigma} : \delta\boldsymbol{\varepsilon} + f(\bar{\alpha})G_V \left[d\delta d + l_c^2 \nabla d \nabla \delta d \right] \right\} dV \tag{9}$$

A variation of the external potential energy W_{ext} is known as [7,8]:

$$\delta W_{ext} = \int_V \mathbf{b} \cdot \delta\mathbf{u} dV + \int_A \mathbf{h} \cdot \delta\mathbf{u} dA \tag{10}$$

where b is a body force field per unit volume, h is a boundary traction per unit area, and u is the displacements vector. The equilibrium of the internal and external potential energy [4-8]:

$$\begin{aligned} &\int_V \left\{ \boldsymbol{\sigma} : \delta\boldsymbol{\varepsilon} + \frac{1}{2} g'(d) \boldsymbol{\varepsilon}_E^T : \boldsymbol{\sigma}_0 \delta d + f(\bar{\alpha})G_V \left[d\delta d + l_c^2 \nabla d \cdot \nabla \delta d \right] \right\} dV \\ &= \int_V \mathbf{b} \cdot \delta\mathbf{u} dV + \int_A \mathbf{h} \cdot \delta\mathbf{u} dA \end{aligned} \tag{11}$$

By the application of total derivatives and by using the Gauss theorem, the following can be obtained [4-8]:

$$\begin{aligned} &\int_V \left\{ -\left[g'(d)\psi_0 + f(\bar{\alpha})G_V \left[d - l_c^2 \nabla^2 d \right] \right] \delta d - \left[Div[\boldsymbol{\sigma}] + \mathbf{b} \right] \cdot \delta\mathbf{u} \right\} dV \\ &+ \int_A \left\{ \left[\boldsymbol{\sigma} \cdot \mathbf{n} - \mathbf{h} \right] \cdot \delta\mathbf{u} \right\} dA + \int_A \left\{ \left[G_V l_c^2 \nabla d \cdot \mathbf{n} \right] \delta d \right\} dA = 0 \end{aligned} \tag{12}$$

where $\mathbf{n}$ is the unit outer normal to the surface A. The Neumann-type boundary conditions are

$$\boldsymbol{\sigma} \cdot \mathbf{n} - \mathbf{h} = 0 \tag{13}$$

$$\nabla d \cdot \mathbf{n} = 0 \tag{14}$$

what leads to the governing balance equations [4-8]:

$$Div[\boldsymbol{\sigma}] + \mathbf{b} = 0 \tag{15}$$

$$f(\bar{\alpha})G_V \left[d - l_c^2 \nabla^2 d \right] + g'(d)\psi_0 = 0 \tag{16}$$

2.2 Fatigue damage

The cyclic loading produces damage increase what is captured by a fatigue degradation function $f(\bar{\alpha})$ [3-6]. This function degrades the material toughness concerning the fatigue history variable. For the pseudo time, the history variable can be defined as [3-6]:

$$\bar{\alpha}(t) = \int_0^t H(\alpha\dot{\alpha})|\dot{\alpha}| d\tau \tag{17}$$

where $H(\alpha\dot{\alpha})$ is the Heaviside step function [6]:

$$H(\alpha\dot{\alpha}) = \begin{cases} 1, & \alpha\dot{\alpha} \geq 0 \text{ for loading} \\ 0, & \text{otherwise for unloading} \end{cases} \tag{18}$$

The fatigue history variable α is defined as [3-6]:

$$\alpha = g(d)\psi \tag{19}$$

while the fatigue degradation function is [6]:

$$f(\bar{\alpha}) = \begin{cases} 1 & \text{if} \quad \bar{\alpha} \leq \alpha_T \\ \left(\dfrac{2\alpha_T}{\bar{\alpha} + \alpha_T} \right)^2 & \text{if} \quad \bar{\alpha} > \alpha_T \end{cases} \tag{20}$$

Here, α_T represents a threshold value, below which the fracture energy remains unaffected, which should be determined experimentally and in this case is adopted according to the literature [6]:

$$\alpha_T = \frac{G_V}{12} \tag{21}$$

3. Results and discussion

The uniaxial loading example of the unit cube is created to simulate the phenomenology of the damage evolution under High Cyclic Fatigue (HCF) loading conditions using the PFDM approach extended by the fatigue degradation function described in the previous section.

The unit cube is loaded on one side by prescribed displacements while the other directions are restrained. The opposite side is fully restrained [9]. Only the elastic material parameters of general metallic material are used as data from the literature [9] and are given in Table 1. According to the literature, the additional material parameters, such as fracture energy, characteristic length, and tolerance of convergence, are set to show the material damaging and fatigue phenomena [9].

Firstly, the monotonic loading is performed to the total strain of 1% to show the stress-strain response of the material. Then, two simulations were performed - one with the influence of the fatigue degradation function and the one without. The examples are solved in 1000 loading steps.

After that, the three loading and unloading cycles are performed for both cases. The results are given in Figure 1. The examples are solved in 1800 loading steps up to a total strain of 0.3%.

As can be noticed in Figure 1, the fatigue degradation function has a significant influence on the material response. The damage value for the total strain is given in Figure 2, where we can see how it increases for each simulation case.

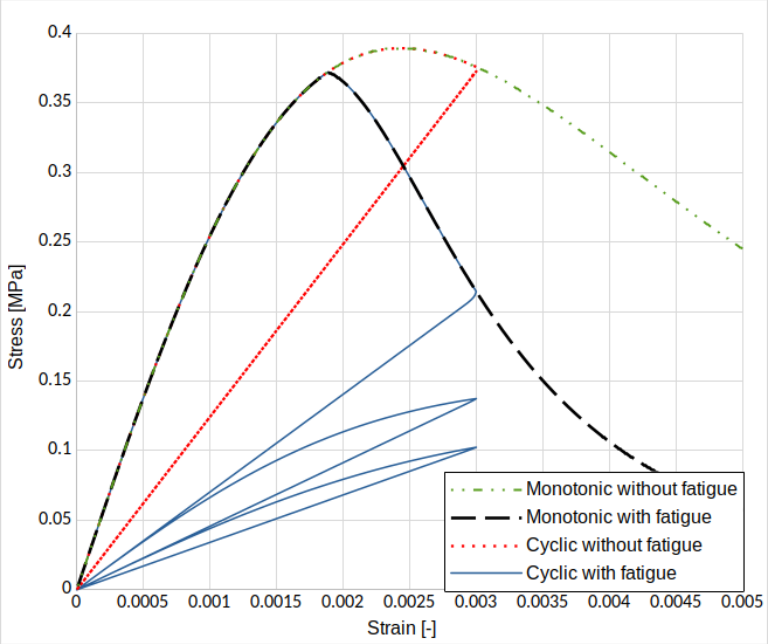

Fig. 1. Stress-strain response for monotonic and cyclic loading conditions with and without fatigue function

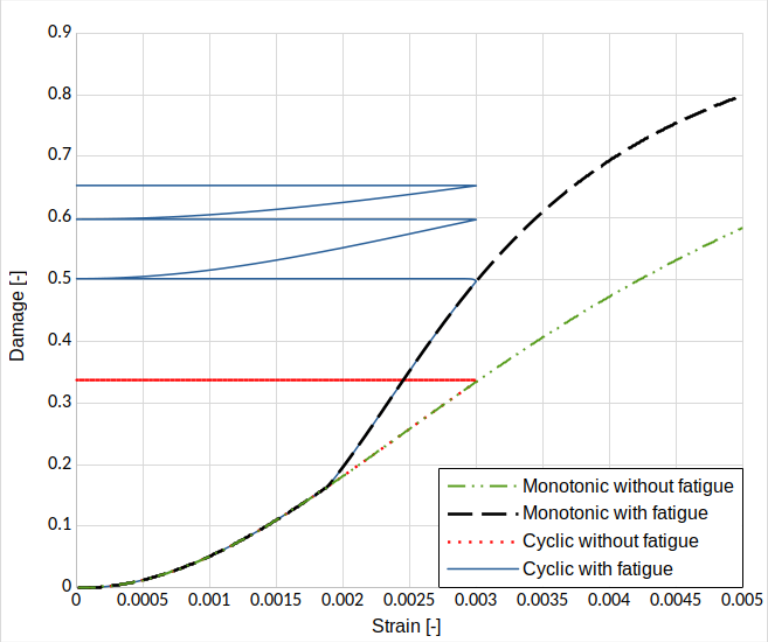

Fig. 2. Damage-strain response for monotonic and cyclic loading conditions with and without fatigue function

E [MPa]	ν [-]	G_V [MPa]	l_c [mm]	tol
210000	0.3	5	0.1	1.e-7

Table 1. Material parameters used in simulation [9]

4. Conclusions

The PFDM is a cutting-edge technique that is nowadays often implemented into FEM software for the prediction of damage and fracture in structures, but also for the evaluation of the structures' safety. By introducing the fatigue degradation function, the PFDM features are enhanced with the capability of simulation fatigue in materials.

In this paper, the authors presented the necessary modifications of the PFDM for that purpose, and the behavior's phenomenology is presented on a simple unit cube model modeled by one finite element. The stress-strain diagram, as well as damage value-strain dependence, show that with the included fatigue degradation function, it is possible to simulate fatigue and that the damage value increases while, at the same time, the stress-strain relationship decreases.

These results are the first step that will be extended by the application on more complex structures and the experimental investigation of the threshold value of the cumulative history variable.

Acknowledgment: This paper is supported by the national funding of research at the Faculty of Engineering, University of Kragujevac after the end of project TR 32036.

References:

[1] Francfort GA, Marigo J-J., Revisiting brittle fracture as an energy minimization problem, J Mech Phys Solids, Vol. 46, 1319–42, 1998.
[2] Bourdin B, Francfort GA, Marigo JJ, The variational approach to fracture. Springer Netherlands; 2008.
[3] Lo YS, Borden MJ, Ravi-Chandar K, Landis CM, A phase-field model for fatigue crack growth, J Mech Phys Solids, Vol. 132, 103684, 2019.
[4] Golahmar A, Niordson CF, Martínez-Pañeda E, A phase field model for high – cycle fatigue: Total-life analysis, International Journal of Fatigue, Vol. 170, 107558, 2023
[5] Carrara P, Ambati M, Alessi R, Lorenzis LD, A framework to model the fatigue behavior of brittle materials based on a variational phase-field approach, Comput Methods Appl Mech Engrg, Vol. 361, 112731, 2020.
[6] Simoes M, Martínez-Pañeda E, Phase field modelling of fracture and fatigue in shape memory alloys, Comput Methods Appl Mech Engrg, Vol. 373, 113504, 2021.
[7] Živković J, Dunić V, Milovanović V, Pavlović A, Živković M, A Modified Phase-Field Damage Model for Metal Plasticity at Finite Strains: Numerical Development and Experimental Validation, Metals, Vol. 11(1), 47, 2021.
[8] Dunić V, Živković J, Milovanović V, Pavlović A, Radovanović A, Živković M, Two-Intervals Hardening Function in a Phase-Field Damage Model for the Simulation of Aluminum Alloy Ductile Behavior, Vol. 11(11), 1685. Metals, 2021
[9] Molnár, G., Gravouil, A. 2D and 3D Abaqus implementation of a robust staggered phase-field solution for modeling brittle fracture, Finite Elements in Analysis and Design, Vol 130, 27–38, 2017

PREDICTING EPILEPTIFORM ACTIVITY USING MEMRISTIVE LONG SHORT-TERM MEMORY

Svetlana A. Gerasimova[1], Nikolay V. Gromov[1], Albina V. Lebedeva[1], Tatiana A. Levanova[1] and Alexander N. Pisarchik[2]

[1] Institute of Information Technology, Mathematics and Mechanics, Lobachevsky University, Nizhniy Novgorod 603022, Russia
e-mail: gerasimova@neuro.nnov.ru, gromov@itmm.unn.ru, lebedeva@neuro.nnov.ru, tatiana.levanova@itmm.unn.ru.
[2] Center for Biomedical Technology, Universidad Politécnica de Madrid, Pozuelo de Alarcón, Madrid, Spain
e-mail: alexander.pisarchik@ctb.upm.es

Abstract

High computational complexity and resource consumption during the training phase is a major challenge for using deep neural networks. One of the promising solutions to this problem is the implementation of neural networks based on memristors, which demonstrate remarkable energy efficiency. In this paper, we propose a long short-term memory (LSTM) memristive network based on a metal-oxide-metal memristive device for analyzing human electroencephalography (EEG) signals in both normal and pathological conditions.

Keywords: memristor, LSTM, epilepsy, human EEG signals.

1. Introduction

More than 50 million people worldwide suffer from epilepsy, which is approximately 1% of the world's population [1]. This pathology is characterized by recurrent and sudden abnormal brain activity. It has been established that the cause of epileptic seizures is excessive hypersynchronous neuronal activity. Antiepileptic drug treatment is not able to cure this disease. On the other hand, drugs often cause neurological deficits, which significantly impair the quality of patient's life. Therefore, the search for alternative ways for predicting and treating epilepsy is one of the important urgent tasks of modern medicine. The causes of epilepsy should be studied using a multidisciplinary approach, including biological (e.g. the study of changes in neuronal activity in deep brain layers [2]), pharmacological (e.g. the use of a particular drug to improve the patient's condition), and physical models (e.g. the development of an implantable neural chip to control epileptiform activity [3]).

In our previous studies, we investigated the behavior of individual metal-oxide-metal memristors in various neuromorphic systems, including their combination with biological neurons, using mathematical models and experiments [4,5]. Neuromorphic systems are not only considered the next step towards efficient and high-speed computing, but also have the potential for medical applications in the treatment and prevention of neurodegenerative diseases. By replicating the

functionality of biological neural networks, neuromorphic systems may allow the development of more effective and personalized therapies for pathologies such as Alzheimer's disease and Parkinson's disease [6,7]. In addition, these systems could play an important role in improving our understanding of neural mechanisms and ultimately lead to breakthroughs in the field of neuroscience.

Previously, in a wide range of studies, numerous attempts were made to build deep neural networks for predicting epilepsy based on EEG signals [8-10], but the optimal solution for predicting epileptic seizures has not yet been developed. Modern deep learning models are quite complex due to the large number of parameters. The use of memristive devices as a hardware platform for inference can help to overcome data transfer bandwidth limitations arising from limited memory capacity and thereby increase computing power [11-13]. However, despite the promising results reported in the literature, more research is needed to prove the applicability of memristive neural networks in clinical settings.

In this study, we propose a memristive deep neural network to predict epileptiform activity based on human EEG data. We propose an implementation of the LSTM architecture using metal-oxide-metal memristive devices [14]. The conducted numerical experiments will allow us to present the circuit design solution for this model in the future. The ability to accurately predict epileptic seizures before they occur based on real-time EEG data will improve the quality of life of patients and reduce the need for massive use of antiepileptic drugs.

2. Memristive devices

In this paper, the elements of the neural network are interconnected through memristive devices of the metal-oxide-metal type [15]. These devices are thin-film structures whose conductivity changes by several orders of magnitude when a voltage is applied. A memristive device is a resistor with memory that can keep the state it received: low or high resistance, indicating the so-called resistive memory. To simulate the behavior of laboratory memristors, a standard approach is used that describes oxidative-reduction processes when a voltage is applied, where the state of the memristor changes due to oxygen ion migration processes with an increase in the effective migration barrier E_m. In turn, migration is provided by Joule heating kT and applied voltage u. The total current density j through the memristor is the sum of linear j_{lin} and nonlinear j_{nonlin} components. The former corresponds to ohmic conductivity with specific resistance ρ, while the latter is determined by the transport of charge carriers through defects in the insulator regions not occupied by filaments (including the filament breakage region). Current transfer is carried out according to the Poole-Frenkel mechanism with an effective barrier E_b. In this paper, we use the equations for memristive switching (1), a detailed description of which is presented in [16].

$$\begin{cases} j = \mathrm{wj}_{\mathrm{lin}} + (1-w)\, j_{\mathrm{nonlin}} \\ j_{\mathrm{lin}} = u / \rho \\ j_{\mathrm{nonlin}} = u\exp\left(B\sqrt{u} - E_b\right) \\ \dfrac{dw}{dt} = \begin{cases} A\exp\left(-E_m - \alpha\, u\right)\left(1-\left(2w-1\right)^{2p}\right), u < u_{set} \\ 0, V_{set} < u < V_{reset} \\ -A\exp\left(-E_m + \alpha\, u\right)\left(1-\left(2w-1\right)^{2p}\right), u > u_{reset} \end{cases} \end{cases} \quad (1)$$

Parameters A, B, and α are taken from experimental data, and parameters V_{set} and V_{reset} are switching threshold voltages of the memristive structure. Parameters E_b and E_m are effective internal parameters characterizing different films ($Au/ZrO_2(Y)/TiN/Ti$, $Au/SiO_2(Y)/TiN/Ti$).

3. LSTM networks

A typical LSTM cell is shown in Fig. 1. Deep neural networks containing such units are recurrent, which means that they not only completely connect nodes in different layers, but also recurrently connect nodes in the same layer at different time steps. The cell remembers values for arbitrary time intervals, while three filters regulate the information flow into and out of the cell.

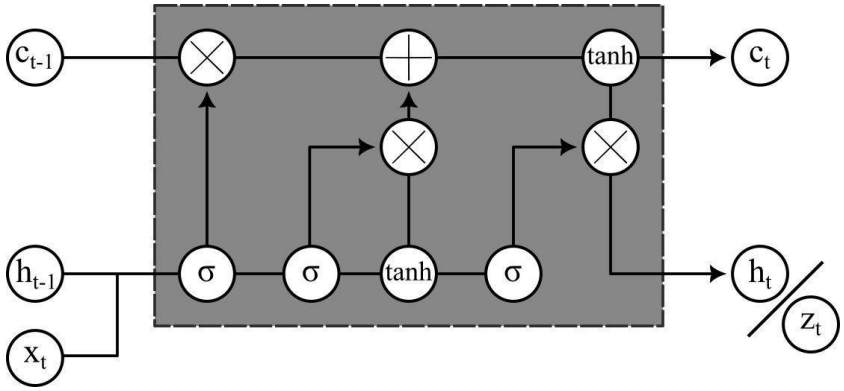

Fig. 1. LSTM cell.

The LSTM cell has two hidden states, one representing short-term memory (h_t) and the other is long-term memory (c_t), which interact as follows. The cell has sigmoid and hyperbolic tangent blocks called gates. The idea of long-term memory is that we want to understand, based on a combination of information from short-term memory and input information, which information we want to forget and what to remember. First, consider the information we want to forget, which is processed by the forget gate, where the sigmoid returns values from 0 to 1. After element-wise multiplication by the long-term memory state, if we get 0, then we forget this information, if 1, then we save it, i.e.

$$f_t = \sigma\left(W_{xf} x_t + W_{hf} h_t + b_f\right)$$

For the information we want to remember, we again use a sigmoid gate to understand which long-term memory state components we want to insert the information into:

$$i_t = \sigma(W_{xi} x_t + W_{hi} h_t + b_i)$$

Once we understand which components of the long-term memory state need to be updated, we use a hyperbolic tangent gate to figure out what information we want to put into those components. The hyperbolic tangent gate outputs values between -1 and 1, indicating how much to update the corresponding components of the long-term memory state based on the input and previously selected information:

$$g_t = TANH\left(W_{xg} x_t + W_{hg} h_t + b_g\right)$$

In other words, in the schema, multiplication means selecting information, and adding means adding information. Thus, the final formula for updating long-term memory is the following:

$$c_t = f_t c_{t-1} + i_t g_t$$

Next, we want the cell to return an output, for which we use an output gate and information from long-term memory:

$$h_t = o_t * TANH(c_t)$$

where

$$o_t = \sigma(W_{xo} x_t + W_{ho} h_t + b_o)$$

We use a model with the following architecture: fully connected layer with ReLU activation, two LSTM layers and another fully connected layer.

The weight matrices W and bias b in the network are trained using backpropagation and the mean squared error (MSE) loss function is used. LSTM networks are well suited for classification, processing, and forecasting based on time series data because there can be intervals of unknown length between important time series events. The relative window length insensitivity is an advantage of LSTM over conventional recurrent networks, hidden Markov models, and other sequence learning methods in many applications.

In our previous paper, an ensemble consisting of neural networks of various types (feedforward, reservoir computing, and LSTM) was tested in the problem of predicting chaotic dynamics based on time series data [14].

The LSTM network in our study was constructed as follows. The model includes a linear input layer of size 1×100 with the Relu activation function. There are also 2 LSTM cells, each with 100 neurons, and the output from these cells goes to a linear layer with a weight matrix of size 200×1. This final output allows us to obtain the predicted value. The model uses new EEG data for each person during the training phase. The prediction step of our proposed model takes approximately 4 ms.

Due to their complicated structure, state-of-the-art LSTM networks include a huge number of model parameters, typically exceeding the usual on-chip memory capacity. Therefore, network inference and training will require parameters to be passed to the processing unit from a separate chip for computation, and inter-chip data communication severely limits the performance of LSTM-based recurrent networks on conventional hardware.

4. Memristive neural network

To create a memristive LSTM network, we implement a memristor crossbar array to storage the weight matrix. Linear matrix multiplication is performed in situ in the memristor crossbar array, eliminating the need to pass weight values back and forth. The model parameters are stored in the same memristor crossbar array that performs the analog matrix multiplications.

In the proposed study, the elements of the neural network are interconnected using metal-oxide-metal memristive devices [16]. Since the weight value in the LSTM cell can take on both positive and negative values, it can be represented as the difference in conductivities of two memristors. This doubles the number of memristors in the array.

The sigmoid and hyperbolic tangent functions are implemented using Simulink. This implementation takes advantage of the property of a differential amplifier to provide a gradual and smooth increase in output voltage when the differential input is in the desired range.

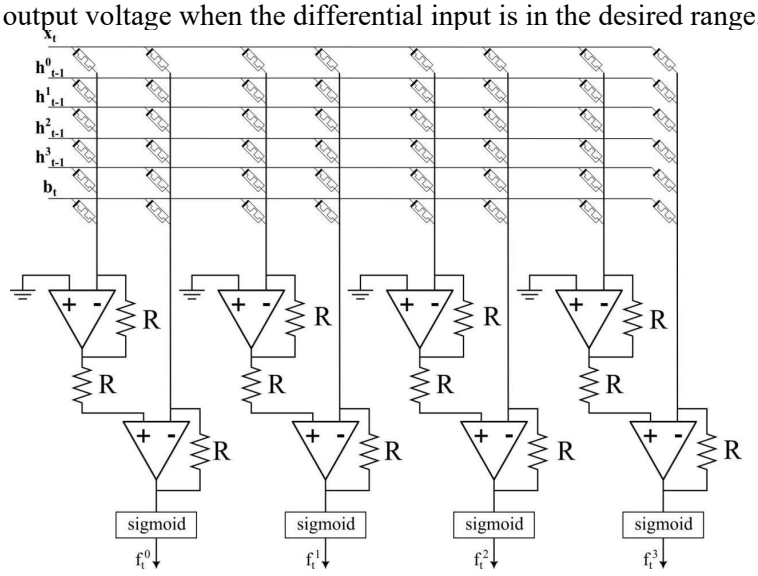

Fig. 2. Scheme of vector-matrix multiplication for the forgetting gate.

The proposed deep neural network is trained on EEG data taken from the open access database https://physionet.org/. This database was collected in 2010 at Children's Hospital Boston and consists of EEG recordings from pediatric subjects with intractable seizures. The subjects were monitored for several days after the withdrawal of anti-seizure medication to characterize their seizures and assess their eligibility for surgical intervention. Epileptic seizures in EEG recordings are characterized by high-amplitude mono- or bilateral spikes and sharp waves. This pathological activity represents a hypersynchronous activation of groups of individual neurons in certain areas of the brain. Physically, patients may experience freezing, loss of consciousness, or a convulsive syndrome.

We conducted numerical experiments and normalized the data by converting it to zero mean and unit variance. The data was then split into an input and output for the model. The input consisted of 20 time samples, and the output was the 21st sample. The optimal number of time samples in an input was determined experimentally during the optimization process. After normalization and splitting the data, we divided it into training and test sets in a 4:1 ratio. The data used in our experiments was from a long EEG recording with epileptic activity.

The simulation results (see Fig. 3 and Fig. 4) show that the proposed architecture is able to achieve high RMSE metric values and adequately predict the appearance of epileptiform activity immediately before its occurrence.

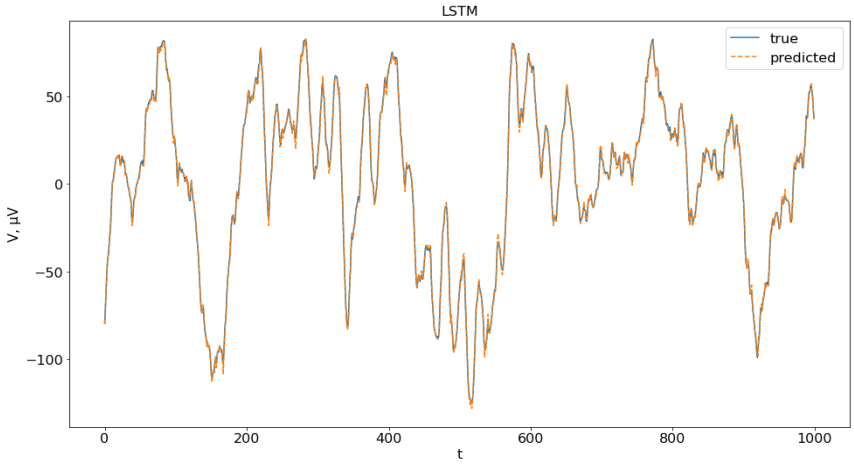

Fig. 3a. True and predicted values for one-step prediction of children EEG, dataset taken at https://physionet.org/. FP1-F7 channel with sampling rate: 256 Hz.

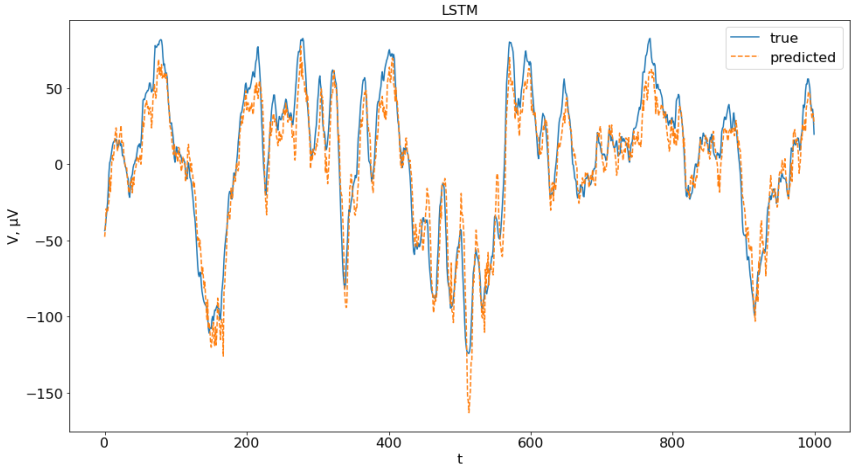

Fig. 3b. True and predicted values for five time steps prediction of children EEG, dataset taken at https://physionet.org/. FP1-F7 channel with sampling rate: 256 Hz.

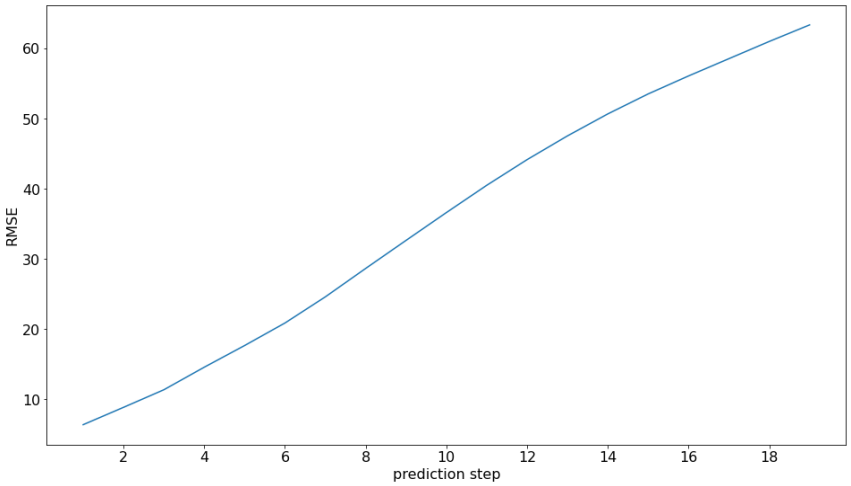

Fig. 4. RMSE metric for truth and predicted values depending on the prediction step length.

3. Conclusions

In this paper, we have proposed a novel approach using memristive deep neural networks to predict epileptiform activity based on human EEG data. The main feature of the proposed technique is the use of memristive devices that make the calculations fast and energy efficient. The obtained results improve our understanding of theoretical and practical aspects of building such architectures and their physical implementations. We hope that, based on this study, effective methods for predicting and controlling epileptic seizures will be developed, which, in turn, will contribute to the creation of new efficient technologies for the treatment of this disease.

Authors thank the Russian Science Foundation grant No. 22-71-00112

References:

[1] Jerome Engel, Jr., Timothy A. Pedley, *Epilepsy: A Comprehensive Textbook*, 1997.
[2] Enes Akyuz, et al., *Elucidating the Visual Phenomena in Epilepsy: A Mini Review*, Epilepsy Research, 107093, 2023.
[3] Alex Plata, et al., *Astrocytic atrophy following status epilepticus parallels reduced Ca^{2+} activity and impaired synaptic plasticity in the rat hippocampus*, Frontiers in Molecular Neuroscience, 11, 215, 2018.
[4] S. A. Gerasimova, et al., *A neurohybrid memristive system for adaptive stimulation of hippocampus*, Chaos, Solitons & Fractals, 1 46, 110804, 2021.
[5] S. A. Gerasimova, et al., *Design of memristive interface between electronic neurons*, AIP Conference Proceedings, 1959, 1, 2018.
[6] Eduardo Perez-Valero, et al., *An automated approach for the detection of Alzheimer's disease from resting state electroencephalography*, Frontiers in Neuroinformatics, 71, 2022
[7] Silvia Battistoni, Victor Erokhin, and Salvatore Iannotta, *Emulation with organic memristive devices of impairment of LTP mechanism in neurodegenerative disease pathology*, Neural Plasticity, 2017, 2017.
[8] Rasheed Khansa, et al, *A generative model to synthesize eeg data for epileptic seizure prediction*, IEEE Transactions on Neural Systems and Rehabilitation Engineering, 29, 2322-2332, 2021.
[9] Xu Yankun, et al., *An end-to-end deep learning approach for epileptic seizure prediction,* 2020 2nd IEEE International Conference on Artificial Intelligence Circuits and Systems (AICAS). IEEE, 2020.

[10] Jemal Imene, et al., *An interpretable deep learning classifier for epileptic seizure prediction using EEG data*, IEEE Access 10, 60141-60150, 2022.
[11] Hosseini Mohammad-Parsa, et al., *Cloud-based deep learning of big EEG data for epileptic seizure prediction*, 2016 IEEE Global Conference on Signal and Information Processing (GlobalSIP). IEEE, 2016.
[12] Daoud Hisham, and Magdy Bayoumi, *Deep learning based reliable early epileptic seizure predictor*, 2018 IEEE Biomedical Circuits and Systems Conference (BioCAS). IEEE, 2018.
[13] Dissanayake Theekshana, et al., *Deep learning for patient-independent epileptic seizure prediction using scalp EEG signals*, IEEE Sensors Journal, 21.7, 9377-9388, 2021.
[14] N. Gromov, et al, *Loss functions in the prediction of extreme events and chaotic dynamics using machine learning approach*, 2022 Fourth International Conference Neurotechnologies and Neurointerfaces (CNN), Kaliningrad, Russian Federation, 2022, pp. 46-50.
[15] A. N Mikhaylov, et al., *Effect of ion irradiation on resistive switching in metal-oxide memristive nanostructures*, Journal of Physics: Conference Series, 1410, No. 1, 2019.
[16] Ivan Kipelkin, et al. *Mathematical and experimental model of neuronal oscillator based on memristor-based nonlinearity*, Mathematics, 11.5, 1268, 2023.

AGE-RELATED PROBLEMS OF POLYPROPYLENE HERNIA MESHES

M. Kirilova-Doneva[1, 2] and D Pashkouleva[2]

[1] Faculty of Pharmacy, Medical University of Sofia, 2 Dunav Str., 1000 Sofia, Bulgaria
e-mail: mdoneva@pharmfac.mu-sofia.bg
[2]Institute of Mechanics, Bulgarian Academy of Sciences, Acad. G. Bonchev Str., Bl. 4, 1113 Sofia, Bulgaria
e-mail: dessip@imbm.bas.bg

Abstract

The repair of the abdominal wall defects with surgical meshes is a common procedure. The implanted meshes stay in the body for many years and it is necessary to know how long the meshes retain its properties. The study aims to investigate the influence of aging on the mechanical properties of surgical meshes.

Five types of meshes made of polypropylene were characterized and compared before and after their expiring date. Long term mesh mechanical properties were determined using quasi-static tensile test. For each specimen maximum tensile stress T_{max}, stretch at maximum stress λ_{max} and elastic secant modulus of mesh E_5 at 5% strain were calculated from derived stress-stretch curves.

The results indicate age-related changes in the mechanical characteristics of investigated surgical meshes. Maximum tensile stress T_{max} and elastic secant modulus of mesh E_5 decrease up to expiring date and after that, the values of parameters increase approximately four years. The stretch at maximum stress λ_{max} decreases before expiring date and remains almost constant after that.

Keywords: hernia meshes, mechanical properties, experimental study.

1. Introduction

Hernia repair is a common surgical procedure in abdominal surgery. In the last decades, surgical meshes were used to improve outcome of operations. Published data focus mainly on the strength and stiffness of biomaterials because the purpose for utilizing biomaterials in hernia repair is mechanical support [1, 2].

The degree to which mechanical mismatch between the repair materials and host tissue contributes to failure has not been evaluated properly in all aspects. The full mechanical properties of biomaterials used in hernia repair need to be quantitatively described and compared as a first step towards matching the mechanics of structures involved in the hernia reoperation [3]. There are studies focused on the tensile mechanical characterization of hernia meshes [4, 5] or compatibility of meshes and abdominal layers at the time of implantation [6-9], but the lack of information exists about age-related changes of the mechanical properties of meshes after implantation.

The long-term performance in mesh materials can be characterized by *in vivo* or *in vitro* experiments. *In vitro* tests of mesh material is a first step toward the validation of its in vivo behaviour. Such tests are: investigation of explanted meshes, or samples placed in the chamber of the thermostatic bath full of buffer solution, to mimic a biological environment similar to human physiology, or comparison of the mechanical behaviour of meshes before and after their expiration date (ED).

The Klosterhalfen et al. reported the results about explanted mesh specimens but the authors analyzed only the tissue reaction to mesh samples and determined the impact of mesh structure on tissue response [10, 11]. The latest study of Lu at al. published results about polypropylene mesh degradation characterized in terms of changes in surface oxidation, crystallinity and mechanical properties. According to authors, infection was a significant factor affecting changes in mesh stiffness [12]. Ryncevic et al. [13] compared pristine control samples with mesh specimens placed in the buffer solution.

The aim of the study is to examine the long term mechanical behaviour of five polypropylene hernia meshes used in surgical practice. Our hypothesis was that the meshes change their properties significantly after their expiration date, which affect the outcomes and lead to insufficient mesh-defect overlap. The recommendations for their application will be discussed.

2. Materials

Five commercially available hernia meshes, namely Microval, Optilene, Surgimesh, Surgipro and TechnoMesh were investigated (Table 1). Information sources for Table 1 are product sheets furnished by the manufacturers.

Brand name	Manufacturer	Type of Material	Filament
Microval	MocroVal, France	polypropylene (nonabsorbable)	monofilament
Optilene	B/Braun, Germany	polypropylene (nonabsorbable)	monofilament
Surgimesh	Aspi Medical, France	polypropylene (nonabsorbable)	monofilament
Surgipro	USSC, USA	polypropylene (nonabsorbable)	monofilament
TecnoMesh	TecnoMedicGmbH, Germany	polypropylene (nonabsorbable)	monofilament

Table 1. A list of the tested meshes

For uniaxial tensile tests 10 samples for every mesh with rectangular shape and length-to-width ratio 7:1 were cut. Each sample was 70 mm long ×10 mm wide and was cut in two orthogonal directions. For every mesh, 5 samples along the loop columns (L direction) and 5 samples across the loop columns (T direction) were tested.

The strips of the tested meshes were gripped with the jaws of a universal testing machine (Fu1000e, Germany, 500N load cell). The distance between the jaws was 40 mm and the jaws were distracted with a constant rate of 0.13 mm/s. The force (F, in N) and the extension (L, in mm) were recorded from the system software. The relationship between the Lagrangian stress T_L and stretch ratio λ of each specimen was obtained where T_L is defined as dividing the applied force F by the initial cross-section area S_0 and stretch ratio λ was defined as the ratio of the obtained displacement L to the initial testing length L_0.From the stress-stretch curves maximum tensile stress T_{max}, stretch at maximum stress λ_{max} and elastic secant modulus of mesh E_5(defined

as a ratio of the Lagrangian stress T_L and 5% strain) were derived for every mesh. The average values of parameters for every mesh in both directions were calculated.

The mechanical properties of the meshes were studied in the interval 34 months before and 60 months after expiration date (ED). Microval, Optilene and Surgipro were tested once 28-34 months before ED and once after ED. Surgimech and TecnoMesh were tested once before and three – five times after ED. The main trends of long term mesh mechanical properties were determined calculating the values of mechanical parameters T_{max}, λ_{max} and E_5 for chosen meshes before and after ED. The origin of a coordinate system coincides with ED. The trend lines were approximated by polynomials of 1to 3-th degrees.

All statistical tests were made using a statistical software package (MedCalc 17.9.7 Software). Quantitative data are represented as mean ± standard error of the mean. The comparison between the average values of parameters was accomplished by procedure which calculates the difference between the observed means in two independent samples. A significance level of $p < 0.05$ was chosen.

3. Results

The mechanical characteristics of investigated surgical meshes showed that the maximum tensile stress T_{max} and elastic secant modulus of mesh E_5 decrease up to expiring date. The values of T_{max} are in the interval 4.41- 16.69 MPa, the mean values of a parameter before and after ED are9.10 ± 3.01vs. 8.15 ± 1.29 MPa ($p = 0.32$). The values ofE_5 are between 3.2 – 35 MPa, while the mean values of a modulus before and after ED are 10.07 ± 9.44 vs. 5.38 ± 1.78 MPa ($p = 0.104$).The values of both parameters increase approximately four years after ED and then begin to decrease again. The results are presented in Fig. 1. The best fit for these parameters are polynomials of 3-th degree where $R^2 = 0.25$ and 0.32 accordingly. The differences between the values of T_{max} and E_5 are more pronounced before ED while after that the parameters change in a narrow interval.

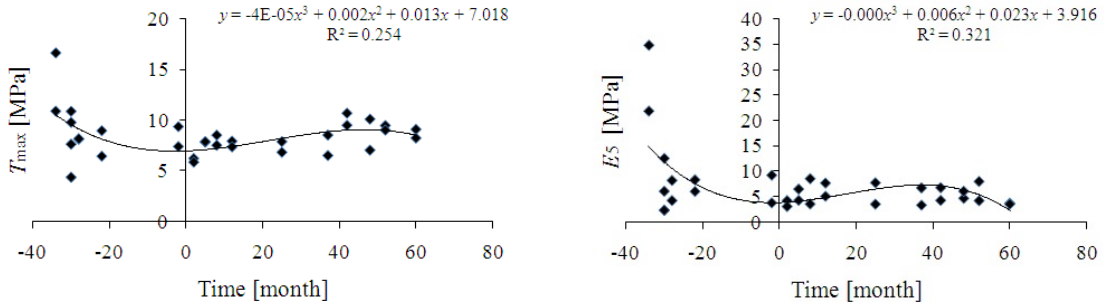

Fig. 1. Age-related changes of the maximum tensile stress T_{max} (left) and elastic secant modulus of mesh E_5 (right)

The opposite trend was observed for the behaviour of stretch at maximum stress λ_{max} plotted in Fig. 2. The stretch λ_{max} increase before expiring date and up to 20 months after ED remain almost constant. The data were fitted with polynomials of second and third order. As $R^2 = 0.16$ for both results, we chose to present the trend with second order polynomial. The values of λ_{max} are in the interval 1.26-2.39 and the mean values of a parameter before and after ED are 1.86±0.45 vs. 2.104±0.17. The difference between the results is not statistically significant (p=0.09).

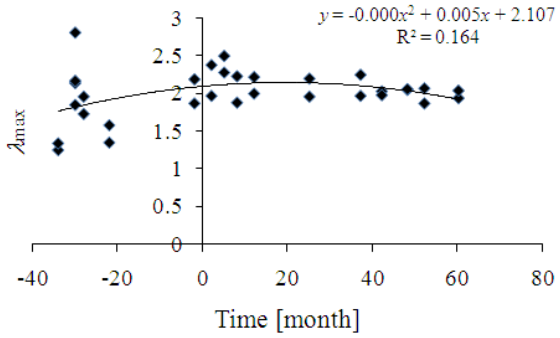

Fig. 2. Age-related changes of the values of λ_{max}

The samples were tested in L and T directions but the values of parameters were not separated according to directions of loading. Although the meshes demonstrated orthotropic properties there is not statistically significant differences between the mean values of maximum tensile stress T_{max} in both directions (7.91 ± 1.71 vs. 9.09 ± 2.35, p = 0.11), the mean values of stretch at maximum stress λ_{max} (2.11± 0.37 vs. 1.91± 0.22, p=0.07) and elastic secant modulus of mesh E_5 (5.44 ± 4.48 vs. 8.85 ± 7.35, p = 0.12).

4. Discussion

Large numbers of mesh brands are available in surgical practice. Considering this fact, particular attention is required when choosing a hernia mesh. Structure, polymer, density, pore size, thickness of material should be clarified in determining the suitability of a hernia mesh. The long-term properties of meshes should be investigated also in order to reduce unsuccessful outcomes.

Recently, attention has been paid to studying the effects of *in-vivo* physiological conditions on the mesh material. The long-term implantation of hernia meshes revealed that the behaviour of polymers in physiological conditions is different. The mechanical properties of the implanted PVDV and PTFE meshes remain unchanged, but the mechanical properties of PP or PE meshes depend on age [14]. Kirscher-Hermans et al. analyzed erosions of PP, polyethylene terephthalate (PET), polytetrafluorethylene (PTFE) and polyvinylidene fluoride (PVDF) used for incontinence and prolapse [15]. It is proved that PTFE is not influenced by hydrolysis and oxidation while PVDF shows excellent resistance to aging and does not increase its stiffness [15-18].

The studies related to the mechanical properties of explanted meshes describe the inflammatory infiltrate, connective tissue on meshes or structural alterations (shrinkage, expansion, adhesion formation, degradation) of the explanted hernia meshes [18]. There are studies which have compared stiffness of surgical mesh before and after exposure to the in-vivo environment. Costello et al. reported that explanted heavy-weight PP meshes increased in stiffness while Burns-Heffner reported an increase in stiffness of heavy-weight mesh Composix E/X (about 7.2-11.2 %) and a decrease for Ultrapro. The average tensile stiffness of Ultrapro decreased by 59.1% [19-20]. A register for mechanical properties of explanted meshes will be very useful but such a registry is not a common practice and at the moment *in vitro* investigations of hernia meshes are reported.

The present study is a part of long lasting investigation of hernia meshes including comparison of pre- and post-implantation mechanical behaviour of composite hernia meshes, long-term investigation of some popular polypropylene and partially absorbable hernia meshes [21-23]. Experimental investigation of long-term behaviour of three polypropylene hernia meshes was accomplished and reported several years ago [23]. The trend of parameters clearly

demonstrates the influence of age on the strength and elasticity of investigated meshes. TechnoMesh become more elastic in both directions, Surgimesh become elastic in the L direction and Surgipro does not change significantly its elasticity.

The main idea in this study was to reveal the trend of polypropylene mesh behaviour years after ED. The results showed that probably this type of meshes loses its elasticity and the strength of the polymer decreases. The results are not statistically significant. Microval, Optilene and Surgipro should be tested several times after ED for confirmation of conclusions.

The study has some limitations. We should increase the number of investigated mesh brands in order to guarantee the generality of the results. The experimental protocol can be enlarged adding more parameters to describe the mechanical behaviour of meshes.

5. Conclusions

Age-related changes in the mechanical characteristics of five commercially used polypropylene surgical meshes were investigated. Maximum tensile stress T_{max} and elastic secant modulus of mesh E_5 decrease up to expiring date and after that the values of parameters increase approximately up to four years. The stretch at maximum stress λ_{max} decreases before expiring date and remain almost constant after that.

A clear understanding of the mechanical properties of hernia meshes, associated with load-bearing is important for outcomes of the operations. The provided results will be useful for clinical recommendations. The information will prevent complications and will improve choice of the meshes.

References:

[1] Pott P., Schwarz M., Gundling R., Nowak K., Hohenberger P., Roessner E., *Mechanical properties of mesh materials used for hernia repair and soft tissue augmentation*, PLoS One, Vol. 7, Nr. 10, e46978, 2012.

[2] Deeken C.R., Abdo M.S., Frisella M.M., Matthews B.D., *Physicomechanical evaluation of polypropylene, polyester, and polytetrafluoroethylene meshes for inguinal hernia repair*, Journal of the American College of Surgeons, Vol. 212, Nr. 1, 68-79, 2011.

[3] Zhu L., Schuster P., Klinge U., *Mesh implants: An overview of crucial mesh parameters*, World Journal Gastrointestinal Surgery, Vol. 7, Nr. 10, 226-236, 2015.

[4] Miao L., Wang F., Wang L., Zou T., Brochu G., Guidoin R., *Physical characteristics of medical textile prostheses designed for hernia repair: a comprehensive analysis of select commercial devices*, Materials, Vol. 8, Nr. 12, 8148–8168, 2015.

[5] Coda A., Lamberti R., Martorana S., *Classification of prosthetics used in hernia repair based on weight and biomaterial*, Hernia, Vol. 16, 9–20, 2012.

[6] Kirilova M., *About mechanical compatibility of some hernia meshes and abdominal wall layers*, Series on Biomechanics, Vol. 25, Nr. 1-2, 134-139, 2010.

[7] Maurer M., Rohrnbauer B., Feola A., Deprest J., Mazza E., *Mechanical biocompatibility of prosthetic meshes: A comprehensive protocol for mechanical characterization*, Journal of the Mechanical Behavior of Biomedical Material, Vol. 40, 42-58, 2014.

[8] He W., Cao G., Gan X., Fan Y., Pei B., Li X., *Evaluation methods for mechanical biocompatibility of hernia repair meshes respective characteristics, application scope and future perspectives*, Journal of Materials Research and Technology, Vol. 13, 1826-1840, 2021.

[9] Deeken C., Lake S., *Mechanical properties of the abdominal wall and biomaterials utilized for hernia repair*, Journal of the Mechanical Behavior of Biomedical Materials, Vol. 74, Nr. 10, 411-427, 2017.

[10] Klosterhalfen B., Junge K, Klinge U., *The lightweight and large porous mesh concept for hernia repair*, Expert Review of Medical Devices, Vol. 2, Nr. 1, 103-117, 2005.
[11] Klosterhalfen B., Klinge U., *Retrieval study at 623 human mesh explants made of polypropylene impact of mesh class and indication for mesh removal on tissue reaction,* Journal of Biomedical Materials Research Part B, Vol. 101, Nr. 8, 1393-1399, 2013.
[12] Lu X., Harman M., Heniford B., Augenstein V., McIver B., Bridges W., *Analyzing material changes consistent with degradation of explanted polymeric hernia mesh related to clinical characteristics*, Surgical Endoscopy, Vol. 36, 5121–5135, 2022.
[13] Rynkevic R., Martins P., Pereira F., Ramiao N., Fernandes, A., *In vitro study of the mechanical performance of hernia mesh under cyclic loading*. Journal Materials Science: Materials in Medicine, Vol. 28, Nr. 11, 176-183, 2017.
[14] Sternschuss G., Ostergard D., Patel H., *Post-implantation alterations of polypropylene in the human*. Journal of Urology, Vol. 188, Nr. 1, 27-32, 2012.
[15] Kirschner-Hermanns R., Klinge U., Klosterhalfen, B., Brehmer B., Heidenreich A., *What can we learn from explanted slings and meshes in pelvic floor surgery*? Journal of Urology, Vol. 183, Nr.4, 686-687, 2010.
[16] Boyce B., *Physical characteristics of expanded polytetrafluoroethylene grafts*. In: Biologic and Synthetic Vascular Prostheses, Stanley JC, Ed; Philadelphia, PA: Grune and Stratton, 553-561, 1982.
[17] Binnebosel M., Trotha K., Jansen P., Conze J., Neumann P., Junge K., *Biocompatibility of prosthetic meshes in abdominal surgery,* Seminars in Immunopathology, Vol.33, Nr. 3, 325-343, 2011.
[18] Bracco P., Brunella V., Trossarelli L., Coda A., *Comparison of polypropylene and polyethylene terephthalate (Dacron) meshes for abdominal wall hernia repair: A chemical and morphological study*, Hernia, Vol. 9, 51-55, 2005.
[19] Costello C., Bachman L., Ramshaw B., Grant S., *Materials characterization of explanted polypropylene hernia meshes*, Journal of Biomedical Materials Research. Part B: Applied Biomaterials*,* Vol. 83, Nr. 1, 44-49, 2007.
[20] Burns-Heffner C., *Development of Explant Registry and Mechanical Testing of Pristine and Explained Surgical Mesh.* PhD thesis, Clemson University, 2014.
[21] Kirilova-Doneva M., Pashkouleva D., Sopotenski S., Petrova G., *Comparison of pre- and post-implantation mechanical behavior of composite hernia meshes*, Journal of Theoretical and Applied Mechanics (JTAM). Poland, Vol.58, Nr. 3,769-778, 2020.
[22] Pashkouleva D., Kirilova- Doneva M., *Mechanical aspects of the degradation process of partially absorbable composite hernia meshe*s, Series of Biomechanics, Vol.36, Nr. 1, 98-104, 2022.
[23] Kirilova-Doneva M., Pashkouleva D., *Long-term mechanical compatibility of polypropylene surgical meshes*, Journal of Mechanics in Medicine and Biology, Vol. 19, Nr. 6, e1950056, 2019.

AN OVERVIEW: ABOUT TWO DOCTORATES IN SERBIAN SCIENCE ON BALL ROLLING AND NEW MODERN RESULTS

Katica R. (Stevanović) Hedrih[1, 2]

[1] Mathematical Institute of Serbian Academy of Sciences and Arts, Belgrade, Serbia
e-mail: katicah@mi.sanu.ac.rs,khedrih@sbb.rs
[2] Faculty of Mechanical Engineering, University of Niš, Niš, Serbia
e-mail: katicahedrih@gmail.com

Abstract

The first part of the short lecture presents the basic contents of two doctorates on ball rolling, defended at the beginning of the last century and in the last millennium, at the University of Belgrade. One doctoral student is Vasilij Demchenko, and the topic of his doctoral thesis is "Rolling without sliding of a gyroscopic ball on a sphere" and was defended in 1924. The second doctoral student is Konstantin Voronec, and the topic of his doctoral thesis is "Rolling of a heavy smooth ball on an elastic surface", and it was defended in 1932. Both doctorates were defended before the Commissions, which consisted of the same members, although the dates for the defense of these doctorates were realized in a time gap of a decade. The composition of both commissions included prominent academicians of the Serbian Academy of Sciences and Arts, and individually, famous Serbian scientists: Anton Bilimonič, Mihailo Petrović and Milutin Milanković. In the second part of this communication, first, a brief overview of the author's previous results is indicated, and then the latest, not yet published, scientific results of the investigation of the rolling, without sliding, of a heavy ball on a stationary sphere from the outside or from the inside are shown, while it is in permanent contact, without sliding, with the moving concentric sphere from the inside, that is, from the outside.

Keywords: two doctoral dissertations, rolling ball without slipping, contact points, angular velocities, nonlinear differential equations, cyclic integral.

1. Introduction as a preliminary

At the beginning of the last century and in the last millennium, at the University of Belgrade two doctorates on ball rolling were defended. The topic of the first doctorate was "Rolling without sliding of a gyroscopic ball on a sphere" and was defended in 1924. The author of this doctoral dissertation is Vasilij Demchenko [7].

The topic of the second doctorate is "Rolling of a heavy, rigid ball on an elastic surface" [8], and the doctorate was defended in 1932. The author of this doctoral dissertation is Konstantin Voronec [10], who was later the founder of the Department of Fluid Mechanics at the Faculty of Mechanical Engineering in Belgrade, as well as the first head of the Department of Mechanics of the Mathematical Institute of the Serbian Academy of Sciences and Arts.

Both doctorates [7] and [8] were defended before the Committees, which consisted of the same members, although the dates for the defense of these doctorates were realized in a time gap of a decade.

The composition of both commissions included the same members, prominent academicians of the Serbian Academy of Sciences and Arts, and individually, famous Serbian scientists: Anton Bilimonič, Mihailo Petrović and Milutin Milanković.

Academician Anton Bilimovich [10] was a scientist in the field of mechanics and one of the initiators of the foundation of Mathematical Institute of Serbian Academy of science and Arts, as well as of the creation of the journal "Publication d' Institut Mathématique", which was originally founded for mathematics and mechanics, but unfortunately, today it has been transformed into a purely specialized mathematical journal.

Academician Mihailo Petrović [10] is a mathematician and the founder of the Serbian School of Mathematics, and the author of the famous and fundamental work "Elements of Mathematical Phenomenon", unfortunately published only in the Serbian language and still insufficiently known and valued in international scientific relations. He is also the author of ten patents in mechanical engineering, and one of the three doctoral students of the famous scientist Julius Henri Poincaré. He is also the author of the hydrointegrator for solving Riccatti's differential equation, and this invention of his is the forerunner of the analog computer.

Academician Milutin Milanković [10] is one of three world-renowned scientists, giants of Serbian science, Nikola Tesla and Mihail Pupin. His most significant work, on a global scale, is the "Canon of Sun insolation". And his Celestial Mechanics, written in Serbian, is significant for Serbian scientific education.

We present the contents of these doctorates in the next section.

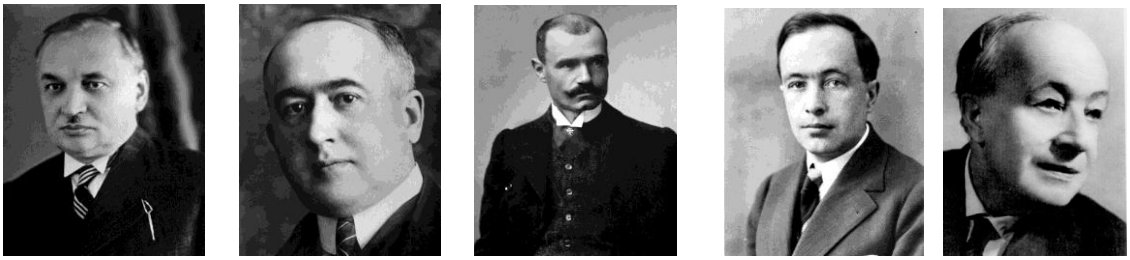

a b c d e

Figure 1. a. ANTON BILIMOVIČ, (Žitomir, 8/20. 7. 1879 − Beograd, 17. 9. 1970); b. MILUTIN MILANKOVIĆ; (Dalj, 16/28. 5. 1879 – Beograd, 12. 12. 1958); c. MIHAILO, ALAS PETROVIĆ; (Beograd, 24. 4/6. 5. 1868 – Beograd, 8. 6. 1943); and d. and e. KONSTANTIN VORONJEC, (Kijev, 17. 1. 1902 – Beograd, 19. 10.1974) (see Refence [10])

2. Contents of two doctorates defended at the beginning of the last century and in the last millennium

2.1. The doctoral dissertation "Rolling without sliding of a gyroscopic ball on a sphere" (94 pages in total), by Vasilij Demchenko, is written on 87 pages, and formulated in six chapters, with an abstract in French and on additional six pages [7].

The titles of the chapters are: 1. Kinematics of a solid body rolling on a constant surface; 2. Equations of a solid body reduced to a moving coordinate system, which has an arbitrarily given movement towards the solid body; 3. Voronets principles; 4. Reduction to quadratures; 5. Solutions in final form; 6. Special cases of movement.

2.2. The doctoral dissertation "Rolling of a heavy smooth ball on an elastic surface" (65 pages in total), by Konstantin Voronec, [10] is written on 62 pages, and formulated in four chapters, with an abstract in French and an additional six pages [8].

The titles of the chapters are: 1. Elastic forces: 2. Equations of motion of a solid body; 3. Approximate solutions to the problem of perturbation motion; 4. Examples.

3. The latest scientific results of the dynamics of rolling, without slipping, a heavy ball on a stationary sphere, in which it is in constant contact, without sliding, with a moving sphere

Figure 2 shows two models of the rolling dynamics, without sliding, of a heavy isotropic and homogeneous ball on a stationary sphere from the outside or inside, where it is in constant contact, without sliding, with a moving and concentric sphere from the inside or outside.

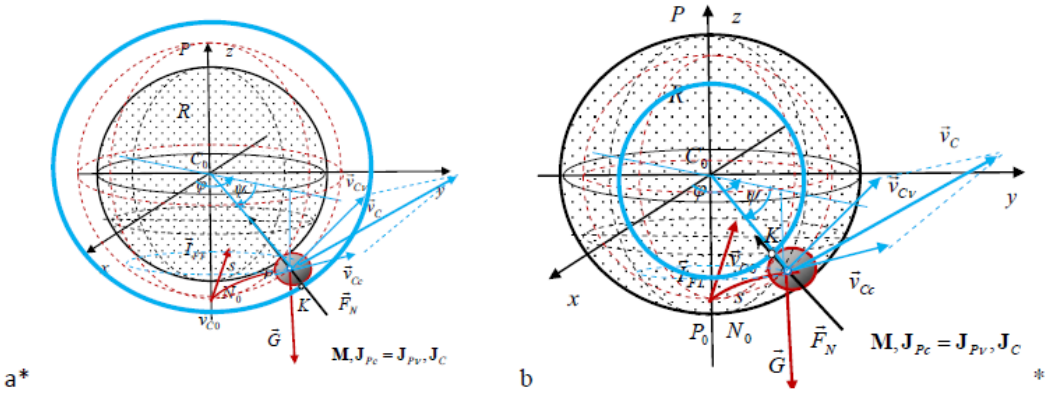

Figure 2. Two models of the rolling dynamics, without sliding, of a heavy isotropic and homogeneous ball on a stationary sphere from a* the outside or b* inside, where it is in constant contact, without sliding, with a moving and concentric sphere from b|* the inside or a* outside

The system is with a finite number of degrees of freedom of dynamic change of the system configuration, and with geometric, stationary and holonomic connections, contacts without sliding of the ball and in contacts with concentric spherical surfaces, movable and immovable. The system has two degrees of freedom of movement, and for independent generalized coordinates we choose meridian ψ and circular φ angular coordinates [9]. Using these independent generalized coordinates, we assemble analytical expressions for kinetic and potential energy. We express the relationship of the component angular velocities of the ball rolling on a stationary sphere using these independent generalized coordinates in the form [1, 2]:

$$\omega_{P,m} = \frac{v_{C,m}}{r} = \frac{(R-r)}{r}\dot{\psi} \qquad \text{and} \qquad \omega_{P,\varphi} = \frac{v_{C,\varphi}}{r} = \frac{(R-r)}{r}\dot{\varphi}\cos\psi \tag{1}$$

From the condition that the rolling ball is in constant contact, without slipping, with the stationary sphere, as well as in permanent contact, without sliding, with the moving sphere, we determine the component angular velocities of rotation of the moving sphere, which revolves around the stationary center. Those component angular velocities are:

$$\dot{\vartheta} = 2\frac{(R-r)}{(R-2r)}\dot{\psi}\,, \qquad \vartheta = 2\frac{(R-r)}{(R-2r)}\psi \quad \text{and} \quad \dot{\delta} = \frac{2(R-r)\dot{\varphi}}{(R-2r)} \tag{2}$$

$$\gamma = \frac{(R-r)\psi}{r} = \gamma = \frac{(R-2r)\vartheta}{2r} \quad \Rightarrow \quad \vartheta = 2\frac{(R-r)\psi}{(R-2r)} \tag{3}$$

In Figure 3a*, the characteristic geometrical elements, characteristic points and arcs in rolling, without sliding, heavy homogeneous and isotropic ball, along the stationary component meridional circular path on the stationary sphere and in contact at the point K, without sliding, along the meridional circle path of the moving sphere are marked. For the analysis of the geometry and kinematics of rolling and contact kinematics, we adopted two angles, one as an independent generalized coordinate ψ and the other dependent coordinate ϑ of the rotation of a moving sphere around an axis through its center, in contact, without sliding, with the ball, in rolling without sliding, according to the stationary meridional component circle path on a moving sphere.

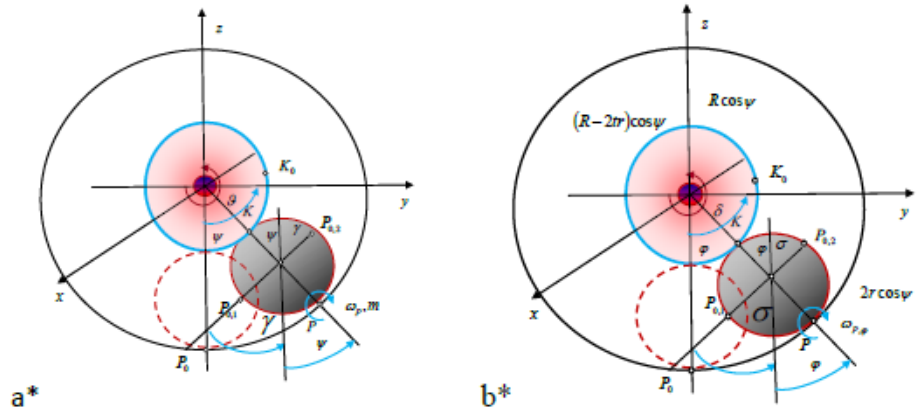

Figure 3. a* The characteristic geometrical elements, characteristic points and arcs in rolling, without sliding, heavy homogeneous and isotropic ball, along the stationary component meridional circular path on the stationary sphere and in contact at the point, without sliding, along the meridional circle path of the moving sphere are marked; b* The characteristic geometrical elements, characteristic points and arcs in rolling, without sliding, heavy homogeneous and isotropic ball, along the stationary component circular circular path on the stationary sphere and in contact at the point , without sliding, along the circular path of the moving sphere are marked

In Figure 3b*, in the component circular direction, the contact points are located on the spherical surfaces of the radius R and $R-2r$, while the center of mass of the rolling ball is always on the spherical surface with radius $R-r$. The ball rolls, without slipping, on a dial on the outer sphere positioned at the meridional angle and at a height $R\sin\psi$ of the center of mass of the ball, during component rolling without sliding, moves along the radius comparator, and on the sphere of radius $R\cos\psi$. The velocity of the center of mass in the circular direction is $v_{C,\varphi}=(R-r)\dot{\varphi}\cos\psi$. The component angular velocity of the ball rolling in a circular direction along that comparator, radius $(R-r)\cos\psi$, is $\omega_{P,\varphi}=\dfrac{v_{C,\varphi}}{r}=\dfrac{(R-r)}{r}\dot{\varphi}\cos\psi$.

The kinetic energy $\mathbf{E}_{\mathbf{k},S}$ of rotation of a moving body (sphere or hollow sphere) in kinematic contact with a rolling ball is the result of two component rotations with angular velocities: and around two orthogonal axis in circular and meridional directions.

$$\mathbf{E}_{\mathbf{k},S}=\frac{1}{2}\mathbf{J}_O\left(\vec{\omega}_O\right)^2=\frac{1}{2}\mathbf{J}_O\omega_0^2=4\frac{1}{2}\mathbf{J}_O\frac{(R-r)^2}{(R-2r)^2}\left(\dot{\varphi}^2+\dot{\psi}^2\right) \tag{5}$$

The kinetic energy $\mathbf{E}_{\mathbf{k},L}$ of rolling without sliding a heavy ball is determined as half the product of the axial moment $\mathbf{J}_P$ of inertia of the ball's mass for the current rolling axis and the square of the resulting rolling angular velocity: $\left(\vec{\omega}_P\right)^2=\left(\dfrac{R-r}{r}\right)^2\left(\dot{\psi}^2+\dot{\varphi}^2\cos^2\psi\right)$ which

consists of the square of the two component angular velocities in the meridional and circular directions:

$$\mathbf{E}_{\mathbf{k},L} = \frac{1}{2}\mathbf{J}_P(\vec{\omega}_P)^2 = \frac{1}{2}\mathbf{J}_P\left(\frac{R-r}{r}\right)^2\left(\dot{\psi}^2 + \dot{\varphi}^2\,\mathbf{cos}^2\,\psi\right) \tag{6}$$

The analytical expression $\mathbf{E}_{\mathbf{k}}$ for the kinetic energy of the dynamics of the complementary system is the sum of the expressions for the component kinetic energies of the rolling ball $\mathbf{E}_{\mathbf{k},L}$ and $\mathbf{E}_{\mathbf{k},S}$ the moving sphere and is in the form:

$$\mathbf{E}_{\mathbf{k}} = \mathbf{E}_{.Lk} + \mathbf{E}_{\mathbf{k},S} = \frac{1}{2}\mathbf{J}_{Pc}\left(\frac{R\pm r}{r}\right)^2\left(\dot{\varphi}^2\,\mathbf{cos}^2\,\psi + \dot{\psi}^2\right) + 2\mathbf{J}_O\frac{(R-r)^2}{(R-2r)^2}\left(\dot{\varphi}^2 + \dot{\psi}^2\right) \tag{7}$$

We get two nonlinear differential equations along two independent generalized coordinates in the meridional angle ψ and circular φ angular coordinate, From the second nonlinear differential equation, we obtain a cyclic integral in which is the integration constant depending of initial conditions. This integral constant depends on the initial conditions, and also on the meridional ψ coordinate ψ_0 and the circular-cyclic coordinate $\dot{\varphi}_0$ at the initial moment of the system's movement.

By means of this cyclic integral, the cyclic φ, circular coordinate can be eliminated from the first nonlinear differential equation and one nonlinear differential equation can be obtained only as a function of the meridional coordinate ψ and using it another integral can be obtained

That integral also represents the equation of the phase trajectory as a function of the meridional coordinate ψ and its velocity $\dot{\psi}$, or the angular velocity of the ball rolling.

We will not show further results here.

4. Concluding considerations

The rolling of a heavy ball on curvilinear paths and curved surfaces [1-6] is a dynamic system, which is a very attractive task for serious and talented researchers, especially important for the dynamics of machine systems, and although many prominent researchers have devoted their research potentials to this task, through previous century, but the dynamics is insufficiently studied. However, even today, in a theoretical sense, the dynamics of the rolling of balls on curved lines and surfaces is insufficiently studied, and it especially refers to the solution of non-linear differential equations, as well as the study of non-linear phenomena that occur. The author of this paper made a significant contribution to the dynamics of the rolling without sliding of a heavy ball on curvilinear surfaces and rotating surfaces, and especially with the analytical theory of the collision of two balls in rolling without sliding. In particular, we point out the series of 15 theorems [2] on the rolling of a ball on surfaces of revolving, and especially the property of this dynamic that, by a suitable choice of independent generalized coordinates, it is easy to show that there is one cyclic coordinate and a cyclic integral, which allows one to derive one nonlinear differential equation by to only one of the more independent generalized coordinates [1]. This is shown in most recently studied nonlinear dynamics of the ball rolling, without slipping, on a stationary sphere, and between a stationary and a moving sphere. Another thing we emphasize here is that when rolling without sliding along plane curvilinear trajectories [3, 4, 5], which rotate around some axis, the beginning of bifurcation and the trigger of coupled singularities can be identified, as well as in the phase trajectory portrait the appearance and disappearance of homoclinic phase trajectories in the form of number “eight” [4, 5].

Many researchers of the problem of the dynamics of rolling, no-slip balls on surfaces, start from the general case of rigid body motion, and choose moving Descartes coordinate systems

related to the rolling ball, assuming that the connections and constraints are non-holonomic. However, by choosing spherical coordinates, the description of the rolling dynamics of the ball leads to obvious results and properties of this non-linear rolling dynamics of the body.

Let's say the dynamics studied by Demchenko [7] in his doctorate, starting from the assumption that it is a non-holonomic system of dynamics, where it is a ball with a gyroscope inside the ball, the whole doctorate can be reworked and studied in a more convenient coordinate system, such as a spherical coordinate system and relative dynamic of inside gyroscope by Euler angles. This would make it possible to arrive at new results with a simpler mathematical description. This proposal could be an inspiration to a young researcher as a topic for doctoral research.

References:

[1] Hedrih (Stevanovic) K. R. (2019) *Rolling heavy ball over the sphere in real Rn3 space*. Nonlinear Dynamics, (2019) 97:63–82, https://doi.org/10.1007/s11071-019-04947-1.

[2] Hedrih (Stevanovic) K., *Rolling a heavy ball on a revolving surface*, (accepted for Springer Proceeding of NODYCON Rome 2023)

[3] Hedrih (Stevanovic) K., *Non-linear phenomena in vibro-impact dynamics: Central collision and energy jumps between two rolling bodies*. Dedicated to memory of Professor and important scientist Ali Nayfeh (December 21, 1933-March 27, 2017). Nonlinear Dynamics, February 2018, Volume 91, Issue 3, pp 1885–1907. DOI :10.1007/s11071-017-3988-x. https://link.springer.com/article/10.1007/s11071-017-3988-x\

[4] Hedrih (Stevanovic) K., *Dynamics of Impacts and Collisions of the Rolling Balls, Dynamical Systems*: Theoretical and Experimental Analysis, Springer Proceedings in Mathematics & Statistics, (2017), Volume Number: 182, Chapter 13, pp. 157-168. © Springer, Part of Springer Science+Business , ISBN 978-3-319-42407-1. ISSN 2194-1009 ISSN 2194-1017 (electronic).

[5] Hedrih (Stevanovic) K., *The Latest Theory of Body Collisions in Rolling and the Dynamics of Vibro-Impact Systems through Scientific Projects over Three Decades*, Special Issue, Guest Editor: Katica R. (Stevanović) Hedrih, Mathematical Institute SASA, Belgrade, NON-PERIODICAL ISSUES – PROCEEDINGS of Mathematical Institute SASA, Belgrade [Collection of Papers], Zbornik radova 19 (27), 2022, pp. 75-160, Series of thematic collection of papers that is published occasionally, Belgrade,
http://elib.mi.sanu.ac.rs/pages/browse_issue.php?db=zr&rbr=27
ttp://elib.mi.sanu.ac.rs/files/journals/zr/27/zrn27p75-160.pdf

[6] Hedrih (Stevanovic) K., *Central collision of two rolling balls: theory and examples*, Advances in Theoretical and Applied Mechanics, Vol. 10, 2017, no. 1, 33-79. https://doi.org/10.12988/atam.2017.765; ISSN 1313-6550. http://www.m-hikari.com/atam/atam2017/atam1-2017/p/hedrihATAM1-2017.pdf
http://www.m-hikari.com/atam/atam2017/atam1-2017/index.html..

[7] Demchnko, V., *Kotrljanje bez klizanja giroskopske lopte po sferi (Rolling without slipping a gyroscopic ball on a sphere)*, doktorska disertacija, odbranjena pred Komisijom u sastavu (doctoral dissertation defended before the Commission composed of): A. Bilimović, M. Petrović, M. Milanković; University of Belgrade, Novem. 15, 1923, pp. 1-94.
hp://www.m-hikari.com/atam/atam2017/atam1-2017/p/hedrihATAM1-2017.pdf
http://www.m-hikari.com/atam/atam2017/atam1-2017/index.html..

[8] Voronec K., *Rolling of a solid body on an elastic surface*, doctoral dissertation, October 9, 1930, 1932, Faculty of Philosophy in Belgrade, Commission Anton Bilimović, Milutin Milanković and Mihailo Petrović; the dissertation is in the Fund of the SANU Library and is kept within the Legacy - Special Library of Academician ANTON BILIMOVĆ (1879–1970) - PB 13, signature PB 13; 221..

[9] Raškovi?, D. *Theory of oscillations, (Theory of oscillations).* (In Serbian), Nau?na knjiga, Belgrade, Serbia, 1965. http://elibrary.matf.bg.ac.rs/handle/123456789/4754..\

[10] Saplememt Book in English: *Lives and Work of the Serbian Scientists*, Volume I-X, Book of Abstracts, 2007p. 458, Edited by Vladan Djordjević, Dragomir Vitorovic and Dragoslav Marinkovic, Edition of Serbian Academy of Sciences and Arts, Beograd. Biographies and Bibliographies. Committee for the Research into the lives and Work of the Scientistts of Serbian Origin/

A NOTE ON THE EFFECT OF STATISTICAL SAMPLE SIZE ON FRACTURE TOUGHNESS CHARACTERIZATION IN THE DTB TRANSITION REGION

Sreten Mastilovic[1,*], Branislav Djordjevic[2] and Aleksandar Sedmak[3]

[1]Institute for Multidisciplinary Research, University of Belgrade, Kneza Viseslava 1a, Belgrade
e-mail: misko.mastilovic@imsi.bg.ac.rs
[2]Innovation Center of Faculty of Mechanical Engineering, Kraljice Marije 16, Belgrade, Serbia
e-mail: brdjordjevic@mas.bg.ac.rs
[3]Faculty of Mechanical Engineering, University of Belgrade, Kraljice Marije 16, Belgrade, Serbia
e-mail: asedmak@mas.bg.ac.rs
[*]*Corresponding author*

Abstract

The ferritic steels, widely used as pressure-vessel materials in nuclear industry, are prone to embrittlement when exposed to neutron irradiation or temperature reduction within the DTB (ductile-to-brittle) transition region. This embrittlement may be accompanied by the increased size effect, which is a pronounced consequence of fracture mechanics not exhibited in the traditional plasticity theory. Therefore, the fracture toughness in the DTB transition temperature region is a stochastic *extrinsic* property well known for its aleatory variability. Consequently, the extremely-pronounced experimental data scatter necessitates the use of the statistical approach to material characterization. The recently proposed two-step-scaling approach to estimate the size effect of fracture toughness CDF (cumulative density function) in the DTB transition region relies heavily on regularity of arrangement of experimental data points for the two *input* sample sizes. This regularity of measurement values becomes an inherently iffy proposition in the case of statistically small data sets. Therefore, the ability of our novel approach to predict objectively the fracture toughness probability outside the experimental domain may be impaired in absence of the sufficient statistical size of the input data sets. Since the large-scale fracture toughness tests for nuclear pressure-vessel steels at low temperatures are very expensive, the present study is concerned with this issue of the statistically sufficient sample size. There are various statistical techniques to determine the sample size needed for a study, including power analysis and sample size calculation formulas. The appropriate method depends on the type of study, the research question, and the statistical analysis planned. These issues are addressed in this article.

Keywords: ferritic steels, embrittlement, fracture toughness, size effect, statistical size.

1. Introduction

The brittle fracture of ferritic steels is characterized by pronounced sample-to-sample variations of fracture toughness (especially for small-size specimens) and a statistical approach is a necessity. The field of Probabilistic Fracture Mechanics emerged from the fact that all fracture toughness measures are inherently distributed quantities (that is, they are best represented by a

range of values and not by a single value) [1]. The Weibull theory is one of the first size-effect theories of the strength of materials that is developed on purely statistical arguments [2]. The Weibull statistics is based on the weakest-link theory, which in this particular case implies lack of stress redistribution prior to cleavage fracture. When it comes to ferritic steels at DTB transition temperatures, addressed in the present study, plasticity mechanisms and stress redistribution are largely suppressed, which results in catastrophic failure of the whole specimen [3]. Consequently, the nature of the size effect appears inherently statistical – that is, of the kind traditionally described by the Weibull distribution. Landes and coworkers (e.g., [4]) based their statistical approach on the premise that the cleavage fracture toughness is controlled by the weakest link at the crack front. They used the two-parameter Weibull distribution, $\mathsf{W}(\beta, \eta)$

$$CDF(x \mid \beta, \eta) = 1 - \exp\left[-\left(\frac{x}{\eta}\right)^{\beta}\right]; \qquad PDF(x \mid \beta, \eta) \equiv \frac{d}{dx} CDF(x) = \frac{\beta}{\eta}\left(\frac{x}{\eta}\right)^{\beta-1} \exp\left[-\left(\frac{x}{\eta}\right)^{\beta}\right] \quad (1)$$

illustrated in Fig. 1, which is a warhorse of DTB fracture toughness assessment to this day (e.g., [3, 5]). The Weibull scale (η) and shape (β) parameters (Fig. 1b) are material constants sensitive to the specimen preparation, surface condition and temperature. Note the general size-effect trend (stemming from the weakest-link theory) that the increase in (sample) size ($W\uparrow$) should results not only in the reduction of the typical fracture toughness value ($\eta\downarrow$) but also in the *reduction* of the fracture toughness *scatter* ($\beta\uparrow$) and the number of necessary tests per CT size ($n_{\max}\downarrow$).

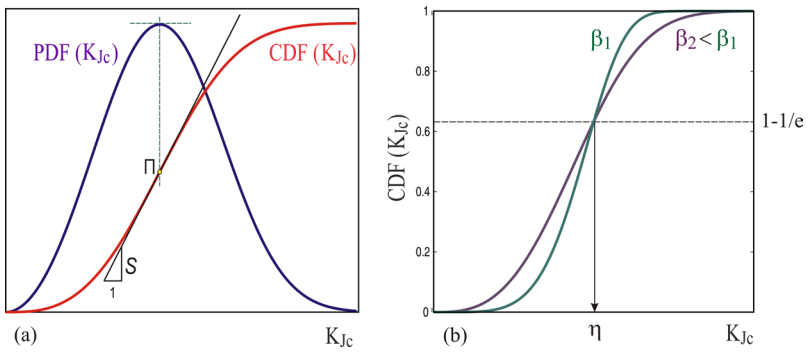

Fig. 1. The Weibull distribution, $\mathsf{W}(\beta, \eta)$. (a) Cumulative distribution function (CDF) and the probability density function (PDF). (b) Illustration of the Weibull parameters of scale (η) and shape (β). K_{Jc} [MPa√m] is the critical value of the stress intensity factor used in the master curve (one of the fracture toughness measures used in Linear Elastic Fracture Mechanics) [7, 8]. (Note that *S* marks the maximum CDF slope.)

A brief historical sketch of some of the, arguably, most influential statistical studies of cleavage fracture toughness of ferritic steels that make use of the Weibull statistics is, for example, recently presented in [6].

The two-step-scaling (2SS) approach has been proposed recently [3, 9] to predict the size effect on the fracture toughness CDF in the DTB transition region. It cannot be overemphasized that it relies crucially on the "regularity of arrangement" of experimental data points for the two *input* sample sizes. This regularity becomes an inherently iffy proposition in the case of *statistically* small data sets (i.e., the small number of realizations of the same statistics, *n*). Therefore, the ability of our novel approach to predict objectively the fracture toughness probability (especially in the extrapolation domain) may be impaired in absence of the sufficient statistical size of the input data sets.

The present study is concerned with this issue of the statistically "large enough" sample size. The very large data sets required to validate statistical methods are already identified as the main problem in the cleavage fracture toughness research [8]. Since the "large" for one analyst may be

"small" for another, what is sufficient in this context? As an example, a sample size of 30 is fairly common in Statistics since it often increases the confidence interval of data sets enough to warrant assertions against findings. Landes [11] suggested that the satisfactory handling of the Weibull slope appears to be achieved with sample sizes between 20 and 50. However, in experimental studies of fracture toughness of ferritic steels in the DTB transition region, the relatively small sample sizes of 10÷12 are often found (e.g., [5, 7]). Obviously, the sample sizes represent a compromise between the statistical analysis confidence and the economic aspects (reflected by judicious and justified use of time and resources). What is a sufficiently large sample size for the purpose? The appropriate method to get an answer, in general, depends on the type of study, the research question, and the statistical analysis planned. The sufficient size of a statistical sample depends on various factors, including the level of precision or accuracy desired, the variability in the population being studied, and the level of confidence required. In general, a larger sample size will provide more precise estimates of population parameters and a higher level of confidence in the results. Again, as a rough guideline, a sample size of at least 30 is often considered sufficient for many statistical analyses. However, this may not be the case in all situations and it is always recommended to investigate the issue on a case-by-case basis.

2. The sources of erratic patterns of experimental data distribution in terms of CDF

The stochasticity of the fracture toughness of ferritic steels in the DTB transition region is "the nature of the beast". In other words, the aleatory variability and epistemic uncertainty are *inherent* in the problem. Nonetheless, when it comes to the above-mentioned "regularity of arrangements" of experimental data points, the primary source of unreliably irregular (non-objective) behavior of fracture toughness CDFs, addressed in this note, appears to be the size of the statistical sample. There are some basics formulas in Statistics for sample size calculation, although sample size calculation differs from technique to technique [10]. (For example, when the means of two populations are compared, if the sample size is less than 30, the t-test is used; if the sample size is greater than 30, the z-test is recommended.) The only aspect a researcher needs in order to justify a sample size based on reliability is the desired width of the confidence interval with respect to their inferential goal, and their assumption about the sample standard deviation of the measure.

As an illustration for the statistical sample size effect of the fracture toughness CDF, the EURO data set is used [7, 8], which is obtained by using CT (compact tension) specimen of the quenched and tempered pressure-vessel steel 22NiMoCr37 frequently used in nuclear power plants. The experimental K_{Jc} data (considered "valid") are actually taken from Annex 2 of the report [7], extracted from the complete EURO data set. This particular data set is selected *exclusively* based on two conveniences: (i) the relatively large size (55 realizations), and (ii) the experimental results are obtained from the same laboratory (see Fig. 2 caption).

It can be observed from Fig. 2 that the progressive reduction of the size of the randomized-order sample eventually results in the break-up of the CDF objectiveness (representativeness). For example, the ½ reduction plot (28 solid green circles) follows reasonably closely the full-deck (55 empty purple squares) CDF plot. The agreement between Weibull slopes is within ±5% and between the Weibull scale factors even better. Then, after further size reductions, the CDFs diverge more and more. Eventually, a simple visual inspection is sufficient to observe that the Weibull parameters (η and β) corresponding to the ⅕ reduction (11 solid red triangles) differ significantly from the original. Interestingly, the ⅕ reduction data set in itself obeys the Weibull CDF sigmoid shape rather well but the parameter values are inconsistent.[1] These conclusions are further supported by the successfully reducing values of the statistical measure of the goodness-of-fit (the adjusted P-value) with the sample size reduction also shown in Fig. 2. (In some other examples, not

[1] For example, the horizontal line corresponding to CDF = 1-1/e ≈ 0.632 reveals the difference in the Weibull scale parameters of more than 10% between the full data set (n = 55) and the ⅕ reduction set (11).

presented herein, the distribution of 11-point set results does not even suggest the sigmoid shape of the Weibull CDF.) It goes without saying that using an experimental set of 11 data points, in this particular case, would bias the CDF (K_{Jc}) predictions obtained by the 2SS approach.

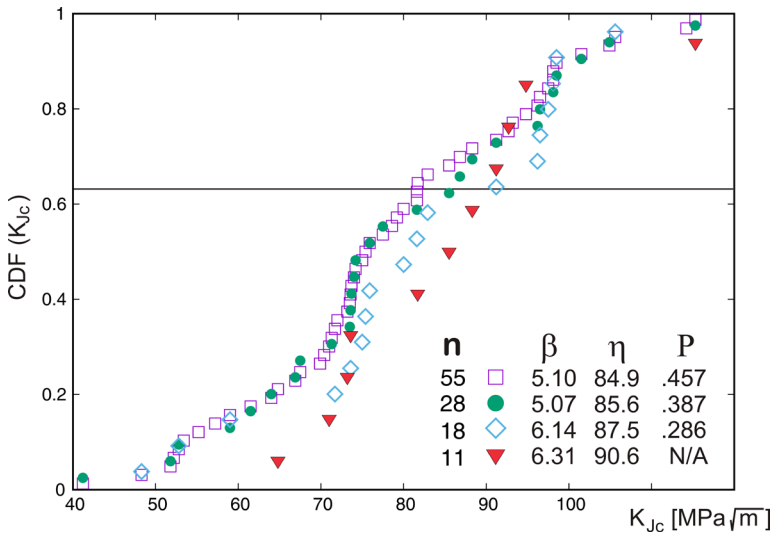

Fig. 2. Effect of random reductions of the data set (1/1, 1/2, 1/3, 1/5) on K_{Jc} CDF for 22NiMoCr37 steel at T=-110ºC and w=25 [7]. The Weibull parameters (β, η) correspond to the calculated P-value (χ^2 test, Appendix A). (Data obtained by the GKSS Research Centre – now: the Helmholtz-Zentrum Hereon, Germany.)

2.1 Random reductions of data set as a source of uncertainty

The random reductions of the original data set are a source of stochasticity in itself. This is an unavoidable consequence (an essential facet) of the process of random reduction. To illustrate this point, the ⅕ random reduction is performed independently four times on the original experimentally obtained fracture toughness set (n = 55 data points). The results are presented in Fig. 3.

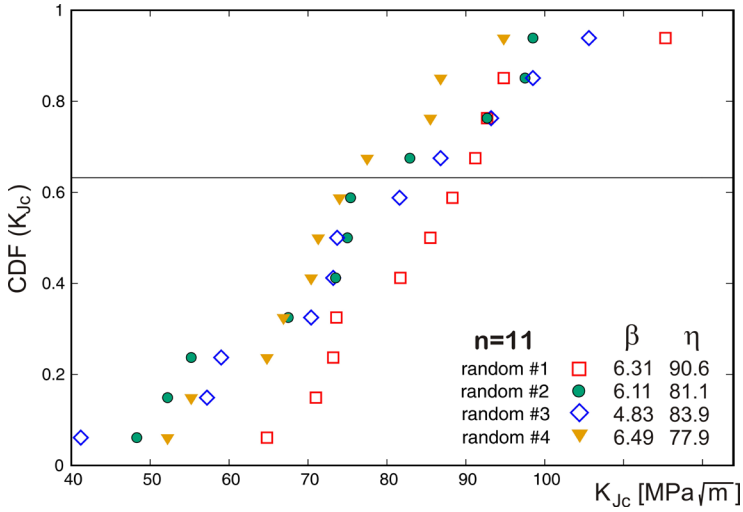

Fig. 3. Four different one-fifth random reductions of the original CDF (K_{Jc}) experimental data set.

Two observations readily come to mind. First, all four CDF patterns that reveal (at least to some extent) the desired sigmoid shape (Fig. 1) are themselves relatively irregular. (This is *apparently* an unavoidable consequence of the small size of the statistical sample; the rule rather than the

exception.) Second, the difference between the four data sets (and the perceived Weibull CDF data fits) is not negligible, to put it mildly, which is evident from the corresponding Weibull parameters (β, η) that are widely different.

Two observations illustrated in Figs. 2 and 3 question representativeness (objectivity) of the 11-point data sets. Fig. 2 suggests that the trend is improving with the increase of the sample size.

3. The use of the experimental data from different laboratories as a source of stochasticity

Assuming that all experimental specimens are cut from the same large segment of the material provided by the same manufacturer, it is a valid question whether testing in different laboratories is, in itself, a source of stochasticity of the fracture toughness measurements.

To investigate this eventuality, the data sets obtained from two laboratories (GKSS and Siemens) for the same CT specimen size (W = 25 mm) and two different temperatures (-154 ºC and -60 ºC) are compared. In this way, the uncertainty due to the specimen size is excluded from consideration. The corresponding CDF (K_{Jc}) plots are shown in Fig. 4.

The CDF comparisons yield the different results for two temperatures. Namely, at T = -154 ºC the Weibull CDFs from two data sets from different labs reveal significantly different Weibull parameters η and β. On the other hand, the Weibull CDFs at T = -60 ºC show a fair level of similarity. One can argue that the more brittle behavior at the lower cryogenic temperature is expected to be more stochastic. But also, it is rational to assume that the discrepancy between the two curves is due to the smaller statistical sample size for the GKSS data set (only 11 points).

Therefore, the analysis is inconclusive at present: it confirmed that the differences between the fracture toughness measurements from different laboratories *may* exist, but the determination of the root cause of this discrepancy with satisfactory certainty requires additional work on new data.

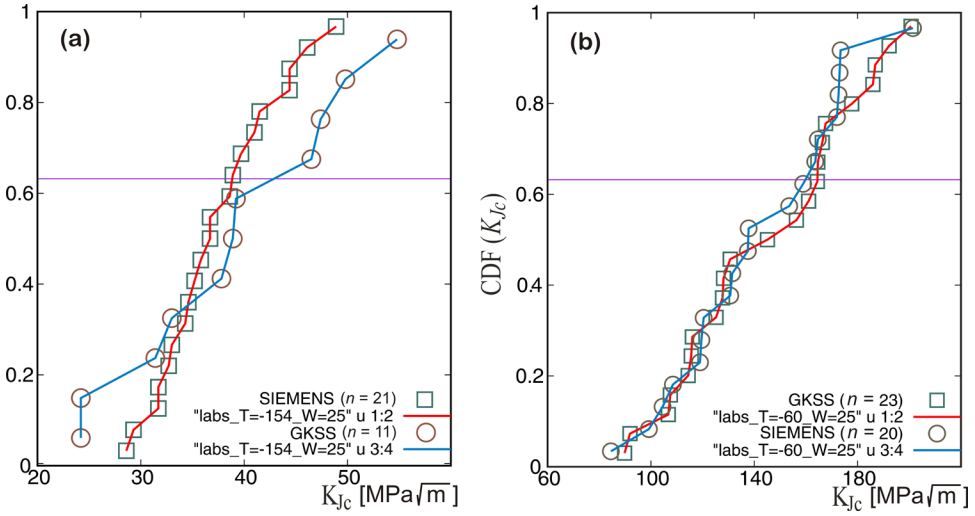

Fig. 4. CDF (K_{Jc}) for 22NiMoCr37 steel obtained from two laboratories: GKSS (squares and red lines) and Siemens AG (Power Generation Group, Erlangen, Germany) (circles and blue lines). The tests are performed at the same CT specimen size (W = 25 mm) at two different temperatures: (a) -154ºC and (b) -60ºC.

4. Summary

The present preliminary study is dedicated to investigation of the effect of the statistical sample size on modeling the Weibull CDF (K_{Jc}) in the DTB transition region by the novel 2SS approach. This approach is sensitive to the objectivity of the fitting of the fracture toughness measurement data sets at two input CT specimen sizes. The big question of every statistical analysis emerges: how many realizations (of the same statistics) are enough in this case?

There are various statistical techniques to determine the sample size needed for a study. At the risk of stating the obvious, in statistical practice "the more the merrier" but in engineering practice using a sample size that is too large could incur a significant waste of both resources and time (the penalty for excess conservatism is increased costs). Thus, based on the data sets examined, it seems reasonable to confirm that small sample sets consisting of less than approximately 15 data points (measurement realizations) are of questionable utility for the above-stated purpose. As a rule of thumb, the minimum data set size can be apparently set from 25 to 30. This observation is consistent with time-honored statistical practices in general and the previous DTB assessments of ferritic steels in particular.

Under these circumstances, bearing in mind that available data set sizes are often limited to 10-12 data points, combining data sets from different laboratories becomes necessary. This practice should be applied judiciously as it might be in itself an additional source of data uncertainty in the case of materials exhibiting the weakest-link type of fracture mechanism.

References:

[1] U.S. NRC, *Important Aspects of Probabilistic Fracture Mechanics Analyses*. Technical Letter Report TLR-RES/DE/CIB-2018-01, 2018.

[2] Weibull, W., A Statistical Theory of the Strength of Materials. Generalstabens Litografiska Anstalts Förlag, Stockholm, 1939.

[3] Mastilovic S., Djordjevic B., Sedmak A. *A scaling approach to size effect modeling of J_c CDF for 20MnMoNi55 reactor steel in transition temperature region*. Engineering Failure Analysis 131: 105838, 2022.

[4] Landes, J., Zerbst, U., Heerens, J., Petrovski, B., Schwalbe, K., *Single-Specimen Test Analysis to Determine Lower-Bound Toughness in the Transition*, in Fracture Mechanics: Twenty-Fourth Volume, ed. J. Landes, D. McCabe, and J. Boulet (West Conshohocken, PA: ASTM International), 171-185, 1994.

[5] Djordjevic B., Sedmak A., Petrovski B., Dimic A., *Probability Distribution on Cleavage Fracture in Function of J_c for Reactor Ferritic Steel in Transition Temperature Region*, Engineering Failure Analysis, 125, 105392, 2021.

[6] Djordjevic B., Sedmak A., Mastilovic S., Popovic O., Kirin S. *History of ductile-to-brittle transition problem of ferritic steels.* Procedia Structural Integrity 42: 88–95, 2022.

[7] Lucon E., Scibetta M., *Application of Advanced Master Curve Approaches to the EURO Fracture Toughness Data Set*. Open Report of the Belgian Nuclear Reserach Centre SCK•CEN-BLG-1036. Mol, Belgium, 2007.

[8] Heerens J., Hellmann D., *Development of the Euro fracture toughness dataset*. Engineering Fracture Mechanics 69: 421–4492002, 2002.

[9] Mastilovic S., Djordjevic B., Sedmak A., *Corrigendum to "A scaling approach to size effect modeling of J_c CDF for 20MnMoNi55 reactor steel in transition temperature region"* [Eng. Fail. Anal. 131 (2022) 105838] Engineering Failure Analysis 142: 106751, 2022.

[10] Hines W.W., Montgomery D.C., *Probability and Statistics in Engineering and Management Science*. John Wiley & Sons; 3rd Edition, 1990.

[11] Landes J.D., The effect of size, thickness and geometry on fracture toughness in the transition. GKSS 92/E/43. GKSS, Geesthacht, Germany, 1992.

Appendix A – The Hypothesis-Testing for Goodness of Fit

The original full (1/1) data set of K_{Jc} CDF for 22NiMoCr37 steel at T = -110ºC and W = 25 mm [7] and the three randomly reduced (1/2, 1/3, 1/5) data sets (Fig. 2) are subjected to the hypothesis testing procedure to establish whether the random variable in question follows the 2-parameter Weibull distribution, $\mathsf{W}(\beta, \eta)$, with the estimated parameters.

The formal goodness-of-fit test procedure is based on the chi-square (χ^2) distribution [10]. The χ^2 is a statistical test that examines whether a random sample data follows a theoretical probability distribution with estimated parameters. The random results of the fracture toughness measurements arranged in the four datasets (1/1, 1/2, 1/3, 1/5) are arrayed in frequency histograms (one for each data set), having k class intervals.[2] The observed frequency in the i-th class interval is marked O_i. From the hypothesized $\mathsf{W}(\beta, \eta)$ with two parameters estimated based on the Weibull plot and the maximum likelihood method (Fig. A1) the expected frequency E_i in the corresponding class interval can be readily computed. (A common practice in constructing the class intervals is to choose their boundaries so that the magnitudes of the expected frequencies are equal for all cells [10].) The test statistics is

$$\chi_0^2 = \sum_{i=1}^{k} \frac{(O_i - E_i)^2}{E_i} \tag{A1}$$

It can be demonstrated that the test statistics (A1) follows approximately the χ^2 distribution with $dof=k–p$-1 degrees of freedom (where p is the number of parameters in the hypothesized distribution; in this case p=2). It cannot be overemphasized that this approximation improves as n increases [10]; the small samples are therefore inherently handicapped. The null hypothesis (H_0) that the random sample conforms to the hypothesized $\mathsf{W}(\beta, \eta)$ is rejected with the confidence level $(1-\alpha)\cdot 100\%$ if the test statistics exceeds the critical statistics, $\chi_0^2 > \chi_{\alpha,dof}^2$. The significance level (α) is the probability of rejecting the null hypothesis when it is true.

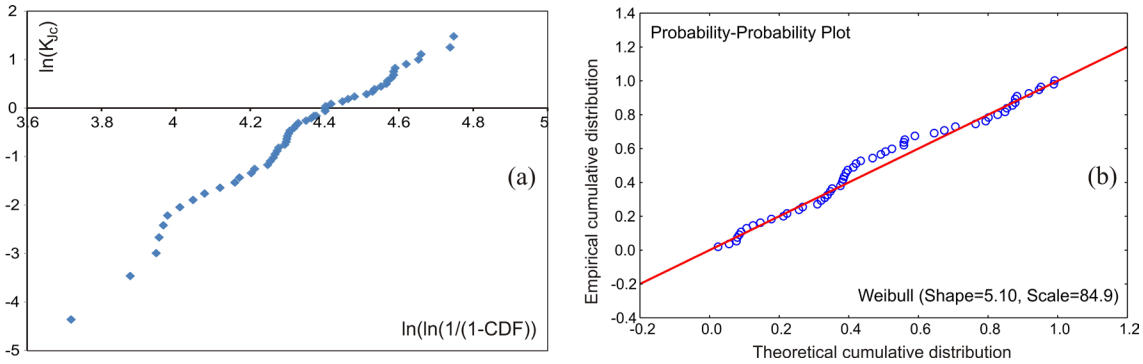

Fig. A1. An example of: (a) the Weibull plot and (b) the probability-probability plot for the full (1/1) data set of K_{Jc} CDF for 22NiMoCr37 steel at T = -110ºC and W = 25 mm.

The χ^2 test is extremely sensitive to the sample size. Since the full data set has a relatively large number of data points (n = 55) an attempt is made to use k = 6 data cells (class intervals). Consequently, the limits of the class intervals (a_i, i = 1, k) in the first column of Table A1 are determined by using Eq. (A2) under the constraint that all expected frequencies have the same

[2] The number of class intervals should be reasonably large. More importantly, although there is no general agreement regarding the minimum value of expected frequencies E_i, the values of 3, 4, and 5 are *commonly* regarded as minimal [10]. This requirement imposes a stringent limitation to the small data sets.

magnitude $E_i = n \cdot p_i = n/k = 55/6 \approx 9.167$:

$$p_i = \int_{a_{i-1}}^{a_i} PDF(x)\,dx = \frac{1}{k}; \quad (i = 1, k),\ a_0 \equiv -\infty \tag{A2}$$

Based on Eq. (A1) and the data in Table A1, the computed value of the chi-square statistics is

$$\chi_0^2 = \frac{(9-9.167)^2}{9.167} + \frac{(8-9.167)^2}{9.167} + \frac{(14-9.167)^2}{9.167} + \frac{(7-9.167)^2}{9.167} + \frac{(6-9.167)^2}{9.167} + \frac{(11-9.167)^2}{9.167} = 4.672 \tag{A3}$$

Since two parameters in the Weibull distribution have been estimated ($\beta = 5.10$, and $\eta = 84.9$; Fig. A1b), the calculated value (A3) should be compared to a chi-square distribution with 3 degrees of freedom. Moreover, the χ^2 P-value for the observed and expected frequencies shown in Table A1 is calculated in Excel to be 0.457. Thus, the null hypothesis that the random sample conforms to W (5.10, 84.9), cannot be rejected since: (i) $\chi_0^2 = 4.672 < \chi^2_{0.05,3} = 7.81$ (Table III,Ref. [10]), and (ii) the corresponding P-value is greater than the significance level ($0.457 > 0.05$). Consequently, it can be concluded that there is *no reason to believe* that the K_{Jc} measurement data **is not** distributed in accordance with W (5.10, 84.9).

	Class Interval	**Observed Frequency, O_i**	**Expected Frequency, E_i**
1	$x \le 60.81$	9	9.167
2	$60.81 \le x \le 71.13$	8	9.167
3	$71.13 \le x \le 79.02$	14	9.167
4	$79.02 \le x \le 86.49$	7	9.167
5	$86.49 \le x \le 95.20$	6	9.167
6	$95.20 \le x$	11	9.167
	sum	**55**	**55.00**

Table A1. Class intervals, observed and expected frequencies for $n = 55$ and $k = 6$.

The χ^2 test applied to the reduced data sets (½) with $n = 28$, yielded the same conclusions. Namely, for $n = 28$ and the estimated Weibull parameters $\beta = 5.07$ and $\eta = 85.6$:

$$\chi_0^2 = 4.143 \quad < \quad \chi^2_{.05,\,5-2-1} = \chi^2_{.05,\,2} = 5.99 \tag{A4}$$

while P-value = $0.387 > \alpha = 0.05$. Similarly, for $n = 18$ (⅓) and the estimated Weibull parameters $\beta = 6.14$ and $\eta = 87.5$:

$$\chi_0^2 = 3.778 \quad < \quad \chi^2_{.05,\,4-2-1} = \chi^2_{.05,\,1} = 3.84 \tag{A5}$$

while P-value = $0.286 > \alpha = 0.05$. Consequently, the two null hypotheses cannot be rejected with the confidence level of 95%. Notably, for the smaller sample size (A5), the hypothesis came very close to be rejected since the two χ^2 values are within 2% from each other and the P-value is smaller than for other samples. Thus, the *n*-reduction trend is toward rejection of the null hypothesis.

Finally, the smallest randomly reduced data set (⅕), with $n = 11$, is evidently too small for the χ^2 test since the expected frequencies ($11 / 4 = 2.5 < 3$) would be below even the most liberally fixed minimal value (= 3; see footnote 2 on the preceding page).

COMPARATIVE STRUCTURAL ANALYSIS OF ALUMINUM AND COMPOSITE WING OF PASSENGER AIRCRAFT

Radoslav D. Radulović , Milica P. Milić and Xun Fei

Faculty of Mechanical Engineering, University of Belgrade, Kraljice Marije 16, 11120 Belgrade, Serbia
e-mail: rradulovic@mas.bg.ac.rs, mmilic@mas.bg.ac.rs, feixunlalala@gmail.com

Abstract

This paper focuses on the conceptual design and structural analysis of winglets attached to the wings of passenger planes, with the aim of improving aircraft performance by reducing fuel consumption and increasing range. Winglets, which are upward and outward extensions of the wings, function by mitigating the drag induced by wingtip vortices. This study underscores the criticality of the winglets' design, as it must strike a balance between structural integrity and lightweight construction. To achieve these objectives, the study proposes the utilization of aluminum and composite materials in a thin-walled construction. Aluminum offers favorable strength-to-weight ratios, rendering it a commonly employed material in aircraft construction. In contrast, composite materials exhibit exceptional strength-to-weight ratios and excellent resistance to corrosion, making them highly suitable for lightweight constructions.

Keywords: conceptual design of wing, static structural analysis, composite and aluminum material.

1. Introduction

The design of modern passenger aircraft wings has evolved to incorporate winglets, which are an essential feature for enhancing overall performance. Winglets, as extensions positioned upward and outward at the wingtips, serve the primary purpose of reducing fuel consumption and increasing the range of the aircraft. This study focuses on the conceptual design and structural analysis of winglets, with a specific emphasis on achieving the desired goals of fuel reduction and range enhancement.

2. Wing model for the structural analysis

One crucial aspect of the Finite Element Method (FEM) pertains to the subdivision of the domain. In this context, the utilization of Computer-Aided Design (CAD) software proves valuable as it facilitates the definition of an object's three-dimensional shape and enables the subdivision of the object into appropriately sized elements based on the desired mesh. The mesh, serving as a three-dimensional grid that outlines the elements, can be tailored to the specific problem at hand. It may comprise uniformly sized and shaped elements such as cubes or pyramids, or it can encompass elements of varying shapes and sizes across different regions of the domain.

By employing the finite element method, the model's behavior can be effectively visualized under designated boundary conditions. This software package offers notable advantages, including cost reduction in production and testing processes, as well as the optimization of geometry and weight. Such benefits are derived from the ability to accurately simulate and analyze the model's performance, enabling engineers to make informed decisions regarding design modifications and improvements. The first step is to import the model saved in the stp to software using the Import function. The model is scaled by a factor of 1000, in order to obtain the true dimensions of the model. View of the wing model is shown in Figure 1.

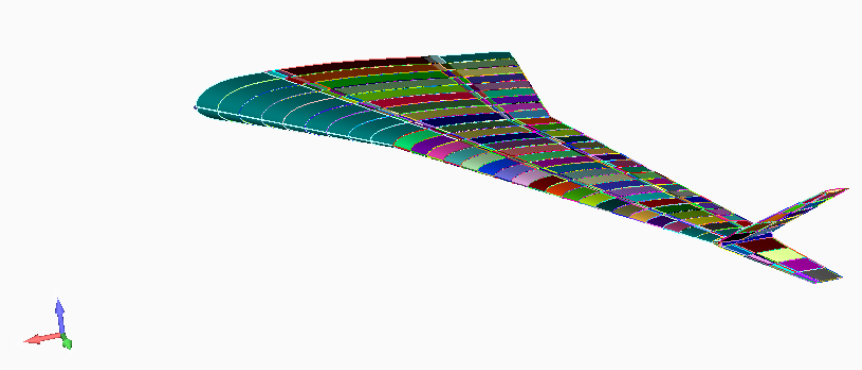

Fig.1. Wing model

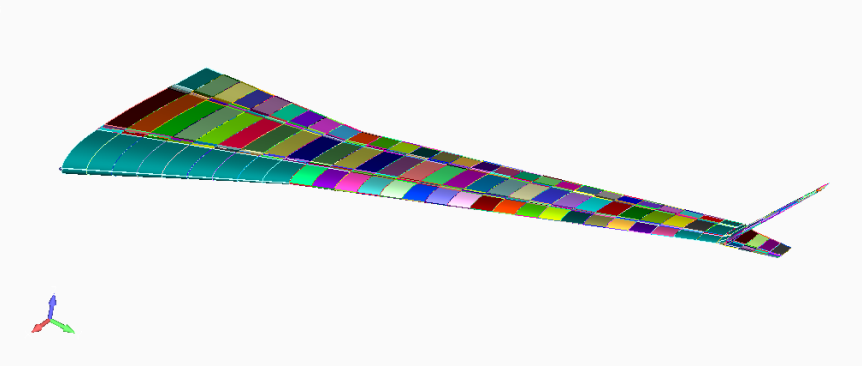

Fig. 2. Wing model

3. Allocation of materials and formation of a network of finite elements' mesh

The process of material definition for an aluminum wing differs from that of a composite wing. For aluminum, it suffices to input specific parameters pertaining to the chosen aluminum material. On the other hand, for a composite wing, the process involves layering the laminae of the selected composite material.

Following the material selection, the subsequent step involves defining the properties in the dedicated section. Here, the thickness of the wing is established and assigned to each respective part of the structure. Subsequently, a finite element mesh is generated to facilitate further analysis. The mesh's appearance, as well as the size of the individual elements comprising the mesh, are determined in the Mesh section.

Lastly, the Boundary Conditions section is defined, encompassing the specification of external forces, moments, and restraints acting upon the structure. These boundary conditions are imposed upon the generated mesh, as depicted in Figure 3, to accurately represent the real-world operating conditions of the wing structure.

Fig. 3. Wing mesh

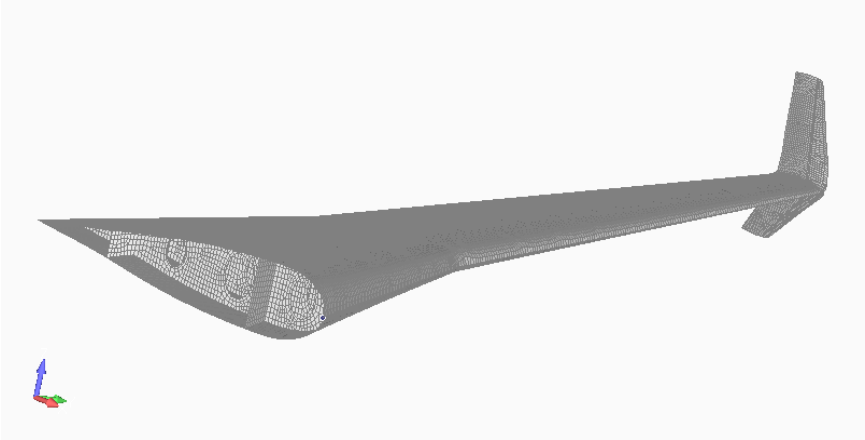

Fig. 4. Wing mesh

4. Aluminum wing

The selected aluminum will be assigned as a material.

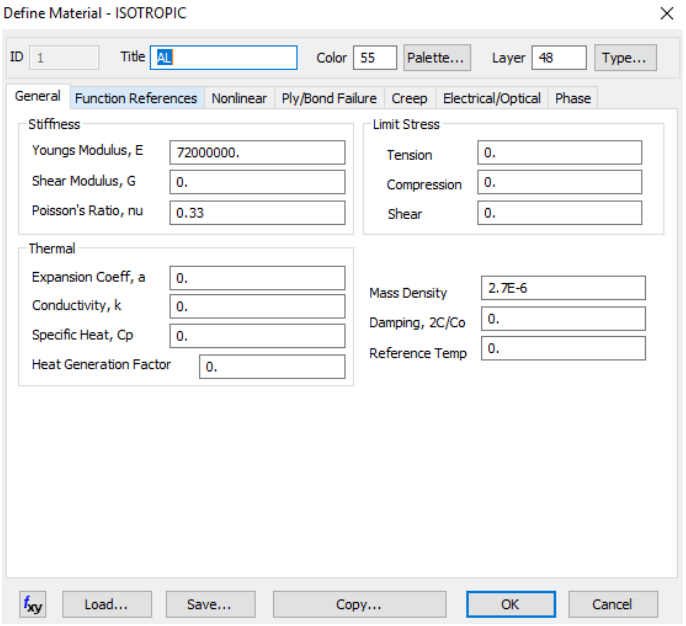

Fig. 5. Defining material

Element	Type of element	Cross section	Thickness [mm]	Material
Ribs	Plate	Rectangle	1.5	Aluminum 7075 T6
Front wall of spar	Plate	Rectangle	3	Aluminum 7075 T6
Rear wall of spar	Plate	Rectangle	2	Aluminum 7075 T6
Upper skin	Plate	Rectangle	1	Aluminum 7075 T6
Lower skin	Plate	Rectangle	1	Aluminum 7075 T6
Back spar	Plate	Rectangle	2.5	Aluminum 7075 T6
Front spar	Plate	Rectangle	3.5	Aluminum 7075 T6

Table 1. Assigning the thickness and material to the elements of the structure

5. Composite wing

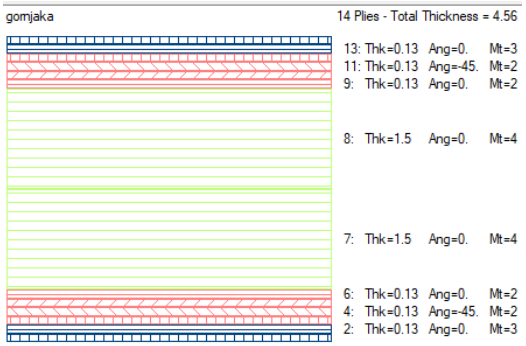

Fig. 6. Layers of materials on the upper skin

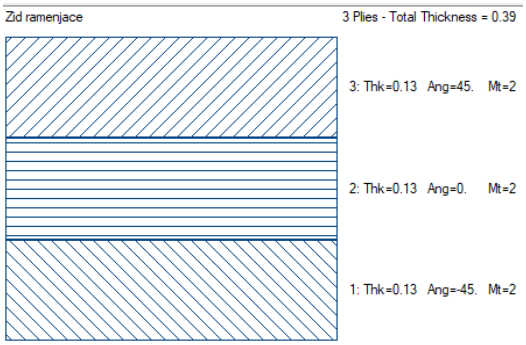

Fig. 7. Layers of materials on the wall of spar

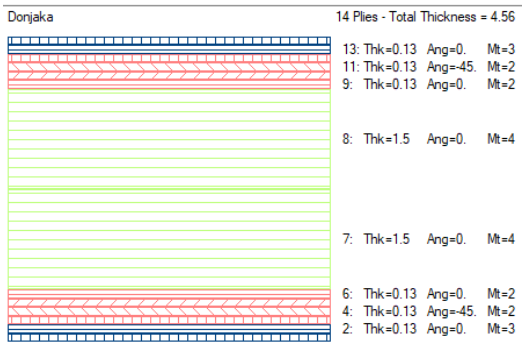

Fig. 8. Layers of materials on the lower skin

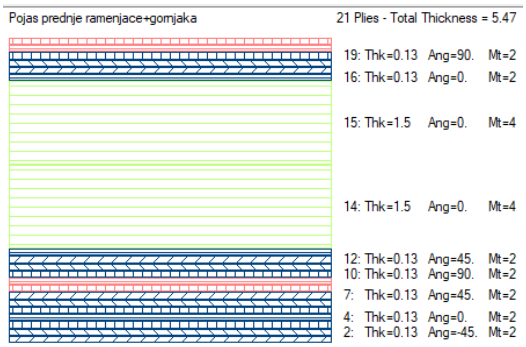

Fig. 9. Layers of materials on the zone + upper skin

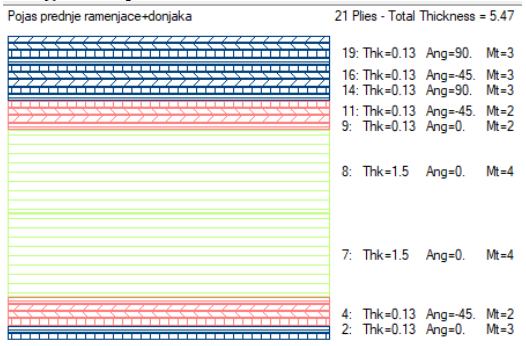

Fig. 10. Layers of materials on the zone + lower skin

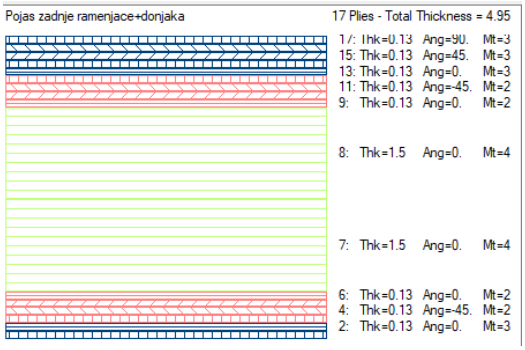

Fig. 11. Layers of materials on the zone + lower skin

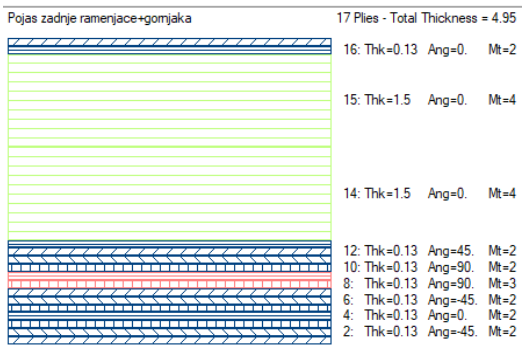

Fig. 12. Layers of materials on the zone + upper skin

6. Input of wing loads and contour boundary conditions for FEM analysis

In Figure 13, the wing mass value in program after assigning the material and thickness to each part of the structure is shown. It was established that the mass of the wing is the same as the mass of the wing of an airplane of real construction in kilograms, without fuel.

	Mass	Center_of_Gravity_in_CSys_0		
	----	X	Y	Z
Structural	639.0419	-5889.479	6388.14	559.0749
NonStructural	0.	0.	0.	0.
Total	639.0419	-5889.479	6388.14	559.0749

Fig. 13. The mass of the wings in program after the assigned material

Subsequent to the preceding procedures, the subsequent stage entails inputting the necessary loads to prepare the model for static analysis. These loads are derived using the methodology described earlier within the Solid Flow software package. The accompanying image depicts the wing model with the applied load, a feature shared by both aluminum and composite wings. The load is introduced along the leading edge, specifically within the primary shoulder region, which bears the predominant weight of the entire wing structure.

$$F_{uk} = R_z = 154944.546[N] \tag{6.1}$$

$$F_g[N] = 0.6 \cdot \left[\frac{F_{uk}}{2} \quad \frac{F_{uk}}{3} \quad \frac{F_{uk}}{6}\right] = [46483{,}3638 \quad 30988{,}9092 \quad 15494{,}4546] \tag{6.2}$$

$$F_d[N] = 0.4 \cdot \left[\frac{F_{uk}}{2} \quad \frac{F_{uk}}{3} \quad \frac{F_{uk}}{6}\right] = [30988{,}9098 \quad 20659{,}2728 \quad 10329{,}6364] \tag{6.3}$$

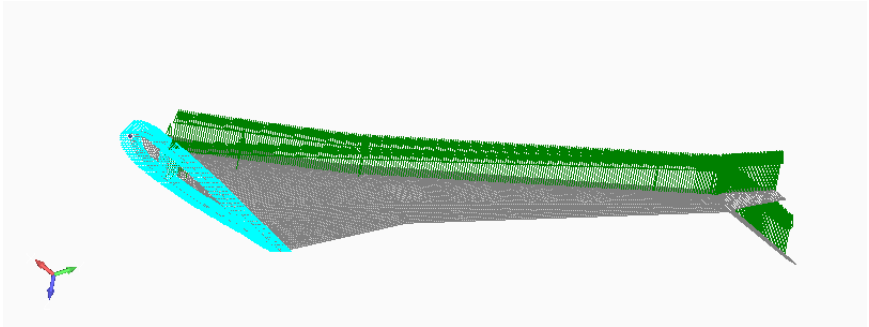

Fig. 13. Wing model with load

The boundary conditions that are set represent the wing-fuselage connection, where, in all analyses, the wing is considered as a cantilever, fixed at one end.

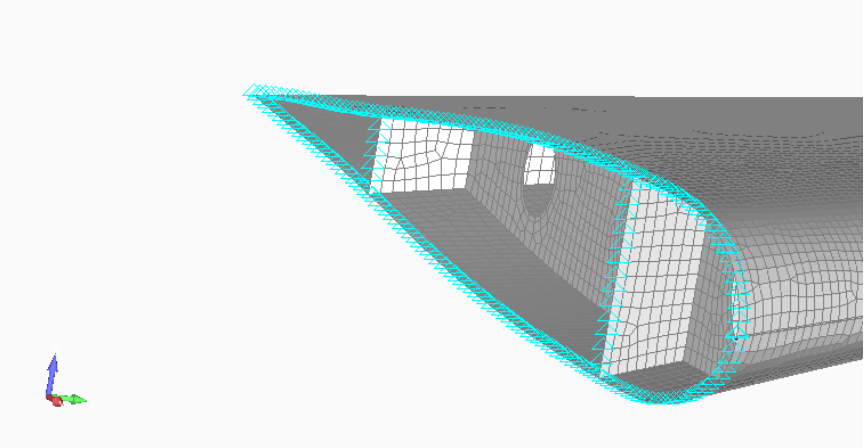

Fig. 14. Constraint definition

7. Static analysis

7.1. Static analysis for aluminum wing

Following the completion of the static analysis, the acquired results encompassing the stress distribution and deformations of the aluminum wing enable a straightforward assessment of potential stress concentrations within the structure that could potentially induce plastic deformation. This determination is facilitated by referring to the predefined maximum stress threshold, specifically known as the critical stress, which serves as a decisive factor for identifying critical regions. Within the scope of this paper, the focus will solely be directed towards normal stresses, disregarding other stress components for the purpose of simplicity and clarity.

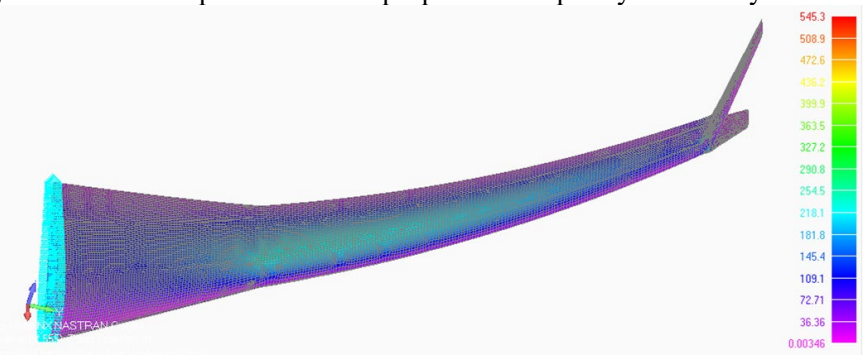

Fig. 15. Characteristic cross section of wing

The value of the maximum normal stress in the construction is: 550 MPa.
Wing deformation is: 12 cm.

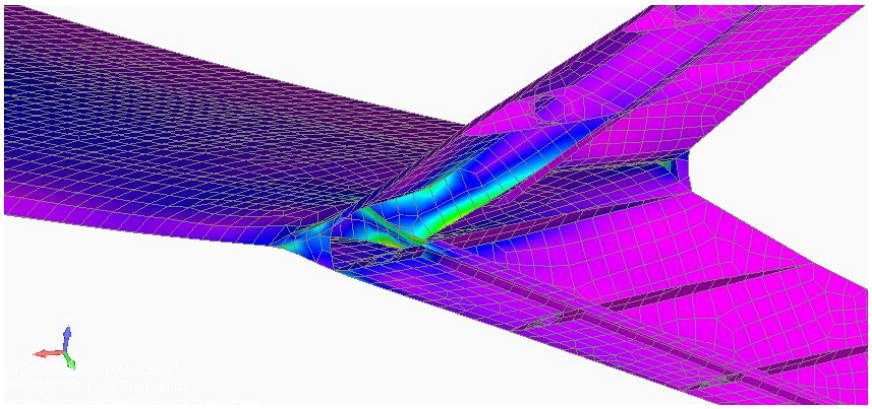

Fig. 16. Characteristic cross section of wing

The results of the static analysis show that the stresses in the construction do not exceed the permitted values, except at the place of connection in between the winglet and the wing, where it is necessary to strengthen the construction.

7.2. Static analysis for composite wing

When it comes to the composite wing, the structure of the composite laminate is such that the maximum allowable stress is not valid for the entire laminate, but it is necessary to consider each layer separately. The combination of multiple composite weaves leads to this, and then to read the stress state of those elements and to determine the limits within which these stress move.

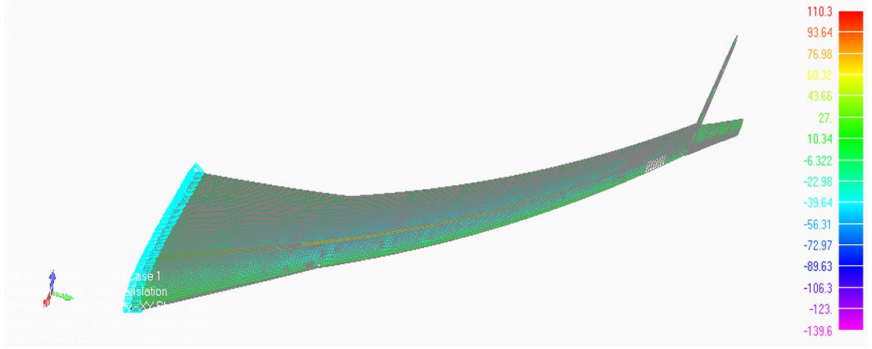

Fig. 17. Characteristic cross section of wing

The value of the maximum normal stress in the construction is: 110.3 MPa.
Wing deformation is: 11.32 cm.

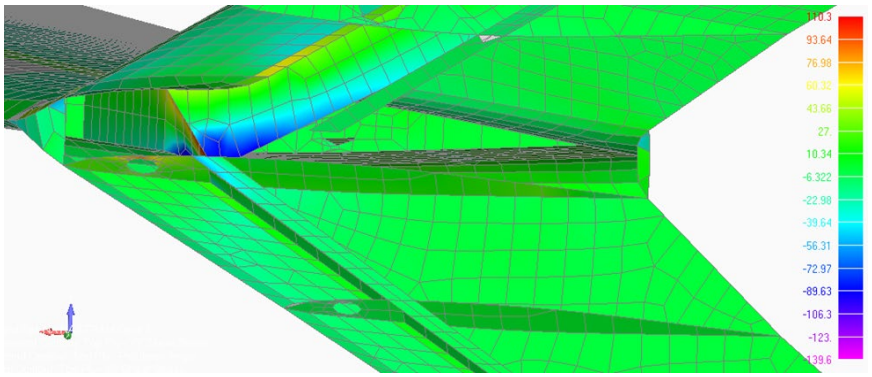

Fig. 18. Characteristic cross section of wing

8. Conclusion

The primary objective of this paper is to gain a comprehensive understanding of the fundamental challenges encountered in wing element construction. The employed software programs facilitate the efficient and seamless modeling of the structural elements, as well as their subsequent analysis. Through the analysis process, the deformations arising from static loading are determined, and the corresponding stress values are evaluated directly on the elements themselves. In order to ensure that these stress values remain within permissible limits, specific elements are reinforced as necessary.

As a result of these efforts, critical phenomena, such as plastic deformations and fractures, are successfully mitigated throughout the structure. Consequently, the objectives of this paper are achieved. Additionally, this outcome indicates that the material selection has been judicious, considering the optimal balance between mass and strength. Given the focus of this paper on the comparative analysis of the aluminum and composite wing with the implemented winglet design, the final results are presented in the subsequent tables for comprehensive evaluation.

Aluminum wing	Composite wing
Wing deformation for the most loaded case of flight: 12 cm.	Wing deformation for the most loaded case of flight: 11.32 cm

Table 2. Comparison results

The static analysis was conducted under the most critical flight conditions, aiming to determine the comparative performance of different wing materials in terms of their deformation characteristics. The primary objective is to identify the material that exhibits superior resistance to deformation in this specific flight scenario. The optimal wing construction, in this context, corresponds to the one demonstrating minimal deformation under the identified flight conditions. It is noteworthy that the structural integrity of the wing is of paramount importance, and the absence of critical stresses that could induce plastic deformation or structural failure further validates the efficacy of this research endeavor.

The overarching goal of this study is to present a prospective methodology for preliminary analysis in the selection of suitable materials and structural elements during the conceptual design phase of aircraft wings. By evaluating and comparing the deformation behaviors of different materials, this work contributes to the development of a framework for informed decision-making regarding material selection in the initial stages of aircraft wing design.

References:

[1] Bruce J. Holmes, Cornelis P. van Dam, Philip W. Brown, and Perry L. Deal (December 1980), NASA Technical Memorandum 81892 “Flight Evaluation of the Effect of Winglets on Performance and Handling Qualities of a Single Engine General Aviation Airplane“
[2] Bruce J. Holmes, Cornelis P. van Dam, Philip W. Brown, and Perry L. Deal (December 1980), NASA Technical Memorandum 81892 “Flight Evaluation of the Effect of Winglets on Performance and Handling Qualities of a Single Engine General Aviation Airplane“
[3] Baki O., Farzad E., Mehmet T. A, Safa B. C.: Transverse Vibration Analysis of Euler- Bernoulli Beams Using Analytical Approximate Techniques, Advances in Vibration Analysis Research, In Tech, 2011.

[4] Megson, T. H. G.: Aircraft Structures for Engineering Students, Fourth edition, Elsevier Aerospace Engineering Series, Burlington USA, 2007.
[5] Dinulović M.: Composite Constructions, University of Belgrade, Faculty of Mechanical Engineering, Belgrade.
[6] Dinulović M.: Aeroelasticity, University of Belgrade, Faculty of Mechanical Engineering, Belgrade.
[7] C. Bisagni, A. Raimondo, I. Atanasovska, M. Milic, R. Troian, G. Frulla, A. Polla, O.N. Cora, M.L. Bekci, B. Henriques, M.F.S.F. de Moura, F. Almudaihesh, S. Grigg: Comparison of numerical analyses of a composite wing component subjected to 4-point bending, Composites Part C: Open Access, doi:10.1016/j.jcomc.2022.100264.
[8] Milić M., Svorcan J., Zorić N.: Numerical simulation of aerodynamic performance of wing with split winglets. The 9th International Scientific Conference on Defensive Technologies, Belgrade, October 15-16, 2020, Proceedings [Elektronski izvor], (ISBN 978-86-81123-83-6).
[9] Milić M., Svorcan J., Jazarević V.:Numerical structural analysis of a composite wind turbine blade. XXXV International Consulting organized by the Energy Federation , Energy , Zlatibor, Jun 24-27,2020,Conference Proceedings [elextronic source],(ISBN 978-86-86199- 02-7).

PREDICTING EPILEPTIFORM ACTIVITY USING MEMRISTIVE LONG SHORT-TERM MEMORY

Svetlana A. Gerasimova[1], Nikolay V. Gromov[1], Albina V. Lebedeva[1], Tatiana A. Levanova[1], and Alexander N. Pisarchik[2]

[1] Institute of Information Technology, Mathematics and Mechanics, Lobachevsky University, Nizhniy Novgorod 603022, Russia
e-mail: gerasimova@neuro.nnov.ru, gromov@itmm.unn.ru, lebedeva@neuro.nnov.ru, tatiana.levanova@itmm.unn.ru.
[2] Center for Biomedical Technology, Universidad Politécnica de Madrid, Pozuelo de Alarcón, Madrid, Spain
e-mail: alexander.pisarchik@ctb.upm.es

Abstract

High computational complexity and resource consumption during the training phase is a major challenge for using deep neural networks. One of the promising solutions to this problem is the implementation of neural networks based on memristors, which demonstrate remarkable energy efficiency. In this paper, we propose a long short-term memory (LSTM) memristive network based on a metal-oxide-metal memristive device for analyzing human electroencephalography (EEG) signals in both normal and pathological conditions.

Keywords: memristor, LSTM, epilepsy, human EEG signals.

1. Introduction

More than 50 million people worldwide suffer from epilepsy, which is approximately 1% of the world's population [1]. This pathology is characterized by recurrent and sudden abnormal brain activity. It has been established that the cause of epileptic seizures is excessive hypersynchronous neuronal activity. Antiepileptic drug treatment is not able to cure this disease. On the other hand, drugs often cause neurological deficits, which significantly impair the quality of patient's life. Therefore, the search for alternative ways for predicting and treating epilepsy is one of the important urgent tasks of modern medicine. The causes of epilepsy should be studied using a multidisciplinary approach, including biological (e.g., the study of changes in neuronal activity in deep brain layers [2]), pharmacological (e.g., the use of a particular drug to improve the patient's condition), and physical models (e.g., the development of an implantable neural chip to control epileptiform activity [3]).

In our previous studies, we investigated the behavior of individual metal-oxide-metal memristors in various neuromorphic systems, including their combination with biological neurons, using mathematical models and experiments [4,5]. Neuromorphic systems are not only considered the next step towards efficient and high-speed computing, but also have the potential for medical applications in the treatment and prevention of neurodegenerative diseases. By replicating the

functionality of biological neural networks, neuromorphic systems may allow the development of more effective and personalized therapies for pathologies such as Alzheimer's disease and Parkinson's disease [6,7]. In addition, these systems could play an important role in improving our understanding of neural mechanisms and ultimately lead to breakthroughs in the field of neuroscience.

Previously, in a wide range of studies, numerous attempts were made to build deep neural networks for predicting epilepsy based on EEG signals [8-10], but the optimal solution for predicting epileptic seizures has not yet been developed. Modern deep learning models are quite complex due to the large number of parameters. The use of memristive devices as a hardware platform for inference can help to overcome data transfer bandwidth limitations arising from limited memory capacity and thereby increase computing power [11-13]. However, despite the promising results reported in the literature, more research is needed to prove the applicability of memristive neural networks in clinical settings.

In this study, we propose a memristive deep neural network to predict epileptiform activity based on human EEG data. We propose an implementation of the LSTM architecture using metal-oxide-metal memristive devices [14]. The conducted numerical experiments will allow us to present the circuit design solution for this model in the future. The ability to accurately predict epileptic seizures before they occur based on real-time EEG data will improve the quality of life of patients and reduce the need for massive use of antiepileptic drugs.

2. Memristive devices

In this work, the elements of the neural network are interconnected through memristive devices of the metal-oxide-metal type [15]. These devices are thin-film structures whose conductivity changes by several orders of magnitude when a voltage is applied. A memristive device is a resistor with memory that can keep the state it received: low or high resistance, indicating the so-called resistive memory. To simulate the behavior of laboratory memristors, a standard approach is used that describes oxidative-reduction processes when a voltage is applied, where the state of the memristor changes due to oxygen ion migration processes with an increase in the effective migration barrier E_m. In turn, migration is provided by Joule heating kT and applied voltage u. The total current density j through the memristor is the sum of linear j_{lin} and nonlinear j_{nonlin} components. The former corresponds to ohmic conductivity with specific resistance ρ, while the latter is determined by the transport of charge carriers through defects in the insulator regions not occupied by filaments (including the filament breakage region). Current transfer is carried out according to the Poole-Frenkel mechanism with an effective barrier E_b. In this work, we use the equations for memristive switching (1), a detailed description of which is presented in [16].

$$\begin{cases} j = \mathrm{wj}_{\mathrm{lin}} + (1-w)\, j_{\mathrm{nonlin}} \\ j_{\mathrm{lin}} = u/\rho \\ j_{\mathrm{nonlin}} = u\exp\left(B\sqrt{u} - E_b\right) \\ \dfrac{dw}{dt} = \begin{cases} A\exp\left(-E_m - \alpha_1 u\right)\left(1-\left(2w-1\right)^{2p}\right), u < u_{set} \\ 0, V_{set} < u < V_{reset} \\ -A\exp\left(-E_m + \alpha\ u\right)\left(1-\left(2w-1\right)^{2p}\right), u > u_{reset} \end{cases} \end{cases} \tag{1}$$

Parameters A, B, and α are taken from experimental data, and parameters u_{set} and u_{reset} are switching threshold voltages of the memristive structure. Parameters E_b and E_m are effective internal parameters characterizing different films ($Au/ZrO_2(Y)/TiN/Ti$, $Au/SiO_2(Y)/TiN/Ti$).

3. LSTM networks

A typical LSTM cell is shown in Fig. 1. Deep neural networks containing such units are recurrent, which means that they not only completely connect nodes in different layers, but also recurrently connect nodes in the same layer at different time steps. The cell remembers values for arbitrary time intervals, while three filters regulate the information flow into and out of the cell.

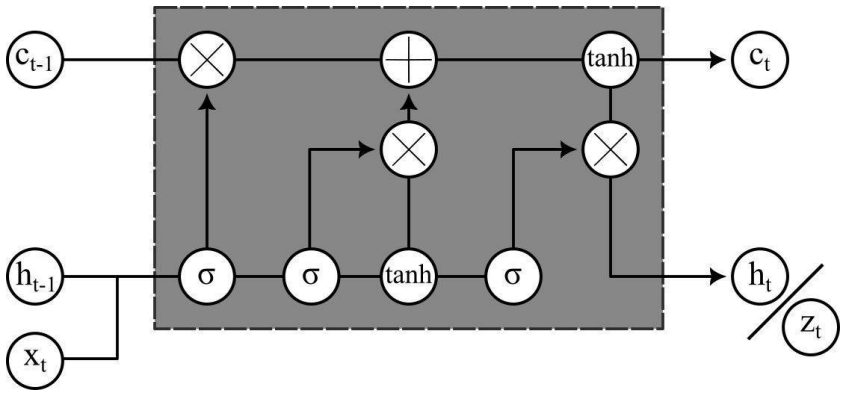

Fig. 1. LSTM cell.

The LSTM cell has two hidden states, one representing short-term memory (h_t) and the other is long-term memory (c_t), which interact as follows. The cell has sigmoid and hyperbolic tangent blocks called gates. The idea of long-term memory is that we want to understand, based on a combination of information from short-term memory and input information, which information we want to forget and what to remember. First, consider the information we want to forget, which is processed by the forget gate, where the sigmoid returns values from 0 to 1. After element-wise multiplication by the long-term memory state, if we get 0, then we forget this information, if 1, then we save it, i.e.

$$f_t = \sigma\left(W_{xf} x_t + W_{hf} h_t + b_f\right)$$

For the information we want to remember, we again use a sigmoid gate to understand which long-term memory state components we want to insert the information into:

$$i_t = \sigma\left(W_{xi} x_t + W_{hi} h_t + b_i\right)$$

Once we understand which components of the long-term memory state need to be updated, we use a hyperbolic tangent gate to figure out what information we want to put into those components. The hyperbolic tangent gate outputs values between -1 and 1, indicating how much to update the corresponding components of the long-term memory state based on the input and previously selected information:

$$g_t = TANH\left(W_{xg} x_t + W_{hg} h_t + b_g\right)$$

In other words, in the schema, multiplication means selecting information, and adding means adding information. Thus, the final formula for updating long-term memory looks like

$$c_t = f_t c_{t-1} + i_t g_t$$

Next, we want the cell to return an output, for which we use an output gate and information from long-term memory:

$$h_t = o_t * TANH(c_t)$$

where

$$o_t = \sigma\left(W_{xo} x_t + W_{ho} h_t + b_o\right)$$

We use a model with the following architecture: fully connected layer with ReLU activation, two LSTM layers and another fully connected layer.

The weight matrices W and bias b in the network are trained using backpropagation and the mean squared error (MSE) loss function is used. LSTM networks are well suited for classification,

processing, and forecasting based on time series data because there can be intervals of unknown length between important time series events. The relative window length insensitivity is an advantage of LSTM over conventional recurrent networks, hidden Markov models, and other sequence learning methods in many applications.

In our previous work, an ensemble consisting of neural networks of various types (feedforward, reservoir computing, and LSTM) was tested in the problem of predicting chaotic dynamics based on time series data [14].

Due to their complicated structure, state-of-the-art LSTM networks include a huge number of model parameters, typically exceeding the usual on-chip memory capacity. Therefore, network inference and training will require parameters to be passed to the processing unit from a separate chip for computation, and inter-chip data communication severely limits the performance of LSTM-based recurrent networks on conventional hardware.

4. Memristive neural network

To create a memristive LSTM network, we implement a memristor crossbar array to storage the weight matrix. Linear matrix multiplication is performed in situ in the memristor crossbar array, eliminating the need to pass weight values back and forth. The model parameters are stored in the same memristor crossbar array that performs the analog matrix multiplications.

In the proposed study, the elements of the neural network are interconnected using metal-oxide-metal memristive devices [16]. Since the weight value in the LSTM cell can take on both positive and negative values, it can be represented as the difference in conductivities of two memristors. This doubles the number of memristors in the array.

The sigmoid and hyperbolic tangent functions are implemented using Simulink. This implementation takes advantage of the property of a differential amplifier to provide a gradual and smooth increase in output voltage when the differential input is in the desired range.

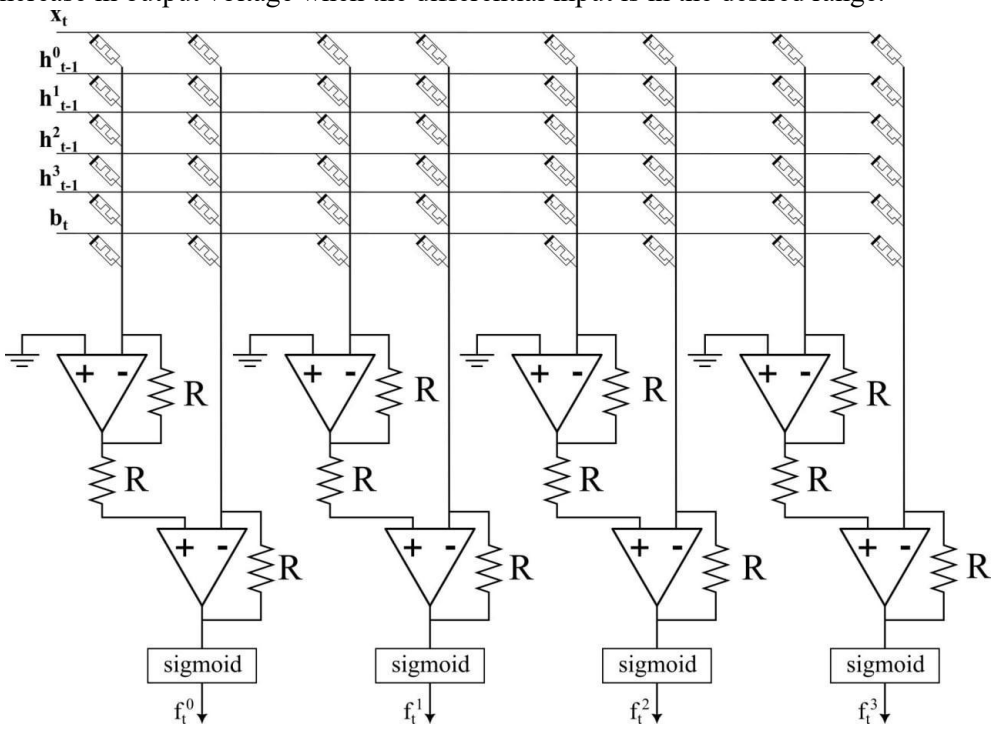

Fig. 2. Scheme of vector-matrix multiplication for the forgetting gate.

The proposed deep neural network is trained on EEG data taken from the open access database https://physionet.org/. The data were recorded both in healthy individuals and in patients with

epilepsy. The simulation results (see Fig. 3 and Fig. 4) show that the proposed architecture is able to achieve high RMSE metric values and adequately predict the appearance of epileptiform activity immediately before its occurrence.

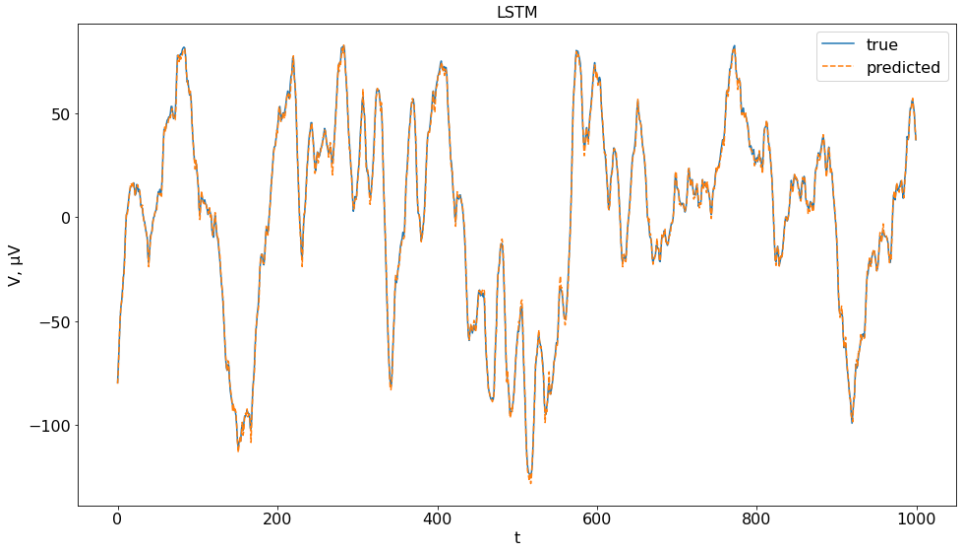

Fig. 3a. True and predicted values for one-step prediction of children EEG, dataset taken at https://physionet.org/. FP1-F7 channel with sampling rate: 256 Hz.

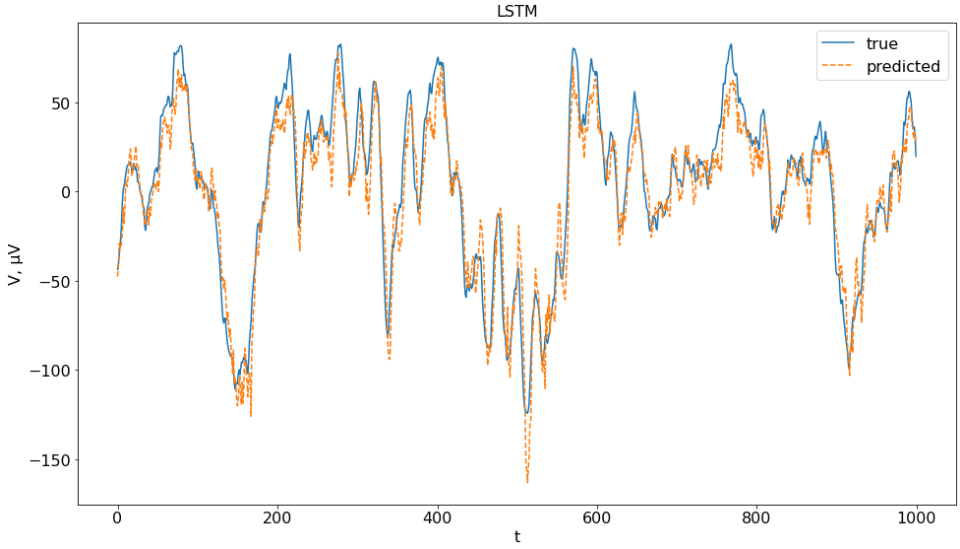

Fig. 3b. True and predicted values for five time steps prediction of children EEG, dataset taken at https://physionet.org/. FP1-F7 channel with sampling rate: 256 Hz.

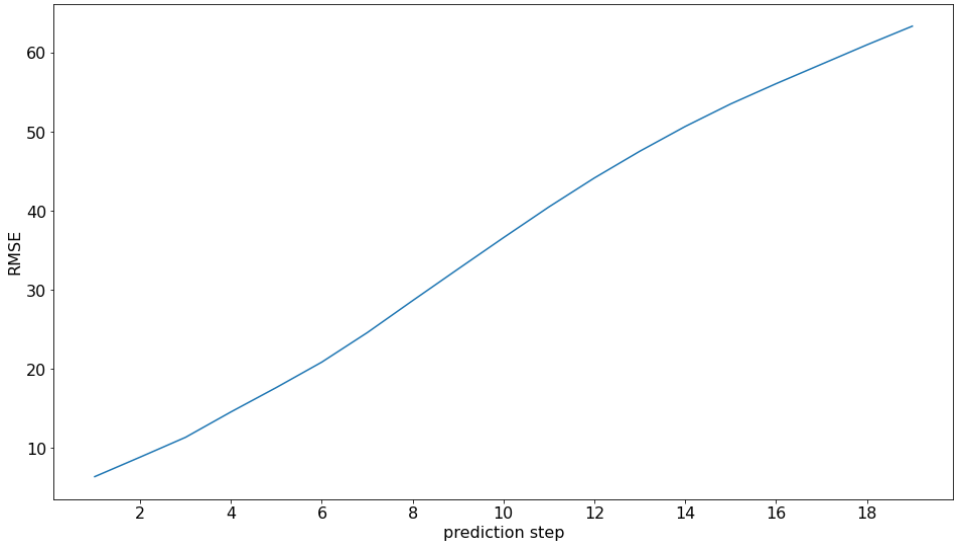

Fig. 4. RMSE metric for truth and predicted values depending on the prediction step length.

3. Conclusions

In this paper, we have proposed a novel approach using memristive deep neural networks to predict epileptiform activity based on human EEG data. The main feature of the proposed technique is the use of memristive devices that make the calculations fast and energy efficient. The obtained results improve our understanding of theoretical and practical aspects of building such architectures and their physical implementations. We hope that based on this study, effective methods for predicting and controlling epileptic seizures will be developed, which, in turn, will contribute to the creation of new efficient technologies for the treatment of this disease.

References:

[1] Jerome Engel, Jr., Timothy A. Pedley, *Epilepsy: A Comprehensive Textbook*, 1997.
[2] Enes Akyuz, et al., *Elucidating the Visual Phenomena in Epilepsy: A Mini Review*, Epilepsy Research, 107093, 2023.
[3] Alex Plata, et al., *Astrocytic atrophy following status epilepticus parallels reduced Ca^{2+} activity and impaired synaptic plasticity in the rat hippocampus*, Frontiers in Molecular Neuroscience, 11, 215, 2018.
[4] S. A. Gerasimova, et al., *A neurohybrid memristive system for adaptive stimulation of hippocampus*, Chaos, Solitons & Fractals, 1 46, 110804, 2021.
[5] S. A. Gerasimova, et al., *Design of memristive interface between electronic neurons*, AIP Conference Proceedings, 1959, 1, 2018.
[6] Eduardo Perez-Valero, et al., *An automated approach for the detection of Alzheimer's disease from resting state electroencephalography*, Frontiers in Neuroinformatics, 71, 2022
[7] Silvia Battistoni, Victor Erokhin, and Salvatore Iannotta, *Emulation with organic memristive devices of impairment of LTP mechanism in neurodegenerative disease pathology*, Neural Plasticity, 2017, 2017.
[8] Rasheed Khansa, et al, *A generative model to synthesize eeg data for epileptic seizure prediction*, IEEE Transactions on Neural Systems and Rehabilitation Engineering, 29, 2322-2332, 2021.
[9] Xu Yankun, et al., *An end-to-end deep learning approach for epileptic seizure prediction,* 2020 2nd IEEE International Conference on Artificial Intelligence Circuits and Systems (AICAS). IEEE, 2020.

[10] Jemal Imene, et al., *An interpretable deep learning classifier for epileptic seizure prediction using EEG data*, IEEE Access 10, 60141-60150, 2022.
[11] Hosseini Mohammad-Parsa, et al., *Cloud-based deep learning of big EEG data for epileptic seizure prediction*, 2016 IEEE Global Conference on Signal and Information Processing (GlobalSIP). IEEE, 2016.
[12] Daoud Hisham, and Magdy Bayoumi, *Deep learning based reliable early epileptic seizure predictor*, 2018 IEEE Biomedical Circuits and Systems Conference (BioCAS). IEEE, 2018.
[13] Dissanayake Theekshana, et al., *Deep learning for patient-independent epileptic seizure prediction using scalp EEG signals*, IEEE Sensors Journal, 21.7, 9377-9388, 2021.
[14] N. Gromov, et al, *Loss functions in the prediction of extreme events and chaotic dynamics using machine learning approach*, 2022 Fourth International Conference Neurotechnologies and Neurointerfaces (CNN), Kaliningrad, Russian Federation, 2022, pp. 46-50.
[15] A. N Mikhaylov, et al., *Effect of ion irradiation on resistive switching in metal-oxide memristive nanostructures*, Journal of Physics: Conference Series, 1410, No. 1, 2019.
[16] Ivan Kipelkin, et al. *Mathematical and experimental model of neuronal oscillator based on memristor-based nonlinearity*, Mathematics, 11.5, 1268, 2023.

ENSTROPHY STUDY OF THE TURBULENT SWIRLING FLOW IN PIPE

Đorđe S. Čantrak, Novica Z. Janković, Dejan B. Ilić, and Lazar M. Lečić

[1]Hydraulic Machinery and Energy Systems Department, Faculty of Mechanical Engineering, University of Belgrade, Kraljice Marije 16, 11120 Belgrade 35, Serbia
e-mail: djcantrak@mas.bg.ac.rs, njankovic@mas.bg.ac.rs, dilic@mas.bg.ac.rs, llecic@mas.bg.ac.rs

Abstract

Turbulent swirling flow is characterized by significant vortex fluctuations, intensive diffusion processes and energy cascade transfer from larger to smaller vortices over a continuous spectrum of wave numbers. The dissipation of the kinetic energy of turbulence occurs in the smallest vortices, because in these areas, both the velocity gradients and the deformation velocities are the largest. In this paper turbulent swirling flow in pipe, generated by the axial fan impellers for three various blade angles (22°, 26° and 30°) is analyzed. Vorticity, enstrophy and lambda 2 values are calculated in order to study the structure of the generated turbulent swirling flows. The axial fan impeller operates in the region of lower flow rates, and it is shown that blade angle does not influence much the integral flow parameters, as well as the enstrophy distribution. It is also shown that the dissipation of the kinetic energy of turbulence is associated with the vorticity fluctuations, i.e., with turbulent fluctuating enstrophy. All these distributions are obtained by use of the high-speed particle image velocimetry data and provided velocity fields. Enstrophy is directly related to kinetic energy, i.e., it corresponds to dissipation effects in this flow. It has maximum in small vortices, i.e., in shear layer, that surrounds vortex core region, where the process of turbulence kinetic energy dissipation occurs.

Keywords: turbulence, swirling flow, axial fan, vorticity, enstrophy, high speed particle image velocimetry.

1. Introduction

Enstrophy and its transport in turbulent swirling flows is recognized as one of the scientific challenges. Enstrophy generation is studied in [1]. Reynolds-averaged enstrophy transport in turbulent swirling flames is studied in [2, 3].

Mechanisms of enstrophy production and destruction are studied in [4].

“An exact non-trivial relation between spatial mean enstrophy and dissipation in closed incompressible flows is derived analytically, which also applies to unbounded fluid domains when the velocity decays to zero sufficiently rapidly at infinity.” [5]

In this paper the study of the turbulent swirling flow behind the axial fan impeller in pipe in the light of the enstrophy is presented. Turbulence structure and dynamics investigation of this turbulent swirling flow, generated by the axial fan impeller in built in pipe after the international standard ISO 5801:2007 "Industrial fans – Performance testing using standardized airways" [6],

category B installation, is presented in [7]. High-speed stereo particle image velocimetry (HSS PIV) system is employed with the aim to gain the 3D velocity fields, and afterwards flow integral parameters, vorticity fields, vortex dynamics, turbulence statistics, structure and invariant maps [7, 8]. The enstophy fields presented in this paper are calculated on the basis of the vorticity field.

2. Experimental rig and HSS PIV equipment

Experimental test facility is designed and assembled at the Institute of Fluid Machinery, Faculty of Mechanical Engineering, Karlsruhe Institute of Technology, Karlsruhe, Germany (FSM KIT), presented in [7,9]. The total length of the experimental rig is 22.67·D + flexible hose, where average inner diameter is D=0.404 m (Fig. 1).

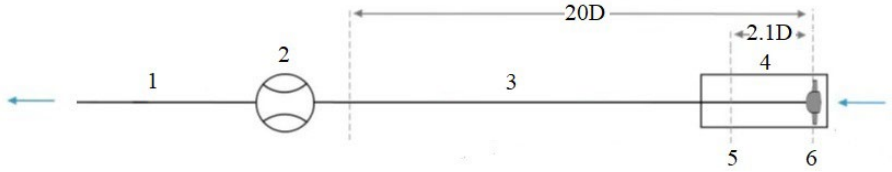

Fig. 1. Experimental rig for investigation of the turbulent swirling flow: 1- flexible hose, 2-Venturi flow meter, 3- straight aluminium duct, 4- transparent pipe section, 5- measuring cross-section (z/D=2.1) and 6- axial fan impeller [7,9]

Measuring cross-section (Fig. 1, pos. 5) with the coordinate system and origin on the pipe axis is presented in Fig 2.

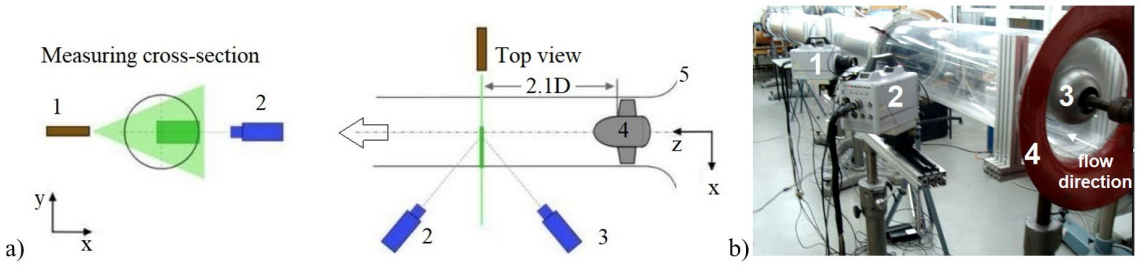

Fig. 2. Measuring cross-section with the software coordinate system: 1- Nd:YLF laser, 2 and 3- left and right PIV fast cameras, respectively, 4- axial fan impeller and 5- profiled free bell-mouth intake [7,9] and b) photo of the measuring section at the installation: 1 and 3-PIV fast cameras, 3- axial fan impeller and 4- profiled free bell-mouth inlet.

The axial fan impeller blade angle at the outer diameter was adjusted to the various positions, i.e., angles 22°, 26° and 30°. The fan rotation speed was n=500 rpm. The axial fan impeller is designed to generate the Rankine vortex.

The usage of HSS PIV equipment and the data processing procedures are presented in [7]. However, some details will be repeated here. A diode-pumped Nd:YLF laser, model Darwin Duo-527-100-M, which generates light with a wavelength 532 nm, was used for flow illumination. Two fast cameras, model FASTCAM SA4, manufactured by Photron, were positioned in Scheimpflug configuration, in a “forward scatter” mode (Figure 2). The camera resolution at 4000 fps was 1024 pix x 1008 pix. Due to the camera memory limitation, only 5542 images were taken during one measurement, so the capturing time was approximately 1.4 s. The flow was by the fog machine Antari Z3000II with liquid Eurolite Smoke Fluid “-X-Extrem A2”. The seeding was naturally sucked in the installation by the axial fan. Data acquisition and processing software was PIVView ver. 3.3.2. Data processing procedure, as well as measuring uncertainty is presented in [7].

HSS PIV measurements and parameters for data analysis are provided in [7, 9, 10].

3. Experimental results – integral flow parameters

Distributions of the time averaged axial (U), radial (V) and circumferential velocities (W) for the impeller blade angle 26° are presented in [7]. Integral flow parameters for all three velocities are presented in [9,10]. In Table 1 the measured and calculated integral flow parameters are presented, such as volume flow rate (Q), average velocity (Um) and Reynolds number (Re) for all three impeller blade angles.

Angle [°]	Q [m³/s]	U_m [m/s]	Re
22	0.16	1.24	32330
26	0.173	1.34	35159
30	0.169	1.31	34245

Table 1. Integral flow parameters for all three impeller blade angles and fan rotation speed n=500 rpm

The Axial fan works for all blade angles with pretty damped flow, i.e., the test rig hydraulic resistance is high, so the influence of the impeller opening, i.e., blade angle on the integral flow parameters is almost negligible.

4. Identification of vortex structures and interpretation of the vorticity and enstrophy fields

Processes of vorticity change, for example, its intensification in the deformation field due to which the vortex fibers are elongated, are often described by the equation for enstrophy $(\underline{\tilde{\omega}}^2/2)$ in the following form:

$$\frac{D}{Dt}\left(\underline{\tilde{\omega}}^2/2\right)=\tilde{\omega}_i\tilde{\omega}_j\tilde{S}_{ij}-\nu\left(\nabla\times\underline{\tilde{\omega}}\right)^2+\nu\nabla\cdot\left[\underline{\tilde{\omega}}\times\left(\nabla\times\underline{\tilde{\omega}}\right)\right] \tag{1}$$

where is $\underline{\tilde{\omega}}$ vorticity vector.

The last term on the right side of the equation can be ignored, because the contribution of the divergence of localized vorticity distributions is insignificant. The generation or reduction of enstrophy due to the elongation or shortening of the vortex filament is described by the first term, and its destruction caused by viscosity by the second term on the right side of equation (1). This physically characterizes, analogously to the case of kinetic energy, the viscous dissipation of enstrophy, i.e., its losses due to friction. In this way, viscosity through physical processes with dissipative effects connects the kinetic energy of the fluid and its field of vorticity.

The dynamics of turbulent enstrophy is described by the equation for the square of the mean vorticity, as well as the equation for the square of the fluctuating vorticity. According to the Reynolds decomposition the mean enstrophy E_Ω and the fluctuation enstrophy e_ω are defined by the expressions as follows:

$$E_\Omega=\frac{1}{2}\underline{\Omega}^2=\frac{1}{2}\Omega_i\Omega_i,\ e_\omega=\frac{1}{2}\overline{\underline{\omega}^2}=\frac{1}{2}\overline{\omega_i\omega_i} \tag{2}$$

The following expression could be derived for the statistically stationary flow, by using the usual notation:

$$U_j\partial_j E_\Omega=-\partial_j\left(\Omega_i\overline{\omega_i u_j}\right)+\overline{u_j\omega_i}\partial_j\Omega_i+\Omega_i\Omega_j S_{ij}+\Omega_i\overline{\omega_j s_{ij}}+\nu\partial_{jj}^2E_\Omega-\nu\partial_j\Omega_i\partial_i\Omega_j \tag{3}$$

Enstrophy (E_Ω) transport by turbulent interaction vorticity-velocity is denoted with the term on the left side of the equation (3). The equation (3) right hand members are the following, respectively: the gradient production of the fluctuating enstrophy, the generation of the average

vorticity with the mean strain rate field, production of the E_Ω quantity caused by the interaction of fluctuating vorticity and fluctuating strain rate components, viscous transport term of mean enstrophy and viscous dissipation of the mean enstrophy.

The interaction of the mean and fluctuating vorticity can be analyzed in the best way by using the dynamical equations for E_Ω and e_ω. The equation for e_ω is derived by an analogous procedure as the equation for the kinetic energy of turbulence. The physical meaning of this equation individual members is analogous to the interpretations given for the equation (3). Since the experimental distributions for e_ω are not considered in this paper, the dynamic equation for the fluctuation enstrophy e_ω is not derived and discussed here in more details, but its connection with the dissipation of kinetic energy of turbulence is given in equation (4). Namely, turbulence is characterized not only by vorticity, but also by high vorticity fluctuations. The following expression, that can be derived, shows that the dissipation of turbulence kinetic energy is related to the vorticity fluctuations, i.e., with turbulent fluctuation enstrophy:

$$\varepsilon \approx 2\nu e_\omega \tag{4}$$

Average vorticity fields, calculated on the basis of the measured velocity field by use of the HSS PIV are presented in Fig. 3.

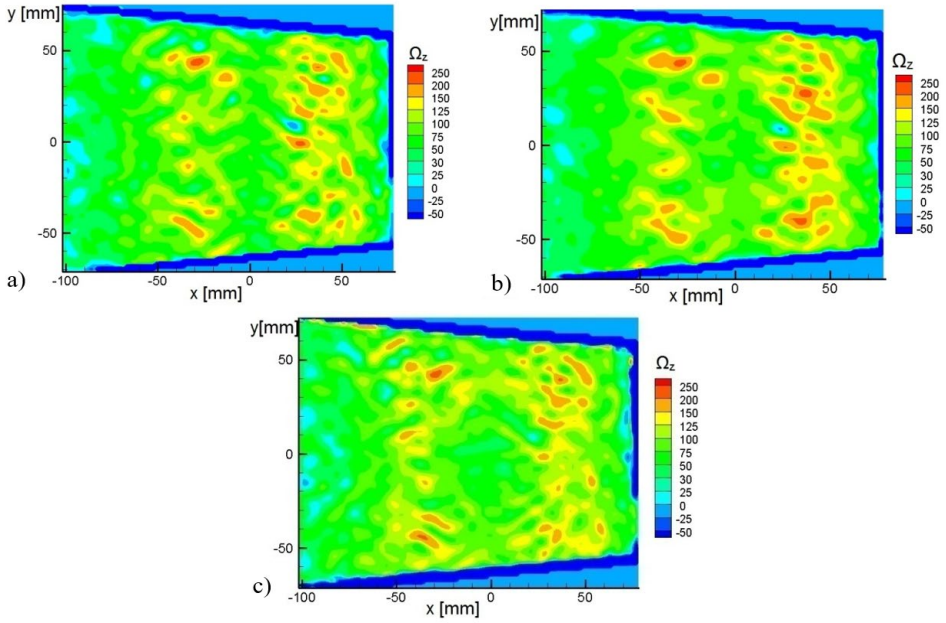

Fig. 3. Average vorticity fields for all three impeller blade angles: a) 22°, b) 26° and c) 30° [7,9,10].

The highest vorticities are achieved in the shear layer region and present for all three blade impeller angles. The mean enstrophy distributions for all three blade angles are presented in the following figure.

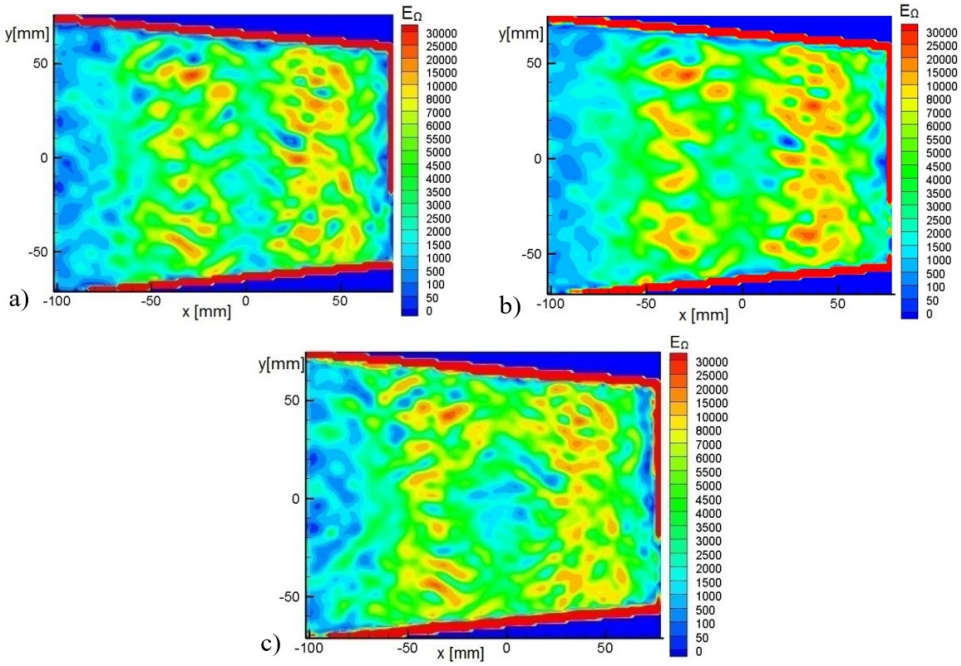

Fig. 4. Mean enstrophy fields for all three impeller blade angles: a) 22°, b) 26° and c) 30° [7,9,10].

Mean enstrophy is directly related to kinetic energy. Namely, it corresponds to the dissipation effects in the flow and is important in the study of turbulence. The increase in enstrophy, according to the equation (4), results in an increase of the rate of dissipation of kinetic energy. Based on equation (2), the enstrophy distribution is directly correlated to the vorticity distribution. It could be concluded, based on the presented experimental results in Figures 3 and 4, that the enstrophy distribution is very similar for all impeller blade angles, which can be explained by small differences in the achieved Reynolds numbers.

The "Lambda 2" method for vortex detection is presented in [11] and used in the study of the turbulent swirling flow in pipe behind the axial fan impeller in [7, 9, 10]. Lambda 2 (λ_2) distributions are provided for all three blade angles in Figure 5. Again, similar distributions are obtained for all blade angles.

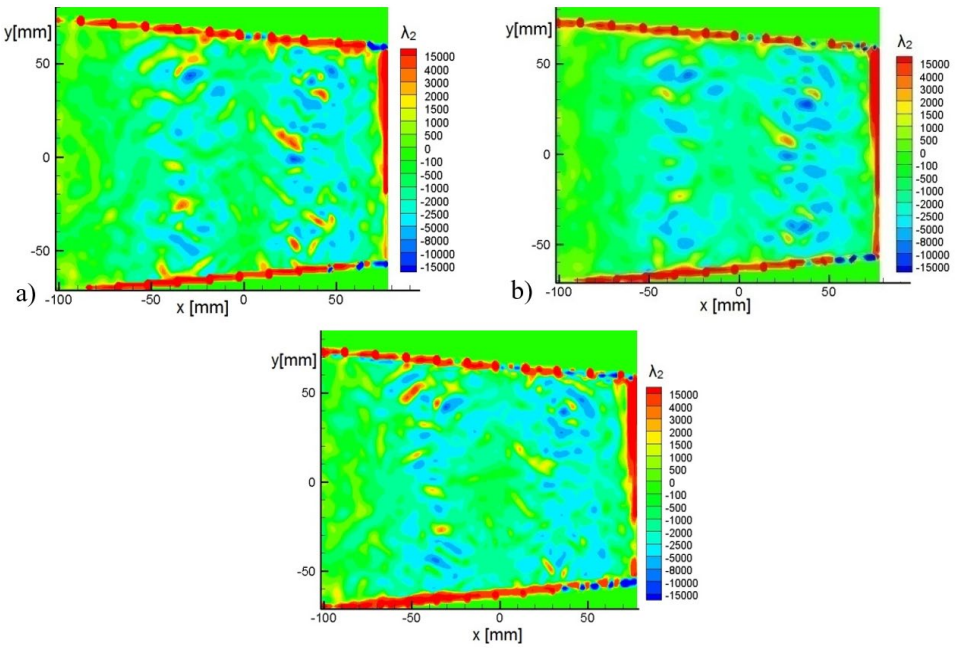

Fig. 5. Distributions of λ_2 for all three impeller blade angles: a) 22°, b) 26° and c) 30° [7,9,10].

It is shown in [7] that this method has a problem when several vortex structures exist. Numerous centers with extreme values are detected in the central flow region for all three blade angles.

Presented results are important for the investigation of the turbulence structures. It can be concluded, based on the Figures 3-5, that intense energy dissipation occurs in the shear layer region bounded by the maximum values of vorticity and enstrophy. Namely, the highest energy is contained in the large vortices, which is here in the central zone around the pipe acis, while enstrophy is found in small-scale vortices (Figure 4). As expected, large vorticity is usually associated with small eddies in turbulence, as this is a case here for all three blade angles (Figure 3). Small eddies have intense vorticity and "dominate" the enstrophy fields and according to the equation (4), the process of dissipation of the kinetic energy of the turbulence occurs in them.

5. Conclusions

Turbulent swirling flow is characterized by significant vorticity fluctuations, intensive diffusion processes, and energy cascade transfer from larger to smaller vortices over a continuous spectrum of wave numbers. The dissipation of the kinetic energy of turbulence occurs in the smallest vortices, because in these areas, both the velocity gradients and the deformation velocities are the largest. The highest vorticities are reached in the shear layer region, surrounding the central vortex zone (Figure 3). Enstrophy is calculated on the basis of the HSS PIV data. It is directly related to the kinetic energy, i.e. it corresponds to dissipation effects in this flow, after equation (4). Mean enstrophy has maximum in small vortices, i.e. in shear layer, that surrounds vortex core region, where the process of turbulence kinetic energy dissipation occurs (Figure 4). The axial fan impeller operates in the test rig with the high hydraulic resistance, so the obtained integral flow parameters are very similar and independent of the blade angle. This is also shown for the presented results for vorticity and enstrophy, and as well as for the λ_2 (Figures 3 to 5). It could be concluded that the enstrophy, with its intensities, clearly reveals the shear layer region with the great dissipation. In addition, it is shown that “Lambda 2” doesn’t provide good result in the generated turbulent swirling flow in pipe. It is planned, in the future, to study the cases for the

higher Reynolds number and the ones with the added booster fan, which would decrease the hydraulic resistance of the test rig.

Acknowledgement: This research is financially supported by the Ministry of Science, Technological Development and Innovation, Republic of Serbia, grant number 451-03-47/2023-01/ 200105, February 3rd, 2023 (subproject TR35046) and German Academic Exchange Service (DAAD) (Bilateral Project, Karlsruhe Institute of Technology, Institute of Fluid Machinery, Germany and Faculty of Mechanical Engineering, University of Belgrade, Serbia, in period 2011-2012) which is gratefully acknowledged.

References:

[1] Tsinober A, Shtilman L and Vaisburd H. A Study of properties of vortex stretching and enstrophy generation in numerical and laboratory turbulence. *Fluid Dynamics Research* 1997; 21(6):477-494.
[2] Kazbekov A, Kumashiro K and Steinberg A. Enstrophy transport in swirl combustion. *Journal of Fluid Mechanics* 2019; 876: 715-732.
[3] Kazbekov A and Steinberg AM. Flame- and flow-conditioned vorticity transport in premixed swirl combustion. *Proceedings of the Combustion Institute*, 2021; 38(2):2949-2956.
[4] Buxton ORH and Ganapathisubramani B. Amplification of enstrophy in the far field of an axisymmetric turbulent jet. *Journal of Fluid Mechanics*, 2010; 651:483-502.
[5] Raynal F. Exact relation between spatial mean enstrophy and dissipation in confined incompressible flows. *Physics of Fluids*, 1996; 8(8): 2242-2244.
[6] ISO 5801:2017. Fans - Performance testing using standardized airways.
[7] Čantrak DjS and Janković NZ. Turbulence structure and dynamics investigation of turbulent swirl flow in pipe using high-speed stereo PIV data. *Energies*, 2022; 15(15): 5417, 13 pages.
[8] Čantrak ĐS and Janković NZ. High speed stereo PIV investigation of the turbuelnce structure of the axially restricted turbulent swirl flow behind the axial fan in pipe. *Advances in Mechanical Engineering*, 2022; 14(11): 1-9.
[9] Čantrak ĐS. *Investigation of the turbulent Rankine vortex in the pipe behind the axial fan impeller using optical (PIV and LDA) measurement methods and visualization*. Belgrade: Military Technical Institute, 2022, p. 163.
[10] Čantrak ĐS. *Analysis of the vortex core and turbulence structure behind axial fans in a straight pipe using PIV, LDA and HWA methods.* PhD Thesis, University of Belgrade, Serbia, 2012.
[11] Jeong J and Hussain F. On the identification of a vortex. *Journal of Fluid Mechanics*, 1995; 285: 69–94.

STOCHASTIC STABILITY OF THE TIMOSHENKO BEAM RESTING ON THE MODIFIED ELASTIC FOUNDATION

Dunja Milić[1], Jian Deng[2], Vladimir Stojanović[1,2] and Marko D. Petković[3]

[1] Faculty of Mechanical Engineering, University of Niš, Aleksandra Medvedeva 14, 18000 Niš
e-mail: stojanovic.s.vladimir@gmail.com, dunja1994milic@gmail.com
[2] Faculty of Engineering, Lakehead University, Thunder Bay, Ontario, Canada P7B 5E1
e-mail: jian.deng@lakeheadu.ca
[3] Faculty of Sciences and Mathematics, University of Niš, Višegradska 33, 18000 Niš
e-mail: dexterofnis@gmail.com

Abstract

The moment and almost-sure stochastic stability of the Timoshenko beam resting on the elastic foundation under parametric excitation of white noise are investigated through moment Lyapunov exponents and Lyapunov exponents. The foundation medium is visualized as modified Kerr-type elastic layer, which consists of three layers of springs connected by two shear layers. The method of regular perturbation is used to determine the explicit expansions of the moment Lyapunov exponent and the Lyapunov exponent. Moment Lyapunov exponent and the Lyapunov exponent are important for determining the stability of a stochastic dynamical system. The effects of the damping coefficient, shear constant, beam thickness and intensity of the random process on the stochastic stability of systems are considered and graphically displayed.

Keywords: Stochastic stability; modified elastic layer; moment Lyapunov exponents; Lyapunov exponents.

1. Introduction

This paper is concerned with stochastic stability of the Timoshenko beam resting on the elastic foundation. Avramidis and Morfidis [1] have discussed the superiority of the Kerr-type foundation model compared to one or two-parameter models through the example of a Timoshenko beam resting on a Kerr-type three-parameter elastic foundation. In this research, we use a modified type of Kerr layer as an elastic foundation, which, in contrast to the classic Kerr layer, has one more layer of springs which is also connected by a shear layer. Sri Namachchivaya and Van Roessel [2] used a perturbation approach to obtain the approximation for the moment Lyapunov exponent of two coupled oscillators with commensurable frequencies driven by a small intensity real noise with dissipation. Deng et al. [3] investigated stochastic stability of two-degree-of-freedom coupled viscoelastic systems under parametric excitation of white noise. In the present study by means of the Lyapunov method, on the basis of the Timoshenko beam theory, the stability and instability of a beam-foundation system subjected to white noise of small intensity is studied.

2. Results

A beam-foundation system is shown in Fig. 1 and it comprises a Timoshenko beam, three layers of springs, with mutually different stiffness moduli, and two intermediate shear layers. Analytical investigation of the stochastic system is conducted through the analysis of moment Lyapunov exponents and Lyapunov exponents. Regions of almost sure stability are obtained and graphically displayed as a function of shear constant, beam thickness, intensity of the random process and the foundation damping coefficients (Fig. 2.).

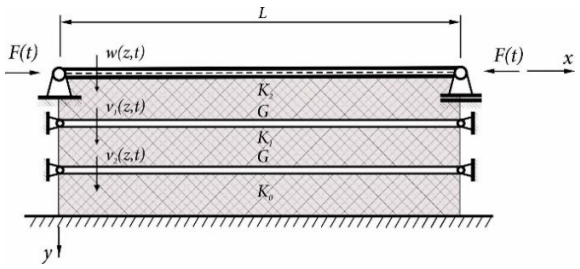

Fig. 1. Beam-foundation system

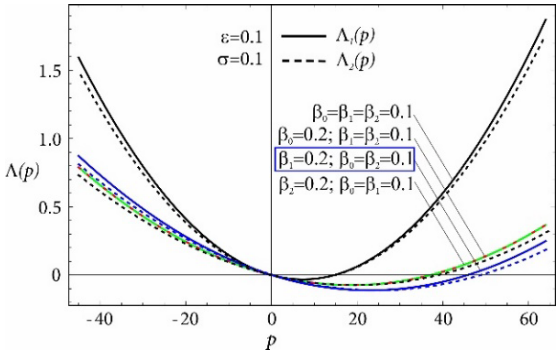

Fig. 2. Moment Lyapunov exponent Λ(p) for varying damping coefficients

3. Discussion

A perturbation approach is used to obtain an approximation for the moment Lyapunov exponent of Timoshenko beam resting on the modified elastic foundation driven by a small intensity white noise. The findings of this study suggest that reducing the shear constant of the foundation, decreasing the intensity of the random process, and increasing the beam thickness leads to an expansion of the stability region. It has also been demonstrated that by varying the damping coefficients of the modified foundation, particularly the damping coefficient of the middle layer of the foundation, a significant increase in the stability region can be achieved.

4. Conclusions

The purpose of this study is to investigate the stochastic stability of Timoshenko beams resting on a complex modified Kerr-type elastic foundation and subjected to compressive axial loadings. The method of regular perturbation is used to determine the explicit expansions of the moment Lyapunov exponent and the Lyapunov exponent. Finally, the effects of the damping coefficient, beam thickness and intensity of the random process on the stochastic stability of system are considered and graphically displayed.

Acknowledgments: This research was financially supported by the Ministry of Science, Technological Development and Innovation of the Republic of Serbia (Contract No. 451-03-47/2023-01/ 200109) and partly by the Natural Sciences and Engineering Research Council of Canada.

References:

[1] Morfidis, K., Avramidis, I.E., *Bending of beams on three-parameter elastic foundation*, International Journal of Solids and Structures, Vol.43, 357-375, 2006.

[2] Sri Namachchivaya, N., Van Roessel, H. J., *Stochastic Stability of Coupled Oscillators in Resonance: A Perturbation Approach*, ASME Journal of Applied Mechanics, Vol.71, 759-767, 2004.
[3] Deng, J., Xie, W.-C., Pandey, M.D., *Moment Lyapunov exponents and stochastic stability of coupled viscoelastic systems driven by white noise*, Journal of mechanics of Materials and Structures, Vol.9(1), 2014.

CHAPLYGIN SYSTEMS WITH GYROSOPIC FORCES

Vladimir Dragović[1,2], Borislav Gajić[1] and Božidar Jovanović[1]

[1] Mathematical Institute SASA, Kneza Mihaila 36, 11000 Belgrade, Serbia
e-mail: vladad@mi.sanu.ac.rs, gajab@mi.sanu.ac.rs, bozaj@mi.sanu.ac.rs,
[2] Department of Mathematical Sciences, University of Texas at Dallas, USA
e-mail: Vladimir.Dragovic@utdallas.edu,

Abstract

In this talk we will present a part of the results obtained in [1]. We introduce and study a general setting for Chaplygin systems with gyroscopic forces, with a special emphasis on the important subclass of the Chaplygin systems with magnetic forces. We pay particular attention to the important subclass of such systems with magnetic forces. The existence of an invariant measure and the problem of Hamiltonization are studied, both within the Lagrangian and the almost-Hamiltonian framework. This class of nonholonomic systems, although quite natural, has not been treated before. In his first PhD thesis [2] (see also [3]), Vasilije Demchenko studied the rolling of a ball with a gyroscope, satisfying the Bobilev-Zhukoviskii condition [4, 5], without slipping over a sphere in $\mathbb{R}^3$, by using the Voronec equations (e.g., see [6]). Inspired by this thesis, in [1] we considered rolling of a ball with a gyroscope without slipping and twisting over a sphere in $\mathbb{R}^n$. This provided us with examples of gyroscopic $SO(n)$-Chaplygin systems that reduce to integrable magnetic geodesic flows on a sphere S^{n-1} [1].

Keywords: Nonholonimic dynamics, Voronec equations, Chaplygin systems, Hamiltonization, invariant measure.

1. Nonholonomic system with gyroscopic forces

Let $(Q, \boldsymbol{G})$ be a Riemannian manifold. Consider a Lagrangian nonholonomic system $(Q, \boldsymbol{L}, D)$, where the constraints define a nonintegrable distribution $D \subset TQ$. The constraints are homogeneous and do not depend on time. The Lagrangian, along with the difference of the kinetic and potential energy, contains an additional term, which is linear in velocities:

$$\boldsymbol{L}(q, \dot{q}) = \frac{1}{2}(\boldsymbol{G}\dot{q}, \dot{q}) + (\boldsymbol{A}, \dot{q}) - V.$$

Here and throughout the text, $(\ ,\ )$ denotes the parring between appropriate dual spaces, while $\boldsymbol{A}$ is a one-form. The metric $\boldsymbol{G}$ is also considered as a mapping from TQ to T^*Q.

A smooth path $q(t) \in Q, t \in \Delta$ is called admissible if the velocity $\dot{q}$ belongs to $D_{q(t)}$ for all $t \in \Delta$. An admissible path $q(t)$ is a motion of the natural mechanical nonholonomic system $(Q, \boldsymbol{L}, D)$ if it satisfies the Lagrange-d'Alembert equations

$$\left(\frac{\partial \boldsymbol{L}}{\partial q} - \frac{d}{dt}\left(\frac{\partial \boldsymbol{L}}{\partial \dot{q}}\right), \delta q\right) = 0, \quad \delta q \in D_q. \tag{1}$$

The equations (1) are equivalent to the equations

$$\left(\frac{\partial L}{\partial q} - \frac{d}{dt}\left(\frac{\partial L}{\partial \dot{q}}\right), \delta q\right) = \boldsymbol{F}(\dot{q}, \delta q), \quad \delta q \in D_q, \tag{2}$$

where L is the part of the Lagrangian $\boldsymbol{L}$ which does not contain the term linear in velocities

$$L(q, \dot{q}) = \frac{1}{2}(\boldsymbol{G}\dot{q}, \dot{q}) - V,$$

and the additional force $\boldsymbol{F}(\dot{q}, \delta q)$ is defined as the exact two-form $\boldsymbol{F} = d\boldsymbol{A}$.

We will subsequently consider a more general class of systems where an additional force is given as a two-form which is neither exact nor even closed. Systems with an additional force defined by a closed two-form $\boldsymbol{F}(\dot{q}, \delta q)$ and without nonholonomic constraints are very well studied. The corresponding Hamiltonian flows are usually called magnetic flows or twisted flows. Following tradition, we introduce

Definition 1. Let $\boldsymbol{F}$ be a 2-form on Q. We refer to a system $(Q, L, \boldsymbol{F}, D)$ as *a natural mechanical nonholonimic system with gyroscopic forces*. The additional gyroscopic force $\boldsymbol{F}(\dot{q}, \delta q)$ is called *magnetic* if the form $\boldsymbol{F}$ is closed, $d\boldsymbol{F} = 0$ and in this case we say that the system $(Q, L, \boldsymbol{F}, D)$ is a *natural mechanical nonholonomic system with a magnetic force*.

The equations of motion of a natural mechanical nonholonomic system with a gyroscopic force $(Q, L, \boldsymbol{F}, D)$ are given in (2).

2. Gyroscopic G-Chaplygin system

Starting from the notion of G-Chaplygin systems for nonholonomic systems without gyroscopic forces (see [7-12]), we introduce the following

Definition 2. Assume that Q is a principal bundle over S with respect to a free action of a Lie group G, $\pi: Q \to S = Q/G$, and that L and $\boldsymbol{F}$ are G-invariant. Suppose that D is a principal connection, that is, D is G-invariant, transverse to the orbits of the G-action, and $rank\ D = dim\ S$. Then we refer to $(Q, L, \boldsymbol{F}, D, G)$ as a gyroscopic G-Chaplygin system.

The distribution D is transverse to the fibers of π: $T_qQ = D_q \oplus \mathcal{V}_q$, $\mathcal{V}_q = ker\ d\pi(q)$. The space $\mathcal{V}_q$ is called the *vertical space* at q. Obviously, a gyroscopic G-Chaplygin system $(Q, L, \boldsymbol{F}, D, G)$ is G-invariant and reduces to the tangent space of the base-manifold $S = Q/G$.

Definition 3. Let G, V, and $\boldsymbol{F}$ be a G-invariant metric, a potential and a two-form on Q. The *reduced metric* $\boldsymbol{g}$, the *reduced potential* v, and the *reduced two-form* $\boldsymbol{f}$ on S are defined by:

$$\boldsymbol{g}(X, Y)|x = \boldsymbol{G}(Xh, Yh)|q, \quad v(x) = V(q), \quad \boldsymbol{f}(X, Y)|x = \boldsymbol{F}(Xh, Yh)|q.$$

Here Xh, Yh are the horizontal lifts of X, Y at a point $q \in \pi^{-1}(x)$ defined by

$$d\pi|q(Xh) = X, \quad d\pi|q(Yh) = Y, \quad Xh, Yh \in D_q.$$

Note that we do not impose any additional assumptions on $\boldsymbol{F}$. The equations (2) are G-invariant and they reduce to TS

$$\left(\frac{\partial l}{\partial x} - \frac{d}{dt}\left(\frac{\partial l}{\partial \dot{x}}\right), \delta x\right) = \mathbf{JK}(\dot{x}, \delta x) + \boldsymbol{f}(\dot{x}, \delta x), \quad \delta x \in T_xS2, \tag{3}$$

where $l(x, \dot{x}) = \frac{1}{2}(\boldsymbol{g}\dot{x}, \dot{x}) - v$ is the reduced Lagrangian and the term $\mathbf{JK}(\cdot, \cdot)$ depends on the metric and the curvature of the connection (see [8, 11]).

Definition 4. We refer to $(S, l, \boldsymbol{f}, \mathbf{JK})$ as *a reduced gyroscopic G-Chaplygin system*. In the case when $\boldsymbol{f}$ is a closed 2-form, we call it *a reduced magnetic G-Chaplygin system*.

The equations of motion of the reduced gyroscopic G-Chaplygin system are given in (3).

Theorem 1. The solutions of the gyroscopic G-Chaplygin system $(Q, L, \boldsymbol{F}, D, G)$ project to solutions of the reduced gyroscopic G-Chaplygin system $(S, l, \boldsymbol{f}, \mathbf{JK})$. Let $x(t)$ be a solution of the reduced system (3) with the initial conditions $x(0) = x_0, \dot{x}(0) = X_0 \in T_{x_0}S$ and let $q_0 \in \pi^{-1}(x_0)$.

Then the horizontal lift $q(t)$ of $x(t)$ through q_0 is the solution of the original system (2), with the initial conditions $q(0) = q_0$, $\dot{q}(0) = Xh_0 \in D_{q_0}$.

The case when the constraints are nonhomogeneous and time-dependent and without gyroscopic forces is considered by Bakša in [13]. If the group G is commutative then we deal with classical Chaplygin systems [14] (see also [6]).

3. Almost Hamiltonian description, an invariant measure, and Hamiltonization

Recall that an almost symplectic structure is a pair (M, ω) of a manifold M and a nondegenerate 2-form ω (see [15]). Here we do not assume that the form ω is closed, in contrast to the symplectic case. As in the symplectic case, since ω is nondegenerate, to a given function H one can associate the *almost Hamiltonian vector field* X_H by the identity

$$i_{X_H}\omega(\cdot) = \omega(X_H, \cdot) = -dH(\cdot).$$

The almost symplectic structure (M, ω) is *locally conformally symplectic*, if in a neighborhood of each point x on M, there exists a function f different from zero such that $f\omega$ is closed. If f is defined globally, then (M, ω) is *conformally symplectic* [15].

Let $(x_1, \cdots, x_n)$ be local coordinates on S in which the metric $\boldsymbol{g}$ is given by the quadratic form $\boldsymbol{g} = \sum g_{ij} dx_i \otimes dx_j$. Then the Lagrangian, the gyroscopic two-form and the **JK**-term read as follows

$$l(x, \dot{x}) = \frac{1}{2}\sum g_{ij}\dot{x}_i\dot{x}_j - v(x)\,, \quad \boldsymbol{f} = \sum_{i<j} f_{ij}\, dx_i \wedge dx_j,$$
$$\mathbf{JK}(X, Y)|(x, \dot{x}) = g(\dot{x}, C(X, Y)) = \sum_{klij} g_{kl} C_{ij}^k X_i Y_j \dot{x}_l,$$

where C_{ij}^k are the components of the (1, 2)-tensor field $\boldsymbol{C}$. We also introduce the Hamiltonian function

$$h(x, p) = \frac{1}{2}(p, g^{-1}(p)) + v(x) = \frac{1}{2}\sum_{ij} g^{ij} p_i p_j + v(x),$$

as the usual Legendre transformation of l. Here $(p_1, \cdots, p_n, x_1, \cdots, x_n)$ are the canonical coordinates of the cotangent bundle T^*S. In canonical coordinates the equations (3) take the form

$$\dot{x}_i = \frac{\partial h}{\partial p_i} = \sum_j g^{ij}(x) p_j, \tag{4}$$

$$\dot{p}_i = -\frac{\partial h}{\partial x_i} + \sum_{jk} C_{ij}^k(x) p_k \frac{\partial h}{\partial p_j} + \sum_j f_{ij}(x) \frac{\partial h}{\partial p_i}. \tag{5}$$

Let $z = (x, p)$. The reduced equations (4), (5) on the cotangent bundle T^*S can be written in the almost Hamiltonian form

$$\dot{z} = X, \qquad i_X(\Omega) = -dh, \qquad \Omega = \omega + \sigma + \boldsymbol{f}, \tag{6}$$

where ω is the canonical symplectic form on T^*S, σ is a semi-basic form defined by the **JK** term (see [9, 12]):

$$\omega = dp_1 \wedge dx_1 + \cdots + dp_n \wedge dx_n, \qquad \sigma = \sum_{1\le k\le n, 1\le i<j\le n} C_{ij}^k p_k dx_i \wedge dx_j.$$

The existence of an invariant measure for nonholomic problems is well studied (see [10, 16–24]). We will consider smooth measures of the form $\mu = \nu\omega^n$, where ω^n is the standard measure on the cotangent bundle T^*S and ν is a nonvanishing smooth function, called the *density* of the measure μ.

In the absence of potential and gyroscopic forces, it was proved in [11] that the equations (4), (5) have an invariant measure if and only if its density is basic, i.e., $\nu = \nu(x)$. Then the system with a potential force $v(x)$ also preserves the same measure (see [9, 12]). For $\boldsymbol{f} = 0$, the existence of the basic density $\nu = \nu(x)$ is equivalent to the condition that the one-form

$$\Theta = \sum_{ij} C_{ij}^{j} dx_i, \qquad \text{i.e.,} \qquad \Theta(\mathrm{X}) = tr\, \boldsymbol{C}(X,\cdot)|x, \qquad X \in T_x S.$$

is exact: a function λ exists such that $\Theta = d\lambda$. Then the function $\nu(x) = exp(\lambda(x))$ is the density of an invariant measure (see [9, 25]).

In the presence of the gyroscopic form $\boldsymbol{f}$ we have a similar situation.

Theorem 2. The reduced gyroscopic Chaplygin (4), (5) have an invariant measure $\mu = \nu\omega^n$ with a basic density $\nu = \nu(x)$ if and only if the one-form Θ is exact $\Theta = d\lambda$. Then the function $\nu(x) = exp(\lambda(x))$ is the density of the invariant measure.

In other words, according to [10, 12], a Chaplygin system with a gyroscopic term possesses a basic invariant measure if and only if the same Chaplygin system without gyroscopic term preserves the same basic invariant measure.

The existence of an invariant measure is closely related to the Hamiltonization problem (e.g., see [9, 10, 14, 18, 20, 25–35]).

Suppose that the form $\Omega = \omega + \sigma + \boldsymbol{f}$ is conformally symplectic, i.e., there exists a nonvanishing function N, such that $d(N\Omega) = 0$. After the time rescaling $d\tau = Ndt$, the equation (6) reads

$$\frac{d}{d\tau} z = N^{-1} z = N^{-1} X =: \tilde{X}.$$

The last relation introduces the rescaled vector field $\tilde{X}$, which is Hamiltonian:

$$i_{\tilde{X}}(N\Omega) = -dh.$$

Therefore, the system in the new time becomes the Hamiltonian system with respect to the symplectic form $N\Omega$. Then, according to the Liouville theorem [15, 16], the Hamiltonian vector field $\tilde{X}$ preserves the standard measure $N^n\Omega^n = N^n\omega^n$,

$$L_{\tilde{X}}(N^n\Omega^n) = d(i_{\tilde{X}}(N^n\Omega^n)) = 0.$$

Thus, for the almost Hamiltonian vector field $X = N\tilde{X}$ we have

$$L_X(N^{n-1}\Omega^n) = d(i_X(N^{n-1}\Omega^n)) = d(i_{\tilde{X}}(N^n\Omega^n)) = 0.$$

and the flow of the reduced gyroscopic Chaplygin system (6) preserves the measure $\mu = N^{n-1}\Omega^n = N^{n-1}\omega^n$.

Theorem 3. The function $N = N(x)$ is a conformal factor for the almost symplectic form $\Omega = \omega + \sigma + \boldsymbol{f}$ if and only if it is a conformal factor for the almost symplectic form $\omega + \sigma$ and the form $\boldsymbol{f}^* = N\,\boldsymbol{f}$ is magnetic, i.e., closed. Assume that $\boldsymbol{f}^* = N\,\boldsymbol{f}$ is closed. The conditions (a) and (b) listed below are equivalent:

(a) The almost symplectic form $\Omega = \omega + \sigma + \boldsymbol{f}$ is conformally symplectic with the base conformal factor $N = N(x)$ and σ is given by $\sigma = N^{-1}dN\wedge\theta$, $\theta = p_1dx_1 + \cdots + p_ndx_n$.

(b) The (1,2)-tensor $\boldsymbol{C}$ is given by $\boldsymbol{C}(X,Y) = N^{-1}X(N)Y - N^{-1}Y(N)X$.

If $N = N(x)$ is a conformal factor for $\Omega = \omega + \sigma + \boldsymbol{f}$, then the reduced gyroscopic Chaplygin system (6) preserves the same measure as in the case of the absence of gyroscopic forces. This is in accordance with Theorem 2.

Examples. The problems of rolling without slipping and twisting of a balanced, dynamically nonsymmetric ball with a gyroscope over a plane and a sphere in $\mathbb{R}^n$ are the examples of gyroscopic $SO(n)$-Chaplygin systems. We described an invariant measure and provided examples of $SO(n-2)$-symmetric systems that allow the Chaplygin Hamiltonization. In the case of additional $SO(2)$-symmetry we proved that the obtained magnetic geodesic flows on the sphere S^{n-1} are integrable. In particular, we introduced the generalized Demchenko case in $\mathbb{R}^n$, where the inertia operator of the system is proportional to the identity operator. The reduced systems are automatically Hamiltonian and represent the magnetic geodesic flows on the spheres S^{n-1} endowed with the round-sphere metric, under the influence of a homogeneous magnetic field. The magnetic geodesic flow problem on the two-dimensional sphere is well known, but for $n > 3$ was not studied before.

We performed explicit integrations in elliptic functions of the systems for $n = 3$ and $n = 4$, and provided the case study of the solutions in both situations (see [1]).

Acknowledgements: This research has been supported by the Project no. 7744592 MEGIC "Integrability and Extremal Problems in Mechanics, Geometry and Combinatorics" of the Science Fund of Serbia, Mathematical Institute of the Serbian Academy of Sciences and Arts and the Ministry for Education, Science, and Technological Development of Serbia, and the Simons Foundation grant no. 854861.

References:

[1] Dragović, V., Gajić, B., Jovanović, B., *Gyroscopic Chaplygin systems and integrable magnetic flows on spheres*, J. Nonlinear Sci. (2023) 33:43, https://doi.org/10.1007/s00332-023-09901-5, arXiv:2110.09938 [math-ph].
[2] Demchenko, V., *Rolling without sliding of a gyroscopic ball over a sphere, doctoral dissertation*, University of Belgrade, 1924, pp. 94, printed ``Makarije" A.D. Beograd-Zemun. (in Serbian), http://elibrary.matf.bg.ac.rs/handle/123456789/118
[3] Dragović, V., Gajić, B., Jovanović, B., *Demchenko's nonholonomic case of a gyroscopic ball rolling without sliding over a sphere after his 1923 Belgrade doctoral thesis*, Theor. Appl. Mech. 47 (2) (2020), 257-287, arXiv:2011.03866.
[4] Bobilev, D.K., *About a ball with an iside gyroscope rollong without sliding over the plane*, Mat. Sb., 1892.
[5] Zhukovskiy, N.E., *About the Bobilev gyroscopic ball*, Trudy Otdela Fiz. Nauk, 1893. (in Russian).
[6] Neimark, J.I., Fufaev, N.A., *Dynamics of nonholonomic systems*, Transl. Math. Monogr. 33, Am. Math. Soc., Providence, 1972.
[7] Bakša, A., *On geometrisation of some nonholonomic systems*, Mat. Vesn. 27 (1975) 233-240. (in Serbian); English transl.: Theor. Appl. Mech. 44(2) (2017) 133-140.
[8] Bloch, A.M., Krishnaprasad, P.S., Marsden, J.E., Murray, R.M., *Nonholonomic mechanical systems with symmetry*, Arch. Ration. Mech. Anal. 136 (1996) 21-99.
[9] Cantrijn, F., Cortes, J., de Leon, M., Martin de Diego, D., *On the geometry of generalized Chaplygin systems*, Math. Proc. Camb. Philos. Soc. 132 (2) (2002) 323-351.
[10] Garcia-Naranjo, L.C., Marrero, J.C., *The geometry of nonholonomic Chaplygin systems revisited*, Nonlinearity, 33 (3) (2020) 1297-1341, arXiv:1812.01422 [math-ph].
[11] Koiller, J., *Reduction of some classical non-holonomic systems with symmetry*, Arch. Rational Mech. Anal. 118 (1992) 113-148.
[12] Stanchenko, S., *Nonholonomic Chaplygin systems*, J. Appl. Math. Mech. 53 (1989) 11-17.
[13] Bakša, A., *Ehresmann connection in the geometry of nonholonomic systems*, Publ. Inst. Math., Nouv. Sér. 91(105) (2012), 19-24.
[14] Chaplygin, S.A., *On the theory of the motion of nonholonomic systems. Theorem on the reducing multiplier*, Mat. Sb. 28 (2) (1911) 303-314. (in Russian)
[15] Libermann, P., Marle, C-M., Symplectic geometry and Analytic Mechanics, Kluwer, 1987.
[16] Arnold, V.I., Kozlov, V.V., Neishtadt, A.I., Mathematical Aspects of Classical and Celestial Mechanics, Encylopaedia of Mathematical Sciences 3, Springer-Verlag, Berlin, 1989.
[17] Fedorov, Yu.N., Kozlov, V.V., *Various aspects of n-dimensional rigid body dynamics*, Transl., Ser. 2, Am. Math. Soc. 168 (1995), 141-171.
[18] Fedorov, Yu.N., Jovanović, B., *Nonholonomic LR systems as generalized Chaplygin systems with an invariant measure and geodesic flows on homogeneous spaces*, J. Nonlinear Sci. 14 (2004) 341-381, arXiv: math-ph/0307016.
[19] Fedorov, Yu.N., Garca-Naranjo, L.C., Marrero, J.C., *Unimodularity and preservation of volumes in nonholonomic mechanics*, J. Nonlinear Sci. 25 (2015) 203-246, arXiv:1304.1788.

[20] Gajić, B., Jovanović, B., *Two integrable cases of a ball rolling over a sphere in* R^n, Rus. J. Nonlin. Dyn., 15 (4) (2019) 457-475.
[21] Jovanović, B., *Invariant measures of modified LR and L+R systems*, Regul. Chaotic Dyn. 20 (2015) 542-552, arXiv:1508.04913 [math-ph].
[22] Kozlov, V.V., *Invariant measures of the Euler-Poincare equations on Lie algebras*, Funct. Anal. Appl. 22 (1) (1988) 58-59.
[23] Zenkov, D.V., Bloch, A.M., *Invariant measures of nonholonomic flows with internal degrees of freedom*, Nonlinearity, 16 (2003) 1793-1807.
[24] Veselov, A.P., Veselova, L.E., *Integrable nonholonomic systems on Lie groups*, Math. Notes, 44 (5-6) (1988), 810-819.
[25] Bolsinov, A.V., Borisov, A.V., Mamaev, I.S. *Hamiltonization of non-holonomic systems in the neighborhood of invariant manifolds*, Regul. Chaotic Dyn. 16 (2011) 443-464.
[26] Bolsinov, A.V., Borisov, A.V., Mamaev, I.S., *Geometrisation of Chaplygins reducing multiplier theorem*, Nonlinearity 28 (2015) 2307-2318.
[27] Borisov, A.V., Mamaev, I.S., *Chaplygin's ball rolling problem is Hamiltonian*, Math. Notes 70 (5-6) (2001) 720-723.
[28] Borisov, A.V., Mamaev, I.S., Tsiganov, A.V., *Non-holonomic dynamics and Poisson geometry*, Russ. Math. Surv. 69 (2014) 481-538.
[29] Ehlers, K., Koiller, J., Montgomery, R., Rios, P., *Nonholonomic systems via moving frames: Cartan's equivalence and Chaplygin Hamiltonization*, In: J. E. Marsden, T. S. Ratiu (eds), *The Breadth of Symplectic and Poisson Geometry*, Prog. Math. 232, Birkhäuser Boston, 2005, arXiv:math-ph/0408005.
[30] Gajić, B., Jovanović, B., *Nonholonomic connections, time reparametrizations, and integrability of the rolling ball over a sphere*, Nonlinearity, 32 (5) (2019) 1675-1694.
[31] Garcia-Naranjo, L.C., *Generalisation of Chaplygin's Reducing Multiplier Theorem with an application to multi-dimensional nonholonomic dynamics*, J. Phys. A, Math. Theor. 52 (2019) 205203, 16 pp, arXiv:1805.06393 [nlin.SI].
[32] Garcia-Naranjo, L.C., *Hamiltonisation, measure preservation and first integrals of the multi-dimensional rubber Routh sphere*, Theor. Appl. Mech. 46 (1) (2019), 65-88..
[33] Jovanović, B., *Hamiltonization and integrability of the Chaplygin sphere in* R^n, J. Nonlinear. Sci. 20 (2010) 569-593, arXiv:0902.4397.
[34] Jovanović, B., *Rolling balls over spheres in* R^n, Nonlinearity, 31 (2018), 4006-4031.
[35] Jovanović, B., *Note on a ball rolling over a sphere: integrable Chaplygin system with an invariant measure without Chaplygin Hamiltonization*, Theor. Appl. Mech. 46 (1) (2019) 97-108.

DEVELOPMENT OF A METHOD FOR THE CALCULATION OF MULTISTAGE GAS TURBINES AND ESTIMATION OF THE REQUIRED AMOUNT OF COOLING AIR

Nikola M. Marković

Mathematical Institute of the Serbian Academy of Sciences and Arts, Kneza Mihaila 36, Belgrade, Serbia
email: nikola.markovic@mi.sanu.ac.rs

Abstract

The main task of designing a gas turbine process is to achieve maximum efficiency by expanding the maximum efficiency coefficient within the limitations related to the stress level of the blades, dimensions of the machine, economic factors or other factors. The mentioned limitations, during design, lead to the creation of a wide range of models and structures (solutions) of Gas Turbines. However, in this paper the emphasis will be placed on pure aerodynamic calculation and achieving the maximum efficiency coefficient. As shown in [1], when it comes to the aerodynamic calculation of a single-stage turbine at the mean diameter, the greatest influence on the efficiency coefficient is due to the dimensionless parameters of the turbines. According to [1], the axial velocity ratio (K) and the inlet-to-outlet mean diameter ratio (D) have a minor effect on the efficiency coefficient than the loading coefficient (ψ) and the flow coefficient (φ). The mentioned dimensionless parameters are defined by the expression (1):

$$\psi = \frac{\Delta h_S}{\frac{u_1^2}{2}}, \qquad \varphi = \frac{c_a}{u_1} \tag{1}$$

For that reason, the loading coefficient and flow coefficient are primarily considered in this paper, whereby the highest priority is given to the loading coefficient as the most influential parameter. The other two parameters can be ignored. According to [1], it is not possible to define any exact mathematical relation that links the dimensionless and other parameters of the turbine with the efficiency coefficient that is achieved. Therefore, the developed mathematical model in this paper is based on the Fielding model [2], where the variation of dimensionless parameters, that have the greatest influence on the efficiency coefficient, is achieved by variating the blade velocity of the first stage in the group (u_1) and flow coefficient. The parameters that directly depend on it include the loading coefficient, flow coefficient, degree of reaction, the ratio of the diameter at the root and the tip of the blade, as well as the minimum permissible ratio of the diameter of the root and the tip. Models of Aerodynamic and internal losses in this work are calculated according to [3] and [4], while flow mixing losses are developed based on research in [5]. The gas flow is considered as a semi-ideal gas, with the attribute of changing thermophysical properties depending on temperature, as according to [6], the pressure change has a negligible effect on the properties of gas. On the other hand, if we took the pressure change into consideration our model and calculations will be extremely complex to solve in real-time.

The solutions obtained in this work assume a one-dimensional calculation of the mean diameter based on the given input parameters. The developed mathematical model can be divided into two parts: 1 - Calculation of the equivalent (imaginary) gas turbine. Calculation of an equivalent turbine consists of three steps: a) variation (optimization) of the loading and flow coefficients and important parameters of the GT, b) definition of physical implementation limits according to [8], c) selection of optimal GTs dimensionless parameters at which the maximum value of the efficiency coefficient will be achieved.

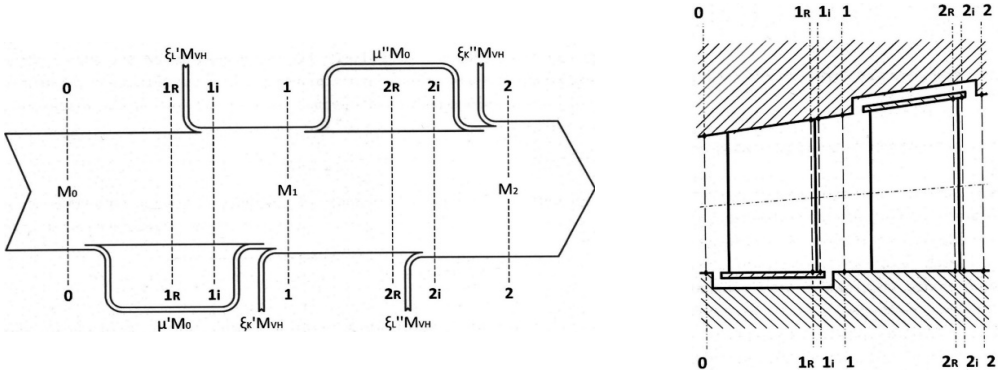

Fig. 1. Calculation planes shown by Sankey diagram and gas turbine stage

2 - Calculation of the GT with blade cooling mechanism. The calculation consists of the following steps: a) definition of the cooling model, b) detailed thermodynamic calculation of the GT stage, c) determination of the required amount of cooling air. This cooling model was developed for film and convective cooling of blades and convective cooling of GT case. It is based on a combination of two models from the works of authors [8] and [9]. For the purpose of thermodynamic calculation of the GT stage with cooling, calculation planes are used, as shown by the Sankey diagram and GT stage in Figure 1. With these calculation planes set up in this way, the gas expansion flow in the GT stage with cooling is shown in Figure 2. The developed algorithm for the mathematical model calculation of GT with cooling is also shown in Figure 2.

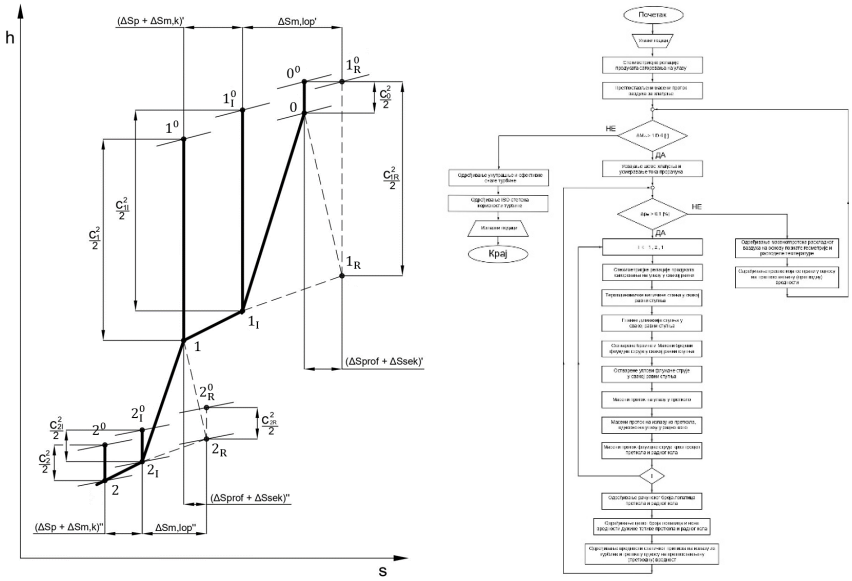

Fig. 2. The gas expansion flow in the GT stage with cooling and the developed algorithm for the calculation of GT – part 2

Acknowledgment: This research was funded by the Ministry of Science, Technological Development and Innovation, Republic of Serbia, Grant numbers: 451-03-47/2023-01/200029. I need to express gratitude to Prof. Petrović for the valuable remarks, guidelines and advice during the presented research.

References:

[1] Zhengping, Z. , Songtao, W. , Huoxing, L., *Weihao, Z., Axial Turbine Aerodynamics for Aeroengines*, Beihang Univeristy Bejing China, 2004.
[2] Fielding, L., *The effect on Axial Flow Turbine Performance of Parameter Variation*, ASME Press, 2000.
[3] Denton, J., *Loss Mechanisms in Turbomachines*, ASME Journal of Turbomachinery, 1993
[4] Petrović, M., *Steam turbine*, Faculty of Mechanical Engineering, Belgrade, 2013
[5] Baehr, D. , Diederichsen, C., *Berechnungsgleichungen für Enthalpie und Entropie der Komponenten von Luft und Verbrennungsgasen*, 40 (1/2), pp. 30 – 33, BWK, 1988
[6] Young, J. , Wilcock, R., *Modeling the Air – Cooled Gas Turbine*, Part 2 – Coolant Flows and Losses, Journal of Turbomachinery, 2002.

WAVE PROPAGATION IN PERIODIC TIMOSHENKO BEAMS ON DIFFERENT ELASTIC FOUNDATION TYPES

Nevena A. Rosić[1], Danilo Z. Karličić[2], Milan S. Cajić[2] and Mihailo P. Lazarević[1]

[1] Faculty of Mechanical Engineering, University of Belgrade, Kraljice Marije 16, 11120 Belgrade
e-mail: nrosic@mas.bg.ac.rs
[2] Mathematical Institute of the Serbian Academy of Sciences and Arts, Kneza Mihaila 36, 11001 Belgrade, Serbia
e-mail: danilok@mi.sanu.ac.rs, mcajic@mi.sanu.ac.rs

Abstract

Here, the transfer matrix method along with the Bloch theorem are employed to study the frequency spectra in various cases of Timoshenko's beam periodicity, such as structural, material and boundary periodicity. We additionally compare the location and size of band gaps, and the shape of the band structure in general for different types of foundation layers and relevant parameter values.

Keywords: elastic wave, Timoshenko beam theory, transfer matrix method, band structure.

1. Introduction

Wave propagation in periodic structures is an ongoing area of scientific research. It has been shown that these phononic-like periodic structures exhibit some very interesting and useful phenomena, such as the appearance of band gaps in the frequency spectrum. A periodic Timoshenko beam is examined and its representative cell is taken into consideration. Various types of periodicity are applied: material, geometric and boundary periodicity. We consider one layer in the cell as a uniform beam and we apply Timoshenko's beam theory to describe its transverse motion [1]. Further on, the transfer matrix method and Bloch's theorem are applied in order to study the frequency spectrum [1], [2]. Thus, we state the eigenvalue problem which can be solved using the so-called "direct" method [3]. By visualizing the frequency band structure and mode shapes, we have achieved a very useful insight into the behavior of such structures, which can be conveniently applied for vibration attenuation without using active control strategies [4]. The transfer matrix method provides any required number of exact results using only one cell, and the order of the global matrix is independent on the number of cells into which the structure is divided, which leads to the decrease of computational effort, but suffers from non-physical numerical instability under certain conditions [5].

2. Problem formulation and methodology

When material periodicity is considered, the cell is divided into two layers made out of different materials, while their other aspects remain the same. The geometric periodicity is achieved by varying the cross section of a homogenous beam, thus, a representative cell is consisted of two layers with different cross sections. Finally, three types of boundary periodicity are studied:

elastic foundation, a series of suspended masses and elastic foundation with inerters whose reaction force is given as $F = b(\ddot{w} - \ddot{w}_0)$, where b is the coefficient of proportionality and w is transverse displacement. The transfer matrix method is applied to each layer in a cell, which is considered to be one uniform Timoshenko beam, thus relating its transverse displacements, rotation angles, forces and moments, which form a state vector $\mathbf{\Phi}(x)$, where x is the longitudinal dimension of the beam. The transfer matrix for one layer is obtained by relating its left and right boundaries, and the general transfer matrix **T** is formed subsequently. The boundary periodicity is applied by taking into consideration the shear force at the right end of the unit cell, which has been shown in detail in [1]. After applying the Bloch's theorem to relate the adjoining cells, we state and solve the required eigenvalue problem:

$$\mathbf{T}(\Omega)\mathbf{\Phi} = \lambda\mathbf{\Phi}, \ \lambda = e^{i\kappa} \tag{1}$$

where **T** is the transfer matrix given as a function of dimensionless frequency Ω, κ is the dimensionless wavenumber, and λ is a Floquet multiplier. The eigenvalue problem (1) is solved by imposing frequency values (the so-called "direct" method [3]), and thus the values of Floquet multipliers are provided. From these results, we can determine real and imaginary parts of the wavenumber and evaluate this propagation constant as a function of frequency.

3. Some results and discussion

The representative unit cell for the case of boundary periodicity which is achieved through the application of an elastic layer with inerters is shown in Fig. 1a, while corresponding band structure is given in Fig. 1b, compared with the uniform beam and the case with bare and inerter-based elastic foundation. The results from Fig. 1b show the imaginary (below zero) and real part (above zero) of dispersion curves and demonstrate the existence of many band gaps in such a continuous system. The analogues of optical and acoustic branch of the simple phononic system can be recognized in the higher frequency ranges as well. By introducing the inerter-based foundation, the band gaps and corresponding dispersion branches shift to lower frequency values and slightly change their shapes due to the inertia amplification effect.

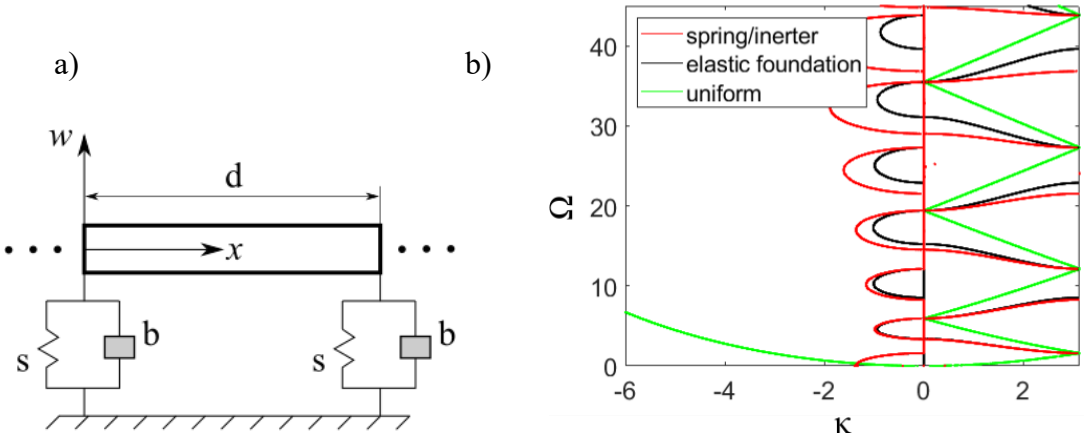

Fig. 1. a) Illustration of a unit cell model and b) Band structures of Timoshenko beam resting on different foundations.

Conclusion

In this paper, the analysis of wave propagation in Timoshenko periodic beams resting on different foundation types is performed with the aid of transfer matrix method. The obtained results reveal a significant effect of different periodicity and foundation types on the band structure of the system. The most pronounced effect of the inerter-based elastic foundation reflects in the

reduction of the frequency of band gaps and certain dispersion branches, especially those in the higher frequency range.

Acknowledgements: This research was supported by the Serbian Ministry of Science, Technological Development and Innovation, through the Mathematical Institute of SASA and grant No. 451-03-47/2023-01/200105 from 03/02/2023. This support is gratefully acknowledged.

References:

[1] Liu L., Hussein I.,M., *Wave Motion in Periodic Flexural Beams and Characterization of the Transition Between Bragg Scattering and Local Resonance*, Journal of Applied Mechanics, Vol. 79, 011003, 2012.
[2] Gangli C., Xiaoyun Z., Xingbao L., Xiaoting R., *Transfer Matrix Method for the Free and Forced Vibration Analyses of Multi-step Timoshenko Beams Coupled with Rigid Bodies on Springs*, Applied Mathematical Modelling, Vol. 87, 152-170, 2020.
[3] Hussein I.,M., Leamy M., J., Ruzzene M., *Dynamics of Phononic Materials and Structures: Historical Origins, Recent Progress, and Future Outlook,* Applied Mechanics Reviews, Vol. 66(4), 040802, 2014.
[4] Santos B., R., Berres G., Inman J., D., Gonzales-Bueno G., C., Bueno D., Douglas, A practical approach to evaluate periodic rods composed of cells with geometric and material periodicity, Journal of Sound and Vibration, Vol. 533, 117646, 2023.
[5] Lee W., J., Lee Y., J., Free vibration analysis of functionally graded Bernoulli-Euler beams using an exact transfer matrix expression, International Journal of Mechanical Sciences, Vol. 122, 1-17, 2017.

EXAMPLES OF INTEGRABLE NONHOLONOMIC SYSTEMS WITH AN INVARIANT MEASURE

Vladimir Dragović[1,2], Borislav Gajić[1] and Božidar Jovanović[1]

[1] Mathematical Institute of SASA, Knez Mihailova 36, Belgrade
e-mail: vladad@mi.sanu.ac.rs, gajab@mi.sanu.ac.rs, bozaj@mi.sanu.ac.rs
[2] Department of Mathematical Sciences, University of Texas, Dallas, USA
e-mail: Vladimir.Dragovic@utdallas.edu

Abstract

We will present a part of the results obtained recently in [1, 2]. We consider a nonholonomic problem of rolling without slipping of n homogeneous balls $B_1, \dots, B_n$ with centers $O_1, \dots, O_n$ and the same radius r over a fixed plane Σ_0. We assume that a moving plane Σ is placed over the balls and moves without slipping over the homogeneous balls. In [1] we proved that this system possesses an invariant measure and that it is integrable. The explicit integration of the reduced system is presented in [2].

Keywords: nonholonomic dynamics, rolling without slipping, invariant measure, integrability.

1. Introduction

A classical result is that nonholonomic systems are not Hamiltonian. One of the consequences is that, in general, they do not preserve an invariant measure. However, there is an important class of nonholonomic systems that admit an invariant measure with a smooth function as a density. They are introduced by Chaplygin. Inspired by pioneer papers by Chaplygin [3, 4], nonholonomic systems with an invariant measure are intensively studied (see for example [5-13]). Recently, in [1, 2], we introduced and studied in details new nonholonomic systems with an invariant measure: *spherical and planar ball bearing systems*. A spherical ball bearing system introduced in [1] consists of n homogeneous balls $B_1, \dots, B_n$ of the same radius r that roll without slipping around a fixed sphere S_0 with center O and radius R. A dynamically nonsymmetric sphere S of radius $\rho = R + 2r$ with the center that coincides with the center O of the fixed sphere rolls without slipping over the moving balls. In [2], the system is considered in four different configurations and two integrable cases are founded. The obtained integrable nonholonomic models are natural extensions of the Chaplygin ball integrable problems. Our focus here will be on planar ball bearing problem. It is the nonholonomic system that consists of n homogeneous balls $B_1, \dots, B_n$ with centers $O_1, \dots, O_n$ and the same radius r. The balls are rolling without slipping over a fixed plane Σ_0 . In addition there is a moving plane Σ of the mass m that moves without slipping over the homogeneous balls. Following [1, 2], we will briefly describe the system and its integration.

2. The planar ball bearing system

Let us denote with O_0 a fixed point of the plane Σ_0 and with $O, O_1, \cdots, O_n$ the centers of masses of the plane Σ and the balls $\boldsymbol{B}_1, \ldots, \boldsymbol{B}_n$, respectively. The coordinates of the points O, O_i with respect to the fixed reference frame, are $O(x, y, 2r), O_i(x_i, y_i, r)$, $i = 1, \ldots, n$. With $A_1, \ldots, A_n$ and $B_1, B_2, \ldots, B_n$ we denote the contact points of the balls $\boldsymbol{B_1}, \ldots, \boldsymbol{B_n}$ with the planes Σ_0 and Σ respectively.

The configuration space Q is $(5n + 3)$-dimensional. Conditions that there is no slipping in points of contact of balls with moving and fixed planes, give us $4n$ independent nonholonomic constraints. Hence, the vector subspaces of the admissible velocities $D_q \subset T_q Q$, $q \in Q$, are $(n + 3)$ – dimensional. Note that the centres O_i of the balls $\boldsymbol{B_i}$ are in rest in relation to each other along the motion and we do not have collisions of the balls (see [1]).

Let φ be an angle that describe rotation of the moving plane with respect to the fixed reference frame. Let us also denote $v_\varphi = \dot{\varphi}$, $v_x = \dot{x}$, $v_y = \dot{y}$ and introduce

$$\vec{N} = (N_1, N_2, 0) = \sum_{i=1}^{n} \delta_i \overrightarrow{OB_i}, \qquad \vec{M} = \sum_{i=1}^{n} \delta_i \langle \overrightarrow{OB_i}, \overrightarrow{OB_i} \rangle,$$

where $\delta_i = \frac{m_i r^2 + I_i}{4r^2}$, $i =, \ldots, n$, $\delta = \delta_1 + \ldots + \delta_n$, and $diag(I_i, I_i, I_i)$ is the inertia operator and m_i is the mass of the i-th ball $\boldsymbol{B_i}$.

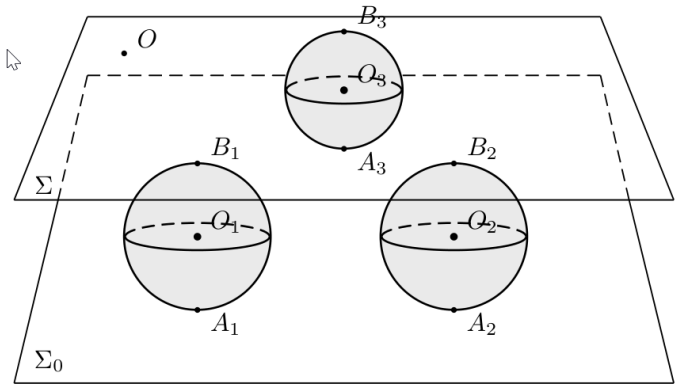

Fig. 1. System with three balls

It is shown in [1] that the equation of motion can be reduced to

$$\mathcal{Q} = \{(v_x, v_y, v_\varphi, N_1, N_2, M) \in \mathbb{R}^6 \mid \delta M > N_1^2 + N_2^2\}.$$

Let I be the moment of inertia of the plane Σ with respect to the line perpendicular to Σ at O. If we introduce

$$\mathbf{v} = (v_x, v_y, v_\varphi), \ \mathbf{n} = (N_1, N_2, M),$$
$$\mathbf{m} = \tfrac{1}{2}(N_1 v_\varphi^2 - \delta v_\varphi v_{y,} N_2 v_\varphi^2 + \delta v_\varphi v_x, v_\varphi (N_1 v_x + N_2 v_y)),$$

and

$$\mathbf{I} = \begin{pmatrix} m+\delta & 0 & -N_2 \\ 0 & m+\delta & N_1 \\ -N_2 & N_1 & I+M \end{pmatrix}, \ \mathbf{J} = -\frac{1}{2}\begin{pmatrix} \delta & 0 & N_2 \\ 0 & \delta & -N_1 \\ 2N_1 & 2N_2 & I+M \end{pmatrix}$$

then we have the following statement.

Theorem 1. [1] The reduced equations of motion on $\mathcal{Q}$ are

$$\mathbf{v} = \mathbf{I}^{-1}\mathbf{m}, \ \mathbf{n} = \mathbf{J}\mathbf{v}. \tag{1}$$

They have the following first integrals

$$f_1 = (m+\delta)\, v_x - \, v_\varphi N_2 = d_1,$$
$$f_2 = (m+\delta)\, v_y \, + \, v_\varphi \, N_1 = d_2,$$
$$f_3 = \delta \, M - (N_1^2 + N_2^2) = d_3,$$
$$f_4 = T = \tfrac{1}{2}(I+M)\, v_\varphi^2 + \tfrac{1}{2}(m+\delta)(v_x^2+v_y^2) + v_\varphi(N_1\, v_y - N_2\, v_x) = d_4.$$

Theorem 2. [1] The reduced equations of motion (1) possess an invariant measure

$$\sqrt{\det(\mathbf{I})}\, dv_x \, \wedge dv_y \wedge \, dv_\varphi \wedge \, dN_1 \wedge \, dN_2 \wedge \, dM,$$

where $\det(\mathbf{I}) = (m+\delta)((m+\delta)I \, + \, m\, M + \, (\delta\, M - (N_1^2 + N_2^2)\,)$.

3. Integration of the reduced system

According to the Euler-Jacobi theorem, as a consequence of Theorems 1 and 2 we have

Theorem 3. The system (1) can be solved in quadratures.

At an invariant level set of the three first integrals $f_1 = d_1, f_2 = d_2, f_3 = d_3,$ one gets a closed system in the space $\mathbb{R}^3\{v_\varphi, N_1, N_2\}$. If we introduce the polar coordinates $N_1 = A\cos\theta$, $N_2 = A\sin\theta$, this system becomes

$$\begin{aligned} \dot{v}_\varphi &= \frac{m v_\varphi A}{2\left(d_5 + \frac{m(m+\delta)}{\delta}A^2\right)}(d_1\cos\theta + d_2\sin\theta), \\ \dot{A} &= \frac{-\delta}{2(m+\delta)}(d_1\cos\theta + d_2\sin\theta), \\ A\dot{\theta} &= \frac{m+2\delta}{2(m+\delta)}A v_\varphi + \frac{\delta}{2(m+\delta)}(d_1\sin\theta - d_2\cos\theta). \end{aligned} \tag{2}$$

When $A \neq 0$, from the first two equations, one calculates

$$\frac{dv_\varphi}{dA} = -\frac{m(m+\delta)}{\delta}\frac{A v_\varphi}{d_5 + \frac{m(m+\delta)}{\delta}A^2}$$

and the integration leads to

$$v_\varphi = v_\varphi(A) = \frac{d_6}{\sqrt{d_5 + \frac{m(m+\delta)}{\delta}A^2}} \tag{3}$$

with d_6 as the constant of integration.

In order to finish the integration of the system, one uses the existence of the invariant measure. The original system has an invariant measure with the density $\mu = \sqrt{det(\mathbb{I})}$. One can check that the density of the invariant measure for the last equations reduces to $\mu = \, A$.

Let us first introduce the constant α such that

$$d_1\cos\theta + d_2\sin\theta = \sqrt{d_1^2+d_2^2}\cos(\theta-\alpha)\,, \quad d_1\sin\theta - d_2\cos\theta = \sqrt{d_1^2+d_2^2}\sin(\theta-\alpha),$$

and the constant k by $k = \frac{\delta}{2(m+\delta)}\sqrt{d_1^2+d_2^2}$. The equations (2) reduce to

$$\dot{A} = -k\cos(\theta-\alpha), \qquad A\dot{\theta} = k\sin(\theta-\alpha) + \frac{m+2\delta}{2(m+\delta)}A v_\varphi(A).$$

The last equations can be rewritten in the form

$$\frac{dA}{-k\cos(\theta-\alpha)} = \frac{A d\theta}{k\sin(\theta-\alpha) + \frac{m+2\delta}{2(m+\delta)}A v_\varphi(A)},$$

or equivalently

$$\left(k\sin(\theta-\alpha)+\frac{m+2\delta}{2(m+\delta)}Av_\varphi(A)\right)dA+k\cos(\theta-\alpha)\,Ad\theta=0.$$

One checks that the expression on the left-hand side is the total differential. Thus, we finally gets:

$$kA\sin(\theta-\alpha)+\frac{m+2\delta}{2m(m+\delta)^2}\sqrt{d_5+\frac{m(m+\delta)}{\delta}A^2}=d_7=const.$$

From the last equation θ can be expressed as a function of A. By plugging it into the second equation of the system (2), one gets a separate differential equation, and performing the integration one calculates A as a function of time. Finally, from (3) one can find v_φ as a function of time.

Acknowledgements: This research has been supported by the Project no. 7744592 MEGIC "Integrability and Extremal Problems in Mechanics, Geometry and Combinatorics" of the Science Fund of Serbia, Mathematical Institute of the Serbian Academy of Sciences and Arts and the Ministry for Education, Science, and Technological Development of Serbia, and the Simons Foundation grant no. 854861.

References:

[1] Dragović V., Gajić B., Jovanović B., *Spherical and Planar Ball Bearings — Nonholonomic Systems with Invariant Measures*, Regul. Chaotic Dyn., vol. 27, no. 4, 424—442, 2022,
[2] Dragović V., Gajić B., and Jovanović B., *Spherical and Planar Ball Bearings — a Study of Integrable Cases,* Regul. Chaotic Dyn., vol. 28, no. 1, 62–77, 2023.
[3] Chaplygin S. A., *On a Ball's Rolling on a Horizontal Plane,* Regul. Chaotic Dyn., vol. 7, no. 2, 131–148, 2002; see also: Math. Sb., vol. 24, no. 1, 139–168, 1903.
[4] Chaplygin S. A., *On the Theory of Motion of Nonholonomic Systems. The Reducing-Multiplier Theorem*, Regul. Chaotic Dyn., vol. 13, no. 4, 369–376, 2008; see also: Mat. Sb., vol. 28, no. 2, 303–314, 1912.
[5] Borisov A. V., Mamaev I. S., *The rolling motion of a rigid body on a plane and a sphere: hierarchy of dynamics*, Regul. Chaotic Dyn., Vol. 7, no. 2, 177–200, 2002.
[6] Borisov A. V., Mamaev I. S., Bizyaev I. A., *The hierarchy of dynamics of a rigid body rolling without slipping and spinning on a plane and a sphere*, Regul. Chaotic Dyn., Vol.18, 277—328, 2013.
[7] Fedorov Yu. N., Jovanović B., *Integrable nonholonomic geodesic flows on compact Lie groups*, In: Topological methods in the theory of integrable systems (Bolsinov A.V., Fomenko A.T., Oshemkov A.A. eds), Cambrige Scientific Publ., 115–152, 2006.
[8] Garcia-Naranjo L. C., *Hamiltonisation, measure preservation and first integrals of the multidimensional rubber Routh sphere*, Theor. Appl. Mech., vol. 46, No.1, 65–88, 2019.
[9] Jovanović B., *LR and L+R systems*, J. Phys. A: Math. Theor., Vol. 42, No 22, 225202 (18pp), 2009, arXiv: 0902.1656 [math-ph].
[10] Jovanović B., *Invariant measures of modified LR and L+R systems*, Regul. Chaotic Dyn., Vol. 20, 542—552, 2015, arXiv:1508.04913.
[11] Jovanović B., *Note on a ball rolling over a sphere: integrable Chaplygin system with an invariant measure without Chaplygin Hamiltonization,* Theor. Appl. Mech., Vol. 46, No. 1, 97–108, 2019.
[12] Kozlov V.V., *Invariant measures of the Euler–Poincare equations on Lie algebras*, Funkts. Anal. Prilozh., Vol. 22, 69–70, 1988, (in Russian); English transl.: Funct. Anal. Appl., Vol. 22, No. 1, 58–59, 1988.

[13] Zenkov D. V., Bloch A. M., *Invariant measures of nonholonomic flows with internal degrees of freedom*, Nonlinearity, Vol. 16, 1793–1807, 2003.

FURTHER RESULTS ON ROBUST FINITE-TIME STABILITY NONSTATIONARY TWO-TERM NEUTRAL NONLINEAR PERTURBED FRACTIONAL - ORDER TIME DELAY SYSTEMS

Mihailo P. Lazarević, Darko Radojević, Petar Mandić, and Stjepko Pišl

[1] Faculty of Mechanical Engineering, University of Belgrade, Kraljice Marije 16, 11120 Belgrade 35, Serbia,
e-mail: mlazarevic@mas.bg.ac.rs, drmasf@yahoo.com, pmandic@mas.bg.ac.rs, stjepko.pisl@gmail.com

Abstract

In this paper, the problem of finite-time stability (FTS) for a class of nonstationary neutral nonlinear perturbed fractional-order time delay systems (FOTDS) is studied. Based on an extended form of generalized Gronwall inequality, a new FTS stability criterion for such systems is established in terms of the Mittag-Leffler function. Finally, a numerical example is given to illustrate the effectiveness and applicability of the proposed theoretical results.

Keywords: finite-time stability, time-varying, fractional order, nonlinear, neutral, delay, perturbed systems.

1. Introduction

Time delay often appears in many real-world engineering systems, and it may lead to bifurcation, chaos and even instability, [1]. The stability and control design of time-delay systems are widely studied due to the effect of delay phenomena on system dynamics, which often leads to poor performance or even instability. While the concept of Lyapunov stability, recognized as infinite time behavior, has been well investigated and developed, here, we consider system stability in the non-Lyapunov sense- *finite-time stability* (FTS) because the system restrains its trajectory to a predefined time-varying domain over a finite time interval for a bounded initial condition [2]. As an important role in the study of the transient behavior of control systems, FTS may help achieve better anti-interference and robustness over a time interval as well as improve the control precision [3]. Also, it is observed that the stability of time delay systems may be destroyed by their uncertainties and nonlinear perturbations, so it is necessary to study the FTS analysis of time delay systems with uncertain parameters and nonlinear perturbation [4].

On the other side, the stability properties of neutral-type systems with delays have been studied in the last decades due to their effectiveness in describing a wide variety of physical phenomena [5]. For neutral time-delay systems, the term with the highest order of derivative involves at least one time delay and it presents a more general class than those of the delayed type.

Also, fractional order dynamical systems have drawn much attention from researchers and engineers over the past few decades, [6,7] particularly for different kinds of stability. FOTDS

stand for dynamical systems with both fractional-order derivative and time delays, and they can be classified into two categories: retarded type and neutral type. Here, we are interested in FTS where FTS analysis of FOTDS of retarded type is initially investigated and presented in [8,9] using generalized Gronwall inequality (GGI).

However, the stability of fractional order neutral systems proves to be a more complex question because the system includes the highest order derivative of the retarded state. Accordingly, a special focus on the FTS of fractional order neutral time-delay systems (FONTDS) has been conducted, see [10-12]. Recently, we obtained and presented new results which are related to FTS of uncertain nonhomogeneous FONTDS which include time-varying delays [13,14].

In this article, inspired by the above discussions, for the first time, we will investigate the FTS problem of a more general class of nonstationary nonlinear two-term FONTDS where a novel delay independent condition for the FTS of the FONTDS has been presented.

2. Preliminaries and problem statement

2.1 Preliminaries

In this subsection, some basic notations and definitions including the definition of Caputo and Riemann–Liouville fractional derivatives are given. Also, the norm $\|(\cdot)\|$ will denote any vector norm, i.e. $\|(\cdot)\|_1$, $\|(\cdot)\|_2$, or $\|(\cdot)\|_\infty$, or the corresponding matrix norm induced by the equivalent vector norm, i.e. $1-$, $2-$, or $\infty-$ norm, respectively.

Definition 2.1: The Riemann–Liouville (RL) fractional integral of order α for an integrable function $f(t):[t_0,\infty)\to R$ is defined as [15]:

$$ {}^{\mathrm{RL}}_{t_0}\mathrm{D}_t^{-\alpha} f(t) \equiv {}_{t_0}\mathrm{I}_t^{\alpha} f(t) = \frac{1}{\Gamma(\alpha)}\int_{t_0}^{t}(t-s)^{\alpha-1} f(s)\,\mathrm{d}s, \quad t\ge t_0, \quad \alpha\in C, \quad t>0, \mathrm{Re}(\alpha)>0. \quad (2.1) $$

where $\Gamma(\cdot)$ is the gamma function defined as

$$ \Gamma(\alpha) = \int_0^{\infty} \mathrm{e}^{-t}t^{\alpha-1}\mathrm{d}t, \quad \Gamma(\alpha+1)=\alpha\Gamma(\alpha), \quad \alpha\in C, \ \mathrm{Re}(\alpha)>0 \quad (2.2) $$

where C is the set of complex numbers. For the left RL fractional derivative is given as:

$$ {}^{\mathrm{RL}}_{t_0}\mathrm{D}_t^{\alpha} f(t) = \frac{1}{\Gamma(1-\alpha)}\frac{d}{dt}\int_{t_0}^{t}(t-s)^{-\alpha} f(s)\,\mathrm{d}s, \quad t\ge t_0, \quad (2.3) $$

Definition 2.2*:* The left Caputo fractional derivative of order $0<\alpha<1$, $\alpha\in C$, $\mathrm{Re}(\alpha)\ge 0$, is defined as:

$$ {}^{\mathrm{C}}_{t_0}\mathrm{D}_t^{\alpha} f(t) = \frac{1}{\Gamma(1-\alpha)}\int_{t_0}^{t}(t-s)^{-\alpha}\frac{df(s)}{ds}\mathrm{d}s, \quad t\ge t_0, \quad (2.4) $$

Definition 2.3 The Mittag-Leffler function with one parameter is given as [16]:

$$E_\alpha(z)=\sum_{k=0}^{\infty} z^k/\Gamma(k\alpha+1),\ \left(\alpha=1,\quad E_1(z)=e^z\right),\quad \alpha>0,\ z\in C \tag{2.5}$$

The following lemmas are introduced and help prove our main stability criterion.

Lemma 2.1 [17] Assume $x(t)\in C^1\left([0,+\infty),R\right), \dot{x}(t)\geq 0$ and $\alpha>0$ .Then,

$\int_0^t\left((t-s)^{\alpha-1}/\Gamma(\alpha)\right)x(s)ds$ is monotonically increasing with respect to *t.*

Lemma 2.2 [15] $$ {}_0I_t^{\alpha}\left({}^cD_0^{\alpha}x(t)\right)=x(t)-\sum_{k=0}^{n-1}\frac{t^k}{k!}x^{(k)}(0),\quad n-1<\alpha<n, t>0 \tag{2.6}$$

Lemma 2.3 Let $\alpha>\beta>0, n-1<\beta<n$ and $x(t)\in AC^n[a,b]$. Then

$$ {}_0I_t^{\alpha}\left({}^cD_0^{\beta}x(t)\right)={}_0I_t^{\alpha-\beta}x(t)-\sum_{k=0}^{n-1}\frac{t^{k+\alpha-\beta}}{\Gamma(\alpha-\beta+k+1)}x^{(k)}(0). \tag{2.7}$$

Lemma 2.4 (*extended form of the GGI***),** [18]

Suppose non-integer orders $\alpha>0,\beta>0$, $q(t)$ is a nonnegative function locally integrable on $[0,T)$, $g_1(t)$ and $g_2(t)$ are nonnegative, nondecreasing, continuous functions defined on $[0,T)$; $g_1(t)\leq N_1, g_2(t)\leq N_2, (N_1,N_2=const)$. Suppose $x(t)$ is nonnegative and locally integrable on $[0,T)$ with

$$x(t)\leq q(t)+g_1(t)\int_0^t(t-s)^{\alpha-1}x(s)ds+g_2(t)\int_0^t(t-s)^{\beta-1}x(s)ds,\quad t\in[0,T) \tag{2.8}$$

It follows,

$$x(t)\leq q(t)+\int_0^t\sum_{n=1}^{\infty}\left[g(t)\right]^n\cdot\sum_{k=0}^{n}\frac{C_n^k\left[\Gamma(\alpha)\right]^{n-k}\left[\Gamma(\beta)\right]^k}{\Gamma\left((n-k)\alpha+k\beta\right)}(t-s)^{(n-k)\alpha+k\beta-1}a(s)ds,\quad t\in[0,T) \tag{2.9}$$

where $g(t)=g_1(t)+g_2(t)$ and $C_n^k=n(n-1)(n-2)...(n-k+1)/k!$.

Corollary 2. Under the hypothesis of Lemma 2.4, let $q(t)$ be a nondecreasing function on $[0,T)$. Then $$x(t)\leq q(t)E_{\omega}\left[g(t)\left(\Gamma(\alpha)t^{\alpha}+\Gamma(\beta)t^{\beta}\right)\right],\ \omega=min(\alpha,\beta). \tag{2.10}$$

2.2 Problem statement

Consider the following nonstationary two-term $0<\beta<\alpha<1$ neutral nonlinear fractional-order delay system with state and control time varying delays given by the following equation:

$$\begin{aligned}&{}^c\mathrm{D}^{\alpha}\boldsymbol{x}(t)=A_0(t)\boldsymbol{x}(t)+A_1(t)\boldsymbol{x}\left(t-\tau_x(t)\right)+A_{N1}(t)^c\,\mathrm{D}^{\beta}\boldsymbol{x}\left(t-\tau_{xN}(t)\right)+\\&+B_0\boldsymbol{u}(t)+B_1\boldsymbol{u}\left(t-\tau_u(t)\right)+\mathrm{g}\left(t,x(t),x\left(t-\tau_x(t)\right),x\left(t-\tau_{xN}(t)\right)\right)+G(t)w(t),\end{aligned} \tag{2.11}$$

with associated continuous functions of initial state and input (control):

$$\boldsymbol{x}(t)=\boldsymbol{\psi}_x(t), t\in[-\tau_{xm},0],\quad \boldsymbol{u}(t)=\boldsymbol{\psi}_u(t), t\in[-\tau_{uM},0], \tag{2.12}$$

where $\tau_u(t)$ is the time varying input delay, $\tau_x(t)$ is the time varying state delay and $\tau_{xN(.)}(t)$ is the neutral time varying delay, where are continuous functions satisfyng (2.13):

$$\begin{aligned} &0 \le \tau_x(t) \le \tau_{xM}, 0 \le \tau_u(t) \le \tau_{uM}, \quad \forall t \in J = [t_0, t_0 + T], \quad t_0 \in \mathbb{R}, \quad T > 0 \\ &0 \le \tau_{xN}(t) \le \tau_{xN}, \qquad \tau_{xm} = \max(\tau_{xM}, \tau_{xN}) \end{aligned} \tag{2.13}$$

${}^{C}\mathrm{D}_t^{\alpha}, {}^{C}\mathrm{D}_t^{\beta}$ denote Caputo fractional derivatives of order α, β, $0 < \beta < \alpha < 1$; $x(t) \in R^n$ is the state vector and $u(t) \in \mathbb{R}^m$ is the control input; $A_0(t), A_1(t), A_{N1}(t), G(t)$, are time-varying matrices as well as B_0, B_1 denote constant matrices with appropriate dimensions; $w(t) \in R^n$ is the disturbance vector, which has the upper bound as follows: $\|w(t)\| < \gamma_w$, $\gamma_w = const > 0$, $\forall t \in J$. $\boldsymbol{\psi}_x(t) \in C([-\tau_{xm}, 0], R^n)$ is the initial function of $x(t)$ with the norm $\|\psi_x\|_C = \sup_{-\tau \le \theta \le 0} \|\psi_x(\theta)\|$. Here, the following assumption for the nonlinear perturbation function $g(.)$ is introduced. The nonlinear perturbation $g(t, x(t), x(t - \tau_x(t)), x(t - \tau_{xN}(t)))$ satisfies the Lipschitz condition, i.e. there is a continuous function $L(t)$ on $[0, +\infty]$ such that

$$\|g(t, x(t), x(t - \tau_x(t)), x(t - \tau_{xN}(t)))\| \le L(t)(\|x(t)\| + \|x(t - \tau_x(t))\| + \|x(t - \tau_{xN}(t))\|) \tag{2.14}$$

The norm $\|x(t)\|_{\infty}$ will be used here as well

$$\begin{aligned} &\sup_{t \in [0,T]} \|A_0(t)\| = a_0, \ \sup_{t \in [0,T]} \|A_1(t)\| = a_1, \ \sup_{t \in [0,T]} \|A_{N_1}(t)\| = a_N \\ &\sup_{t \in [0,T]} (\|A_0(t)\| + \|A_1(t)\|) < \infty, \ \sup_{t \in [0,T]} (\|G(t)\|) = g, \ \sup_{t \in [0,T]} (L(t)) = l \end{aligned} \tag{2.15}$$

3. Main Results

3.1 Robust FTS of nonstationary two-term neutral nonlinear perturbed fractional-order time delay system

In this section, we derive FTS criteria for time-varying two-term $0 < \beta < \alpha < 1$ neutral nonlinear perturbed FOTDS with state and control time varying delay using an extended form of generalized Gronwall inequality. Further, the appropriate definition of FTS for the time-varying nonhomogeneous system (2.11) with the associated initial functions (2.12) respectively is given.

Definition 2.3 [9, 19]: The fractional nonstationary two-term neutral perturbed time-delay system given by nonhomogeneous state equation (2.11) satisfying initial conditions (2.12) is *finite-time stable* w.r.t. $\{\delta, \varepsilon, t_0, \gamma_u, \gamma_0, J, \|(\cdot)\|\}$, $\delta < \varepsilon$, if and only if:

$$\left.\begin{aligned} &\|\boldsymbol{\psi}_x\|_C < \delta, \quad \|\boldsymbol{\psi}_u\|_C < \gamma_0, \\ &\|\boldsymbol{u}(t)\| < \gamma_u, \quad \forall t \in J, \end{aligned}\right\} \ \Rightarrow \ \|\boldsymbol{x}(t)\| < \varepsilon, \quad \forall t \in J. \tag{3.1}$$

where $\delta, \varepsilon, \gamma_0, \gamma_u$ are positive constants, Fig.1. Now it is possible to formulate the following theorem.

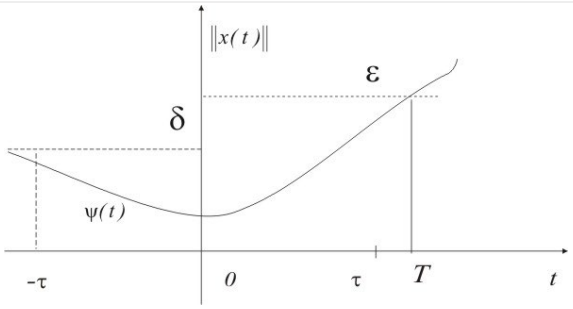

Fig. 1. Finite time stability conception

Theorem A: The nonstationary nonlinear neutral two-term fractional order time varying delay system (2.11) satisfying initial conditions (2.12) is *finite-time stable* w.r.t. $\left\{\delta,\varepsilon,t_0,\gamma_u,\gamma_0,J,\|(\cdot)\|\right\},\ \delta<\varepsilon,$ if the following condition holds:

$$\left[1+\frac{a_N|t|^{\alpha-\beta}}{\Gamma(\alpha-\beta+1)}\right]E_{\alpha-\beta}\left[\left(\frac{a_N}{\Gamma(\alpha-\beta)}+\frac{a_l^*}{\Gamma(\alpha)}\right)\left(\Gamma(\alpha-\beta)t^{\alpha-\beta}+\Gamma(\alpha)t^{\alpha}\right)\right]$$
$$+\frac{\gamma_{0w}|t|^{\alpha}}{\Gamma(\alpha+1)}+\frac{\gamma_{0u}|t|^{\alpha}}{\Gamma(\alpha+1)}+\frac{\gamma_{01}\tau_{uM}{}^{\alpha}}{\Gamma(\alpha+1)}+\frac{\gamma_{1u}|t-\tau_u|^{\alpha}}{\Gamma(\alpha+1)}\le\frac{\varepsilon}{\delta},\quad\forall t\in J_0, \tag{3.2}$$

where: $$\gamma_{0u}=b_0\gamma_u/\delta,\gamma_{1u}=b_1\gamma_u/\delta,\gamma_{01}=b_1\gamma_0/\delta,\gamma_{0w}=g\gamma_w/\delta \tag{3.3}$$

Proof: The fractional order satisfy $0<\beta<\alpha<1,$ and solution can be obtained in the form of the equivalent Volterra integral equation, where is $t_0=0$:

$$\boldsymbol{x}(t)=\psi_x(0)-A_{N1}(t)\psi_x(-\tau_{xm})\frac{t^{\alpha-\beta}}{\Gamma(\alpha-\beta+1)}+\frac{1}{\Gamma(\alpha-\beta)}\int_0^t(t-s)^{\alpha-\beta-1}A_{N1}(s)x(s-\tau_{xN}(s))ds+$$
$$+\frac{1}{\Gamma(\alpha)}\int_0^t(t-s)^{\alpha-1}\begin{bmatrix}A_0(s)\boldsymbol{x}(s)+A_1(s)\boldsymbol{x}(s-\tau_x(s))\\+B_0u(s)+B_1u(s-\tau_u(s))+G(s)w(s)\\+g(s,x(s),\boldsymbol{x}(t-\tau_x(s)),x(s-\tau_{xN}(s)))\end{bmatrix}ds \tag{3.4}$$

Applying the norm $\|(.)\|$ and previous assumptions to the previous expression it follows:

$$\|\boldsymbol{x}(t)\|\le\|\psi_x(0)\|+\|A_{N1}(t)\|\|\psi_x(-\tau_{xm})\|\frac{|t|^{\alpha-\beta}}{\Gamma(\alpha-\beta+1)}+$$
$$+\frac{1}{\Gamma(\alpha-\beta)}\int_0^t|t-s|^{\alpha-\beta-1}\|A_{N1}(s)\|\|x(s-\tau_{xN}(s))\|ds+ \tag{3.5}$$
$$+\frac{1}{\Gamma(\alpha)}\int_0^t|t-s|^{\alpha-1}\begin{bmatrix}\|A_0(s)\|\|\boldsymbol{x}(s)\|+\|A_1(s)\|\|\boldsymbol{x}(s-\tau_x(s))\|\\+\|B_0\|\|u(s)\|+\|B_1\|\|u(s-\tau_u(s))\|+\|G(s)\|\|w(s)\|\\+L(s)\left(\|x(s)\|+\|x(s-\tau_x(s))\|+\|x(s-\tau_{xN}(s))\|\right)\end{bmatrix}ds$$

or:

$$\|\boldsymbol{x}(t)\| \le \|\psi_x\|_C \left[1+\frac{a_N |t|^{\alpha-\beta}}{\Gamma(\alpha-\beta+1)}\right] + \frac{a_N}{\Gamma(\alpha-\beta)}\int_0^t |t-s|^{\alpha-\beta-1} \|x(s-\tau_{xN}(s))\| ds +$$

$$+\frac{1}{\Gamma(\alpha)}\int_0^t |t-s|^{\alpha-1} \begin{bmatrix} (\|A_0(s)\|+L(s))\|\boldsymbol{x}(s)\| + (\|A_1(s)\|+L(s))\|\boldsymbol{x}(s-\tau_x(s))\| \\ +\|B_0\|\|u(s)\| + \|B_1\|\|u(s-\tau_u(s))\| + \|G(s)\|\|w(s)\| \\ +L(s)\|\boldsymbol{x}(t-\tau_{xN}(s))\| \end{bmatrix} ds \tag{3.6}$$

On the other hand, there are:

$$\begin{aligned} &\left\| \begin{matrix} A_0(t)\boldsymbol{x}(t) + A_1(t)\boldsymbol{x}(t-\tau_x(t)) + B_0\boldsymbol{u}(t) + B_1\boldsymbol{u}(t-\tau_u(t)) \\ +\mathrm{g}(t,x(t),x(t-\tau_x(t)),x(t-\tau_{xN}(t))) + G(t)w(t) \end{matrix} \right\| \le \\ &\le \|A_0(t)\|\|\boldsymbol{x}(t)\| + \|A_1(t)\|\|\boldsymbol{x}(t-\tau_x(t))\| + \|B_0\|\|u(t)\| + \|B_1\|\|u(t-\tau_u(t))\| + \|G(t)\|\|w(t)\| \\ &+L(t)\left(\|x(t)\| + \|x(t-\tau_x(t))\| + \|x(t-\tau_{xN}(t))\|\right) \\ &\le (a_0+l)\|\boldsymbol{x}(t)\| + (a_1+l)\|\boldsymbol{x}(t-\tau_x(t))\| + b_0\|u(t)\| + b_1\|u(t-\tau_u(t))\| + g\|w(t)\| \\ &+l\|x(t-\tau_{xN}(t))\| = a_{ol}\|\boldsymbol{x}(t)\| + a_{1l}\|\boldsymbol{x}(t-\tau_x(t))\| + l\|x(t-\tau_{xN}(t))\| + \\ &b_0\|u(t)\| + b_1\|u(t-\tau_u(t))\| + g\|w(t)\| \end{aligned} \tag{3.7}$$

Combining the previous two expressions, taking into account $\|\boldsymbol{u}(t)\| < \gamma_u$, $\|w(t)\| < \gamma_w, \forall t \in J$, it yields: (3.8)

$$\|\boldsymbol{x}(t)\| \le \|\psi_x\|_C \left[1+\frac{a_N |t|^{\alpha-\beta}}{\Gamma(\alpha-\beta+1)}\right] + \frac{a_N}{\Gamma(\alpha-\beta)}\int_0^t |t-s|^{\alpha-\beta-1} \|x(s-\tau_{xN}(s))\| ds +$$

$$+\frac{1}{\Gamma(\alpha)}\int_0^t |t-s|^{\alpha-1} \begin{bmatrix} a_{0l}\|\boldsymbol{x}(s)\| + a_{1l}\|\boldsymbol{x}(s-\tau_x(s))\| \\ +l\|\boldsymbol{x}(t-\tau_{xN}(s))\| \end{bmatrix} ds + \frac{b_0\gamma_u |t|^{\alpha}}{\Gamma(\alpha+1)} + \frac{b_1\gamma_0{\tau_{uM}}^{\alpha}}{\Gamma(\alpha+1)} + \frac{g\gamma_w |t|^{\alpha}}{\Gamma(\alpha+1)} + \frac{b_1\gamma_u |t-\tau_{uM}|^{\alpha}}{\Gamma(\alpha+1)}$$

Also, the next nondecreasing function is introduced $z(t) = \sup_{\theta\in[-\tau_{xm},t]} \|x(\theta)\|, \quad \forall t \in [0,T]$, [20],

where for $\forall t^{\bullet} \in [0,t]$, the following conditions satisfy

$$\|x(t^*)\| \le \sup_{t^*\in[t-\tau_{xm},t]} \{\|\boldsymbol{x}(t^*)\|\} \le z(t^*), \ \|x(t^*-\tau_{x*}(t^*))\| \le z(t^*), \cdot \tag{3.9}$$

Applying the previous inequalities, the expression (3.8) takes the following form:

$$\|\boldsymbol{x}(t)\| \le \|\psi_x\|_C \left[1+\frac{a_N |t|^{\alpha-\beta}}{\Gamma(\alpha-\beta+1)}\right] + \frac{a_N}{\Gamma(\alpha-\beta)}\int_0^t |t-s|^{\alpha-\beta-1} z(s) ds +$$

$$+\frac{a_l^*}{\Gamma(\alpha)}\int_0^t |t-s|^{\alpha-1} z(s) ds + \frac{b_0\gamma_u |t|^{\alpha}}{\Gamma(\alpha+1)} + \frac{b_1\gamma_0{\tau_{uM}}^{\alpha}}{\Gamma(\alpha+1)} + \frac{g_l\gamma_w |t|^{\alpha}}{\Gamma(\alpha+1)} + \frac{b_1\gamma_u |t-\tau_{uM}|^{\alpha}}{\Gamma(\alpha+1)} \tag{3.10}$$

where is $a_l^* = (a_{0l} + a_{1l} + l)$. Taking into account $\forall \theta \in [0,t]$ and $\theta - s \to s^* \to s$ one obtain

$$\begin{aligned}\left\|\boldsymbol{x}(t)\right\| &\le \left\|\psi_x\right\|_C\left[1+\frac{a_N|\theta|^{\alpha-\beta}}{\Gamma(\alpha-\beta+1)}\right]+\frac{a_N}{\Gamma(\alpha-\beta)}\int_0^{\theta}\left|s^*\right|^{\alpha-\beta-1} z\left(\theta-s^*\right)ds^*+\\ &+\frac{a_l^*}{\Gamma(\alpha)}\int_0^{\theta}\left|s^*\right|^{\alpha-1} z(\theta-s^*)ds^*+\frac{b_0\gamma_u|\theta|^{\alpha}}{\Gamma(\alpha+1)}+\frac{b_1\gamma_0{\tau_{uM}}^{\alpha}}{\Gamma(\alpha+1)}+\frac{g\gamma_w|\theta|^{\alpha}}{\Gamma(\alpha+1)}+\frac{b_1\gamma_u|\theta-\tau_{uM}|^{\alpha}}{\Gamma(\alpha+1)}\end{aligned} \tag{3.11}$$

or:

$$\begin{aligned}\left\|\boldsymbol{x}(t)\right\| &\le \left\|\psi_x\right\|_C\left[1+\frac{a_N|t|^{\alpha-\beta}}{\Gamma(\alpha-\beta+1)}\right]+\frac{a_N}{\Gamma(\alpha-\beta)}\int_0^{t}|t-s|^{\alpha-\beta-1} z(s)ds+\\ &+\frac{a_l^*}{\Gamma(\alpha)}\int_0^{t}|t-s|^{\alpha-1} z(s)ds+\frac{b_0\gamma_u|t|^{\alpha}}{\Gamma(\alpha+1)}+\frac{b_1\gamma_0{\tau_{uM}}^{\alpha}}{\Gamma(\alpha+1)}+\frac{g\gamma_w|t|^{\alpha}}{\Gamma(\alpha+1)}+\frac{b_1\gamma_u|t-\tau_{uM}|^{\alpha}}{\Gamma(\alpha+1)}\end{aligned} \tag{3.12}$$

Moreover, based on the property of the function $z(t)$, we have:

$$\begin{aligned}z(t) &= \sup_{\theta\in[-\tau_{xm},t]}\left\|x(\theta)\right\| \le \max\left\{\sup_{\theta\in[-\tau_{xm},0]}\left\|x(\theta)\right\|,\ \sup_{\theta\in[0,t]}\left\|x(\theta)\right\|,\right\}\le\\ &\le \max\left\{\begin{array}{l}\left\|\psi_x\right\|_C,\left\|\psi_x\right\|_C\left[1+\frac{a_N|t|^{\alpha-\beta}}{\Gamma(\alpha-\beta+1)}\right]+\frac{a_N}{\Gamma(\alpha-\beta)}\int_0^{t}|t-s|^{\alpha-\beta-1} z(s)ds+\\ +\frac{a_l^*}{\Gamma(\alpha)}\int_0^{t}|t-s|^{\alpha-1} z(s)ds+\frac{b_0\gamma_u|t|^{\alpha}}{\Gamma(\alpha+1)}+\frac{b_1\gamma_0{\tau_{uM}}^{\alpha}}{\Gamma(\alpha+1)}+\frac{g\gamma_w|t|^{\alpha}}{\Gamma(\alpha+1)}+\frac{b_1\gamma_u|t-\tau_{uM}|^{\alpha}}{\Gamma(\alpha+1)}\end{array}\right\}\\ &= \left\|\psi_x\right\|_C\left[1+\frac{a_N|t|^{\alpha-\beta}}{\Gamma(\alpha-\beta+1)}\right]+\frac{a_N}{\Gamma(\alpha-\beta)}\int_0^{t}|t-s|^{\alpha-\beta-1} z(s)ds+\\ &+\frac{a_l^*}{\Gamma(\alpha)}\int_0^{t}|t-s|^{\alpha-1} z(s)ds+\frac{b_0\gamma_u|t|^{\alpha}}{\Gamma(\alpha+1)}+\frac{b_1\gamma_0{\tau_{uM}}^{\alpha}}{\Gamma(\alpha+1)}+\frac{g\gamma_w|t|^{\alpha}}{\Gamma(\alpha+1)}+\frac{b_1\gamma_u|t-\tau_{uM}|^{\alpha}}{\Gamma(\alpha+1)}\end{aligned} \tag{3.13}$$

Now, one can observe that $q(t)$ is a nondecreasing function on $J_0=[0,T]$

$$q(t)=\left\|\psi_x\right\|_C\left[1+\frac{a_N|t|^{\alpha-\beta}}{\Gamma(\alpha-\beta+1)}\right]. \tag{3.14}$$

and applying Lemma 2.4, we obtain

$$\begin{aligned}x(t)\le z(t)\le q(t)E_{\alpha-\beta}&\left[\left(\frac{a_N}{\Gamma(\alpha-\beta)}+\frac{a_l^*}{\Gamma(\alpha)}\right)\left(\Gamma(\alpha-\beta)t^{\alpha-\beta}+\Gamma(\alpha)t^{\alpha}\right)\right]+\\ &+\frac{b_0\gamma_u|t|^{\alpha}}{\Gamma(\alpha+1)}+\frac{b_1\gamma_0{\tau_{uM}}^{\alpha}}{\Gamma(\alpha+1)}+\frac{g\gamma_w|t|^{\alpha}}{\Gamma(\alpha+1)}+\frac{b_1\gamma_u|t-\tau_{uM}|^{\alpha}}{\Gamma(\alpha+1)}\end{aligned} \tag{3.15}$$

Finally, using the basic condition of Theorem A, we can obtain the required FTS condition:

$$\left\|\boldsymbol{x}(t)\right\|<\varepsilon,\quad \forall t\in J. \tag{3.16}$$

4. Numerical example

Consider the nonstacionary nonlinear neutral two-term fractional order time varying delay system (2.11) satisfying initial conditions (2.12) having the fractional-orders $\alpha = 0.5,\ \beta = 0.1$ For the sake of simplicity, it is assumed $\tau_x(t) = \tau_{xN1}(t) = \tau_u(t) = \tau(t),\ \tau_{xm} = \max(\tau_{xM}, \tau_{xN}) = \tau_{uM}$. Here all notation $\|(.)\|$ means the ∞ – norm of a matrix or a vector.

$$\begin{aligned} &{}^{c}\mathrm{D}^{0.5}\boldsymbol{x}(t) = A_0(t)\boldsymbol{x}(t) + A_1(t)\boldsymbol{x}(t-\tau_x(t)) + A_{N1}(t)\,{}^{c}\mathrm{D}^{0.1}\boldsymbol{x}(t-\tau_{xN}(t)) + \\ &+B_0\boldsymbol{u}(t) + B_1\boldsymbol{u}(t-\tau_u(t)) + \mathrm{g}(t, x(t), x(t-\tau_x(t)), x(t-\tau_{xN}(t))) + G(t)w(t), \end{aligned} \tag{3.17}$$

where

$$A_0(t) = \begin{bmatrix} 0.2\cos t & 0 \\ 0 & 0.4\cos t \end{bmatrix}, A_1(t) = \begin{bmatrix} 0.2\sin t & 0 \\ 0 & 0.3\cos t \end{bmatrix}, A_{N1} = \begin{bmatrix} 0.3\sin t & 0 \\ -0.05 & 0.2\sin t \end{bmatrix},$$

$$B_0 = \begin{bmatrix} 0 \\ 0.5 \end{bmatrix}, B_1 = \begin{bmatrix} 0.5 \\ 0 \end{bmatrix}, \quad G(t) = \begin{bmatrix} 0.01\cos t \\ 0.01\cos t \end{bmatrix}, w(t) = \begin{bmatrix} sin(t) \\ 0 \end{bmatrix}$$

$$\mathrm{g}(t, x(t), x(t-\tau(t))) = 0.01\begin{bmatrix} 0.01\cos x_2(t) \\ 0.01\cos x_1(t-\tau) \end{bmatrix} \tag{3.18}$$

and $t_0 = 0, \alpha = 0.5, \beta = 0.1, \tau = 0.1$,with associated functions: $\boldsymbol{\psi}_x(t) = [0.05 \quad 0.05]^{\mathrm{T}}$, $t \in [-0{,}1 \ \ 0]$; $\boldsymbol{\psi}_u(t) = 0.05,\ t \in [-0{,}1 \ \ 0]$. The task is to analyze the FTS with respect to $\{\delta = 0.06 \ \ \varepsilon = 10, \ \ \gamma_u = 1\}$. From the initial functions and given state equation, we have: $\|\boldsymbol{\psi}_x\|_{\mathcal{C}} = \max\limits_{t\in[-0.1,0]} \|\boldsymbol{\psi}_x(t)\|_\infty = 0.05 < \delta = 0.06$, $\|\boldsymbol{\psi}_u\|_{\mathcal{C}} = \max\limits_{t\in[-0.1,0]} \|\boldsymbol{\psi}_u(t)\|_\infty = 0.05 < \gamma_0 = 0.06$.

Based on assumption (2.14) it holds with $\sup_{t\in[0,T]}(L(t)) = 0.01$ and $\gamma_w = 1.01, \gamma_u = 1$.

It is obviously that $\|A_0\| = 0.4|\cos t|, \|A_1\| = 0.3|\sin t|, \|A_{N1}\| = 0.3|\sin t|, \|G\| = 0.01|\cos t|$ $\|B_0\| = 0.5, \|B_1\| = 0.5$. Also, one can find

$$\sup_{t\in[0,T]}(\|A_0\| = 0.4|\cos t|) = 0.4, \ \ \sup_{t\in[0,T]}(\|A_1(t)\| = 0.3|\sin t|) = 0.3$$

$$\sup_{t\in[0,T]}(\|A_{N_1}(t)\| = 0.3|\sin t|) = 0.3, \ \ \sup_{t\in[0,T]}(\|G\| = 0.01|\cos t|) = 0.01.$$

Using the condition of Theorem A, it is easy to attain the estimated time of the FTS, which is $T_{\mathrm{e}} \approx 0.92$ s .

5. Conclusion remarks

In this contribution, the FTS of (non)homogeneous nonlinear neutral two-term FOS with order $\beta, \alpha \in (0,1)$ with time-varying input and state delays is studied. By use of the extended form of generalized Gronwall inequality, new FTS criterion is obtained where sufficient conditions are derived for the FTS of considered FOTDS. Finally, the simulation example shows the validation of the proposed novel stability criterion of FTS.

Acknowledgement: This work is supported by the Ministry of Education, Science and Technological Development of the Republic of Serbia under the Grant No. 451-03-47/2023-01/ 200105 from 03.02.2023.

References:

[1] Zavarei M., Jamshidi M., *Time-Delay Systems: Analysis, Optimization and Applications*, North-Holland, Amsterdam, 1987.
[2] Gu, K., Kharitonov, V.L., Chen, J.*: Stability of Time-Delay Systems.* Birkhauser, Boston, MA 2003.
[3] Lee, J.; Haddad, W.M. *On finite-time stability and stabilization of nonlinear hybrid dynamical systems.* AIMS Math. 6, 5535–5562,2021.
[4] Liu P.L., *A delay decomposition approach to robust stability analysis of uncertain systems with time-varying delay*, ISA Trans. 51 (6),694-701, 2012.
[5] Kolmanovskii,V.andMyshkis,A. *Introduction to the theory and applications of functional differential equations.*KluwerAcademicPublishers,Dordrecht,1999.
[6] Monje, C. A., Chen, Y., Vinagre, B. M., Xue, D. and Feliu-Batlle, V., *Fractional-Order Systems and Controls: Fundamentals and Applications,* Springer, ISBN 9781849963350, 2010. https://link.springer.com/book/10.1007/978-1-84996-335-0.
[7] Caponetto R. *Fractional order systems: Modeling and control applications*, Vol. 72. World Scientific; 2010, http://dx.doi.org/10.1142/7709.
[8] Lazarević M. P., *Finite Time Stability Analysis of PDα Fractional Control of Robotic Time-Delay Systems,* Mechanics Research Communications, Vol. 33, No. 2, 269–279, 2006.
[9] Lazarević M., A.Spasić, *Finite-Time Stability Analysis of Fractional Order Time Delay Systems:Gronwall`s Approach,* Mathematical and Computer Modelling, 49, pp.475-481,2009.
[10] Denghao P., J. Wei, *Finite-time stability of neutral fractional time-delay systems via generalized Gronwalls inequality,* Abstr. Appl. Anal. 2014 1–4 , p. 610547, 2014.
[11] Li Z., G. Cunchen, R. Qifeng, *Robust finite-time stability of neutral fractional time-delay systems, Journal of Shanghai Normal University* Vol.49, No.3,pp.344-360,2020.
[12] Du F., J-G Lu, *Finite-time stability of neutral fractional order time delay systems with Lipschitz nonlinearities*, Applied Mathematics and Computation 375, 125079, https://doi.org/10.1016/j.amc.2020.125079,2020.
[13] Lazarević P.M., D. Radojević, S. Pišl, and G. Maione, *Robust finite-time stability of uncertain neutral nonhomogeneous fractional-order systems with time-varying delays*, Theoretical and applied mechanics (TAM), Vol.47 issue 2, 241–255. 2020.
[14] Lazarević P.M., D. Radojević, G. Maione, S. Pišl, *Finite-time stability of neutral fractional-order time varying delay systems with nonlinear parameter uncertainties and perturbations*, 8th International Congress of Serbian Society of Mechanics Kragujevac, ISBN 978-86-909973-8-1 Serbia, June 28-30, 2021,pp.652-661.
[15] Kilbas A., Srivastava H., Trujillo J., *Theory and Applications of Fractional Differential Equations*, Elsevier, Amsterdam, 2006.
[16] Kochubei A., Y.Luchko,Eds, *Handbook of Fractional Calculus with Applications,Volume 1: Basic Theory*,Walter de Gruyter GmbH, Berlin/Boston,2019.
[17] J. Ren, C. Zhai, *Stability analysis of generalized neutral fractional differential systems with time delays*, Applied Mathematics Letters 116 (2021) 106987, https://doi.org/10.1016/j.aml.2020.106987.
[18] Sheng J., W. Jiang, *Existence and uniqueness of the solution of fractional damped dynamical systems,* Advances in Difference Equations, (2017) 1-16, 2017. https://doi.org/10.1186/s13662-016-1049-2

[19] Liang C.,W.Wei, J.Wang, *Stability of delay differential equations via delayed matrix sine and cosine of polynomial degrees,* Adv. Difference Equ., (1):1–17, https://doi.org/10.1186/s13662-017-1188-0,2017.

[20] Naifar O, Nagy AM, Makhlouf AB, Kharrat M, Hammami MA. *Finite-time stability of linear fractional-order time-delay systems.* Int J Robust Nonlinear Control., 29:180–187. https://doi.org/10.1002/rnc.4388, 2019.

EXPERIMENTAL AND NUMERICAL APPROACH TO NATURAL FREQUENCY OF TAPERED 3D PRINTED CANTILEVER BEAM A TIP BODY

Marko Veg[1], Aleksandar Tomović[1], Goran Šiniković[1], Stefan Dikić[2], Nemanja Zorić[1], Slaviša Šalinić[3], Aleksandar Obradović[1], and Zoran Mitrović[1]

[1] Faculty of Mechanical Engineering, University of Belgrade, Kraljice Marije 16, 11120 Belgrade
e-mail: mveg@mas.bg.ac.rs, atomovic@mas.bg.ac.rs, gsinikovic@mas.bg.ac.rs, nzoric@mas.bg.ac.rs, aobradovic@mas.bg.ac.rs, zmitrovic@mas.bg.ac.rs
[2] Faculty of Technology and Metalurgy, University of Belgrade, Karnegijeva 4, 11120 Belgrade
e-mail: s.dikic@tmf.bg.ac.rs
[3] Faculty of Mechanical and Civil Engineering in Kraljevo, University of Kragujevac, Dositejeva 19, 36000 Kraljevo
e-mail: salinic.s@mfkv.kg.ac.rs

Abstract

This paper presents the continuation of the research by the authors on the topics of vibration analysis. Namely, a tapered cantilever beam has been studied in theoretical and experimental terms. The beam is 3D printed using the FDM technique of PLA material with two characteristics patterns, linear layered and the two-dimensional periodic structure. The former of the two is conducted to tensile test in order to determine elasticity modulus, so the computations of natural frequencies could be conducted. The experimental part of the research, in terms of natural frequency, is conducted on six specimens with various eccentricities. The angular frequencies of one representative sample, obtained by analytical computations and experimental measurement are compared.

Keywords: coupled vibrations, natural frequency, 3D printed material, cantilever beam.

1. Introduction

Elastic beams have been widely used and studied in the structural mechanics. Due to the increasing use of additive manufacturing processes, novel materials have become more available for structural design. Also, functionally graded materials have been present for almost half a century [1]. The use of 3D printed and functionally graded materials have several advantages. In order to tackle vibration problem of inhomogeneous structures and compute natural frequencies several procedures have been developed. One of them is the Symbolic Numeric Method of Initial Parameters in Differential Form (SNMIP) which enables researchers to solve natural frequencies directly from governing equations [2] for inhomogeneous beams with variable cross sectional characteristics. Also, there are several methods based on discretization of elastic elements as presented by the researcher in [3].

The 3D printed material is inhomogeneous and its mass and mechanical characteristics may differ from the homogeneous material of the used filament. Mechanical parameters of the 3D

printed material have been analyzed in [4] and the impact of the inclination angle among layers on the mechanical properties has been discussed.

Material design is an emerging engineering and scientific field. Many authors look for inspiration in natural shapes or traditional patterns in order to find optimal lattice shape for vibration control or energy harvesting purposes as in [5-7].

In this paper the material for cantilever beam is produced by 3D printing and two characteristic patterns are be presented, the linear-layered and the two dimensional periodic structure. For both pattern types, the fundamental natural frequency of cantilever beams is measured. Furthermore, for one case the comparison with computed results is conducted. For linear layered structure, the mass and mechanical characteristics have been determined in order to examine the deviation of characteristics of printed material to homogeneous filament. Measured results were used for computation of natural frequencies.

2. Formulation of the problem

The natural frequencies of an elastic tapered cantilever beam with the rigid body eccentrically displaced with respect to the free end are investigated. The eccentricity causes coupling between axial and bending vibrations. Similar problem was theoretically analyzed in the paper [8] for an axially functionally graded cantilever beam. In this paper the coupled vibrations of a 3D printed cantilever beam will be examined by practical measurement. The rigid body at the free end of the beam will be introduced via accelerometer used for measuring. Three cases of mass eccentricities and two different patterns in material design will be used.

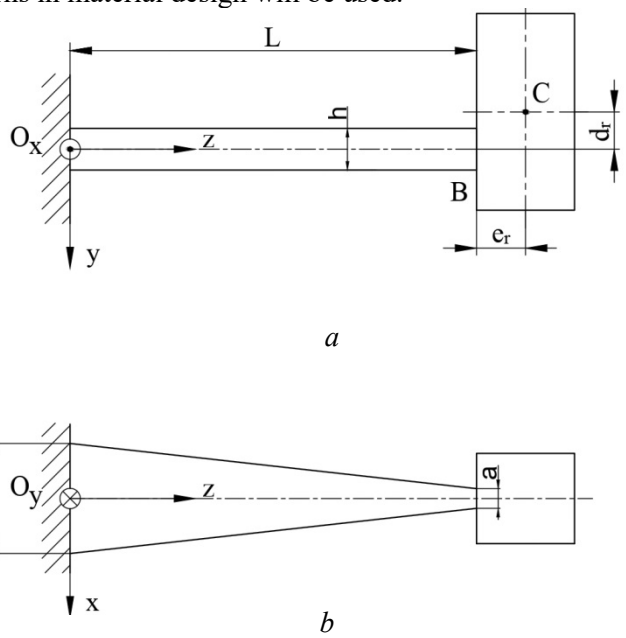

Fig. 1. An undeformed shape of the tapered cantilever beam wıth a tip mass presented schematically in: *a* – front and *b* – top view

Governing equations of motion in transverse and axial direction of presented cantilever beam, under the assuption of validity of Euler-Bernouli beam theory, read as [9]

$$\frac{\partial}{\partial z}\left[F_t(z,t)\right]-\rho(z)A(z)\frac{\partial^2 w(z,t)}{\partial t^2}=0,\frac{\partial}{\partial z}\left[F_a(z,t)\right]-\rho(z)A(z)\frac{\partial^2 u(z,t)}{\partial t^2}=0 \tag{1.1}$$

Even though the equations are not mutually coupled, the coupling originates from boundary conditions as it will be presented.

After implementing the method of separation of variables as presented in [9], one may write a system of ordinary differential equations in matrix form as in [8]

$$\frac{d}{dz}\boldsymbol{X}(z)=\boldsymbol{T}(z)\times\boldsymbol{X}(z) \tag{1.2}$$

where a vector ***X(z)*** and a vector of derivatives of arguments of ***X(z)*** and a matrix ***T(z)*** are as in [8]

$$\boldsymbol{X}(\mathrm{z})=\begin{bmatrix}U(z) & W(z) & W'(z) & F_a(z) & F_t(z) & M_f(z)\end{bmatrix}^T \tag{1.3}$$

$$\frac{d}{dz}\boldsymbol{X}(z)=\begin{bmatrix}\frac{dU(z)}{dz} & \frac{dW(z)}{dz} & \frac{dW'(z)}{dz} & \frac{dF_a(z)}{dz} & \frac{dF_t(z)}{dz} & \frac{dM_f(z)}{dz}\end{bmatrix}^T \tag{1.4}$$

$$\boldsymbol{T}(z)=\begin{bmatrix}0 & 0 & 0 & \frac{1}{E(z)A(z)} & 0 & 0\\ 0 & 0 & 1 & 0 & 0 & 0\\ 0 & 0 & 0 & 0 & 0 & \frac{-1}{E(z)I_x(z)}\\ -\omega^2\rho(z)A(z) & 0 & 0 & 0 & 0 & 0\\ 0 & -\omega^2\rho(z)A(z) & 0 & 0 & 0 & 0\\ 0 & 0 & 0 & 0 & 1 & 0\end{bmatrix} \tag{1.5}$$

The free body diagram is presented in Fig. 2. and it creates the foundation for the derivation of boundary conditions.

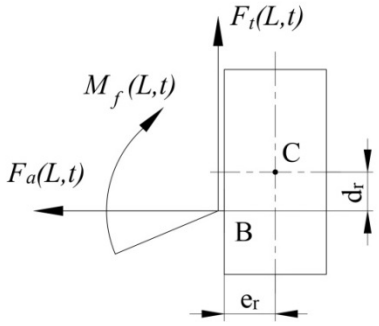

Fig. 2. A free body diagram of the attached rigid body

Boundary conditions at the left and right end of the cantilever beam (*z=0, z=L*) shown in Figure 1 read as in [8]

$$U(0)=0, W(0)=0, W'(0)=0 \tag{1.6}$$

$$-\omega^2 J_{C_r}W'(L)=M_f(L)+F_a(L)d_r+F_t(L)e_r, \tag{1.7}$$

$$m_r\omega^2\left[U(L)+W'(L)d_r\right]=F_a(L), m_r\omega^2\left[W(L)+W'(L)e_r\right]=F_t(L) \tag{1.8}$$

The third, rotational motion equation is written about mass center *C*, thus J_{Cr} stands for the centroidal mass moment of inertia for *x* axis.

3. Numerical procedure

By using the Symbolic numeric procedure in differential form, as presented in [2,10] the angular frequencies will be determined. Similarly to the model presented in [8], based on the linearity of the presented system, and the implementation of the method of initial parameters in differential form one may write a solution as a sum of particular solutions as

$$\boldsymbol{X}(z,\omega) = C_1\boldsymbol{X_1}(z,\omega) + C_2\boldsymbol{X_2}(z,\omega) + C_3\boldsymbol{X_3}(z,\omega) \tag{1.9}$$

Where, C_1, C_2 and C_3 are integration constants. Particular solutions, with respect to axial coordinate and angular frequency as symbolic variables in vector form may read:

$$\boldsymbol{X_i}(z,\omega) = \left[U_i(z,\omega) \quad W_i(z,\omega) \quad W_i^{'}(z,\omega) \quad F_{ai}(z,\omega) \quad F_{ti}(z,\omega) \quad M_{fi}(z,\omega)\right]^T, i = 1,2,3 \tag{1.10}$$

Presented particular solutions shall satisfy the folowing boundary conditions (z=0)

$$\boldsymbol{X}_1(0,\omega) = \begin{bmatrix}0 & 0 & 0 & 1 & 0 & 0\end{bmatrix}^T, \boldsymbol{X}_2(0,\omega) = \begin{bmatrix}0 & 0 & 0 & 0 & 1 & 0\end{bmatrix}^T,$$
$$\boldsymbol{X}_3(0,\omega) = \begin{bmatrix}0 & 0 & 0 & 0 & 0 & 1\end{bmatrix}^T \tag{1.11}$$

According to the SNMIP procedure, let us define expressions $a_{ji}(\omega)$, i,j=1,2,3 based on the boundary conditions at the free end of the beam

$$a_{1i}(\omega) = -F_{ai}(L,\omega) + m_r\omega^2\left(U_i(L,\omega) + W_i^{'}(L,\omega)d_r\right), i = 1,2,3 \tag{1.12}$$

$$a_{2i}(\omega) = -F_{ti}(L,\omega) + m_r\omega^2\left(W_i(L,\omega) + W_i^{'}(L,\omega)e_r\right), i = 1,2,3 \tag{1.13}$$

$$a_{3i}(\omega) = M_{fi}(L,\omega) + \omega^2 J_{Cr}W_i^{'}(\mathrm{L},\omega) + F_a(\mathrm{L},\omega)d_r + F_t(\mathrm{L},\omega)e_r, i = 1,2,3 \tag{1.14}$$

The system of equations, obtained in that manner one may read

$$\begin{bmatrix} a_{11}(\omega) & a_{12}(\omega) & a_{13}(\omega) \\ a_{21}(\omega) & a_{22}(\omega) & a_{23}(\omega) \\ a_{31}(\omega) & a_{32}(\omega) & a_{33}(\omega) \end{bmatrix}\begin{bmatrix} C_1 \\ C_2 \\ C_3 \end{bmatrix} = \begin{bmatrix} 0 \\ 0 \\ 0 \end{bmatrix} \tag{1.15}$$

The latter system of equations will have nontrivial solutions if

$$h(\omega) \equiv \begin{vmatrix} a_{11}(\omega) & a_{12}(\omega) & a_{13}(\omega) \\ a_{21}(\omega) & a_{22}(\omega) & a_{23}(\omega) \\ a_{31}(\omega) & a_{32}(\omega) & a_{33}(\omega) \end{vmatrix} = 0 \tag{1.16}$$

Where *h(ω)* presents the frequency equation of the presented problem from which the angular frequency can be determined for coupled axial and bending vibrations.

4. Material structure

The Fuse Deposition Modeling (FDM) technique is applied for printing a cantilever beam of Polylactic Acid (PLA) material. The reason for choosing the PLA as the material for this study is in its mechanical and thermal characteristics. These characteristics enable the detailed printing that can be exploited when printing periodic structures. Thus, two representative structures are presented in Fig. 3. The linear layered structure is presented in Fig. 3a, while the two-dimensional periodic structure is presented in Fig. 3b.

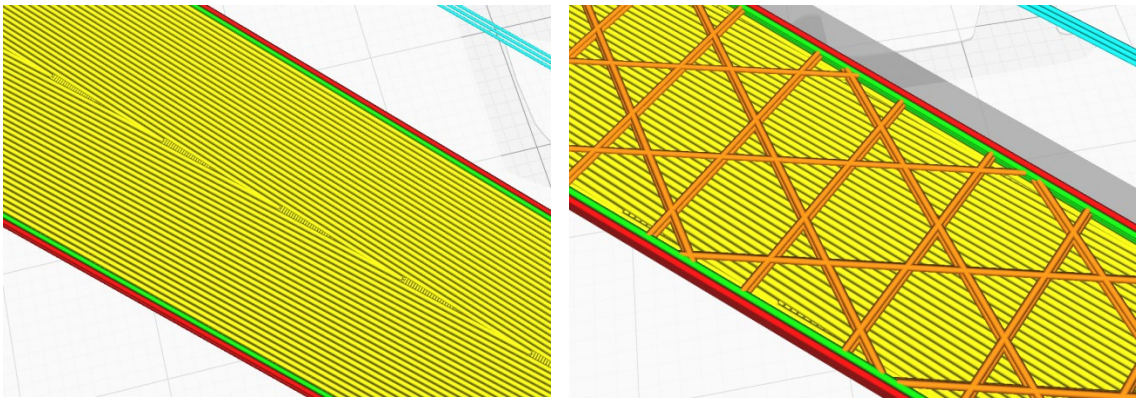

a *b*

Fig. 3. 3D printed material structure: *a* – linear layered material, *b* – two-dimensional periodic structure

The two cantilever beams of same dimensions will be introduced with different internal structures. One will have linear layered structure and the second one will have a two-dimensional periodic structure as presented in Fig. 3. The comparable dimensions with different inner structure will result in different frequencies. In Fig. 4a, the cantilever beam of linear layered structure prepared for 3D printing is presented while Fig. 4b shows the beam of two-dimensional periodic structure.

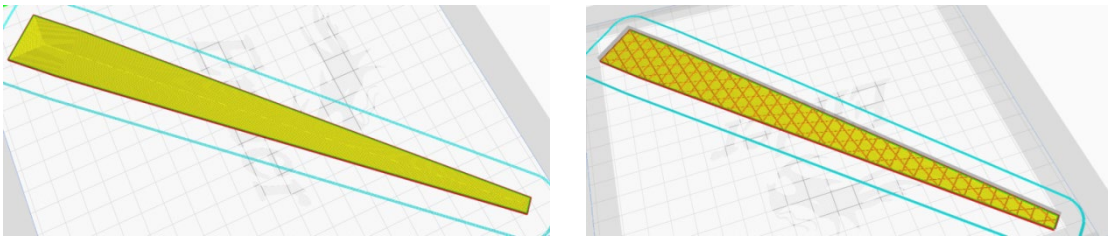

a *b*

Fig. 4. Beams prepared for 3D print: *a* – linear layered structured beam, *b* – two-dimensional periodic structured beam

5. Mechanical testing

5.1 Preparation for mechanical testing

The experimental determination of elasticity modulus is conducted only for linear layered structure using specimens that are designed according to ISO 527-2-2012 (International standard, plastics determination of tensile properties Part 2: Test conditions for molding and extrusion plastics) as in [4]. The zoomed structure is presented in Fig. 5, and six specimens prepared for testing are presented in Fig. 6, while characteristic dimensions are presented in Table 1.

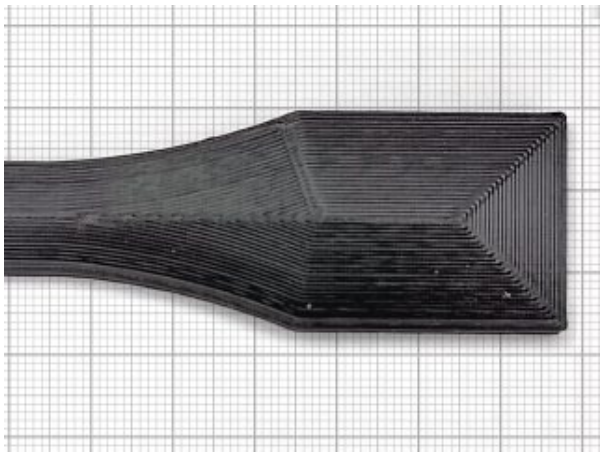

Fig. 5. 3D printed linear layered structure

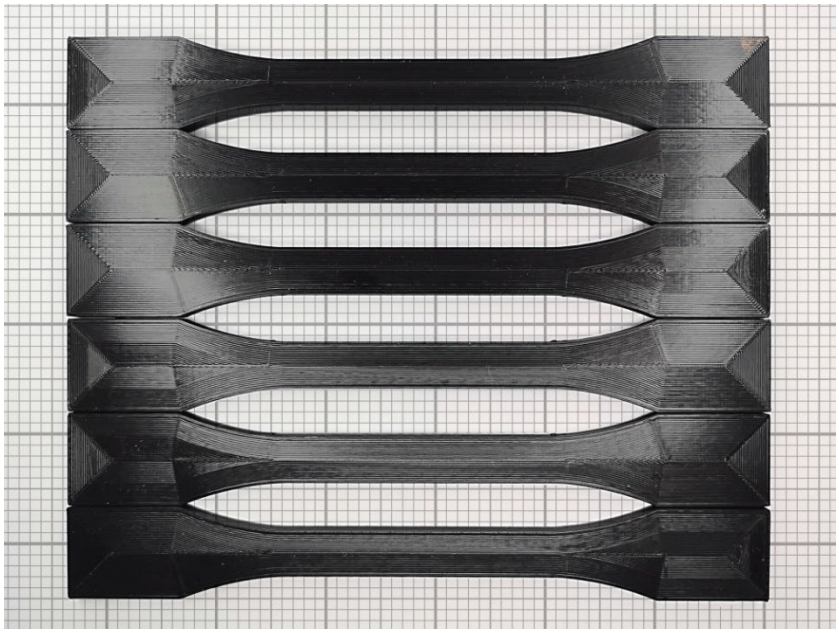

Fig. 6. Testing specimens

Thickness, mm	4
Width, mm	10.3
Gauge Length, mm	110

Table 1. Dimensions of tested specimens

5.2 Elasticity modulus

In order to examine the elasticity modulus, the universal tensile test machine, see Fig. 7, is used. Testing is conducted under standard conditions on six specimens and tested data is collected using digital collector. In Table 2 experimental results are presented.

During tensile testing eight specimens are used, of which two were exploited for setting up test machine and data acquisition, while six are considered to be relevant test samples.

Sample number	Elasticity modulus, MPa
1	2334.37
2	2816.3
3	2774.7
4	2800.04
5	2732.44
6	2763.4

Table 2. Test results of six samples

Average result is 2703.54 MPa with standard deviation of 183.192 MPa.

Fig. 7. Tensile test machine

Mass density and average elasticity modulus of printed material are presented in Table 3. It can be noted that the mass and mechanical characteristics of printed element decrease when compared to the homogeneous PLA material. When compared to 3D printed material in the paper [4] slight deviations can be observed.

Mass density (kg/m^3)	Elasticity modulus (MPa)
1.170,35	2703.54

Table 3. Average characteristics of the material of cantilever beam

The mechanical properties of linear layered structure will be used for the computations of angular frequencies of cantilever beam.

6. Determination of frequencies

The fundamental natural frequency of a cantilever beam has been determined experimentally for six configurations. One configuration has been chosen as the representative and angular frequencies have been computed numerically.

6.1 Experimental approach

The structure prepared for experiment consists of: the cantilever beam prepared for experiment, the 3D printed adaptive ring for accelerometer placement and the accelerometer itself, as modeled in

Fig. 8. The accelerometer presents the rigid body eccentrically displaced with respect to the free tip of the cantilever beam.

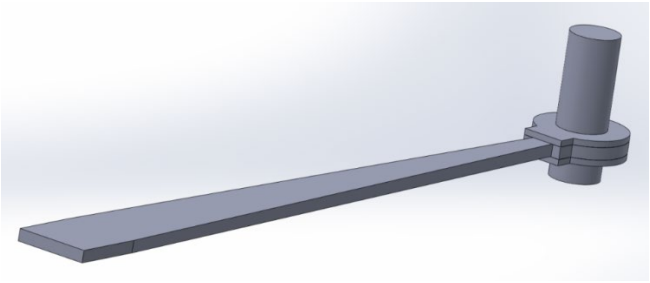

Fig. 8. Schematic representation of tapered cantilever beam with eccentrically displaced rigid body

The following equipment is applied for the measurement of the natural frequency: Microlog CMVA60-SKF with Wilcoxon 793 accelerometer. The accelerometer is a high performance general purpose with characteristics 100mV/g.

In order to obtain different eccentricities different masses were placed at the end of the beam.

By using the FFT analysis the results for the obtained natural frequency are presented in Table 4.

Measurement	f [Hz]	ω [rad/s]
1a	3.375	21.195
1b	3	18.84
1c	3.687	23.15436
2a	3.562	22.36936
2b	3.125	19.625
2c	3.937	24.72436

Table 4. Measured Natural frequencies/Angular frequencies

Different experimental setups are presented in Fig. 9., the number denotes the type of material structure and the letter mass of the eccentrically placed body. Number 1 stands for two-dimensional pattern, while, 2 stands for linear layered structure. Letter “a” stands for the case where rigid body consists of accelerometer and additional weight, “b” stands for case “a” with additional two M12 screws and “c” shows accelerometer without attached masses.

Configuration 1a and 2a

a

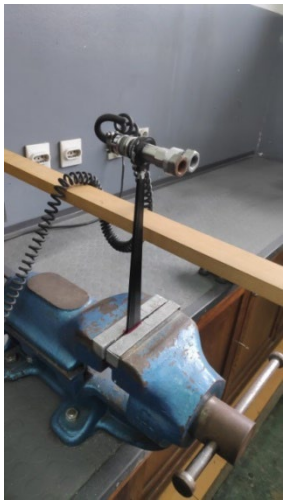

Configuration 1b and 2b

b

Configuration 1c and 2c

c

Fig. 9. Experimental setup

6.2 Numerical approach

A representative sample is considered. The fundamental natural frequency is computed using the Symbolic numeric method of initial parameters in differential form as explained in Chapter 3 of the paper.

Geometrical characteristics of the cross section with respect to the axial coordinate (z) are:

$$A(z) = 0.004(0.025 - 0.0625z); I_x(z) = (0.025 - 0.0625z)(0.004\,\hat{}\,3)/12. \tag{1.17}$$

The free length of the cantilever beam is L=228mm.

Elasticity modulus (MPa)		
2520.34	2703.54	2886.7
ω [rad/s]		
24.667384	25.548178	26.399423

Table 5. Computed natural frequencies for configuration 2c

5. Conclusions

A detailed study on coupled bending and axial vibrations of 3D printed cantilever beams with different boundary conditions is conducted in this paper. The study presents an upgrade of the practical work of the group of authors that studied coupled vibrations of axially functionally graded on theoretical level. The two material structures are designed, namely a linear layered and a two-dimensional periodic one. For each of the structures, the three different boundary conditions were imposed by changing mass and mechanical characteristics of the rigid body at the free end. The linear layered structured material is conducted to tensile test in order to obtain the elasticity modulus, which is implemented in numerical calculations. One experimental case has been chosen as the representative, and computations have been conducted. The obtained results of the measured and computed angular frequencies are comparable. Cantilever beams of specific material design are treated in this paper, both experimentally and numerically. Numerical model is applicable to the general beam designed, yet limitations are in the available experimental capacity. The presented paper is the introduction to more complex research in the field of vibrations of periodic structures made of novel materials.

Acknowledgment: Support for this research was provided by the Ministry of Education, Science and Technological Development of the Republic of Serbia under Grants Nos. 451-03-47/2023-01/200105 and 451-03-47/2023-01/200108. This support is gratefully acknowledged.

References:

[1] Koizumi M., *FGM activities in Japan*, Composites Part B, no. 28, pp. 1–4, 1997.
[2] Šalinić S.,Obradović A., Tomović A*., Free vibration analysis of axially functionally graded tapered, stepped, and continuously segmented rods and beams*, Composites Part B, no. 150, pp. 135–143, 2018.
[3] Nikolić A., *Free vibration analysis of a non-uniform axially functionally graded cantilever beam with a tip body*, Arch Appl Mech, no. 87, pp. 1227–1241, 2017.
[4] Zhao Y., Chen Y., Zhou Y., *Novel mechanical models of tensile strength and elastic property of FDM AM PLA materials: Experimental and theoretical analyses*, Materials and Design, no. 181, pp. 108089, 2019.
[5] Miniaci M., Krushynska A., Gliozzi A., Kherraz N., Bosia F., Pugno N., *Design and Fabrication of Bioinspired Hierarchical Dissipative Elastic Metamaterials*, Phys. Rev.

Applied 10, 024012, 2018.
[6] De Ponti J., Colombi A., Ardito R., Braghin F., Corigliano A., CrasterR., *Graded elastic metasurface for enhanced energy harvesting*, New J. Phys. 22, 013013, 2020.
[7] Aguzzi G., Colombi A., Dertimanis V., Chatzi E., *Metamaterials for groundborne vibration absorption in pillars*, 29th International Conference on Noise and Vibration Engineering (ISMA 2020) (virtual), Leuven, 2020.
[8] Tomović A., Šalinić S., Obradović A., Lazarević M., Mitrović Z., *The exact natural frequency solution of a free axial-bending vibration problem of a non-uniform afg cantilever beam with a tip body*, The 7th International Congress of Serbian Society of Mechanics, Sremski Karlovci, 2019.
[9] Rao S. S., *Vibration of Continuous Systems*. Hoboken, New Jersey: John Wiley & Sons inc., 2007.
[10] Biderman V.L., *Theory of mechanical Vibration*. USSR, Moscow: Vysshaya Shkola, 1980.

MECHANICAL RESPONSE OF V-SHAPED PROTECTIVE PLATES WITH DIFFERENT ANGLES UNDER BLAST LOADING

Miloš S. Pešić[1], Aleksandar S. Bodić[2], Živana M. Jovanović Pešić[2], Nikola B. Jović[2] and Miroslav M. Živković[2]

[1] Institute for Information Technologies, University of Kragujevac, Jovana Cvijica bb, 34000 Kragujevac, Serbia
e-mail: milospesic@uni.kg.ac.rs
[2] Faculty of Engineering, University of Kragujevac, Sestre Janjic 6, 34000 Kragujevac
e-mail: abodic@uni.kg.ac.rs, zixi90@gmail.com, njovic1995@gmail.com, miroslav.zivkovic.mfkg@gmail.com

Abstract

The effective design of armored personal vehicles requires an evaluation of the structural response of blast-resistant constructions such as Infantry Fighting Vehicles (IFVs), known as Mechanized Infantry Combat Vehicles (MICVs), or Armored Personal Vehicles (APVs), or Mine-Resistant Ambush-Protected (MRAP) vehicles. These structures' rigid designs will transmit blast forces into the troop's cabins, while their softer designs will result in excessive structure deformation that is hazardous to the troops. The troops in the cabin should experience the least amount of vibration and the least amount of blast-loading energy transmission in an ideal configuration. In this paper, the efficiency of different angled V-shaped plates under blast loading is examined. This study focuses on blast modeling for STRENX700 (S690QL) armor steel, which is utilized for blast protection in Anti-Landmine (ALM) Vehicles, using the Conventional Weapon (ConWep) method. The Johnson-Cook material model is applied to define the plate as a deformable solid. The V-shaped protective structure is subject to significant elastoplastic deformation as a result of landmine detonation within 4 milliseconds of the explosion. Blast-wave is associated with large deformation, erosion, high strain rate, dependent nonlinear material behavior, and fragmentation. In this paper, the results of numerical simulation for failure in V-shaped plates subjected to localized blasts at different included angles (from 145 to 180 degrees) are presented. The parameters chosen to represent the results were the maximal value of the vertical displacement of the central node on the protective plate and the maximal value of the von Mises equivalent stress.

Keywords: V-shaped plate, blast load, structural response, finite element method, explicit dynamic analysis.

1. Introduction

The threat posed by blast loading to both public and military infrastructure is severe. The soldiers in armored vehicles are seriously at risk of death due to the blast loading caused by landmines and improvised explosive devices (IEDs). For structural components like columns and plates, blast

loading has the potential to cause significant damage. Because there are so many factors to consider, like the angle of the V-shaped plate, the position, and shape of the charge, etc., it is challenging to determine how the armored vehicle will respond to a blast loading.

Examining the effects of the blast wave on the vehicle and its systems is vital to limit the deformation of the vehicle [1] and hence increase troop safety within the armored vehicle. The use of numerical simulations, which require fewer prototypes and take less time to develop, is validated in the paper [2] as a strategy for designing armored vehicles. In numerical simulations, FE models can be modeled with different types and with different sizes of finite elements. In order to achieve convergence, the floor and protective plates of the armored vehicle are modeled with five different mesh densities [3]. The body of the vehicle is covered with armored steel plates to protect it from explosions, making it an armored vehicle. The explosion protection plates can have different geometries [4]. Geometries that are investigated in papers [5-7] are V-shaped. Determining the ideal angle for the V-shaped protective plates is vital to ensure that the armored vehicle sustains the least amount of damage acceptable.

Levels 2, 3, and 4 of the NATO AEP-55 STANAG 4569 standard were followed in the research for this paper [8].

Determining the ideal angle for the V-shaped protective plates is the main objective of this paper. It is vital to ensure that the armored vehicle sustains the least amount of possible damage in order to protect troops and armored vehicles from the blast wave generated by ALM.

2. Problem description and FE models

A V-shaped protective plate is one of the best possible geometries to provide adequate protection to the troops, armored vehicles, and military equipment from the anti-landmine blasts. The hull is made of a metal plate that is installed beneath the floor of the armored vehicle and bent into a V shape. In order to determine the best angle, eight geometries of the V-shaped hull were developed (Fig.1). The explosion originated from an anti-landmine that is located directly under the V-shaped hull at a distance of 500 mm as shown in Fig.1. The protective plate is 2 m wide and 3 m long.

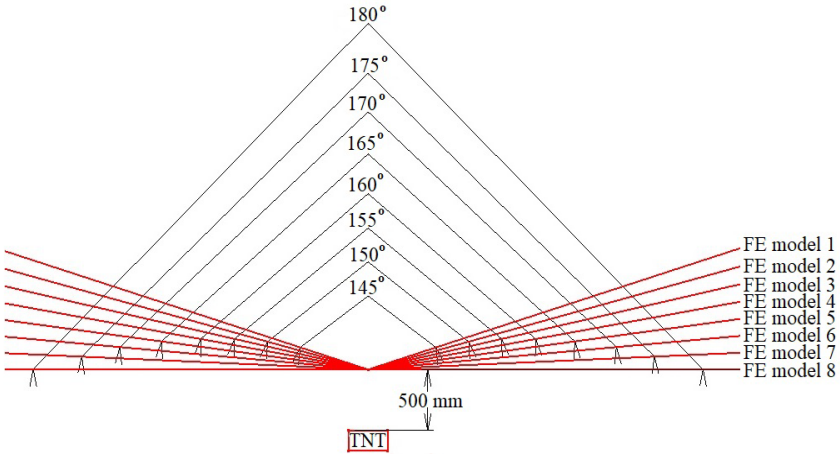

Fig. 1. Angles for V-shaped protective plate

All four edges of the plate are fixed to the floor of the armored vehicle. The material chosen for the protective plate is an appropriate type of steel. The V-shaped protective plates were numerically tested in order to resist 6 kg, 8 kg, and 10 kg of trinitrotoluene (TNT) exploding directly under the V-shaped hull. Many variables affect the parameters of the explosion: depth of burial, the composition of sand, the shape of the explosive, etc., but for this research, a simplified model of the explosion is used.

In this paper, the significance of the V-shaped protective plate angle in the reduction of incident explosion waves is examined. The clearance value for all analyzed models is the same. The mass of TNT explosives corresponds to levels 2, 3, and 4 of protection according to the NATO standard [8] and their mass is 6 kg, 8 kg, and 10 kg. The V-shaped protective plate thickness for all FE models is 12 mm. The input file for the LS-DYNA software [9] was exported after the FE model was created in the FEMAP v2021.2 program [10] using the CAD model. All other settings of the FE model for explicit dynamic analysis were performed in LS-DYNA software. FEMAP v2021.2 software was used for pre-processing and post-processing. All protective plates were exposed to a hemispherical incident wave. The floor of the vehicle is modeled with 3D hexahedral eight-noded finite elements, while the four-noded plate elements were used to model the V-shaped protective plates as shown in Fig. 2.

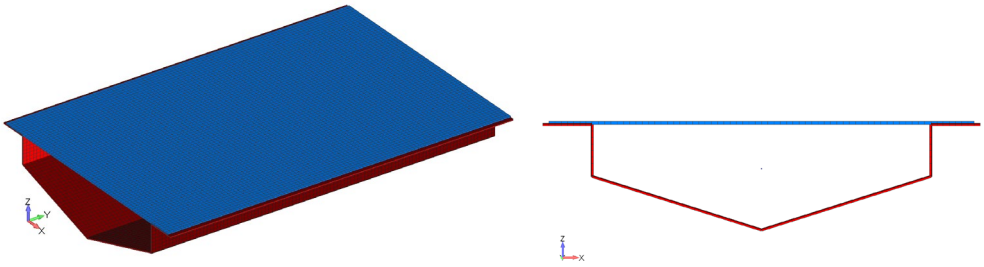

Fig. 2. FE model

The size of 3D hexahedral eight-noded finite elements is 30 mm x 30 mm x 15 mm, and the size of the four-noded plate elements is 30 mm x 30 mm.

3. Material model

Armor steel was chosen as the material for the V-shaped protective plate. When subjected to high strain rates, the material suffers plastic flow, temperature increase, and final possible failure as a consequence of the blast wave. In numerical simulations, the Johnson-Cook material model is frequently used to perform simulations that use temperature and high strain rate effects. The von Mises flow stress is expressed as:

$$\sigma = \left[A + B\varepsilon^{n}\right]\left[1 + C\ln\dot{\varepsilon}^{*}\right]\left[1 - T^{*m}\right] \tag{1}$$

the reference strain rate. T^{*} is the homologous temperature defined as $T^{*} = \dfrac{T - T_0}{T_{melt} - T_0}$. T is the material temperature, T_{melt} is the melting point temperature of the material, and T_0 is the reference temperature (room temperature). The material constants A, B, C, n, and m can be calculated using the tests suggested by Johnson and Cook (1985) or by fitting the flow stress data based on static and dynamic tests. The Johnson-Cook material model can also be used to simulate the material damage beginning and its development. The material damage is calculated using the value of the parameter D, which is defined as:

$$D = \sum \frac{\Delta\varepsilon}{\varepsilon^{f}} \tag{2}$$

where $\Delta\varepsilon$ is the equivalent plastic strain and ε^{f} is the equivalent strain to fracture. The fracture occurs when the parameter D reaches the value 1. The basic form of the fracture strain is given as:

$$\varepsilon^{f} = \left[D_1 + D_2 \exp D_3\sigma^{*}\right]\left[1 + D_4 \ln\dot{\varepsilon}^{*}\right]\left[1 + D_5 T^{*}\right] \tag{3}$$

where $\sigma^* = \frac{\sigma_m}{\bar{\sigma}}$ and σ_m is the average normal stress and $\bar{\sigma}$ is the von Mises equivalent stress. $D_1 - D_5$ are material damage parameters.

A number of armored steel varieties with differing degrees of ductility and strength are available. Steel with a moderate amount of ductility and enough strength is chosen for the analysis because ductility is a key factor in the energy dissipation caused by blast loading. Young's Modulus (E=228 GPa), Poisson's ratio (ν=0.3), and density (ρ=7850 kg/m^3) of S690QL steel are equal to mild steel, but because of its increased strength, S690QL steel is substantially stiffer when loaded (σ_y=750-800 MPa). In the Table 1 are shown Johnson-Cook material characteristics for S690QL steel.

Parameters	Values
Density ρ (t/mm^3)	7.85E-9
Young's Modulus E (MPa)	228368.9
Poisson's ratio v	0.3
Yield stress A (MPa)	767.38
Proportionality coefficient B	445.13
Reinforcement exponent n	0.5075
Strain rate Impact parameter C	0.0265
Temperature Impact parameter m	1.354
Damage parameter D_1	-0.066
Damage parameter D_2	3.028
Damage parameter D_3	-1.408
Damage parameter D_4	-0.00851
Damage parameter D_5	0.633

Table 1. Johnson-Cook material parameters for S690QL steel

The material parameters shown in table 1 were experimentally obtained on the split Hopkinson tension bar (SHTB) and validated using the finite element simulations in LS-DYNA.

4. Results and discussion

In order to decide which geometry would be the best to use as anti-mining protection, the results of explicit dynamic analysis of all eight FE models were compared. All FE models were tested with a simulated TNT weight of 6 kg, 8 kg, and 10 kg which corresponds to levels 2, 3, and 4 of the NATO AEP-55 STANAG 4569 standard.

The maximum value of the vertical displacement of the central node on the protective plate, which is located on the longitudinal plane of symmetry in the direction perpendicular to the protective plate, and the maximum value of the von Mises equivalent stress, has been chosen as the parameters to compare the results of each model.

The maximal value of vertical displacement of the central node on the protective plate and the maximal value of von Mises stress for all eight FE models are shown in Table 2.

FE model ID	TNT – 6 kg		TNT – 8 kg		TNT – 10 kg	
	Vertical	von Mises	Vertical	von Mises	Vertical	von Mises

	displacement (m)	stress (MPa)	displacement (m)	stress (MPa)	displacement (m)	stress (MPa)
ID 1 - 145°	0.10	977.79	0.15	1029.2	0.23	1108.37
ID 2 - 150°	0.13	987.78	0.21	1079.18	0.27	1124.09
ID 3 - 155°	0.18	1026.2	0.24	1076.77	0.27	1095.68
ID 4 - 160°	0.20	1024.29	0.23	1048.53	0.26	1065.86
ID 5 - 165°	0.19	993.64	0.22	997.88	0.25	1012.47
ID 6 - 170°	0.17	957.35	0.20	977.83	0.24	992.86
ID 7 - 175°	0.14	959.1	0.18	988.97	0.23	1004.57
ID 8 - 180°	0.12	957.76	0.16	1007.79	0.21	1048.41

Table 2. Results of numerical analysis for all eight FE models

Maximal values of the vertical displacement of the central node on the protective plate which is located on the longitudinal plane of symmetry in the direction perpendicular to the protective plate for a TNT mass of 6 kg are shown in the diagram in Fig. 3.

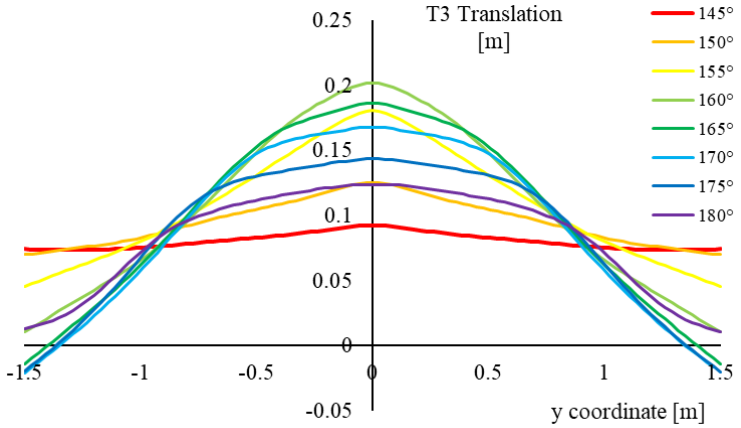

Fig. 3. Values of vertical displacement of the central node on the protective plate for all eight FE models under blast loading for a TNT mass of 6 kg

Based on the obtained results, which are shown in Table 2 and the diagram in Fig. 3, it can be concluded that FE models with the smallest (ID 1 - 145°) and the largest (ID 8 - 180°) angle have the smallest vertical displacement (highest stiffness). As can be seen from Table 2 FE models (ID 2 - 150°) and (ID 7 - 175°) also have high stiffness. The lowest values of von Mises stress have FE models (ID 1 - 145°), (ID 6 - 170°), (ID 7 - 175°), and (ID 8 - 180°). The smallest value of von Mises stress has an FE model (ID 6 - 170°) 957.35 MPa.

Maximal values of the vertical displacement of the central node on the protective plate which is located on the longitudinal plane of symmetry in the direction perpendicular to the protective plate for a TNT mass of 8 kg are shown in the diagram in Fig. 4.

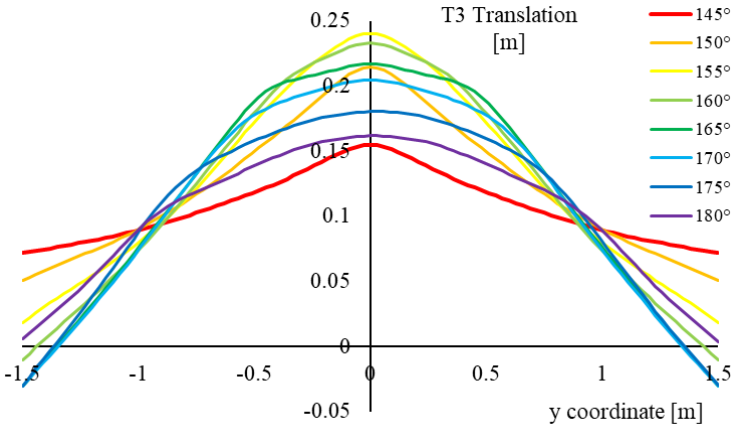

Fig. 4. Values of vertical displacement of the central node on the protective plate for all eight FE models under blast loading for a TNT mass of 8 kg

Based on the obtained results, which are shown in Table 2 and the diagram in Fig. 4, it can be concluded that FE models with the smallest (ID 1 - 145°) and the largest (ID 8 - 180°) angle have the smallest vertical displacement (highest stiffness). As can be seen from Table 2 FE model (ID 7 - 175°) also have high stiffness. The lowest values of von Mises stress have FE models (ID 5 - 165°), (ID 6 - 170°), (ID 7 - 175°), and (ID 8 - 180°). The smallest value of von Mises stress has an FE model (ID 6 - 170°) 977.83 MPa.

Maximal values of the vertical displacement of the central node on the protective plate which is located on the longitudinal plane of symmetry in the direction perpendicular to the protective plate for a TNT mass of 10 kg are shown in the diagram in Fig. 5.

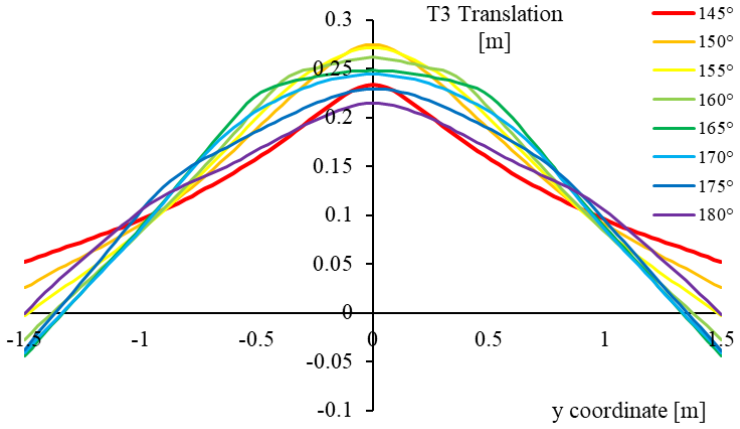

Fig. 5. Values of vertical displacement of the central node on the protective plate for all eight FE models under blast loading for a TNT mass of 10 kg

Based on the obtained results, which are shown in Table 2 and the diagram in Fig. 5, it can be concluded that FE models with the smallest (ID 1 - 145°) and the largest (ID 7 - 175° and ID 8 - 180°) angle have the smallest vertical displacement (highest stiffness). The highest value of vertical displacement has FE models (ID 2 - 150°), and (ID 3 - 155°). The lowest values of von Mises stress have FE models (ID 5 - 165°), (ID 6 - 170°), and (ID 7 - 175°). The smallest value of von Mises stress has an FE model (ID 6 - 170°) 992.86 MPa.

An example of vertical displacement of the central node on the protective plate for FE model 6 with a simulated TNT weight of 8 kg is shown in Fig. 6.

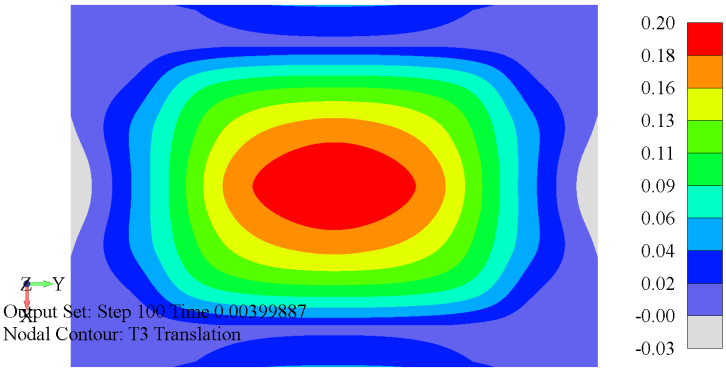

Fig. 6. Vertical displacement distribution

Von Mises equivalent stress distribution for FE model 6 with a simulated TNT weight of 8 kg is shown in Fig. 7.

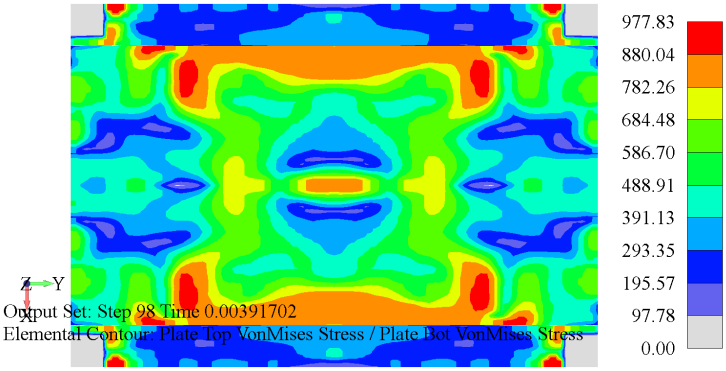

Fig. 7. Von Mises equivalent stress distribution

5. Conclusions

This study uses numerical simulation to analyze the mechanical response of V-shaped protective plates with different angles subjected to blast loading. The focus of this study is to determine the optimal angle of the V-shaped protective plate which can be used for Infantry Fighting Vehicles (IFVs), known as Mechanized Infantry Combat Vehicles (MICVs), or Armored Personal Vehicles (APVs), or Mine-Resistant Ambush-Protected (MRAP) vehicles. From the analysis using FEM, the following conclusions, which are based on the maximal value of the vertical displacement of the central node on the protective plate and the maximal value of the von Mises equivalent stress, are reached:

- In general, the maximal value of the protective plate vertical displacement increases with the increase of the TNT mass;
- Maximal value of the von Mises equivalent stress increases with the increase of the TNT mass;
- The smallest vertical displacement of the central node on the protective plate, i.e., the highest stiffness has a protective plate in the FE model (ID 1 - 145°) and (ID 8 - 180°).
- The smallest value of von Mises stress has an FE model (ID 6 - 170°) for all three load cases (6 kg, 8 kg, and 10 kg of TNT).
- In order to achieve a more efficient configuration of protection, developing anti-mining protection should be a major step in the process of developing a complete vehicle.

Further study will concentrate on the use of various protective plate geometries, as well as various types of high-strength steels, sandwich constructions, and composite materials to protect troops, armored vehicles, and military equipment from the effects of ALMs and IEDs.

Acknowledgements: This research is partly supported by the Ministry of Science, Technological Development and Innovation, Republic of Serbia, Agreement No. 451-03-47/2023-01/200378 and Grant TR32036.

References:

[1] Sunil Kumar M.R., Schmidova E., *Deformation Response of Dual Phase Steel in Static and Dynamic Conditions*, Applied Engineering Letters, Vol. 4, 41–47, 2019.

[2] Mahajan S., Muralidharan R., *Simulation of an Armoured Vehicle for Blast Loading*, Defence Science Journal, Vol. 67, 449, 2017.

[3] Pešić M., Jović N., Milovanović V., Pantić M., Živković M., *FE Mesh Density Influence on Blast Loading Analysis*, IOP Conference Series: Materials Science and Engineering, Vol. 1271, 012016, 2022.

[4] Pešić M., Jović N., Milovanović V., Savić D., Aničić A., Živković M., Savić S., *FEM Analysis of Anti-Mining Protection of Armored Vehicles*, Applied Engineering Letters, Vol. 7, 89–99, 2022.

[5] Trajkovski J., Perenda J., Kunc R., *Blast Response of Light Armoured Vehicles (LAVs) with Flat and V-Hull Floor*, Thin-Walled Structures, Vol. 131, 238–244, 2018.

[6] Cong M., Zhou Y., Zhang M., Sun X., Chen C., Ji C., *Design and Optimization of Multi-V Hulls of Light Armoured Vehicles under Blast Loads*, Thin-Walled Structures, Vol. 168, 108311, 2021.

[7] Markose A., Rao C.L., *Mechanical Response of V Shaped Plates under Blast Loading*. Thin-Walled Structures, Vol. 115, 12–20, 2017.

[8] NATO, *AEP-55 Procedures for Evaluating the Protection Level of Armored Vehicles – Mine Threat*, NATO Standardization Agency, Vol. 2, 2014.

[9] LS-DYNA, *LS-PrePost-4.5-A New Post Processor for Use LSDYNA*, California: Livermore, 2014.

[10] Femap, *Finite Element Modeling and PostProcessing Application FEMAP v2021.2*, Siemens, 2021.

COMPARATIVE ANALYSIS OF SPH AND FVM NUMERICAL SIMULATIONS OF BLOOD FLOW THROUGH LEFT VENTRICLE

Aleksandar S. Bodić[1], Marko D. Topalović[2], Miljan S. Milošević[2,3] Miroslav M. Živković[1], and Miloš S. Pešić[2]

[1] Faculty of of Engineering, University of Kragujevac, Kragujevac 34000, Serbia
e-mail: abodic@uni.kg.ac.rs , zile@kg.ac.rs
[2] Institute for Information Technologies, University of Kragujevac, Kragujevac 34000, Serbia
e-mail: topalovic@kg.ac.rs , miljan.m@kg.ac.rs , milospesic1736@gmail.com
[3] Belgrade Metropolitan University, Belgrade, Serbia

Abstract

The purpose of this research was to compare blood flow modeling inside the heart's left ventricle using commercial smoothed particle hydrodynamics (SPH) and finite volume method (FVM) solvers. These two methods are both based on continuum mechanics, and while FVM uses Eulerian material framework, SPH uses a Lagrangian formulation. In this study, the focus was only on CFD analysis of blood flow through the left ventricle using the two mentioned methods. Therefore, in the numerical analysis using FVM, walls were modeled as boundary conditions where fluid velocity was set to zero. The ventricle wall in the SPH was modeled using larger, fixed fluid particles, so at this point, there is no need for a specific contact definition. *LS-DYNA* software was used for modeling the left ventricle using the SPH method. In order to generate realistic fluid flow injection particles at the mitral valve and deactivation planes at the aortic semilunar valve were used where particle velocity was defined by time functions. *Ansys Fluent* software was used for modeling the left ventricle using FVM, within which a finite volume mesh was generated. Velocities at the inlet and outlet of the model are defined by functions using User Defined Function (UDF) so that the fluid flow corresponds to the realistic blood flow through the left ventricle. The results obtained by FVM were used as a verification of the results obtained using the SPH method. In the results section of the paper, the velocity field obtained by SPH and FVM methods is shown and compared. SPH offers greater possibilities to study FSI phenomena like the effects of wall deformations, or tracking the movement of solid particle inclusion, all within the single numerical domain. On the other hand, it requires elaborate contact definition, and prolonged analysis time in comparison to the finite volume CFD analysis.

Keywords: SPH, FVM, Lagrangian formulation, Eulerian formulation, left ventricle model, Bioengineering, Fluid flow

1. Introduction

Despite significant advances in medicine, cardiovascular diseases are still one of the leading causes of death in the world. For this reason, studies related to the evaluation of heart function are increasing significantly. Understanding cardiac blood flow patterns has various applications in

studying haemodynamics as well as for the clinical evaluation of heart function [1]. Various experimental techniques are used to investigate blood flow patterns. Among the experimental techniques, imaging techniques such as Doppler ultrasound echocardiography [2, 3] and magnetic resonance imaging (MRI) [4, 5] are most common. Although these techniques have advanced significantly and provide a lot of information about the blood flow pattern through the left ventricle, there is still plenty of room for improvement, especially in terms of increasing the spatial and/or temporal resolution [6]. In addition to experimental techniques, computer simulations such as computational fluid dynamics (CFD) are also applied for these purposes, which are most often performed using the finite volume method (FVM), finite element method (FEM) and smoothed particle hydrodynamics (SPH). Their advantage is that they provide a much more complete picture of blood flow through the left ventricle with more details compared to classical methods.

SPH is a mesh-free numerical method [7], based on continuum mechanics, where the analyzed continuum is divided into sub-domains called pseudo-particles [8]. Originally designed for astrophysical problems [9,10], it was later extended to CFD [11] and solid mechanics [12]. SPH uses the Lagrangian material framework to observe the motion of a particular domain section [7], no matter the state or the composition, while the FVM which is also based on continuum mechanics, uses the Eulerian spatial formulation to observe a fixed volume through which the fluid flows [13]. While Eulerian formulation is accurate in predicting pressure and fluid velocity, a Lagrangian formulation is needed to observe particle movements and interactions within the fluid flow. Fig. 1 shows the difference between Lagrangian and Eulerian formulation using the finite element method (FEM) as an example [14], because this method can use both, although it was not used in this paper.

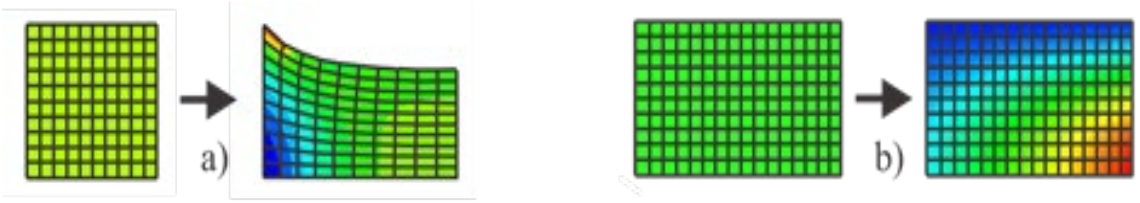

Fig. 1. Numerical formulations: a) Lagrangian b) Eulerian

In this paper, numerical simulations of blood flow through the left ventricle using commercial SPH and FVM solvers are conducted and results obtained from both methods are compared. This paper aims to facilitate the utilization of the SPH method in bioengineering modeling [15] of the cardiovascular system by addressing its challenges, primarily the need for comprehensive boundary conditions [16] and high computational demands that can be seen as a limitation or drawback, as SPH requires significant computing power and time to produce accurate results.

The paper also gives the procedure for modeling blood flow through the left ventricle using FVM. The results obtained by FVM within *Ansys Fluent* software were used as a verification of the results from *LS-DYNA* software obtained using the SPH method.

In chapter 2 of this paper, a brief retrospective of SPH kernel and particle approximation is given, as well as the procedure for modeling the left ventricle using the SPH method within the *LS-DYNA* software. In chapter 3, governing equations of fluid dynamics are given, as well as the procedure for numerical analysis of the left ventricle using FVM in the *Ansys Fluent* software. Also, the procedure for creating a model, defining regions on the model and setting boundary conditions on them is given. A comparison of the results obtained using both methods is given in chapter 4. The conclusion summarizes the outcomes shown in this paper and points out our future research.

2. Numerical analysis of blood flow through left ventricle using SPH method

2.1 SPH method

SPH models continuous matter with the kernel and particle approximations [7] and express the conservation laws of continuum mechanics as partial differential equations. These equations are transformed into integral equations with interpolation functions that estimate field variables at specific points. The exact value of the function $f(\mathbf{x})$ in integral form is given by equation (1):

$$f(\mathbf{x}) = \int_{\Omega} f(\mathbf{x}')\delta(\mathbf{x}-\mathbf{x}')d\mathbf{x}' \tag{1}$$

where $f(\mathbf{x})$ is a function of the position vector $\mathbf{x}$ of the observed pseudo-particle and $\mathbf{x}'$ is the position vector of the material point that belongs to the domain of influence Ω.

The Dirac delta measure [7] $\delta(\mathbf{x}-\mathbf{x}') = \begin{cases} 1 & \mathbf{x}=\mathbf{x}' \\ 0 & \mathbf{x}\neq\mathbf{x}' \end{cases}$ is not practical for computational applications, therefore it is replaced with bell-shaped kernel function $W(|\mathbf{x}-\mathbf{x}'|,h)$ where h is the smoothing length (bell base radius), which gives us a kernel approximation [7] of function $f(\mathbf{x})$:

$$\langle f(\mathbf{x})\rangle = \int_{\Omega} f(\mathbf{x}')W(|\mathbf{x}-\mathbf{x}'|,h)d\mathbf{x}' \tag{2}$$

Likewise, the integral form of equation (2) is not appropriate for numerical implementation because the continuous material being analyzed is divided into a finite number of particles, each with its own mass and occupying individual space. As a result, equation (2) is converted into a discrete form, which is expressed as a sum over all particles within the support domain [7]. The infinitesimal volume $d\mathbf{x}'$ is replaced by finite volume of the particle $\Delta V_\beta = m_\beta/\rho_\beta$ where m_β and ρ_β are particle mass and particle density [7]. With the summation of all particles within the support domain implemented in Eq. (2) we get particle approximation of a function $f(\mathbf{x})$ for particle α:

$$\langle f(\mathbf{x}_\alpha)\rangle \cong \sum_{\beta=1}^{NNP} f(\mathbf{x}_\beta)W(|\mathbf{x}_\alpha-\mathbf{x}_\beta|,h)dV_\beta = \sum_{\beta=1}^{NNP}\frac{m_\beta}{\rho_\beta}f(\mathbf{x}_\beta)W(|\mathbf{x}_\alpha-\mathbf{x}_\beta|,h) \tag{3}$$

where NNP is the number of nearest neighbouring particles [7].

Using the equation (3), which incorporates kernel and particle approximations, the conservation laws of continuum mechanics are programmed into the SPH solvers, which use an explicit integration scheme to calculate acceleration, velocity, displacement, energy and other values of interest, such as total stress tensor σ_{ij}, which in the viscous fluid [8] consists of the hydrostatic pressure p and viscous stress ${}^{visc}\tau_{ij}$:

$$\sigma_{ij} = -p\delta_{ij} + {}^{visc}\tau_{ij} \tag{4}$$

Viscous stress [7] can be calculated as:

$${}^{visc}\tau_{ij} = \mu\left(\partial_i v_j + \partial_j v_i - \frac{2}{3}\partial_k v_k \delta_{ij}\right) = \mu\varepsilon_{ij} \tag{5}$$

where μ is the coefficient of dynamic viscosity and ε_{ij} is the strain rate tensor [7]:

$$\varepsilon_{ij}^{\alpha} = \sum_{\beta=1}^{NNP} \frac{m_\beta}{\rho_\beta} v_j^{\beta\alpha} \frac{\partial W^{\alpha\beta}}{\partial x_i^{\alpha}} + \sum_{\beta=1}^{NNP} \frac{m_\beta}{\rho_\beta} v_i^{\beta\alpha} \frac{\partial W^{\alpha\beta}}{\partial x_j^{\alpha}} - \left(\frac{2}{3} \sum_{\beta=1}^{NNP} \frac{m_\beta}{\rho_\beta} \mathbf{v}^{\beta\alpha} \cdot \nabla_\alpha W^{\alpha\beta} \right) \delta_{ij} \tag{6}$$

Hydrostatic pressure p is calculated using the Murnaghan equation of state [7]:

$$p = k_0 \left[\left(\frac{\rho}{\rho_0} \right)^{\gamma} - 1 \right] \tag{7}$$

where ρ_0 is the density of the fluid at rest, while k_0 and γ are the material parameters.

2.2 SPH analysis of the left ventricle using LS-DYNA

The primary research and development focus of the commercial *LS-DYNA* solver [17] is not on fluid flow in SPH, especially not its application in the field of bioengineering. There are numerous published papers and examples utilizing academic or open-source SPH solvers, but they all have some solution for generation and deletion of SPH particles. Nevertheless, the LS-DYNA manual [17] contains a description of keywords such as BOX, BOX_LOCAL, BOUNDARY_SPH_FLOW, SPH_INJECTION, PRESCRIBED_MOTION_SET_BOX, CONTROL_SPH (BOXID) and SET_NODE_LIST_GENERATE which can activate and deactivate SPH particles. These can be used to create the variable fluid flow [18] shown in Figure 2. The inlet velocity function at mitral valve corresponds to realistic cardiac cycle (Fig. 2a). In the first approximately 0.5 seconds mitral valve is opened and the blood flows into the left ventricle from the atrium part. Subsequently, due to the ventricle contraction, blood is forced out through the aortic valve at a velocity defined by the function shown in Fig. 2b.

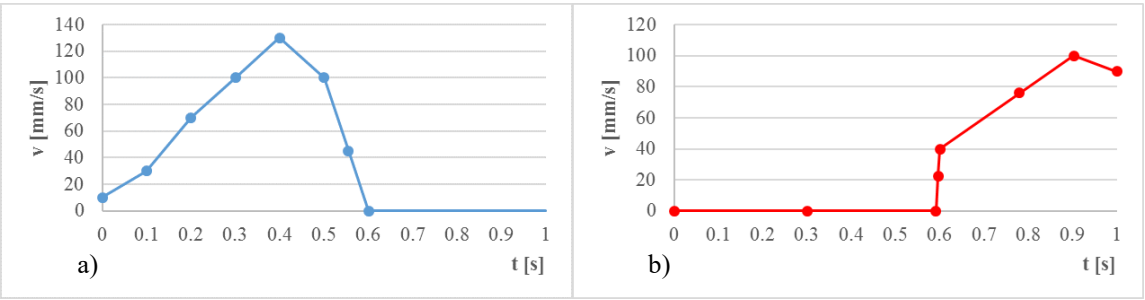

Fig. 2. Boundary flow: a) inlet velocity at mitral valve, b) outlet velocity at the aortic semilunar valve

Before *LS-DYNA* version R12.0.0 from 2020 which added option to define a variable speed of injection in the SPH_INJECTION keyword [17], this option could only produce a constant particle flow and could not be used for hemodynamic analysis. The only alternative was to use a BOUNDARY_SPH_FLOW keyword [17] with a long streak of SPH particles shown in Fig. 3.

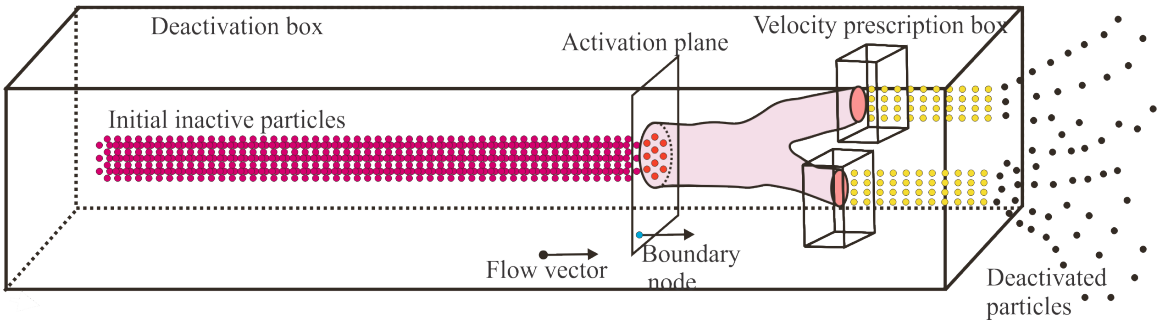

Fig. 3. Obsolete generation of fluid flow using BOUNDARY_SPH_FLOW keyword

The latest versions of LS-DYNA require a negative injection speed scale factor to be set for the SPH_INJECTION keyword [17] to prescribe a variable speed. This means that instead of a constant value, the scale factor now takes values from a DEFINE_CURVE keyword [17]. However, the new problem with this approach is that new SPH particles can collide with existing ones and cause an explosion or bounce away. To overcome this, a PRESCRIBED_MOTION_SET_BOX keyword is used, which creates a box in front of the injected particles that is at least two inter-particle distance wide. Within the PRESCRIBED_MOTION_SET_BOX keyword parameters [17], a DEFINE_CURVE is used to prescribe a continuous inflow of particles into the left ventricle of the heart according to Fig. 2 a). A similar approach is used at the aortic semilunar valve to define outlet velocity according to Figure 2 b). These keywords do not define motion for all of the SPH particles in the model, but only to those particles specified in the NODE_LIST keyword. To solve this issue, a PRESCRIBED_MOTION_SET_BOX keyword [17] is used twice at the aortic semilunar valve outlet: once with NODE_LIST for preexisting particles and the second time with NODE_LIST_GENERATE [17] for the new, injected particles. The functionality of the model is illustrated in the Fig. 4.

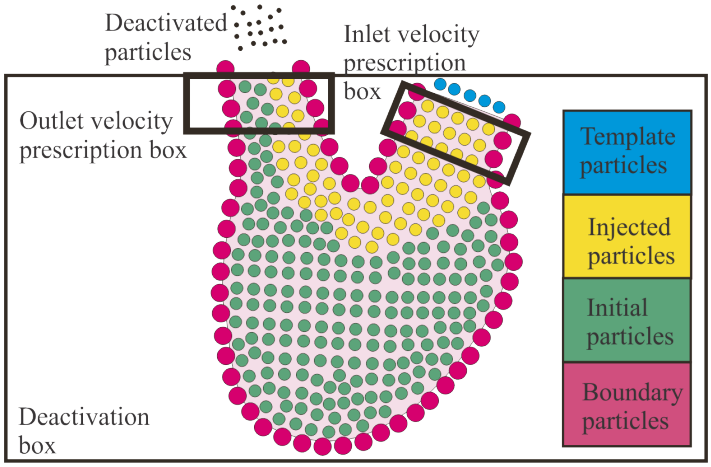

Fig. 4. Improved generation of fluid flow using SPH_INJECTION keyword

3. CFD analysis of left ventricle using Fluent

Blood flow through left ventricle is considered as laminar flow of incompressible fluid and can be defined by Navier–Stokes equations and continuity equation [15]:

$$-\mu\nabla^2 v_l+\rho\left(v_l\cdot\nabla\right)v_l+\nabla p_l=0 \tag{8}$$

$$\nabla v_l=0 \tag{9}$$

where v_l represents fluid velocity, p_l is the pressure, μ is the dynamic viscosity coefficient, and ρ is the fluid density.

Material parameters of blood used in numerical simulations are given in Table 1.

Material parameter	Value
Density [kg/m^3]	1060
Viscosity [Pa·s]	0.001

Table 1. Material parameters of blood

Geometry of left ventricle [18] is created using user interface software CAD Field & Solid [19]. Based on this geometry, finite volume mesh is generated in software *Ansys Fluent*. The

model is created using tetrahedral finite volume cells. Quality of the mesh is checked using Fluent Meshing, and maximum cell skewness was 0.84. The average size of cell is set as 2 mm, while the entire model consists of 62208 cells and 11972 nodes. The finite volume model of the left ventricle is shown in Fig. 5a.

Within the fluent meshing, regions are created on the model that represent the inlet, outlet, wall, and symmetry plane (Fig. 5b). Based on these regions, boundary conditions are set on the model. At inlet and outlet prescribed velocity functions are set as shown in Fig. 2.

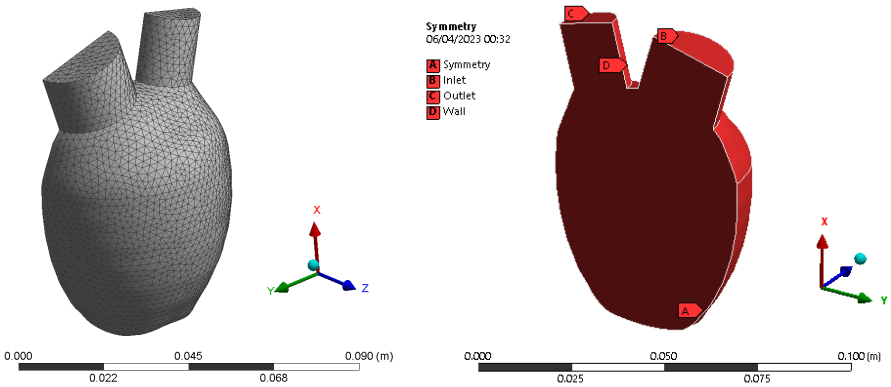

Fig. 5. a) Finite volume mesh of left ventricle and b) Defined regions on the left ventricle model

For the purpose of defining the prescribed velocities at inlet and outlet a User Defined Function (UDF) is created. As within the used version of *Fluent* there is no way to define fluid velocity at the outlet, the model consisted of "two inlet regions". At the inlet region from atrium part, a velocity is set using the UDF so that it corresponds to the function in Fig. 2a. On the other hand, at the "inlet region of the aortic valve" (model output), the velocity is set using UDF so that the function in Fig. 2b is reversed. In this way, the outflow of blood from the left ventricle through the aortic valve due to the contraction of the heart muscle walls was simulated. Transient analysis is performed in 500 time steps with time step size of 0.002 s.

4. Results and Discussion

As can be seen from Figure 2, the maximum value of inlet velocity occurs at 0.4 seconds [18], and we will compare velocity fields obtained using *LS-DYNA* and *Fluent* at that particular time, which will be shown in Figure 6. The maximum prescribed outlet velocity is defined at 0.9 seconds [18], but at that time fluid velocities within the volume of the ventricle are negligible, so more appropriate time of 0.8 seconds is shown in Fig. 7.

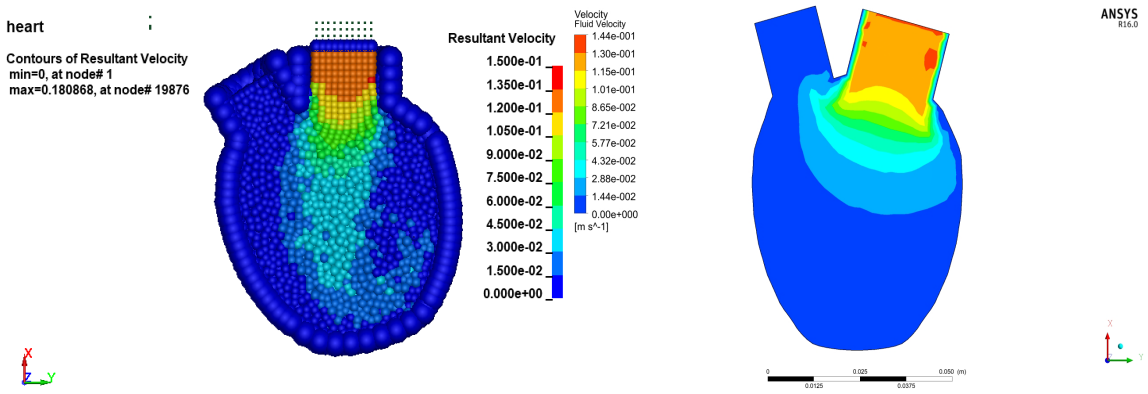

Fig. 6. Velocity field at 0.4 s: a) Ls-DYNA b) Fluent

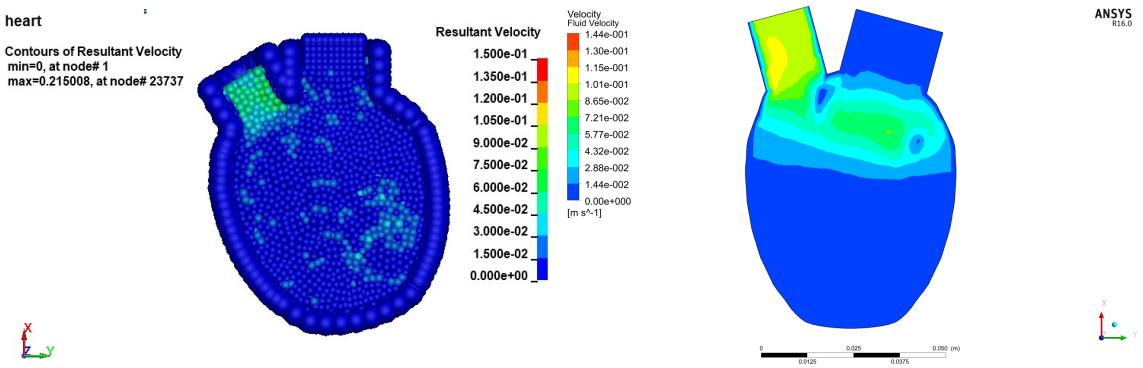

Fig. 7. Velocity field at 0.8 s: a) Ls-DYNA b) Fluent

As can be seen from previous figures, both SPH and FVM solvers produced similar velocity fields. Smaller deviations in the results can be observed after 0.6 s, when the blood starts to flow through the aortic valve. These deviations can be explained by the nature of the SPH method, due to which small fluctuations of particle velocity occur. It should also be noted that SPH analysis lasted 25 hours, while FVM took about 30 minutes on AMD Ryzen 7 5800X with 128 GB DDR4. For purely CFD simulations, FVM method is obviously the best choice, but if the multyphysics and multiscale calculations are required, SPH represents a flexible, scalable and unified base for further research.

5. Conclusions

SPH method is often used in maritime engineering to predict fluid-structure interaction between vessels and surrounding water, as well as in aeronautical engineering to predict bird strikes or crash-landing. However, these calculations are done with static fluid, and vessels or objects that impact these vessels travelling at high speeds. In this paper, we used SPH for bioengineering analysis that required modeling of continuous, variable fluid flow. Within the *LS-DYNA* software, blood flow through the left ventricle was modeled using the SPH method. Additionally, the same problem is modeled using FVM within the *Ansys Fluent* software. The results obtained using the FVM were used as a verification of the numerical analysis using the SPH method. By comparing the results obtained using both methods, it can be concluded that the results obtained within the *LS-DYNA* software are similar to the results obtained in the *Ansys Fluent* software.

Although the results in both software are similar, it should be noted that the prescription of boundaries is much more difficult in *LS-DYNA* in comparison to *Fluent*. In order to achieve realistic blood flow, we used a combination of several keywords in *LS-DYNA* input file and prescribed inlet and outlet velocities by defining appropriate boxes. Execution time is also significantly longer for SPH analysis, but this method can be used for more sophisticated analysis of fluid-structure interaction within the Lagrangian material framework, which will be the focus of our future research.

Acknowledgements: This research is supported by the Ministry of Science, Technological Development and Innovations, Republic of Serbia, Agreement No. 451-03-47/2023-01/200378 and Grant TR32036.

References:

[1] Moosavi MH, Fatouraee N, Katoozian H, Pashaei A, Camara O, Frangi AF. Numerical simulation of blood flow in the left ventricle and aortic sinus using magnetic resonance

imaging and computational fluid dynamics, Comput Methods Biomech Biomed Engin., Vol. 17, Iss. 7, 740-749, 2012.
[2] Pedrizzetti, G., La Canna, G., Alfieri, O. et al., The vortex—an early predictor of cardiovascular outcome?, Nat Rev Cardiol, Vol 11, 545–553, 2014
[3] Mele, D., Smarrazzo, V., Pedrizzetti, G., Capasso, F., Pepe, M., Severino, S et al., Intracardiac Flow Analysis: Techniques and Potential Clinical Applications, Journal of the American Society of Echocardiography, Vol. 32, Iss. 3, 319-332, 2019.
[4] Elbaz, M. S. M., van der Geest, R. J., Calkoen, E. E., de Roos, A., Lelieveldt, B. P. F., Roest, A. A. W., Westenberg, J. J. M., Assessment of viscous energy loss and the association with three-dimensional vortex ring formation in left ventricular inflow: In vivo evaluation using four-dimensional flow MRI, Magnetic Resonance in Medicine, Vol. 77, Iss. 2, 794-805, 2016.
[5] Eriksson, J., Dyverfeldt, P., Engvall, J., Bolger, A. F., Ebbers, T., Carlhäll, C. J., Quantification of presystolic blood flow organization and energetics in the human left ventricle, American Journal of Physiology-Heart and Circulatory Physiology, Vol. 300, Iss. 6, H2135-H2141, 2011.
[6] Xu F., Kenjereš S., Numerical simulations of flow patterns in the human left ventricle model with a novel dynamic mesh morphing approach based on radial basis function, Computers in Biology and Medicine, Vol. 130, 2021.
[7] Liu G., Liu M., Smoothed Particle Hydrodynamics, World Scientific Publishing, 2003.
[8] Vignjević R., Campbell J., Brief review of development of the smooth particle hydrodynamics (SPH) method, IConSSM 2011 - The 3rd International Congress of Serbian Society of Mechanics, Vlasina lake, Serbia, 5-8 July 2011, 24-43.
[9] Gingold R. A., Monaghan J. J., Smoothed particle hydrodynamics: theory and application to non-spherical stars, Monthly Notices Royal Astronomical Society, Vol. 181, 375-389, 1997.
[10] Lucy L. B., A numerical approach to the testing of fusion process, Astronomical Journal, Vol. 88, 1013-1024, 1997.
[11] Monaghan, J., J., Pongracic H., Artificial viscosity for particle methods, Applied Numerical Mathematics Vol. 1, 187-194, 1985.
[12] Libersky L. D., Petschek A. G., Carney T. C., Hipp J. R., Allahdadi F. A., High Strain Lagrangian Hydrodynamics: A Three-Dimensional SPH Code for Dynamic Material Response, Journal of Computational Physics, Vol. 109. 67-75, 1993.
[13] ANSYS Fluent Theory Guide, Ansys Inc., 2013.
[14] Bathe K., Finite element Procedures, Prentice Hall: Pearson Education, Inc., 2006.
[15] Kojic M., Filipovic N., Stojanovic B., Kojic N., Computer Modeling in Bioengineering: Theoretical Background, Examples and Software, John Wiley & Sons, 2009.
[16] Vacondio R., Altomare C., De Leffe M., Hu X., Le Touzé D., Lind S., Marongiu J-C., Marrone S., Rogers B., D., Souto-Iglesias A., Grand challenges for Smoothed Particle Hydrodynamics numerical schemes. Computational Particle Mechanics, Vol. 8. 575–588, 2021.
[17] LS-DYNA Theory Manual, Livermore Software Technology Corporation, 2022.
[18] Tomasevic S., Milosevic M., Milicevic B., Vladimir Simic V., Prodanovic M., Mijailovich S., Filipovic N., Computational Modeling on Drugs Effects for Left Ventricle in Cardiomyopathy Disease, Pharmaceutics, Vol. 15, No. 3. 793, 2023.
[19] Milošević M., CAD Solid and Field, https://github.com/miljanmilos/CAD-Solid-Field

PHASE-FIELD MODELING OF LOW CYCLIC FATIGUE IN DUCTILE MATERIALS

Vladimir Lj. Dunić[1], Miroslav M. Živković[1], Vladimir P. Milovanović[1] and Jelena M. Živković[1]

[1] Faculty of Engineering, University of Kragujevac, Sestre Janjić 6, 34000 Kragujevac, Serbia
e-mail: dunic@kg.ac.rs

Abstract

Plastic strains in engineering structures occur if the loading conditions exceed the designed values. The loading above the yield strength of the material leads to fatigue of the structure and fracture. The fracture occurs after a lower number of cycles, in comparison to the high cyclic fatigue when the material operates in the elastic range. However, the fatigue behavior of structures made of ductile materials in the range above the yield strength can be simulated by Phase-Field Damage Modeling (PFDM) approach, which includes a fatigue degradation function. In this paper, the cyclic tensile loading-unloading behavior is simulated by PAK finite element method software with Von Mises plasticity constitutive model and Simo's hardening function. The material parameters are proposed for generic metal with the phase-field constants set to show the phenomena which can be simulated. The results show that the proposed theory and implementation should be further investigated and applied to simulate the experimental testing of ductile materials under cyclic loading and fatigue conditions.

Keywords: cyclic loading, fatigue, plasticity, phase-field modeling, damage, ductile materials.

1. Introduction

Low cyclic fatigue (LCF) can be defined as repeated loading-unloading of material that exhibits plastic strains. The loading amplitude is above the yield strength, leading to fatigue and fracture after fewer cycles compared to the high cyclic fatigue (HCF) when the structures operate in an elastic range.

There are various constitutive models for the plasticity of engineering materials, such as metals, alloys, polymers, etc., but steel and aluminum are the most used mechanical engineering materials. The well-known Von Mises plasticity constitutive model can be used for that purpose. Besides the constitutive model, the Phase-Field Damage Model (PFDM) can be used to create multifield finite elements with an additional degree of freedom to compute the damage field in the structure. The PFDM is based on Griffith's thermodynamical framework, which defines that the crack will increase if the released energy exceeds the material toughness, explained in detail in Francfort and Marigo [1] and Bourdin et al. [2].

The fatigue life is estimated as the relationship between cyclic stress or strain range and the number of cycles in the form of Wöhler diagrams or S-N curves. In LCF, the material is subjected to high-stress amplitude in a plastic regime, leading to fewer cycles until fracture. Various

researchers are working on developing PFDM and implementing fatigue features into FEM software, mainly for HCF [3, 4]. However, the extension of this approach to the ductile behavior and the LCF need further investigation. A fatigue degradation function describing the fatigue history is also used to reduce the material toughness [4-6]. The PFDM approach has already been used by the authors [7,8] for the simulation of damage in metals and aluminum. In this paper, the authors present the PFDM implementation for modeling the LCF behavior of metallic ductile materials, and the first simulation results are shown.

The theoretical background of the phase field fatigue framework is described in Section 2. Then, the obtained results and discussion are provided in Section 3. Finally, the article ends with conclusions in Section 4.

2. Methods

2.1 A phase field model for LCF

By the formulation of cracks in one-dimensional solids, and the extension of the regularized crack functional to multi-dimensional problems [7,8], the crack surface is defined as follows:

$$S(d) = \int_V \gamma(d, \nabla d) dV \tag{1}$$

where γ is the crack surface density function per unit volume. The internal potential energy density ψ is considered as the sum of elastic $\psi^E(\boldsymbol{\varepsilon}_E, d)$, plastic $\psi^P(\bar{\varepsilon}_P)$, plastic dissipation $\varphi^P(\bar{\varepsilon}_P)$ and fracture surface energy density $\varphi^S(d, \nabla d)$ [7,8]:

$$\psi = \psi^E(\boldsymbol{\varepsilon}_E, d) + \psi^P(\bar{\varepsilon}_P) + \varphi^S(d, \nabla d) + \varphi^P(\bar{\varepsilon}_P) \tag{2}$$

where $\boldsymbol{\varepsilon}_E$ is the elastic strain tensor, $\bar{\varepsilon}_P$ is the equivalent plastic strain, and d is the damage variable. The elastic strain energy density of virgin material $\psi_0^E(\boldsymbol{\varepsilon}_E)$ is multiplied by degradation function $g(d)$ to define the elastic strain energy density $\psi^E(\boldsymbol{\varepsilon}_E, d)$ as [7,8]:

$$\psi^E(\boldsymbol{\varepsilon}_E, d) = g(d)\psi_0^E(\boldsymbol{\varepsilon}_E) = g(d)\frac{1}{2}\boldsymbol{\varepsilon}_E^T : \boldsymbol{\sigma}_0 \tag{3}$$

where $\boldsymbol{\sigma}_0$ is the Cauchy stress tensor of an undamaged solid. Similarly, the "damaged" Cauchy stress $\boldsymbol{\sigma}$ is given in the following form [7,8]:

$$\boldsymbol{\sigma} = g(d)\boldsymbol{\sigma}_0 = g(d)\mathbf{C}_0 : \boldsymbol{\varepsilon}_E \tag{4}$$

where $\mathbf{C}_0$ is the fourth-order elastic constitutive matrix. The fracture surface energy Φ^S at the crack surface S is defined as [7,8]:

$$\Phi^S = \int_S G_c dS \approx \int_V G_c \gamma(d, \nabla d) dV = \int_V \varphi^S(d, \nabla d) dV \tag{5}$$

where the fracture surface energy density dissipated by the formation of the crack is:

$$\varphi^S(d, \nabla d) = G_c \gamma(d, \nabla d) \tag{6}$$

and G_c is the Griffith-type critical fracture energy release rate. For a cumulative history variable $\bar{\alpha} \geq 0$, and a fatigue degradation function $f(\bar{\alpha})$, the fracture surface energy density can be re-formulated as follows [4,5]:

$$\overline{\varphi}^{S}\left(d,\nabla d,\overline{\alpha}\right)=f\left(\overline{\alpha}\right)G_{c}\gamma\left(d,\nabla d\right) \tag{7}$$

The plastic energy density for Simo hardening function is [7]:

$$\psi^{P}\left(\overline{\varepsilon}_{P}\right)=\left(\sigma_{y0,\infty}-\sigma_{yv}\right)\left(\overline{\varepsilon}_{P}+\frac{1}{n}e^{-n\overline{\varepsilon}_{P}}\right)+\frac{1}{2}H\overline{\varepsilon}_{P}^{2} \tag{8}$$

while the plastic dissipated energy density is [7]:

$$\varphi^{P}\left(\overline{\varepsilon}_{P}\right)=\sigma_{yv}\overline{\varepsilon}_{P} \tag{9}$$

The total internal potential energy W_{int} functional is defined as [6,7,8]

$$W_{\text{int}}=\int_{V}\psi dV=\int_{V}\left\{g\left(d\right)\frac{1}{2}\boldsymbol{\varepsilon}_{E}^{T}:\boldsymbol{\sigma}_{0}+\psi^{P}\left(\overline{\varepsilon}_{P}\right)+f\left(\overline{\alpha}\right)G_{V}\left[\frac{d^{2}}{2}+\frac{l_{c}^{2}}{2}\left|\nabla d\right|^{2}\right]+\sigma_{yv}\overline{\varepsilon}_{P}\right\}dV \tag{10}$$

where a critical fracture energy release rate per unit volume is $G_{V}=G_{c}/l_{c}$ and l_{c} is the characteristic length. The variation of the internal potential energy over the total strain, equivalent plastic strain and damage is given as [4-8]:

$$\begin{aligned}\delta W_{int}=&\int_{V}\left\{\boldsymbol{\sigma}:\delta\boldsymbol{\varepsilon}_{E}+\frac{1}{2}g'\left(d\right)\boldsymbol{\varepsilon}_{E}^{T}:\boldsymbol{\sigma}_{0}\delta d+f\left(\overline{\alpha}\right)G_{V}\left[d\delta d+l_{c}^{2}\nabla d\nabla\delta d\right]+\right.\\&\left.+\left(-\boldsymbol{\sigma}:\frac{\partial\boldsymbol{\varepsilon}_{P}}{\partial\overline{\varepsilon}_{P}}+\left(\sigma_{y0,\infty}-\sigma_{yv}\right)\left(1-e^{-n\overline{\varepsilon}_{P}}\right)+H\overline{\varepsilon}_{P}+\sigma_{yv}\right)\delta\overline{\varepsilon}_{P}\right\}dV\end{aligned} \tag{11}$$

A variation of the external potential energy W_{ext} is known as [7,8]:

$$\delta W_{ext}=\int_{V}\mathbf{b}\cdot\delta\mathbf{u}dV+\int_{A}\mathbf{h}\cdot\delta\mathbf{u}dA \tag{12}$$

where b is a body force field per unit volume, h is a boundary traction per unit area, and u is the displacements vector. The equilibrium of the internal and external potential energy can be transformed by the application of total derivatives and by using the Gauss theorem, as [4-8]:

$$\begin{aligned}&\int_{V}\left\{-\left[g'\left(d\right)\psi_{0}+f\left(\overline{\alpha}\right)G_{V}\left[d-l_{c}^{2}\nabla^{2}d\right]\right]\delta d-\left[Div\left[\boldsymbol{\sigma}\right]+\mathbf{b}\right]\cdot\delta\mathbf{u}+\right.\\&\left.+\left(-\boldsymbol{\sigma}:\frac{\partial\boldsymbol{\varepsilon}_{P}}{\partial\overline{\varepsilon}_{P}}+\left(\sigma_{y0,\infty}-\sigma_{yv}\right)\left(1-e^{-n\overline{\varepsilon}_{P}}\right)+H\overline{\varepsilon}_{P}+\sigma_{yv}\right)\delta\overline{\varepsilon}_{P}\right\}dV\\&+\int_{A}\left\{\left[\boldsymbol{\sigma}\cdot\mathbf{n}-\mathbf{h}\right]\cdot\delta\mathbf{u}\right\}dA+\int_{A}\left\{\left[G_{V}l_{c}^{2}\nabla d\cdot\mathbf{n}\right]\delta d\right\}dA=0\end{aligned} \tag{14}$$

where $\mathbf{n}$ is the unit outer normal to the surface A. The Neumann-type boundary conditions are

$$\boldsymbol{\sigma}\cdot\mathbf{n}-\mathbf{h}=0 \tag{15}$$

$$\nabla d\cdot\mathbf{n}=0 \tag{16}$$

what leads to the governing balance equations [4-8]:

$$Div\left[\boldsymbol{\sigma}\right]+\mathbf{b}=0 \tag{17}$$

$$f\left(\overline{\alpha}\right)G_{V}\left[d-l_{c}^{2}\nabla^{2}d\right]+g'\left(d\right)\psi_{0}=0 \tag{18}$$

$$\bar{\sigma}_{eq} - \sigma_{yv} - \left(\sigma_{y0,\infty} - \sigma_{yv}\right)\left(1 - e^{-n\bar{\varepsilon}_P}\right) - H\bar{\varepsilon}_P = 0 \tag{19}$$

2.2 Fatigue degradation function

The cyclic loading produces damage increasing what is captured by a fatigue degradation function $f(\bar{\alpha})$ [3-6]. This function degrades the material toughness concerning the fatigue history variable. For the pseudo time, the history variable can be defined as [3-6]:

$$\bar{\alpha}(t) = \int_0^t H(\alpha\dot{\alpha})|\dot{\alpha}|\,d\tau \tag{20}$$

where $H(\alpha\dot{\alpha})$ is the Heaviside step function [6], where $\alpha = g(d)\psi_0$ is the fatigue history variable and $\dot{\alpha}$ is its derivative. The fatigue degradation function is [6]:

$$f(\bar{\alpha}) = \begin{cases} 1 & \text{if} \quad \bar{\alpha} \le \alpha_T \\ \left(\dfrac{2\alpha_T}{\bar{\alpha} + \alpha_T}\right)^2 & \text{if} \quad \bar{\alpha} > \alpha_T \end{cases} \tag{21}$$

Here, α_T represents a threshold value, below which the fracture energy remains unaffected, which should be determined experimentally and in this case is adopted according to literature [6]:

$$\alpha_T = \frac{G_V}{12} \tag{22}$$

3. Results and discussion

The uniaxial loading example of the unit cube is created to simulate the phenomenology of the damage evolution under Low Cyclic Fatigue (HCF) loading conditions for ductile materials using the PFDM approach extended by the fatigue degradation function described in the previous section.

The unit cube is loaded on one side by prescribed displacements while the other directions are restrained. The opposite side is restrained in the direction of prescribed displacements [9]. Elasticity and plasticity parameters of arbitrary metallic material are used and given in Table 1. The additional material parameters, such as fracture energy, characteristic length, and tolerance of convergence, are set to show the material damaging and fatigue phenomena [9].

Simulations are performed for the case of Von Mises plasticity and Simo hardening function without PFDM, only with PFDM, and with PFDM and fatigue. For each case, three loading and unloading cycles are performed. The results are given in Fig. 1. The examples are solved in 500 loading steps up to a different strain for each cycle: first cycle - 2%, second cycle – 3%, and third cycle – 4%.

As can be noticed in Fig. 1, the fatigue degradation function has a significant influence on the material response. The damage value for the total strain is given in Fig. 2, where we can see how it increases for each simulation case, except for the plasticity without PFDM because there is no damage.

E [MPa]	ν [-]	G_V [MPa]	σ_{y0} [MPa]	$\sigma_{y\infty}$ [MPa]	H [MPa]	n [-]	l_c [mm]	tol
199000	0.29	3.09	345	635	9	18	0.01	1.e-7

Table 1. Material parameters used in simulation.

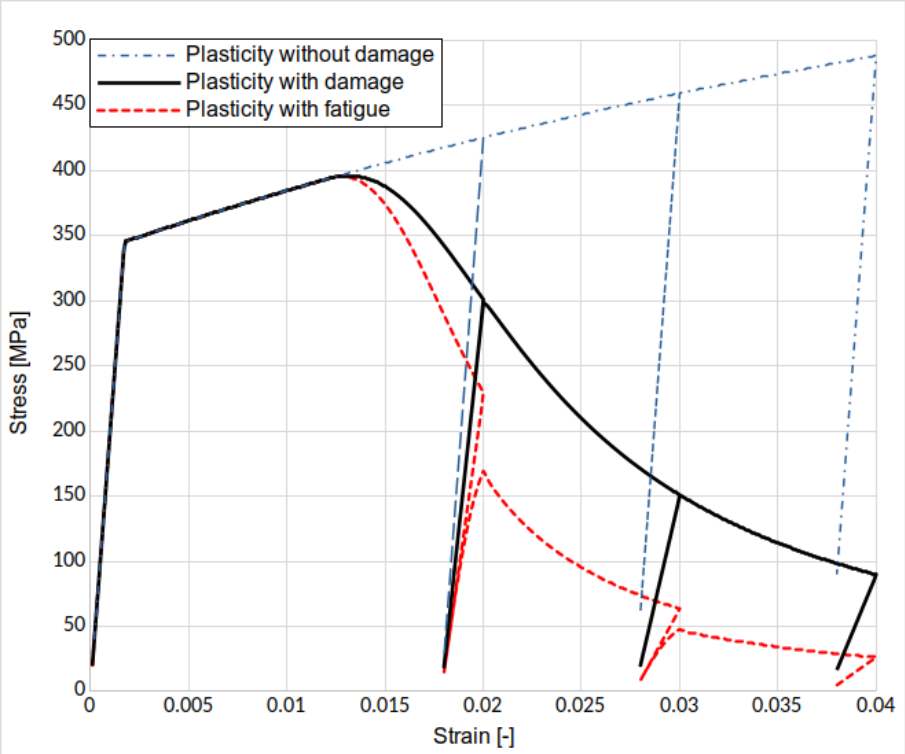

Fig. 1. Stress-strain response for monotonic and cyclic loading conditions with and without fatigue function.

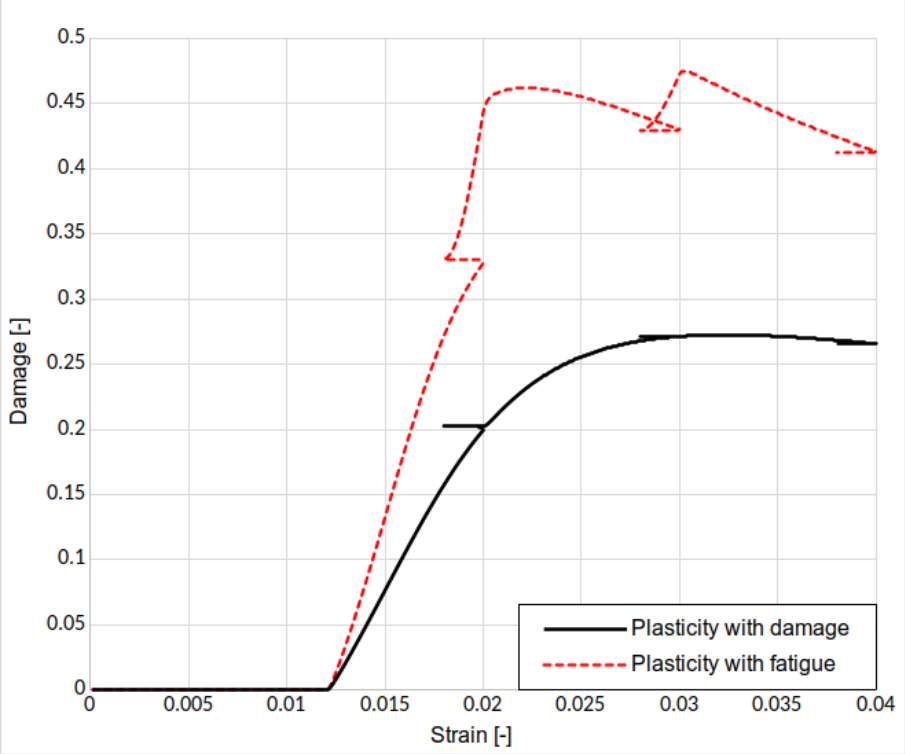

Fig. 2. Damage-strain response for monotonic and cyclic loading conditions with and without fatigue function.

4. Conclusions

The PFDM is a technique widely used for various simulations of damage in materials. For example, it is often implemented into FEM software to create multifield finite elements for predicting damage and fracture in structures. Recently, the fatigue degradation function opened the possibility of simulation of damage accumulation and fatigue.

In this paper, the authors presented the extension of Von Mises plasticity constitutive model with Simo hardening function with the PFDM and fatigue degradation function to show how it influences the simulation of ductile materials behavior under the cyclic loading. A simple unit cube model is used to show the phenomenology of the implementation. The stress-strain diagram, as well as damage value-strain dependence, show that it is possible to simulate fatigue and that the damage value increases while, at the same time, the stress-strain relationship decreases.

These results are the first step that will be extended by application on more complex structures.

Acknowledgement: This work is supported by national funding of research work at the Faculty of Engineering, University of Kragujevac after the end of project TR 32036.

References:

[1] Francfort GA, Marigo J-J., Revisiting brittle fracture as an energy minimization problem, J Mech Phys Solids, Vol. 46, 1319–42, 1998.
[2] Bourdin B, Francfort GA, Marigo JJ, The variational approach to fracture. Springer Netherlands; 2008.
[3] Lo YS, Borden MJ, Ravi-Chandar K, Landis CM, A phase-field model for fatigue crack growth, J Mech Phys Solids, Vol. 132, 103684, 2019.
[4] Golahmar A, Niordson CF, Martínez-Pañeda E, A phase field model for high – cycle fatigue: Total-life analysis, International Journal of Fatigue, Vol. 170, 107558, 2023
[5] Carrara P, Ambati M, Alessi R, Lorenzis LD, A framework to model the fatigue behavior of brittle materials based on a variational phase-field approach, Comput Methods Appl Mech Engrg, Vol. 361, 112731, 2020.
[6] Simoes M, Martínez-Pañeda E, Phase field modelling of fracture and fatigue in shape memory alloys, Comput Methods Appl Mech Engrg, Vol. 373, 113504, 2021.
[7] Živković J, Dunić V, Milovanović V, Pavlović A, Živković M, A Modified Phase-Field Damage Model for Metal Plasticity at Finite Strains: Numerical Development and Experimental Validation, Metals, Vol. 11(1), 47, 2021.
[8] Dunić V, Živković J, Milovanović V, Pavlović A, Radovanović A, Živković M, Two-Intervals Hardening Function in a Phase-Field Damage Model for the Simulation of Aluminum Alloy Ductile Behavior, Vol. 11(11), 1685. Metals, 2021
[9] Molnár, G., Gravouil, A. 2D and 3D Abaqus implementation of a robust staggered phase-field solution for modeling brittle fracture, Finite Elements in Analysis and Design, Vol 130, 27–38, 2017

AN OVERVIEW: ABOUT THREE MODELS OF MITOTIC SPINDLE OSCILLATIONS AND THEIR MODS

Andjelka Hedrih[1] and Katica R. (Stevanović) Hedrih[1, 2]

[1] Mathematical Institute of Serbian Academy of Sciences and Arts, Belgrade, Serbia
e-mail: handjelka@gmail.com,
[2] Faculty of Mechanical Engineering, University of Niš, Niš, Serbia
e-mail: katicahedrih@gmail.com, katicah@mi.sanu.ac.rs, khedrih@sbb.rs

Abstract

We present three oscillatory models of forced oscillating dynamics of mitotic spindle where interconnections between sister chromatids and microtubules are represented by different types of coupling: 1) ideally elastic elements, 2) viscoelastic elements and third model 3) connections whose properties are expressed by fractional derivatives. Each model consists of a system of oscillators. Each oscillator consists of sister chromatids of a certain chromosome that are interconnected with centrosomes (represent a rheonomic centres of oscillations) through microtubules. The rheonomic centers introduce kinematic excitation by external frequency force. Each oscillator in all three models oscillates with two degrees of freedom.

Analytical expressions for the corresponding forced modes of oscillations for all three models are determined. It is shown that the model of fractional properties is the most general, because for the range of derivatives of non-integer order from zero to one, the primary modes were practically obtained for all three models of mitotic spindle. For the limiting values of the derivative parameter of fractional order, zero and one, the modes are transformed into the modes of the ideally elastic model, or into the modes of the ideally viscous model, respectively.

Those modes, in each of the three models, are independent: there is neither interaction between the modes, nor energy transfer from one mode to another.

Keywords: oscillatory model of the mitotic spindle, fractional modes, rheonomic system.

1. Introduction

A theoretical model of mitotic spindle oscillations was presented in [1] as transversal repositioning of the mitotic spindle during unequal cell division. The authors set an oscillatory model of mitotic spindle to explain its behavior during meta- and anaphase of the normal cell division cycle [2]. According to this model [2], the mitotic spindle is considered as a system of coupled oscillators, and it oscillates along the axis that interconnects the spindle poles. In [1], transversal oscillations of the spindle are considered as a result of the mitotic spindle lateral displacement. The model [2] is based on the theory of oscillations [3] and specific patterns of chromosome movements observed both in prometaphase and in metaphase [4, 5].

In metaphase plate and during anaphase, chromosomes have specific dynamics, and their movements exhibit oscillatory properties. At the spindle equator, some chromosomes undergo

continuous oscillations throughout the metaphase, other chromosomes remain motionless, and some switch between periods of oscillations and irregular movements [4]. Recently, the oscillatory model of mitotic spindle [2] is improved by adding the Rayleigh function of energy dissipation in the model as chromosomes have to move through the cytoplasm that is considered a viscous fluid with a low Reynolds number [6].

In this paper, three types of oscillatory models of mitotic spindle will be presented and their forced oscillatory modes. All of them considered the mitotic spindle as a system of coupled oscillators. The models differ in the properties of the coupling elements within the single oscillator that consists of sister chromatids, microtubules and centrosomes. The biological explanation for using different models is that with this methodology we can model the viscoelastic properties of chromatin and microtubules that represent interconnecting material in this oscillatory model. We supposed that, during the aging process of the cell, these materials (chromatin and microtubules) age and change its mechanical properties from ideally elastic to viscoelastic.

The models presented in this paper are based on application of fractional calculus on oscillatory systems [7-10]. The differences between the models are discussed below.

2. Analytical expression of the main forced modes of sister chromatids oscillations of the fractional type model of mitotic spindle

According to the oscillatory model of mitotic spindle [2], the mitotic spindle is considered to be a system of coupled oscillators: each subsystem is an oscillator that consists of a homologue chromosome pair, a pair of microtubules that are attached to homologue chromosomes and two centrosomes located on the opposite poles of the cell. Centrosomes are presented in the model as mass particles that represent two rheonomic centers of oscillations; microtubules are represented as standard light visco-elastic elements modeled by fractional derivatives. Sister chromatids are represented as mass particles that are connected by a standard light massless elastic/viscoelastic spring (See Fig. 1.). Homologue chromosomes have equal masses and different chromosomes have different masses. Each subsystem of oscillators is a rheonomic system with two degrees of freedom whose oscillations are described by a system of two ordinary differential equations of fractional order and with two generalized coordinates. Three different models of the subsystems of mitotic spindle is presented in Fig. 1.

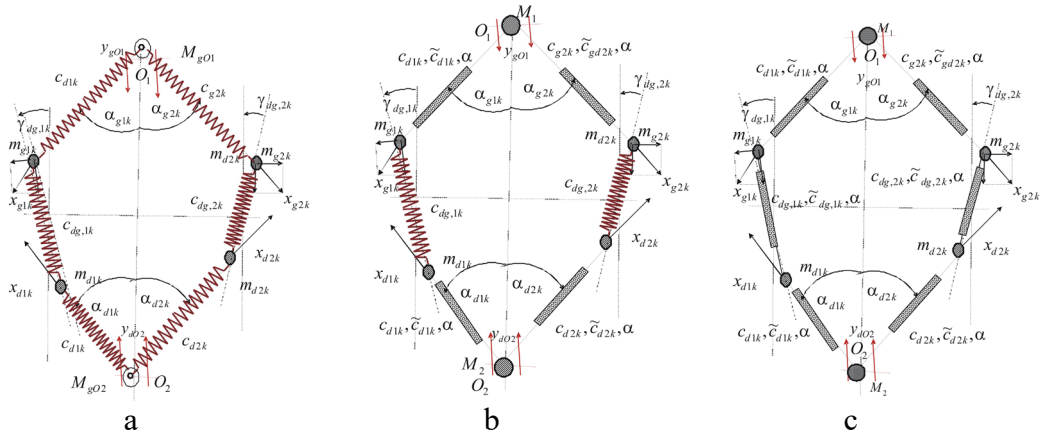

Fig. 1. Three general subsystems of the oscillatory models of mitotic spindle in metaphase plate with inertia elements on the rheonomic poles of the cell, that represent centrosomes. Only two pairs of homologues chromosomes are presented. Kinematical excitation of mitotic spindle occurs in the rheonomic centers in vertical axis with synchronous or asynchronous kinematic excitation; a. pure ideal elastic subsystem; b. subsystem with combinations of fractional type and elastic elements and c. model with all fractional elements.

A system of two coupled ordinary differential equations of fractional order expressed by generalized coordinates is then transformed into two uncoupled and independent ordinary differential equations of fractional order expressed by eigen main coordinates. The transformations are obtained by using the transformation formulas of the corresponding linear differential equations for the transformation of the generalized coordinates to the eigen main coordinates. Each of those differential equations of fractional order contains only one principal eigen coordinate and can be solved independently of each other in the analytical approximate form.

Each of those independent differential equations of fractional order describes one partial oscillator of fractional type with one degree of freedom of oscillations and represents the oscillation of one forced eigen principal mode of forced oscillations of fractional type.

In the analytical form, the approximate solutions of those two independent differential equations of fractional order are of the form:

$$\xi_k\left(t,\alpha,\omega_{k,1},\omega_{k,\alpha,1},\Omega_g,\Omega_d\right)=\xi_{k,free}\left(t,\alpha,\omega_{k,1},\omega_{k,\alpha,1}\right)+\xi_{k,particularree}\left(t,\alpha,\omega_{k,1},\omega_{k,\alpha,1},\Omega_g,\Omega_d\right)=$$

$$=\xi_k(0)\sum_{i=0}^{\infty}(-1)^i\omega_{k,\alpha,1}^{2i}t^{2i}\sum_{j=0}^{i}\binom{i}{j}\frac{(\mp1)^j\omega_{k,\alpha,1}^{-2j}t^{-\alpha j}}{\omega_{k,1}^{2j}\Gamma(2i+1-\alpha j)}+$$

$$+\dot{\xi}_k(0)\sum_{i=0}^{\infty}(-1)^i\omega_{k,\alpha,1}^{2i}t^{2i+1}\sum_{j=0}^{i}\binom{i}{j}\frac{(\mp1)^j\omega_{k,\alpha,1}^{-2j}t^{-\alpha j}}{\omega_{l,1}^{2j}\Gamma(2i+2-\alpha j)}+$$

$$+\int_0^t\left\langle\left(v_{g,k}h_{0,gk}-\tilde{h}_{0,gk}-\tilde{\tilde{h}}_{0,dk}\right)\cos\Omega_g(t-\tau)-\left(v_{d,k}h_{0,dk}+\tilde{h}_{0,dk}+\tilde{\tilde{h}}_{0,gk}\right)\cos\Omega_d(t-\tau)\right\rangle\cdot$$

$$\cdot\left\langle\sum_{i=0}^{\infty}(-1)^i\omega_{k,\alpha,1}^{2i}t^{2i+1}\sum_{j=0}^{i}\binom{i}{j}\frac{(\mp1)^j\omega_{k,\alpha,1}^{-2j}t^{-\alpha j}}{\omega_{l,1}^{2j}\Gamma(2i+2-\alpha j)}\right\rangle d\tau,\quad for\quad k=1,2,3,.....,\ n$$

$$and\quad \alpha\in(0.1),t\in(0.b) \tag{1}$$

$$\eta_k\left(t,\alpha,\omega_{k,2},\omega_{k,\alpha,2},\Omega_g,\Omega_d\right)=\eta_{k,free}\left(t,\alpha,\omega_{k,2},\omega_{k,\alpha,2}\right)+\eta_{k,particularr}\left(t,\alpha,\omega_{k,2},\omega_{k,\alpha,2},\Omega_g,\Omega_d\right)=$$

$$=\eta_k(0)\sum_{i=0}^{\infty}(-1)^i\omega_{k,\alpha,2}^{2i}t^{2i}\sum_{j=0}^{i}\binom{i}{j}\frac{(\mp1)^j\omega_{k,\alpha,2}^{-2j}t^{-\alpha j}}{\omega_{k,2}^{2j}\Gamma(2i+1-\alpha j)}+$$

$$+\dot{\eta}_k(0)\sum_{i=0}^{\infty}(-1)^i\omega_{k,\alpha,2}^{2i}t^{2i+1}\sum_{j=0}^{i}\binom{i}{j}\frac{(\mp1)^j\omega_{k,\alpha,2}^{-2j}t^{-\alpha j}}{\omega_{l,2}^{2j}\Gamma(2i+2-\alpha j)}+$$

$$+\int_0^t\left\langle\left(v_{g,k}h_{0,gk}-\tilde{h}_{0,gk}+\tilde{\tilde{h}}_{0,dk}\right)\cos\Omega_g(t-\tau)+\left(v_{d,k}h_{0,dk}+\tilde{h}_{0,dk}-\tilde{\tilde{h}}_{0,gk}\right)\cos\Omega_d(t-\tau)\right\rangle\cdot$$

$$\cdot\left\langle\sum_{i=0}^{\infty}(-1)^i\omega_{k,\alpha,2}^{2i}t^{2i+1}\sum_{j=0}^{i}\binom{i}{j}\frac{(\mp1)^j\omega_{k,\alpha,2}^{-2j}t^{-\alpha j}}{\omega_{l,2}^{2j}\Gamma(2i+2-\alpha j)}\right\rangle d\tau,\quad for\quad k=1,2,3,.....,\ n$$

$$and\quad \alpha\in(0.1),t\in(0.b) \tag{2}$$

In previous general approximate solutions, (1) and (2), ξ_k as well as η_k, $k=1,2,3,.....,n$, for forced vibrations of a fractional type partial oscillators, with one degree of freedom, loaded by a two frequency external excitations is in the form of sum of analytical approximate solutions for free vibrations modes $\xi_{k,free}\left(t,\alpha,\omega_{k,1},\omega_{k,\alpha,1}\right)$, as well as $\eta_{k,free}\left(t,\alpha,\omega_{k,2},\omega_{k,\alpha,2}\right)$ and particular approximate solution for a forced complex mode $\xi_{k,particularree}\left(t,\alpha,\omega_{k,1},\omega_{k,\alpha,1},\Omega_g,\Omega_d\right)$ as well as $\eta_{k,particularr}\left(t,\alpha,\omega_{k,2},\omega_{k,\alpha,2},\Omega_g,\Omega_d\right)$.

3. Analysis of the eigen main cos-like and sin- like oscillatory modes of three models of mitotic spindle from ideally elastic properties to fractional type properties

In this part of the paper, we analyze and determine analytical approximate expressions for the main eigen modes of free oscillations, oscillations expressed by fractional type derivatives, similar to the sine (sin-like) or cosine (cos-like) form. When we put in the approximate analytical expressions for fractional-type modes, the value of the parameter of the fractional derivative with time equal to zero, we obtained exact analytical expressions for periodic modes of linear properties; when we put the value of the fractional derivative parameter with time equal to one, we obtained linearly damped modes.

In Figure 2.a, by first term in expression (1) or (2) like cosines mode $T_{s,\cos}(t,\alpha)=\sum_{k=0}^{\infty}(-1)^k\,\omega_{\alpha,s}^{2k}t^{2k}\sum_{j=0}^{k}\binom{k}{j}\frac{\omega_{\alpha,s}^{-2j}t^{-\alpha j}}{\omega_s^{2j}\Gamma(2k+1-\alpha j)}$ as surface in space $\left(t,\alpha,T_{s,\cos}(t,\alpha)\right)$ is presented and for $\alpha=0$ vibrations linear and pure periodic and mode is $T_{s,\cos}(t,\alpha)\big|_{\alpha=0}=\cos\left(t\sqrt{\omega_s^2+\omega_{(\alpha=0)s}^2}\right)$ and for $\alpha=1$ vibrations are in the form $T_{s,\cos}(t,\alpha)\big|_{\alpha=1}=e^{-\frac{1}{2}\omega_{(\alpha=1)s}^2t}\cos\left(t\sqrt{\omega_s^2+\frac{1}{4}\omega_{(\alpha=1)s}^4}\right)$ and are visible as contour of surface at coordinates $\alpha=0$ and $\alpha=1$.

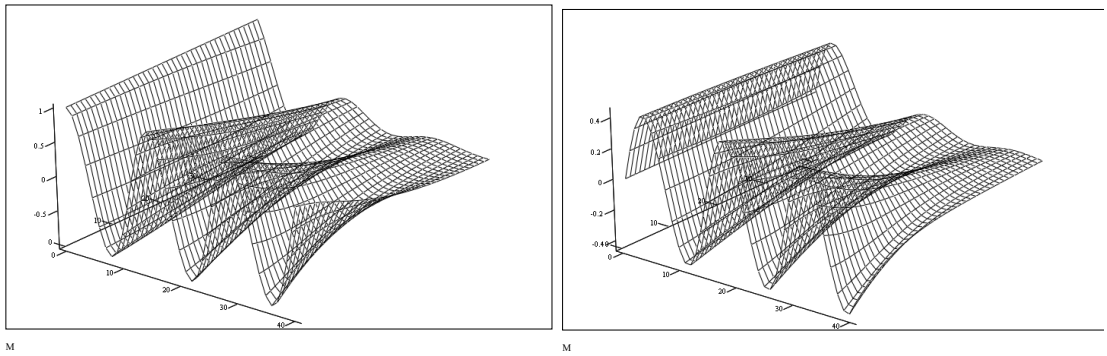

a b

Fig. 2. Shapes of components like cos $T_{s,\cos}(t,\alpha)$ in (a) and like sin $T_{s,\sin}(t,\alpha)$ in (b) of eigen fractional order normal modes.

In Fig. 2.b, by second term in expression (1) or (2) eigen main fractional order like sinus mode $T_{s,\sin}(t,\alpha)=\sum_{k=0}^{\infty}(-1)^k\,\omega_{\alpha,s}^{2k}t^{2k+1}\sum_{j=0}^{k}\binom{k}{j}\frac{\omega_{\alpha,s}^{-2j}t^{-\alpha j}}{\omega_s^{2j}\Gamma(2k+2-\alpha j)}$ is presented in space $\left(t,\alpha,T_{s,\sin}(t,\alpha)\right)$, and for $\alpha=0$ vibration is linear and pure periodic and mode is $T_{s,\sin}(t,\alpha)\big|_{\alpha=0}=\sin\left(t\sqrt{\omega_s^2+\omega_{(\alpha=0)s}^2}\right)$. For $\alpha=1$, vibrations are in the form $T_{s,\sin}(t,\alpha)\big|_{\alpha=1}=e^{-\frac{1}{2}\omega_{(\alpha=1)s}^2t}\sin\left(t\sqrt{\omega_s^2+\frac{1}{4}\omega_{(\alpha=1)s}^4}\right)$ and are visible as contour of surface at coordinates $\alpha=0$ and $\alpha=1$.

In Fig. 3.a, derivative of fractional order like cosines modes

$$T_{s,\cos}(t,\alpha)=\sum_{k=0}^{\infty}(-1)^k\,\omega_{(\alpha)s}^{2k}t^{2k}\sum_{m=0}^{k}\binom{k}{m}\frac{\omega_{(\alpha)s}^{-2m}t^{-\alpha m}}{\omega_s^{2m}\Gamma(2k+1-\alpha m)}$$ is minus like sin

$$\dot{T}_{\cos}(t,\alpha)=\sum_{k=1}^{\infty}(-1)^k\,\omega_{\alpha}^{2k}t^{2k}\sum_{m=0}^{k}\binom{k}{m}\frac{(2k-\alpha m)\omega_{\alpha}^{-2m}t^{-\alpha m}}{\omega_o^{2m}\Gamma(2k+1-\alpha m)}$$ is presented.

In Figure 3.b derivative of fractional order like sinus modes

$$T_{s,\sin}(t,\alpha)=\sum_{k=0}^{\infty}(-1)^k\,\omega_{(\alpha)s}^{2k}t^{2k+1}\sum_{m=0}^{k}\binom{k}{m}\frac{\omega_{(\alpha)s}^{-2m}t^{-\alpha m}}{\omega_s^{2m}\Gamma(2k+2-\alpha m)}$$

is like cos $\dot{T}_{\sin}(t,\alpha)=\sum_{k=0}^{\infty}(-1)^k\,\omega_{\alpha}^{2k}t^{2k}\sum_{m=0}^{k}\binom{k}{m}\frac{(2k+1-\alpha m)\omega_{\alpha}^{-2m}t^{-\alpha m}}{\omega_o^{2m}\Gamma(2k+2-\alpha m)}$ is presented.

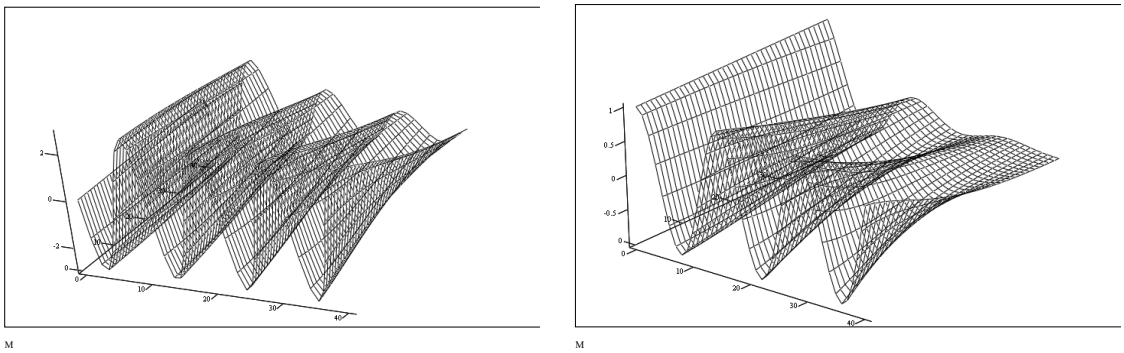

a b

Fig. 3. Shapes of derivatives of components of like cos $\dot{T}_{s,\cos}(t,\alpha)$ in a) and like sin $\dot{T}_{s,\sin}(t,\alpha)$ in b) of eigen fractional order normal modes.

In Fig. 4, some variants of eigen main modes of fractional order are presented.

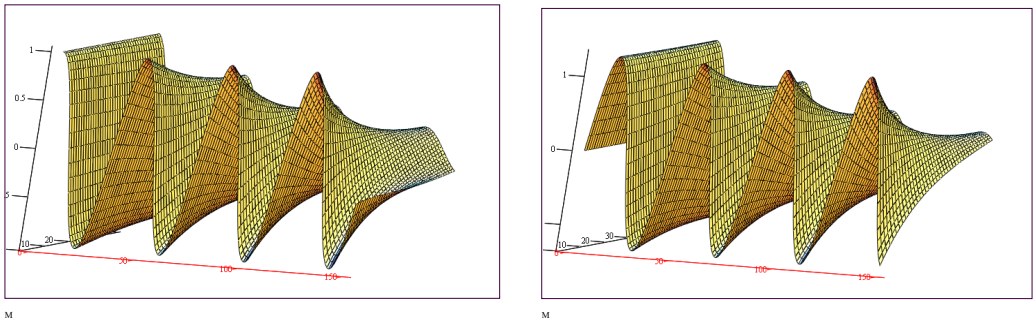

a b

Fig. 4. a. Eigen main modes of fractional order. $T_{s,\cos}(t,\alpha)$ is on ordinate; b. Eigen main modes of fractional order. $T_{s,\sin}(t,\alpha)$ is on ordinate. Time t and α, for $0<\alpha<1$ are on two abscissa axes.

4. Analysis of the main forced particular oscillatory modes of three models of mitotic spindle from ideally elastic properties to fractional type properties

The third term in expression (1) presents $\xi_{k,p}(t,\alpha,\omega_{k,1},\omega_{k,\alpha,1},\Omega_g,\Omega_d)$ approximate particular solution of the main forced mode of fractional type oscillation of the system under the external single frequenency force and is in the form:

$$\xi_{k,p}\left(t,\alpha,\omega_{k,1},\omega_{k,\alpha,1},\Omega_g,\Omega_d\right)=$$
$$=\int_0^t\left\langle\left(v_{g,k}h_{0,gk}-\tilde{h}_{0,gk}-\tilde{\tilde{h}}_{0,dk}\right)\cos\Omega_g\left(t-\tau\right)-\left(v_{d,k}h_{0,dk}+\tilde{h}_{0,dk}+\tilde{\tilde{h}}_{0,gk}\right)\cos\Omega_d\left(t-\tau\right)\right\rangle\cdot$$
$$\cdot\left\langle\sum_{i=0}^{\infty}\left(-1\right)^i\omega_{k,\alpha,1}^{2i}t^{2i+1}\sum_{j=0}^{i}\binom{i}{j}\frac{\left(\mp1\right)^j\omega_{k,\alpha,1}^{-2j}t^{-\alpha j}}{\omega_{l,1}^{2j}\Gamma\left(2i+2-\alpha j\right)}\right\rangle d\tau,\quad for\quad k=1,2,3,.....,n \tag{3}$$
$$and\quad \alpha\in\left(0.1\right),t\in\left(0.b\right)$$

The third term in expression (2) presents $\eta_{k,p}\left(t,\alpha,\omega_{k,2},\omega_{k,\alpha,2},\Omega_g,\Omega_d\right)$ approximate particular solution of the main forced mode of fractional type oscillation of the system under the external single frequenency force and is in the form:

$$\eta_{k,p}\left(t,\alpha,\omega_{k,2},\omega_{k,\alpha,2},\Omega_g,\Omega_d\right)=$$
$$=\int_0^t\left\langle\left(v_{g,k}h_{0,gk}-\tilde{h}_{0,gk}+\tilde{\tilde{h}}_{0,dk}\right)\cos\Omega_g\left(t-\tau\right)+\left(v_{d,k}h_{0,dk}+\tilde{h}_{0,dk}-\tilde{\tilde{h}}_{0,gk}\right)\cos\Omega_d\left(t-\tau\right)\right\rangle\cdot$$
$$\cdot\left\langle\sum_{i=0}^{\infty}\left(-1\right)^i\omega_{k,\alpha,2}^{2i}t^{2i+1}\sum_{j=0}^{i}\binom{i}{j}\frac{\left(\mp1\right)^j\omega_{k,\alpha,2}^{-2j}t^{-\alpha j}}{\omega_{l,2}^{2j}\Gamma\left(2i+2-\alpha j\right)}\right\rangle d\tau,\quad for\quad k=1,2,3,.....,\ n \tag{4}$$
$$and\quad \alpha\in\left(0.1\right),t\in\left(0.b\right)$$

Forced modes are caused by kinematic excitation of rheonomic centres.

6. Conclusions

In this paper, three types of oscillatory models of mitotic spindle are presented and their forced oscillatory modes. All of them considered the mitotic spindle as a system of coupled oscillators. The models differ in the properties of the coupling elements within the single oscillator.

It was shown that the model of fractional properties is the most general. In this model, the range of derivatives of non-integer order goes from zero to one. For the limiting values of the derivative parameter of fractional order, zero and one, the modes are transformed into the modes of the ideally elastic model, or into the modes of the ideally viscous model, respectively.

Those modes, in each of the three models, are independent: there is neither interaction between the modes, nor energy transfer from one mode to another.

In [11], a method for simulating the electric fields from vibrating microtubules was presented. Five vibrational modes were simulated [11] and, based on conventional definitions of interaction, they did not identify any cases where the fields produced by the microtubule could interact with biomolecules at large distances (>100 nm) [11]. In [11], a numerical transient method to determine the fields generated by microtubule vibrations was used. Numerical studies in [11] suggest that all modes have lower resonant frequencies for longer microtubules, except for the flexing mode. Using coupled-mode-theory relationships of energy transfer, Thackston et al. [12] studied energy transfer between two neighboring microtubules trough numerical simulation. They consider microtubules as electrically coupled mechanical resonators. The key assumption in their work is that the resonator must be able to store more energy from electromagnetic interactions than thermal energy [12]. A region where near-field communication would be most efficient and might be sustained is identified via numerical experiment (around 100 MHz) [12].

We supposed that during the aging process of the cell, chromatin and microtubules age and change its mechanical properties from ideally elastic to viscoelastic.

The presented model of fractional properties is suitable for modeling oscillations in the mitotic spindle when we want to study how oscillations are affected by changing the elasticity of chromatin that interconnects sister chromatids or microtubules in aged cells.

Acknowledgement: This work was supported by the Ministry of Science, Technological Development and Innovation of the Republic of Serbia through Mathematical Institute SANU, Belgrade, Serbia.

References:

[1] Grill W.S., Kruse K., and Jüicher F., *Theory of Mitotic Spindle Oscillations*, Physical Review Letters, Prl 94, 108104, 2005. DOI: 10.1103/PhysRevLett.94.108104

[2] Hedrih A., (Stevanovic) Hedrih K., *Relation between centrosome excitation and oscillatory energy of mitotic spindle in metaphase trough biomechanical oscillatory model of mitotic spindle*, in: Antonov I., Serow W.D. (Eds.), "Mathematics XXI Century & Natural Science". Envied Lecture. Book of Abstracts: IV International Seminar "Nonlinear henomenology Advances" (October 6, 2017); III International Wokshop "Scientific & Educational Problems of Belarusian Nuclear Power Plant. St. Petersburg: Publishing House of SPbPU., St. Petersburg, Russia, p. 27.

[3] Raškovic D. P., Teorija oscilacija (Theory of oscillatins), Naucna knjiga, 1952.

[4] Magidson V., O'Connell C.B., Loncarek J., Paul R., Mogilner A., and Khodjakov A., *The spatial arrangement of chromosomes during prometaphase facilitates spindle assembly*, Cell, Vol.146, 555-567, 2011.

[5] Maly I.V., *Systems biomechanics of centrosome positioning: A conserved complexity*, Communicative and Integrative Biology, Vol. 4, 230-235, 2011.

[6] Hedrih A.N., (Stevanovic) Hedrih K., Bogdanovic-Jovanovic J., *Rayleigh function of energy dissipation in modelling oscillatory behaviour of moving sister chromatids in anaphase of mitosis,* In International Conference on Mathematical Analysis and Applications in Science and Engineering - Book of Extended Abstracts. Series Editors Carla M.A. Pinto, School of Engineering, Polytechnic of Porto and Centre for Mathematics, University of Porto Jorge Mendonça, School of Engineering, Polytechnic of Porto Lurdes Babo, Porto Accounting and Business School Dumitru Baleanu, Cankaya University. 2022: 111-114, Publisher ISEP, P.Porto, pp 646. Book ISBN & DOI: 978-989-53496-3-0; https://doi.org/10.34630/20734

[7] Baclic BS, Atanackovic TM., *Stability and creep of a fractional derivative order viscoelastic rod. Bulletin (Académie serbe des sciences et des arts Classe des sciences mathématiques et naturelles Sciences mathématiques)* pp 115-131, 2000.

[8] Hedrih (Stevanovic) K., Machado T.J.A., *Discrete fractional order system vibrations*, International Journal Non-Linear Mechanics, Vol. 73, 2-11, 2015. DOI: 10.1016/j.ijnonlinmec.2014.11.009.

[9] Hedrih (Stevanović) K., *Generalized function of fractional order dissipation of system energy and extended Lagrange differential Lagrange equation in matrix form*, Dedicated to 86th Anniversary of Radu MIRON'S Birth., Tensor, Vol. 75, No. 1, 35-51, 2014.

[10] (Stevanovic) Hedrih K.R., (2020), *Forced Longitudinal Fractional Type Vibrations of a Rod with Variable Cross Section*, in Developments and Novel Approaches in Nonlinear Solid Body Mechanics, Editors: Bilen Emek Abali and Ivan Giorgio, Chapter 18, 325-344, 2020. Springer Nature Switzerland AG 2020. DOI https://doi.org/10.1007/978-3-030-50460-1.

[11] Thackston K.A., Deheyn D.D., and Sievenpiper D.F., *Simulation of electric fields generated from microtubule vibrations*, Physical Review E 100, 022410, 2019. DOI: 10.1103/PhysRevE.100.022410

[12] Thackston K.A., Deheyn D.D., and Sievenpiper D.F., *Limitations on electromagnetic communication by vibrational resonances in biological systems,* Physical Review E 101, 062401, 2020. DOI: 10.1103/PhysRevE.101.062401.

ANALYTICAL DESIGN OF RESONANT CONTROLLER APPLIED FOR SOLVING ROBOT ARM TRACKING PROBLEM

Petar D. Mandić[1], Tomislav B. Šekara[2] and Mihailo P. Lazarević[1]

[1]Faculty of Mechanical Engineering, University of Belgrade, Kraljice Marije 16, Belgrade 11120, Serbia
e-mail: pmandic@mas.bg.ac.rs, mlazarevic@mas.bg.ac.rs
[2]School of Electrical Engineering, University of Belgrade, Bulevar kralja Aleksandra 73, Belgrade 11120, Serbia
e-mail: tomi@etf.rs

Abstract

This paper deals with a topic of robot following a trajectory in three-dimensional space with a prescribed velocity law. Considering the nonlinear nature of robot manipulators, and high demands regarding tracking performances, this task is very challenging, but also very popular in control community because of its importance in industrial applications. To successfully tackle this problem, we propose a resonant controller, which outperforms classical control schemes usually employed in this situation. In this case, the robot manipulator needs to follow an ellipse trajectory with constant speed along the curve. First, a mathematical model of the three degrees of freedom robot arm is derived with included actuator dynamics. Then, a numerical solution of the inverse kinematics problem is calculated in order to obtain a desired trajectory in joint space. Third, an analytical procedure for designing a resonant controller is given, with parameters of the controller chosen in order to achieve a good performance/robustness trade-off, which is a key element in modern control design. Finally, the proposed control scheme is tested, and results of robot simulation are provided before the concluding remarks.

Keywords: robot trajectory control, resonant controller, robust control, inverse kinematics.

1. Introduction

Robotics is a multidisciplinary field wherein knowledge of several different disciplines such as electrical, mechanical and systems engineering are needed in order to successfully cope with it. Moreover, advances in computer science have been the main cause of rapid development of robotics over the past decades [1]. The majority of robot applications deal within industrial conditions, executing tasks such as welding, packaging, cutting, paint spraying, moving objects etc. Industrial manipulators need to fulfill high demands in terms of accuracy, precision and repeatability. One of such typical applications is a task of following a trajectory in space with prescribed velocity law.

Designing a controller for such a task is not so straightforward. Scientific community reports a large number of different control strategies for robotic manipulators [2]. Most of them are based on linear control theory from a practical reason. Namely, linear controllers are intuitive, easy to

understand and last but not least, easy to implement. This approach gains even more importance when robot dynamics can be regarded as linear, which can be achieved by using motors with high gear ratios, or by using feedback linearization techniques. This way, dynamic coupling effects can be neglected, and control of each robotic joint can be designed independently. This is the reason why classical PID controllers are still an inevitable part of control of robot manipulators in industry [3-9].

Besides classical control strategies, improving performances of the closed loop system can be achieved by applying a bit more complex algorithms such as resonant controllers [10]. These regulators are capable of tracking sinusoidal references (with or without offsets) of arbitrary frequencies with zero steady state error, and they achieve it while preserving good transient response [11]. They have been applied successfully in cases such as alternate current systems, wind turbines, active rectifiers, motor drives, etc. [12,13].

Having in mind the task of robot following the desired path, the resonant controller proposed in this paper imposes as a reasonable choice. Namely, following a closed trajectory in space with constant speed several times in a row is a repetitive task for the robot manipulator, meaning that robot joints need to track complex periodic signals with the same fundamental frequency. In order to do so, several steps need to be resolved successfully. Deriving a mathematical model of robot manipulator with the actuator dynamics is a first one. Then, solving an inverse kinematics problem is necessary in order to obtain desired trajectories in joint space. Design of a robust controller with good closed-loop system performances is the next important step. Finally, simulation of the robot performing the abovementioned task is necessary to validate the effectiveness of the proposed procedure. All these steps are described in more detail in the following sections.

2. Mathematical model of robotic manipulator and solution of the inverse kinematics problem

The mechanical structure of robot arm can be described as a sequence of rigid bodies interconnected by means of joints. Dynamic equations of the robotic system can be written in the following form [14]:

$$A(q)\ddot{q} + C(q,\dot{q})\dot{q} - Q^g = Q^m, \tag{1}$$

wherein: $\boldsymbol{q}(t) \in R^3$ is the vector of the generalized coordinates, $A(q) \in R^{3\times3}$ represents basic metric tensor (or inertia matrix), $C(q,\dot{q}) \in R^{3\times3}$ is a matrix that includes centrifugal and Coriolis effects, $Q^g \in R^3$ and $Q^m \in R^3$ are gravity term and torque vectors applied to the joints, respectively. For details of the calculation of the basic metric tensor and matrix $C(q,\dot{q})$ for robot manipulators, the reader is referred to [15].

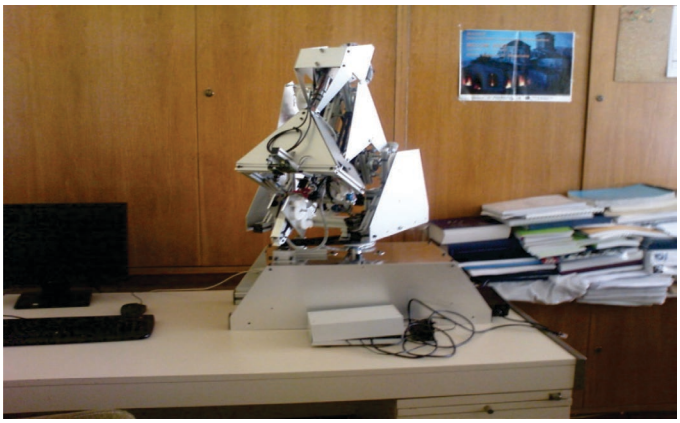

Fig. 1. Robotic manipulator with seven DOFs.

In this paper, we considered a robotic system which is an integral part of the Laboratory of Applied Mechanics at the Faculty of Mechanical Engineering in Belgrade (Fig. 1). It has seven degrees of freedom (DOFs), but only the first three revolute joints are responsible for placing the end-effector into the demanded position in space [16]. The following three DOFs are in the form of the spherical wrist, and they are responsible for the end-effector's orientation. The 7th DOF is the gripper. Herein, robot arm with first three revolute joints is considered since these robot links are engaged in tracking the desired path in space.

Usually, robot links are driven by DC motors. Since the motor's optimal working condition include high angular speeds, while controlling the movement of robot link demands low speeds [17], it is necessary to interpose a gear transmission between motors and joints. If N represents diagonal matrix of the gear ratios, the following equations describe connection between motors and robot links:

$$q_m = Nq,\ \mathrm{Q}^m = N\tau_l, \tag{2}$$

wherein $\boldsymbol{q}_m$ represents the positions of the actuators shafts, while $\boldsymbol{\tau}_l$ is the vector of torques resulting from the robot manipulator and acting on the motors shafts. It can be easily shown [18] that torque $\boldsymbol{\tau}_l$ is equal to:

$$\tau_l = (N^2)^{-1}(A(q)\ddot{q}_m + C(q,\dot{q})\dot{q}_m) - N^{-1}Q^g \tag{3}$$

Torque $\boldsymbol{\tau}_l$ can be described as a disturbance acting on the motor shafts. The influence of this disturbance on the motor's dynamics decreases with the increase of the reduction ratio N. Consequently, it means that the presence of large reduction ratio tends to linearize the dynamic equations of the robot. This allows us to introduce a major simplification in our mathematical model. Instead of nonlinear dynamic equations of the robot given by (1), we can use a linear model of the DC motor instead.

The robot manipulator from the above picture uses three identical Maxon DC motors for controlling the position of the first three links. The transfer function $G_m(s)$ of these motors can be described as:

$$G_m(s) = \frac{K}{s(Ts+1)}, \tag{4}$$

wherein K=22.515 and $T = 0.0056409$. Finally, to sum up, the original nonlinear robotic system, due to high reduction ratio $\left(N = \mathrm{diag}\{185,632,140\}\right)$ can be represented by 3 linear, decoupled subsystems, using the motor transfer function $G_{\mathrm{m}}(s)$.

2.1 Inverse kinematics problem

The inverse kinematics problem consists of the determination of the joint variables corresponding to a given end-effector position. As mentioned before, tip of the robot arm needs to follow an ellipse curve with constant speed along the path. In this example, ellipse lies in a plane parallel to the referential horizontal plane, with the value of 0.2 m corresponding to the semi-major axis, and 0.1 m for the semi-minor axis. Desired end-effector speed along the path is 0.2 m/s. Before tackling the inverse kinematics, coordinates of the robot tip with respect to the inertial reference frame need to be calculated. This is achieved by applying numerical procedures, since an analytical solution is not possible in this case. Graphical representations of equations of motion of the robot tip obtained in Cartesian coordinates are depicted in Fig. 2.

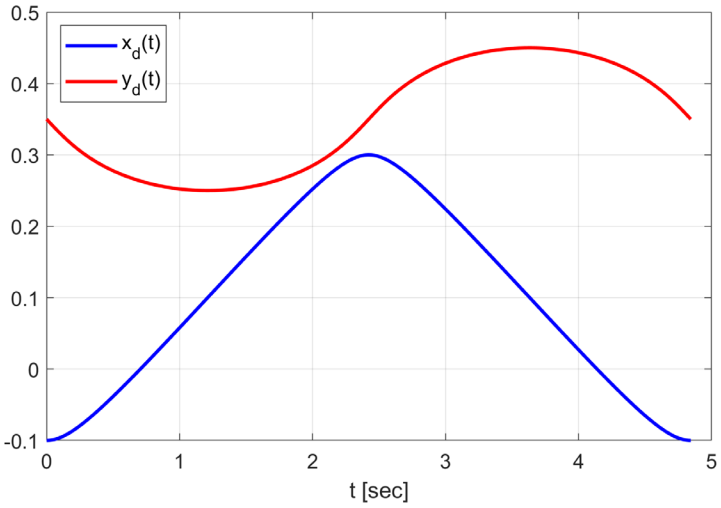

Fig. 2. Cartesian coordinates of reference trajectory.

Now, knowing the position of the end-effector with respect to the inertial frame at each time instance, we can determine desired values of joint variables $\boldsymbol{q}_d$. In this case, for the given robot configuration, analytical solution is possible and is graphically illustrated in Fig. 3. For more details about solving inverse kinematics problem, the reader is referred to [19,20].

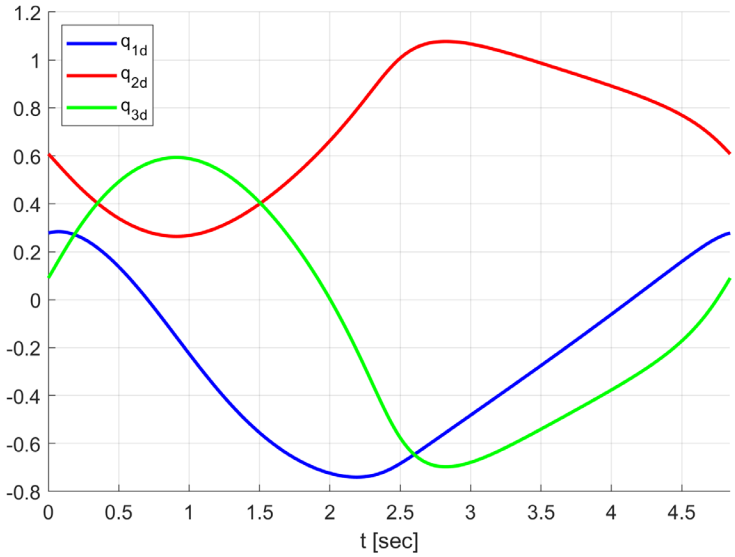

Fig. 3. Graphical solution of inverse kinematics problem.

Here, we should notice that the oscillatory period is approx. 4,85 seconds, which corresponds to the value of natural frequency $\omega_0 \approx 1,295\ \mathrm{s}^{-1}$.

3. Controller design

The control scheme of the closed loop system is depicted in Fig. 4, where $G_\mathrm{m}(s)$ is the model of the motor given by (4), $C(s)$ is the employed controller, while *r*, *d*, *u* and *y* represent the reference, disturbance, control and output signal, respectively.

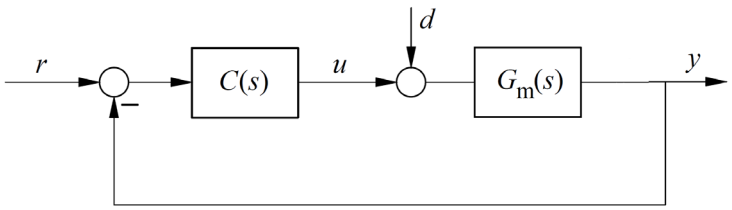

Fig. 4. Block diagram of closed loop control system.

In this paper, parameters of the resonant controller $C(s)$ are derived specifically for the plant $G_{\mathrm{m}}(s)$, but described procedure can be applied to any other plant model [21]. To begin with, we start with the complementary transfer function $T(s)$ given by [22,23]:

$$T(s)=\frac{\eta_4 s^4+\eta_3 s^3+\eta_2 s^2+\eta_1 s+1}{(\lambda s+1)^2(Ts+1)^4} \tag{5}$$

where time constant $\lambda>0$, and η_4, η_3, η_2 and η_1 are free parameters which will be determined to obtain the desired dynamic characteristics of the closed loop system. Having in mind that $T(s)$ can be formulated also as $T(s)=C(s)G_m(s)/\left(1+C(s)G_m(s)\right)$, then after some calculations, the controller $C(s)$ is obtained in the following form:

$$C(s)=\frac{\eta_4 s^4+\eta_3 s^3+\eta_2 s^2+\eta_1 s+1}{(\lambda s+1)^2(Ts+1)^4-\eta_4 s^4-\eta_3 s^3-\eta_2 s^2-\eta_1 s-1}\frac{1}{G_m(s)}, \tag{6}$$

Free parameters η_4, η_3, η_2 and η_1 are determined in order to cancel the poles of $G_{\mathrm{m}}(s)$ and the poles of the controller: $s=0$, $s_{1,2}=\pm i\omega_0$. Applying these conditions, we obtain:

$$\begin{aligned}
\eta_1&=2\lambda+4T,\\
\eta_2&=-2T^3\lambda\omega_0^2\ \hat{}\ 2-3T^2\lambda^2\omega_0^2+6T^2+8T\lambda+\lambda^2,\\
\eta_3&=-2T\left(T^3\lambda\omega_0^2+2T^2\lambda^2\omega_0^2-2T^2-6T\lambda-2\lambda^2\right),\\
\eta_4&=-T^4\lambda^2\omega_0^2+T^4+6T^3\lambda+3T^2\lambda^2
\end{aligned} \tag{7}$$

Substituting expressions from (7) into (6) we obtain $C(s)$ as a function of one tuning parameter λ:

$$C(s)=\frac{(Ts+1)\left(1+T((1-\lambda^2\omega_0^2)T^2+6T\lambda+3\lambda^2)s^3+(-2T^3\lambda\omega_0^2+(3-3\lambda^2\omega_0^2)T^2+6T\lambda+\lambda^2)s^2+(3T+2\lambda)s\right)}{sK(s^2+\omega_0^2)(T\lambda s+2T+3\lambda)T^2\lambda} \tag{8}$$

By adjusting λ, one can obtain very good robustness/performance trade-off, which is a key issue in modern control system design. Robustness with respect to modelling uncertainties is ensured by constraining the largest value of the sensitivity function $M_{\mathrm{s}}=\max_{\omega}\left|1-T(i\omega)\right|$. Sensitivity to model uncertainties can also be expressed with the largest value of the complementary sensitivity function $M_{\mathrm{p}}=\max_{\omega}\left|\mathrm{T}(i\omega)\right|$. The sensitivity to measurement noise M_{n} is defined as $M_{\mathrm{n}}=\max_{\omega}\left|C(i\omega)/(1+C(i\omega)G_m(i\omega))\right|$.

The reader should observe the term $s^2+\omega_0^2$ in the denominator of the above expression. While this term is capable of tracking fundamental frequency ω_0 of periodic signal $\boldsymbol{q}_d$, another pole $s=0$ of the controller is responsible for bringing the offset of $\boldsymbol{q}_d$ to zero steady state error.

4. Simulation results

To validate the performance of the resonant controller given by (8), simulation of robotic manipulator executing the given task is performed [24]. Choosing $\lambda = 10T \approx 0.056409$, a very good compromise between robustness and performance is obtained $\left(M_s \approx 1.36,\ M_{\mathrm{p}} \approx 1.48\right)$, in which case transfer function of resonant controller equals to:

$$C(s) = \frac{29.368(s+15.620)(s+27.620)(s+39.455)(s+183.161)}{s(s+586.116)(s^2+1.677)} \tag{9}$$

Controller (9) written in the above form is not suitable for practical realization. In order to be implemented in real time application, one should perform partial fraction decomposition of the given transfer function to obtain:

$$C(s) = \frac{93149.09}{s} + \frac{29.368s + 6976.05}{s + 586.1162704} + \frac{-92317.59s + 20182.47}{s^2 + 1.677} \tag{10}$$

Now, resonant controller can be realized in parallel series according to (10). Regarding simulation, robot arm is programmed to follow ellipse curve several times in a row. Results of the simulation are depicted in Fig. 5.

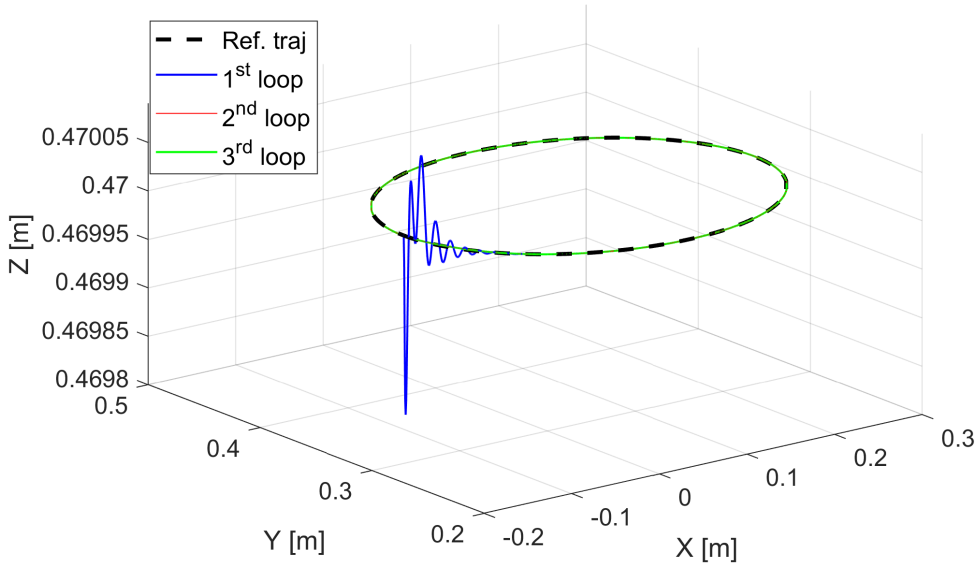

Fig. 5. Comparison between reference and actual trajectories for different loops.

As a measure of tracking performance, maximum absolute error between actual and reference path is calculated after every loop. Results are summarized in Table 1. We can see the biggest error occurred during the first loop, which was expected due to initial conditions mismatch. During the second loop, error decreased significantly, and remained stable in the following iterations. Similar conclusions can be derived by observing trajectories in Fig. 5.

Loop No.	1	2	3	4, 5 etc.
Max. error [mm]	5,408e^{-01}	1,3606e^{-02}	1,3606e^{-02}	1,3606e^{-02}

Table 1. Evolution of maximum absolute error (in milimeters).

It is worth saying that the tracking error would be even smaller if we chose to track not only fundamental frequency ω_0, but also higher harmonics of periodic signal $\boldsymbol{q}_d$. The analytical

procedure described above for the design of resonant controller could be employed with insignificant changes, but in that case the price would be paid in terms of complexity of the regulator, which would be of a higher degree.

5. Conclusion

In this paper, a resonant controller is employed for executing robots' repetitive tasks. In order to do it successfully, several steps need to be overcome. A mathematical model of a robot is derived, followed by an inverse kinematics problem solution. A resonant controller is designed analytically as a function of one adjustable parameter. Choosing λ appropriately, a good compromise between robustness and system performance is obtained. Simulation of robot following a desired ellipse curve in space shows effectiveness of the proposed controller. Designed procedure can be generalized for different type of plants, but also for different end-effectors' trajectories and velocity laws along the path. Future work will include routines for optimization of controller parameters, as well as comparison of different control strategies for the given task.

Acknowledgment: The authors gratefully acknowledge the support of Ministry of Education, Science and Technological Development of the Republic of Serbia under the contract 451-03-47/2023-01/200105 from 03.02.2023 (Projects TR 33047 (P.D.M), TR 35006, III 41006 (M.P.L.)), and 451-03-47/2023-01/200103 (T.B.Š.)

References:

[1] B. Siciliano, L. Sciavicco, L. Villani, G. Oriolo, *Robotics*, London: Springer-Verlag, 2009.
[2] H. G. Sage, M. F. De Mathelin, E. Ostertag, "Robust control of robot manipulators: A survey," *Inter J Control*, vol. 76, no. 16, pp. 1498-1522, 1999.
[3] G.K. McMillan, *Industrial applications of PID control*. In: Vilanova R, Visioli A, eds. PID control in the third millenium. London: Springer, pp. 415-461, 2012.
[4] Astrom, K. J., & Hagglund, T. (2006). *Advanced PID control*. The Instrumentation Systems and Automation Society, 2006.
[5] T.B. Šekara, M.R. Mataušek, *Optimization of PID Controller Based on Maximization of the Proportional Gain Under Constraints on Robustness and Sensitivity to Measurement Noise*, IEEE Trans Automat Contr, vol. 54, pp. 184-189, 2009.
[6] Šekara, T. B., & Mataušek, M. R. (2010). *Revisiting the Ziegler-Nichols process dynamics characterization*. Journal of Process Control, 20(3), 360–363.
[7] Šekara, T. B., & Mataušek, M. R. (2011). *Classification of dynamic processes and PID controller tuning in a parameter plane*. Journal of Process Control, 21(4), 620–626.
[8] Mataušek, M. R., & Šekara, T. B. (2011). *PID controller frequency-domain tuning for stable, integrating and unstable processes, including dead-time*. Journal of Process Control, 21(1), 17–27.
[9] P. D. Mandić, M. Č. Bošković, T. B. Šekara, M. P. Lazarević, *A new optimisation method of PIDC controller under constraints on robustness and sensitivity to measurement noise using amplitude optimum principle*, International Journal of Control. doi.org/10.1080/00207179.2021.1912392
[10] A. Kuperman, *Proportional-Resonant Current Controllers Design Based on Desired Transient Performance*, in IEEE Transactions on Power Electronics, vol. 30, no. 10, pp. 5341-5345, Oct. 2015, doi: 10.1109/TPEL.2015.2408053
[11] Đ. M. Stojić and T. B. Šekara, *Digital Resonant Current Controller for LCL-Filtered Inverter Based on Modified Current Sampling and Delay Modeling*, in IEEE Journal of

Emerging and Selected Topics in Power Electronics, vol. 10, no. 6, pp. 7109-7119, Dec. 2022.

[12] M. -C. Chou and C. -M. Liaw, *Development of Robust Current 2-DOF Controllers for a Permanent Magnet Synchronous Motor Drive With Reaction Wheel Load*, in *IEEE Transactions on Power Electronics*, vol. 24, no. 5, pp. 1304-1320, May 2009.

[13] Đ. M. Stojić and T. B. Šekara, *A new digital resonant current controller for AC power converters based on the advanced Z-transform*, ISA Transactions, Vol. 129 (part B), pp. 535-545, 2022

[14] J. Wittenburg, Dynamics of Multibody Systems, Springer Verlag Berlin Heidelberg, 2008.

[15] V. Čović, M. P. Lazarević, *Robot Mechanics*, Faculty of Mechanical Engineering, Belgrade, Serbia, 2009.

[16] P. D. Mandić, M. P. Lazarević, Z. Stokić, T. B. Šekara, M., *Dynamic Modelling and Control Design of Seven Degrees of Freedom Robotic Arm,* 6th International Congress of Serbian Society of Mechanics, Tara, Serbia, June 19-21, 2017.

[17] F. L. Lewis, D. M. Dawson, C. T. Abdallah, Robot Manipulator Control, Marcel Dekker, New York, 2004.

[18] P. D. Mandić, M. P. Lazarević, T. B. Šekara, M. Č. Bošković, G. Maione, *Robust control of robot manipulators using fractional order lag compensator,* 7th International Congress of Serbian Society of Mechanics, Sr. Karlovci, Serbia, June 24-26, 2019.

[19] P. D. Mandić, Advanced modeling of complex robotic systems and mechanisms and applications of modern control theory, PhD Dissertation, Faculty of Mechanical Engineering, 2019.

[20] P. D. Mandić, M. P. Lazarević, *An Application Example of Webots in Solving Control Tasks of Robotic System*, FME Transactions (41), pp. 153-162, 2013.

[21] M. Č. Bošković, M. R. Rapaić, T. B. Šekara, P. D. Mandić, M. P. Lazarević, *A novel method for design of complex compensators in control systems,* 18th International Symposium INFOTEH-JAHORINA, March 20-22, 2019.

[22] K. J. Åström, R. M. Murray, *Feedback Systems- An Introduction for Scientists and Engineers*, Princeton, USA: Princeton University Press, 2008.

[23] K. J. Åström, R. H. Panagopoulos, T. Hägglund, *Design of PI Controllers based on Non-Convex Optimization*, Automatica 34(5), pp. 585-601.

[24] M. P. Lazarević, P. D. Mandić, S. Ostojić, *Further results on advanced robust iterative learning control and modeling of robotic systems*, Proc IMechE Part C: J Mechanical Engineering Science, pp. 1-16, 2020.

ANALYSIS OF PLANAR COMPLEX MOTION OF A HOMOGENEOUS DISK AND A MATERIAL POINT WITH EULER-LAGRANGE EQUATIONS IN QUASI-VELOCITIES

Marko M. Gavrilovic

Faculty of Mechanical Engineering, University of Belgrade, Kraljice Marije 16, 11060 Belgrade, Serbia
e-mail: mgavrilovic@mas.bg.ac.rs

Abstract

The purpose of this paper is to present quasi-coordinates and quasi-velocities as quantities of the state of the motion of material systems. In the paper, by applying the Lagrange formalism, Euler-Lagrange differential equations of motion were formed, i.e., Lagrange equations of the second kind in quasi-velocities for mechanical systems with a finite number of degrees of freedom. It could be said that the Euler-Lagrange differential equations of motions have an important role in the analysis of a rigid body motion and, in general, control of nonholonomic mechanical systems.

The paper contains the analysis of complex planar motion of a material system that consist of platform (rigid body) – homogenous disk, that is rolling over a horizontal plane without slipping, and one material point that moves relative to the disk, in the groove on the disk, with Euler-Lagrange differential equations of motion in quasi-velocities, which together with corresponding quasi-coordinates uniquely determine the state of the disk motion relative to the referent coordinate system and Lagrange equations of the second kind over relative generalized coordinates that uniquely determine the motion of the material point.

On the other hand, the equations of motion thus obtained will be compared with the differential equations of the described motion of the material system obtained from the Lagrange equations of the second kind for non-holonomic material systems, where the advantage of applying the Euler-Lagrange differential equations in quasi-velocities over the Lagrange differential equations of the second kind for nonholonomic mechanical systems will be demonstrated.

Likewise, at the very beginning of the paper, the relations between Euler-Lagrange equations over quasi-velocities and the theorems of classical mechanics will be shown. That means that all of the differential equations that uniquely determine equations of motions of the material system will be expressed with dynamic quantities such as momentum and angular momentum of the mentioned system.

Keywords: nonholonomic mechanics, rigid body, homogenous disk, rolling without slipping, dynamics, point contact, quasi-velocities, quasi-coordinates, Euler-Lagrange equations, Boltzmann-Hamel equations.

1. Introduction

The Euler-Lagrange equations were developed by Boltzmann (Ludwig Eduard Boltzmann, 1844-1906) and Hamel (Georg Karl Wilhelm Hamel, 1877-1954) at the very beginning of the twentieth

century, and therefore some call this Lagrange formalism the Boltzmann-Hamel equations. The first time that these equations have been published in original was in the papers [3-5] but at that time they did not use Hamel coefficients which are the key parts in these differential equations. The first idea about this way of analysis of nonholonomic system was initially published by H. Hertz in the paper [6]. Important works on which Hamel had relied are the works of H. Poincaré [14], V. Voltera [17], P. Voronets [18], Tzénoff [15-16] together with the work of Boltzmann [1-2], and formed a final form of the equations.

Euler-Lagrange differential equations are most often used for the formation of differential equations of spherical and general motion of a rigid body, but they can also be used for complex motions analysis of material systems in 3D space. In the case of the movement of a free rigid body, for the quasi-velocity of the body, the projections of the velocity vector of its pole of translation and the projection of the current angular velocity vector of the body on the axes of the Cartesian coordinate system are most often used, which can be seen in a textbook [21] (N. V. Butenin, J. L. Lunc, D. R. Merkin). The structure of the Euler-Lagrange differential equations of motion for the case of general motion of a rigid body can be related to the law of change of the momentum of a free rigid body and the law of change of the body angular momentum for its translation pole or its center of mass [8] (A. I. Lurie).

The formation of the Euler-Lagrange differential equations of observed material systems requires that the kinetic energy of those systems must be expressed as a function of quasi-velocity and quasi-coordinates (generalized coordinates). In the case of complex motion of mechanical system that consists of platform - rigid body and a system of material points, that are in a motion relative to the platform, Euler-Lagrange differential equations are being written over quasi-velocities that, with corresponding quasi-coordinates, determine the state of the motion of the platform (in relation to non-moving reference object/coordinate system) [21]; and Lagrange equations of the second kind over relative generalized which uniquely determine the motion of the mass points [8].

Some texts on mechanics such as Sir Edmund Taylor Whittaker's [19-20] and Leonard Meirovitch's [9-10] contain advanced analysis of these equations and show the advantage of their use over Lagrange equations of the second kind and many other formalisms for nonholonomic mechanical systems. According to Neimark (Mark Aronovich Naimark, 1909-1978) and Fufaev (N.A. Fufaev) (1967) [11], Lagrange equations over quasi-coordinates, i.e., Euler-Lagrange differential equations of motion are developed as a form that is appliable for every dynamical system with or without imposed mechanical constraints. Recent development of the Euler-Lagrange differential equations of motion has been influenced by Passeron [13], Houston [7], Passerello (1980) and Oz [12] with their works.

2. Equations of motion in Quasi-Velocities

2.1 Quasi-Velocities

Velocities of the points of material system, in most cases, could be obtained with n mutually independent parameters ω^s that represent linear form of generalized velocities $\dot{q}^r$, whose coefficient are functions of generalized coordinates:

$$\omega^s = a_r^s(q^p)\,\dot{q}^r, \quad p,s,r,l = 1,2,\dots,n \tag{1}$$

For quantities ω^s, that determine the velocities of system points, could be assumed that represent time derivations d'/dt of some functions $\pi^s = \pi^s(t)$:

$$\omega^s = \frac{\mathrm{d}'\pi^s}{\mathrm{dt}} \rightarrow \mathrm{d}'\pi^s = \omega^s \mathrm{dt}$$

thus equations (1) could be written as:

$$\mathrm{d}'\pi^{\mathrm{s}} = a_{\mathrm{r}}^{s}(\mathrm{q}^{\mathrm{p}})\mathrm{dq}^{\mathrm{r}} \tag{2}$$

In the case when $\partial a_r^s/\partial q^p = \partial a_p^s/\partial q^r$, quantities $\mathrm{d}'\pi^{\mathrm{s}}$ given with equation (2) represent total derivatives of scalar functions $\pi^{\mathrm{s}} = \pi^{\mathrm{s}}(q^r)$, so quantities π^{s} could be adopted as new generalized coordinates of a material system. On the other hand, when $\partial a_r^s/\partial q^p \neq \partial a_p^s/\partial q^r$, quantities $\mathrm{d}'\pi^{\mathrm{s}}$ do not represent total derivatives of functions $\pi^{\mathrm{s}} = \pi^{\mathrm{s}}(q^r)$, and it would be possible to obtain π^{s} as:

$$\pi^{\mathrm{s}}(t) - \pi^{\mathrm{s}}(t_0) = \int_{t_0}^{t} a_r^s \, \dot{q}^r \, \mathrm{dt}$$

but now, in general sense, quantities π^{s} couldn't be generalized coordinates of the material system. Due to that, these quantities π^{s} are called Quasi-Coordinates. In this paper, we introduce the assumption that the determinant of the matrix of coefficients of the linear form (1) is different from zero: $\det[a_r^s] \neq 0$, and now generalized velocities of material system could be expressed as a function of quasi-velocities

$$\dot{q}^s = b_r^s(q^p)\omega^r \tag{3}$$

where $[b_r^s] = \left[a_k^p\right]^{-1}$. We could also introduce Kronecker delta symbols as $\delta_p^s = b_r^s a_k^r$. Now, from relation (3) we could obtain derivatives of generalized coordinates as:

$$\mathrm{d}q^s = b_r^s(q^p)\mathrm{d}'\pi^r$$

2.1 The Euler-Lagrange equations

Let the motion of a stationary, holonomic material system in configuration space of *n* generalized coordinates q^s be described with Lagrange differential equations of the second kind:

$$\frac{\mathrm{d}}{\mathrm{dt}}\left(\frac{\partial T\prime}{\partial \dot{q}^s}\right) - \frac{\partial T'}{\partial q^s} = Q_s, \quad s,r,p,l,m = 1,2,\dots,n, \tag{4}$$

where $T' = T'(q^r, \dot{q}^r)$ is the kinetic energy written as a function of generalized coordinates q^r and generalized velocities $\dot{q}^r$ of the observed system. With relation (3), we could write kinetic energy as a function of generalized coordinates and quasi-velocities of the system $T'\left(q^r, \dot{q}^r = b_p^r\omega^p\right) = T(q^r, \omega^r)$ [3-5]. Now, partial derivatives in equation (4) are given with the next relations:

$$\begin{gathered}\frac{\partial T'}{\partial \dot{q}^s} = \frac{\partial T}{\partial \omega^r} a_s^r \\ \frac{\partial T'}{\partial q^s} = \frac{\partial T}{\partial q^s} + \frac{\partial T}{\partial \omega^r}\frac{\partial a_p^r}{\partial q^s}\,\dot{q}^p \\ \frac{\mathrm{d}}{\mathrm{dt}}\left(\frac{\partial T'}{\partial \dot{q}^s}\right) = \frac{\mathrm{d}}{\mathrm{dt}}\left(\frac{\partial T}{\partial \omega^r}\right) a_s^r + \frac{\partial T}{\partial \omega^r}\frac{\partial a_s^r}{\partial q^p}\,\dot{q}^p\end{gathered} \tag{5}$$

To derive Euler-Lagrange differential equations, Lagrange differential equations of the second kind (4) must be multiplied with coefficient b_l^s, and then it is needed to make contraction over counter *l* of all equations (4) including in them values of partial derivatives given with (5) [5]:

$$\frac{\mathrm{d}}{\mathrm{dt}}\left(\frac{\partial T}{\partial \omega^l}\right) + b_l^s\frac{\partial T}{\partial \omega^r}\frac{\partial a_s^r}{\partial q^p}\,\dot{q}^p - b_l^s\frac{\partial T}{\partial q^s} - b_l^s\frac{\partial T}{\partial \omega^r}\frac{\partial a_s^r}{\partial q^p}\,\dot{q}^p = b_l^s Q_s \tag{6}$$

With the elimination of generalized velocities $\dot{q}^p$ from equations (6), with relation (3), and with relation $\partial T/\,\partial \pi^r = b_r^s \partial T/\partial q^s$ the Euler-Lagrange differential equations are obtained [1-5]

$$\frac{\mathrm{d}}{\mathrm{dt}}\left(\frac{\partial T}{\partial \omega^r}\right) - \frac{\partial T}{\partial \pi^r} + \gamma_{pr}^s \frac{\partial T}{\partial \omega^s}\omega^p = P_r \tag{7}$$

where γ_{pr}^s are Hamel coefficients [3], [8], [20]:

$$\gamma_{ml}^r = \left(\frac{\partial a_s^r}{\partial q^p} - \frac{\partial a_p^r}{\partial q^s}\right) b_l^s b_m^p \tag{8}$$

and P_r are generalized forces over quasi-coordinates π^r, whose virtual work is given as

$$\delta' A = Q_s b_r^s(q^p)\delta\pi^r = P_r(t, q^p, \omega^p)\delta\pi^r \tag{9}$$

2.1 Differential equations of complex motion of material system

The state of the motion of observed material system, that consists of platform - rigid body with mass *M* and *N* material points that are in relative motion in relation to the platform, could be described with two groups of equations. One group consists of relative generalized coordinates q^i and relative generalized velocities $\dot{q}^i$. Nonetheless, the other group contains quasi-coordinates π^s, that is generalized coordinates q^{n+s} and quasi-velocities $\omega^s = \dot{\pi}^s$. It's necessary to write differential equations of the system motion for the given initial condition at the moment $t_0 = 0$:

$$q_0^i = q_0^i(0),\ \ \dot{q}_0^i = \dot{q}_0^i(0),\ \ \omega_0^s = \omega_0^s(o) \ \text{ and } \ q_0^{n+s} = q_0^{n+s}(0)$$

and to obtain its equations of motions:

$$q^i = q^i(t) \ \text{ and } \ q^{n+s} = q^{n+s}(t)$$

Based on the fact that there are two types of equations, i.e. two groups, the motion of the material system will be described with two groups of differential equations of motion. One group is described with the Lagrange equations of the second kind written over relative generalized coordinates q^i:

$$\mathcal{L}_i(T) = \frac{\mathrm{d}}{\mathrm{dt}}\left(\frac{\partial T}{\partial \dot{q}^i}\right) - \frac{\partial T}{\partial q^i} = Q_i \tag{10}$$

where *T* is kinetic energy of the system, and Q_i are generalised forces over generalized coordinates q^i. The other group of differential equations of motions is represented with Euler-Lagrange equations over quasi-coordinates ω^s, where they can be divided into two groups with three equations due to six degrees of body freedom. Also, $\partial T/\partial \pi^r = 0$ thus the equations are:

$$\begin{aligned} &\frac{\mathrm{d}}{\mathrm{dt}}\left(\frac{\partial T}{\partial \omega^t}\right) + \gamma_{pt}^s \frac{\partial T}{\partial \omega^s}\omega^p = P_t \\ &\frac{\mathrm{d}}{\mathrm{dt}}\left(\frac{\partial T}{\partial \omega^{t+3}}\right) + \gamma_{pt+3}^s \frac{\partial T}{\partial \omega^s}\omega^p = P_{t+3} \end{aligned} \tag{11}$$

Kinetic energy of material system *T* consists of three additions: $T = T_m + T_p + T_r$, where T_r is the kinetic energy of material points – relative kinetic energy, T_m is mixed part and T_p is kinetic energy of the platform with the mass points that are "frozen" on that platform, and they are given as [8]:

$$T_r = \frac{1}{2}\sum_{\nu=1}^{N} m_\nu v_\nu'^2 = \frac{1}{2} a_{ij}(q^p)\dot{q}^i\dot{q}^j$$

$$T_p = \frac{1}{2}\left[m v_O^2 + 2m(\vec{v}_O \times \vec{\omega}) \cdot \vec{r}_C'(q^i) + \vec{\omega} \cdot \boldsymbol{J}^O(q^i) \cdot \vec{\omega}\right]$$

$$T_m = \vec{v}_O \cdot \vec{K}_r + \vec{\omega} \cdot \vec{L}_r^O$$

where v_O is velocity of translation pole of the platform, $\vec{\omega}$ - current angular velocity vector, $\vec{r}_C'(q^i)$ – vector of the centre of mass of the platform, $\boldsymbol{J}^O(q^i)$ – system inertia tensor, $\vec{K}_r$ – relative momentum and $\vec{L}_r^O$ – relative angular momentum in relation to the pole of the body translation *O*. Now differential equations of the relative motion (10) become:

$$\mathcal{L}_i(T_r) = Q_i - \frac{\partial}{\partial q^i}(\Pi^O + \Pi^\omega) + Q_i^{\dot{\omega}} + \Gamma_i$$

where Q_i are generalised forces, Π^O - potential energy of inertial forces of translational movement given as $\Pi^O = M\vec{a}_O \cdot \vec{r}_C'$, Π^ω – potential energy of centrifugal forces given as $\Pi^\omega = -1/2\ \vec{\omega} \cdot \boldsymbol{J}^O \cdot \vec{\omega}$, $Q_i^{\dot{\omega}}$ – generalized rotary inertial forces over generalized coordinates q^i given with relation:

$$Q_i^{\dot{\omega}} = -\dot{\vec{\omega}} \cdot \frac{\partial \vec{L}_r^O}{\partial \dot{q}^i} = -\sum_{\nu=1}^{N} (m_\nu\, \dot{\vec{\omega}} \times \vec{r}_\nu') \cdot \frac{\partial \vec{r}_\nu'}{\partial q^i}$$

and Γ_i are gyroscopic forces given with relation:

$$\Gamma_i = 2\vec{\omega} \cdot \sum_{\nu=1}^{N} m_\nu \frac{\partial \vec{r}_\nu'}{\partial q^i} \times \frac{\partial \vec{r}_\nu'}{\partial q^j} \dot{q}^j = \gamma_{ij}\dot{q}^j$$

where γ_{ij} are gyroscope coefficients.

3. Complex motion of a homogenous disk and material point

3.1 Problem statement

Homogenous disk *A* with mass *m* and radius *r* is rolling on the horizontal plate without slipping. The point *T*, whose mass is also m, is in motion relative to the disk as it moves in a groove *AB*. The point *T* is connected with the disk with its centre, point *A*, with the spring whose stiffness is *k*. The length of the spring in undeformed position is l_0. Force couple with an intensity *M* is also acting on the disk into direction showed in Fig. 1. The system is moving in the space of three generalized coordinates: *x* – disk translation, θ – disk rotation and ζ – relative coordinate of point mass *T*. Mechanical system is in motion in a vertical plane. The main goal of the paper is to show that it is much easier to obtain differential equations of motion with the Euler-Lagrange differential equations instead of the Lagrange equations of the second kind.

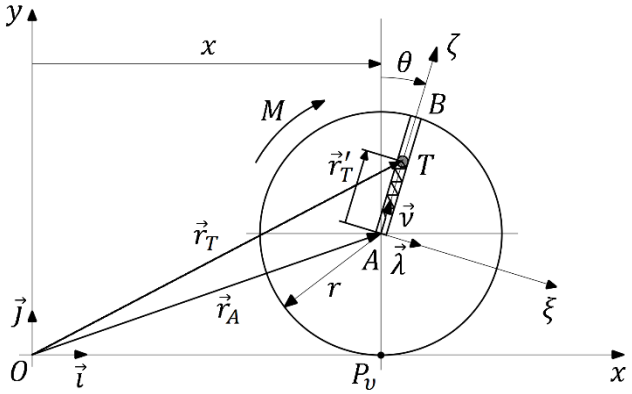

Fig. 1. Problem setting.

2.1 Differential equations obtained with the Lagrange equations of the second kind

Kinetic energy of the system consists of two additions: kinetic energy of the disk and point:

$$T = T_T + T_d = \frac{1}{2}mv_T^2 + \frac{1}{2}mv_A^2 + \frac{1}{2}J_{Az}\omega_d^2$$

Where are:

$$\vec{v}_A = \dot{x}\vec{\imath}, \quad J_{Az} = \frac{1}{2}mr^2, \quad \omega_d = \dot{\theta}$$

$$\vec{v}_T = \vec{v}_A + \dot{\vec{r}}_T' = \dot{x}\vec{\imath} + \vec{\omega} \times \vec{r}_T' + \frac{\mathrm{d_r}\vec{r}_T'}{\mathrm{d}t} = \left(\dot{x} + \dot{\zeta}\sin\theta + \zeta\dot{\theta}\cos\theta\right)\vec{\imath} + \left(\dot{\zeta}\cos\theta - \zeta\dot{\theta}\sin\theta\right)\vec{\jmath}$$

Therefore, the kinetic energy of the observed system is obtained as:

$$T = m\dot{x}^2 + \frac{1}{2}m\dot{\zeta}^2 + \frac{1}{4}mr^2\dot{\theta}^2 + \frac{1}{2}m\zeta^2\dot{\theta}^2 + m\dot{x}\dot{\zeta}\sin\theta + m\zeta\dot{x}\dot{\theta}\cos\theta$$

We know that the velocity of the point contact between disk and the horizontal plane is equal to zero, because there is no slipping, which implicates that there is one nonholonomic (kinematic) constrain in the system. Accordingly, the motion of material system is limited due to that one nonholonomic constraint that is imposed to it. So, the following could be concluded:

$$\vec{v}_{p_v} = \vec{v}_A + \frac{\mathrm{d}}{\mathrm{d}t}\overrightarrow{AP_v} = \dot{x}\vec{\imath} + \vec{\omega} \times \overrightarrow{AP_v} = (\dot{x} - r\dot{\varphi})\vec{\imath} = 0$$

from which the equation of nonholonomic constraint could be obtained as:

$$\Phi = \dot{x} - r\dot{\varphi} = 0 \tag{12}$$

Despite the fact that there are three generalized coordinates, there will also be three Lagrange equations of the second kind over these generalized coordinates. The equations are:

$$\begin{gathered}
\frac{\mathrm{d}}{\mathrm{d}t}\left(\frac{\partial T}{\partial \dot{x}}\right) - \frac{\partial T}{\partial x} = Q_x + \lambda\frac{\partial \Phi}{\partial \dot{x}} = Q_x + \lambda \\
\frac{\mathrm{d}}{\mathrm{d}t}\left(\frac{\partial T}{\partial \dot{\theta}}\right) - \frac{\partial T}{\partial \theta} = Q_\theta + \lambda\frac{\partial \Phi}{\partial \dot{\theta}} = Q_\theta - r\lambda \\
\frac{\mathrm{d}}{\mathrm{d}t}\left(\frac{\partial T}{\partial \dot{\zeta}}\right) - \frac{\partial T}{\partial \zeta} = Q_\zeta + \lambda\frac{\partial \Phi}{\partial \dot{\zeta}} = Q_\zeta
\end{gathered} \tag{13}$$

To close this system of equations (13), the constraint equation (12) must be added to it. As we can see, the main difficulty of the Lagrange equations of the second kind is that the Lagrange multiplier λ must be, somehow, removed from the system of equations. Imagine how the solving of the mechanical system that has got just two nonholonomic constraints would be difficult due to the need to remove all of the Lagrange multipliers. So, the system of equations that we have to solve this problem is:

$$\begin{gathered}
\frac{\mathrm{d}}{\mathrm{d}t}\left(\frac{\partial T}{\partial \dot{\theta}}\right) + r\frac{\mathrm{d}}{\mathrm{d}t}\left(\frac{\partial T}{\partial \dot{x}}\right) - \frac{\partial T}{\partial \theta} - r\frac{\partial T}{\partial x} = Q_\theta + rQ_x \\
\frac{\mathrm{d}}{\mathrm{d}t}\left(\frac{\partial T}{\partial \dot{\zeta}}\right) - \frac{\partial T}{\partial \zeta} = Q_\zeta \\
\dot{x} - r\dot{\varphi} = 0
\end{gathered} \tag{14}$$

The values of the partial derivatives in the equations (14) are:

$$\frac{\partial T}{\partial x} = 0, \quad \frac{\partial T}{\partial \zeta} = m\zeta\dot{\theta}^2 + m\dot{x}\dot{\theta}\cos\theta, \quad \frac{\partial T}{\partial \theta} = m\dot{x}\dot{\zeta}\cos\theta - m\zeta\dot{x}\dot{\theta}\sin\theta$$

$$\frac{\mathrm{d}}{\mathrm{dt}}\left(\frac{\partial T}{\partial \dot{\zeta}}\right) = m\ddot{\zeta} + m\ddot{x}\sin\theta + m\dot{x}\dot{\theta}\cos\theta \tag{15}$$

$$\frac{\mathrm{d}}{\mathrm{dt}}\left(\frac{\partial T}{\partial \dot{x}}\right) = 2m\ddot{x} + m\ddot{\zeta}\sin\theta + 2m\dot{\zeta}\dot{\theta}\cos\theta + m\zeta\ddot{\theta}\cos\theta - m\zeta\dot{\theta}^2\sin\theta$$

$$\frac{\mathrm{d}}{\mathrm{dt}}\left(\frac{\partial T}{\partial \dot{\theta}}\right) = \frac{1}{2}mr^2\ddot{\theta} + 2m\zeta\dot{\zeta}\dot{\theta} + m\zeta^2\ddot{\theta} + m\dot{\zeta}\dot{x}\cos\theta + m\zeta\ddot{x}\cos\theta - m\zeta\dot{x}\dot{\theta}\sin\theta$$

The virtual work of the forces that act on the material system is described as:

$$\delta' A = -mg\vec{j}\cdot\delta[\,(r+\zeta\cos\theta)\vec{j}\,] + M\delta\theta = -mg\delta\zeta\cos\theta + mg\zeta\sin\theta\,\delta\theta + M\delta\theta \tag{16}$$

Potential energy of the spring whose stiffness is *k* is:

$$\Pi = \frac{1}{2}k(\zeta - l_0)^2 + c \tag{17}$$

Based on (16) and (17) generalized forces of the material system are:

$$\begin{gathered} Q_x = 0 \\ Q_\theta = mg\zeta\sin\theta + M \\ Q_\zeta = -mg\cos\theta - k(\zeta - l_0) \end{gathered} \tag{18}$$

When we put (15) and (18) into system (14), system (14) becomes:

$$\begin{gathered} \frac{1}{2}mr^2\ddot{\theta} + 2m\zeta\dot{\zeta}\dot{\theta} + m\zeta^2\ddot{\theta} + m\dot{\zeta}\dot{x}\cos\theta + m\zeta\ddot{x}\cos\theta - m\zeta\dot{x}\dot{\theta}\sin\theta \\ + r\left(2m\ddot{x} + m\ddot{\zeta}\sin\theta + 2m\dot{\zeta}\dot{\theta}\cos\theta + m\zeta\ddot{\theta}\cos\theta - m\zeta\dot{\theta}^2\sin\theta\right) - m\dot{x}\dot{\zeta}\cos\theta \\ + m\zeta\dot{x}\dot{\theta}\sin\theta = mg\zeta\sin\theta + M \\ m\ddot{\zeta} + m\ddot{x}\sin\theta - m\zeta\dot{\theta}^2 = -mg\cos\theta - k(\zeta - l_0) \\ \dot{x} - r\dot{\varphi} = 0 \end{gathered}$$

Finally, two differential equations of the system motion are obtained as:

$$\begin{gathered} \frac{5}{2}mr^2\ddot{\theta} + 2m\zeta\dot{\zeta}\dot{\theta} + m\zeta^2\ddot{\theta} + mr\ddot{\zeta}\sin\theta + 2mr\dot{\zeta}\dot{\theta}\cos\theta + 2mr\zeta\ddot{\theta}\cos\theta - mr\zeta\dot{\theta}^2\sin\theta \\ = mg\zeta\sin\theta + M \\ m\ddot{\zeta} + m\ddot{x}\sin\theta - m\zeta\dot{\theta}^2 = -mg\cos\theta - k(\zeta - l_0) \end{gathered} \tag{19}$$

2.1 Differential equations obtained with the Euler-Lagrange equations

Now, differential equations of the same system motion (19) are going to be derived by using the Euler-Lagrange equations over quasi-velocities and quasi-coordinates. Now for the quasi-velocities we could take the rotation of the disk θ and the nonholonomic (kinematic) constraint Φ. So, the quasi-velocities of the given problem are:

$$\begin{gathered} \omega^1 = \dot{\theta} \\ \Phi = \omega^2 = \dot{x} - r\dot{\theta} \end{gathered} \tag{20}$$

From (20), generalized coordinates must be expressed with quasi-velocities because the kinetic energy of the system must be written as a function of them. So they are:

$$\begin{gathered} \dot{\theta} = \omega^1 \\ \dot{x} = \omega^2 + r\omega^1 \end{gathered} \tag{21}$$

The kinetic energy of the system, written as a function of generalized velocities and coordinates is, normally, the same as in the previous subsection 2.1:

$$T' = m\dot{x}^2 + \frac{1}{2}m\dot{\zeta}^2 + \frac{1}{4}mr^2\dot{\theta}^2 + \frac{1}{2}m\zeta^2\dot{\theta}^2 + m\dot{x}\dot{\zeta}\sin\theta + m\zeta\dot{x}\dot{\theta}\cos\theta$$

However, we must put (21) in the kinetic energy and express it as a function of quasi-velocities and quasi coordinates. Now, generalized velocities are ready, but an angle θ is unknown as a function of quasi-coordinates. Equation (8) could be used for that, but for more complex systems it would be very difficult. The trick that can be used here is to examine commutativity of the operator of differentiation and variation:

$$\frac{\mathrm{d}}{\mathrm{d}t}(\delta\pi^1) - \delta(\omega^1) = 0 \quad \text{and} \quad \frac{\mathrm{d}}{\mathrm{d}t}(\delta\pi^2) - \delta(\omega^2) = 0 \tag{22}$$

which means that, in the case of this material system, generalized coordinates are actually quasi-coordinates of the system. Also, the conclusion is that the quasi-coordinates are actually integrable functions. That means the following:

$$\pi^1 = \theta(t) - \theta(0) = \theta$$

Now, kinetic energy of the system as a function of quasi-coordinates and quasi-velocities is given:

$$T = m(\omega^2 + r\omega^1)^2 + \frac{1}{2}m\,\dot{\zeta}^2 + + \frac{1}{4}mr^2(\omega^1)^2 + \frac{1}{2}m\zeta^2(\omega^1)^2 + m(\omega^2 + r\omega^1)\dot{\zeta}\sin\pi^1 + m\zeta(\omega^2 + r\omega^1)\omega^1\cos\pi^1$$

The advantage of the Euler-Lagrange differential equations is that there are only two differential equations, instead of 4 as in the previous subsection, and one equation is over ω^1, the other equation is over quasi-velocity ω^2 and it is equal to zero, so the second one is over relative motion of point:

$$\frac{\mathrm{d}}{\mathrm{dt}}\left(\frac{\partial T}{\partial\dot{\zeta}}\right) - \frac{\partial T}{\partial\zeta} = Q_\zeta \tag{23}$$

$$\frac{\mathrm{d}}{\mathrm{dt}}\left(\frac{\partial T}{\partial\omega^1}\right) - \frac{\partial T}{\partial\pi^1} + \gamma_{p1}^s\frac{\partial T}{\partial\omega^s}\omega^p = P_1 \tag{24}$$

Equation (23) stays unchanged in this case, and it is the same as in the subsection 2.1. Now, the part in the equation (24) with Hamel coefficients is:

$$\gamma_{p1}^s\frac{\partial T}{\partial\omega^s}\omega^p = \gamma_{11}^1\frac{\partial T}{\partial\omega^1}\omega^1 + \gamma_{11}^2\frac{\partial T}{\partial\omega^2}\omega^1 + \gamma_{21}^1\frac{\partial T}{\partial\omega^1}\omega^2 + \gamma_{21}^2\frac{\partial T}{\partial\omega^2}\omega^2 = 0$$

The real reason why this part of the equations (24) is equal to zero are relations (22). Therefore, there is also one important conclusion. The kinematic constraint Φ is quasi-kinematic/quasi-nonholonomic constraint, and with that fact, every time the quasi-coordinates of the system are going to be generalized coordinates of the system. Also, the Hamel coefficients are always equal to zero when the relation (22) is, likewise, zero. Thus, partial derivatives of the equation (24) are:

$$\frac{\partial T}{\partial\pi^1} = m(\omega^2 + r\omega^1)\dot{\zeta}\cos\pi^1 - m\zeta(\omega^2 + r\omega^1)\omega^1\sin\pi^1$$

$$\frac{\mathrm{d}}{\mathrm{dt}}\left(\frac{\partial T}{\partial\omega^1}\right) = 2mr(\dot{\omega}^2 + r\dot{\omega}^1) + \frac{1}{2}mr^2\dot{\omega}^1 + 2m\zeta\dot{\zeta}\omega^1 + m\zeta^2\dot{\omega}^1 + mr\ddot{\zeta}\sin\pi^1 + mr\dot{\zeta}\omega^1\cos\pi^1 + m\dot{\zeta}\omega^2\cos\pi^1 + m\zeta\dot{\omega}^2\cos\pi^1 - m\zeta\omega^1\omega^2\sin\pi^1 + 2mr\dot{\zeta}\omega^1\cos\pi^1 + 2mr\zeta\dot{\omega}^1\cos\pi^1 - 2mr\zeta(\omega^1)^2\sin\pi^1$$

Another fact to prove that this is much easier than Lagrange equations of the second kind is that quantities ω^2 and $\dot{\omega}^2$ are equal to zero. Thus, previous partial derivatives become:

$$\frac{\partial T}{\partial \pi^1} = mr\omega^1\dot{\zeta}\cos\pi^1 - m\zeta r(\omega^1)^2\sin\pi^1$$

$$\frac{\mathrm{d}}{\mathrm{dt}}\left(\frac{\partial T}{\partial \omega^1}\right) = \frac{5}{2}mr^2\dot{\omega}^1 + 2m\zeta\dot{\zeta}\omega^1 + m\zeta^2\dot{\omega}^1 + mr\ddot{\zeta}\sin\pi^1 + 3mr\dot{\zeta}\omega^1\cos\pi^1 + 2mr\zeta\dot{\omega}^1\cos\pi^1 - 2mr\zeta(\omega^1)^2\sin\pi^1$$

When return quasi-velocities and quasi-coordinates as a function of generalized velocities and coordinates, the final equations of the system motions are proved, and they are:

$$\frac{5}{2}mr^2\ddot{\theta} + 2m\zeta\dot{\zeta}\dot{\theta} + m\zeta^2\ddot{\theta} + mr\ddot{\zeta}\sin\theta + 2mr\dot{\zeta}\dot{\theta}\cos\theta + 2mr\zeta\ddot{\theta}\cos\theta - mr\zeta\dot{\theta}^2\sin\theta = mg\zeta\sin\theta + M$$

$$m\ddot{\zeta} + m\ddot{x}\sin\theta - m\zeta\dot{\theta}^2 = -mg\cos\theta - k(\zeta - l_0)$$

3. Conclusions

The Euler-Lagrange differential equations of motion of both holonomic and non-holonomic material systems are discussed in the paper. As examples of holonomic material systems to which Euler-Lagrange differential equations were applied, the general movement in Euclidean space was considered, as well as the complex movement of a material system consisting of a platform, a free rigid body and a supported system - material points. The results of such an approach show a much greater efficiency and transparency of the Euler-Lagrangian differential equations of motion compared to the application of other formalisms of Lagrangian mechanics to the considered problems of motion.

On the basis of this example, the advantage of applying the Euler-Lagrange differential equations of motion in the analysis of the motion of non-holonomic material systems, compared to other formalisms of analytical mechanics, was demonstrated. This advantage is reflected, among other things, in the fact that in the Euler-Lagrange differential equations of motion of non-holonomic mechanical systems, the problem of determining the reactions of ideal kinematic restraining links is separated from the problem of determining its final equations of motion.

In future work, the complex movement of material systems consisting of a supporting body-platform and with supported moving body systems on them, whose movement is limited by external and internal geometric and kinematic non-stationary restraining connections, will be analyzed.

Acknowledgment: This publication is based upon work from COST Action CA21106 COSMIC WISPers and CA21155 HISTRATE supported by COST (European Cooperation in Science and Technology) and research supported by the Ministry of Science, Technological Development and Innovation of the RS under Contract 451-03-47/2023-01/ 200105 dated 02/03/2023. This work is a continuation of research started in my master's thesis [22]. I would also like to thank Professor Olivera Jeremic who, as a mentor, introduced me to this field.

References:

[1] Boltzmann, L.: *Über die Form der Lagrange'schen Gleichungen für nicht holonome generalisierte Coordinaten*, Sitzungsberichte der Kaiserlichen Akademie der Wissenschaften in Wien, No. 111, pp. 1603–1614 (1902). Published as F. Hasenöhrl (ed.): Wissenschaftliche Abhandlungen, by Ludwig Boltzmann, Friedrich Hasenöhrl, Cambridge University Press, 2012

[2] Boltzmann, L.: *Vorlesungen über die Prinzipe der Mechanik*. Verlag von Johann Ambrosius Barth, Leipzig, II. Teil (1904)
[3] Hamel G., *Die Lagrange–Eulersche Gleichungen der Mechanik*. Z. Math. Phys. 50(1), 1–57 (1904a)
[4] Hamel G., *Über die virtuellen Verschiebungen in der Mechanik*, Math. Ann. Vol. LIX, pp. 416–434 (1904b)
[5] Hamel G., *Über nichtholonome Systeme*. Math. Ann. 92, 33–41 (1924)
[6] Hertz, H.: *Die Prinzipien der Mechanik in neuem Zusammenhange dargestellt*, (1894) (Ges. Werke. Bd. III. Leipzig. 1910)
[7] Huston, R. L., and Passerello, C. E., 1980, *Multibody Structural Dynamics Including Translation Between the Bodies*, Computers and Structures, Vol. 12, pp. 713-720.
[8] Lurie, I.A.: *Analytical Mechanics*. Springer, Berlin (2002)
[9] Meirovitch, L., 1980, *Computational Methods in Structural Dynamics*, Sijthoff and, Noordhoff, The Netherlands, pp. 242-252.
[10] Meirovitch, L., and Quinn, R. D., 1987, *Equations of Motion for Maneuvering Flexible Spacecraft*, Journal of Guidance and Control, Vol. 10, pp. 453-465.
[11] Neimark, Ju. I., and Fufaev, N. A., 1972, *Dynamics of Nonholonomic Systems*, American Mathematical Society, Providence, R.I., (translated from Russian, 1967).
[12] Oz, H., Meirovitch, L., and Montgomery, R. C , 1980, *On Maneuvering Large Flexible Spacecraft Using an Annular Momentum Control Device*, AIAA and AAS, Astrodynamics Conference, Danvers Mass., Aug. 11-13.
[13] Passeron, L., Gamier, Ch., and Sevennec, B., *Dynamic Modeling and Optimal Control Design for Large Flexible Space Structures*, Mechanical Qualification of Large Flexible Spacecraft Structures, AGARD, Paris, France, 1986, pp. 3-1 to 3-13.
[14] Poincaré, H.: *Les méthodes nouvelles de la m écanique céleste* (1892)
[15] Tzénoff, I.: *Sur les équations du mouvement des systèmes matériels non holonomes*. J. de Math. pures et applique (1920)
[16] Tzénoff, I.: *Sur les équations du mouvement des systèmes matériels non holonomes*. Math. Ann. 91(1/2), 161–168 (1924). https://doi.org/10.1007/BF01498387
[17] Volterra, V.: *Sopra una classe di equazioni dinamiche*. Atti della Reale Accademia delle Scieze, Torino 33, 451–475 (1898)
[18] Voronets, P.: *Equations of motion for nonholonomic systems*. Matematicheskii Sbornik, 22(4) (1901)
[19] Whittaker, E. T., 1944, *Analytical Dynamics of Particles and Rigid Bodies*, Dover Publications, New York, pp. 41-44
[20] Whittaker, E.T.: *A Treatise on the Analytical Dynamics of Particles and Rigid Bodies*, Cambridge, 1904 (available as 4th ed., Cambridge, 1988)
[21] Бутенин Н. В., ЛунцЯ. Л., МеркинД. Р. *Курс теоретической механики*: Учебник. В 2-х томах. Т. II.: Динамика. - 2-е изд., перераб. и доп. - М.: Наука. Главная редакция физико-математической литературы, 1979. - 544 стр.
[22] Гавриловић, М.: *Квазибрзине и квазикоординате. Ојлер-Лагранжеве диференцијалне једначине и Лагранжеве једначине друге врсте сложеног кретања материјалног система.* Мастер рад, Београд 2022, Машински факултет

EXPERIMENTAL AND NUMERICAL ANALYSIS OF THE STRENGTH OF A DRONE ARM MADE OF COMPOSITE MATERIAL

Petar R. Ćosić[1], Miloš D. Petrašinović[1], Aleksandar Grbović[1], Danilo Petrašinović[1], Mihailo Petrović[1], Veljko Petrović[1], Nikola Raičević[1] and Boško Rašuo[1]

[1] Faculty of Mechanical Engineering, University of Belgrade, Kraljice Marije 16, 11120 Belgrade 35, Serbia
e-mail: cpetar112@gmail.com, mpetrasinovic@mas.bg.ac.rs, agrbovic@mas.bg.ac.rs, dpetrasinovic@mas.bg.ac.rs, petrovicmiha@gmail.com, vpetrovic@mas.bg.ac.rs, nraicevic@mas.bg.ac.rs, brasuo@mas.bg.ac.rs

Abstract

Aerospace engineering, as a field in which the reduction of mass has always been one of the primary tasks of its engineers, has made significant progress as a result of numerous developments and advancements in the field of composite materials in the sense of gaining large benefits from the relatively low density that characterizes composites. In the spirit of the increasing use of composite materials on aerospace structures, in this paper we will conduct an experimental and numerical analysis of the strength of a drone arm made of a composite material. Every method of analysis, whether it is analytical, numerical, or experimental, has some advantages and disadvantages. Experimental results are easily affected by random and instrumental errors and numerical methods are highly affected by the chosen physical model. In order to obtain the most reliable analysis solution, a mixture of numerical analysis backed up by experimental data is required. In the hope of bypassing the expensive and time-consuming experiments in the future, in this paper we will conduct a numerical analysis on a drone arm made of composite materials which will then be replicated by an experiment verifying its validity.

Keywords: composites, composite materials, drones, UAV, structural analysis, numerical analysis, experimental analysis.

1. Introduction

Due to their high specific strength ratio, relatively low density, and many other advantages, composite materials have found application in various fields of engineering and applied sciences and continue to be used more and more intensively as production processes develop and enable the production of composite parts without (or with less) manual labor. As mentioned before, aerospace engineering, in particular, has had significant benefits from the properties that characterize composite materials. In the case of drones and UAVs, composite materials play an even greater role in the task of improving their performance. Since UAVs are unmanned vehicles, they rely on sensors, cameras, and other electronics that are powered by batteries which have a large drawback in the form of large relative mass, which along with the mass of sensors, cameras,

and electronics drastically affect the overall performance of UAVs. With this in mind, it is easy to understand why composites are so heavily used on drones and UAVs today [1].

The specific composite drone arm that we are going to be analyzing in this paper can be seen in Fig. 1 (a) along with its CAD model (b). As far as materials are concerned, the arm is made out of woven epoxy-carbon fabrics whose thickness is 0.21 mm.

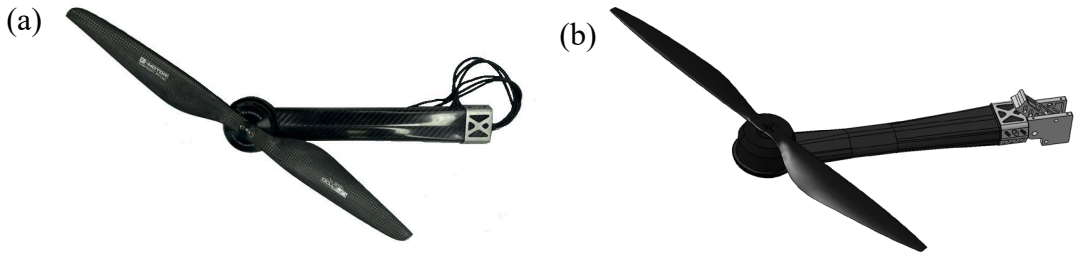

Fig. 1. Drone arm assembly.

2. Experimental analysis

Before presenting the plan of the experiment, it is necessary to give a more detailed breakdown of the scaffolding and the elements on which the experiment is going to be carried out. Figure 2 shows the CAD model of the scaffolding and the main elements connected to it.

One of the crucial elements of the experimental setup is the force loading joint which has the task of applying the load on the drone arm in such a way that it mimics the actual surface loading produced by the thrust force of the propeller. The actual value of the force being applied on the drone arm can be measured using a load cell, while the displacement can be measured using a displacement transducer.

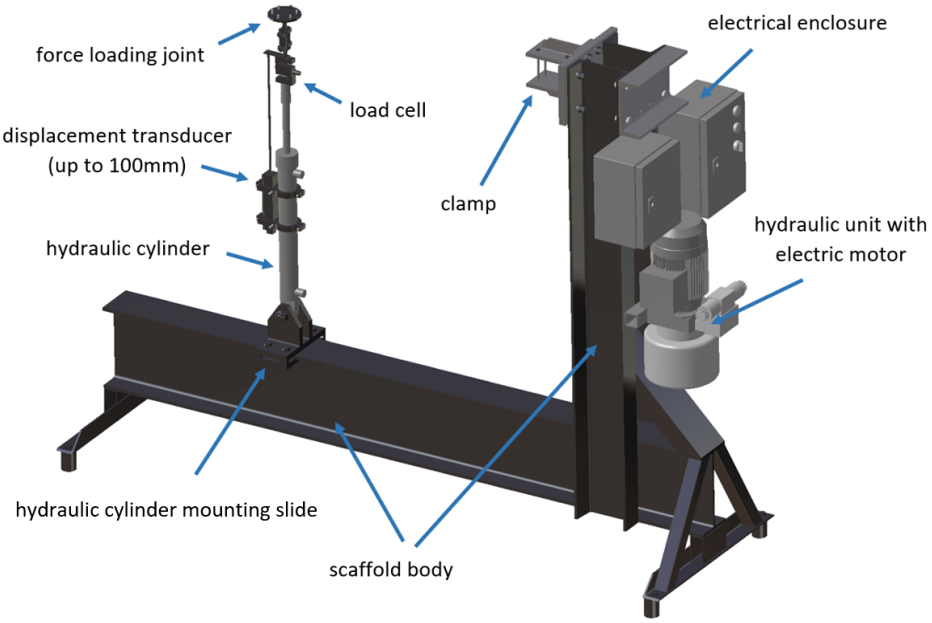

Fig. 2. Scaffolding and main elements.

To simulate the arm-body connection, we can fix one end of the arm in a way that can be seen in Fig. 3. The other end of the arm will be connected to the force loading joint that is, as mentioned, going to attempt to simulate the effect of the propeller's thrust force.

Once we have the drone arm set up, we can connect all the necessary equipment needed for data acquisition (Fig. 4).

The data we are aiming to extract from this experiment is the change in intensity of force in time acquired by the load cell and the change of displacement in time collected from the displacement transducer.

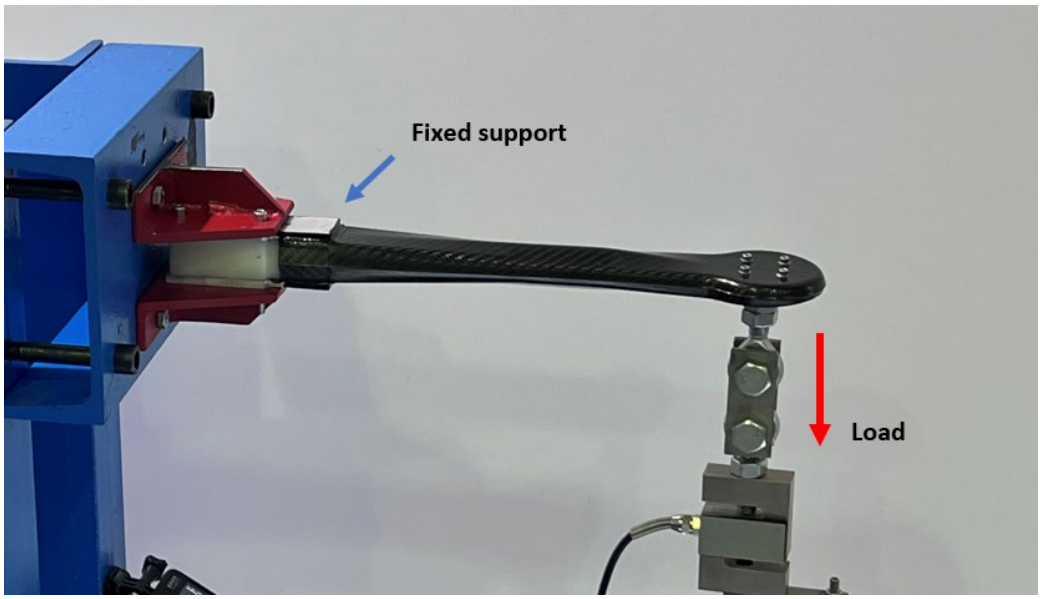

Fig. 3. Loads and constraints.

Once we have the data collected, we can form the connection between the force applied and the displacement produced by removing time from consideration. This connection is what is of crucial value as we are going to try to verify the numerical results that give us the mentioned force-displacement connection.

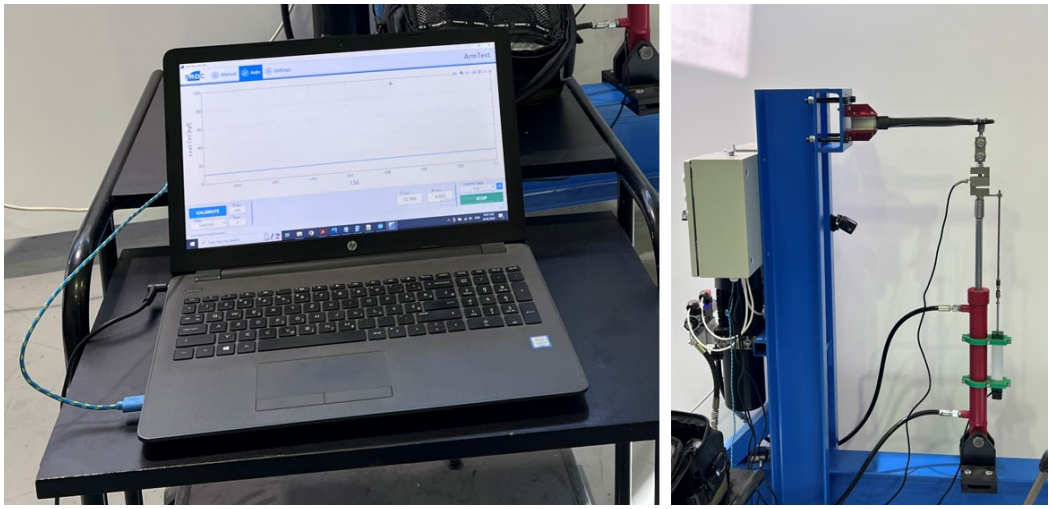

Fig. 4. Experiment setup.

2.1 First experiment – applying the force on the arm until failure

The first experiment will consist of applying force on the drone arm until failure. We can then repeat this four times while monitoring the force-displacement correlation.

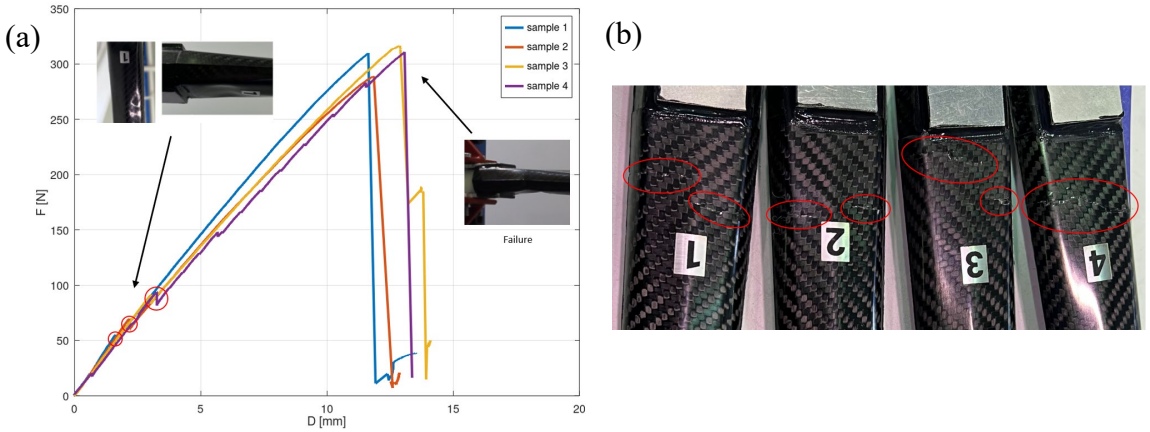

Fig. 5. First experiment results (a) Force-displacement graph and (b) failure location.

On the graph shown in Fig. 5 (a), we can see that failure occurs at roughly 320 N of force. Another interesting thing to notice in this experiment is that for all four samples, failure occurs on the lower part at the base of the arm Fig. 5 (b).

2.2 Second experiment – periodically loading and unloading the arm

Now that we roughly know the force at which our drone arm breaks, we can reduce the applied force (approximately 1/1.5 of its maximum intensity) and periodically load and unload the arm so we can produce a clear force-displacement correlation.

Once we execute this, the data acquired from the sensors will give us the results of the experiment in the form of a set of data that can be represented in the form of three graphs. The first graph shows us the force-time correlation (Fig. 5 (a)), the second one displacement-time correlation (Fig. 5 (b)), and the last graph gives us the key force-displacement correlation (Fig. 6).

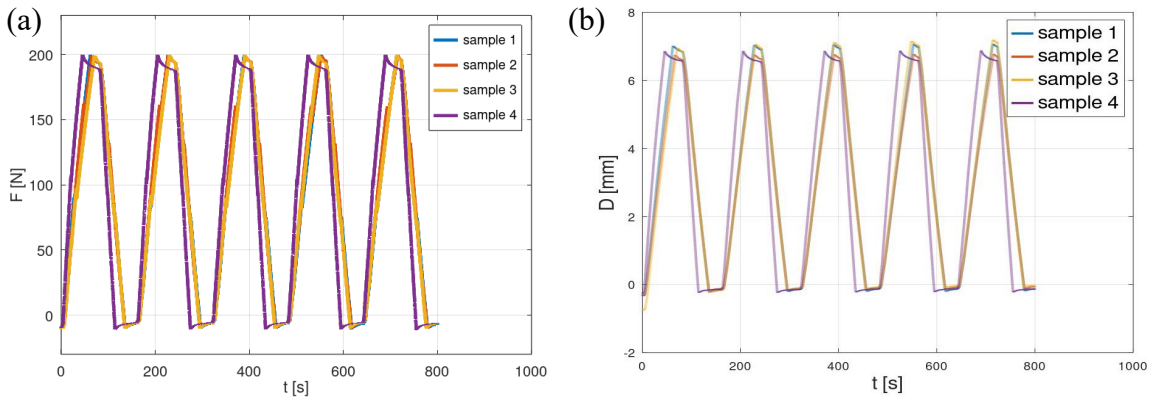

Fig. 6. (a) Force-time graph and (b) displacement-time graph.

Given that we periodically loaded and unloaded the drone arm, on the graph shown in Fig. 6 (a) we can see the occurrence of a slight hysteresis that is the consequence of the dependence of the behavior of the arm on the history of its state.

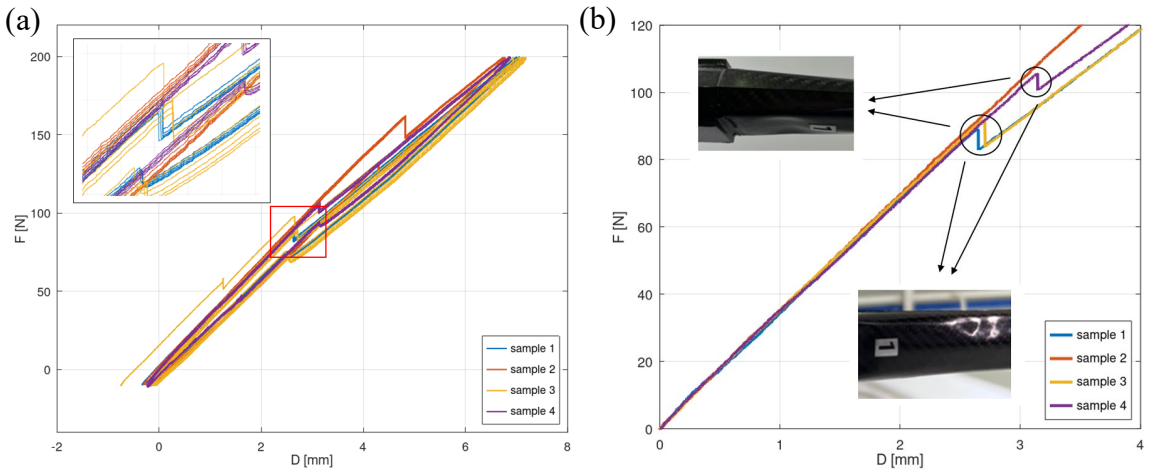

Fig. 7. Force-displacement graph (a) original and (b) filtered.

We are currently not interested in the unloading behavior of the arm so we can filter the results and only show the loading part in the domain that is of interest to us (Fig. 6 (b)).

As we can see in Fig. 6 (b), another anomaly occurs in our analysis in the form of a discontinuity of the linear part as a consequence of slight buckling of the structure of the arm.

Although this is an interesting occurrence, it is not a serious obstacle in our analysis as we are only interested in the linear part from 0 up to 75 N (50 N with a safety factor of 1.5) as that is the domain in which our drone arm is going to be exploited in.

3. Determining the mechanical characteristics of the material

Given that we are going to be conducting a numerical analysis with FEM software, we will need the information on the mechanical characteristics of said material which forces us to conduct an experiment using a tensile test machine in the hope of determining their value.

The first part of the analysis will consist of determining the needed mechanical characteristics of the material using a tensile test machine and the appropriate test samples composed of the same epoxy-carbon woven composite material that the drone arm is made of (Fig. 8).

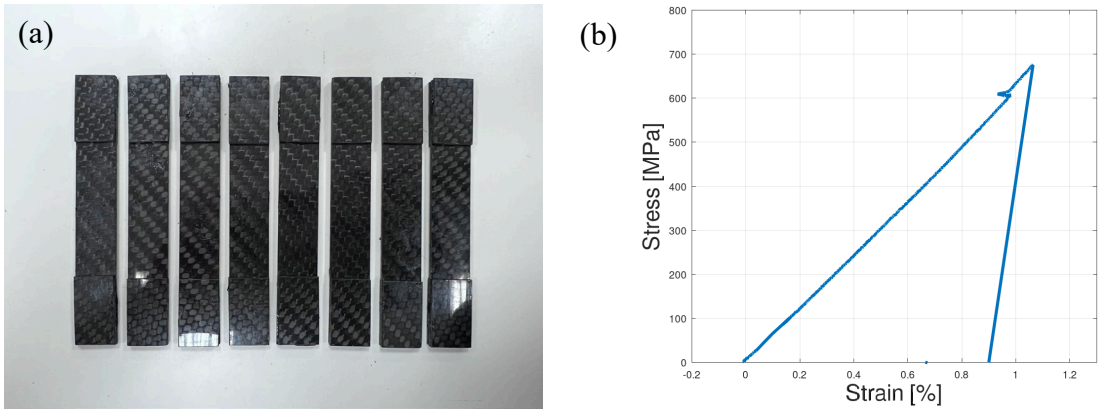

Fig. 8. Test samples (a) and the representative Stress-Strain graph (b).

Out of all the test samples shown in Fig. 8 (a), the behavior of the most representative one can be seen in Fig. 8 (b). Given that we are going to be conducting a numerical analysis in the ANSYS environment, we will need a value of Young's modulus which for the given material

based on the experiment conducted on the tensile test machine is 61 GPa, more specifically, given that we are working with woven fabrics, both modulus E1 and E2 are going to have a value of 61 GPa. Even though, as some of the authors have already shown in [2], elastic properties of carbon fiber reinforced composites vary with temperature changes, in this analysis these properties will have a constant value.

4. Numerical analysis

Now that we have gathered the results from the experimental analysis, we can try to recreate the analysis but this time in a numerical way. In this chapter we will briefly show the process of conducting the numerical analysis. The end goal of this analysis is to gather the data that will allow us to verify the numerical analysis which should produce the same results as the experimental one.

The numerical analysis that is presented was carried out in the ANSYS environment according to the following plan. Firstly, we can analyze the constraints and the loads that the drone arm is subjected to. Then we can extract the adequate geometry from the CAD model of the entire drone arm assembly in accordance with the considered physicality of the problem (Fig. 9).

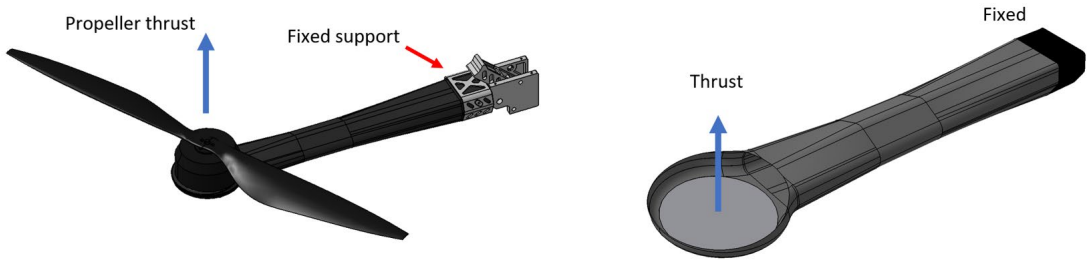

Fig. 9. Loads and constraints.

As can be seen in Fig. 9, we can approximate the fixed support of the arm by restricting all translations and rotations on part of the drone arm that the support is applied on [3].

In the case of loads, the only force acting on the arm is the thrust force of the propeller [4]. Given that we are trying to replicate the conducted experiment, we need to model the entire assembly so we can apply the appropriate contacts while conducting the numerical analysis (Fig. 10).

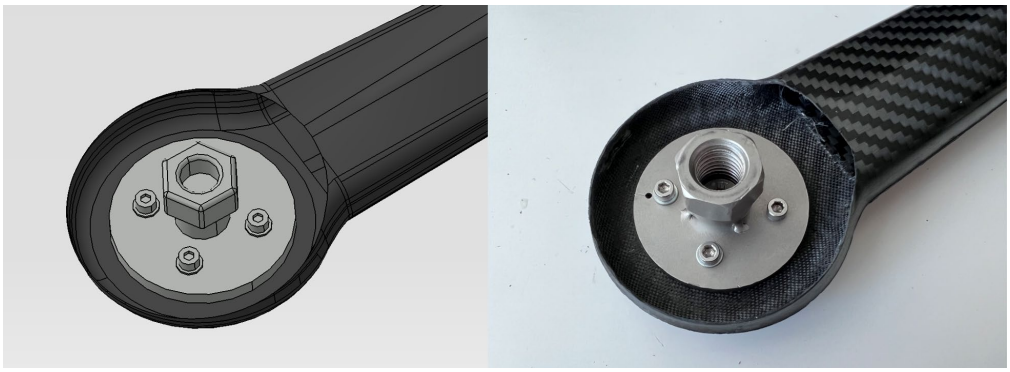

Fig. 10. Model of the attachment part used for creating appropriate contacts.

The next step is to form the fabrics and the laminate stackups by following the number of layers that are, for the specific drone arm that we are going to be observing, placed in the way that can be seen in Fig. 11.

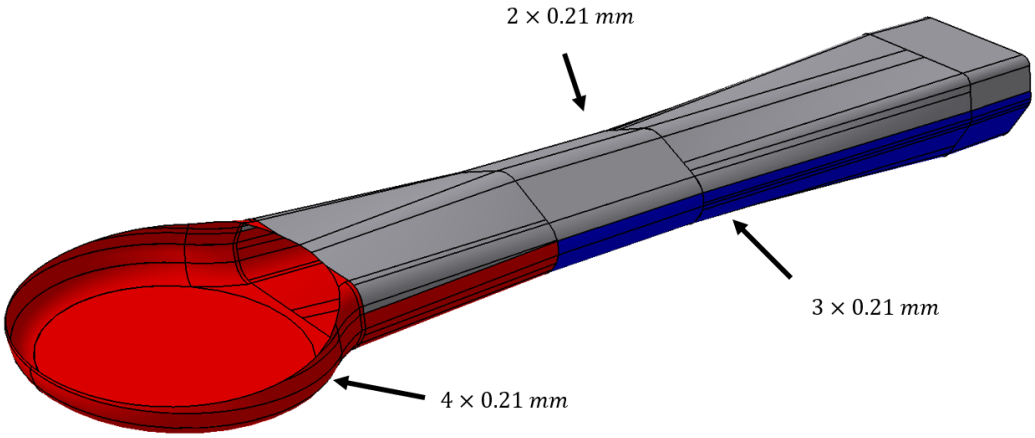

Fig. 11. Number of layers on a given section.

In order to be able to assess the accuracy of the fiber orientation, we can simultaneously display the actual sample arm and the simulation model (Fig. 12) and compare the fiber orientation in both cases. In Fig. 12, we can notice that the fibers are, in both cases, oriented along and perpendicular to the arm's length.

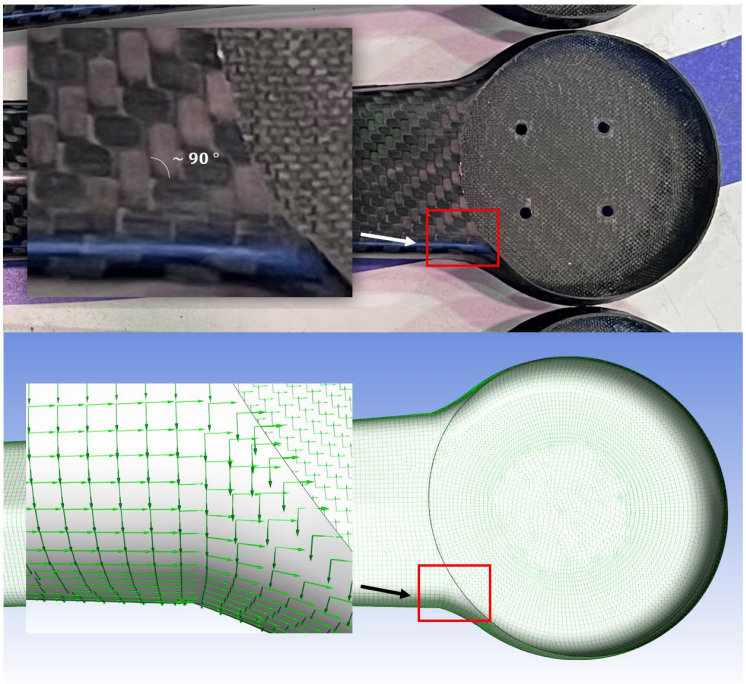

Fig. 12. Fiber orientation validation.

5. Results verification

The crucial part of this paper is the verification of the results of the numerical analysis with the experimental data. The best way to do this is to form the linear part of the force-displacement curve using the numerical model that we previously formed. We can do this by forming two points and drawing a line through them. We can acquire these points [displacement, force] by loading our drone arm with a force of an arbitrary intensity and reading the displacement value of the appropriate node (Fig. 13 (a)). Once this is done twice, there are two points in a plane from which a numerically produced linear part can be formed (Fig. 13 (b)).

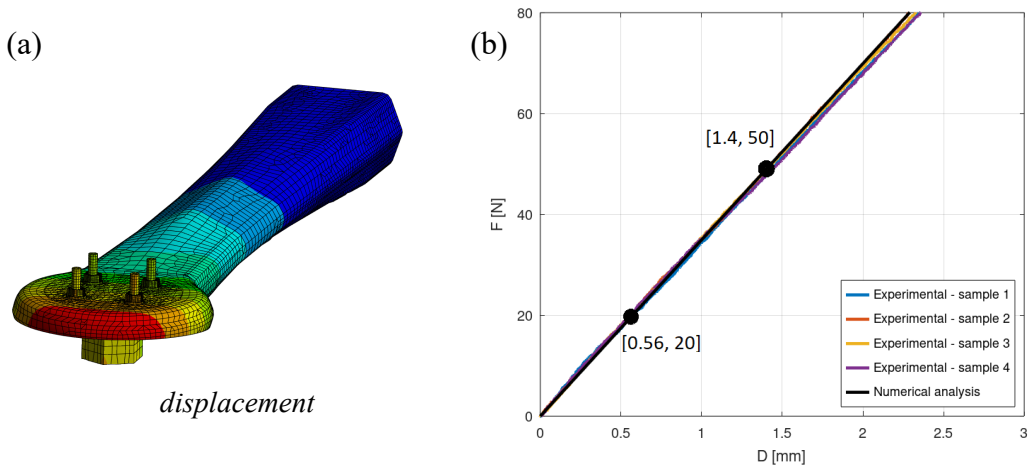

Fig. 13. Results verification (a) ANSYS simulation and (b) Force-displacement comparison.

6. Conclusions

As we can see in Fig. 13 (b), the slope of the numerical curve is roughly the same as the slope of the experimental one which tells us that the numerical model is correctly formed and is valid for further use. The validity of this analysis allows us to bypass the entire expensive and risky experimental process, and it allows us to safely conduct the numerical analysis for any given geometry without worrying about the validity of the results. Another important thing that we concluded in this paper is the load at which the arm will break. This data on the maximum load is important both for practical reasons of drone exploitation and for future failure analyses.

References:

[1] Sönmez M., Pelin C.E, Georgescu M., Pelin G., Stelescu M.D., Niruica M., Stoian G., Alexandrescu L., Gurau. D., *Unmanned Aerial Vehicles – Classification, Types of Composite Materials Used in Their Structure and Applications,* ICAMS 2022 – 9th International Conference on Advanced Materials and Systems, https://doi.org/10.24264/icams-2022.I.11

[2] Taha S. A., Petrović V., Grbović A., Lozanović-Šaljić J., Balać I., *Numerical Evaluation of the Elastic Properties of Carbon Fiber Reinforced Composite Material at Elevated and Lowered Temperatures,* Science of Sintering, Vol 53, 127-136, 2021.

[3] Brischetto S., Torre R., *Preliminary Finite Element Analysis and Flight Simulations of a Modular Drone Built through Fused Filament Fabrication,* J. Compos. Sci. 2021, 5, 293. https://doi.org/10.3390/jcs5110293

[4] Bahrom M. Z., Manshoor B., Zain B.A.M., Zaman I., Didane D.H., Haq R.H.A., Ibrahim M.N., *Thrust Force for Drone Propeller with Normal and Serrated Trailing Edge,* Journal of Advanced Research in Fluid Mechanics and Thermal Sciences 101, Issue 1 (2023) 160-173.

A SIMPLIFIED NONLINEAR DYNAMIC MATHEMATICAL MODEL OF A CONTROLLED REAL TURBOJET ENGINE

Miloš M. Živanović

EDePro, Kralja Milutina 33, Belgrade, Serbia
e-mail: miloszivanoviccar@gmail.com

Abstract

A turbojet engine is considered to be a mechanical system with one degree of freedom. The engine operation is controlled by a control system. A nonlinear differential equation of motion of the engine's rotating part (spool) is obtained on the basis of an adopted interaction between the spool and the working fluid which holds for all phases of the engine's run. An analytical solution of the differential equation with constant control input is given. The recorded data of motion of a real turbojet engine at a test stand are used to identify the model's parameters. The recorded input is applied to the model and spool's motion is simulated. Simulation results are compared with recorded data and discussed.

Keywords: turbojet engine, gas turbine, modelling.

1. Introduction

A vast amount of literature exists on gas turbine modelling. Few existing literature reviews [1], [2], [3], [4], [5] primarily consider modelling of power plant gas turbines. According to [1] gas turbine modelling may be classified in three groups: physical, empirical and simplified one. Physical or "white box" modelling [2], [3] is based on the physical laws that describe processes in a gas turbine. These models can be most accurate, and models' equations have complete physical background. On the other hand, "black box" modelling, in which empirical and simplified models can be put, may have very little or not any connection with physical processes in a gas turbine. It is based on the correlation between chosen inputs and outputs [6], [7], [8], [9].

All physical gas turbine models are obtained by applying the principles of conservation of mass, conservation of momentum and conservation of energy. The engine is divided into control volumes and balance equations are written for each volume. The model is more accurate if the control volume is smaller. The most accurate model would be if the control volume had a size of a fluid particle where balance equations are applied in their differential form. However, this model requires vast computational effort, and it is not convenient for fast simulations and real time applications. Hence, some approximations in the form of assumptions are done. The first approximation is that flow through the engine is one-dimensional [10]. Secondly, the engine is divided into components such are inlet, compressor, combustion chamber, turbine and nozzle and interaction between contiguous components are considered [11].

Two methods can be recognized that describe interaction between components in transient phases of a gas turbine engine. They are the constant mass flow (CMF) method and inter-component value (ICV) method [12]. The CMF method assumes that mass flow along the fluid path through the engine is constant all the time, that is, the mass flow field is homogenous and, in transient phases, non-stationary. A transient phase arises only due to an imbalance in the compressor and turbine work done on the spool. A model based on CMF method [13] contains algebraic dependencies where outputs cannot be explicitly expressed and, hence, require an iterative procedure to be solved. The ICV method allows non-homogeneity of the mass flow field but only in adopted control volumes or plena [10] that connect neighboring components in the engine. A transient phase arises due to an imbalance of not only work but also mass flow. These models [14], [15], [16] can be expressed as ordinary differential equations in a normal form which may be solved non-iteratively.

In this paper, we present the operation of a turbojet engine TJE45 developed by the EDePro company. A controlled engine's run is showed and described, and the engine's run phases are defined. Physical interactions in the control system of the engine are considered and those which influence spool dynamics are highlighted. The mechanical interaction between the spool and the working fluid is modelled both when the working fluid combustion is established and when there is no combustion. The model gives relation between the angular velocity of the spool and control signal for the fuel pump. The model parameters are indentified on the basis of the presented engine's run. The control input that is used for the real engine is applied to the model of the engine and the angular velocity of the spool obtained by simulation is compared to the angular velocity of the real spool. A slow thermal influence on the angular velocity is noticed and how it can be incorporated in spool dynamics is discussed.

2. Turbojet engine TJE45 and its control system

Turbojet engine TJE45 is a small one-spool gas turbine. It is intended for propulsion of unmanned flying vehicles. The engine produces 43 daN of thrust at maximum angular velocity of the spool, which is 83000 rpm[1].

The engine is driven by a control system which is shown in Fig. 1.

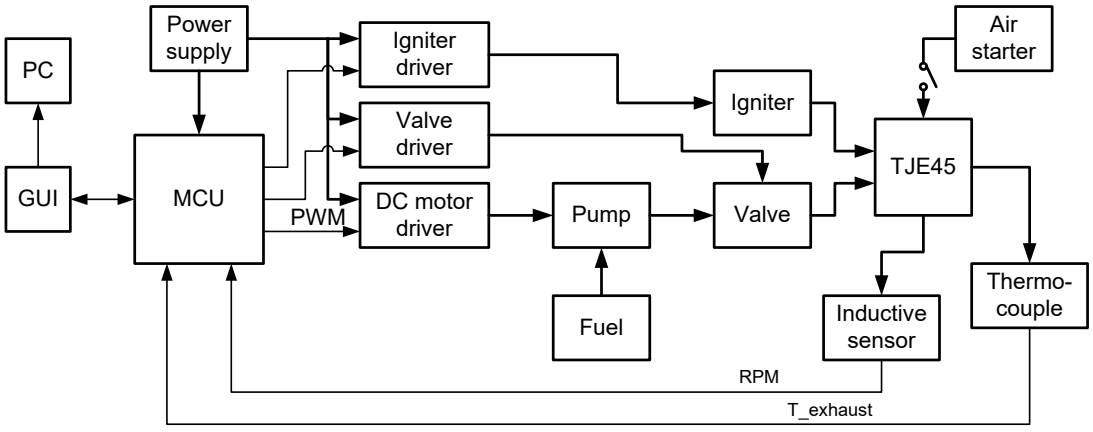

Fig. 1. TJE45 control system.

The engine's spool starts to rotate when the air starter is activated manually. The microcontroller unit (MCU) measures the angular velocity of the spool and temperature of exhaust gases. It can activate the igniter and fuel valve by an ON/OFF signal sent to the corresponding drivers. The fuel, which is kerosene, is injected to the combustion chamber of

[1]More about the engine can be found at www.edepro.com.

TJE45 by a gear pump driven by an electric DC motor. The MCU controls the fuel injection by a pulse-width-modulated (PWM) signal sent to the DC motor driver. The MCU communicates with a graphical user interface (GUI) that is an interface between an operator and the MCU. The GUI receives relevant data from MCU, shows them to the operator and sends them to a PC for recording. Using the GUI, an operator can manually drive the igniter, valve and pump, but also it can start and stop an automatic run of the TJE45.

3. Turbojet engine phases of run

An automatic run of a TJE45 is shown in Fig. 2. The engine was mounted on a stationary test stand in an EDePro's laboratory hall in Leštane. The test was done on 16th December 2022 around noon.

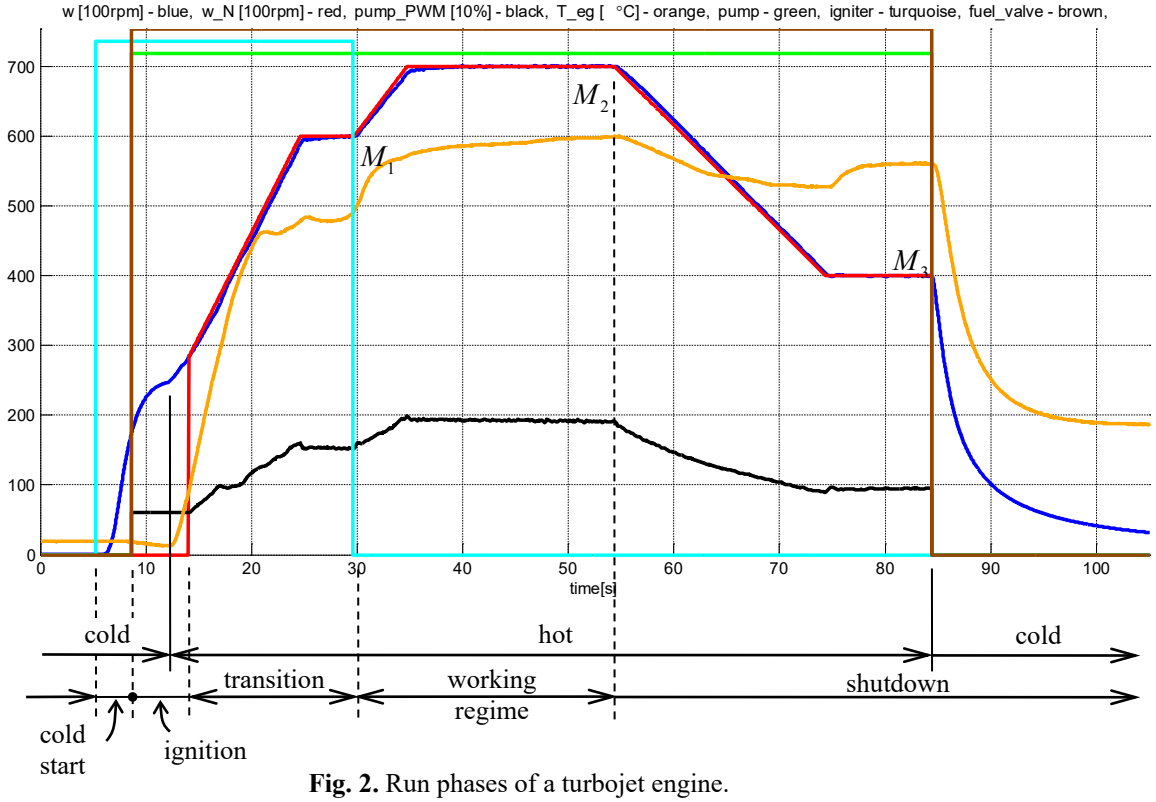

Fig. 2. Run phases of a turbojet engine.

After the spark plug has been activated (turquoise line), the cold start phase of engine's run begins. The spool is accelerated by bringing the compressed air to turbine's blades. The spool speeds up (blue line) with acceleration that starts decreasing. When the angular velocity of the spool crosses 17000 rpm, the fuel valve (brown line) and fuel pump (green line), which is driven by a constant duty cycle of the PWM signal (black line) in the next phase, are activated and the fuel starts entering the combustion chamber. At this moment, the cold start phase is completed, and the ignition phase begins.

After a short time, the fuel is ignited and the spool's angular acceleration increases instantly but then, it continues to decrease. When the angular velocity crosses 28000 rpm, the combustion is considered to be established and the angular acceleration is monitored. When it drops below 3000 rpm/s, the ignition phase is finished, and the transition phase begins.

In the transition phase, the angular velocity of the spool is controlled to track the nominal angular velocity of the spool (red line). Five seconds after the nominal velocity has reached 60000 rpm, the transition phase is finished, and the working regime phase begins. If the spool's angular velocity is not between 57600 rpm and 62400 rpm at the end of the transition phase, the

transition fails, and the engine is turned off. The igniter and starter are turned off at 60000 rpm of the spool.

The spool's angular velocity continues to track the nominal one in the working regime phase until the operator commands the finish of the phase. When it happens, the working regime phase is completed, and the shutdown phase begins.

The shutdown phase begins with controlled decrease of the angular velocity to 40000 rpm. Ten seconds after the nominal velocity has reached 40000 rpm, the fuel pump is deactivated, the valve is closed, and the spool decelerates up to the zero angular velocity.

The engine's operation can also be divided into the cold phase and hot phase. The hot phase is the part of engine's operation in which the combustion is established, while the other part is the cold phase.

4. Physical interactions in a turbojet engine control system

Four types of interactions in a turbojet engine control system may be distinguished. They are mechanical, thermal, chemical and electromagnetic one and they exist between elements of the system, Fig. 3.

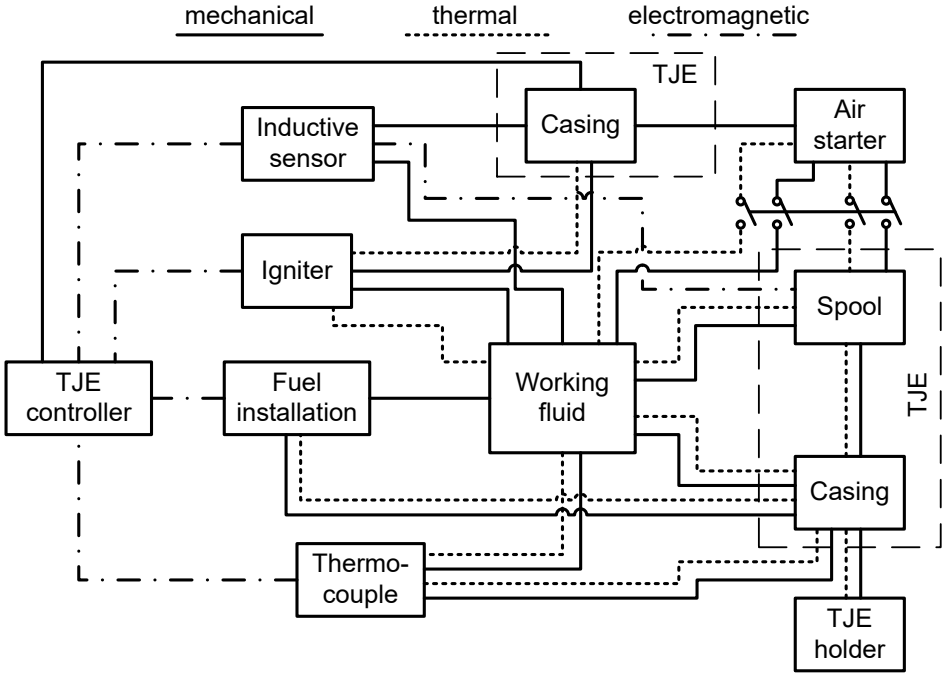

Fig. 3. Physical interaction in a turbojet engine control system.

A turbojet engine consists of the spool and casing in which the spool is placed. The spool and casing interact through the bearings whose outer rings belong to the casing while the inner rings belong to the spool. The bearing balls and their cages are considered only as a transmitter of interaction between the spool and the casing, and their dynamics is neglected. The spool also interacts with the starter during the cold start, ignition and transition phase.

The turbojet engine interacts with the working fluid which contains the air, fuel, and combustion products of the mixture of the air and fuel. The working fluid interacts with both the spool and casing and the interaction is both mechanical and thermal. The thermal interaction during the cold start phase and cold part of the ignition phase may be usually neglected. The working fluid also interacts with the fuel installation that "feeds" the working fluid with the fuel. This interaction is mechanical which is represented by the pressure at the exit of combustion chamber nozzles. While the air starter is active, the working fluid iteracts with the air from the

starter and that air becomes part of the working fluid. The combustion is a hemical interaction in the working fluid between the air and the fuel.

The turbojet engine controller has primarily electromagnetic interaction with the sensors and executive organs such are the fuel pump, igniter and valves. The interaction with the sensors is represented by low power voltage and current signals while interaction with the executive organs is of higher power. The mechanical interaction of the controller and the engine exists if the controller is mounted on the engine's casing. In this case a thermal interaction may exist too, but if the controller is thermally isolated it can be neglected. Although there is no direct interaction between the controller and the spool, the controller has great influence on spool dynamics.

5. Interactions that influence spool dynamics

The mechanical, as well as thermal, interaction with the spool may be considered in the axial direction along the spool's axis of symmetry, which is its axis of rotation in the casing, and in planes perpendicular to the axial direction. The mechanical interaction with the spool along the axis of rotation in the casing is reduced to a force and moment that act on the spool. Only the moment has influence on the spool's rotation around the axis. If the casing motion is approximately translational, the spool's rotation may be described by the differential equation

$$J\dot{\omega} = M\,, \tag{1}$$

where J is the axial moment of inertia of the spool, ω is the angular velocity of the spool, and M is the total moment that acts on the spool along its axis of rotation. The total moment M may be expressed by

$$M = M_{wf} + M_c + M_s\,, \tag{2}$$

where M_{wf} is the moment by which the working fluid acts on the spool, M_c is the moment by which casing acts on the spool, and M_s is the moment by which the starter acts on the spool. The moment M_c stems from the friction in the bearings which is here neglected, so that

$$M_c \approx 0\text{Nm}\,. \tag{3}$$

6. Spool dynamics in cold phase

During the cold start phase and cold part of the ignition phase, the spool dynamics is described by the following equation

$$J\dot{\omega} = M_{wf} + M_s\,, \tag{4}$$

while in the cold part of the shutdown phase we have

$$J\dot{\omega} = M_{wf}\,. \tag{5}$$

In this part of the shutdown phase, the working fluid is only the air and the spool's motion is only influenced by the air resistance. Therefore, it is reasonable to assume that moment M_{wf} has the following form

$$M_{wf} = -k_{wf}\omega^2\,, \tag{6}$$

where k_{wf} is a positive number. If we assume that k_{wf} is constant, then its value may be determined from the deceleration curve of the spool in shutdown phase which is given in Fig. 4 by blue line. Knowing the axial moment of inertia of the spool $J = 0.000667\text{kgm}^2$ and determining angular acceleration from the deceleration curve, we can determine the moment M_{wf} during deceleration from the equation (5). Absolute value of M_{wf} is shown in Fig. 4 by black

line. As can be seen, the moment does not follow angular velocity change in a period of around one second after the pump and valve are deactivated and especially in the first half of the second. This can be explained by the fact that the fuel flow is not totally stopped at the moment when the valve is closed. and combustion still exist some short time. After this critical interval, the moment M_{wf} has almost perfect quadratic dependence on the angular velocity, which is represented by the pink line. The coefficient k_{wf} is calculated at the 85.66th second on the basis of the values of the angular velocity and moment of the air resistance at that instant.

$$k_{wf} = \frac{\left|M_{wf}\left(85.66s\right)\right|}{\left(\omega\left(85.66s\right)\right)^2} = \frac{63.01\text{Ncm}}{\left(25340\text{rpm}\right)^2} = \frac{0.6301\text{Nm}}{\left(2\pi \cdot 25340/60 \cdot \text{rad/s}\right)^2} = 8.95*10^{-8}\frac{\text{Nm}}{\left(\text{rad/s}\right)^2} \tag{7}$$

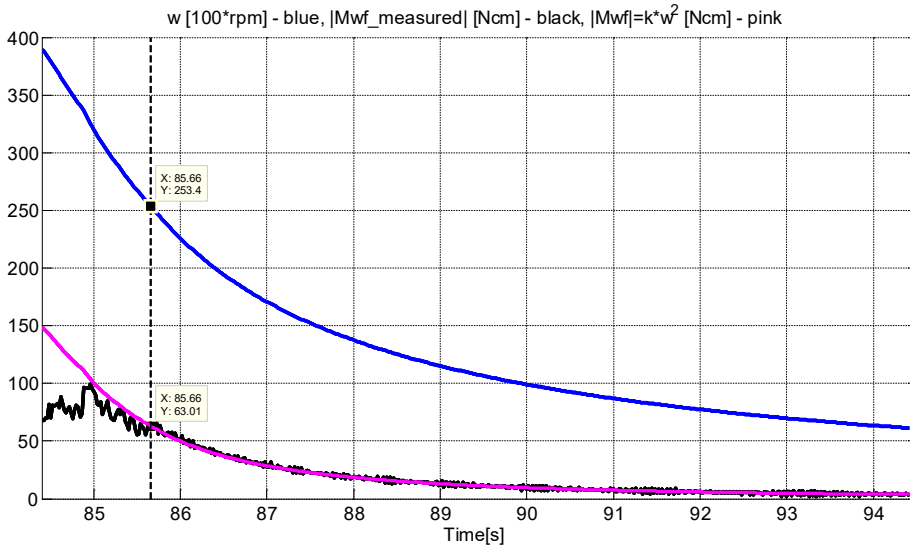

Fig. 4. Deceleration line of the spool in shutdown phase.

Certain tests in which the engine is turned off at higher angular velocities show that air resistance moment deviates from quadratic dependence with the constant coefficient k_{wf} determined in lower angular velocities. It deviates toward higher values which can be explained by elastic deformation of the spool in radial direction at higher angular velocities. This deformation decreases the gap between the blades and the casing and gives rise to the air resistance to be higher than that which would be if the gap stayed unchanged. Therefore, better model for the air resistance would be in the form

$$M_{wf} = -k_{wf}\left(\omega\right)\omega^2, \tag{8}$$

where $k_{wf}\left(\omega\right)$ is a positive monotonically increasing function. From now on, we adopt the form (6) of the working fluid resistance and we assume that this moment acts in all phases of an engine's run.

The air starter moment M_s can be modelled as quadratic function of ω , too, since when the spool is at rest the resistance of the air from the starter is what drives the spool. At some angular velocity ω_s the air starter does not impart mechanical energy to the spool, that is, $M_s = 0$, and from that angular velocity up it starts to break the spool. This suggests the following function for the moment of the air starter

$$M_s = k_s \,\text{sign}\left(\omega_s - \omega\right)\left(\omega_s - \omega\right)^2. \tag{9}$$

The parameters k_s and ω_s may be determined from the conditions $\omega = 0$ and $\dot{\omega} = 0$. The first condition may be used when an air valve between the starter and the engine is opened very fast. In that case, we have

$$J\dot{\omega}|_{\omega=0} = k_s \omega_s^2 . \tag{10}$$

The second condition happens when the moment from the air starter equals the moment of air resistance M_{wf} but with opposite direction. It will happen at some equilibrium angular velocity ω_{eq}, which can be determined experimentally. So, the second condition has the following form

$$k_s \left(\omega_{eq} - \omega_s \right)^2 = k_{wf} \omega_{eq}^2 . \tag{11}$$

In this paper, we shall not simulate the influence of the starter in cold phase since the acceleration of the spool may be done by a starter in various ways in this phase, not only in the way just presented.

7. Spool dynamics in hot phase

A turbojet engine behaves differently depending on which part of the hot phase it is running in. We can distinguish a controllable self-sustained run from the passing run of the engine in hot phase. Self-sustained run means that the engine is working without any help from the starter. Controllable run means that the spool can reach any angular velocity in the self-sustained run starting from arbitrarily chosen angular velocity in the self-sustained run. The passing run can be unsustainable without starter's help, or it can be self-sustainable but uncontrollable. The unsustainable passing run happens when turning off the starter leads to turning off the engine. The uncontrollable passing run happens when turning off the starter leads to self-sustained run without possibility to increase the angular velocity of the spool. Any adding the fuel into the engine is converted to heat and does not result in significant angular velocity increase. For this engine, the passing run is the run between approximately 20000 rpm and 40000 rpm. Here, we shall consider only controllable self-sustained run.

We assume that the engine is working inside its limitations which are determined by the engine's components. This means that the compressor is working between choke and surge lines, the combustion chamber does not cross flameout limit, the turbine inlet temperature does not exceed allowed maximal values, the spool rotates below maximal angular velocity limit, vibrations are in allowed limits, and the flows through the inlet and exhaust nozzle are not choked.

In considered hot phase, the working fluid produces active moment M_{wf}^a on the turbine that provides self-sustained run. This moment arises as a consequence of temperature increase in front of the turbine and, according to the first law of thermodynamics [17], it is proportional to the temperature difference T_{ti} and T_{ta} in front and after the turbine, respectively

$$M_{wf}^a = \dot{m}_{wf} \frac{c_{p,wf} \left(T_{ti} - T_{ta} \right)}{\omega} , \tag{12}$$

where $\dot{m}_{wf}$ is the working fluid mass flow and $c_{p,wf}$ is the specific heat of the working fluid at constant pressure. Besides the active moment, a working fluid resistance moment defined by (6) acts on the spool, as it has been already assumed. If we denote it by M_{wf}^r, the spool dynamics has the following form

$$J\dot{\omega} = M_{wf}^a + M_{wf}^r . \tag{13}$$

Substituting M_{wf}^r from (6), we obtain

$$J\dot{\omega} + k_{wf}\omega^2 = M_{wf}^a . \tag{14}$$

One can find that the solutions of this differential equation for $M_{wf}^{a} = const.$ and $\omega_{\mathrm{i}} = \omega(t_{\mathrm{i}}) \geq 0\,\mathrm{rad/s}$, where t is time ant t_{i} is the initial instant, is given by

$$\omega = \begin{cases} \omega_s \dfrac{-1 + C_{p_0} e^{k(t-t_{\mathrm{i}})}}{1 + C_{p_0} e^{k(t-t_{\mathrm{i}})}}, & \omega_{\mathrm{i}} \in [0, \omega_s) \cup (\omega_s, \infty) \\ \omega_{\mathrm{i}}, & \omega_{\mathrm{i}} = \omega_s \end{cases}, \tag{15}$$

where

$$\omega_s = \sqrt{\frac{M_{wf}^{a}}{k_{wf}}}, \qquad C_{p_0} = \frac{1 - p_0}{1 + p_0}, \qquad p_0 = \frac{\omega_{\mathrm{i}}}{\omega_s}, \qquad k = 2\frac{\sqrt{k_{wf} M_{wf}^{a}}}{J}. \tag{16}$$

The expression (12) for the active moment is not practical for our simplified model. It requires knowing two temperatures and the mass flow, but we need dependence between the control input and the active moment. Let u be the duty cycle of PWM signal which controls the fuel pump. It is clear that the active moment depends on u and the simplest case is to assume that it depends only on u, that is,

$$M_{wf}^{a} = M_{wf}^{a}(u). \tag{17}$$

One also logical assumption is that active moment cannot be negative

$$M_{wf}^{a} \geq 0\mathrm{Nm}. \tag{18}$$

The function (17) may be determined on the basis of equation (14) and the steady-state characteristic of the engine control system that connects the angular velocity in steady state ω_{st} with duty cycle in steady state u_{st}. For steady-state condition $\dot{\omega}$ is zero and the characteristic must satisfy

$$k_{wf} \omega_{st}^2 = M_{wf}^{a}(u_{st}). \tag{19}$$

In Fig. 5, the dependence of ω from u during the automatic engine's run is drawn. Three points M_1 (15.28 %, 59850 rpm), M_2 (19.38 %, 69900 rpm) and M_3 (9.4 %, 40000 rpm) are chosen to belong to the steady-state characteristic $\omega_{st}(u_{st})$, see also Fig. 2.

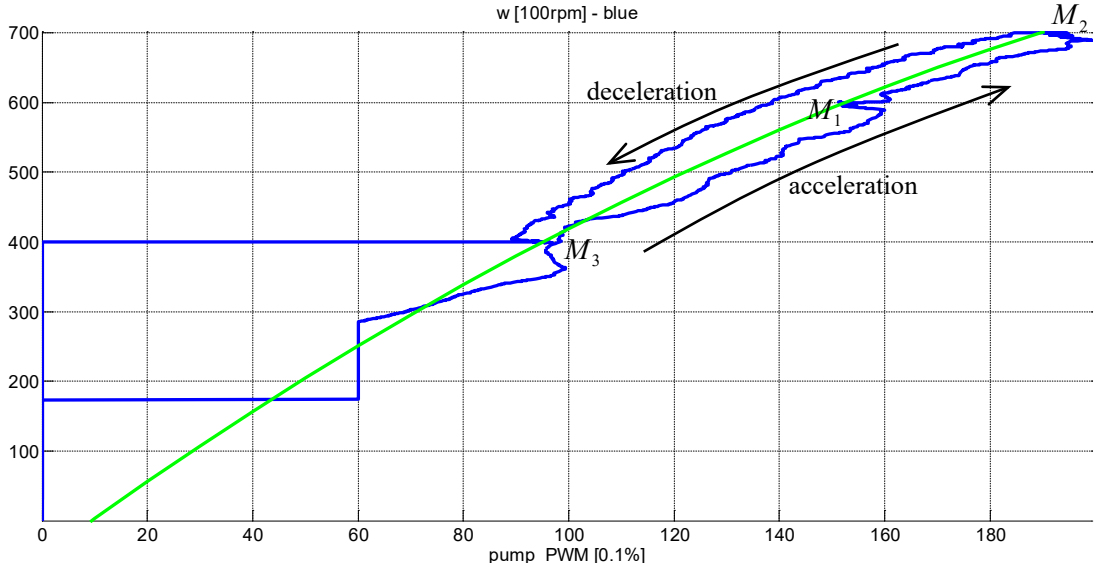

Fig. 5. $\omega(u)$ graph and obtained steady-state characteristics (green line).

The location of the points M_1, M_2 and M_3, acceleration line, and especially deceleration (slower than acceleration) line suggest that the steady state characteristic is not a linear function. Since we have only three points, our first guess is a quadratic function in the form

$$\omega_{st} = -k\left(u_{st} - u_0\right)^2 + \omega_0, \tag{20}$$

where k, u_0 and ω_0 are coefficients which ought to be determined on the basis of chosen points $M_1\left(u_{st1}, \omega_{st1}\right)$, $M_2\left(u_{st2}, \omega_{st2}\right)$ and $M_3\left(u_{st3}, \omega_{st3}\right)$. We have a system of linear equations

$$\begin{aligned} u_{st1}^2 x + u_{st1} y + z &= \omega_{st1} \\ u_{st2}^2 x + u_{st2} y + z &= \omega_{st2} \\ u_{st3}^2 x + u_{st3} y + z &= \omega_{st3} \end{aligned}, \tag{21}$$

where $x = -k$, $y = 2ku_0$, $z = -ku_0^2 + \omega_0$, so that the coefficients are found from

$$k = -x, \quad u_0 = \frac{y}{2k}, \quad \omega_0 = z + ku_0^2. \tag{22}$$

According to Cramer's rule, the solutions of the linear equations are

$$x = \frac{\det\left(A_x\right)}{\det\left(A\right)}, \quad y = \frac{\det\left(A_y\right)}{\det\left(A\right)}, \quad z = \frac{\det\left(A_z\right)}{\det\left(A\right)}, \tag{23}$$

where $A_x = \begin{vmatrix} \omega_{st1} & u_{st1} & 1 \\ \omega_{st2} & u_{st2} & 1 \\ \omega_{st3} & u_{st3} & 1 \end{vmatrix}$, $A_y = \begin{vmatrix} u_{st1}^2 & \omega_{st1} & 1 \\ u_{st2}^2 & \omega_{st2} & 1 \\ u_{st3}^2 & \omega_{st3} & 1 \end{vmatrix}$, $A_z = \begin{vmatrix} u_{st1}^2 & u_{st1} & \omega_{st1} \\ u_{st2}^2 & u_{st2} & \omega_{st2} \\ u_{st3}^2 & u_{st3} & \omega_{st3} \end{vmatrix}$, and $A = \begin{vmatrix} u_{st1}^2 & u_{st1} & 1 \\ u_{st2}^2 & u_{st2} & 1 \\ u_{st3}^2 & u_{st3} & 1 \end{vmatrix}$.

Substituting them in equations (22), we obtain the following values

$$k = 1.3704 \frac{\text{Hz}}{\%^2}, \quad u_0 = 33.5676\%, \quad \omega_0 = 1459{,}2\text{Hz} = 87552\text{rpm}. \tag{24}$$

From (19) and (20), the active moment gets the following form in steady-state operation of the engine

$$M_{wf}^a\left(u_{st}\right) = k_{wf}\left(-k\left(u_{st} - u_0\right)^2 + \omega_0\right)^2. \tag{25}$$

We assume that the same expression for the active moment holds for transient engine's runs in the hot controllable self-sustained phase, too, that is,

$$M_{wf}^a\left(u\right) = k_{wf}\left(-k\left(u - u_0\right)^2 + \omega_0\right)^2, \qquad \omega_0 > \omega > 39000\text{rpm}. \tag{26}$$

8. Simulation results and discussion

The model simulation is done by taking the recorded duty cycle of the fuel pump PWM signal during the automatic run shown in Fig. 2 and applying it to the obtained model for spool dynamics (14). Although the active moment is taken to be valid in the controllable self-sustained hot phase, it is applied to whole hot phase. For this simulation, it is implemented in the following form

$$M_{wf}^a\left(u\right) = \begin{cases} k_{wf}\left(-k\left(u - u_0\right)^2 + \omega_0\right)^2 & u \geq 5\% \\ 0\text{Nm} & u < 5\% \end{cases}. \tag{27}$$

The air starter's moment is taken to be zero in the simulation. The initial angular velocity is $\omega_{\text{i}} = 25070\text{rpm}$. The simulation result is shown in Fig. 6 by red line.

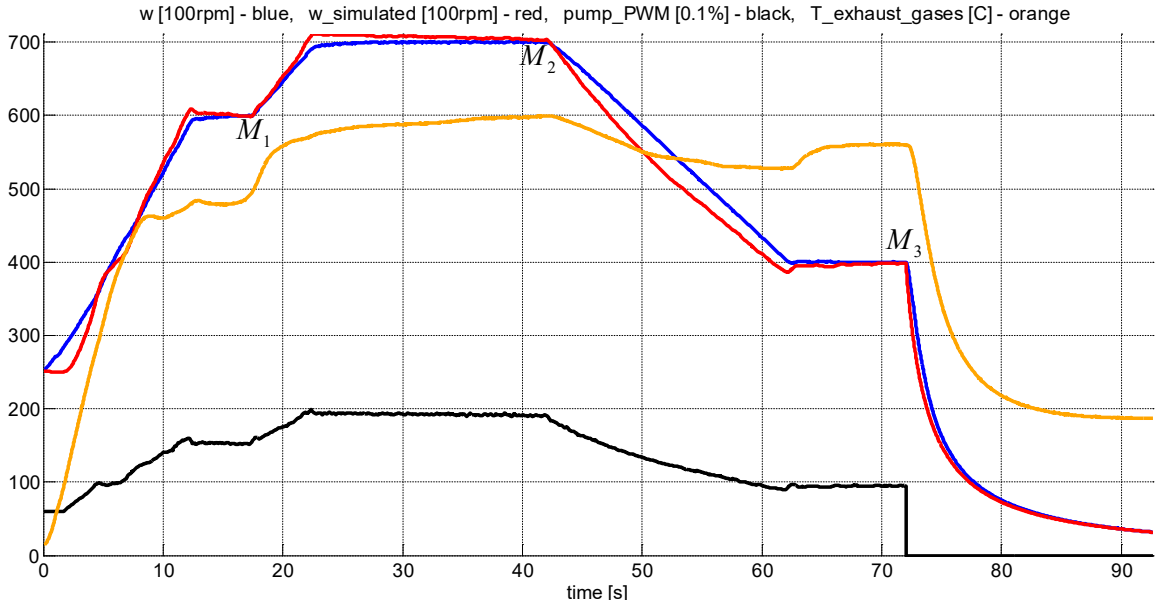

Fig. 6. Simulated spool's angular velocity compared with its real one.

As can be seen, the steady-state points M_1, M_2, and M_3 are simulated well. We can say that the character of the transient behavior is also well simulated, except in the passing phase where the starter's moment is not included in the simulation. Although the starter is turned off at 60000 rpm, we can see it has not much effect on the spool dynamics above 45000 rpm since the transition from 45000 rpm to 60000 rpm and transition from 60000 rpm to70000 rpm are similar by character both real and simulated one, and the starter is not active in the latter transitions.

It can be now seen that change of the working fluid temperature influences the spool angular velocity. During the period when the angular velocity is kept at 70000 rpm, the temperature of the exhaust gases slowly increases and the duty cycle slowly decreases which leads to slow, but better observable, decrease of the simulated angular velocity. If the duty cycle was constant, the real angular velocity would slowly increase. This behavior is a consequence of a phenomenon called heat soakage [18]. Heat soakage is an unsteady heat transfer between the working fluid and the engine. This transfer exists up to new steady state.

Heat soakage is the slowest process in a transition from one steady-state to another one. Hence, the disagreement in angular velocity at the transition from 45000 rpm to 60000 rpm and transition from 60000 rpm to 70000 rpm cannot be considered as a consequence of heat soakage, but as a consequence of the clearances between the spool's edge and the casing called the tip clearances [18]. The tip clearances decrease with increase in angular velocity. This leads, as we have already discussed, in increase in resistive moment of the working fluid which can be modelled in the form (8).

To compensate the influence of heat soakage, the controller decreases the duty cycle after accelerations and increases it after deceleration. The resistive moment behaves as if it slowly decreases after accelerations and slowly increases after decelerations. Physically, this might be explained by working fluid average density decrease with its average temperature increase in the engine. Since heat soakage is a thermal process, we need to measure some appropriate temperature that behaves similarly as the resistive moment due to heat soakage, which the exhaust working fluid temperature obviously is not one. If such a temperature T can be found, the resistive moment may be modelled in the form

$$M_{wf}^{r} = -\left(k_{wf}\left(\omega\right) + k_{T}\left(T - T_{st}\left(u\right)\right)\right)\omega^{2}, \tag{28}$$

where $T_{st}(u)$ is the steady state characteristics between the duty cycle and the temperature T, while $k_T(x)$ is a monotonically decreasing function for which $k_T(0) = 0$.

These are simplified suggestions for modelling the influences of the tip clearance and heat soakage to spool dynamics. One can find more physically based models in [16] and [19].

9. Conclusion

A new approach in modelling turbojet engine spool dynamics has been presented. The net moment that acts on the spool is not presented as a sum of the compressor and turbine power at certain angular velocity, which is commonly done in literature, but as a sum of active and resistive moment. These moments arise as a consequence of interaction of the working fluid, casing and starter with the spool. It is adopted that the working fluid and casing resistive moment act during entire engine operation.

The resistive moment due to friction in bearings is neglected, while the resistive moment between the working fluid and the spool is modelled as a common aerodynamic drag proportional to the square of the spool's angular velocity. The coefficient of proportionality is not constant but increases with increase of the angular velocity, which is explained by the tip clearance decrease between the spool and casing. The power obtained by the working fluid resistive moment at certain angular velocity of the spool defines minimum starter's power necessary for accelerating the spool to that velocity.

The active moment stems from the starter and working fluid. It opposes the resistive moment, and it may increase the angular velocity of the spool. The starter active moment is applied during starting of the engine while it is not in controllable self-sustained run. A model for the air starter active moment is suggested as an aerodynamic moment proportional to the square of the angular velocity.

The working fluid active moment arises in the hot phase as a consequence of combustion of the air and fuel mixture. It is assumed that the working fluid active moment cannot decelerate the spool and that it depends only on the pump control signal which controls the fuel flow. Its model is obtained by using the condition that the active and resistive moment of the working fluid must be equal in a steady run of the engine. Moreover, the static characteristic between the angular velocity and pump control signal is used to obtain an analytical dependence of the working fluid active moment on the control signal which tells that the active moment is proportional to the fourth power of the pump signal. So, small change in the control signal has great influence on the active moment.

The model is verified by applying the same control signal used in a real test to the model. The obtained simulation result shows that the character of the angular velocity change and steady states are modelled well. Certain disagreements in real and simulated angular velocities during the transients exist, where maximal deviation of angular velocity is less than 4000rpm in modulus. They are unmodelled influences of tip clearances and heat soakage. It is suggested that these influences may be modelled as a change in the resistive moment of the working fluid. Decrease of the tip clearances produces increase of the resistive moment. The heat soakage influence is represented through the deviation of a characteristic temperature from its value in the steady state for given control signal. If the deviation is positive, which means the characteristic temperature is higher than its considered steady state value, the resistive moment is less than that which would be if the temperature had its steady state value, and conversely.

Acknowledgement: The author obtained permission from EDePro to use TJE45 test results presented in the paper.

References:

[1] Mohamed O., Khalil A., *Progress in Modeling and Control of Gas Turbine Power Generation Systems: A Survey*, Energies, Vol 13, No 9, 2358, 2020.

[2] Hashmi M.B., et al., *Transient Behaviour in Variable Geometry Industrial Gas Turbines: A Comprehensive Overview of Pertinent Modeling Techniques,* Entropy, Vol 23., 250, 2021.

[3] Asgari H., Chen X., *Considerations in Modeling and Control of Gas Turbines – a Review*, Proc. The 2nd International Conference on Control, Instrumentation and Automation, Shiraz, Iran, December 27-29, 2011, 84-89.

[4] Yee S.K., Milanović J.V., Hughes F.M., *Overview and Comparative Analysis of Gas Turbine Models for System Stability Studies*, IEEE Transactions on Power Systems, Vol. 23, No. 1 108 – 118, 2008.

[5] Kulikov G., Thompson H.A (Eds.), *Dynamic Modelling of Gas Turbines,* Springer, London, 2004.

[6] Rowen V.I., *Simplified Mathematical Representation of Heavy-Duty Gas Turbines,* Journal of Engineering for Power, Vol 105., No 4., 865-869, 1983.

[7] Lichtsinder M., Levy Y.., *Jet Engine Model for Control and Real-Time Simulations*, Journal of Engineering for Gas Turbines and Power, Vol. 128, 745-753, 2006.

[8] Jiali Y., Jihong Z., *Dynamic Modeling of a Small Scale Turbojet Engine,* Proc. European Control Conference, Linz, Austria, July 15-17, 2015, 2750-2755.

[9] Ekinci M., Yavrucuk I., *Fast Engine Model for FMU-less Small Turbojet Engine*, Proc. of the Institution of Mechanical Engineers, Part G: Journal of Aerospace Engineering, Vol 234, No. 2, 416-427, 2019.

[10] Schobeiri M.T., *Turbomachinery Flow Physics and Dynamic Performance*, Springer, Berlin, 2012.

[11] Bettochi R., Spina P.R., *Dynamic Modeling of Single –Shaft Industrial Gas Turbine*, Proc. The International Gas Turbine and Aeroengine Congress, Birmingham, UK, June 10-13, 1996.

[12] Fawake A.J., Saravanamutto H.I.H., *Digital Computer Methods for Prediction of Gas Turbine Dynamic Response,* SAE Technical Paper 710550, 1805-1813, 1971.

[13] Medici G., Chiesa S., Balbo M., Sbuttoni A., *Tutbojet Seady State and Transient Analytical Model Development and Validation*, The Journal of Aerospace Science, Technology and Systems, Vol 93., 41-50, 2014.

[14] Rahman N.U., Whidborne J.F., *A Numerical Invastigation into the Efect of Engine Bleed on Performance of a Single-Spool Turbojet Engine*, Proc. Institution of Mechanical Engineering, Part G: Journal of Aerospace Engineering, Vol. 222., No. 7, 939-949, 2008.

[15] Wang C., Li Y.G., Yang B.Y., *Transient Performance Simulation of Aircraft Engine Integrated with Fuel and Control Systems,* Applied Thermal Engineering, Vol. 114, 1029-1037, 2017.

[16] Petkovic Dj., et al., *Modeling the Transient Behavior of Gas Turbines*, Journal of Turbomachinery, Vol. 142, No. 8, 081005:1-10, 2020.

[17] Mattingly J.D., *Elements of Gas Turbine Propulsion,* McGraw-Hill, New Delhi, 1996.

[18] Walsh P.P, Fletcher P., *Gas Turbine Performance,* Blackwell Science, Oxford, 2004.

[19] Li Z., Li Y.-G., Sampath S., *Aeroengine Transient Performance Simulation Integrated with Generic Heat Soakage and Tip Clearance Model*, The Aeronautical Journal, Vol. 126, 1265-1287, 2022.

PARAMETER IDENTIFICATION OF VISCOELASTIC MATERIALS USING DIFFERENT DEFORMATION VELOCITIES

Iva R. Janković, Nenad M. Grahovac and Miodrag M. Žigić

Faculty of Technical Sciences, University of Novi Sad, Trg Dositeja Obradovica 6, 21000 Novi Sad, Serbia
e-mail: jankovic.bi3.2021@uns.ac.rs, ngraho@uns.ac.rs, mzigic@uns.ac.rs

Abstract

In this paper, the fractional Kelvin-Zener model of viscoelastic body was used for modeling the behavior of monofilament and fluorocarbon during the ramp and hold type of experiment, using diferent deformation velocities. First, experimental measurements were made on 9 samples of each material. Three sample groups were tested at different deformation rates during the first phase of the experiment. Afterward, the relaxation phase was kept consistent across all samples. Riemann-Liouville fractional derivatives were approximated numerically using the Grünwald-Letnikov definition. Four model parameters have been determined for each sample by numerical procedure. Finally, the experimental results were compared with the results provided by the fractional Kelvin-Zener model.

Keywords: viscoelasticity, stress relaxation experiment, fractional derivative.

1. Introduction

Over the past few decades, polymers have gained popularity as a preferred engineering structural material due to their affordability, ease of processing, weight savings, corrosion resistance, and other notable benefits. The use of polymeric materials is ubiquitous, both in our daily lives and in the engineering profession. Viscoelastic properties of polymer fibers have attracted considerable attention in different scientific areas. Experimental studies conducted with different polymers revealed rheological behavior which manifests non-linear elasticity, and almost ideal plasticity, or plasticity with strain hardening, strain-rate effects, creep and viscoelastic relaxation effects. Those kinds of properties of polymer materials play an important role in their application. One of the most important representatives of polymeric materials nylon 6,6 is characterized with high mechanical tensile strength, elasticity, and luster while being wrinkle proof and highly resistant to abrasion [1].

Polymeric materials prolene, ethylene (nylon) and Ticron, otherwise threads that are usually used in plastic surgery, were subjected to tests of time-dependent mechanical properties responsible for the quality of tendon repair flexors in terms of crack formation also by experiments crawling. Due to its specific viscoelastic properties, Ticron proved to be the most suitable [2].

Monofilament made of fishing nylon has attracted special attention in medicine due to its mechanical properties. A case-control study of sensitivity, specificity, and comparison with

standardized sensory modalities of a homemade monofilament for screening of diabetic peripheral neuropathy. A low-cost instrument has been proven to be equivalent to the internationally accepted instrument in assessing the risk of foot ulcers in diabetes patients, and that it has the potential to become standard for detecting diabetic neuropathy [3]. As an advantage of fishing nylon in the detection of diabetic neuropathy in a case-control study in addition to its mechanical features, a feature that stood out was its economy, as well as its simplicity and the speed of conducting the test, which shows its potential in daily clinical practice [4].

It was demonstrated that inexpensive high-strength polymer fibers used for fishing line and sewing thread can be easily transformed by twist insertion to provide fast, scalable, nonhysteretic, long-life tensile and torsional muscles. Extreme twisting produces coiled muscles that can contract by 49%, lift loads over 100 times heavier in comparison to a human muscle of the same length and weight and generate amount of mechanical work per kilogram of muscle weight, similar to that produced by a jet engine [5].

The identification of model parameters for viscoelastic materials has been conducted in numerous studies, see for example [6], [7] and [8]. The values of model parameters determined on the bases of relatively simple experiments of stress relaxation and creep are sometimes used for modeling in collision problems, where deformation rates are much higher. This paper investigates the influence of deformation rate on the values of parameters of the fractional Kelvin-Zener model.

2. Experiment and parameter identification

2.1 Stress-relaxation experiment

Eighteen different samples of polymer materials, i.e. nine fluorocarbon (FC) samples with a thickness 0.3 mm, linear density 1.116 10^{-4} kg/m and nine monofilament (MF) samples with a thickness 0.28 mm and linear density 7.078 10^{-5} kg/m, were tested with the test system Instron 2710-204.

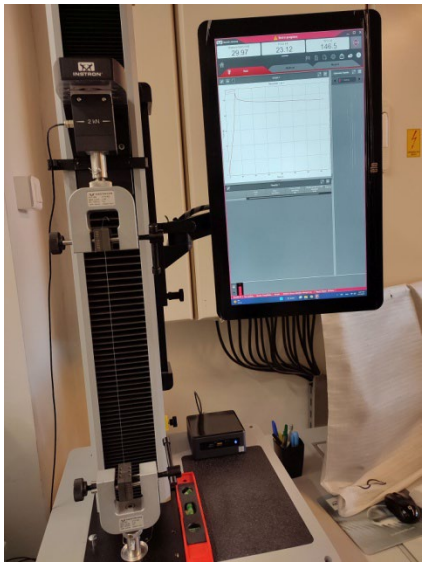

Fig. 1. Experimental apparatus.

All samples had an initial length of 30 cm. The experimental apparatus is shown in Fig. 1. During the first phase, the ramp phase, the samples were loaded under constant strain rate until a predetermined strain value of 10% was achieved. Three sample groups were subjected to different deformation rates, specifically 60 mm/min, 120 mm/min, and 360 mm/min, so that the tension

phase lasted 30 s, 15 s, and 5 s, respectively, for these three sample groups. After that, the samples were exposed to a relaxation phase in which the achieved deformation was held constant for a period of 180 s for all samples. Figure 2 shows the experimental results for 9 samples of fluorocarbons, which were grouped into sets of three samples each. The experimental results for the monofilament samples are shown in Fig. 3.

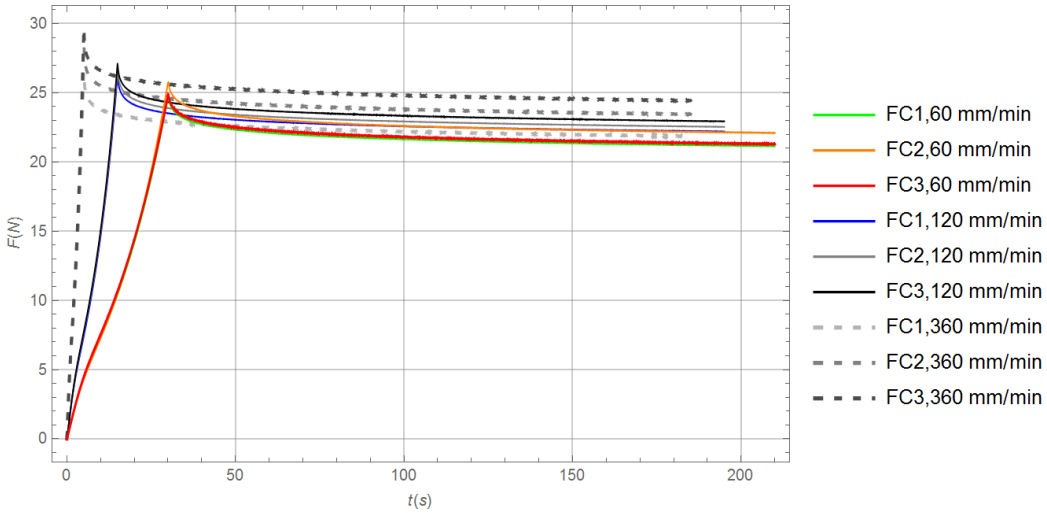

Fig. 2. Experimental results for nine fluorocarbon samples that were subjected to different deformation rates.

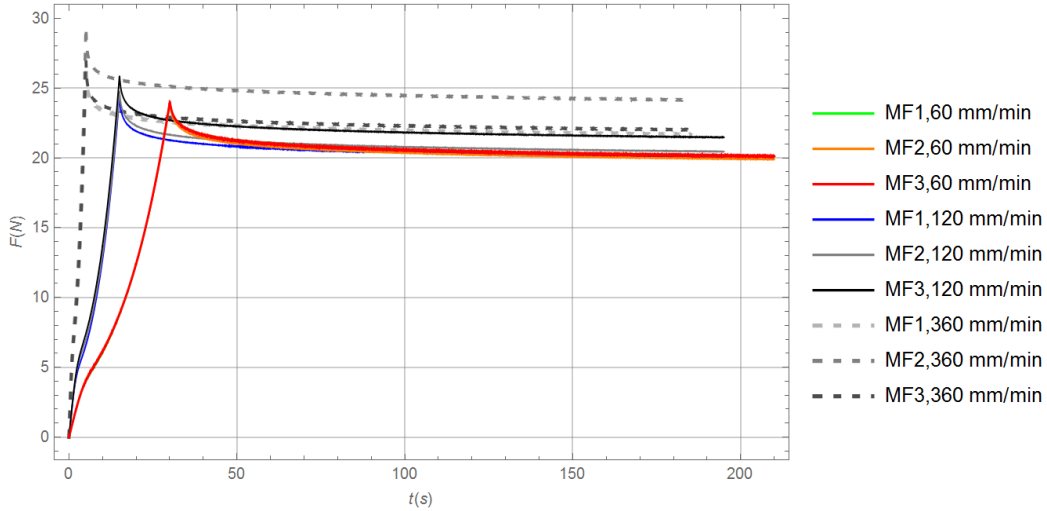

Fig. 3. Experimental results for nine monofilament samples that were subjected to different deformation rates.

By observing the obtained experimental results, certain mutual deviations of the curves within the same group of three samples can be noticed, but from a phenomenological point of view, there is no difference in the behavior of the material during the experiment. From Fig. 3, which shows the behavior of the monofilament samples, very good agreement of results for all three samples can be observed at a deformation rate of 60 mm/min. At higher deformation rates, two curves in each group are close, while one curve in each of these groups deviates slightly. The reason for the observed deviation could be the imperfections of the tested samples.

2.2 The model

The appropriate selection of rheological model is important for testing viscoelastic materials. Considering that stress is directly related to the zeroth derivative of strain in solids and to the first derivative of strain in fluids, it is reasonable to hypothesize that in viscoelastic materials, which exhibit characteristics of both solids and fluids, stress could be proportional to the αth derivative of strain, where α is a real number between 0 and 1, see [10]. In this analysis we chose the Fractional Kelvin-Zener model which yields accurate results that match experimental data while using only four parameters. The constitutive equation has the following form:

$$f + \tau_{f\alpha} f^{(\alpha)} = E\left(x + \tau_{x\alpha} x^{(\alpha)}\right) \tag{1}$$

where f and x stand for tensile force and elongation, $\tau_{f\alpha}$, $\tau_{x\alpha}$ are model parameters expressed in s^{α}, E is expressed in N/m, while the real number α ($0<\alpha<1$) represents the derivative order in the standard Riemann-Liouville form. Parameters $\tau_{f\alpha}$, $\tau_{x\alpha}$ and E must satisfy certain restrictions:

$$E > 0,\ \tau_{f\alpha} > 0,\ \tau_{x\alpha} > \tau_{f\alpha}, \tag{2}$$

according to the second law of thermodynamics, [9]. Our objective is to calculate the values of the model parameters (α, E, $\tau_{x\alpha}$, $\tau_{f\alpha}$) for all samples and examine how changes in deformation velocity affect the obtained results.

3. Results

Following the procedure for parameter identification described in [7], where the Grünwald-Letnikov definition of fractional derivatives was used, the values of parameters of the viscoelastic model are determined for all samples, see also [10]. The obtained results are shown in Table 1 for fluorocarbon samples, and in Table 2 for monofilament samples.

Sample	α	E[N/mm]	$\tau_{x\alpha}[s^{\alpha}]$	$\tau_{f\alpha}[s^{\alpha}]$
FC1 (60 mm/min)	0.527	0.681	1.127	$4.882\cdot10^{-4}$
FC2 (60 mm/min)	0.529	0.712	1.104	$4.957\cdot10^{-4}$
FC3 (60 mm/min)	0.515	0.684	1.088	$4.958\cdot10^{-4}$
FC1 (120 mm/min)	0.437	0.71	0.671	$4.783\cdot10^{-4}$
FC2 (120 mm/min)	0.436	0.721	0.679	0.011
FC3 (120 mm/min)	0.447	0.734	0.862	0.153
FC1 (360 mm/min)	0.434	0.712	0.437	$2.971\cdot10^{-3}$
FC2 (360 mm/min)	0.43	0.763	0.431	$4.912\cdot10^{-4}$
FC3 (360 mm/min)	0.426	0.795	0.433	$4.912\cdot10^{-4}$

Table 1. Model parameter values for fluorocarbon at deformation rates of 60, 120, and 360 mm/min.

Sample	α	E[N/mm]	$\tau_{x\alpha}[s^{\alpha}]$	$\tau_{f\alpha}[s^{\alpha}]$
MF1 (60 mm/min)	0.585	0.652	1.463	$4.888\cdot10^{-4}$
MF2 (60 mm/min)	0.583	0.643	1.479	10^{-3}
MF3 (60 mm/min)	0.598	0.652	1.533	$4.962\cdot10^{-4}$
MF1 (120 mm/min)	0.513	0.648	0.898	$4.949\cdot10^{-4}$
MF2 (120 mm/min)	0.517	0.661	0.893	$4.95\cdot10^{-4}$
MF3 (120 mm/min)	0.514	0.694	0.86	$1.798\cdot10^{-5}$
MF1 (360 mm/min)	0.525	0.714	0.505	$2.466\cdot10^{-4}$
MF2 (360 mm/min)	0.532	0.797	0.481	$4.974\cdot10^{-4}$
MF3 (360 mm/min)	0.533	0.725	0.507	$4.971\cdot10^{-4}$

Table 2. Model parameter values for monofilament at deformation rates of 60, 120, and 360 mm/min.

From the obtained results, it can be noticed that there are no significant deviations in the parameter values within each group of three samples for both tested materials, indicating result repeatability. By observing the obtained results for the derivative order α, it can be concluded that the values of α at a deformation rate of 60 mm/min are slightly higher for both materials compared to the values obtained at higher speeds. With the increase of the deformation rate, there is a slight increase in the values of the parameter E. The biggest change in the parameter values is observed in the parameter $\tau_{x\alpha}$, where the values decrease with the increase of the deformation rate. The values of the parameter $\tau_{f\alpha}$ are very small for most of the samples compared to the obtained values of other parameters. Considering that this parameter multiplies the αth derivative of the tensile force in equation (1), it can be concluded that the influence of this term is reduced.

4. Conclusions

In this paper, we analyzed the influence of strain rate on the value of parameters of the fractional Kelvin-Zener viscoelastic model in a stress relaxation experiment. The behavior of two viscoelastic materials was tested, with three sample groups formed for each material, all subjected to the same deformation speed. Very similar behavior was observed within each sample group, as evidenced by the small deviations in the parameter values obtained for each group. The change in deformation speed affected the parameter values in a very similar manner for both materials. The highest and lowest deformation speeds for the tested samples were in a 6:1 ratio. It would be interesting to investigate the effect of a much larger ratio between the maximum and minimum deformation speeds, and to analyze the potential application of relatively simple relaxation and creep experiments to collision problems where deformation speeds are very high.

Acknowledgement: This research has been supported by the Ministry of Science, Technological Development and Innovation through project no. 451-03-47/2023-01/200156 “Innovative scientific and artistic research from the FTS (activity) domain”. This study was done using equipment purchased in the framework of the STRENTEX project of European Union's Horizon 2020 research and innovation program under grant agreement no. 854194.

References:

[1] Yarin, L. Aleksander, Sankaran, Abhilash, An, Seongpil, Pourdeyhimi, Behnam, *Constitutive modeling of polymers accounting for their hyperelasticity, plasticity, creep and viscoelastic relaxation*, Polymer Testing, 85, 106444, 2020.

[2] Brandon, J., A., *Strategies for Structural Dynamic Modification*, John Wiley & Sons INC, New York, 1990.

[3] Parisi, Maria Candida Ribeiro, Giannella, Daniel, Fernandes, Tulio Diniz, Rezende, Karla Freire, Nery, Marcia, *Diabetic foot screening: study of a 3000 times cheaper instrument*, Clinics, 66, 1105-1107, 2011.

[4] Bourcier, E. Mattew, Ullal, Jagdeesh, Parson, K. Henri, Dublin, B. Charlotte, Witherspoon, A. G. Crystal, Ward, A. Sheila, Vinik, I. Aaron, *Diabetic peripheral neuropathy: how reliable is a homemade 1-g monofilament for screening?*, Journal of family practice 55(6), 505-509, 2006.

[5] Haines, S. Carter, Lima, D. Márcio, Li, Na, Spinks, M. Geoffrey, Foroughi, Javad, Madden, D. W. John, Kim, Shi Hyeong, Shaoli, Fang, Jung de Andrade, Mônica, Göktepe, Fatma, Göktepe, Özer, Mirvakili, M. Seyed, Naficy, Sina, Lepró, Xavier, Oh, Jiyoung, Kozlov, E. Mikhail, Kim, Jeong Seon, Xu, Xiuru, Swedlove, J. Benjamin, Wallace, G. Gordon, Baughman, H. Ray, *Artificial muscles from fishing line and sewing thread*, Science, 343, 868-872, 2014.

[6] Zigic, M., Grahovac, N., *Dynamical behavior of a polymer gel during impact*. *Fractional derivative viscoelastic model*, In: Proceedings of the Third Serbian (28th Yu) Congress on Theoretical and Applied Mechanics Vlasina lake, Serbia, 5-8 July 2011.
[7] Zigic, M., Viscoelastic response of the human hamstring muscle during a ramp-and-hold type of experiment, In: Proceedings of the 2nd International Congress of Serbian Society of Mechanics, Palić (Subotica), Serbia, 1-5 June 2009.
[8] Shen, K. L., Soong, T. T., Modeling of Viscoelastic Dampers for Structural Applications, Journal of Engineering Mechanics, 121(6), 1995.
[9] Atanackovic, T. M., A modified Zener model of a viscoelastic body, *Continuum Mech. Thermodyn.*, 14, pp. 137-148, 2002.
[10] Podlubny, I., *Fractional differential equations*, Academic Press, London, 1999.

SYSTEMATIC DESIGN OF A DESKTOP ROBOT ARM IN SOLIDWORKS AND MATLAB SIMULINK

Andrija A. Dević[1], Jelena Z. Vidaković[1], Nikola Lj. Živković[1] and Mihailo P. Lazarević[2]

[1] Lola institute, Kneza Viseslava 70a, 11030 Belgrade, Serbia
e-mail: andrija.devic@li.rs, jelena.vidakovic@li.rs, nikola.zivkovic@li.rs
[2] Faculty of Mechanical Engineering, University of Belgrade, Kraljice Marije 16, 11120 Belgrade 35, Serbia
e-mail: mlazarevic@mas.bg.ac.rs

Abstract

Robot arms are complex mechatronic systems whose design is a challenging and time-consuming task. Low-cost small-size desktop robot arms have been increasingly used in education, research, households, etc. This paper presents the systematic design of a 6DoF desktop robot arm with cylindrical joints actuated with stepper motors. Within the design, the main goals were to achieve cost-effectiveness of the construction, to enable the simplicity of the control unit, and to achieve fast dynamics and good repeatability. The virtual simulation system of the manipulator, built using the integration of 3D design and modern multibody simulation environment, improves the robot design and the efficiency of the robot control system. 3D modeling of the robot arm is performed in SolidWorks. The location of each motor as well as the selection of the power transmission method achieve a reduction of the required moments in the joints during the robot movement. The verification of the motors' dimensioning is performed using numerical simulations of the inverse dynamics problem of the robot based on the SolidWorks 3D robot model for the desired robot operations within the Simulink environment using Simscape Multibody.

Keywords: desktop robot, design, virtual model, stepper motors, SolidWorks, Simscape Multibody.

1. Introduction

The number of technologies that turn to the employment of industrial robots to facilitate their production process is on a constant increase [1]. Robot arms are used in many industrial applications, such as handling, painting, assembling, welding, etc. [2]. However, the costs of industrial robots of renowned manufacturers are high. Recently, there has been a demand on the market for small-size (desktop) and low-cost robots where low-cost implementation prevails over the need for high dynamic performance [3]. Under the background of strategies such as Industry 4.0, Made in China 2025, Advanced Manufacturing Partnership (AMP), Industry 4.1J, etc., increasing number of vocational schools have been setting up industrial robot majors. As a solution, low-cost desktop robots are proposed for academic and research purposes [4].

Three main components in developing a robot arm system include: 1) the mechanical design and structure, 2) an interface device, actuators, and sensors, and 3) a controller [5]. Within the design of desktop robots, designers' goals are oriented to make the robotic system cost-effective, with simple constructions, fast dynamics, and a good repeatability of movements. Considering the practical realization of a robot, significant costs are related with applied actuators with transmission systems, a control unit, and custom-machined components. Nowadays, engineers use CAD software for design and simulation, where their compatibility with the modern multibody simulation environment for 3D mechanical systems provides a time and cost-effective method of research and development.

In desktop manipulators, stepper motors are frequently used due to the ease of control of their position without feedback. Feedforward control, often chosen as a control strategy for stepper motors due to the simplicity of control algorithms, as well as the cost-effectiveness of the solution, is chosen as a control method in this study. The absence of feedback implies that the conditions (trajectory scope) under which the robot arm operates are strictly defined in order to avoid the occurrence of "step skipping" throughout the robot operation. Selection/dimensioning of actuators have to be carefully performed depending on intended robot applications. Dimensioning of motors plays an important role in the design of the desktop robot mechanical structure [6], as their mass/inertia often makes up most of the desktop robot's mass/inertia.

This paper presents the systematic design of a desktop robot arm with six degrees of freedom actuated with stepper motors using available modern software multibody design and simulation tools. The virtual simulation system of the manipulator is built, which improves the robot design and the efficiency of the manipulator control system [7] using Solidworks [8] and Simscape Multibody simulation platform [9]. Modeling of 6Dof desktop robot arm in Solidworks is presented. The design of the transmission system, as one of the most important aspects of robot mechanical design, is described in the paper in detail. 3D assembly from SolidWorks was integrated into Simulink Simscape Multibody via a plug-in, and numerical solution of inverse dynamics problem is simulated in order to verify the motor dimensioning for intended applications.

This paper is divided as follows. In Section 2, the 3D design of the robot arm, including the design of the torque transmission system, is presented. In Section 3, the verification of the dimensioning of the robot based on Simscape Multibody numerical simulation of inverse dynamics is presented. Concluding remarks are given in Section 4.

2. 3D modeling of the robot arm including the design of the torque transmission system

Modern software tools for 3D modeling of machine assemblies ease the problem of constructing machine parts and assemblies but also have the ability to synchronize with multi-body dynamics simulation software by creating suitable files that can be exported and executed via the plugins. The definition of the kinematic structure of the 6DoF robot arm with cylindrical joints is followed by the design and coupling of the robot links. The constructed desktop robot with six degrees of freedom is shown in Fig. 1. The links of the robotic arm are named herein in the following order: shoulder, upper arm, elbow, forearm, hand, and finger [10]. In order to achieve the fastest dynamics of the robot, it is necessary to position the center of mass of the robot be as close as possible to the stationary support (base) to reduce the required motors' moments/forces for the given movement. Guided by this, the motors that drive the joints were placed as close as possible to the stationary support, which allowed the motors to be smaller in mass, dimensions, and cost. The electronics with the microcontroller that controls the motors are also located in the base.

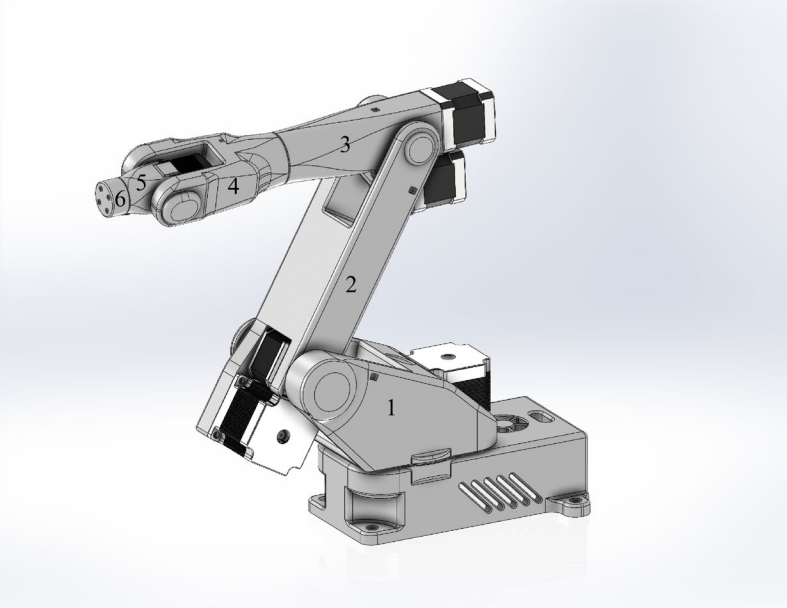

Fig. 1. Designed robot arm with six degrees of freedom. Legend: 1-shoulder, 2-upper arm, 3-elbow, 4-forearm, 5-hand, 6-finger.

The design of the transmission system is one of the most important aspects of robot mechanical design. The most well-known transmission systems used in robot manipulators are strain wave gearing (harmonic drives) and toothed belt pulleys [6]. Toothed belts are used herein as a cost-effective solution that enables transmission of power from the stepper motor to the joints so that the motors are as close as possible to the base. Toothed belts are characterized by smaller backlash compared to conventional gears and enable easy change of the transmission ratio by using pulleys of different sizes. The specific design of the transmission system for the constructed desktop robot arm is described in this section. In Fig. 2, the designed transmission method of the torque from the motor by the belt to the shoulder joint is presented.

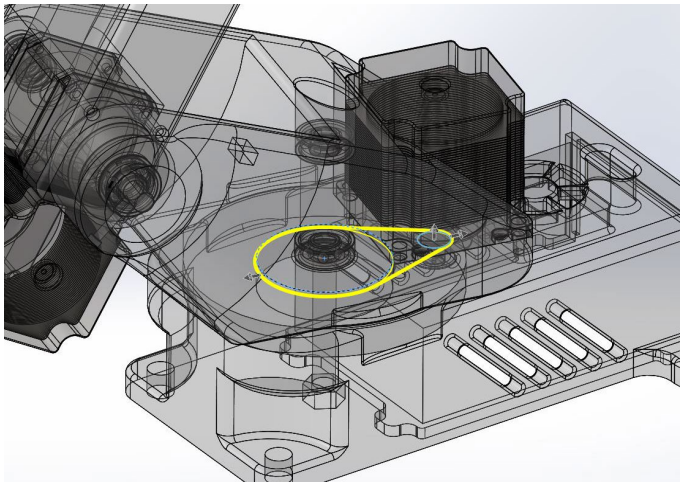

Fig. 2. Transmission of power method of the motor by the belt to the shoulder joint.

In Fig. 3a, the elbow (3rd link) belt transmission method is depicted. The motor located below the motor that drives the second link (in grey color in Fig. 3a) drives the elbow link. In Fig. 3.b, the forearm (4th link) joint's belt transmission method from the motor which is attached at the end of the upper arm (2nd link), is described.

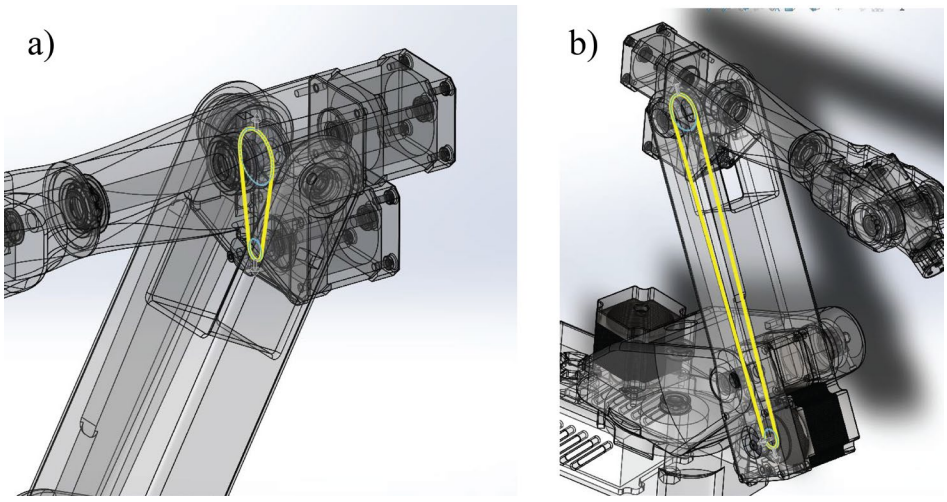

Fig. 3. a) Elbow joint belt transmission method, b) 4. Forearm joint belt transmission method.

One of the biggest challenges was placing the motor that drives the hand (5^{th}) link onto the elbow (3^{rd}) link. It was necessary to find a way to couple the motor of the hand link through the elbow and the forearm link to the hand joints. That construction problem was solved in such a way that the forearm rotates about an elbow axis of symmetry, and the shaft of the hand motor is placed along the forearm rotational axis. At the end of the motor shaft, there is a pulley rigidly attached to the motor shaft and coupled by a toothed belt to the hand joint. The rotational axes of the two pulleys are at an angle of 90 degrees. In order to couple those two belts, the belt had to change direction using two additional pulleys, as presented in Fig. 4.

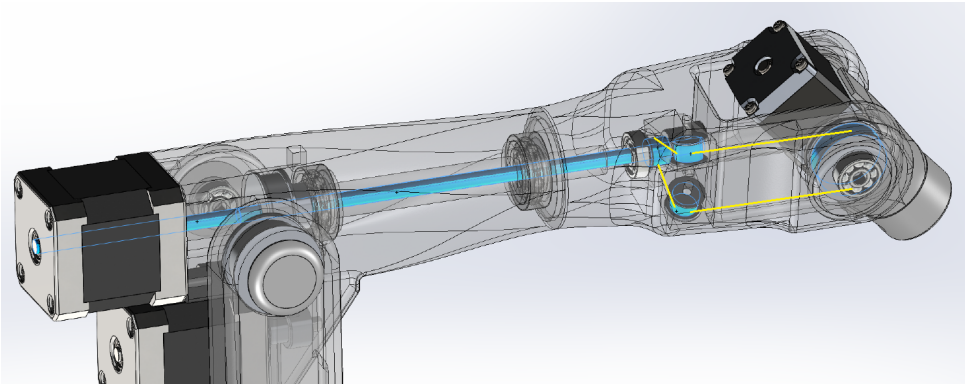

Fig. 4. Hand joint belt transmission method inside forearm link.

Presented low-cost and efficient design of the transmission system enabled placements of the motors as near the base as possible, reducing the required motor torques and sizes.

3. Verification of stepper motors using numerical solution of inverse dynamics problem in Simscape Multibody

Feedforward control of a stepper motor can only achieve successful trajectory tracking under the condition that the required motor torques/forces for the programmed trajectory can be achieved by the installed motors throughout the entire robot operation. Due to the absence of feedback, i.e., the inability to compensate for an error, it is of paramount importance to make sure that the robot motors are dimensioned according to the intended application in order for the motors not to “lose” (“skip”) steps. For this reason, the possibility of considering the integration of high degree

precision 3D mechanical model and modern multibody simulation environment is highly beneficial for verifying the dimensioning of the applied motors.

The initial selection of stepper motors is performed based on simple static calculation for the robot configuration with the maximum static load in the joints, which is the configuration in which the robot arm is completely horizontally positioned so that the robotic gripper can withstand a vertical force of up to 10 N. Based on initial static calculations, stepper motors with torque up to 0.6 Nm are initially selected [11]. The motor manufacturer provides a torque/speed curve which is shown in Fig. 5a. By defining the moment-angular velocity plot for every robot joint by the desired robot movement using the numerical simulation of the inverse the robot dynamics problem, a simple comparison of the two graphs for each motor can verify the dimensioning of the selected stepper motors.

a)

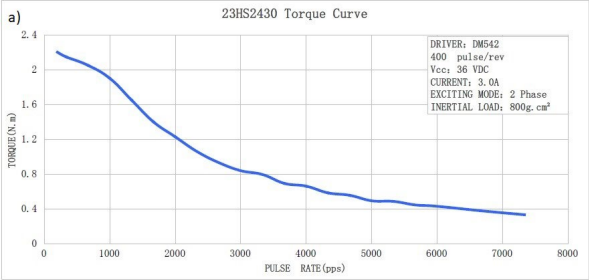

b)

	Motor	Holding torque
Joint 1	23HS5628	504 Ncm
Joint 2	17HS3401	608 Ncm
Joint 3	23HS5628	236 Ncm
Joint 4	17HS3401	96 Ncm
Joint 5	17HS3401	96 Ncm
Joint 6	11HS3410	60 Ncm

Fig. 5. a) Stepper motor torque-speed curve [11], b) Holding torque of chosen stepper motors with reducers.

A robot dynamic model is time variable, highly non-linear, and characterized by coupling effects among the robot joints [12]. The solution of the robot inverse dynamic problem, i.e., the calculation of the required robot actuators' torques/forces from a specification of the robot's trajectory can be obtained analytically, or by using ready-made modeler/simulator software solutions based on 3D software robot models. The latter avoids solving complicated mathematical expressions [12].

Matlab supports the installation of additional packages (add-ons), such as Simscape Multibody Link, which is used to import assembly models from CAD applications to Simscape Multibody. Using Simscape Multibody, a 3D model of the robot arm designed in SolidWorks is transformed into a dynamic model in Simulink environment. In SolidWorks, by selecting the Simscape Multibody Link option, a file with the extension .hml is created, which contains all the necessary parameters for creating a dynamic model in Simscape Multibody, such as mass, inertia, a center of mass, etc., for each part of the assembly separately, as well as the type of joints by which they are connected. For the purpose of inverse dynamics simulation, the cylindrical joint function blocks with two ports, an actuator and a sensor port, were used. The input value of the joint bloc, a series of discrete joint positions in radians obtained from the trajectory planner, is brought to the actuator port, while the output of the sensor port is the series of the calculated joint moments for the given input.

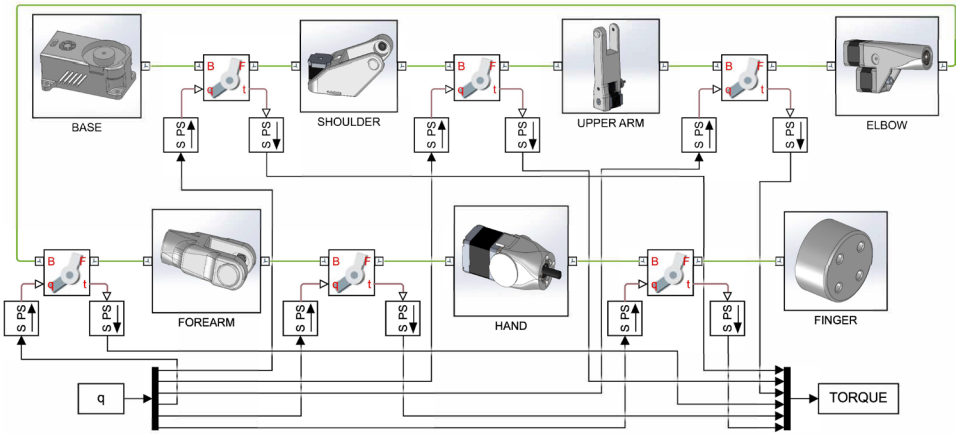

Fig. 6. Simscape Multibody dynamic model of the designed desktop 6DoF robot arm obtained from SolidWorks .hml file.

In Fig. 7a, a time change of the required moment for the upper arm joint and the desired robot motion obtained by Simscape Multibody simulation model in Fig. 6 is given, while the angular velocity for the same joint calculated from the trajectory planer is given in Fig. 7b. The upper arm joint is chosen here since it is the most loaded motor.

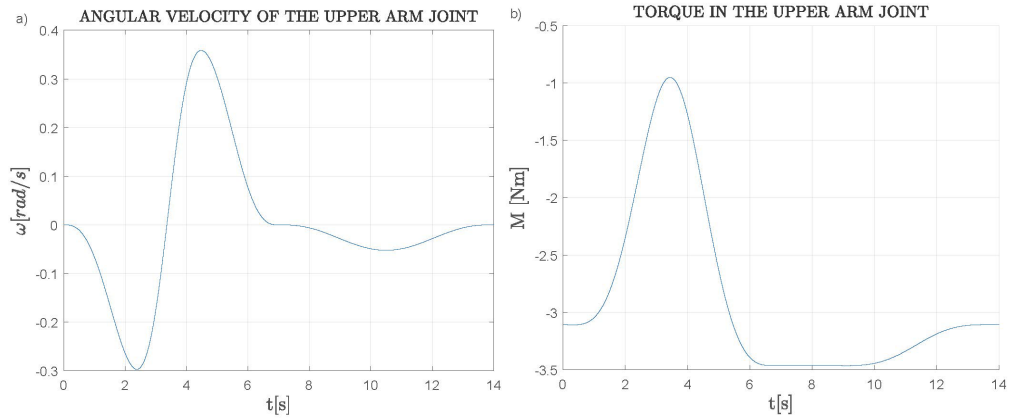

Fig. 7. a) Angular velocity of the upper arm joint calculated in the trajectory planner, b) Torque in the upper arm joint obtained by simulation model in Simscape Multibody.

In Fig. 8.a, the torque/angular velocity plot composed from the time change of the calculated motor's moment and the time change of calculated angular velocity for the desired robot motion and the considered joint is presented. In Fig. 8b, the mentioned torque/angular velocity dependence is presented in absolute coordinates for the simplicity of display and comparisons with the manufacturer's torque/speed curve.

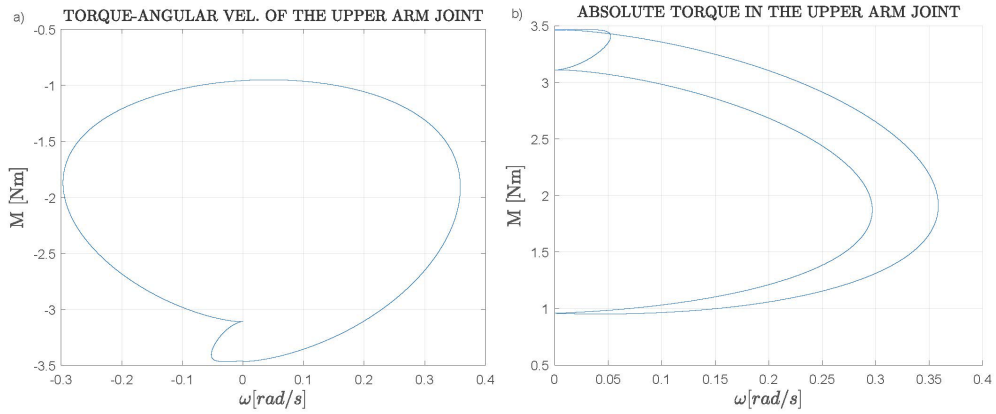

Fig. 8. a) Torque/angular velocity plot for the upper arm joint, b) Absolute torque/angular in the upper arm joint.

In Fig. 9, the comparison of the obtained torque/angular velocity plot from Fig. 8.b (yellow curve) and the manufacturer's torque/speed curve that presents the maximum moments motors can produce depending on rotor speed without causing the desynchronization of the stepper motor, is presented. The blue curve is the curve obtained from the manufacturer documentation [11], while the red curve is the "scaled" motor torque/speed curve obtained by applying a safety degree of 20 % to account for friction and other unmodelled uncertainties of the dynamic model. It has to be noted that the load of mass 1 kg was simulated, which corresponds to the maximum load capacity of the constructed robot.

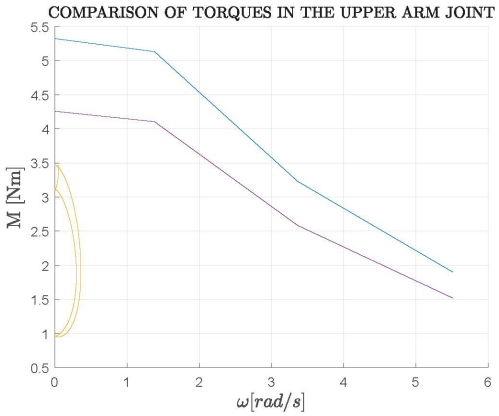

Fig. 9. Comparison of torques/speed curves in the upper arm joint during manipulation.

As can be seen in Fig. 9, the obtained torque/angular velocity plot for the selected motor is located below the curve for the entire robot operation, which implies that the desired robot motion will not cause the occurrence of steps skipping. Also, the resulting curve is not excessively smaller compared to the manufacturer's torque/speed curves, from which it can be concluded that the selected motor is not oversized, which is in compliance with the designer guidelines-selecting small motor as possible (which decreases the mass and the price of the construction) for the desired robot applications.

4. Conclusion

In this study, the systematic design of the mechanical structure for the 6DoF desktop robot arm with cylindrical joints actuated with stepper motors based on the usage of available modern software multibody design and simulation tools is presented. The adopted principles and the followed guidelines for designing a low-cost desktop robotic arm are described. Stepper motors

are selected for ease of control of their position without feedback motors. The design of the transmission system, as one of the most important aspects of robot mechanical design, is described. The virtual simulation system of the manipulator is built, which improves the robot design, and the efficiency of the manipulator control system using Solidworks and Simscape Multibody simulation platform. The verification of the motors' dimensioning is performed using numerical simulation of robot inverse dynamics problem based on the SolidWorks 3D robot model for the desired robot operations. Application of software tools that simulate a solution of the inverse robot dynamics problem could be especially suitable for quick and simple adaptation of the designed robot's mechanical structure.

Acknowledgment: This research has been supported by the research grants of the Serbian Ministry of Science, Technological Development and Innovations, grant No. 451-03-68/2023-14/200066 and 451-03-47/2023-01/ 200105 from 03.02.2023.

References:

[1] Sobaszek, L., Gola, A., & Varga, J. *Virtual designing of robotic workstations*. In Applied Mechanics and Materials. Vol. 844, pp. 31-37. Trans Tech Publications Ltd, 2016.
[2] Vidaković, J. Z., Kvrgić, V. M., Lazarević, M. P., Dimić, Z. Z., & Mitrović, S. M. *Procedure for definition of end-effector orientation in planar surfaces robot applications*. Tehnika, Belgrade 72(6), 845-851, 2017.
[3] Siciliano, B., Sciavicco, L., Villani, L., & Oriolo, G. *Actuators and sensors. Robotics: Modelling, Planning and Control*, Springer, pp. 191-231, 2009.
[4] Tiansong, L., Feng, G., & Yilong, Y. *Design of low-cost desktop robot based on 3D printing technology and open-source control system*. In 2019 IEEE 3rd Information Technology, Networking, Electronic and Automation Control Conference (ITNEC) (pp. 739-742). IEEE, 2019.
[5] Zainudin, W. M. L. W., Shauri, R. L. A., Roslan, M. I., Rosli, M. A., & Ariffin, M. F. M. *New Interface using Beaglebone Black for 4-DOF Robot Arm System*. IEEE Symposium on Industrial Electronics & Applications (ISIEA) (pp. 1-6). IEEE, 2020.
[6] Benotsmane, R., Dudás, L., & Kovács, G. *Simulation and trajectory optimization of collaborating robots by application of solidworks and matlab software in industry 4.0*. Academic Journal of Manufacturing Engineering, 18(4), 2020.
[7] Tang, Y., & Li, X. *Simulation research of manipulator control system based on Solidworks and SimMechanics*. Academic Journal of Computing & Information Science, 1(1), 2018.
[8] Dassault Systems, Solidworks, https://www.solidworks.com, accessed on: 1.4.2023
[9] MathWorks. Model and simulate multidomain physical systems. From: https://www.mathworks.com/products/simscape.html, accessed on: 9.2.2023.
[10] Devic, A.: *Design and control of a robotic system with six degrees of freedom*, Master thesis, Faculty of Mechanical Engineering Belgrade, 2020.
[11] *LAM Technologies electronic equipment*, https://www.lamtechnologies.com/Product.aspx?lng=EN&idp=M1233032, accessed on: 20.8.2020.
[12] Vidakovic, J., Devic, A., Zivkovic, N., Kvrgic, V., & Stepanic, P. *Practical Approaches for Robot Dynamic Model Implementation for Control and Simulation Purposes*. In Experimental Research and Numerical Simulation in Applied Sciences: Proceedings of the International Conference of Experimental and Numerical Investigations and New Technologies, CNNTech 2022 (pp. 147-163). Cham: Springer International Publishing, 2022.

AN ALTERNATIVE FOR THE GRÜNWALD-LETNIKOV-TURNER METHOD FOR SOLVING SET-VALUED FRACTIONAL DIFFERENTIAL EQUATIONS OF MOTION

Filip V. Jakovljević, Miodrag M. Žigić, Nenad M. Grahovac and Dragan T. Spasić

Faculty of Technical Sciences, Department of Mechanics, University of Novi Sad,
Trg Dositeja Obradovica 6, 21000 Novi Sad, Serbia
e-mail: jakovljevic@uns.ac.rs, mzigic@uns.ac.rs, ngraho@uns.ac.rs, spasic@uns.ac.rs

Abstract:

In this paper an impact problem with both fractional type of dissipation and dry friction governed by a set-valued fractional differential equation is re-examined. The problem was previously numerically solved by the Grünwald-Letnikov-Turner method that combines the Grünwald-Letnikov form of the classical left Riemann-Liouville fractional derivative with the event driven, non-iterative Turner's slack variable algorithm used for handling discontinuous model motion phases. We suggest an alternative method that is based on the partly applied Laplace transform and the convolution theorem is proposed. It yields the closed form solution. The time instants separating the discontinuous model motion phases are determined by use of the Newton method applied to velocity and contact force. It is shown that this alternative can handle both sequences of motions and histories of stress and strain.

Keywords: non-smooth mechanics, fractional calculus, impact.

1. Introduction

The problems of contact mechanics are very important for modern society. If posed and solved correctly, they reduce the energy dissipated by unduly high friction, decrease the number of accidents caused by erratically low friction, and prevent the premature wear and failures of many machines. The assumption that the bodies in contact are rigid will simplify the analysis, but at the same time, when used with the Coulomb dry friction law, will lead to mathematical and physical inconsistencies. The Painlevé paradox published in 1895, the homonym paradox (also Painlevé in 1905) or impact problems with an energetic inconsistency, are some of the examples. These problems can be resolved by use of either the Frémond approach or compliant contact models. Namely, if the system includes all bodies in contact, even if each of the bodies is rigid, the system is deformable since the distance between the points of the bodies changes. Therefore, the contact forces between the bodies in the system are interior forces. These interior forces are to be determined by constitutive laws as a result of experiments and should obey the second principle of thermodynamics [1]. The same can be recognized in the compliant contact models dealing with the rigid bodies with viscoelastic layer particularly when fractional viscoelasticity is used [2]. Namely, the concept of change given in terms of fractional derivatives yields more accurate description of the physical process under

consideration since it takes into account memory effects. In mechanical systems, this concept changes the classical Cauchy problems for ordinary differential equations to the Cauchy problems for integro-differential equations of motion. Further, mechanical systems stop in finite time so in order to cover sticking phases of motion, occurring when both velocity and acceleration vanish, the Coulomb friction law should be taken in the set-valued form [3]. Generally speaking, motions of the bodies having a rigid core and a fractional viscoelastic layer (made of an elastomer, polymer or some biomaterials), in the presence of dry friction, can be described by the set-valued fractional differential equations and in turn the Cauchy problem for integro-differential inclusions. This form of the Cauchy problem has a chance to describe motions shown in experiments.

When a rigid body with fractional viscoelastic layer in the presence of dry friction impinges against the rigid wall, three different impact scripts are observed: rebound, capture in the approach phase, and capture in the rebound phase. The problem was posed and solved in [4]. It was described by the Cauchy problem given in terms of the integro-differential inclusion and numerically solved by use of the first approximation known as the Grünwald-Letnikov form of the fractional derivative [5] complemented with the event-driven, non-iterative method known as the Turner slack variable algorithm, see [4, 6] for the details. Later an impact of two bodies [7] and a seismic base isolation problem [8], both with two strictly dissipative processes: deformation of the viscoelastic layer and dry friction, were solved numerically by the same method, say the Grünwald-Letnikov-Turner method, GLTM for short. In order to keep the histories of stress and strain from the previous to the next model motion phase, GLTM requires resizing of the integration step. Namely, after the switching time instant separating two phases of motion is determined (in just one step, as shown in [6]), repeating the integration process from the beginning with a slightly larger integration step ensures that the switching between the motion phases will take place between two steps, so integration according to the next discontinuous model can be easily continued including the memory effects. Besides numerical procedures, the existence results for the derived set-valued fractional differential equations and the equivalent Cauchy problem given in terms of two coupled integro-differential inclusions at velocity level, can be found in [7, 8].

In this paper a new method, as the alternative for GLTM, for solving set-valued fractional differential equations of motion will be suggested. It is motivated by § 20. of [9], where the Laplace transform (LT) was used for solving nonlinear equations. Namely, LT will be partly applied to selected parts of the governing equations of motion, the corresponding kernel will be found and the convolution theorem will be applied yielding the closed form solution for position, velocity and the contact force. Then the Newton method will be used for determining the time instants separating the discontinuous model motion phases. In doing so, the convolution integrals should be split on time intervals with no jumps [10].

2. The set-valued fractional differential equations as the impact model

For the sake of simplicity, we shall re-examine the impact problem presented in [4] dealingwith a rectilinear motion of a rigid block of mass m with a fractional viscoelastic layer in the presence of dry friction. Let us assume that the viscoelastic layer is given in the form of a rod made of the standard fractional linear viscoelastic material, see Fig. 1.:

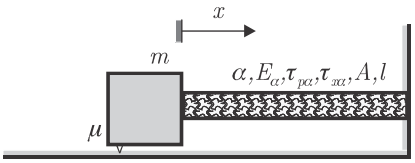

Fig. 1. System under consideration.

In what follows, we use $f = f(t)$ and $q = q(t)$ to denote the force in the viscoelastic layer and the dry friction force, respectively. We start with the Newton axiom and the Newton-Laplace Determination Principle, say

$$mx^{(2)} = -f(t) - q(t), \qquad x(0) = 0, \qquad x^{(1)}(0) = v_0, \tag{1}$$

where $x = x(t)$ stands for the coordinate declaring both the position of the block as well as the deformation of the viscoelastic layer, and $(\cdot)^{(k)}, k = 1,2$ are integer order derivatives. Next we complement (1) with the following constitutive axioms.
We relate $f(t)$ and $x(t)$ with

$$f + \tau_{f\alpha} f^{(\alpha)} = \frac{E_\alpha A}{l}[x + \tau_{x\alpha} x^{(\alpha)}], \qquad f(0) = 0, \tag{2}$$

where we assume that the layer will start to deform from its virginal state and where $(\cdot)^{(\alpha)}$ stands for the classical left Reimann-Liouville derivative of real order α, $0 < \alpha \leq 1$, E_α is the modulus of elasticity, $\tau_{x\alpha}$ and $\tau_{f\alpha}$ are relaxation constants of dimension [time]$^\alpha$, A is the cross-section area of the rod and l is its length in the undeformed state which we assume to correspond to time instant $t = 0$. According to the Clausius--Duhem inequality (2) goes with the following restrictions $E_\alpha > 0$, $\tau_{f\alpha} > 0$, $\tau_{x\alpha} > \tau_{f\alpha}$ ensuring energy dissipation during the deformation process. The axiom (2) is also known as the fractional Kelvin Zener viscoelastic model.

Among all existing dry friction models we assume that the force q obeys the associated Coulomb friction law given in the following set-valued form

$$q \in \mu N \operatorname{Sgn}\left(x^{(1)}\right), \tag{3}$$

with μ representing the friction coefficient, $N = mg$ i.e. the normal force is known in advance, and where $\operatorname{Sgn}(u)$ stands for the maximal monotone set-valued map (the filled-in relay function) defined as

$$\operatorname{Sgn}\left(x^{(1)}\right) = \begin{cases} 1, & \text{if} \quad x^{(1)} > 0, \quad \text{positive sliding,} \\ [-1,1], & \text{if} \quad x^{(1)} = 0, \quad \text{sticking,} \\ -1, & \text{if} \quad x^{(1)} < 0, \quad \text{negative sliding.} \end{cases} \tag{4}$$

The set-valued dry friction law is crucial for modeling transitions from sliding to sticking and vice versa. Namely, during sliding the friction force is in opposite direction to others, it equals its maximal value, and when the motion ceases the friction force will instantaneously jump to another value within its set to maintain equilibrium with the others. During the sticking phase, this equilibrium may take place on a finite time interval since the friction force can change in time as long as it stays within declared set. If it reaches its maximum again the transition from sticking to sliding may occur. Thus we may say that the friction force is of double dual nature: it is the set-valued function with respect to sliding velocity and, at the same time, it is a function of time, also, when preventing motions it acts like a reaction force and is determined from equilibrium equations, while during sliding it has a prescribed structure like an active force, [11].

Introducing the dimensionless quantities: the coordinate, forces and time

$$\overline{x} = \frac{xE_\alpha A}{mgl}, \quad \overline{f} = \frac{f}{mg}, \quad \overline{q} = \frac{q}{mg}, \quad \overline{t} = t\sqrt{\frac{E_\alpha A}{ml}}, \tag{5}$$

as well as the dimensionless relaxation constants and initial velocity

$$a = \tau_{f\alpha}\left(\frac{E_\alpha A}{ml}\right)^{\frac{\alpha}{2}}, \quad b = \tau_{x\alpha}\left(\frac{E_\alpha A}{ml}\right)^{\frac{\alpha}{2}}, \quad \xi = \frac{v_0}{g}\sqrt{\frac{E_\alpha A}{ml}}, \tag{6}$$

our problem becomes

$$x^{(2)} = -f - q, \quad x(0) = 0, \quad x^{(1)}(0) = \xi, \tag{7}$$

$$f + af^{(\alpha)} = x + bx^{(\alpha)}, \quad f(0) = 0, \tag{8}$$

$$q \in \mu\,\mathrm{Sgn}\left(x^{(1)}\right), \tag{9}$$

where the bar was omitted. Note that the impact ends at time instant T determined by either $f(T) = 0$ corresponding to rebound (the block separates from the wall), say R&S, or $x^{(1)}(T) = x^{(2)}(T) = 0$ corresponding to the capture scenario (the block is captured between the wall and asperities below it). The latter can happen in either approaching or rebound phase, say A&C and R&C respectively, and is feasible due to the fact that the friction force being a multifunction (i.e. set-valued function) can change its sign instantaneously as explained above. Namely, when the motion stops the friction force q may jump to any point within the set $[-\mu, \mu]$ to maintain the equilibrium of the forces $f(t)$ and $q(t)$ When captured, for $t > T$ the viscoelastic rod will exhibit some kind of relaxation process which we do not treat here. Note that if the classical sign function is used instead of the filled-in relay function, these capture scenarios can not be covered by the model.

3. The GLTM alternative

Applying the Laplace transform (LT) *to what we can*, with $X = X(s) = \mathcal{L}\{x(t)\} = \int_0^\infty e^{-st}x(t)\,dt$ and $F = F(s) = \mathcal{L}\{f(t)\} = \int_0^\infty e^{-st}f(t)\,dt$, from (7) and (8) we get

$$s^2X - \xi = -F - \mathcal{L}\{q(t)\}, \tag{10}$$

$$F(1 + as^\alpha) = (1 + bs^\alpha)X. \tag{11}$$

Remark: being a set-valued function with respect to sliding velocity as well as a function of time, the dry friction force $q(T) = 0$ is unknown on $[0, \infty)$ so its LT is a priori unknown. Thus we avoid to write an expression for $\mathcal{L}\{q(t)\}$ and keep it under the LT operator until the application of the convolution theorem.

Noting that $sX = \mathcal{L}\{v(t)\}$ since $v(t) = x^{(1)}(t)$ and $x(0) = 0$ we cast (11) in the following form

$$F = \frac{1 + bs^\alpha}{1 + as^\alpha}X = \frac{1 + bs^\alpha + as^\alpha - as^\alpha}{1 + as^\alpha}\frac{Xs}{s} = \left\{\frac{1}{s} + \frac{(b-a)}{a}\left[\frac{s^{\alpha-1}}{\frac{1}{a} + s^\alpha}\right]\right\}\mathcal{L}\{v(t)\},$$

and using the convolution theorem, we get

$$f\left(t\right)=\int_0^t\left[1+\left(\frac{b}{a}-1\right)\cdot E_\alpha\left(-\frac{\eta^\alpha}{a}\right)\right]v\left(t-\eta\right)d\eta, \tag{12}$$

with $E_\alpha\left(z\right)$ standing for the Mittag-Leffler type function

$$E_\alpha\left(z\right)=\begin{cases}\sum_{n=0}^{\infty}\dfrac{z^n}{\Gamma\left(\alpha n+1\right)}, & \left|z\right|<M,\\[2ex] -\sum_{n=1}^{\infty}\dfrac{z^{-n}}{\Gamma\left(1-\alpha n\right)}, & \left|z\right|>M,\end{cases}$$

see [12] for details. There is no adhesion between the block and the wall so $f\left(t\right)$ is positive, i.e. $f\left(t\right)>0$.

On the hand, the partly applied LT to (10) with (11), yields

$$\left(s^2+\frac{1+bs^\alpha}{1+as^\alpha}\right)X=\xi-\mathcal{L}\left\{q\left(t\right)\right\}. \tag{13}$$

Note that the beginning of the argument we use here is the same as the one used in § 20. of [9]. Namely, instead of the unknown LT of the nonlinear terms therein, the unknown LT of the set-valued Coulomb law (that is also nonlinear) stands here.
Rewriting the left hand side of (13) as

$$\left(s^2+\frac{1+bs^\alpha}{1+as^\alpha}\right)X=\frac{as^{2+\alpha}+s^2+bs^\alpha+1}{1+as^\alpha}\frac{sX}{s},$$

and following the lines of Doetsch [9] we introduce the kernel $\psi(\mathrm{t})=\mathcal{L}^{-1}\{\Psi\left(s\right)\}$ with

$$\Psi\left(s\right)=\frac{s+as^{1+\alpha}}{as^{2+\alpha}+s^2+bs^\alpha+1}, \tag{14}$$

so the convolution theorem applied to (11) yields

$$v\left(t\right)=\xi\psi\left(t\right)-\int_0^t\psi\left(t-\eta\right)\cdot q\left(\eta\right)d\eta. \tag{15}$$

This resembles to eq. (20.4) of [9]. Note that the first term on the right hand side of (15) is also a convolution product (of $\psi\left(t\right)$ with the Dirac delta).

Finally, we integrate (15) to get

$$x\left(t\right)=\int_0^t v\left(\eta\right)d\eta. \tag{16}$$

Remark: by the use of (7), (9) and (12) the problem under consideration is governed by a single integro-differential inclusion, that is

$$v^{(1)}+\int_0^t\left[1+\left(\frac{b}{a}-1\right)\cdot E_\alpha\left(-\frac{\eta^\alpha}{a}\right)\right]v(t-\eta)d\eta\in-\mu\mathrm{Sgn}\left(x^{(1)}\right),\quad\text{i.e.}\quad\text{on }[0,T], \tag{17}$$

with

$$v^{(1)}(0) = \xi.$$

The split of the time interval $\left[\,0,T\,\right]$ should follow discontinuous model motion phases determined by either $v(t) = 0$ or $f(t) = 0$. Namely, after the impact the block will slide towards the wall so

$$v\left(t\right) = \xi\psi\left(t\right) - \mu\int_0^t \psi\left(\eta\right)d\eta, \qquad \text{for} \;\; 0 < t \le t_1, \tag{18}$$

will decrease until time instant t_1 determined by $v\left(t_1\right) = 0$. The friction force at t_1 changes its sign instantaneously and becomes of the opposite sign to $f\left(t\right)$. Then, there are two possible scripts after time instant t_1. If the corresponding force $f\left(t_1\right)$ determined by (12) satisfies $f\left(t_1\right) \le \mu$ the motion will cease, due to the instantaneous jump of the friction force from its limiting value during the sliding phase to the value within the interval $\left[-\mu,\mu\right]$. This maintains the equilibrium $f\left(t_1\right) - q\left(t_1\right) = 0$, ensuring $x^{(2)}\left(t_1\right) = 0$ so the impact ends with $T = t_1$. This script correspond to the capture in the approaching phase, A&C. In case of the opposite $f\left(t_1\right) > \mu$ the rebound will starts and the motion will be continued in the opposite direction, it reads

$$v\left(t\right) = \xi\psi\left(t\right) - \int_0^{t_1}\psi\left(\eta\right)q\left(t-\eta\right)d\eta - \int_{t_1}^{t_2}\psi\left(\eta\right)q\left(t-\eta\right)d\eta, \quad \text{for} \;\; t_1 < t \le t_2. \tag{19}$$

Note that $q\left(t\right)$ does not have the same sign within time intervals $\left[0,t_1\right]$ and $\left[t_1,t_2\right]$. Time instant t_2 is to be determined either by $f\left(t_2\right) = 0$ or $v\left(t_2\right) = 0$. The first case $f\left(t_2\right) = 0$ with $v\left(t_2\right) < 0$, corresponds to the rebound after impact (separation from the wall), R&S. The second one, $v\left(t_2\right) = 0$ followed by $f\left(t_2\right) > 0$ and $f\left(t_2\right) \le \mu$ corresponds to the capture in the rebound phase, R&C. As before the instantaneous jump of the friction force from its limiting value to the value equal to $f\left(t_2\right)$ and of opposite sign of it, within the set $\left[-\mu,\mu\right]$ will maintain the equilibrium for $t > t_2$ In either case the impact ends so $T = t_2$.

4. The kernel $\psi(t)$ and the closed form solutions

The image of the kernel $\Psi\left(s\right)$, (14) is given in the Müntz quotient form, so in order to find the original $\psi\left(t\right)$ one may use the complex inversion formula

$$\psi\left(t\right) = \lim_{Y\to\infty}\frac{1}{2\pi j}\int_{c-Yj}^{c+Yj} e^{st}\Psi\left(s\right)ds, \quad t > 0, \tag{20}$$

where c is suitably chosen so all poles of $\Psi\left(s\right)$ lie to the left of the line $s = c$. Following the standard procedure, first, the Bromwitch contour with a cut along the negative real axis, say *ABDEFGHA* or κ for short, was chosen.

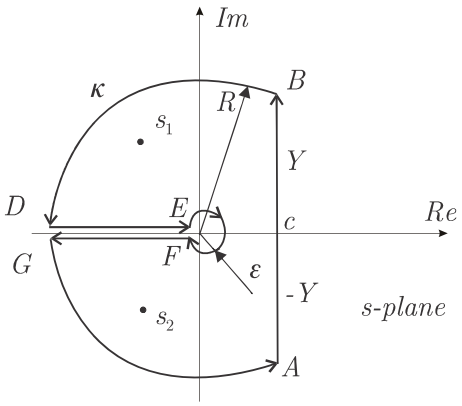

Fig. 2. Contour of integration.

Then the number of poles of $\Psi(s)$ inside γ were analyzed by use of the Rouché theorem. It can be shown that $\Psi(s)$ has two poles, see [13, p.187] and [14] for details. To find the poles one has to split the equation $as^{2+\alpha}+s^2+bs^{\alpha}+1=0$ into the system

$$\begin{aligned} a\rho^{2+\alpha}\cos\big(2+\alpha\big)\theta+\rho^2\cos 2\theta+b\rho^{\alpha}\cos\alpha\theta+1=0,\\ a\rho^{2+\alpha}\sin\big(2+\alpha\big)\theta+\rho^2\sin 2\theta+b\rho^{\alpha}\sin\alpha\theta=0. \end{aligned} \tag{21}$$

Applying the Newton method one may find the solutions corresponding to the principal branch, say $\overline{\rho}$ and $-\pi<\overline{\theta}<\pi$, so the poles of Ψ say $s_1=\overline{\rho}e^{\overline{\theta}j}$, $s_2=\overline{\rho}e^{-\overline{\theta}j}$ are assumed to be known. With this preparation done, it remains to explore the residue theorem, see § 34. of [9]. According to it, the integral along the closed path κ is $2\pi j$ times the sum of the residues of $e^{st}\Psi\big(s\big)$ calculated at the singularities enclosed by κ. Rewriting $e^{st}\Psi\big(s\big)$ as $F_1\big(s,t\big)/F_2\big(s\big)$ with

$$F_1\big(s,t\big)=s\big(1+as^{\alpha}\big)e^{st},\quad F_2\big(s\big)=as^{2+\alpha}+s^2+bs^{\alpha}+1, \tag{22}$$

the residue of $F_1\big(s,t\big)/F_2\big(s\big)$, at the point s_0 reads $F_1\big(s_o,t\big)/F_2'\big(s_o\big)$ where prime represents the derivative with respect to s. After calculating the sum of the integrals along the lines above *DE* and below *FG* the negative real axis, the introduced kernel $\psi\big(t\big)$ in its integral form reads

$$\psi\big(t\big)=\sum_{k=1}^{2}\frac{F_1\big(s_k,t\big)}{F_2'\big(s_k\big)}-I\big(\alpha,a,b,t\big), \tag{23}$$

with $I\big(t\big)=I\big(\alpha,a,b,t\big)$ given by

$$\begin{aligned} I\big(t\big)=&\frac{\big(b-a\big)\sin\alpha\pi}{\pi}\cdot\\ &\cdot\int_0^{\infty}\frac{r^{1+\alpha}e^{-rt}dr}{\big(1+r^2\big)^2+\big(ar^{2+\alpha}+br^{\alpha}\big)^2+2\big(1+r^2\big)\big(ar^{2+\alpha}+br^{\alpha}\big)\cos\alpha\pi}. \end{aligned} \tag{24}$$

With this preparation done, the model of the impact problem under consideration reads

$$
\begin{aligned}
v(t) &= \begin{cases} \xi\psi(t) - \int_0^t \psi(\eta) q(t-\eta)\, d\eta, & \text{for } 0 < t \le t_1, \\ \xi\psi(t) - \int_0^{t_1} \psi(\eta) q(t-\eta)\, d\eta - \int_{t_1}^{t_2} \psi(\eta) q(t-\eta)\, d\eta, & \text{for } t_1 < t \le t_2, \end{cases} \\
f(t) &= \int_0^t \left[1 + \left(\frac{b}{a} - 1 \right) \cdot E_\alpha \left(-\frac{\eta^\alpha}{a} \right) \right] v(t-\eta)\, d\eta, \\
x(t) &= \int_0^t v(\eta)\, d\eta,
\end{aligned}
\tag{25}
$$

with (9), (23) and the following impact scripts

$$
\begin{array}{llll}
\text{A\&C} & v(t_1) = 0 & f(t_1) \le \mu & q(t_1) = -f(t_1) < \mu, \\
\text{R\&C} & v(t_2) = 0 & f(t_2) \le \mu & q(t_2) = -f(t_2) < \mu, \\
\text{R\&S} & v(t_2) < 0 & f(t_2 = 0) & q(t_2) = -\mu.
\end{array}
\tag{26}
$$

Note that both parameters of the viscoelastic layer attached to rigid block, and memory effects are included in the convolution integrals.

5. The verification of the method

In order to verify the method we shall pick the same values of system parameters: $\alpha = 0.23,\ a = 0.004, b = 1.183$ and $\xi = 1$ as in [4], use (25), (26) to solve the problem and compare the results with the ones obtained by use of GLMT therein. We shall keep this values in all calculations. Since the coefficients of friction for collision phenomena cannot be accurately determined we choose several values of μ, $\mu \in [0,1]$. These values are assumed as for non-collision processes.

First we solve (21) to find $\overline{\rho} = 1.4991$ and $\overline{\theta} = 1.6792$ corresponding to the principal branch of the Riemann surface for multivalued analytic function in the complex plane. Then we find poles of $\Psi(s)$ in our case $s_1 = -0.16222 + 1.4903j$ and $s_2 = -0.16222 - 1.4903j$, (j being the imaginary unit $\sqrt{-1}$), so after the contour integration and some algebra from [2] we get the kernel $\psi(t)$ in the following form

$$
\psi(t) = 2e^{-0.1622t} \left(0.5346 \cos(1.4903t) - 0.0062 \sin(1.4903t) \right) - I(0.23, 0.004, 1.183, t), \tag{27}
$$

with the upper boundary in the integral of (24) was equal to 2000 instead of infinity. The difference between the values of $I(0.23, 0.004, 1.183)$ obtained for the upper bounds 2000 and 3000 was not significant. After completing (23), (26) we apply the proposed procedure complemented with some non-linear equation solver in our case either Newton's or secant method. The obtained results are as follows.

As expected for the smooth model $\mu = 0$ we recover the numerical results of [2] where the rebound and separation from the wall, R&S, was the only script covered. Note that this method yields $v(t)$, $f(t)$ and $x(t)$ in the closed form what was not the case therein. The obtained values of the impact duration $T = 2.0244$, the residual deformation $x(T) = 0.1353$ and the rebound velocity $v(T) = -0.7730$ fully agree with the values obtained by both Post's inversion

formula and the Grünwald-Letnikov type algorithm used in [2]. Since we deal here with the closed form solutions for $v(t)$, $f(t)$ and $x(t)$ we do not present graphics of these functions.

For $\mu > 0$ we recover the results of [4] and confirm three different impact scripts shown therein. The results summarized in the following table correspond to initially chosen values $\alpha = 0.23$, $a = 0.004, b = 1.183$ and $\xi = 1$. The values of the friction force after its instantaneous jump at the end of the capture scenarios are given in the last column.

Description of impact							
Script	μ	T	$v(t)$	$f(t)$	$x(t)$	$q(T)$	$q(T^+)$
R&S,	0	2.0244	-0.7730	0	0.1353	-	-
R&S,	0.2	2.0862	-0.5376	0	0.1096	-0.2	-0.2
R&C,	0.6	2.7054	0	0.3807	0.2351	-0.6	0.3807
A&C,	0.9	0.6676	0	0.8028	0.3618	0.9	-0.8028

In Fig. 3. we show the impact duration T and the distance travelled during impact, say $DT = 2x(t_1) - x(T)$ since $x_{\max} = x(t_1)$ for several values of the friction coefficient μ. As expected increasing μ the distance travelled *DT* decreases. The threshold values of μ separating three impact scenarios considered are also shown. Namely, for $\mu \in [0, 0.415)$, $\mu \in (0.415, 0.831)$ and $\mu \in (0.831, \infty)$ the corresponding impact scripts respectively read R&S, R&C and A&C.

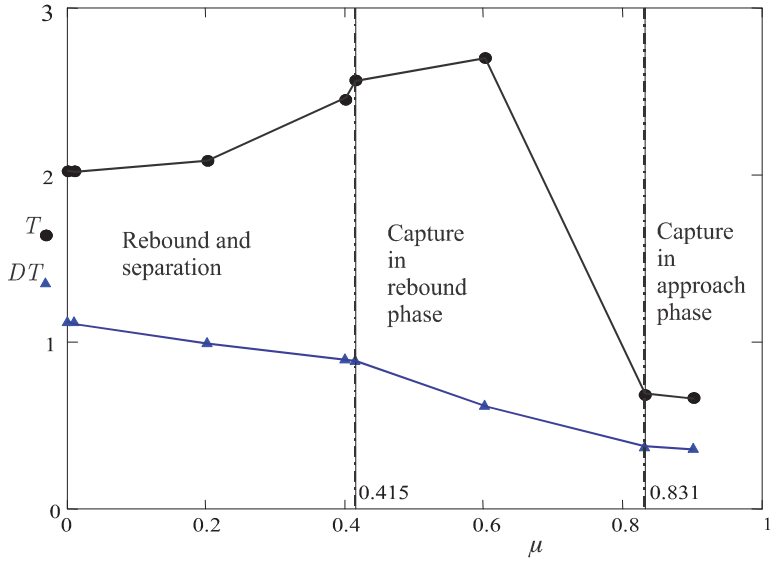

Fig. 3. Distance traveled during impact, its duration and the threshold values of μ.

Note that the dependence of the impact duration T on the friction coefficient μ exhibits non- m onotonic behavior. Also note that due to the closed form of the variables characterizing the state and forces, the variation of any of the model parameters does not seem to be a problem.

6. Closure

In this paper the impact problem with both fractional and dry friction type of dissipation, described by the set-valued system of fractional differential equations was re-examined. The problem was previously numerically solved by use of the Grünwald-Letnikov-Turner method. The new method for solving this kind of equations of motion was proposed and the solution of the impact problem was obtained by the Laplace transform, partially applied to selected part of the governing equations, and the convolution theorem. The closed integral form of the velocity, contact force and position were obtained. The memory effects were included in the convolution integrals. Time instants separating discontinuous model motion phases were determined by the Newton method and the secant method. We believe that this new method can serve as an alternative for the Grünwald-Letnikov-Turner method not only for the short time duration processes but also for different kind of structural applications too.

Acknowledgment: This paper has been supported by the Ministry of Science, Technological Development and Innovation through project no. 451-03-47/2023-01/200156 "Innovative scientific and artistic research from the FTS (activity) domain".

References:

[1] Frémond, M., *Non-Smooth Thermomechanics,* Springer, 2002.
[2] Atanackovic T.M., Spasic, D.T., On *viscoelastic compliant contact-impact models*, Transactions of ASME Journal of Applied Mechanics, 71, 134-138, 2004.
[3] Leine R.I., Nijmeijer H., *Dynamics and Bifurcations of Non-Smooth Mechanical Systems*, Springer, 2004.
[4] Grahovac N.M., Zigic M.M., Spasic D. T., *On impact scripts with both fractional and dry friction type of dissipation*, Int. J. Bifircation and Chaos, 22, 4, 1250076, 2012. DOI:10.1142/S0218127412500769.
[5] Podlubny, I., *Fractional Differential Equations,* Academic Press, 1999.
[6] Turner J.D., *On simulation of discontinious functions*, Transactions of ASME, Journal of Applied Mechanics, 68: 751--757, 2001.
[7] Grahovac N.M., Spasic D.T., *Multivalued fractional differential equations as a model for an impact of two bodies*, Journal of Vibration and Control, 20(7), 1017--1032, 2014.
[8] Zigic M.M., *Seismic response of a column like structure with both fractional and dry friction type of dissipation*, (in Serbian) Ph.D. thesis, Novi Sad, 2012.
[9] Doetsch, G., *Guide to the applications of Laplace transforms*, D. Van Nostrand, 1961.
[10] Adkins, W.A., Davidson, M.G., *Ordinary Differential Equations*, Springer 2010.
[11] Spasic D.T., *A Thermodynamically Consistent Rheological Model for Engineering Applications,* book chapter in Advanced Topics on Applications of Fractional Calculus on Control Problems, System Stability and Modeling, (Eds: V. Mladenov, N. Mastorakis; Com. M. Lazarevic), WSEAS Press, 2014.
[12] Mainardi F., Gorenflo R., *On Mittag-Leffler-Type Functions in Fractional Evolution Processes*, Journal of Computational and Applied mathematics, 118, 283-299, 2000.
[13] Shabat, B.V., *Introduction to complex analysis*, 2nd Russian ed., Nauka, Moscow, 1976.
[14] Spasic D.T., Charalambakis N.C., *Forced vibrations with fractional type of dissipation*, Proceedings of the International Conference on Nonsmooth/Nonconvex Mechanics with Applications in Engineering, Thessaloniki, p. 323-330, 2002.

DESIGNING, OPTIMISING AND FABRICATING OF MICROFLUIDIC DEVICES, BASED ON TOPOLOGY OPTIMISATION AND 3D PRINTING

Dalibor Nikolić[1,2], Nevena Milivojević[1], Ana Mirić[1], Marko Živanović[1,2] and Nenad Filipović[2,3]

[1]Institute for Information Technologies, University of Kragujevac, Jovana Cvijića bb, 34000 Kragujevac, Serbia
e-mail: markovac85@kg.ac.rs, nevena_milivojevic@live.com, anamiric53@gmail.com, zivanovicmkg@gmail.com
[2]BioIRC - Bioengineering Research and Development Center, University of Kragujevac, Prvoslava Stojanovića 6, 34000 Kragujevac, Serbia
e-mail: markovac85@kg.ac.rs, fica@kg.ac.rs
[3]Faculty of Engineering, University of Kragujevac, Sestre Janjić 6, 34000 Kragujevac, Serbia
e-mail: fica@kg.ac.rs

Abstract

Preclinical studies are based on consistent, relevant systems that can be used to better understand basic physiological processes. Until recently, flat biology offered many answers in examining model systems needed to study biological processes. However, the reduced use of animal model systems and limitations of 2D flat biology cell models can be replaced successfully by newer technological *in vitro* solutions. Flat biology technology is based on static working conditions, in which vasculature and shear forces in most experiments lack. Also, mimicking of rheological properties of physiological processes are missing. Nowadays, microfluidic chips are one of the most advanced and widely used technologies for *in vitro* testing of 3D constructs that mimic *in vivo* processes in a very successful manner. The main challenge in the design of these devices is the consistent distribution of nutrients and drugs. Even the smallest detail in the construction of channels, chambers and other compartments are crucial. This paper presents a unique approach to the design of chip devices by using the computational fluid dynamics (CFD) based on the discretization finite element method (FEM) and topological optimization (TO) method for in silico testing and optimizing the shape of the features (chambers and channels). This approach minimizes mistakes in feature design by minimizing local backflow and recirculation and provides the full potential of novel microfluidic devices.

Keywords: microfluidic device, 3D print, topology optimization, Tosca, organ-on-chip.

1. Introduction

Biomedical experiments continue to use traditional tissue culture dishes or flasks for cell and tissue cultivation, despite their limitations. These models are generally static and lack vasculature and shear stress forces, typically failing to reproduce the rheological properties of the physiological processes [1]. Similarly, *in vivo* animal models poorly mimic the human condition

and cannot accurately predict drug efficacy, and they are ethically controversial. In this regard, preclinical *in vitro* experimentation requires highly reliable and physiologically relevant systems that could recapitulate complex human physiology [2]. Over the last two decades, the combination of advanced tissue engineering principles, nanotechnology tools, computer methods and cell biology methods has resulted in the development of a state-of-the-art microfluidic model with an unprecedented ability to reproduce the natural habitat of cells and tissues in microfluidic devices. These biomimetic devices, called organ-on-a-chip, have become a promising approach that has been applied in numerous research areas. They are beginning to attract the attention of physicians due to their unprecedented predictive capacity and their compatibility with existing technologies, such as optical microscopy, screening techniques or biosensor probes. This provides microfluidic platforms with advanced capabilities that are very attractive for biomedical experimentation, healthcare and the pharmaceutical sector [3, 4].

A wide variety of micro- and bio-fabrication methods have been used to develop these microfluidic devices that contain miniature features (chambers, microchannels). Usually, this type of device is produced by UV photolithography and soft lithography methods, such as replica molding, due to its simplicity and efficiency [5]. In this paper, we are presenting a new approach to fabrication of microfluidic chip devices.

The *in vivo* environment guarantees the presence of basic molecular factors that direct cell behavior, while vascularization ensures the supply of nutrients and the removal of waste. Therefore, the presence of molecular factors that influence cell division, shape, expansion, proliferation, death and secretion of extracellular matrix components is necessary for successful modeling of morphogenetic events. When designing a 3D model, it should be considered that cells in the middle of the construct might behave differently than cells growing on the surface, depending on the nutrient concentration gradient. Specifically, cells respond to dynamic signals, such as electric fields, osmotic and hydrostatic pressure, stress, strain, fluid flow, and flow potential, modifying the surrounding extracellular matrix [6].

The three-dimensional cellular environment plays a synergistic role in directing cell fate and behavior, thus a good replication of the *in vivo* environment in terms of architecture and mechanical properties is required. The development of a dynamic biomimetic environment is a key aspect in the long-term culture of any cell type or tissue [7, 8]. The main issue with those microfluidic devices is a consistent fluid distribution trues them. The construction of chambers and channels has a huge impact on the distribution of nutrients and drugs in each part of the device (to each testing cells or tissue on a microfluidic chip). This paper also describes a novel approach in designing chip devices using the computational fluid dynamics (CFD) based on discretization finite element method (FEM) and topological optimization (TO) method for in silico testing and optimizing the shape of the features (chambers and channels). This approach minimizes mistakes in features design by minimizing local backflow and recirculation and provides the full potential of novel microfluidic devices.

2. Material and methods

2.1 Desing of microfluid device

The features of interest, such as chambers and microfluidic channels in the form of virtual 3D models, were first designed in the computer-aided design (CAD) software package SolidWorks® Premium 2022 SP0.0 (Fig. 1). The first model was created as a single-chamber chip with one input and one output channel, the simplest lab-on-a-chip device design (Fig. 1 - right). Afterwards, through a series of iterations, that model was updated with the goal of achieving a uniform flow through the chamber.

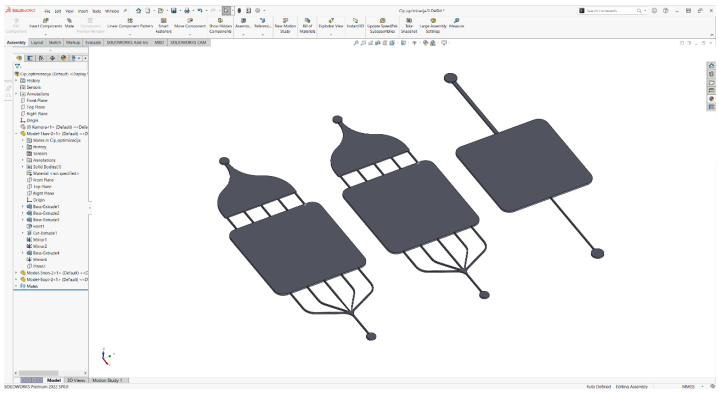

Fig. 1. SolidWorks® design.

2.2 DS SIMULIA® - Tosca fluid topology and non-parametric optimization

The Tosca optimization suite provides dedicated fast and powerful flow optimization solutions based on computational fluid dynamics (CFD) simulations. Fluid Optimization enables topology optimization-driven design concepts for fluid flow systems and components. Usually, engineers have to develop innovative products in the shortest development time possible. Tosca has the capability to create innovative design ideas automatically for a defined flow task and optimized flow canals. Fluid Optimization's unique technology helps you achieve the highest flow performance and quality. In the design of the chip, it is very important that, depending on the complexity of the chip, the communication channels must be optimized in such a way that the flow is fully balanced. Also, flow noise must be reduced and flow instabilities eliminated. In this way, all places inside the chamber/chambers will be equally covered with the same medium concentration. Zhou et al. [9] presented an industrial application of TO for combined conductive and convective heat transfer problems. Flow solution was performed in SIMULIA-Abaqus and optimization process was performed in SIMULIA-Tosca and design dependent convection is modelled. For chip optimization we used 3D model designed by SolidWorks® Premium 2022 SP0.0 software. Ansys® Academic Research Mechanical, Release 19.1 was used for CFD simulations and SIMULIA-Tosca for topology optimization. Topology optimization was performed on inlet canals of the microfluid device (Fig. 2 green area), aim of TO was to create a model with an equal flow in all inlet channels/all camber inputs (Fig. 2 out-A to out-E). Equal flow on all chamber inlets produces a uniform flow through the chamber.

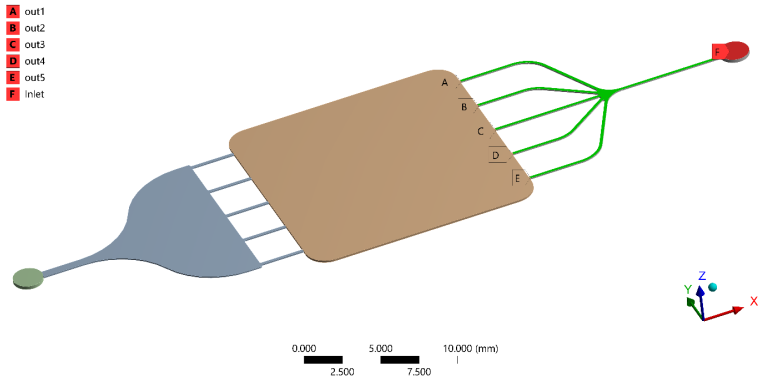

Fig. 2. CFD Ansys model, boundary conditions.

2.3 Fabrication of microfluidic chip device

Designed and optimized 3D CAD models were exported to stereolithography (STL) file format. They are precisely delineated to reproduce the desired biological event or microenvironment under study. The STL files were then imported into the 3D printing software. With mask-stereolithography (mSLA) technology, master mold was printed layer by layer.

After 3D printing, replica molding was used to replicate the master. A biocompatible and optically transparent polymeric material, polydimethylsiloxane (PDMS), was used. PDMS elastomer was poured over the mold and cured in the oven (Fig. 3). The obtained PDMS replica was gently peeled off and cut into appropriate sizes and shapes, and the inlet/outlets were drilled out for tube connection. Finally, controlled UV and ozone radiation was used for bonding the PDMS chip replica to another PDMS part or to a standard microscopy glass slide.

Fig. 3. Cured PDMS chips in mold.

3. Results

The first model was created as a single-chamber chip with one input and one output channel, the simplest lab-on-chip device design (Fig. 1 - right). By using the CFD model simulations, the flow through this device was simulated, and the results of the velocity field were presented in Fig. 4. By analyzing the result from the CFD simulation, we conclude that the flow through the chamber is unequally distributed, and design needs to be updated. Streamlines very well represent the initial state of the flow in the microfluidic device, as shown in Fig. 4.

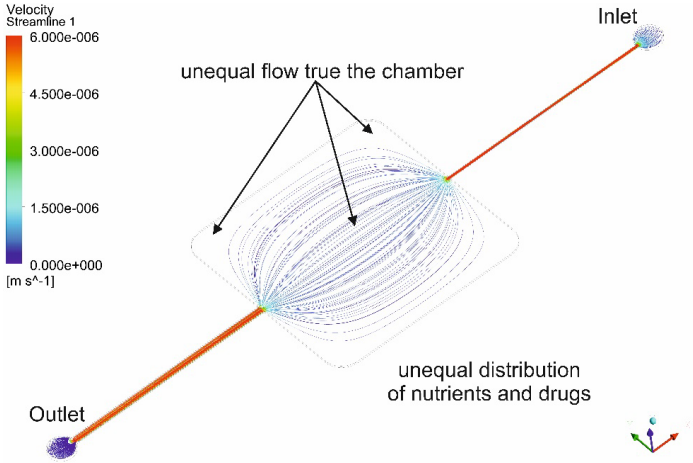

Fig. 4. Initial model velocity field – streamlines.

To improve the performance of the device, our aim was to add several inlet and outlet channels equally distributed on the inlet/outlet chamber plane. By adding several more inlet channels, the expectation was to create a more uniform flow through the device. The second design was manually updated in CAD software (Fig. 1 - middle) with 5 input/output channels. The CDF results of fluid flow through that device are presented in Fig. 5. In this computer model, different inlet canal lengths cause unequal flow and nutrient distribution through the cross-section of the chamber. The flow was better than in single canal devices but still showed some small distribution irregularities.

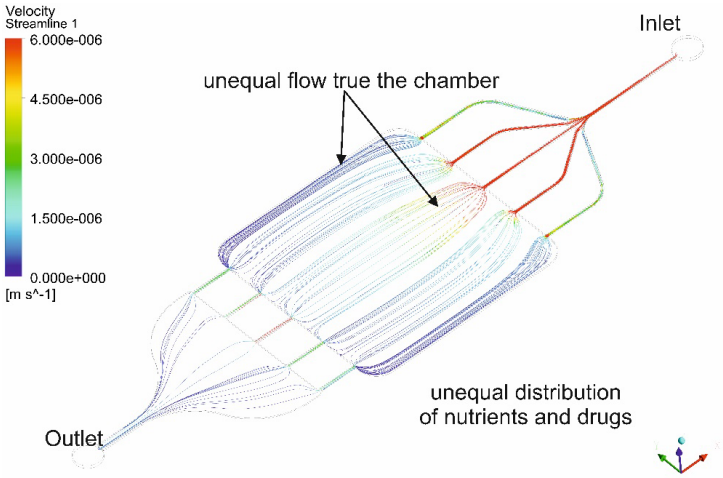

Fig. 53. Base model after manual design.

In order to improve the deviceand achieve a uniform fluid flow through it, an advanced topological optimization technique was applied. Tosca Fluid - CFD Topology optimization for high-end CFD Software (Fig. 6).

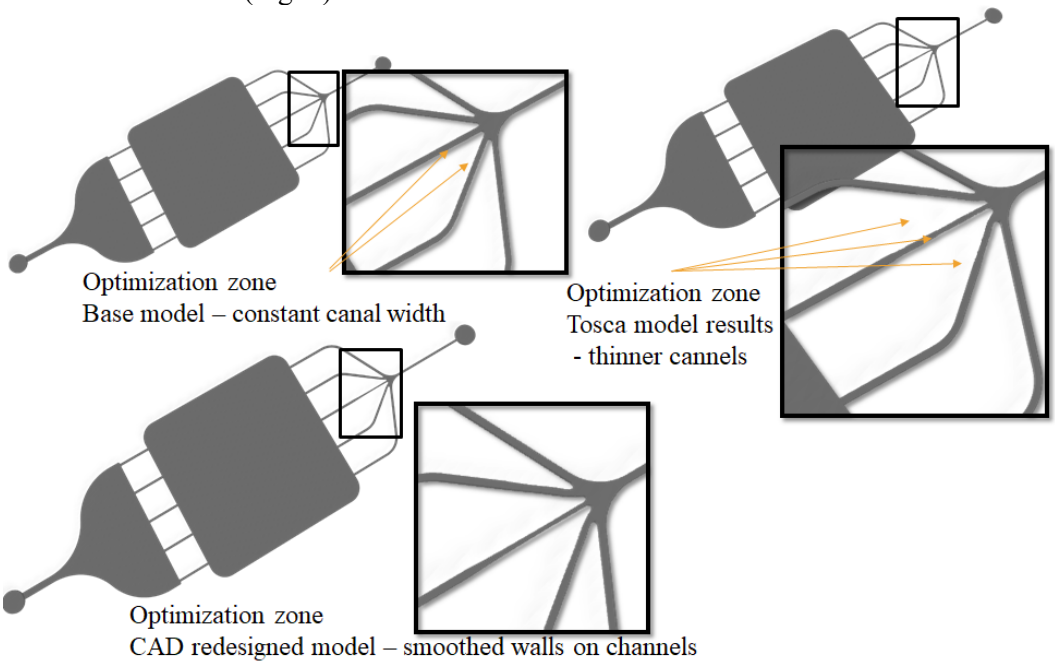

Fig. 64. Optimization process – Tosca Fluid.

Topology optimization process began from 3D model with constant canal width (Fig. 6 up left image). Through a series of iterations and flow simulations using the mass flow balancing

algorithm, Tosca changed the geometry of canals by removing discretization elements to achieve the desired flow distribution (Fig. 6 up right). In this way, TO generates rough design concepts for a desired flow split ratio with multiple given outlets. This design we used as a guide for creating a new smooth CAD model with adequate channel width (Fig. 6 down left image).

The results of CFD velocity distribution in the final model after topology optimization are shown in Fig. 7. Analyzing the fluid flow streamlines, it can be concluded that this design has achieved uniform fluid flow through the front chamber.

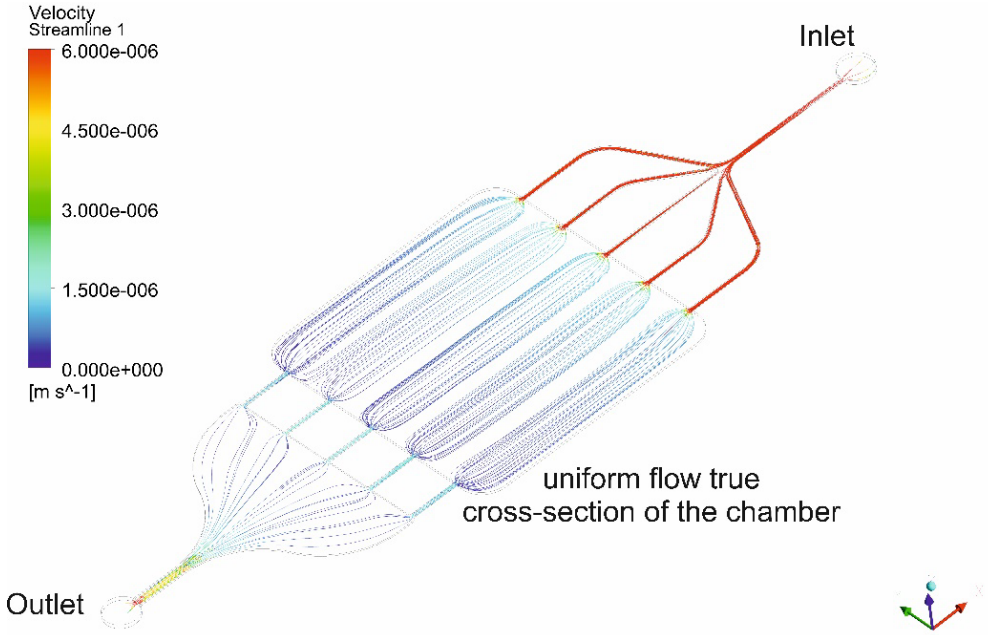

Fig. 7. Final model after optimization.

Channels whose width is not uniform can be very complicated to manufacture; therefore, to test the optimized model, we printed the master mold for chip replica molding. Figure 8 shows the fabricated mold (3D printed) before (left) and the final model after optimization (right). Differences in channel width can be easily recognized.

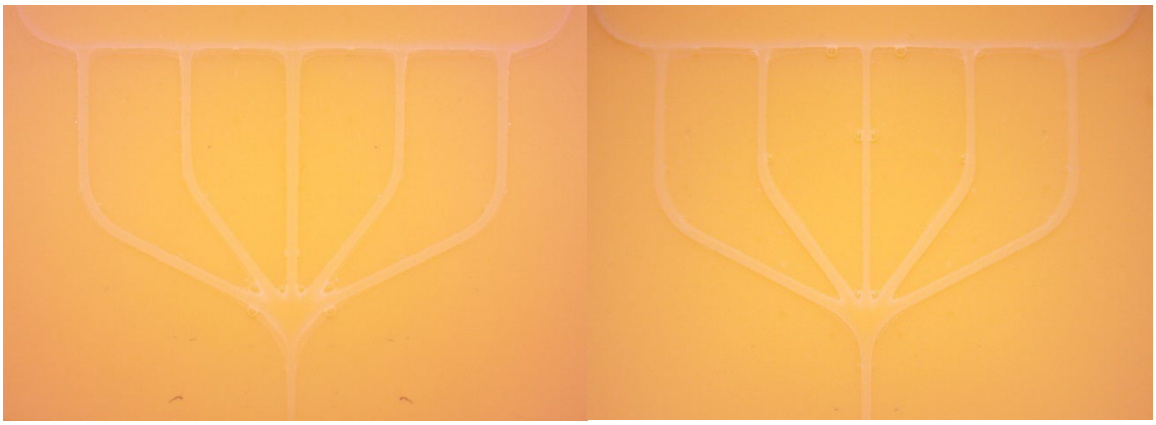

Fig. 85. Fabricated mold channels optimization preview; non-optimized inlet canals – left; optimized inlet canals – right.

4. Discussion

Compared to conventional microfluidic chip device fabrication techniques, the approach presented in this paper has several advantages. For example, fused deposition-modeling has some

restrictions related to the rough surface obtained and the velocity of printing is slow, while LCD printing does not have these disadvantages. Also, another technique such as Inkjet modeling shows certain limitations, including the removal of the support material and the amount of waste produced during the printing process, while there are no such losses with the LCD method. As for stereolithography, there are two main variables along the process, photopolymerizable promoter and resin features. The obtained resolution depends on these two variables, and resolution with this LCD technology is very high [10, 11].

Tosca – topological optimization tool generates models that are difficult to fabricate using conventional fabrication techniques. Therefore, 3D printing is an ideal tool for manufacturing optimized models that can be very complex and, in some cases, can be impossible to manufacture the other way.

5. Conclusions

Using modern computer-aided engineering methods - CFD for in-silico fluid flow analysis, combined with a topological optimization method, it is possible to create a chip microfluidic device that will have an equal distribution of fluid flow in all parts, and therefore the examined tissues and cells will have an equal chance of survival. Also, using modern manufacturing techniques such as 3D printing, that kind of custom-made device is possible to produce and test easily and very fast.

Considering the biological value of this approach in the creation of microfluidic chip devices, we come to conclusions that can be crucial for the *in vitro* simulation of *in vivo* processes. Whatever the dimensions of the chamber in which the 3D culture of the cells being tested is located, the number of cells in most experiments is measured in tens or even hundreds of thousands. If we have a heterogeneous distribution of nutrients and/or drugs in the chip, after a certain time period of the experiment we will get a heterogeneous distribution of (bio)markers that are monitored experimentally. In this sense, the obtained biological results are the mean value of biomarker expression in the 3D culture zones that were treated differently. The question is if we really want multiple different treatments within one chip, or we are focused on 1 treatment per 1 chip. On the other hand, using the proposed combination of advanced technologies, we can actually create only that. Namely, if we want, for example, different distribution of drugs, nutrients, oxygen, etc. in different chip compartments, because we mimic a certain physiological process, it is possible.

To our knowledge, there is no available published literature on the optimization of microfluidic chip devices in this way. Customized chip design will be imperative in many *in vivo* like experiments on chip devices in the future, and this work will certainly contribute to a better understanding of the topic being addressed.

Acknowledgments: This work was supported by Ministry of Education, Science and Technological Development of the Republic of Serbia (Agreement no. 451-03-68/2022-14/200107). Also, we owe special thanks to Dr. J Miguel Oliveira (3BS Research Group, University of Minho, Portugal) for introducing our research group to the scientific field of using PDMS in the production of microfluidic chip devices. This work is supported by the European Union’s Horizon 2020 research and innovation pro-gramme under grant agreement No 952603 (SGABU). This article reflects only the author's view. The Commission is not responsible for any use that may be made of the information it contains.

References:

[1] Carvalho MR, Barata D, Teixeira LM, Giselbrecht S, Reis RL, Oliveira JM, Truckenmüller R, Habibovic P. Colorectal tumor-on-a-chip system: A 3D tool for precision onco-nanomedicine.Sci Adv. 2019 May 22;5(5): eaaw1317. doi: 10.1126/sciadv. aaw1317.

[2] Zhang YS, Aleman J, Shin SR, Kilic T, Kim D, Mousavi Shaegh SA, Massa S, Riahi R, Chae S, Hu N, Avci H, Zhang W, Silvestri A, Sanati Nezhad A, Manbohi A, De Ferrari F, Polini A, Calzone G, Shaikh N, Alerasool P, Budina E, Kang J, Bhise N, Ribas J, Pourmand A, Skardal A, Shupe T, Bishop CE, Dokmeci MR, Atala A, Khademhosseini A. Multisensor-integrated organs-on-chips platform for automated and continual in situ monitoring of organoid behaviors. Proc Natl Acad Sci U S A. 2017 Mar 21;114(12): E2293-E2302. doi: 10.1073/pnas.1612906114.

[3] David Caballero, Maria AngélicaLuque-González, Rui L. Reis, Subhas C. Kundu, Chapter 15 - Microfluidic systems in cancer research, Biomaterials for 3D Tumor Modeling, Elsevier, 2020, Pages 331-377, ISBN 9780128181287, doi: 10.1016/B978-0-12-818128-7.00015-0.

[4] Bower R, Green VL, Kuvshinova E, Kuvshinov D, Karsai L, Crank ST, Stafford ND, Greenman J. Maintenance of head and neck tumor on-chip: gateway to personalized treatment? Future Sci OA. 2017 Mar 7;3(2): FSO174. doi: 10.4155/fsoa-2016-0089.

[5] Carvalho, M.R., Carvalho, C.R., Maia, F.R., Caballero, D., Kundu, S.C., Reis, R.L. and Oliveira, J.M. (2019), Peptide-Modified Dendrimer Nanoparticles for Targeted Therapy of Colorectal Cancer. Adv. Therap., 2: 1900132. doi: 10.1002/adtp.201900132.

[6] Raimondi MT. Engineered tissue as a model to study cell and tissue function from a biophysical perspective. Curr. Drug Discov. Technol. 2006. 3, 245–268. doi: 10.2174/157016306780368126.

[7] Baker M. Tissue models: a living system on a chip. Nature. 2011. 471, 661–665. doi:10.1038/471661a.

[8] Esch EW, Bahinski A, Huh D. Organs-on-chips at the frontiers of drug discovery. Nat. Rev. Drug Discov. 2015. 14, 248–260. doi: 10.1038/nrd4539.

[9] Zhou, M., Alexandersen, J., Sigmund, O. et al. Industrial application of topology optimization for combined conductive and convective heat transfer problems. Struct Multidisc Optim 54, 1045–1060 (2016). https://doi.org/10.1007/s00158-016-1433-2

[10] Waheed S, Cabot JM, Macdonald NP, Lewis T, Guijt RM, Paull B, Breadmore MC. 3D printed microfluidic devices: enablers and barriers. Lab Chip. 2016 May 24; 16(11): 1993-2013. doi: 10.1039/c6lc00284f.

[11] Macdonald NP, Cabot JM, Smejkal P, Guijt RM, Paull B, Breadmore MC. Comparing Microfluidic Performance of Three-Dimensional (3D) Printing Platforms. Anal Chem. 2017 Apr 4; 89(7): 3858-3866. doi: 10.1021/acs.analchem.7b00136.

APPLICATION OF COMPOSITE SMEARED FINITE ELEMENT FOR MECHANICS (CSFEM) ON TUMOR GROWTH MODEL

Vladimir Simic[1,2], Miljan Milosevic[1,2,3] and Milos Kojic[2,4,5]

[1]Institute for Information Technologies, University of Kragujevac, Department of Technical-Technological Sciences, Jovana Cvijica bb, 34000 Kragujevac, Serbia.
e-mail: vsimic@kg.ac.rs, miljan.m@kg.ac.rs
[2]Bioengineering Research and Development Center, BioIRC, Prvoslava Stojanovica 6, 34000, Kragujevac, Serbia.
[3]Belgrade Metropolitan University, Tadeuša Košćuška 63, 11158, Belgrade, Serbia.
[4]Houston Methodist Research Institute, The Department of Nanomedicine, 6670 Bertner Ave., R7 117, Houston, TX 77030, USA.
e-mail: mkojic42@gmail.com
[5]Serbian Academy of Sciences and Arts, Kneza Mihaila 35, 11000, Belgrade, Serbia.

Abstract

Cells inside tissues have ability to integrate mechanical cues, which results in regulation of cells' fate and direct tissue-specific development. These forces play a crucial role in maintaining tissue structure, functionality and homeostasis [1]. They also have a crucial role in describing tumor growth models, which are important to create an engineering background for cancer treatment either by using the models for simulations and evaluation of treatment protocol. Growing tumors consist of dead tumor cells (the necrotic part) and living cells (proliferating part). Most of the known tumor growth models nowadays do not include modeling of the necrotic part. Computational models' complexity and efforts required for their development needed robustness and usage of different approaches in the modeling process. Certain simplifications had to be applied; hence, smeared mechanics concept was introduced (author Milos Kojic) as a general concept for modeling the deformation of composite continua. Along with this concept, authors formulated composite smeared finite element for mechanics (CSFEM), consisting of the supporting medium and immersed subdomains of deformable continua (called compartments) which can mutually interact. This interaction is modeled using 1D contact elements applied to tangential and normal directions. Presented results give insight into the application of the CSFEMs to planar tumor growth model. These models can serve as a basis for possible 3D models (obtained from CT images) in order to have realistic framework for developing patient specific tumor growth models.

Keywords: smeared mechanics, tissue mechanics, composite smeared finite element for mechanics, tumor growth.

1. Introduction

Complex biological systems consist of numerous cells that have demonstrated the property to absorb various physico-chemical, mechanical and electrical signals. Forces acting on the cells and surrounding space (shear and loading force, as well as stresses and strains) have the ability to manage drug and biological responses. Previous publications in this research area displayed the complexity of computational models within different fields' representations (regarding small tissue part as well as a specific organ); therefore, it is desirable to create a computational methodology which is primarily feasible and robust, which would lead to a less-demanding modeling process for practical applications. This novel smeared concept (presented in [2,3]) is applied to the mechanical behavior modeling, considering tissue with various immersed cells (cancerous or healthy ones).

Smeared concept, in our previous scientific publications, is presented for mass transport, both in the capillary/tissue space [4,5] where the accuracy of the concept was shown, in comparison to traditional modeling methods. The presented concept is implemented into our in-house code PAK (abbreviation in Serbian of 'Program za Analizu Konstrukcija' - 'Program for Structural Analysis'), a high-performance finite element analysis (FEA) software. Regarding graphical representation of computational results, we used the CAD Field & Solid visualization software for pre- and post-processing. Here, we will present the applicability of the method and give an insight into a simple 2D tumor growth model, as a next step in modeling of tumor mechanical behavior as a result of prescribed volumetric growth inside cancer cells.

2. Methodology

The steps, necessary for formulating composite smeared finite element for mechanics (CSFEM), are analogous to those presented in [2,3]. The primary and basic goal of the smeared model is to generate a composite continuum finite element (CSFEM) that will consider all the constituents of the physical fields (continuum and 1D domains) represented in "true" model (Fig. 1a). Fundamental assumption is that each of the compartments has its own FE continuum mesh, while for 1D domain we use 1D finite elements which can represent blood vessels or fibers. Simplification of this "true" model is shown in Fig. 1.b, where the smeared model constituents are presented with a supporting domain and numerous immersed domains with boundary velocities (Cells 1 to 8, Fig. 1b). Closer insight into contact phenomena, between two immersed domains (Cells 7 and 8), with denoted velocities in tangent and normal directions is provided in Fig. 1c. A computational model (FE mesh), that consists of a circular growing tumor surrounded by tissue (1/4 of the entire space modeled) of circular shape is shown in Fig. 1d.

The mass growth in this model is represented using the rate of the volumetric deformation due to the tumor growth as

$$\frac{d\left(\Delta V^{growth}\right)}{dt\Delta V} = \frac{c_{mass}^{growth}}{\rho_{mass}^{growth}} = \frac{d(\Delta V)}{dt\Delta V} = \dot{e}_V \tag{1}$$

where $c_{mass}^{growth}\left[\frac{kg}{m^3 s}\right]$ is the mass rate constant, ρ_{mass}^{growth} is the density of additional mass and $\dot{e}_V$ is volumetric strain rate [6].

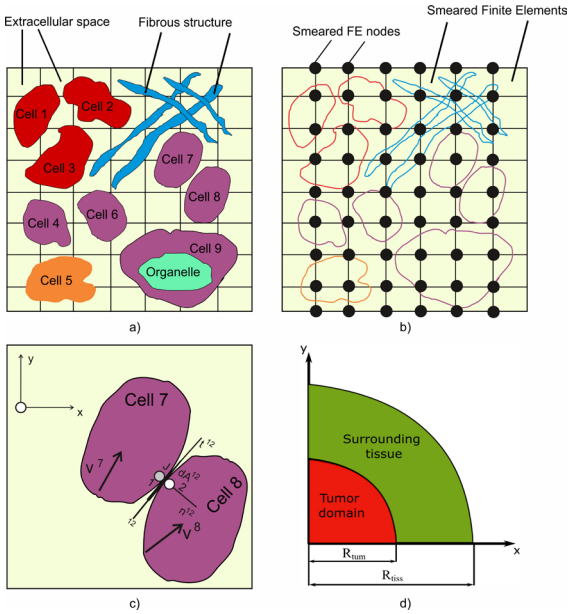

Fig. 1. a) Schematic representation of a "true" model. b) Smeared representation of true a) model c) Detailed form of contact between two domains (Cells 7 and 8, (velocities noted) d) Representation of ¼ of circular tumor domain and surrounding tissue space.

3. Conclusions

The authors have presented the smeared modeling concept for the mechanical field and introduced the composite smeared finite element for mechanics (CSFEM). The main improvement, related to the previous research work, is the implementation of the necessary equations into the finite element software PAK. The accuracy and applicability of this methodology are assessed on a simple 2D tumor growth model, where we considered an early-stage growth of a 2D circular shape tumor. This methodology can also be extended to 3D problems, which would lead to more realistic models of volumetric deformations with geometry obtained from CT scans or uMRIs [6].

References:

[1] Hayward M.K., Muncie M.J., Weaver M.V. *Tissue mechanics in stem cell fate, development, and cancer*, Developmental Cell, Vol. 56 (13), 1833-1847, ISSN 1534-5807, https://doi.org/10.1016/j.devcel.2021.05.011, 2021.

[2] Kojic M, *Smeared concept as a general methodology in finite element modeling of physical fields and mechanical problems in composite media*. J. Serb. Soc. Comput. Mech. 12(2), 1-16, ISSN 1820-6530, https://doi.org/10.24874/jsscm.2018.12.02.01, 2018

[3] Kojic M, Milosevic M, Ziemys A, *Computational Models in Biomedical Engineering – Finite Element Models Based on Smeared Physical Fields - Theory, Solutions and Software*, Elsevier 2022 (to be published).

[4] Kojic M, Milosevic M, Simic V, Koay EJ, Kojic N, Ziemys A, et al. *Extension of the Composite Smeared Finite Element (CSFE) to Include Lymphatic System in Modeling Mass Transport in Capillary Systems and Biological Tissue*. J. Serb. Soc. Comp. Mech. 11(2), 108-120, ISSN 1820-6530, https://doi.org/10.24874/jsscm.2017.11.02.09, 2017.

[5] Milosevic M, Simic V, Milicevic B, Koay EJ, Ferrari M, Ziemys A, et al. *Correction function for accuracy improvement of the Composite Smeared Finite Element for diffusive transport in*

biological tissue systems, Comp. Meth. Appl. Mech. Engrg, 338(1), 97-116, ISSN 457-825, https://doi.org/10.1016/j.cma.2018.04.012, 2018.

[6] Simic V., Milosevic M., Milicevic V., Filipovic N., Kojic M., *A novel composite smeared finite element for mechanics (CSFEM): Some applications*. Technology and Health Care. https://doi.org/10.3233/THC-220414, Epub ahead of print. PMID: 36314177, 2022.

FORCED VIBRATIONS WITH BURGERS TYPE OF DAMPING

Dragan T. Spasić

Department of Mechanics, Faculty of Technical Sciences, University of Novi Sad,
Trg Dositeja Obradovića 6, 21000 Novi Sad, Serbia
e-mail: spasic@uns.ac.rs

Abstract

This paper deals with energy dissipation during forced vibrations of a simple mechanical system. It combines the Newton axiom, the Newton-Laplace principle and a constitutive axiom corresponding to the classical Burgers type of viscoelastic body in which the internal friction occurs. Despite the fact that this constitutive equation relates force and its derivatives, on one side with velocity and acceleration, on the other side the problem belongs to the classical Newtonian mechanics. As an example, the energy dissipation within the Burgers structural element under the action of the Ricker type disturbing force was estimated using the Laplace transform method.

Keywords: forced vibrations, Burgers element, Ricker wavelet.

1. Introduction and preparatory results

Energy loss is a very important issue, no matter if it has to be minimized (to reduce cost) or maximized to reduce damages during impact or seismic activities or designed to maintain some stability or control criteria. In mechanics it appears in various viscoelastic elements springs commonly used in conjunction with dashpots. Besides energy dissipation, these elements have a role to limit the motion between the elements of the mechanical system. Some of the classical examples are known as Kelvin-Voigt, Kelvin-Zener, Burgers and anti-Zener model of viscoelastic body, see [1].

In what follows, we shall consider the classical Burgers element, comprising 4 parameters: two elasticities $E_i > 0$ and two viscosities $\eta_i > 0$, $i = 1,2,$ see Fig. 1. Let us recall some facts about it and confirm that its deformation is a strictly dissipative process. In the direction of relating force $f = f(t)$ and deformation $x(t)$ in this element, it is obvious that the deformations of an elastic spring x_1, a dashpot x_2 and a Kelvin-Voigt element x_3 are additive $x = x_1 + x_2 + x_3$ with f representing an internal force passing through each of these elements. Thus, $f = E_1 x_1 = \eta_1 \dot{x}_2 = E_2 x_3 + \eta_2 \dot{x}_3$ where dot over the symbol represents the derivative with respect to time t. Eliminating x_l, $l = 1,2,3$ from these 4 equations complemented with expressions for $\dot{x}$, $\ddot{x}$ and $\dot{f}$, yields the constitutive relation describing the classic Burgers material

$$\frac{\ddot{f}}{E_1}+\left(\frac{1}{\eta_1}+\frac{1}{\eta_2}+\frac{E_2}{E_1\eta_2}\right)\dot{f}+\frac{E_2}{\eta_1\eta_2}f=\frac{E_2}{\eta_2}\dot{x}+\ddot{x}. \tag{1}$$

The four parameters of the model should be determined by a system identification procedure from either stress relaxation or creep experiments usually starting from a virginal state $x\left(0^-\right)=0,\quad f\left(0^-\right)=0$ with a required additional initial conditions either $\dot{x}\left(0^-\right)=0$ or $\dot{f}\left(0^-\right)=0.$

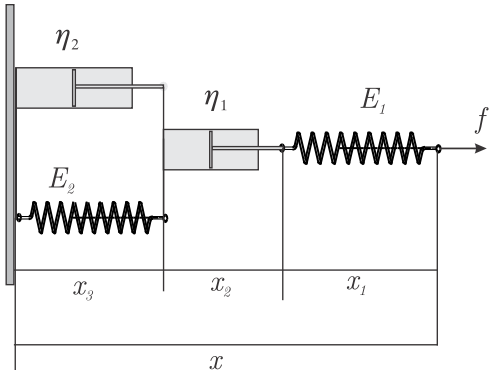

Fig. 1. The Lord Kelvin type of the classical Burgers element.

Namely, in the stress relaxation test $x\left(t\right)=x_0H\left(t\right)$ with a prescribed deformation x_0 and $H\left(t\right)$ being the Heaviside unit step function i.e. the material has to reach the constant deformation instantaneously and maintain it. Therefore, its initial velocity should be infinite as well as its initial acceleration. After reaching x_0 an infinite deceleration should be applied to maintain x_0. Note that $\delta\left(t\right)=\dot{H}\left(t\right)$ being the Dirac delta, as well as $\dot{\delta}\left(t\right),$ shown in Fig. 2, perfectly cover this pattern.

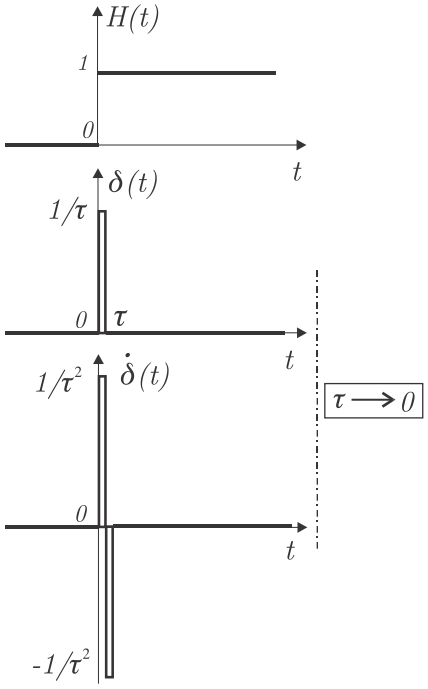

Fig. 2. The Heaviside unit step function and its derivatives, see [2].

Therefore, in the classical stress relaxation experiments the derivatives in (1) should be taken in sense of distributions, i.e. continuous functions complemented with discontinuous but infinitely differentiable functions. The corresponding measure differential equation reads

$$\frac{\ddot{f}}{E_1}+\left(\frac{1}{\eta_1}+\frac{1}{\eta_2}+\frac{E_2}{E_1\eta_2}\right)\dot{f}+\frac{E_2}{\eta_1\eta_2}f=\frac{E_2}{\eta_2}x_0\delta\left(t\right)+x_0\dot{\delta}\left(t\right) \tag{2}$$

The same pattern of change can be recognized in the creep test with $f\left(t\right)=f_0H\left(t\right)$ with prescribed load f_0, and its derivatives also taken in sense of distributions leading to the distributional model of creep, say

$$\ddot{x}+\frac{E_2}{\eta_2}\dot{x}=\frac{f_0}{E_1}\dot{\delta}\left(t\right)+\left(\frac{1}{\eta_1}+\frac{1}{\eta_2}+\frac{E_2}{E_1\eta_2}\right)f_0\delta\left(t\right)+\frac{E_2}{\eta_1\eta_2}f_0H\left(t\right) \tag{3}$$

In order to find creep compliance, say $J\left(t\right)$, the standard procedure based on the Laplace transform can be applied to (3) yielding

$$J\left(t\right)=\frac{x\left(t\right)}{f_0}=\frac{1}{E_1}+\frac{t}{\eta_1}+\frac{1}{E_2}\left(1-\exp\left(-E_2t\ /\ \eta_2\right)\right) \tag{4}$$

Note that $J\left(t\right)$ is positive on $\mathbb{R}_+$, its derivative exists and is completely monotonic function so $J\left(t\right)$ is a Bernstein type function.

In order to find the relaxation modulus corresponding to (1), we apply the Laplace transform to (2), that is

$$\frac{s^2F-sf\left(0^-\right)-\dot{f}\left(0^-\right)}{E_1}+\left(\frac{1}{\eta_1}+\frac{1}{\eta_2}+\frac{E_2}{E_1\eta_2}\right)\left[sF-f\left(0^-\right)\right]+\frac{E_2}{\eta_1\eta_2}F$$
$$=\frac{E_2}{\eta_2}x_0\cdot 1+x_0s,$$

and get

$$\frac{F}{E_1x_0}=\frac{\frac{E_2}{\eta_2}+s}{s^2+\left(\frac{E_1}{\eta_1}+\frac{E_1}{\eta_2}+\frac{E_2}{\eta_2}\right)s+\frac{E_1E_2}{\eta_1\eta_2}} \tag{5}$$

Note that $\left(\frac{E_1}{\eta_1}+\frac{E_1}{\eta_2}+\frac{E_2}{\eta_2}\right)^2-4\frac{E_1E_2}{\eta_1\eta_2}=\left(-\frac{E_1}{\eta_1}+\frac{E_1}{\eta_2}+\frac{E_2}{\eta_2}\right)^2+4\frac{E_1^2}{\eta_1\eta_2}>0,$ so denominator in (5) has two different negative real roots say s_1 and s_2. Rewriting (5) as

$$\frac{F}{E_1x_0}=\frac{E_2}{\eta_2}\frac{1}{\left(s-s_1\right)\left(s-s_2\right)}+\frac{s}{\left(s-s_1\right)\left(s-s_2\right)}$$

and using the tables given at the end of [3] we get the relaxation modulus in the form

$$\frac{f\left(t\right)}{E_1x_0}=\frac{E_2}{\eta_2}\frac{\exp\left(s_1t\right)-\exp\left(s_2t\right)}{s_1-s_2}+\frac{s_1\exp\left(s_1t\right)-s_2\exp\left(s_2t\right)}{s_1-s_2} \tag{6}$$

It can be shown that (6) is a non-negative and completely monotonic function. However, instead of showing so, we recall Theorem 6 of the Hanyga paper [4], stating that if the

corresponding creep compliance is a Bernstein function and $J\left(0^+\right) > 0$ (what was already shown) then the relaxation modulus is a locally integrable and completely monotonic function. Thus, the classical Burgers viscoelastic model is physically acceptable, i.e. its deformation causes energy dissipation.

2. The forced vibration problem

Consider a rigid block of mass m that can move on the smooth and straight horizontal line under the action of a known disturbing force $w = w\left(t\right)$. The motion of the block is limited since the Burgers viscoelastic body undergoing uniaxial deformation shown in Fig. 1 is attached to it. The other end of the body is anchored to a rigid wall. Therefore, (1) holds with $x = x\left(t\right)$ representing both position of the block and the deformation of the body and f is as above. Initially, the block is in the state of rest while the viscoelastic body is in its virginal state. One may cast this motion problem into the language of equations by use of the Newton axiom and the Newton-Laplace Determination Principle . It reads

$$m\ddot{x} = -f + w \tag{7}$$

$$x\left(0\right) = 0, \quad \dot{x}\left(0\right) = 0, \quad f\left(0\right) = 0, \quad \dot{f}\left(0\right) = 0 \tag{8}$$

Equation (7) should be complemented with the constitutive equation describing the classical Burgers material (1). Note that in the Newtonian mechanics it is implicitly assumed that the right hand side of (7) should be a function of time, position and velocity, i.e. $-f\left(t, x, \dot{x}\right) + q\left(t\right)$, see [5]. However, (1) comprises force f and its derivatives $\dot{f}$ and $\ddot{f}$, as well as velocity $\dot{x}$ and acceleration $\ddot{x}$, so further preparations are needed. Before, let us introduce the following dimensionless quantities

$$\overline{x} = \frac{xE_2^2}{g\eta_2^2}, \quad \overline{t} = t\frac{E_2}{\eta_2}, \quad \overline{f} = \frac{f}{mg}, \quad \overline{w} = \frac{w}{mg}$$

$$\overline{a} = \frac{mE_2}{\eta_1\eta_2}, \quad \overline{b} = \frac{mE_2}{\eta_2}\left(\frac{1}{\eta_1} + \frac{1}{\eta_2} + \frac{E_2}{E_1\eta_2}\right), \quad \overline{c} = \frac{mE_2^2}{E_1\eta_2^2}$$

into (7) and (1). Then, after omitting the bar, one gets more compact form of the problem

$$x'' = -f + w, \qquad x\left(0\right) = 0, \quad x'\left(0\right) = 0, \quad f\left(0\right) = 0, \quad f'\left(0\right) = 0, \tag{9}$$

$$x'' + x' = af + bf' + cf'' \tag{10}$$

where prime denotes the derivative with respect to dimensionless time. With this preparation done, it is still not obvious that the problem (9), (10) fits into the classical Newtonian mechanics framework.

Remark: In order to relate constitutive equation (10) with a dynamics equation comprising f used in eq. (6) of [6], Parietti et al. solved (10) with respect to f', and integrate it to eliminate the acceleration term yielding in our notation

$$f\left(t\right) = f\left(0\right) + \left[\frac{c}{b}\left(f'\left(0\right) - f'\left(t\right)\right) - \frac{a}{b}\int_0^t f\left(\xi\right)d\xi + \frac{x\left(t\right) - x\left(0\right) + x'\left(t\right) - x'\left(0\right)}{b}\right]$$

what is quite complicated expression for the force, but it fits into the framework of Newtonian mechanics, see eq. (5) of [6].

In what follows a different procedure will be used to relate (9) and (10) so the framework of Newtonian mechanics for the vibration problem at hand will be easily recognized. Namely, the

Laplace transform of (10) for given initial conditions leads to:

$$F = \frac{s+1}{cs^2 + bs + a}\left(sX\right) \tag{11}$$

Noting that

$$b^2 - 4ac = \left(\frac{1}{\eta_1} - \frac{E_2}{E_1\eta_2}\right)^2 + 2\left(\frac{1}{\eta_1} + \frac{E_2}{E_1\eta_2}\right) + \frac{1}{\eta_2} > 0$$

and introducing negative distinct real roots of $cs^2 + bs + a = 0$, say $-\sigma_1$ and $-\sigma_2$, the straightforward inversion of (11) yields

$$f\left(t\right) = \int_0^t \kappa\left(\tau - \xi\right) x'\left(\xi\right) d\xi \tag{12}$$

with

$$\kappa\left(t\right) = \frac{1}{c}\frac{\left(1-\sigma_1\right)\exp\left(-\sigma_1 t\right) + \left(1-\sigma_2\right)\exp\left(-\sigma_2 t\right)}{\sigma_2 - \sigma_1} \tag{13}$$

Now with $v = x'$ it is obvious that the forced oscillation problem with the Burgers internal friction element fits into Newtonian mechanics framework, since

$$v' = -\int_0^t \kappa\left(t - \xi\right) v\left(\xi\right) d\xi + w \tag{14}$$

to be solved with $v\left(0\right) = 0$.

3. An example

Consider the above problem with the disturbing force given in the form of linear combination of 5 wavelets of the Ricker type, i.e.

$$w\left(t\right) = u_0 \sum_{k=1}^{5} \left\{\left[2\frac{\pi^2\left(t - t_s\right)^2}{t_p^2} - 1\right]\exp\left[-\frac{\pi^2\left(t - t_s\right)^2}{t_p^2}\right]\right\} \tag{15}$$

for $u_0 = 1$, $t_1 = 1.25$, $t_2 = 3$, $t_3 = 4$, $t_4 = 1.75$, $t_5 = 1$ and $\omega_1 = 2/3$, $\omega_2 = 1$, $\omega_3 = 4/3$, $\omega_4 = 0.5$, $\omega_5 = 0.8$, shown below

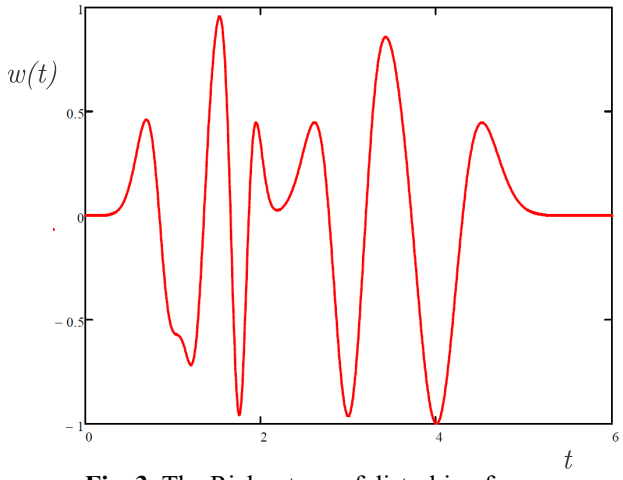

Fig. 3. The Ricker type of disturbing force.

We assume the following values of the Burgers parameters: $E_1 = E_2 = E = 6670$, N/m

corresponding to helical coil springs $\eta_1 = \eta_2 = \eta = 1200$ Ns/m and $m = 1$. Thus $a = 0.00463,\ b = 0.014,\ c = 0.00463,$ and

$$\kappa(t) = 171.2989\exp(-3.8416) + 44.5906\exp(-0.2603t).$$

The solution of (14) obtained by use of the Bulirsch-Stoer algorithm is shown in the following figure.

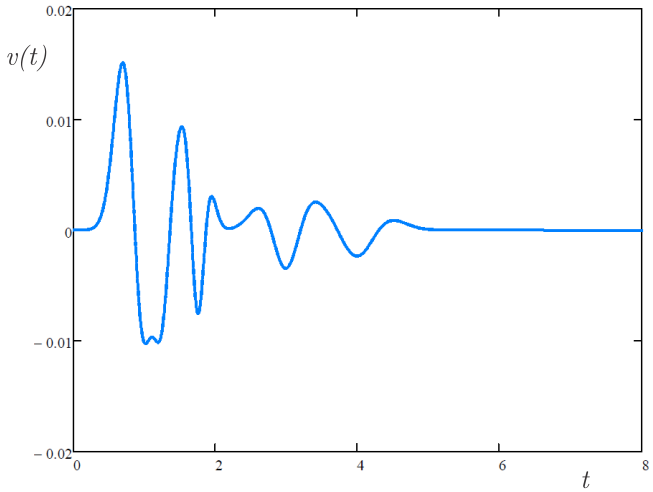

Fig. 4. The solution of (14), (15) for $E = 6670$ N/m and $\eta = 1200$ Ns/m.

Note that for $t > 5.34$ the corresponding velocity satisfies $|v(t)| < 5 \times 10^{-5}$. It can be shown that if η increases, the velocity of the block decreases and more energy is be dissipated as expected.

4. Closure

In this paper the forced oscillations with the classical Burgers type of dissipation were examined. It was shown that the problem fits into the framework of Newtonian mechanics. The solution of the problem was obtained by use of the Laplace transform and the convolution theorem. The example with the disturbing force of the Ricker type was given at the end.

Acknowledgment: This research was supported by the Serbian Ministry of Science.

References:

[1] Mainardi F., *Fractional Calculus and Waves in Linear Viscoelasticity, An Introduction to Mathematical Models*, Imperial College Press, 2010.
[2] Martinenko V. S., *Operational calculs (in Russian),* Kiev, 1973.
[3] Doetch G., *Guide to the applications of the Laplace transforms*, D Van Nostrand Comp., London, 1961.
[4] Hanyga A., *Physically acceptable viscoelastic models*, in Trends in applications of mathematics and mechanics, edited by Wang Y. and Hutter K., Shaker Verlag, Aachen 2005.
[5] Markeev A.P., *Theoretical Mechanics*, Moscow, (in Russian) 1999.
[6] Parietti, F., Baud-Bovy, G., Gatti, E., Riener, R., Guzzella, L., and Vallery H. *Series viscoelastic actuators can match human force perception,* IEEE/ASME Transactions on mechatronics, Vol. 16, 853-860, 2011.

COMPARATIVE NUMERICAL ANALYSES OF TOOTH RESTORED WITH HYDROXYAPATITE CERAMIC INSERT VERSUS TRADITIONAL COMPOSITE RESTORATION

Aleksandar Bodić[1], Maja Ležaja Zebić[2], Milan Bojović[1], Djordje Veljović[3] and Vladimir Milovanović[1]

[1] Faculty of Engineering, University of Kragujevac, Serbia
e-mail: abodic@uni.kg.ac.rs, mbojovic@outlook.com, vladicka@kg.ac.rs
[2] School of Dental Medicine, University of Belgrade, Serbia
e-mail: dr.maja.zebic@gmail.com
[3] Faculty of Technology and Metallurgy, University of Belgrade, Serbia
e-mail: djveljovic@tmf.bg.ac.rs

Abstract:

The aim of this study was to compare traditional composite restoration and restoration which include hydroxyapatite ceramic insert in replacing healthy tooth structures using comparative numerical analysis. The dental inserts discussed in this paper are based on nanostructured hydroxyapatite/yttrium stabilized zirconia and suits for dentin substitution only. Hydroxyapatite insert is biocompatible, and supposed to be used as is, without potential changes in dimensions unlike the composite which polymerize and shrink in the cavity. A 3D CAD model of a healthy tooth is created based on a 3D scan. The internal geometry of the healthy tooth was modified to contain I class cavity restored in one case with composite alone and in another case using dental inserts in combination with composite. For all three cases, a finite element mesh was created using prepared geometries. Boundary conditions and loads are set to simulate the real tooth testing procedure. The models pre- and post-processing was performed using the *Femap* software, while the calculation was carried out in the *Nastran* software. Comparing the calculation results, it can be observed that lower values of von Mises stress in dentin occur in the case of a restored tooth using a dental insert. Based on this, it can be concluded that restoration procedure using dental insert is more effective than classic one.

Keywords: finite element method, dental insert, tooth, 3D model.

1. Introduction

In order to restore the back teeth, direct restorations are most often used because of the lower cost, less need to remove healthy tooth substance compared to indirect restorations, and acceptable clinical performance [1]. The most commonly used material for direct posterior filling is resin composite, which has shown acceptable longevity in various studies [2, 3]. However, these materials still exhibit deficiencies despite significant improvements. The main reasons for long-term failure are secondary caries and fractures [4]. The use of dental inserts based on hydroxyapatite and yttrium-stabilized zirconium investigated in [5] shows significant potential for restoration of the major part of the tooth cavity with the material which does not change its dimensions after placement in the cavity and is made of completely biocompatible material at the same time.

This paper presents comparative numerical analyses of a healthy tooth, tooth restored using composite alone and tooth restored using dental insert as dentin substitute, in combination with composite used as enamel substitute. The tooth geometry was created based on 3D scan. Healthy tooth morphology CAD model was modified for two tooth restoration situations with the same total dimensions and shape. After that, within the *Femap* software, a finite element mesh was created, and boundary conditions and loads were set. Calculation was performed in the *Nastran* software [6].

A brief description of dental inserts for tooth restoration and the materials they are made of is given in section 2 of the paper.

In the third section of the paper, the procedure for creating tooth geometry based on 3D scans is presented.

In the fourth section of the paper, the created FE model of the tooth is shown as well as definition of boundary conditions and loads on it.

At the end of the paper, a comparison of the numerical analysis results for all three cases is given.

2. Composite nanostructured hydroxyapatite/yttrium stabilized zirconia dental inserts

Hydroxyapatite (HAp), or more accurately calcium hydroxyapatite, has been an attractive biomaterial for hard tissue replacement [7, 8, 9]. Due to its chemical and mechanical characteristics, as well as good bioactivity and biocompatibility, it is frequently used in orthopaedics, but also in dentistry [10, 11]. HAp can be used in dentistry in various ways, such as dental cements, scaffolds for replacement of damaged parts of the jawbone, filler in dental composites and adhesives etc [4, 5]. In addition to these applications, HAp can be used as a substitute for dentin in the form of dental inserts [12]. The use of dental restorative inserts (Fig. 1) can simplify the procedure, reduce the number of steps in the clinical protocol, and potentially reduce polymerization shrinkage stress due to the central position of the insert in the cavity [5].

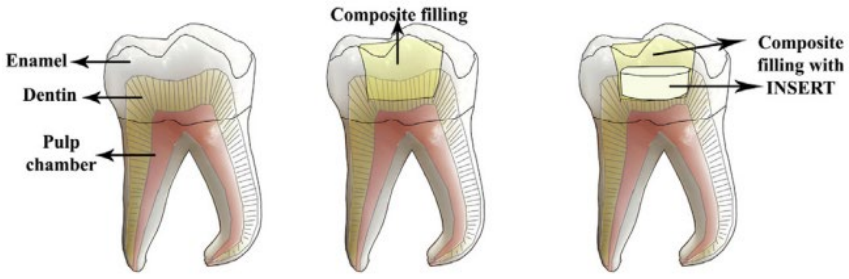

Fig. 1 Schematic representation of dental implants placement.

In order to increase the fracture toughness of HAp bioceramics, various sintering procedures are applied, as well as the addition of various nanoparticles. The procedure of adding optimal amount of tough partially stabilized zirconia particles of different sizes and shapes to optimize the mechanical properties of the HAp matrix is investigated in [5]. In this way, the composite material based on hydroxyapatite and yttrium-stabilized zirconium (YSZ) can be used as a dental insert. The use of dental insert on mechanical properties of restored tooth is still uninvestigated.

The material characteristics of the composite restoration and hydroxyapatite dental insert in the model are taken from [13].

3. Tooth geometry

The object of geometry reconstruction is the first molar in the lower right position shown in Fig. 2. To minimise the impact of boundary conditions in numerical simulations, immediate vicinity of the jaws is also reconstructed to set the boundary conditions.

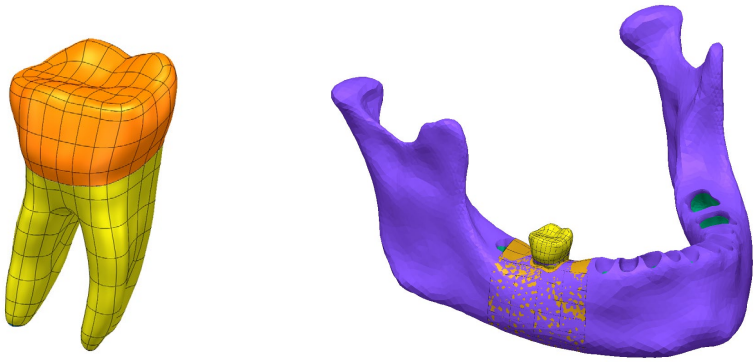

Fig. 2. Geometry of first molar (left); lower jaw mesh with reconstructed tooth geometry (right).

Tooth geometry is created using NURBS surfaces inside of patch boundaries based on polygonised points. The boundaries are defined by a 3D patch network (Fig. 3). The patch network can be created automatically or drawn manually. Although manual patching requires more time, it yields better results in terms of creating a clean and high-quality surface, which is very important for further geometry processing and FEA mesh generation. The deviation of created surface from the mesh is shown in Fig. 3. SThe deviation is less the 0.1mm.

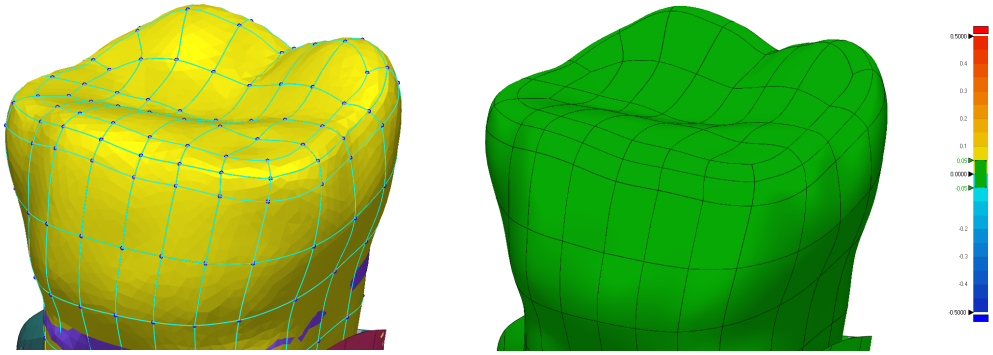

Fig. 3. Constructed patch network over mesh (left); surface deviation from mesh (right).

Surface Fitting is a unique method used in the Reverse Design process (creating geometry from 3D scanned data) that provides an efficient way in creating a 3D freeform surface body easily and precisely from the mesh's freeform shape.

4. Finite element model of tooth

Finite element model of tooth was created using *Femap software* (Fig. 4). The model was created based on tooth geometry for three situations: healthy tooth, restored tooth using a composite alone, and restored tooth using an insert in combination with composite.

The finite element model of tooth includes the following parts: mandible, dentine, pulp, enamel, cement, composite and insert (in the case of tooth restoration with an insert). The average size of the elements in the tooth is 0.2 mm with an increase of up to 1 mm in the mandible. All three tooth models were created using tetrahedral finite elements with midside nodes and consist of approximately 510 000 finite elements and 740 000 nodes.

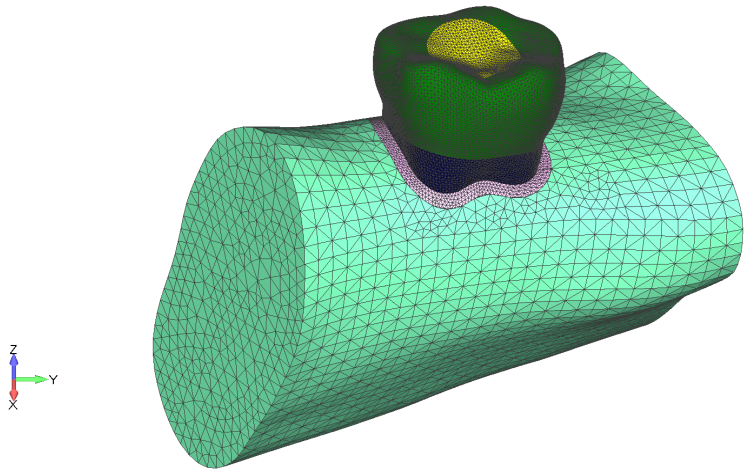

Fig. 4. Tooth tetrahedral mesh.

The loading of the model is set to match the real conditions of dental testing. For the purposes of testing the tooth model, a "ball" was created, through which the directional load was set. Contact is set between the surface of the test ball and the upper surface of the tooth. The ball touches the tooth in three points on the upper surface of the tooth and presses it with a force of 2000 N (Fig. 5).

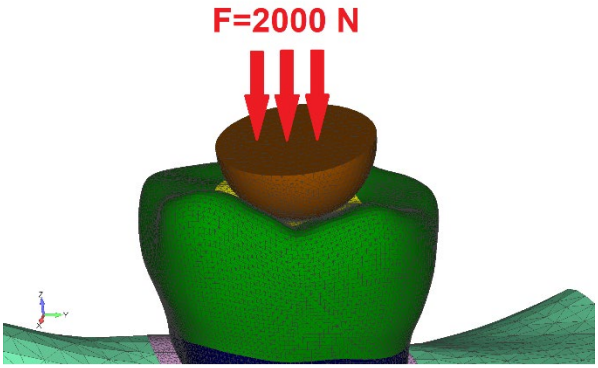

Fig. 5. Applying pressure to the upper surface of the tooth with a test ball.

The hardening (polymerization contraction) effect of the composite is achieved by setting the temperature difference between the composite and the external surfaces on the model. First, a thermal analysis was performed with set temperatures of 10° C on the composite surfaces and 36° C on the outer surfaces of the model. The temperature field obtained by the thermal analysis was then used as a load in the static calculation (Fig. 6).

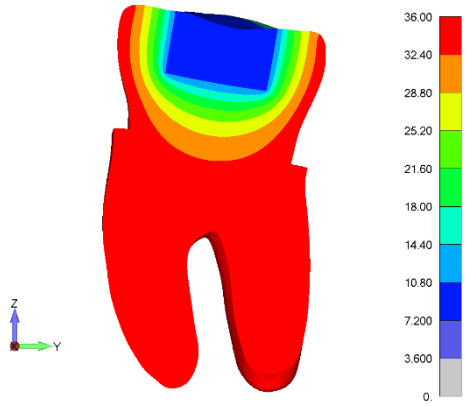

Fig. 6. Composite hardening effect - assigned temperature field as the difference between external and composite temperatures.

The material parameters of the tooth models are given in Table 1.

Environment of model	E [MPa]	ν [-]
Pulp	6.8	0.45
Dentine	18600	0.31
Enamel	84100	0.3
Cement	16600	0.24
Mandible	199.5	0.3
Cement (below and side)	4000	0.35
Composite	16600	0.24
Insert	5220	0.3

Table 1. Material parameters.

The calculation was performed using *Nastran* solver. A comparative analysis of the results for three tooth models is given in the next section.

5. Results

As dentin represents the key component that makes up the largest part of the tooth and gives it its shape, it the focus of the numerical analysis results. The results are presented in the form of Von Mises stress fields for all three models.

The Von Mises Stress field for the healthy tooth model is given in Fig. 7 and Fig. 8.

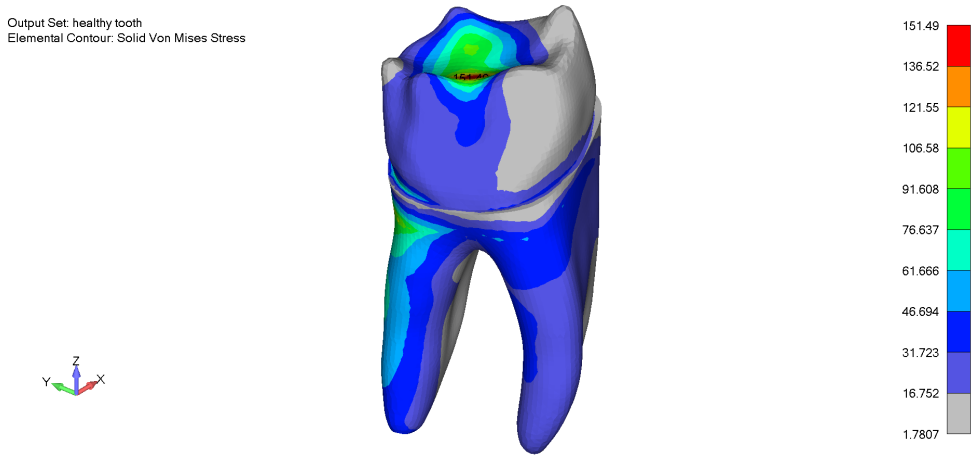

Fig. 7. Von Mises Stress – isometry.

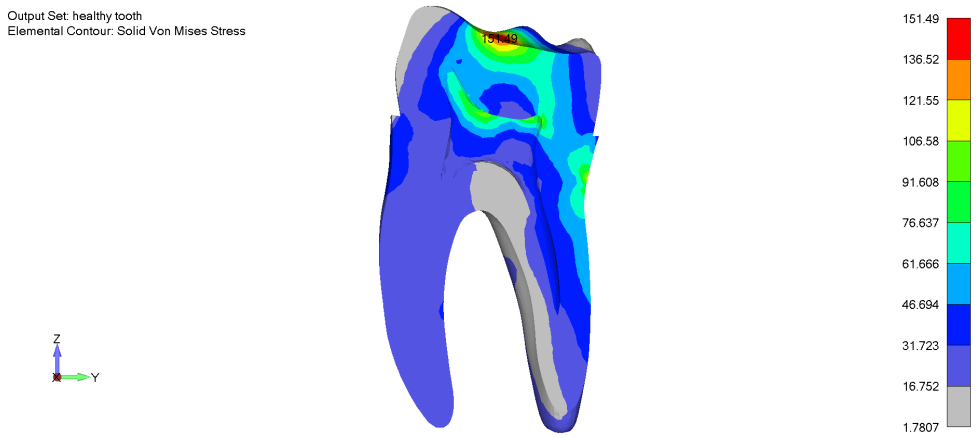

Fig. 8. Von Mises Stress – vertical cross section.

The Von Mises Stress field for the model of tooth restored using composite is given in Fig. 9 and Fig. 10.

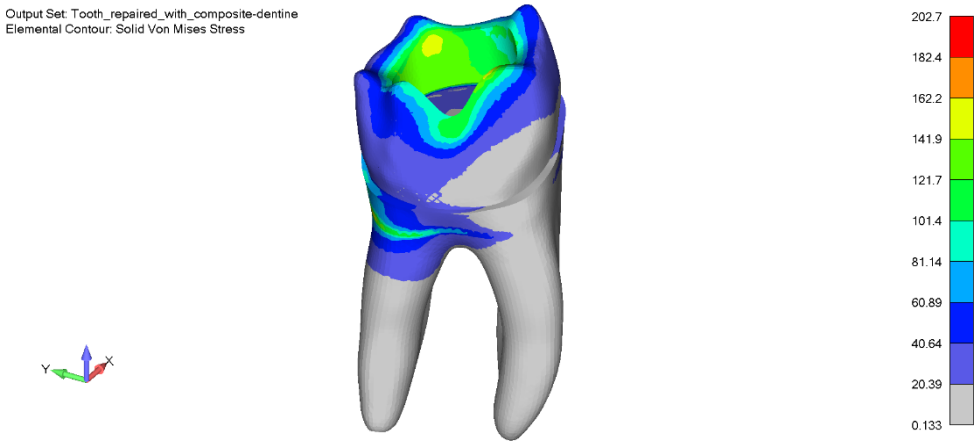

Fig. 9. Von Mises Stress – isometry.

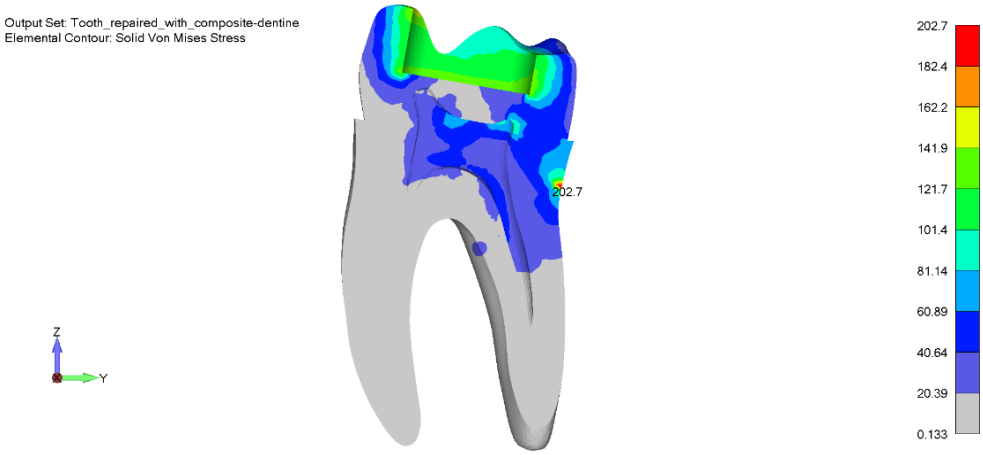

Fig. 10. Von Mises Stress – vertical cross section.

The Von Mises Stress field for the model of tooth restored using insert is given in Fig. 11 and Fig. 12.

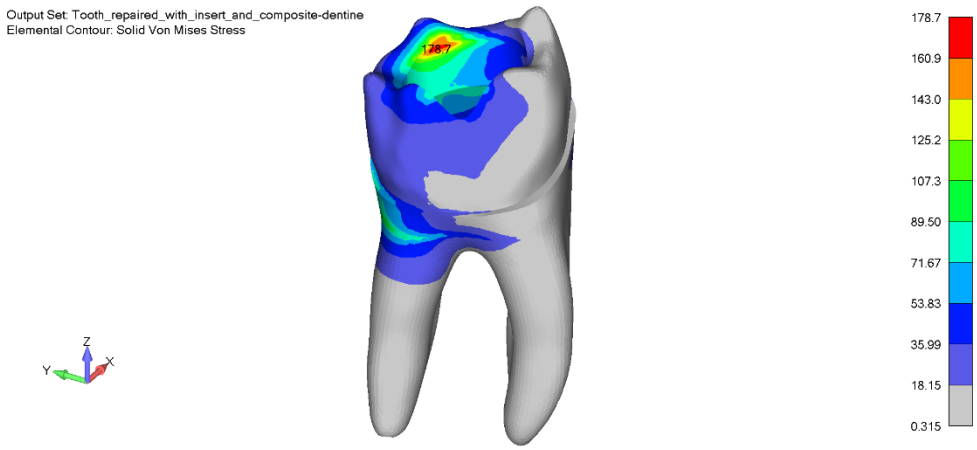

Fig. 11. Von Mises Stress – isometry.

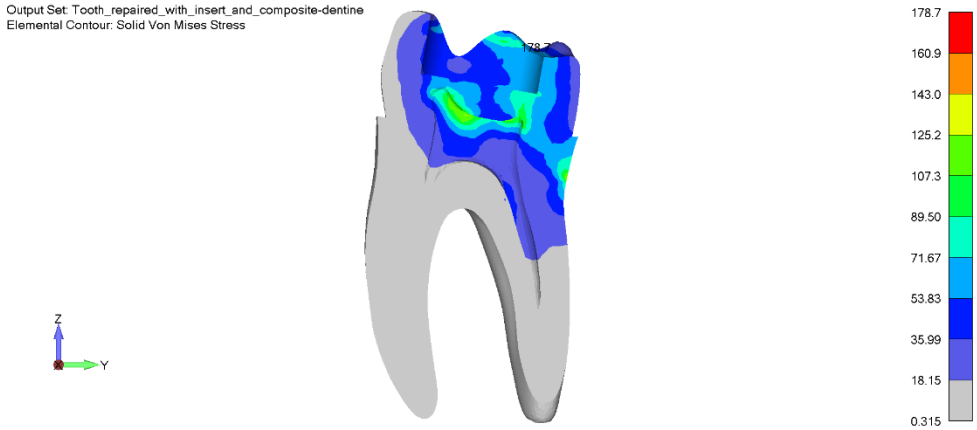

Fig. 12. Von Mises Stress – vertical cross section.

Analysing the results from the previous figures, it can be concluded that the most favourable variant is the healthy tooth in which the lowest Von Mises stress values occur. In addition, looking at the results for both situations of tooth restoration, it can be concluded that lower stress values occur for the case of a restored tooth with a dental insert. Therefore, using this method of restoration, better mechanical characteristics of the tooth are obtained, and the incidence of tooth fracture occurrence is lowered.

6. Conclusions

In this paper, a numerical analysis was conducted to compare a healthy tooth, tooth restored with composite, and a tooth restored with dental insert. Dental inserts based on nanostructured hydroxyapatite/yttrium stabilized zirconia composite were considered. First, a three-dimensional CAD model of a healthy tooth was created based on a 3D scan. After that, two models of the restored tooth were created by modifying a healthy tooth geometry: using composite and using dental insert. Based on these geometries, finite element meshes were created for all three situations. Boundary conditions and loads where set to correspond to real tooth testing conditions.

By comparing the calculation results, it can be concluded that lowest values of von Mises stress in dentine occur in the case of a healthy tooth. When it comes to the two tooth restoration procedures considered in this paper, based on the presented results, it can be observed that lower stress values occur in the tooth restored using dental insert. Considering that the use of a dental insert can

potentially simplify and shorten the duration of the tooth restoration process, it can be concluded that this procedure has great potential to be applied as standard tooth restoration procedures.

References

[1] F. Demarco, M. Corrêa, M. Cenci, R. Moraes and N. Opdam, "Longevity of posterior composite restorations: Not only a matter of materials," *Dental Materials,* vol. 28, no. 1, pp. 87-101, 2012.

[2] F. Demarco, T. Pereira-Cenci, D. de Almeida André, R. P. de Sousa Barbosa, E. Piva and M. S. Cenci, "Effects of metallic or translucent matrices for class II composite restorations: 4-year clinical follow-up findings," *Clin. Oral Invest.,* vol. 15, no. 1, pp. 39-47, 2010.

[3] A. Wilder jr, K. May jr, S. Bayne, D. Taylor and K. Leinfelder, "Seventeen-Year Clinical Study of Ultraviolet-Cured Posterior Composite Class I and II Restorations," *Journal of Esthetic and Restorative Dentistry,* vol. 11, no. 3, pp. 135-142, 1999.

[4] M. Ležaja, Đ. Veljović, B. Jokić, I. Cvijović-Alagić, M. Zrilić and V. Miletić, "Effect of hydroxyapatite spheres, whiskers, and nanoparticles on mechanical properties of a model BisGMA/TEGDMA composite initially and after storage," *Journal of Biomedical Materials Research Part B: Applied Biomaterials,* vol. 101, no. 8, pp. 1469-1476, 2013.

[5] G. Ayoub, Đ. Veljović, M. Ležaja Zebic, V. Miletić, E. Palcevskis, R. Petrović and Đ. Janackovic, "Composite nanostructured hydroxyapatite/yttrium stabilized zirconia dental inserts – The processing and application as dentin substitutes," *Ceramics International,* vol. 44, no. 15, pp. 18200-18208, 2018.

[6] Siemens, FEMAP User Guide Version 11.2, Siemens PLM Software Inc, 2015.

[7] R. LeGeros and J. LeGeros, "DENSE HYDROXYAPATITE," *An Introduction to Bioceramics,* pp. 139-180, 1993.

[8] J. Chevalier and L. Gremillard, "Ceramics for medical applications: A picture for the next 20 years," *Journal of the European Ceramic Society,* vol. 29, no. 7, pp. 1245-1255, 2009.

[9] L. Hench, "Bioceramics: From Concept to Clinic," *Journal of the American Ceramic Society,* vol. 74, no. 7, pp. 1487-1510, 1991.

[10] M. J. Uzeda, R. F. de Brito Resende, S. C. Sartoretto, A. T. N. N. Alves, J. M. Granjeiro and M. D. Calasans-Maia, "Randomized clinical trial for the biological evaluation of two nanostructured biphasic calcium phosphate biomaterials as a bone substitute," *Clinical Implant Dentistry and Related Research,* vol. 19, no. 5, pp. 802-811, 2017.

[11] I. R. Bordea, S. Candrea, G. T. Alexescu, S. Bran, M. Băciuț, G. Băciuț, O. Lucaciu, C. M. Dinu and D. A. Todea, "Nano-hydroxyapatite use in dentistry: a systematic review," *Drug Metabolism Reviews,* vol. 52, no. 2, pp. 319-332, 2020.

[12] G. Ayoub, M. Ležaja Zebić, V. Miletić, R. Petrović, Đ. Veljović and Đ. Janaćković, "Dissimilar sintered calcium phosphate dental inserts as dentine substitutes: Shear bond strength to restorative materials," *J Biomed Mater Res. Part B: Applied Biomaterials,* vol. 108, no. 6, p. 2461– 2470, 2020.

[13] A. Vukićević, K. Zelić, G. Jovičić, M. Đurić and N. Filipović, "Influence of dental restorations and mastication loadings on dentine fatigue behaviour: Image-based modelling approach," *Journal of dentistry,* vol. 43, no. 5, pp. 556-67, 2015.

NUMERICAL SIMULATIONS IN THE DESIGN AND OPTIMIZATION OF A FLUID-DYNAMICAL VALVE IN REGENERATIVE BURNERS INSTALLATION

Mirjana S. Stamenić

Faculty of Mechanical Engineering, University of Belgrade, Kraljice Marije 16, 11120 Belgrade 35
e-mail: mstamenic@mas.bg.ac.rs

Abstract

An experimental installation of regenerative burners consists of two regenerative Pebble-bed heaters (PH), one fluid-dynamical valve (FDV), two burners, one fan for flue gas exhaust, and one fan for combustion air supply. The experimental installation is mounted at the stand for tundish preheating in a steel factory. This facility aims to reduce natural gas as fuel consumption at half of the current (200-250 m^3/h at p=101325 Pa, T=273,15 K) using high-preheated air for combustion.

Design optimization of the FDV and optimization of the position of burner heads and off-gas exit at the tundish top cover by application of StarCD software for numerical simulation was performed.

Input parameters for numerical simulation and design optimization of the FDV are the pressure difference between two inlet streams – high-preheated air and off-gas, and the pressure value at the outlet of high-preheated air. The 3D model was made based on real valve geometry and consists of 177744 cells (control volumes). The result of the numerical calculation and optimization procedure of FDV is optimal geometry definition, lowest pressure drop through the FDV, and minimal value of two streams (high-preheated air and off-gas) mixing coefficient.

Keywords: numerical simulation, fluid-dynamical valve, design optimization, regenerative burners, pebble-bed technology.

1. Introduction

Fuel consumption in energy-intensive high-temperature processes takes an important part in the cost summary of the whole process. The following paper will present the procedure used in geometry optimization for a specific part of the experimental regenerative burner system installation to reduce fuel consumption and obtain a more efficient tundish preheating process. Presently, the process of tundish preheating is relatively inefficient, with average fuel consumption of 200-250 m^3/h (at p=101325 Pa, T=273,15 K). The purpose of installing regenerative burners is to utilize the waste heat of exhaust gases from tundish and to return it to the combustion process

via high-preheated combustion air. The expected result is to reduce fuel consumption (over 50 %) and the amount of CO_2 emitted in the atmosphere.

In the optimization procedure, computational fluid dynamic code StarCD was used for numerical calculations. This method is very efficient in solving such problems (geometry optimization) since the virtual models allow significant changes and determine the consequences of such action without actual experiments. Depending on the complexity of model optimization, the procedure may be quick and low-cost.

2. Experimental installation of regenerative burners

An experimental installation of regenerative burners consists of two compact Pebble-Heaters (PH), a Fluid-Dynamical Valve (FDV) for the switching between two hot gas streams, and auxiliary equipment - one fan for off-gas exhaust, one fan for combustion air supply, piping, two burners, measuring and regulation devices.

Pebble-Heater is a common name for regenerators filled with bulk material, mainly spherical shape (pebbles). The state-of-the-art design has a vertical column of pebbles through which gas flows axially. The problems connected with this design, such as channeling, wall heat losses, pressure drop, scaling problems, and inhomogeneous temperature field, are also well-known in technical practice.

A new concept of the PH has been introduced. The main difference is in the flow direction: gas flows radially through the pebble bed, which is fixed between two coaxial cylindrical grids. The inner grid, the so-called hot grid, is made of porous ceramic bricks. The outer grid, called the cold grid, is made of gas-permeable steel construction (e.g., perforated steel plate). All other extraordinary characteristics result from that, at first sight, slight difference. Higher flow velocity and smaller pebble diameters may be used. That provides a very high specific surface (or surface-to-volume ratio) and an excellent heat transfer. That results in a high thermal efficiency (units with more than 98% are in operation) and a temperature gradient in the range of 1500 – 2000 K/m. The pebble bed does not have to be thick in a radial direction, so the pressure drop is also low. Ultimately, it leads to a very compact unit at low investment costs. The new technology has been developed primarily to substitute the technology of hot wind stoves (Cowpers) for supplying blast furnaces with a hot blast. With those characteristics, PH is suitable for combustion air preheating in the scope of a regenerative burner system [2].

The Pebble Heaters in experimental installation have been designed for 2,000 m^3/h (p=101325 Pa, T=273,15 K) and 1200 °C. The dimensions of a PH are presented in Table 1.

Item	Unit	Value
Inside diameter of the hot grid	mm	300
Outside diameter of the hot grid	mm	400
Cold grid diameter	mm	754
Pebble-bed thickness	mm	177
Outer shell diameter	mm	790
Active height of the hot grid	mm	750
Height of the cold grid	mm	1015
Total height of the outer shell	mm	1200

Table 1. PH dimensions.

An important part of the installation of regenerative burners is Fluid-Dynamical Valve (FDV). The usage of FDV makes it possible to rapidly switch between two hot gas streams (above 1000°C) without movable mechanical parts. The principle is based on the interaction between velocity and pressure field in fluid channels of FDV. With a suitable design of flow ducts, it is possible to increase the velocity and decrease pressure and vice versa at specific parts of FDV so that two hot gas streams flow in different directions without considerably mixing. As a result, FDV operates

faster and more reliably (without movable mechanical parts at high temperatures), and it has a simpler design and is much cheaper than the conventional switching valve at the hot gas stream side [2].

The facility is compact due to the short switching time – the designed value is 1 min. The pebble bed consists of alumna pebbles (resistant at high temperatures) with a mean diameter of 4,5 mm. The hot grid is brick-layered with honeycombs made of mullite. Each brick has dimensions of 150 x 150 x 50 mm. The cold grid is manufactured from perforated steel with horizontal slots. Figures 1 and 2 show a view of the separate system of two PH and the experimental installation of regenerative burners at the stand for tundish preheating in the steel plant.

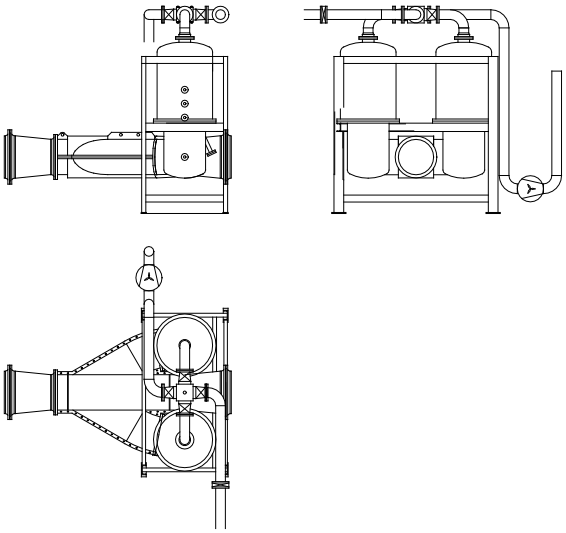

Fig.1. View of two PH connected with FDV [1].

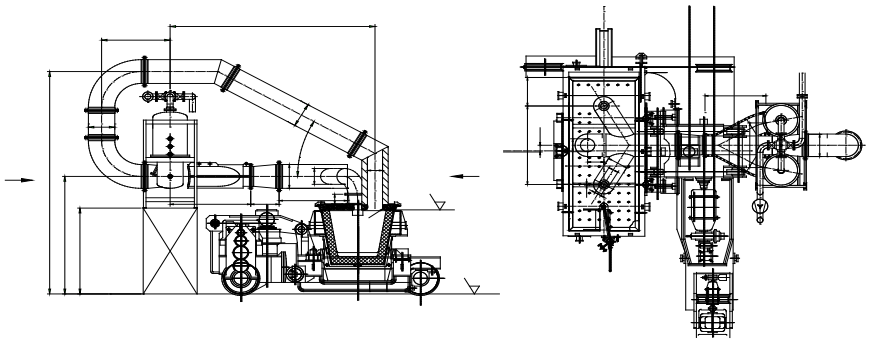

Fig. 2. View experimental installation of regenerative burners connected to the stand for tundish preheating in steel plant [1].

3. Optimisation procedure and results

3.1 Design and Optimisation of the FDV

The design and optimization of the FDV and tundish top cover was done using the numerical CFD code StarCD. A steady-state model was used. Due to simplification, a rectangular cross-section of all flow channels of FDV was adopted, although some are circular. Some previous experience has shown that such an approach is justified due to significantly faster geometry modeling in pre-processing and minor deviations from the actual conditions.

The basic characteristics of the simulation model are given in Table 2. Table 3 shows parameters used in numerical simulation to optimize FDV geometry.

Item	Characteristics
Number of blocks	22
Number of cells in the grid	177744
Type of the grid	Uniform
Cross section of FDV	Rectangular – with an equivalent area of the round cross-section
Geometry of: - Inlets: Preheated air Off-gas - Outlets: Preheated air Off-gas	 ϕ_{ekv} = 220 mm ϕ_{ekv} = 300 mm ϕ_{ekv} = 270 mm ϕ_{ekv} = 220 mm
Boundary conditions: - Inlets: Preheated air Off-gas - Outlets: Preheated air Off-gas	 V=67.2 m/s, t=1000 °C, ρ=0.285 kg/m^3 V=44.0 m/s, t=1100 °C, ρ=0.232 kg/m^3 Splited Splited
Reference pressure	100900 Pa
Used models in simulation: Turbulence model Thermal model	 K-ε High Reynolds number Calculation of temperature field

Table 2. Characteristic parameters in numerical modeling and design optimization of FDV [1].

Solution method		Steady-state		
Solution algorithm		Simple		
Max. global residual tolerance		$1 \cdot 10^{-5}$		
Solver type		Scalar		
Primary variables	**Relaxation factor**	**Number of sweeps**	**Residual tolerance**	**Difference scheme**
U-Momentum V-Momentum W-Momentum	0.5 0.5 0.5	100 100 100	0.01 0.01 0.01	UD
Pressure	0.15	1000	0.005	UD
Turbulence K-ε Turbulence Dissipation	0.5 0.5	100 100	0.01 0.01	UD
Temperature	0.7	100	0.01	UD
Density Viscosity	1 1			MARS

Table 3. Parameters used in solution and numerical simulation for FDV design optimization [1].

As can be seen, most of the parameters for both models are equal. The solution method for FDV design optimization was only steady state (Simple solution algorithm), and the radiation model was omitted.

The relaxation factor for pressure had to be kept low – 0.15 due to the sensitivity of the solution, and for other variables, the relaxation factor was kept in the range of 0.5 to 1. Upwind (UD) and MARS differencing schemes were used for model solving.

The optimization of the FDV design was performed with slight changes in the geometry of the flow channels, especially in the middle part of FDV, where the two hot gas streams come in contact.

The criteria for optimization were to:

- obtain the same pressure difference at the entrance channels of FDV as calculated using the pressure drop estimation (Table 2);
- achieve acceptable pressure drop through FDV and obtain required pressure value at the outlet channel for preheated air due to necessary flow potential for burners at tundish top, and
- achieve relatively small mixing between two hot gas streams.

The geometry of FDV, which is used for numerical simulation, is shown in Fig. 3.

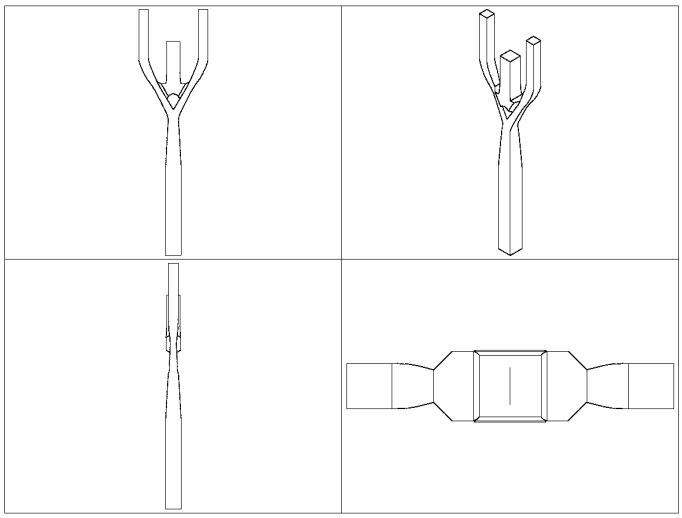

Fig. 3. The geometry of the model of FDV used in numerical simulation [1].

In the case of regenerative burner systems, mixing (up to 12 %) of flue gas and hot combustion air may help minimize NO_x formation. Namely, it is favorable to have some combustion gases mixed in the preheated air, thus reducing oxygen concentration, which is a relevant factor for the kinetics of NO_x formation. It is the well-known technique of off-gas recirculation. In this case, mixing is carried out on the hot side - inside the FDV, without a costly recirculation piping system. Hence, it is called *in-situ* recirculation.

The results achieved with the final geometry are given in Figs. 4-8. Figure 4 shows the pressure field in the middle plane of the whole FDV. The detailed pressure field for the middle part of the FDV is presented in Fig. 5. In both cases, the hot air enters through the top right-side pipe and leaves the FDV through the bottom central tube. The hot off-gas stream enters through the top central pipe, turns left, and goes out through the top left-side pipe. Figure 6 shows the intensity of the velocity field in the middle plane of FDV, which strongly depends on the pressure field. Figure 7 shows the detailed velocity field of the middle part of FDV. The nozzle accelerates the hot air stream reducing its pressure so that at the location where the two streams get in contact, the pressure is almost identical from both sides (ochre yellow colored field in Fig. 5). In that way, there is no potential for significant convective mixing between the two streams. In addition, the long diffuser at the hot air outlet (see Fig. 4) slows down the gas stream and recovers the pressure loss to some extent. Figure 6 shows the velocity vectors in the middle section of FDV. The hot air accelerates (up to 170 m/s), while the velocity of the off-gas at the contact location is considerably lower (approx. 10 m/s). The concentration field in the middle plane of the whole Fluid-Dynamical Valve is given in Fig. 8. The air concentration at the outlet is higher than 92,8 % (red field), which means that about 7 % of off-gas is recirculated and goes into the tundish.

Pipeline for hot air	**Pipeline for off-gasses**	**Pipeline for hot air**	**Pipeline for off-gasses**
Pipeline part	Pressure drop, Pa	Pipeline part	Pressure drop, Pa
I part	1021	I part	185
Pebble-Heater	2000	II part	335
II part	745	Fluid-Dynamical Valve	2860
Fluid-Dynamical Valve	1475	III part	-180
III part	115	Pebble-Heater	2000
IV part	65	IV part	1375
Pipeline for hot air		Pipeline for off-gasses	
Burners	760		
Sum:	Σ6181 Pa	Sum:	Σ6575 Pa
Characteristics of pipeline parts: ϕ, l, ζ,λ, V			
High preheated air		Off-gas	
I part - cold side of air from fan to the Pebble Heater entrance.	ϕ 200 mm; l=13.5 m; $\Sigma\zeta$=3.3; λ=0.0252; V=17.88 m/s	I part - from tundish to first knee in horizontal part of the pipeline	ϕ 350 mm; l=8 m; $\Sigma\zeta$=1.1; λ=0.0253; V=30.48 m/s
II part - knee from Pebble Heater to Fluid-Dynamical Valve	ϕ 300 mm; l=1 m; $\Sigma\zeta$=0.4; λ=0.026; V=50.78 m/s	II part - two knees to the FDV	ϕ 350 mm; l=3.5 m; $\Sigma\zeta$=0.8; λ=0.0253; V=30.53 m/s
III part - from Fluid-Dynamical Valve to Y part	ϕ 350 mm; l=13.5 m; $\Sigma\zeta$=1; λ=0,0251; V=26.66 m/s	III part - diffusing knee	ϕ 350 mm; l=1 m; $\Sigma\zeta$=0.4; λ=0.0252; V=61.32 m/s
IV part - from Y part to burners exit	ϕ 250 mm; l=2.5 m; $\Sigma\zeta$=0.4; λ=0.0274; V=26.16 m/s	IV part – cold off gasses from Pebble-Heaters	ϕ 200 mm; l=2.5 m; $\Sigma\zeta$=3.4; λ=0.0264; V=33.94 m/s

Table 4. Pressure loss estimation through the installation of regenerative burner [1].

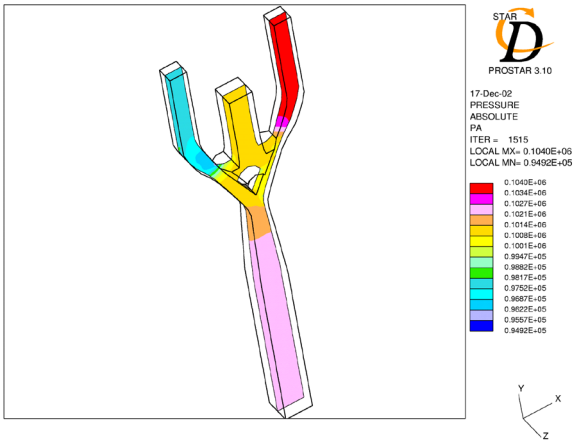

Fig. 4. Pressure field in the middle cross-section of FDV [1].

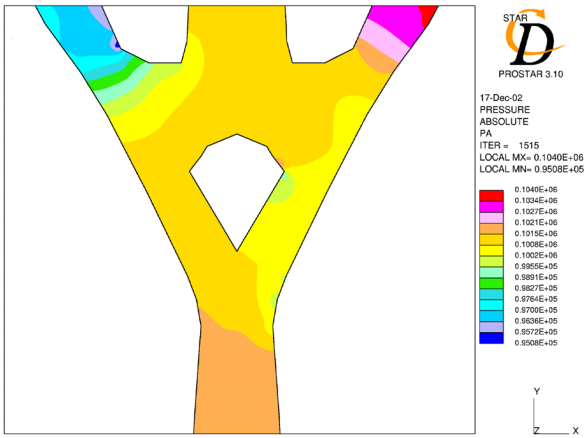

Fig. 5. Detail of pressure field in the central part of FDV [1].

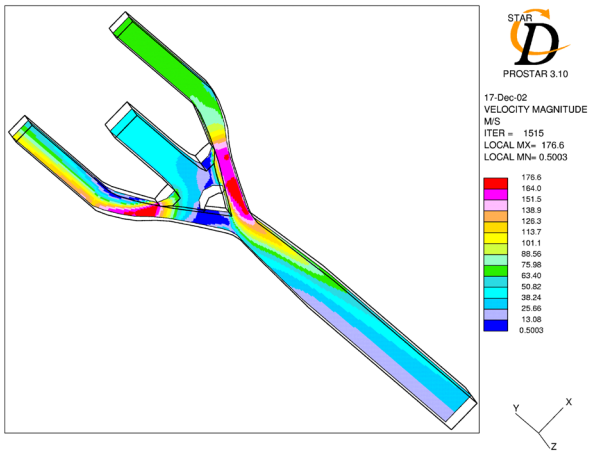

Fig. 6. Velocity field in middle cross-section of FDV [1].

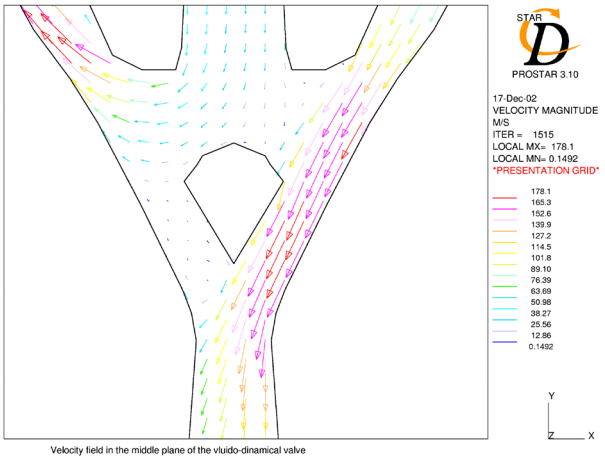

Fig. 7. Detail of velocity vectors in the central part of FDV [1].

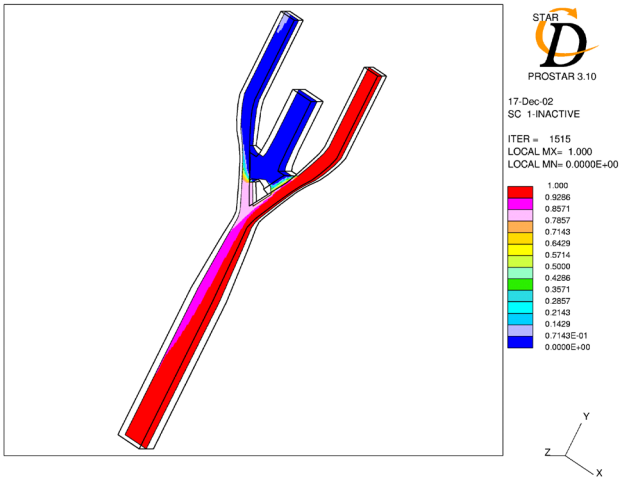

Fig. 8. Concentration field in middle cross-section of FDV [1].

A model core for real FDV (shown in Fig. 9) was built to verify obtained results of the numerical simulation of FDV optimization in the experiment.

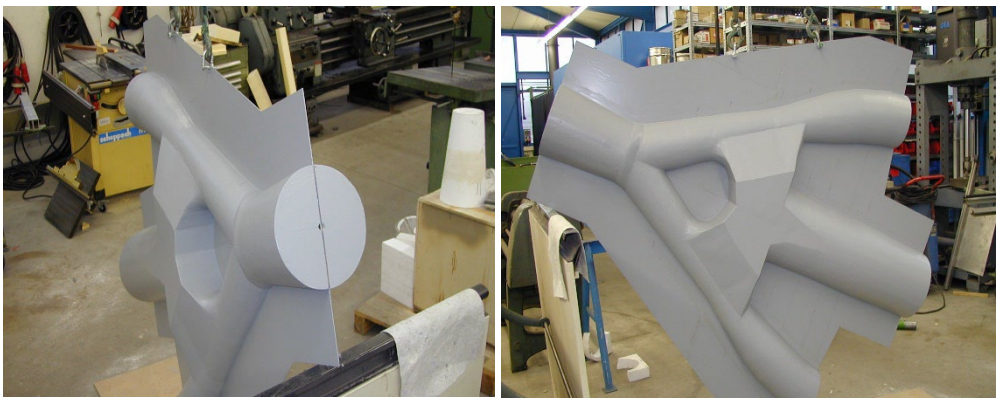

Fig. 9. The core model of FDV [1].

4. Conclusions

With existing physical models, CFD can offer cost-effective solutions for many complex systems of interest in the metallurgical industry. For example, numerical simulations in the design and optimization of FDV of experimental installation of regenerative burners for tundish preheating have been performed by using CFD code StarCD v 3.15 A. According to the obtained result, the solution for the geometry of FDV was suggested.

Due to the considerable pressure difference between two hot streams at the inlets of FDV, one of the streams (the hot air) should accelerate (up to 170 m/s), while the velocity of the other (off-gas) at the contact location should be considerably lower (approx. 10 m/s). Adequate geometry of FDV channels was obtained as a result of numerical optimization. The air concentration at the outlet is higher than 92,8 %, which means that about 7 % of off-gas is recirculated and goes into the tundish.

References:

[1] Stevanović, D., Tran, van C., Scholz R., Quicker, P., Jankes, G., Stamenić, M., Dimitrov, A., Kamberović, Ž., Butala, V.: *Reducing fuel consumption and air pollution of industrial furnaces*

by high-efficiency pebble-heaters and fluid-dynamical valve, Contract Number: ICA2-CT-2002-10004, Progress Report No. 1, November 2003.

[2] Stevanović, D., Fischer, W.: *Pebble-Heater Twins with Fluid-dynamic valve: an efficient possibility for high combustion air preheating,* 6th European Conference on Industrial Furnaces and Boilers, Estoril - Lisbon - Portugal, 02.-05. April 2002.

EXPERIMENTAL INVESTIGATION AND MATHEMATICAL MODELLING OF VORTEX STRUCTURES FOUND AT IMPINGING TURBULENT AXISYMMETRIC AIR JET MODIFIED BY LOW-AMPLITUDE SOUND MODULATION

Dejan Cvetinović[1], Aleksandar Erić[1], Nikola Ćetenović[2], Djordje Čantrak[2], Jaroslav Tihon[3] and Kazuyoshi Nakabe[4]

[1]«Vinča» Institute of Nuclear Sciences, National Institute of the Republic of Serbia, University of Belgrade, Laboratory for Thermal Engineering and Energy, Belgrade, Serbia
e-mail: deki@vinca.rs, erica@vin.bg.ac.rs
[2]Faculty of Mechanical Engineering, University of Belgrade, Kraljice Marije 16, P.O.Box 35, 11120 Belgrade, Serbia
e-mail: nikolacetenovic99@gmail.com, djcantrak@mas.bg.ac.rs
[3]Institute of Chemical Process Fundamentals, Academy of Sciences of the Czech Republic, Prague, Czechia
e-mail: tihon@icpf.cas.cz
[4]Mechanical Engineering, Faculty of Engineering, Kyoto University, Kyoto, Japan
e-mail: nakabe@me.kyoto-u.ac.jp

Abstract

The controlled modulation of the nozzle exit velocity acts as a disturbance source, superimposing the natural disturbances in axisymmetric turbulent air jets. The modulation controls the vortex roll-up, and thus the overall vortex structure in the jet. The vortex structures have a significant influence on the heat transfer properties of the jet configurations. The jet can be modulated by an external source of low amplitude oscillations or by self-sustaining oscillations generated by the operation of the specially designed whistler nozzles. The aim of the experimental investigations, mathematical modelling and numerical simulations was to investigate the properties and vortex structures of acoustically modified and non-modified jets and to find an efficient way to control them.

This study can serve as a basis for further development and optimisation of technological processes related to air nozzles. The paper presents the results of experimental research and mathematical modelling and numerical simulation of free and impinging turbulent axisymmetric modified and not modified air jets.

Keywords: turbulent axisymmetric air jet, impinging jet, vortex structures, experimental investigations, mathematical modelling, heat transfer, flow control.

1. Introduction

Impingement nozzles are a widely used means of effective and flexible transfer of energy or mass in various industrial applications. Liquid or gaseous streams impinging on a surface can efficiently

transfer heat energy or mass between the surface and the fluid. Heat transfer applications include cooling in material forming, heat treatment of various materials, cooling of electronic components, heating of surfaces for defogging, cooling of turbine components, cooling of critical machinery structures and many other similar industrial processes. Typical mass transfer applications include drying and removal of small surface particles. Abrasion and heat transfer are of interest for vertical/short take-off and landing jet devices in the case of direct lift propulsion systems. The heat transfer rate can be assumed to be a complex function of many parameters: Reynolds number (Re), Prandtl number (Pr), the non-dimensional distance between nozzle and plate (L/D) and the non-dimensional displacement from the stagnation point (r/D), also the nozzle geometry, the flow confinement, the initial turbulence intensity of the jet, the jet temperature dissipation, etc. [1], [2], [3]. A number of authors confirm that the vortex structures of the impinging jet are of great importance for heat transfer. Primary vortices that roll up in the shear layer of the jet lead to unsteady flow separation at the wall, which prevents heat transfer between the wall and the fluid jet. Control of these vortices results in control of heat transfer from the jet to the wall and vice versa. It was found that vortex roll-up can be controlled by a small amplitude modulation of the nozzle exit velocity.

The subject of the present paper is an immersed, round, unconfined, impinging air jet exiting from a bell-shaped converging nozzle [4], [5], [6] and from the specially designed Whistler nozzle [7]. The aim of the study is to qualitatively describe the vortex structure of the free and impinging jet and to test the possibility of controlling it by modulating the exit velocity of the low-amplitude nozzle by an external sound source and by self-sustaining resonant sound oscillations generated during the operation of the Whistler nozzles. The vortex roll-up is generally triggered by a disturbance of the shear layer, which is amplified by the shear layer instability [8], [9]. The disturbance can also be a random noise wave coming from the environment, from an upstream flow system or from a downstream flow event. The modulation of the nozzle exit velocity acts as an additional source of disturbance that overlays the natural disturbances if the modulation is strong enough. The modulation of the nozzle exit velocity controls the vortex roll-up and thus the entire structure of the turbulent axisymmetric jet [10]. The development of suitable mathematical models can save time for extensive experimental investigations and is a good basis for understanding this very complex phenomenon.

2 Experimental Setup

The experimental setup for the measurements of the flow field in the impinging jet configuration is shown schematically in Fig. 1. It consisted of a bell-shaped converging nozzle, a settling chamber, a flow disturbance system, an impingement plate perpendicular to the jet axis, an air supply system and a control and data acquisition system. The bell-shaped nozzle with an outlet diameter of 25 mm was made of a plastic material. The air entered the settling chamber through two pipes fixed in the centre and flowed through four grids and a honeycomb. The last element of the settling chamber contained a pressure tap and a temperature sensor. The reference sensor of the anemometer temperature sensor had a diameter of 1.7 mm and its end was about 30 mm from the chamber wall.

The rear part of the settling chamber was equipped with a loudspeaker to induce the flow disturbance. This eight-ohm loudspeaker (8 Ω), with 20 W mid-tone class loudspeaker had a diameter of 100 mm. It was located behind two additional grilles and a honeycomb element. The air was supplied by a laboratory compressed air circuit. The manometer used to measure the pressure in the settling chamber was used to precisely measure the flow velocity.

The measurement system consists of a hot-wire probe operated in constant temperature mode and controlled by a Dantec Streamline anemometer system. The probe was mounted on a 2D traversing device. The system resolution, corresponding to one-step movement, was 0.025 mm. The mean jet temperature was measured with the temperature sensor of the Streamline anemometer.

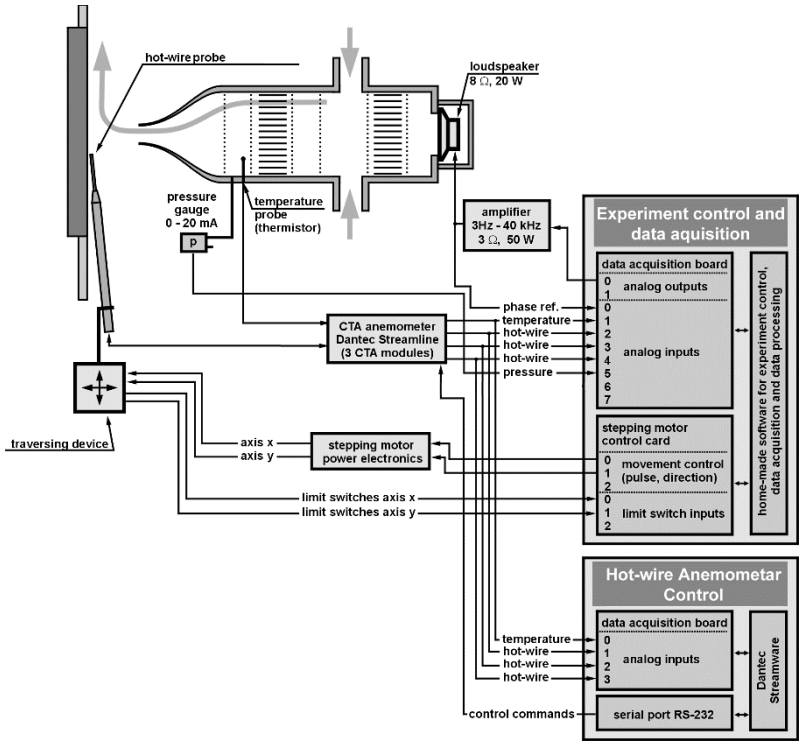

Fig. 1. Experimental setup for experiments in an impinging jet configuration.

During the experiments, the loudspeaker was fed from an analogue output of the data acquisition board, the signal of which was amplified by a 50 W amplifier with a flat frequency response in the range from 3 Hz to 40 kHz.

An impingement plate was very carefully aligned perpendicular to the axis of the air jet to avoid the influence of jet inclination. A large part of the measurements was carried out in the perturbed jet. The perturbation level was defined as the normalised velocity rms u'/U_e in the middle of the nozzle exit. The level was in the range u'/U_e=1÷3% (in some cases even higher – up to 7%). The dependence of the required loudspeaker voltage on the frequency, i.e. the Strouhal number of the excitation, is shown in [9, 11].

During the experiments, the signals were sampled at a sampling rate of 12 kS/s. The signals were displayed online and stored on the hard drive. Data acquisition was started at least half a second after the probe was moved to the next grid point. This delay was sufficient to attenuate the vibrations of the probe.

3. Experimental results

A series of measurements are made near the impingement plate and in the plane perpendicular to the jet at the nozzle exit to investigate the influence of the low-amplitude disturbance on the structure of the axisymmetric turbulent air jet exiting a bell-shaped nozzle. Evaluations of the initial conditions of the jet for a complete range of jet Reynolds numbers are presented for the free jet case in [9, 11].

2.1 Velocity along the line at distance y/D=0.04 from the impinging plate

Normalised mean velocity profiles and normalised velocity rms profiles measured along the line at distance y/D=0.04 from the impinging plate for the experimental case Re=10000, not excited jet and selected excitations, are shown in Figure 2.

During the preparatory measurements, it was found that the radial velocity profiles have their maximum value at distance y/D=0.04 from the impinging plate, which is why this line was chosen as representative for the measurements.

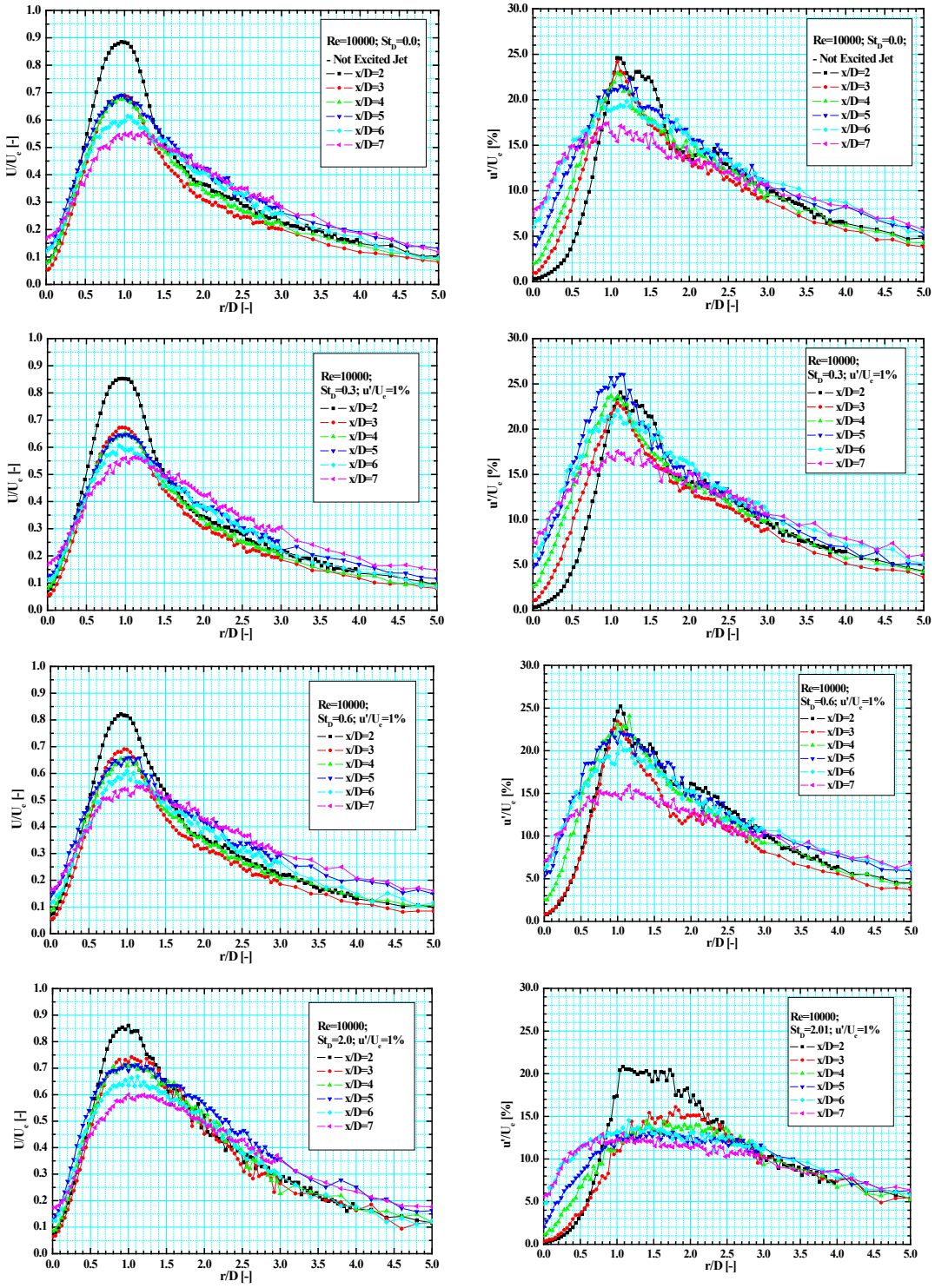

Fig. 2. Normalised velocity and normalised velocity rms along the line y/D=0.04; – Re=10000; St_D=0.0, 0.3, 0.6 and 2.0; u′/U_e=1%; x/D=2–7.

Figure 2 shows the profiles of normalised velocity and normalised velocity rms profiles along the line y/D=0.04 for the experimental case Re=10000 and the excitation Strouhal number St_D=0.0, 0.3, 0.6 and 2.0 and the excitation amplitude 1% for impinging distances x/D=2-7.

The first pair of plots in Fig. 2 is for the unexcited case, St_D=0.0, where there is clearly a tendency for the normalised velocity and its rms profiles to change as we move the impinging plate away from the nozzle lip. From the images shown, we can conclude that the profiles for impinging distance x/D=2 show a different behaviour than the other profiles measured for the impinging plate located inside the potential core. This is probably due to the influence of the impinging plate, i.e. the sudden deceleration of the jet in the stagnation zone is dominant in adjusting the jet structure for minimal impinging distances. The normalised velocity profiles show a maximum value around the radial distance r/D=1 for the small distance between the nozzle and plate and a small shift to the higher radial distances when the plate is far from the nozzle lip, followed by the highest values in the normalised velocity rms, even though these profiles show a small drift around the maximum value. In addition, a slight shift in the position of the maximum in the profiles towards the lower radial distances is observed in the case of a higher Reynolds number.

From the plots in Fig. 2, which show the normalised velocity and rms profiles for not excited jet it can be seen that the normalised velocity and rms profiles around the radial position where the maximum is found in the profiles are almost the same when the plate is inside the potential core (x/D=3, 4 and 5). Differences in the profiles are observed at the other radial distances, as the rms values increase at radial distances smaller than r/D=1, which can be explained by the entrainment of the vortex structures closer to the jet axis and the thickening of the jet shear layer at larger axial lengths from the nozzle lip. The profiles measured at higher impinging distances showed the expected behaviour. The value of the normalised velocity is decreased for some excitation conditions St_D=0.3 and 0.6 and increased for the others St_D=2.0. An increase and a decrease of the profiles of the normalised velocity rms also showed a similar tendency as for the free jet [9]. The presence of the maximum in the normalised velocity rms can be explained by the separation from the wall by the radial distance r/D=1.

The most interesting excitation cases remain those belonging to the Strouhal number around St_D=2.0, as already observed for the free-jet configuration [9, 11]. The profiles of the normalised velocity rms have a very uniform shape for all impinging distances, except for the impinging length of 2D, where the most dominant influence on the jet structure is the presence of the plate very close to the nozzle.

4. Mathematical modelling

In most practical engineering situations, the impinging jets are modelled using different turbulent models. Most of the turbulence models were developed for flows parallel to the wall. Therefore, their applicability to the impinging jet is limited because it significantly differs from parallel flows: the kinetic energy of turbulence in the vicinity of the axis of symmetry (i.e. stagnation point or zone) is generated by the normal stresses (for flows parallel to the wall this role have shear stresses); the velocity fluctuation component normal to the wall is of the same order, or even larger than the component parallel to the wall; in parallel flows, the normal component is much smaller; the local turbulent length scales near the wall are strongly affected by the length scale of the jet turbulence; in parallel flows, the length scales are determined by the distance from the wall; in impinging jets, there is an important convective transport of turbulence toward the stagnation point; in parallel flow, the convective transport is usually negligible and the turbulence production and dissipation are approximately in equilibrium.

The initial assumption of the model is that the air is an incompressible Newtonian fluid with temperature-dependent characteristics. Numerical simulation of temperature and calculation of the flow field in a numeric domain requires solving the continuity equation (1), Reynolds averaged Navier-Stokes equations of motion (2) and time-averaged energy equation (3), presented in the index tensor notation in the form of:

$$\frac{\partial U_i}{\partial x_i} = 0 \tag{1}$$

$$\frac{\partial U_i}{\partial t}+U_i\frac{\partial U_j}{\partial x_j}=-\frac{1}{\rho}\frac{\partial P}{\partial x_i}+\frac{\partial}{\partial x_j}\left[\nu\left(\frac{\partial U_i}{\partial x_j}+\frac{\partial U_j}{\partial x_i}\right)-\overline{u_iu_j}\right] \tag{2}$$

$$\rho\frac{DT}{Dt}=\rho\frac{\partial T}{\partial t}+\rho U_j\frac{\partial T}{\partial x_j}=\frac{\partial}{\partial x_i}\left[\frac{\mu}{\mathrm{Pr}}\frac{\partial T}{\partial x_i}-\rho\overline{\theta u_i}\right] \tag{3}$$

Attempts of the numerical calculation of the flow and temperature field of the fluid flow, formed in the case of the jet impinging on a flat heated plate, carried out using standard two-equation turbulence models and standard Reynolds-stress models, showed disagreements with the experimentally determined physical situation. The highest degree of disagreement was observed in the stagnation area of the jets, especially in the calculation of local values of Nusselt numbers. In the case of two-equation models of turbulence, the reason for these disagreements is usually their known property, to provide relatively wrong predictions for extremely non-isotropic flows. This property is a consequence of their design based on differential transport equations for scalar quantities (k and ε, or k and ω), and the fact that practically all two-equation turbulent models are developed for shear turbulent flows.

Based on Boussinesq's turbulent viscosity hypothesis, Reynolds stress is a function of the local gradient of velocity and turbulent viscosity ν_t. The coefficient of the turbulent viscosity takes into account the viscous interactions of the fluid and is not a physical property of the fluid. By analogy with the constituent relation between the laminar stresses and the deformation rate, the dependence between the turbulent stress and the velocity gradient of averaged fluid flow can be obtained in the form:

$$-\rho\overline{u_iu_j}=\tau_{ij}=\mu_t\left(\frac{\partial U_i}{\partial x_j}+\frac{\partial U_j}{\partial x_i}\right)=\mu_tS_{ij}$$

known in the literature as the linear concept of turbulent viscosity. The introduction of the coefficient μ_t enables the closure of the system of equations of turbulent motion and the method of its calculation defines the type of model for turbulence modelling (μ_t is not a model itself).

In the case of shear turbulent flows, this coincidence and proportionality are more or less present, but in the stagnation zone of the flow generated by impingement of the jet to the surface, the presumption of such dependence is no longer adequate. In this zone, instead of the appearance of the shear, the processes of the compression of the fluid particles are the dominant ones. This means that those parts of the averaged velocity tensor responsible for the normal, rather than shear deformations, dominantly change.

If the turbulent stresses for this case of physical fluid flow are modeled in accordance with Boussinesq's hypothesis, this results in a wrong prediction of the turbulence kinetic energy and the linear increase of the corresponding normal turbulent stresses. This erroneous prediction process, for k-ε and k-ω models, is reflected through an enlarged term of the modelled turbulent viscosity, since the increase in the kinetic energy of turbulence causes the turbulent viscosity to increase in proportion to the square of its value.

Energy equation (3) has a term $\frac{\mu_t}{\mathrm{Pr}}\frac{\partial T}{\partial x_i}$, which is not capable to distinguish the difference between the effects of certain Reynolds stresses, consequently leading to an excessive increase in the enthalpy flow that increases local value Nusselt numbers in the stagnation area.

By moving away from the stagnation point and transforming into the wall jet, the results of numerical calculations are increasingly approaching experimentally measured values. These approximations are not surprising, as, with the transition from "non-shear" to a shear turbulent flow, Boussinesq's hypothesis accurately predicts the relationships between the Reynolds stress tensors and the averaged fluid particle deformation rate tensor. Correctly establishing these relationships leads to increased accuracy of numerical/mathematical predictions.

In this paper will be shown mathematical models that use turbulent scalar quantities k and ε to calculate ν_t, which are obtained by solving the set of modelled transport equations:

$$\rho U_i \frac{\partial k}{\partial x_i} = \frac{\partial}{\partial x_i}\left[\left(\mu + \frac{\mu_t}{\sigma_k}\right)\frac{\partial k}{\partial x_i}\right] + \mu_t\left(\frac{\partial U_i}{\partial x_j} + \frac{\partial U_j}{\partial x_i}\right)\frac{\partial U_i}{\partial x_j} - \rho\tilde{\varepsilon} \tag{4}$$

$$\rho U_i \frac{\partial \varepsilon}{\partial x_i} = \frac{\partial}{\partial x_i}\left[\left(\mu + \frac{\mu_t}{\sigma_\varepsilon}\right)\frac{\partial \varepsilon}{\partial x_i}\right] + f_1 C_1 \mu_t \frac{\varepsilon}{k}\left(\frac{\partial U_i}{\partial x_j} + \frac{\partial U_j}{\partial x_i}\right)\frac{\partial U_i}{\partial x_j} - \rho f_2 C_2 \frac{\varepsilon^2}{k} + E \tag{5}$$

$$\mu_t = \rho f_\mu C_\mu \frac{k^2}{\varepsilon} \tag{6}$$

$$\tilde{\varepsilon} = \varepsilon + D \tag{7}$$

$$\mathrm{Re}_T = \frac{\rho k^2}{\mu\varepsilon}; \qquad \mathrm{Re}_{x_2} = \frac{\rho\sqrt{k}x_j}{\mu}; \qquad \mathrm{Re}_\varepsilon = \frac{\rho\left(\mu\varepsilon/\rho\right)^{1/4} x_j}{\mu} \tag{8}$$

where C_μ, C_1, C_2, σ_k and σ_ε are the same empirical constants for turbulent models as those used in k-ε models for large Reynolds numbers. The "dumping functions" f_μ, f_1 and f_2, and in some models, the used terms D and E are used to improve the accuracy of the flow model near the wall. The detailed physical meaning of these "dumping functions", as well as terms D and E, with the criteria for determining the correctness of these functions for the flow near the wall are given in the reference Patel et al., 1985 [11].

The modification of the *k-ε* model developed for lower Reynolds turbulent numbers (so-called Low-Reynolds number models) allows their use in the vicinity of the wall. The modification involves inserting a “dumping function” into the original term of the transport equation for ε and in the expression for turbulent viscosity μ_t.

The "damping functions" allow these equations to be used in a turbulent boundary layer, including a viscous sublayer, but on the other hand, they apply only to this case of flow and cannot be applied in other fluid flows. A modified transport equation for ε (5) for using the dumping functions f_μ, f_1 and f_2 takes the form:

$$\rho U_i \frac{\partial \varepsilon}{\partial x_i} = \frac{\partial}{\partial x_i}\left[\left(\mu + \frac{\mu_t}{\sigma_\varepsilon}\right)\frac{\partial \varepsilon}{\partial x_i}\right] + \frac{\varepsilon}{k}\left(f_1 C_{1\varepsilon}\mu_t S^2 - \rho f_2 C_{2\varepsilon}\varepsilon\right) \tag{9}$$

Tables 1 and 2 give the values for the five basic constants and the dumping functions used in most *k-ε* models modified for Low-Reynolds turbulent numbers. Modifications of the basic *k-ε* model that will be presented in the paper are Abid (AB and AB1 in following Table 1), 1993, [12], Lam and Bremhorst (LB), 1981, [13], Launder and Sharma (LS), 1974, [14] Abe, Kondoh and Nagano (AKN and AKN1), 1994, [15], and Chang, Hsieh and Chen (CHC) 1995, [16].

Model	*D*	*E*	ε_w – *boundary condition*	C_μ	C_1	C_2	σ_k	σ_ε
AB	*0*	*0*	$\varepsilon_w = \nu\left(\frac{\partial^2 k}{\partial x_j^2}\right)$	*0.09*	*1.44*	*1.92*	*1.0*	*1.3*
AB1				*0.09*	*1.45*	*1.83*	*1.0*	*1.4*
LB	*0*	*0*	$\left(\frac{\partial \varepsilon}{\partial x_j}\right)_w = 0$	*0.09*	*1.44*	*1.92*	*1.0*	*1.3*
LS	$2\nu\left(\frac{\partial\sqrt{k}}{\partial x_j}\right)^2$	$2\mu\nu_t\left(\frac{\partial^2 U}{\partial x_j^2}\right)^2$	*0*	*0.09*	*1.44*	*1.92*	*1.0*	*1.3*
AKN	*0*	*0*	$\varepsilon_w = \nu\left(\frac{\partial^2 k}{\partial x_j^2}\right)$	*0.09*	*1.44*	*1.92*	*1.0*	*1.3*
AKN1				*0.09*	*1.5*	*1.9*	*1.4*	*1.4*
CHC	*0*	*0*	$\varepsilon_w = \nu\left(\frac{\partial^2 k}{\partial x_j^2}\right)$	*0.09*	*1.44*	*1.92*	*1.0*	*1.3*

Table 1. List of model constants and functions that occur in basic model equations.

Model	f_μ	f_1	f_2
AB	$\tanh\left(0.008Re_{x_j}\right)\left(1+4Re_t^{-3/4}\right)$	*1*	$\left[1-\frac{2}{9}e^{-\frac{Re_t^2}{36}}\right]\left[1-e^{-\frac{Re_{x_j}}{12}}\right]$
LB	$\left[1-e^{-0.0165\mathrm{Re}_{x_j}}\right]^2\left(1+20.5/Re_t\right)$	$1+\left(\frac{0.005}{f_\mu}\right)^3$	$1-e^{-Re_t^2}$
LS	$e^{-3.4/\left(1+Re_t/50\right)^2}$	*1*	$1-0.3e^{-Re_t^2}$
AKN	$\left[1-e^{-Re_\varepsilon/14}\right]^2\left[\left(1+5.0/Re_t^{3/4}\right)e^{-\left(Re_t/200\right)^2}\right]$	*1*	$\left[1-e^{-\left(Re_\varepsilon/3.1\right)}\right]^2\left[1-0.3e^{-\left(\mathrm{Re}_t/6.5\right)^2}\right]$
CHC	$\left[1-e^{-0.0215Re_{x_j}}\right]^2\left(1+31.66/Re_t^{5/4}\right)$	*1*	$\left[1-0.01e^{-Re_t^2}\right]^2\left[1-e^{-0.0631Re_{x_j}}\right]$

Table 2. List of „damping functions“ that occur in basic model equations.

5. Results of numerical simulations

The subject of numerical analysis in this research was to investigate the performance of various so-called low-Reynolds number modification of the basic *k-ε* model using the commercial CFD code Fluent-Ansys, applied to the problem of jet on a flat surface positioned perpendicular to its propagation.

Applying the low Reynolds number modification of the *k-ε* model to this phenomenon requires a very high density of the network with the wall itself, y^+ on a cell on the wall must be at least 1. The preferred optimum is 10 cells in the viscous sublayer. The calculation was performed with a coupled solver with double precision and convergence was achieved when the normalised residuals of the dependent variable are smaller than 10^{-7} in the last 10 iterations. First, the not-modified jet was calculated (at about 40000 iterations required for a very strong convergence criterion), and then for the computation of the different low Reynolds number models, iteration was started from this convergent case. Depending on the case, another 10000-35000 iterations were needed for convergence.

The changes in the value of the local Nusselt number (for comparison with other authors in the form of $NuRe^{0.7}$) for different distances from the nozzle are shown in the following figures, Figs. 3-6.

The calculated heat transfer coefficients for the smallest distance of the impinging surface from the nozzle exit L/D=2 are shown in Fig. 3. In general, all 5 modifications of the standard low Reynolds turbulence model k-ε improve the prediction of the local heat transfer coefficients in the impact zone jet compared to the base model.

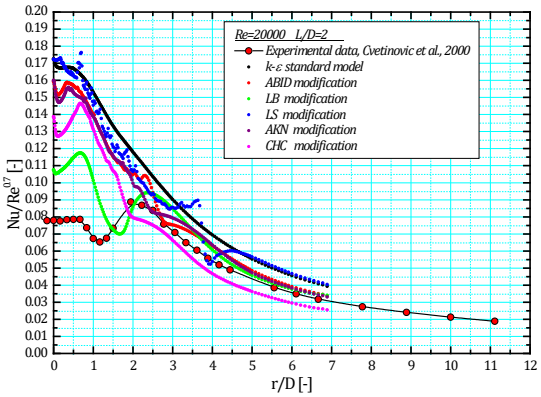

Fig. 3. Local Nusselt number profiles for Re_D=20000, L/D=2

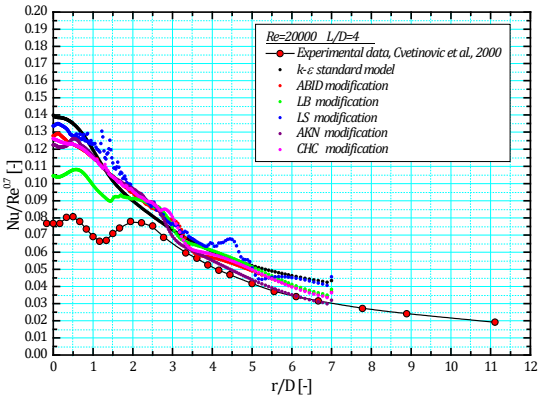

Fig. 4. Local Nusselt number profiles for Re_D=20000, L/D=4

However, the prediction also exceeds the values of the Nusselt numbers determined experimentally in the r/D<2 zones. It can be noticed that some of the proposed modifications and numerically unstable, there was a slight divergence of the solution. There is a particularly notable disagreement with experimentally determined values at higher radial distances from the jet stream which is unacceptable and can be explained by poor selection of damping functions and/or the lack of a justified criterion in the calculation for the application of "damping functions" whose role is to damp production of the kinetic turbulence energy in this zone.

By moving the impinging surface to greater distances from the nozzle outlet, the results of the calculation approach the measured values, as can be seen in Fig. 4, which represents the calculated values of the local heat transfer coefficients in the case of distance L/D = 4 from the impinging plate from the output from the nozzle. The presented results of calculations of the distance L/D = 4 are still above the measured but still can claim to better anticipate local Nusselt numbers of the basic k-ε model in the stagnation zone of the jet. Calculations instability is retained in some modifications of the standard turbulence model for low Reynolds turbulent numbers, which is also reflected in the jumps at some of the radial distributions shown in Fig. 5. Also, the observed distributions indicate a deviation from the measured values at higher radial distances from the jet axis.

For larger distances of the impinging surface from the outlet of the nozzle of L/D = 6 and 8, shown in Figs. 5 and 6, it is evident much better agreement with the measured values and, also, an evident improvement over the standard k-e turbulence model.

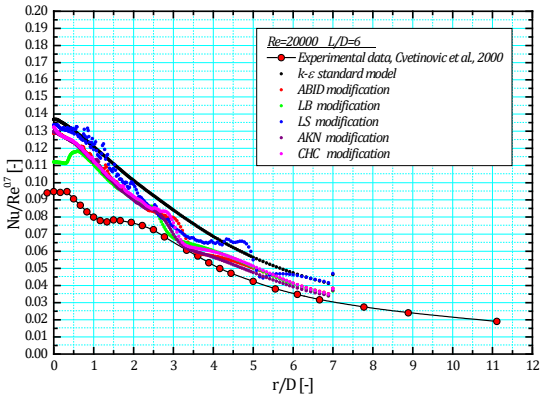

Fig. 5. Local Nusselt number profiles for Re_D=20000, L/D=6.

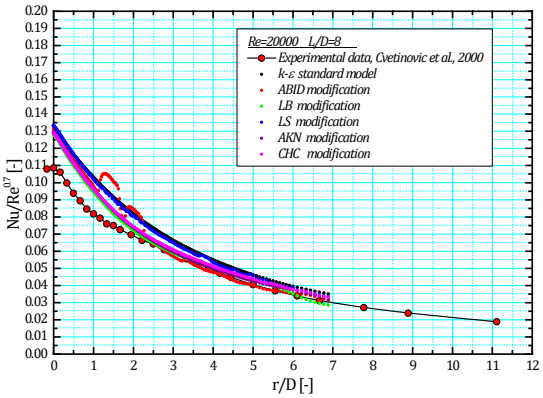

Fig. 6. Local Nusselt number profiles for Re_D=20000, L/D=8.

The objective of the numerical investigation of the heat transfer from a turbulent axisymmetric jet to a flat surface that was set up normally on the jet centerline was to examine the performance and possibilities in predicting local Nusselt numbers of the simplest two-equation turbulence models, and by several authors of the proposed modifications of the standard two-equation k-ε turbulence model for low Reynolds turbulent numbers.

Although the prediction of the local heat transfer coefficients overpredicts the experimental data, better predictive results have been achieved than some that are listed in the literature. The reason for this is in the correctly taken input parameters in the calculations corresponding to the experimental results with which the comparison was made.

6. Conclusions

Heat transfer near stagnation point can be enhanced by increasing not only the time-averaged approaching velocity and turbulence intensity, but also the characteristic frequency of the jet to strike the impinging surface with a large-scale vortex structure, which is the main feature of the late transition region of the jet. In such regions, the gradients of the instantaneous surface pressure are very often unfavourable because the gradients of the time-averaged surface pressure are almost zero there. Therefore, when a target plate is located in the transition region of a turbulent free jet, a transient, the unsteady separation-like reverse flow may occur at and near the stagnation point because large vortex structures temporarily impinge on the target plate.

In this paper, the ability to control the vortex structure in an axisymmetric turbulent jet by sound modulations of the jet velocity at the nozzle exit was demonstrated as an attractive possibility for technological processes. Indeed, it is sometimes necessary to enhance the mixing of the primary fluid flow and the surrounding fluid (in the chemical reactor) by sound modulation that amplifies the vortex structures in a jet shear layer, while, for example, to achieve a uniform heat transfer coefficient on a larger surface area of the impinging surface, it is necessary to apply a modulation with a completely different frequency.

The aim of the numerical study of the heat transfer from a turbulent axisymmetric jet to a plane surface set up normal to the centreline of the jet was to investigate the performance and capabilities in predicting the local Nusselt numbers of the simplest two-equation turbulence models and the modifications of the standard two-equation turbulence model k-ε for low Reynolds turbulence numbers proposed by several authors.

The prediction of the local heat transfer coefficients is better than some of those reported in the literature. The reason for this is the correctly stated input parameters in the calculations, which correspond to the experimental results with which the comparison was made. This study can serve

as a basis for the development and optimisation of the technological processes in which air jets are used.

Acknowledgement: This research was funded by the Ministry of Science, Technological Development and Innovation of the Republic of Serbia, Grant no. 451-03-47/2023-01/ 200017 («Vinča» Institute of Nuclear Sciences, National Institute of the Republic of Serbia, University of Belgrade); European Community FP5 program through BEMUSAC project; and Ministry of Education, Science and Culture, Japan through MONBUSHO program.

References:

[1] Jambunathan, K., Lai, E., Moss, M. A., Button, B. L., 1992: A review of heat transfer data for single circular jet impingement, International Journal of Heat and Fluid Flow, vol. 13, no. 2, pp. 106-115

[2] Zuckerman, N. and Lior, N., 2006: Jet Impingement Heat Transfer: Physics, Correlations and Mathematical Modelling, Advances in Heat Transfer, Volume 39, ISSN: 0065-2717, DOI: 10.1016-S0065-2717(06)39006-5, pp. 565-631

[3] Behnia, M., Parneix, S., Durbin, P. A., 1998: Prediction of heat transfer in an axisymmetric turbulent jet impinging on a flat plate, International Journal of Heat and Mass Transfer, vol. 41, no. 12, pp. 1845-1855

[4] Cvetinovic D., Tihon J., Verjazka J., Drahos J., 2004: "Effect of external excitations on the axisymmetrical air jet flow structures - Investigations of the Free Jet", CHISA 2004, 22-26. August 2004, Prague, Czech Republic, P5.237, ISBN 80-86059-40-5

[5] Cvetinovic D., Tihon J., Verjazka J., Drahos J., 2004: "Effect of external excitations on the axisymmetrical air jet flow structures - investigations of the jet impinging on a flat surface", CHISA 2004, 22-26. August 2004, Prague, Czech Republic, P5.236, ISBN 80-86059-40-5

[6] Dejan Cvetinović, Rastko Jovanović, Jiří Vejražka, Jaroslav Tihon, Kazuyoshi Nakabe, Kazuya Tatsumi. 2017: Possibility of Vortex Structures Control by modulation of the Nozzle Exit Velocity Using Low-amplitude Oscillations, 6th International Congress of Serbian Society of Mechanics, Tara, Serbia, June 19-21, 2017, Paper M2b

[7] Hussain A.K.M.F. and Hasan M.A.Z., 1983: The "Whistler-nozzle" Phenomenon, J. Fluid Mech., vol. 134, pp. 431-458

[8] Zaman, K. B. M. Q., Hussain, A. K. M. F., 1980: Vortex pairing in a circular jet under controlled excitation, Part 1. General jet response, Journal of Fluid Mechanics, vol. 101, part 3, pp. 449-491

[9] Hussain, A. K. M. F., Zaman, K. B. M. Q., 1980: Vortex pairing in a circular jet under controlled excitation. Part 2. Coherent structure dynamics, Journal of Fluid Mechanics, vol. 101, part 3, pp. 493-544

[10] Hussain, A. K. M. F., 1986: Coherent structure and turbulence, Journal of Fluid Mechanics, vol. 173, pp. 303-356

[11] V. C. Patel, W. Rodi and G. Scheuerer: Turbulence Models for Near-Wall and Low Reynolds Number Flows: A Review August 1985, AIAA Journal 23(9):1308-1319, https://doi.org/10.2514/3.9086

[12] Abid, R., 1993: Evaluation of two-equation turbulence models for predicting transitional flows, International Journal of Engineering Science 31 (6) (1993) 831–840.

[13] Lam, C.K.G., Bremhost, K., 1981: A modified form of the k–ε model for prediction wall turbulence, Transactions of the ASME, Journal of Fluids Engineering 103 (1981) 456–460.

[14] Launder, B.E., Sharma, B.I., 1974: Application of the energy-dissipation model of turbulence to the calculation of flow near a spinning disc, Letters in Heat and Mass Transfer 1 (1974) 131–138.

[15] Abe, K., Kondoh, T., Nagano, Y., 1994: A new turbulence model for predicting fluid flow and heat transfer in separating and reattaching flows I: Flow field calculations, International Journal of Heat and Mass Transfer 37 (1) (1994) 139–151.

[16] Chang, K.C., Hsieh, W.D., Chen, C. S., 1995: A modified low-Reynolds-number turbulence model applicable to recirculating flow in pipe expansion, Transactions of the ASME, Journal of Fluids Engineering, 117, pp. 417–423.

NUMERICAL INVESTIGATION OF FLOWS AROUND SMALL-SCALE PROPELLERS: POSSIBILITIES AND CHALLENGES

Jelena Svorcan

Department of Aerospace Engineering, Faculty of Mechanical Engineering, University of Belgrade, Kraljice Marije 16, 11120 Belgrade 35
e-mail: jsvorcan@mas.bg.ac.rs

Abstract

This paper focuses on flows induced by small-scale propeller blades and the wakes shedding from their tips. Flows around propellers for unmanned air vehicles (approximately 25-75 cm in diameter) in hover are simulated by different approaches to considering turbulence. The challenges to simulating these kinds of flows mainly arise from the relatively low values of Reynolds numbers (several tens to several hundreds of thousands) when transition and other flow phenomena may be expected. The adopted numerical set-ups are validated though comparisons with available experimental data. It can be concluded that global aerodynamic performance can be determined with satisfactory accuracy (the discrepancies between computed and measured values of thrust and torque remain below several percents). However, discerning the actual flow characteristics remains challenging. Here, some distinguishing features of small Re rotational flows are accentuated and discussed. Vortex wakes shedding from the blades are visualized and analyzed. These two benchmark examples provide useful guidelines for further numerical and experimental studies of small-scale propellers.

Key words: UAV propeller, aerodynamic performance, hover, turbulence, wake.

1. Introduction

Modern day small-scale rotors common for unmanned aircraft or future urban air vehicles should satisfy several requirements: increased aerodynamic performance, reliability in various operating regimes, low noise. To satisfy these goals, engineers should first comprehend the induced flow fields in hover. For that reason, both numerical and experimental investigations of small-scale rotors have been intensifying over the past years [1-7]. This research also builds on previous studies [8,9] and focuses on low-to-medium Reynolds number (Re) flows forming around two different small-scale propeller rotors in hover.

Distributions of aerodynamic loads along rotating blades influence the two fundamental global aerodynamic quantifiers of propellers: generated thrust T at a required torque Q (power P), that are necessary for subsequent analyses (such as flight dynamics, stability and control, structural reliability) and determine the success of the complete system/aircraft. Unfortunately, there are numerous challenges to their accurate determination, both experimental and computational. On one hand, blade dimensions are small and real geometric features deviate from the modeled, airfoils designed for low Re are somewhat specific, insufficiently tested and highly

sensitive to outer disturbances, whilst high angular velocities require the use of sophisticated measuring equipment. Even when great care is taken, error bars appear quite wide, particularly when torque is investigated [6]. On the other hand, to provide reliable and usable results, contemporary numerical simulations require refined meshes, miniscule time scales and advanced approach to modeling/partially resolving turbulence [9,10].

In order to assess the possibilities and benefits of different numerical approaches, flows around two hovering small-scale propellers (approximately 25 cm and 75 cm in diameter) are computed and analyzed in more detail. Different flow assumptions befitting rotational lifting surfaces are employed, ranging from the simplest (BEMT, vortex models) to more complex, such as RANS and ultimately wall-modelled large eddy simulation (WMLES).

2. Formulation of the numerical models

Propeller analysis usually starts with hover, the most basic flight condition. Just how challenging this topic is, can be proved by the fact that AIAA Rotorcraft Hover Prediction Workshop is held every year at AIAA SciTech international conference (https://www.aiaa-hpw.org/hpw-vision). Challenges to both simulation and experimental measurements include zero inflow across outer boundaries, induced velocity field around the rotor, accurate load prediction, transition to turbulence, wake/tip vortex formation, expansion, development, interaction with the blades and final breakdown, aeroelasticity of the blades, appropriate visualization of the flow field, unconventional configurations (mutual effects of multiple rotors), performance of channeled rotors, aerodynamic noise, etc. To deal with these challenges, one (or all) of the following three categories of computational models is usually employed.

2.1 BEMT

Blade Element Momentum Theory (BEMT), derived from combining MT and BET, is a very simple but surprisingly accurate computational model, that is still very much employed [7,11]. Its major advantages are simplicity, ease of implementation, speed, and usable results. Some of the main disadvantages are that it assumes stationary, inviscid flow (which can be implicitly mitigated to some extent) and requires the knowledge of airfoil aerodynamic characteristics (which is often not available, particularly for novel/unconventional airfoils). The main outcomes from the computation are total thrust and torque (as well as the distributions of their derivatives along the blade) resulting from the complete velocity triangles on blade segments that are known once the induced velocity field is iteratively determined.

2.2 Vortex models

Whereas many variants exist (a very nice review is provided in [12]), vortex methods assume potential and most often unsteady flow. The leading result is a truthful representation of the wake that enables the analysis of its shape and effects on surrounding objects/structures. However, given that the computational cost is not negligible, computational fluid dynamics (CFD) techniques are much more common today.

2.3 CFD

Here, we also encounter many different approaches. The most employed are still the (unsteady) Reynolds-averaged Navier-Stokes, (U)RANS, equations [7,8], but more complex models, that resolve at least a portion of the turbulence spectrum (like DES or LES) are also being tested [9,10]. The primary advantage of RANS approach is computational simplicity. By assuming a quasi-steady flow field where inertial terms from the rotation are added to the equations, it is

possible to obtain a reasonable preliminary estimation of averaged aerodynamic loads. In the second phase, it is also possible to simulate the rotor rotation by actually moving a part of the mesh, which enables the consideration of transient effects. On the other hand, LES and DES are computationally still very costly since they require small spatial and temporal scales. They perform spatial filtering, which in turn, requires adequate sub-grid scale (SGS) modelling as well as special treatment of flow adjacent to the walls. In wall-modelled large eddy simulation (WMLES) larger-scale turbulent motion is resolved, while subgrid-scale motion (appearing in the wall vicinity) is considered more isotropic and can be modelled [13].

The choice of the numerical model dictates the way the geometry and computational mesh are generated. Usually, the domain is in a shape of a revolution body, whereas grids are hybrid unstructured, refined in the wall vicinity (to capture the sudden changes of flow quantities inside the boundary layer) and aft of the rotor to better capture the tip vortices and the developing wake. It is very important to perform valid grid convergence studies since numerical dissipation and instabilities are common. Adequate representation of the blade leading edge is also imperative since it directly influences transition to turbulence and profile drag, particularly at low-to-medium Re (several tens to hundreds of thousands). Trip is often introduced to enforce the transition end ensure dominantly turbulent flow since transition may be quite hard to accurately simulate. One should either come very close to the wall (and drastically increase the mesh size) or use appropriate wall functions. Since transition to turbulence and the accompanying laminar separation bubble (LSB) are still unresolved flow phenomena, different wall functions are tried and used. Important contributors to drag and wake formation are blade root and tip segments so special attention should be paid to them as well. It is now known and confirmed that the shed wake is very complex, comprising both primary (helicoidal) and secondary structures (rings around the main helicoids) that evolve and break down [14]. Adaptive mesh refinement may be employed to capture the wake shape, but many rotor rotations are needed, in turn causing numerical instabilities [15]. For that reason, experimental validation is still very much desired and necessary.

The problem becomes even more complicated if we take a step from the idealized, isolated, and rigid rotor to the installed elastic rotor (in full configuration) or in ground effect. Even the comparison to experimental measurements is not straightforward since the experimental results are affected by the fuselage, test stand and measuring equipment or wind tunnel walls and should be corrected (which introduces additional uncertainties to the analysis).

Possible outcomes from CFD analyses are extensive, both quantitative (thrust and torque/power, pressure and wall shear stress distributions) and qualitative (different visualizations of the flow field such as pressure or velocity contours, velocity vectors, wake shape, etc.).

3. Problem description

The geometric shape of small-scale propeller blades is usually quite complex and curved. It is defined by the spanwise distributions of airfoil (thickness and curvature), pitch and chord, which may be dominantly non-linear due to the use of modern materials and manufacturing technologies. Here, two different rotors (approximately 25 cm and 75 cm in diameter) are considered. Their detailed geometric descriptions may be found in [6,7].

Computations are performed using the finite-volume-based flow solvers charLES (compressible) and ANSYS FLUENT (incompressible). Fine meshes are generated to achieve fine spatial length scales. Small time steps and higher order discretization schemes are used. Zero-gauge pressures are assumed at the outer boundaries. To simulate rotation, computational domains are split into two zones where the inner zones, encompassing the propellers, rotate.

4. Results and discussion

Firstly, computed thrust and torque/power values are compared to the available experimental data [6,7]. As illustrated in Fig. 1, very satisfactory correspondence of thrust forces can be achieved even at Re spanning from approximately 80 to 300 thousand. For both rotors, the slightly bigger (diameter 75 cm) on the left, and the smaller (diameter 25 cm) on the right, differences between numerical and measured values remain within the error bars.

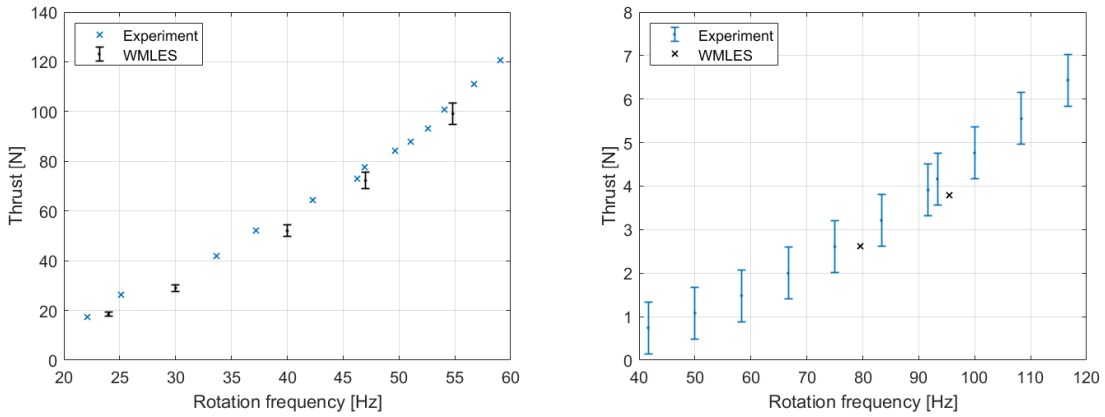

Fig. 1. Computed vs. measured thrust force: the 75 cm diameter propeller (left), the 25 cm diameter propeller (right).

The computed vortices, coloured by velocity, shedding from the blade tips of the 25 cm diameter propeller, viewed from two different angles, are illustrated in Fig. 2. It can be observed that even the mesh of approximately 8 million control volumes may not be sufficient to accurately capture all the complexities of the wake that should comprise both primary helicoidal and secondary vortices (forming around the primary structures). However, primary structures as well as blade/wake interaction seem well apprehended. More representative flow visualizations, obtained on more refined meshes around the 75 cm diameter propeller and by the flow solver charLES, are available in [9].

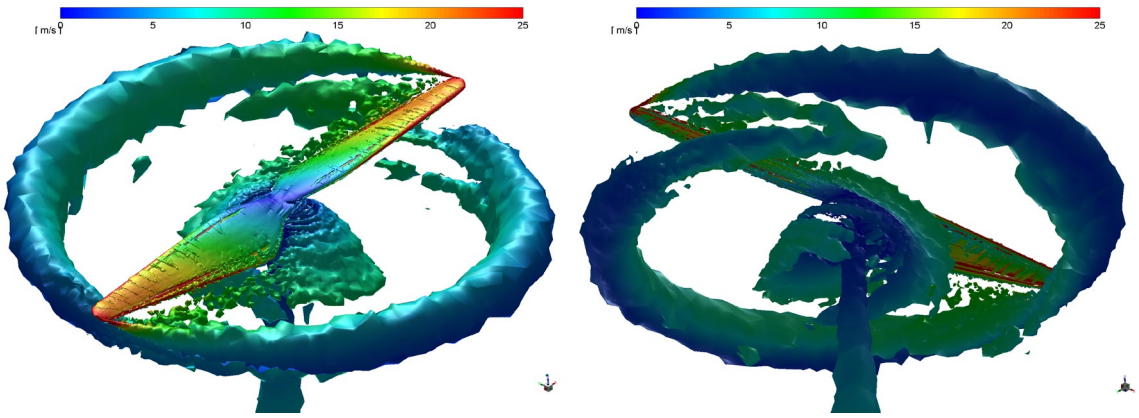

Fig. 2. Wake behind the 25 cm propeller computed by ANSYS FLUENT.

5. Conclusions

The paper addresses some of the issues present when simulating flows around propeller rotors. Some basic distinctions between large- and small-scale structures are outlined, in terms of geometry (small-scale ones are usually more curved), structural behavior (small-scale structures

are less susceptible to aeroelastic effects), control algorithms (small-scale structures are frequency controlled), operating conditions (small-scale structures usually operate in "filthier" flows) and flow physics (small-scale structures usually involve both laminar and turbulent flows, as well as the computationally very delicate transitional flows).

The most employed computational techniques can roughly be divided into three main groups: BEMT, vortex, and CFD methods. Generally, BEMT is excellent for preliminary and optimization studies (estimated thrust error can be around 10%). Vortex methods are used when the wake is in focus, but may simplify the flow too much, and their computational cost is almost comparable to RANS, whereas CFD methods offer the most comprehensive results, but that will also depend on the starting assumptions (thrust errors may range from less than 1% to more than 10%). Ideally, experiment and LES should be used and combined whenever possible. In that respect, this study demonstrates that WMLES presents a valuable tool for the design and analysis of small-scale propeller blades. Additionally, some important flow features as well as the hovering propeller wake are discerned.

Current and future trends in the analysis of these flows move towards more complex simulations (hybrid DES and LES), stronger correlation to experimental measurements, further inclusion of AI methods, smart control, etc.

Acknowledgement: This research work is supported by the Ministry of Science, Technological Development and Innovation of the Republic of Serbia through contract no. 451-03-47/2023-01/200105.

References:

[1] Carreño Ruiz M., Scanavino M., D'Ambrosio D., Guglieri G., Vilardi A., *Experimental and numerical analysis of hovering multicopter performance in low-Reynolds number conditions*, Aerospace Science and Technology, Vol. 128, 107777, 2022.

[2] Wang C., Li P., Guo C., Wang L., Sun S., *Numerical research on the instabilities of CLT propeller wake*, Ocean Engineering, Vol. 243, 110305, 2022.

[3] Zhang T., Barakos G.N., *High-fidelity numerical analysis and optimisation of ducted propeller aerodynamics and acoustics*, Aerospace Science and Technology, Vol. 113, 106708, 2021.

[4] Garofano-Soldado A., Sanchez-Cuevas P.J., Heredia G., Ollero A., *Numerical-experimental evaluation and modelling of aerodynamic ground effect for small-scale tilted propellers at low Reynolds numbers*, Aerospace Science and Technology, Vol. 126, 107625, 2022.

[5] Nathanael J.C., Wang C.-H.J., Low K.H., *Numerical studies on modeling the near- and far-field wake vortex of a quadrotor in forward flight*, Proceedings of the Institution of Mechanical Engineers, Part G: Journal of Aerospace Engineering, Vol. 236(6), 1166-1183, 2022.

[6] Russell C., Willink G., Theodore C., Jung J., Glasner B., *Wind tunnel and hover performance test results for multicopter UAS vehicles*, NASA/TM−2018−219758, NASA Ames Research Center, Moffett Field, CA, 2018.

[7] Kovačević A., Svorcan J., Hasan M.S., Ivanov T., Jovanović M., *Optimal propeller blade design, computation, manufacturing and experimental testing*, Aircraft Engineering and Aerospace Technology, Vol. 93(8), 1323-1332, 2021.

[8] Svorcan J., Kovačević A., Tanović D., Hasan M.S., *Towards viable flow simulations of small-scale rotors and blade segments*, Theoretical and Applied Mechanics, Vol. 48(2), 143-157, 2021.

[9] Svorcan J., Wang K., Ivey C., Kovačević A., *Estimating the performance of a small-scale non-isolated propeller in hover using WMLES*, Center for Turbulence Research Annual Research Briefs, 87-95, 2022.

[10] Stratton Z., Spyropoulos J.T., Bose S., Svorcan J., *Rotor performance and turbulent wake simulations of a scaled helicopter rotor in hover using wall-modeled large-eddy simulations*, AIAA SciTech Forum, AIAA 2023-2636, 2023.
[11] Svorcan J., Hasan M.S., Kovačević A., Ivanov T., *Design of HALE propeller through multi-objective optimization*, AIAA Propulsion and Energy Forum, AIAA 2021-3730, 2021.
[12] Lee H., Sengupta B., Araghizadeh M.S., Myong R.S., *Review of vortex methods for rotor aerodynamics and wake dynamics*, Advances in Aerodynamics, Vol. 4(1), 20, 2022.
[13] Moin P., Bodart J., Bose S., Park G.I., *Wall-modeling in complex turbulent flows*, Notes on Numerical Fluid Mechanics and Multidisciplinary Design, Vol. 133, 207-219, 2016.
[14] Schwarz C., Bodling A., Wolf C.C., Brinkema R., Potsdam M., Gardner A.D., *Development of secondary vortex structures in rotor wakes*, Experiments in Fluids, Vol. 63(1), 4, 2022.
[15] Abras J.N., Narducci R., Hariharan N., *Impact of high-fidelity simulation variations on wake breakdown of a rotor in hover*, AIAA SciTech 2020 Forum, AIAA 2020-0531, 2020.

VIBRATIONS OF FLUID-CONVEYING FUNCTIONALLY GRADED NANOTUBES

Nikola Despenić and Goran Janevski

Faculty of Mechanical Engineering, University of Niš
Aleksandra Medvedeva 14, Niš
e-mail: nikola.despenic@masfak.ni.ac.rs, gocky.jane@gmail.com

Abstract

In this study, a size-dependent Euler-Bernoulli nanobeam model is used for free vibration of a fluid-conveying functionally graded nanotube. The variation of material properties is supposed along the radial direction of the nanotube, and the effective material properties are expressed using the power-law distribution. The thermal effect is presented using two different cases, uniform temperature rise, where the temperature changes uniformly through the nanotube, and linear temperature rise, in which the temperature of functionally graded nanotube varies linearly along the radius of the nanotube. The governing equations are derived, based on Eringen's nonlocal elasticity theory, through Hamilton's principle. The results are obtained using Galerkin's method as well as from the available literature. Natural frequencies, critical fluid velocity and thermal buckling load are presented. As mentioned above, material of the nanotube model is based on the power-law distribution, so the effect of the power-law index and nonlocal parameter on the natural frequency, critical fluid velocity and thermal buckling load are analyzed.

Key words: nanotube, vibration, fluid-conveying, functionally graded materials, critical fluid velocity, thermal buckling.

1. Introduction

It is well known that nanotechnology is in expansion, with a huge application in engineering. Nanostructures are applied in many fields of engineering industry, especially in nano-electro-mechanical-systems (NEMS), with applications in nanosensors and nanoactuators. Investigations in this field have been of interest for the scientific community in the past decade, where nanobeams, nanoplates, nanoshells and others are some of the topics already explored by scientists. Also, another interesting topic that appears in papers is composite materials, where a relatively new class of composite materials called functionally graded materials (FGM) is observed. The main characteristic of FGM is that material properties (Young's modules, density, Poisson's ratio etc.) smoothly changes through the nanostructure, whose ends are pure materials. The combination of these topics has been the focus of many investigations, and this field has been found attractive for many industries such as electrical engineering, aerospace engineering, biomedical engineering, etc.

The investigation of the mechanical behavior of nanostructures is of great interest. The fact that the classical continuum theory has its limitations when it comes to small structures, created a

need for a theory that can be acceptable for modeling small (nanoscale) devices. Based on that, Eringen's nonlocal elasticity theory [1-2], which includes size-dependent effects where the stress at a reference point depends on the strain in the region near that point, has become applicable for nano-scale devices.

Based on Eringen's nonlocal elasticity theory, dynamic behavior of single-walled and double-walled carbon nanotube are investigated in [3-4] with influence of nonlocal parameter, temperature change, Winkler type coefficients, etc.

Dynamic behavior of multibeam system has not gone unnoticed by researchers [5-6]. Stochastic stability, vibration and buckling analysis of multi-nanobeam systems has been analyzed.

Vibration analysis of nonlocal FGM nanobeam model was analyzed in [7-8]. The impact of temperature change, nonlocal parameter, power-law exponent, axial load, etc. were also considered. Natural frequencies and vibrational analysis of porous nanotubes were considered in [9-10] with varying values of nonlocal and strain gradient parameters.

Fluid-structure interactions are always attractive for research, especially because of huge applications in the industry. Fluid conveying on the nano level finds application in nuclear reactors, transportation, electronics, biomedicine and so on [11]. Based on that claim, many papers have investigated vibrations of nanopipes with a fluid being conveyed through them [12-13]. The effects of the magnetic field, Knudsen number and fluid velocity are one of the many effects which are considered through the mentioned papers.

In this paper, based on the Euler - Bernoulli nanobeam models, nondimensional frequency, critical temperature load and dimensionless critical fluid velocity will be examined. The material varies along the radial direction of the nanotube, where the effective material properties are expressed using the power-law distribution. Within the framework of Eringen's nonlocal elasticity model, the governing equations are obtained through Hamilton's principle, and solved with the Galerkin method approach. The effect of thermal load is presented in the form of uniform temperature rise and linear temperature rise where results will be obtained and figured. The fluid velocity effect is also considered in the paper, and critical fluid velocity will be examined and analyzed. The effect of nonlocal parameter on the nondimensional frequency, dimensionless critical fluid velocity and critical temperature will also be considered. Finally, the present work draws certain important conclusions which will be summarized at the end.

2. Mathematical model

2.1 Problem description

Consider a nanotube of functionally graded material, where the graded material properties are assumed to be in the radial direction. The system of interest is a cylindrical functionally graded nanobeam of length L, inner radius R_0 and outer radius R_1 (Fig. 1). The nanotube is subjected to an in-plane thermal loading, where, according to the rule of mixture, the effective material properties P_f are distributed as follows [14]:

$$P(r,T)=\left(P_c(T)-P_m(T)\right)\left(\frac{r-R_0}{R_1-R_0}\right)^p+P_m(T) \tag{1}$$

where $P_c(T)$ and $P_m(T)$ are corresponding temperature dependent material properties for ceramic and metal, respectively. The inner surface $(r=R_0)$ of the FG nanotube is pure metal $(SUS304)$ and the outer surface $(r=R_1)$ is pure ceramic (Si_3N_4). A table with the values of

temperature-dependent coefficient of material properties for Si_3N_4 and $SUS304$ can be seen in [7].

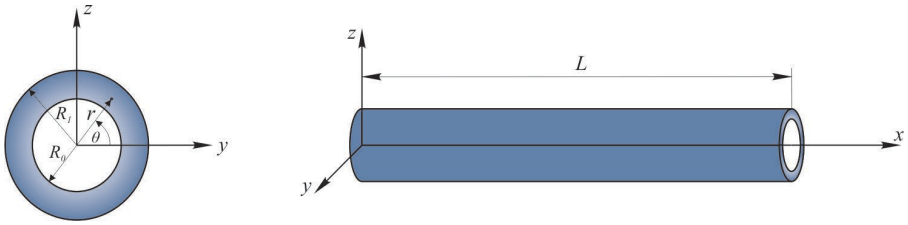

Fig. 1. Geometry and coordinates of the functionally graded nanotube.

2.2 Kinematic relations

Based on the Euler-Bernoulli beam theory, the displacement field of the nanotube can be written as:

$$q_x = u(x,t) - z\frac{\partial w}{\partial x} \tag{2}$$

$$q_z = w(x,t) \tag{3}$$

where u and w are the displacement components of the mid-plane in the x and z directions, respectively. Strain field, based on equations (2) and (3) and in line with the used theory, can be written as:

$$\varepsilon_{xx} = \frac{\partial u}{\partial x} - z\frac{\partial^2 w}{\partial x^2} \tag{4}$$

Hamilton's principle is used to obtain the governing equations of motion, which are expressed as:

$$\int_{t_1}^{t_2}\left(\delta U + \delta V - \delta T_p - \delta T_f\right)dt = 0 \tag{5}$$

in a time interval $t_1 < t < t_2$. Virtual strain energy is expressed as:

$$\delta U = \int_V \sigma_{xx}\delta\varepsilon_{xx}dv = \int_L\left(N_{xx}\delta\frac{\partial u}{\partial x} - M_{xx}\delta\frac{\partial^2 w}{\partial x^2}\right)dx \tag{6}$$

where the following stress resultant are expressed as:

$$N_{xx} = \int_A \sigma_{xx}dA,\ \ M_{xx} = \int_A z\sigma_{xx}dA \tag{7}$$

The virtual kinetic energy of the nanotube model δT_p can be defined in the following form:

$$\begin{aligned}\delta T_p &= \frac{1}{2}\int_v \rho(T,r)\delta\left(\left(\frac{\partial q_x}{\partial t}\right)^2 + \left(\frac{\partial q_y}{\partial t}\right)^2 + \left(\frac{\partial q_z}{\partial t}\right)^2\right)dv = \\ &= \int_0^L\left(I_0\left(\frac{\partial u}{\partial t}\delta\left(\frac{\partial u}{\partial t}\right) + \frac{\partial w}{\partial t}\delta\left(\frac{\partial w}{\partial t}\right)\right) - I_1\left(\frac{\partial u}{\partial t}\delta\left(\frac{\partial^2 w}{\partial x\partial t}\right) + \frac{\partial^2 w}{\partial x\partial t}\delta\left(\frac{\partial u}{\partial t}\right)\right)\right.\end{aligned} \tag{8}$$

where the mass moments of inertia are defined as follows:

$$\left(I_0, I_1, I_2\right) = \int_{R_0}^{R_1}\int_0^{2\pi}\left(1, z, z^2\right)\rho\left(r,T\right) r dr d\theta \tag{9}$$

The variation of the work δV by thermal expansion:

$$\delta V = -\int_v E\left(T,r\right)\alpha\left(T,r\right)\left(T-T_0\right)\frac{\partial w}{\partial x}\frac{\partial}{\partial x}\left(\delta w\right) dv = -\int_0^L\left(N^T\frac{\partial w}{\partial x}\frac{\partial}{\partial x}\left(\delta w\right)\right) dx \tag{10}$$

where N^T is thermal resultant expressed as:

$$N^T = \int_{R_0}^{R_1}\int_0^{2\pi} E\left(T,r\right)\alpha\left(T,r\right)\left(T-T_0\right) r dr d\theta \tag{11}$$

and $T_0 = 300K$ is the reference temperature. The virtual kinetic energy of the fluid can be written as:

$$\begin{aligned}\delta T_f &= \frac{1}{2}\int_v \rho_f \delta\left(\left(\frac{\partial u}{\partial t} + V + V\frac{\partial u}{\partial x}\right)^2 + \left(\frac{\partial w}{\partial t} + V\frac{\partial w}{\partial x}\right)^2\right) dv = \\ &= m_f\int_0^L\left(\left(\frac{\partial u}{\partial t} + V + V\frac{\partial u}{\partial x}\right)\left(\frac{\partial \delta u}{\partial t} + V\frac{\partial \delta u}{\partial x}\right) + \left(\frac{\partial w}{\partial t} + V\frac{\partial w}{\partial x}\right)\left(\frac{\partial \delta w}{\partial t} + V\frac{\partial \delta w}{\partial x}\right)\right) dx\end{aligned} \tag{12}$$

where $m_f = \rho_f A_f$ is the mass per unit length of the fluid.

The governing equations of motion can be achieved by substituting Eqs. (6), (8), (10) and (12) into Eq. (5), using integration by parts and setting the coefficients of δu and δw to zero:

$$\delta u\text{:}\ \frac{\partial N_{xx}}{\partial x} = \left(I_0 + m_f\right)\frac{\partial^2 u}{\partial t^2} - I_1\frac{\partial^3 w}{\partial x \partial t^2} + 2m_f V\frac{\partial^2 u}{\partial x \partial t} + m_f V^2\frac{\partial^2 u}{\partial x^2} \tag{13}$$

$$\delta w\text{:}\ \frac{\partial^2 M_{xx}}{\partial x^2} - N^T\frac{\partial^2 w}{\partial x^2} = \left(I_0 + m_f\right)\frac{\partial^2 w}{\partial t^2} + I_1\frac{\partial^3 u}{\partial x \partial t^2} - I_2\frac{\partial^4 w}{\partial x^2 \partial t^2} + 2m_f V\frac{\partial^2 w}{\partial x \partial t} + m_f V^2\frac{\partial^2 w}{\partial x^2} \tag{14}$$

Based on Eringen's nonlocal elasticity theory [1-2], which includes size-dependent effects where the stress at a reference point depends on the strain in the region near that point, for the one-dimensional case, the relationship between the stress and strain can be written as:

$$\sigma_{xx} - \mu^2\frac{\partial^2 \sigma_{xx}}{\partial x^2} = E\left(r,T\right)\varepsilon_{xx} \tag{15}$$

where $\mu = ea$ is a nonlocal parameter. By applying Eringen's nonlocal elasticity theory and substituting the derivative for N_{xx} and M_{xx} into Eqs. (13) and (14), the nonlocal governing equations of the FG nanotube model can be derived as follows:

$$A_{xx}\frac{\partial^2 u}{\partial x^2} - B_{xx}\frac{\partial^3 w}{\partial x^3} = \left(1 - \mu^2\frac{\partial^2}{\partial x^2}\right)\left[\left(I_0 + m_f\right)\frac{\partial^2 u}{\partial t^2} - I_1\frac{\partial^3 w}{\partial x \partial t^2} + 2m_f V\frac{\partial^2 u}{\partial x \partial t} + m_f V^2\frac{\partial^2 u}{\partial x^2}\right] \tag{16}$$

$$B_{xx}\frac{\partial^3 u}{\partial x^3} - D_{xx}\frac{\partial^4 w}{\partial x^4} = \left(1-\mu^2\frac{\partial^2}{\partial x^2}\right)\left[\left(I_0+m_f\right)\frac{\partial^2 w}{\partial t^2} + I_1\frac{\partial^3 u}{\partial x\partial t^2} - I_2\frac{\partial^4 w}{\partial x^2\partial t^2} + 2m_f V\frac{\partial^2 w}{\partial x\partial t} + m_f V^2\frac{\partial^2 w}{\partial x^2} + N^T\frac{\partial^2 w}{\partial x^2}\right] \quad (17)$$

3. Solution procedure

By eliminating u from Eqs. (16) -(17), the governing differential equation becomes:

$$P_1\frac{\partial^4 w}{\partial t^4} + P_2\frac{\partial^3 w}{\partial t^3} + P_3\frac{\partial^2 w}{\partial t^2} + P_4\frac{\partial w}{\partial t} + P_5 w = 0 \quad (18)$$

where $P_1,...P_5$ are operators which consist of material and mass coefficients of the nanotube and coefficients that belongs to fluid and thermal effect. Using the method of separating variables, the transverse displacement function can be supposed as:

$$w(x,t) = \sum_{k=1}^{N}\varphi_k(x)e^{i\omega_k t} = \sum_{k=1}^{N} sin(\lambda x)e^{i\omega_k t} \quad (19)$$

where $i=\sqrt{-1}$ and $\lambda = k\pi/L$. After substituting Eq. (19) into Eq. (18), and applying Galerkin method to solve the governing equation of the FG nanotube model, the frequency equation becomes:

$$A_\omega\omega_k^4 + B_\omega\omega_k^2 + C_\omega = 0 \quad (20)$$

in which the smaller root of Eq. (20) is

$$\omega_\kappa^2 = \frac{-B_\omega + \sqrt{B_\omega^2 - 4A_\omega C_\omega}}{2A_\omega} \quad (20)$$

4. Results and discussion

This section presents the results that determine the impact of conveying fluid, temperature change, gradient index p and nonlocal parameter μ on the nondimensional natural frequencies. For different values of the nonlocal parameter and gradient index, dimensionless critical velocity and buckling temperature are examined. Also, nondimensional natural frequencies are obtained. The geometry of the nanotube is presented in Fig. 1, with the dimensions: $L=100$ nm, inner radius $R_0=0.5$ nm and outer radius $R_1=1$ nm. The functionally graded nanotube is composed of metal (SUS304) for the inner surface and ceramic (Si_3N_4), for the outer surface.

$\mu\ (nm)$	Ω_1			Ω_2			Ω_3	
	[15]	Present		[15]	Present		[15]	Present
0	8.234	8.3764		31.154	33.1699		64.833	73.4224
1	8.134	8.2749		29.752	31.6450		58.647	66.4173
2	7.855	7.9913		26.739	28.0860		47.180	53.4315
3	7.449	7.5772		22.672	24.1386		37.440	42.4003

Table 1. Comparison with Ref. [16] of the nondimensional natural frequency for a SS FG nanotube.

The presented method is confirmed by comparing it with the results from the literature, for the same parameters [16]. For different values of the nonlocal parameter μ, results are presented in Table 1. For this purpose, dimensionless velocity $v = V\sqrt{m_f L^2 / E_{m0} I_f}$ is set to zero. It should be noted that the reference paper used the refined beam theory as opposed to this paper which used Euler-Bernoulli beam theory.

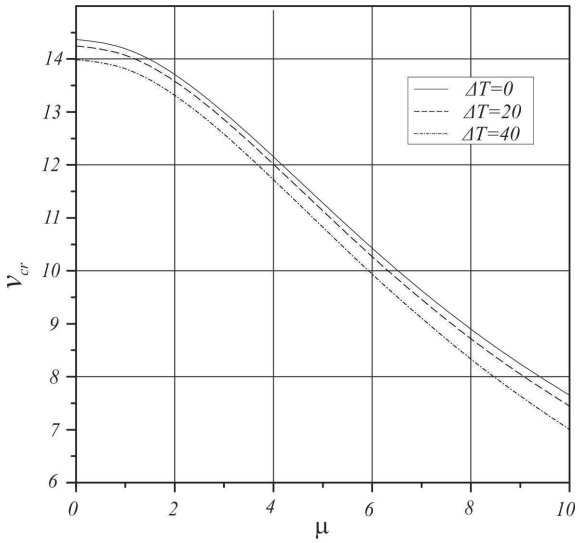

Fig. 2. Dimensionless critical fluid velocity versus nonlocal parameter with different values of temperature change ($p = 1$, $L/R_1 = 20$).

The influence of the nonlocal parameter on the critical fluid velocity is shown in Fig. 2. As it is illustrated, the increasing nonlocal parameter causes a decrease in critical fluid velocity. The decreasing of critical fluid velocity is more noticeable with higher values of the nonlocal parameter. Figure 3. shows the impact of dimensionless fluid velocity on the nondimensional frequency of the nanotube model, for different values of temperature change. It should be noted that increase in dimensionless critical fluid velocity results in a decrease in nondimensional frequency until it reaches zero, where critical fluid velocity is obtained.

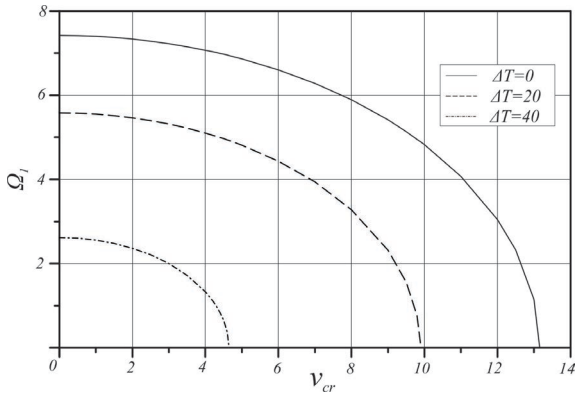

Fig. 3. Dependance of nondimensional frequency and dimensionless critical fluid velocity with different values of thermal load ($p = 1$, $L/R_1 = 100$, $\mu = 0$).

Also, an increase in temperature change results in a decrease in nondimensional frequency. Another finding is illustrated in Fig. 4. which shows the dependence of the critical buckling temperature load and nonlocal parameter. The impact of dimensionless fluid velocity can also be seen. It is observable from this figure that higher values of nonlocal parameter led to lower

critical temperature loads. The dependence of nondimensional natural frequency and critical fluid velocity is shown in Fig. 3. with different temperature values. The question arises as to how the dependence of the nondimensional frequency and the critical buckling temperature load, which is presented in Fig. 5, looks like. It is concluded that nondimensional frequency has higher values for lower values of temperature load. An increase in temperature load leads to a decrease in nondimensional frequency, until it becomes zero. A sharp decrease was observed in the zone where temperature load reaches a critical value.

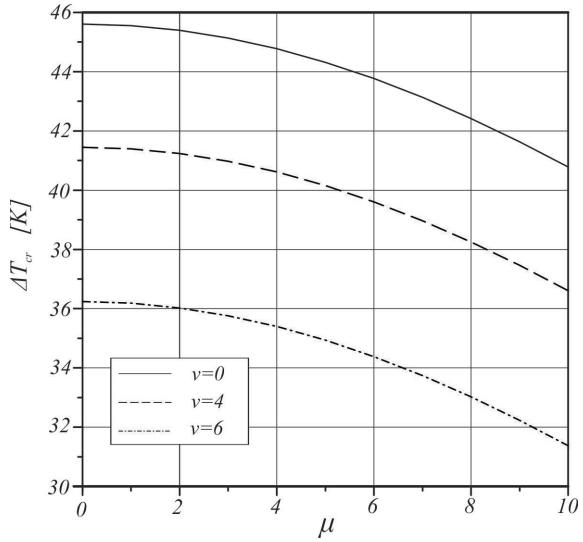

Fig. 4. Dependence of critical buckling temperature load and nonlocal parameter with different fluid velocities ($p=1$, $L/R_1=100$).

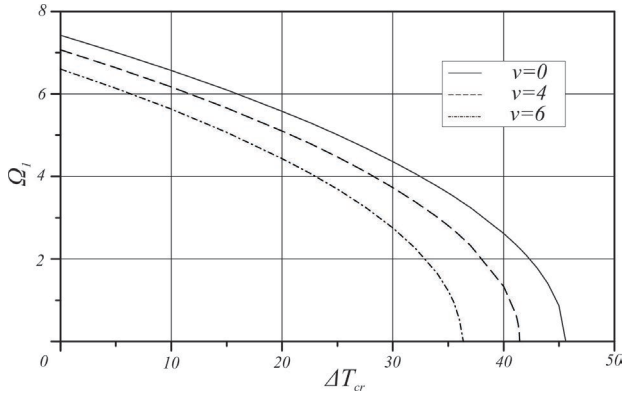

Fig. 5. Dependence of nondimensional frequency and critical buckling load with different values of fluid velocity ($p=1$, $L/R_1=100$, $\mu=0$).

5. Conclusion

This paper investigates the vibration, thermal buckling load and critical fluid velocity of the fluid-conveying FG nanotube model. The equations of motion are obtained through Hamilton's principle and based on the Euler-Bernoulli beam theory within the framework of Eringen's nonlocal elasticity theory. The investigation is based on the impact of fluid velocity and temperature load on nondimensional natural frequency. Also, the effect of the nonlocal parameter is observed. Numerical results are obtained by using Galerkin's method. It can be concluded that there is an obvious impact of nonlocal parameter, where an increase in the nonlocal parameter will decrease the nondimensional frequency, critical buckling load and critical fluid velocity. The influence of fluid velocity on the change in nondimensional frequency is observed, reflected in

increasing fluid velocity and decreasing frequency that leads to zero, which represents the critical fluid velocity. A similar observation comes from the investigation into the impact of temperature change on nondimensional frequency, where an increase in thermal load leads to a decrease in natural frequency until it reaches critical buckling load. The effect of the power law exponent can be seen through the results shown in the tables. It can be observed that lower values of the power law exponent lead to higher values of frequency, thermal buckling load and critical fluid velocity.

References:

[1] Eringen, A.,C., *On differential equations on nonlocal elasticity and solutions of screw dislocation and surface waves,* Journal of Applied Physics, Vol. 54, 138-155, 1983.

[2] Eringen, A.,C., *Nonlocal continuous field theories,* Springer Science & Business Media, New York, 2002.

[3] Murmu T., Pradhan S., C., *Thermo-mechanical vibration of a single-walled carbon nanotube embedded in an elastic medium based on nonlocal elasticity theory,* Computational Material Science, Vol. 46, 854-859, 2009.

[4] Ke L., L., Xiang Y., Tang J., Kitipornchai S., *Nonlinear free vibration of embedded double-walled carbon nanotubes based on nonlocal Timoshenko beam theory,* Computational Material Science, Vol. 47, 409-417, 2009.

[5] Pavlović I., Karličić D., Pavlović R., Janevski G., Ćirić I., *Stochastic stability of multi-nanobeam system,* International Journal of Engineering Science, Vol. 109, 88-105, 2016.

[6] Stamenković Atanasov M., Karličić D., Kozić P., Janevski G., *Thermal effect on free vibration and buckling of a double-microbeam system,* Facta Universitatis, Vol. 15, 45-62, 2017.

[7] Ebrahimi F., Salari E., *Nonlocal thermo-mechanical vibration analysis of functionally graded nanobeams in thermal environment,* Acta Astronautica, Vol. 113, 29-50, 2015.

[8] Ebrahimi F., Salari E., *Thermal buckling and free vibration analysis of size dependent Timoshenko FG nanobeams in thermal environments,* Composite Structures, Vol. 113, 29-50, 2015.

[9] Karami B., Janghorban M., *On the dynamics of porous nanotubes with variable material properties and variable thickness,* International Journal of Engineering Science, Vol. 136, 53-66, 2019.

[10] She G., Ren Y., Yuan F., Xiao W., *On vibrations of porous nanotubes,* International Journal of Engineering Science, Vol. 125, 23-35, 2018.

[11] Wong K., V., De Leon O., *Applications of Nanofluids: Current and Future,* Advances in Mechanical Engineering, Vol. 2, 1-11, 2010.

[12] Liu H., Lv Y., Tang H., *Nonlinear vibration and instability of functionally graded nanopipes with inital imperfection conveying fluid,* Applied Mathematical Modelling, Vol. 76, 133-150, 2019.

[13] Bahaadini R., Saidi A., R., Hosseini M., *On dynamics of nanotubes conveying nanoflow,* International Journal of Engineering Science, Vol. 123, 181-196, 2018.

[14] Janevski G., Despenić N., Pavlović I., *Thermal buckling and free vibration of Euler-Bernoulli FG nanobeams on the higher-order nonlocal strain gradient thoery,* Archives of Mechanics, Vol. 72, 139-167, 2020.

ON THE TRAIL OF VUJIČIĆ'S COORDINATES-INDEPENDENT POSITION VECTOR FORM: ROTATIONALLY-INVARIANT/(CLASSICALLY-)COVARIANT TRAJECTORIAL COORDINATES SYSTEM FORMULATION AND OTHER REPERCUSIOS FOR THE MECHANICS / DYNAMICS MODELING[1]

Slobodan Nedić

Faculty of Technical Sciences, University of Novi Sad, Dr. Zorana Đinđića 1, 21102 Novi Sad
e-mail: nedics@uns.ac.rs, nedic.slbdn@gmail.com

Abstract

Starting from strictly distinguishing between the 'transformation' of the coordinates of a point defined by their functional relation itself and the transformation of the coordinates of a vector/tensor (velocity, acceleration, gradient, displacement) - at the point (in line with the Vujičić's coordinates-independent point's position vector formulation), by applying the unified procedure of forming the corresponding basis vectors, derivation of the covariantly consistent components of the acceleration in the trajectories' coordinates base is accomplished, which turn out formally (presence of the second instead of the third derivatives of coordinates) and substantively (tractability of non-autonomous non-linear differential equations modeling) to be different from traditionally used heuristically/ad-hoc formulated "natural" tangent-normal coordinates. As a very important and far-reaching implication, by relying on numerical integration for the case of Orbital Motion, illustrated is the importance and effectiveness of a consistent (rotational-invariant) approach as an indicator of possible essential (in)correctness of the formed dynamic models, as well as the need for separation of kinematics and dynamics related parts of non-linear differential equations. Also, a kind of tensor's 'vectorization' is suggested to be thought of as the means to check for the validity of various tensors calculus formalisms, including the spatial derivatives.

Keywords: transformation of coordinates, rotational invariance, covariant differentiation.

1. Introduction

Ever since the Descartes' 'algebrization' of geometry through introduction of the rectangular system's coordinates, the analysis and modeling of physical and dynamical systems were proceeded with introduction of quantities and concepts referred to systems of coordinates that appeared suitable for the systems' geometries, going over polar and tangential-normal coordinates for respectively orbital motion and technical/aero-nautical applications, to the relativistic-Lorentz transformations for STR and GTR, along transitioning from the flat Euclidian (extrinsic, 3-D) to the curved surfaces (intrinsic, 2-D Riemannian) abstracted geometry. Although the notions of invariance of a particular point as an element of trajectory in space, distance between such two

[1] *Dedicated to the memory of the late professor Veljko Vujičić.*

points, rate of change of that distance (velocity), acceleration and so on have officially been deeply rooted in the foundations of mechanics and physics, it is due mainly to inadequate and deficient formulations of physical and dynamical laws that instead the invariance, in the sense of independence of their very differential-algebraic forms, have largely been taking precedence.

In the course of development of the concepts of absolute and/or covariant differentiation, on one side motivated by simplification of the related procedures of the analytic and/or numerical integrations pertinent to the straightforwardly applied differential calculus to vector-valued functions, and on the other – ensuring invariant representation of differential quantities as quadratic forms and differential parameters, it turns out that the since long present and used expressions for the components of acceleration in the so-called "non-inertial" polar coordinate system actually are the long searched for "reduced forms" of the coordinates transformation, whereby the partial derivatives representing the entries of the corresponding Jacobian matrix are eliminated, and only the targeted coordinates time-derivatives remain. While the feasibility of such goal had already been demonstrated by both the Hertz's "Principles of Mechanics," [1], and was the main goal of one of pioneers of the covariant and absolute differentiation development, [2], the reliance on Christoffel symbols of the 2nd kind has remained virtually indispensable in the process of differentiation and integration in the (locally orthogonal) curvilinear coordinates.

Thus, for no other viable reason other than the deliberately 'proclaimed' inadequacy of the formally equivalent formulation of the position vector of a point in the rectangular and the polar systems of coordinates, respectively $\boldsymbol{r} = y^i \cdot \boldsymbol{e}_i = x^i \cdot \boldsymbol{g}_i$ - although implied in all textbooks for the very basis vectors determination[2] -, the attempts of V. Vujičić [4] (coauthored by the late Prof. V. Nikolić) to promote and justify formulation of covariant and absolute differentiation which essentially 'obsoletes' the modern procedures in the context of the so-called intrinsic Riemannian differential geometry (where the surface parameterization by u and υ essentially is same as the 2-D flat surface parameterization by distance/radius ($x^1 = \rho$) and polar angle ($x^2 = \varphi$), have been fiercely opposed. Although not referred to directly, in [5] has – as only viable option – rather been advocated the brute-force approach with the untenable 'enforcement' of the velocity-invariance for numerous curvilinear coordinate systems by imposing the conditions on the very Christoffel symbols, with the involvement of - by large not needed - time-differentiations of the basis vectors themselves, despite their "covariant constancy", that is their zero-valued covariant derivatives.

In this submission it will be shown that the consequent application of the concept of "vector at the point" of [6] essentially represents the very same formulation of the tensors' components transformational definition, and that the covariant differentiation/integration essentially reduces to the simple rotationally-invariant transformation between the two coordinates systems, the related rotation matrix essentially 'absorbing' the location/time variant components of the (normalized) basis vectors, thus avoiding the problematic geometrizing of/in the essentially algebraic realm.

Firstly, in Section 2 –offers straightforward, coordinates line-integral based proof for the equivalence, a kind of invariance of the material point position vector formulation. Then, Section 3 shows the derivation of the expressions for the (classically) covariant and/or rotationally-invariant velocities and accelerations at the point of trajectory derived in the coordinate-lines tangential space, along with the derivation of equivalence of the rotational-invariance and classical covariance. The consistency of the absolute differentiation/integration without the necessity to use the Christoffel symbols in the context of orbital mechanics and the Newton-Keplerian elliptic trajectories [7] is referred to, as well as the inadequacy of the traditional orbital mechanics formulation[3]. Further, in Section 4, the covariant/invariant velocities and accelerations in the trajectorial tangential coordinates are derived by pure extension and compared through

[2] It has been only recently that the tensor-like equivalence of the two expressions was demonstrated in [3].
[3] Analysis of inadequate transformation of coordinates in the context of Euler's top-equation is done in [8].

analytic expression and numerical differentiation with the heuristic/ad-hoc natural one. In Section 5 are discussed some spatial covariant differentiation and models equations related issues.

2. Resolving Controversy over nature, formulation and transformation of position vector[4]

The arguments for alleged impossibility of the fully operational representation of point-P position vector in the two systems of coordinates – the Cartesian ($y^1 = x$ i $y^2 = y$) and the polar one ($x^1 = \rho$ and $x^2 = \varphi$) –, with their functional (mutually invertible/inversible) relations $y^1 = x^1 \cdot cos\left(x^2\right) = \rho \cdot cos(\varphi)$; $y^2 = x^1 \cdot sin\left(x^2\right) = \rho \cdot sin(\varphi)$ and $x^1 = \rho = \sqrt{\left(y^1\right)^2 + \left(y^2\right)^2}$ $= \sqrt{(x)^2 + (y)^2}$; $x^2 = \varphi = arctng\left(\frac{y^2}{y^1}\right) = arctng\left(\frac{y}{x}\right)$ in the unified form $\boldsymbol{r} = y^i \cdot \boldsymbol{e}_i = x^i \cdot \boldsymbol{g}_i$, with $i = 1,2$, where the respective basis vectors are determined by unified definitional relations $\boldsymbol{g}_i = \frac{\partial \boldsymbol{r}}{\partial x^i}$ and $\boldsymbol{e}_i = \frac{\partial \boldsymbol{r}}{\partial y^i}$, whereby the location-dependent polar coordinates basis vectors are produced (with application of the differentiation chain-rule) are $\mathbf{g}_1 = cos(\varphi) \cdot \mathbf{e}_{1/x} + sin(\varphi) \cdot \mathbf{e}_{2/y}$ and $\mathbf{g}_2 = \rho \cdot \left[-sin(\varphi) \cdot \mathbf{e}_{1/x} + cos(\varphi) \cdot \mathbf{e}_y\right]$, or expressed through the corresponding orthonormal (unit) basis vectors $\mathbf{g}_1 = \mathbf{e}_\rho$ and $\mathbf{g}_2 / |\mathbf{g}_2| = \mathbf{e}_\varphi$ as $\mathbf{r}^P = \rho \cdot \mathbf{e}_\rho + \rho \cdot \varphi \cdot \mathbf{e}_\varphi$ --- are found to be twofold:

1. The position vector representation in polar coordinates is reduced to its radial part $\rho \cdot \mathbf{e}_\rho$;
2. By essentially naïve direct replacement of polar basis vectors as functions of Cartesian coordinates basis vectors, the position vector gets produced in the form $\mathbf{r} = \rho \cdot \left[cos(\varphi) - \varphi \cdot sin(\varphi)\right] \cdot \mathbf{e}_x + \rho \cdot \left[sin(\varphi) + \varphi \cdot cos(\varphi)\right] \cdot \mathbf{e}_y$, different from the one in which the coordinates substitutions are performed, i.e. $\mathbf{r}^C = \rho \cdot cos(\varphi) \cdot \mathbf{e}_x + \rho \cdot sin(\varphi) \cdot \mathbf{e}_y$.

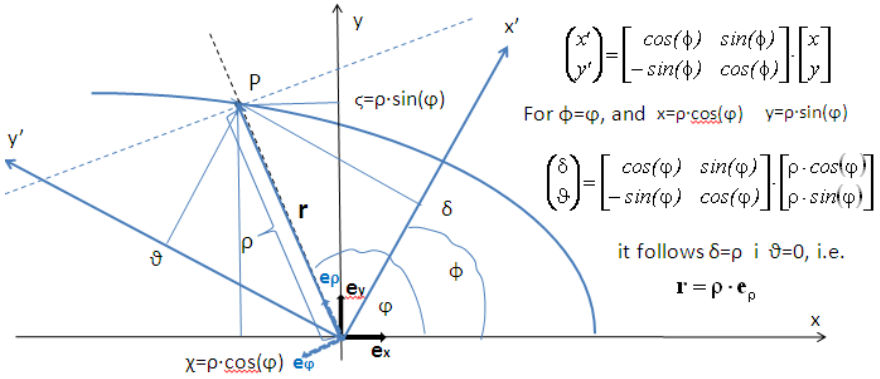

Fig. 1. Illustration of rotational and 'tensorial' transformation (w.r.t. coordinates origin) of position vector.

With reference to Fig. 1, which shows the transformation of the Cartesian coordinates (*x,y*) into the (*x',y'*) ones by rotation by an angle ϕ, so that for the particular *x*- and *y*-components determined by the very functional relation between the Cartesian and polar coordinates in case that the rotation angle is exactly the polar coordinates angle, the 'degenerated' form of position vector under 1. arises, what is nothing else but the principal possibility to choose the coordinates systems' transformations to effectuate the single non-zero vectors component, [9]. The same result, arrived at by consistent replacement of Cartesian basis vectors by those of polar

[4] Only two-dimensional Euclidian space(s) and the basic polar coordinates are referred to. Extensions to 3D case, as cylindrical and spherical, and other locally orthogonal curvilinear coordinates - are straightforward.

coordinates basis vectors, was used for explicit 'proclamation' of the impossibility of the unified, coordinates-independent representation/formulation of the point's position vector, [10] (within the Introductory section). Such statement is commonly made even w/o concrete justification, [11].

As for the case 2., it turnes out that the largely contradictory representation of the position vector comes from the quasi-tensorial/tautological formulation of the coordinates transformation $y^i = \frac{\partial y^i}{\partial x^j} \cdot x^j$, leading to untennable rotational relationship[5] $\begin{bmatrix} x \\ y \end{bmatrix} = \begin{bmatrix} cos(\varphi) & -sin(\varphi) \\ sin(\varphi) & cos(\varphi) \end{bmatrix} . \begin{bmatrix} \rho \\ \rho \cdot \varphi \end{bmatrix}$. The only if at all plausible 'tensorial' formulation would be $z^i = \frac{\partial y^i}{\partial x^j} \partial \cdot x^j$, relating differring coordinates.

The ways directed to consistently establish the validity of the unified/coordinates-independent formulation of the position vector is to formally follow the definitional relations, either in terms of the numbers of units on one of the coordinates, while the other is kept constant (Fig. 2a), or by the integration along the coordinate lines, obeying definitional relation of basis vectors (Fig. 2b):

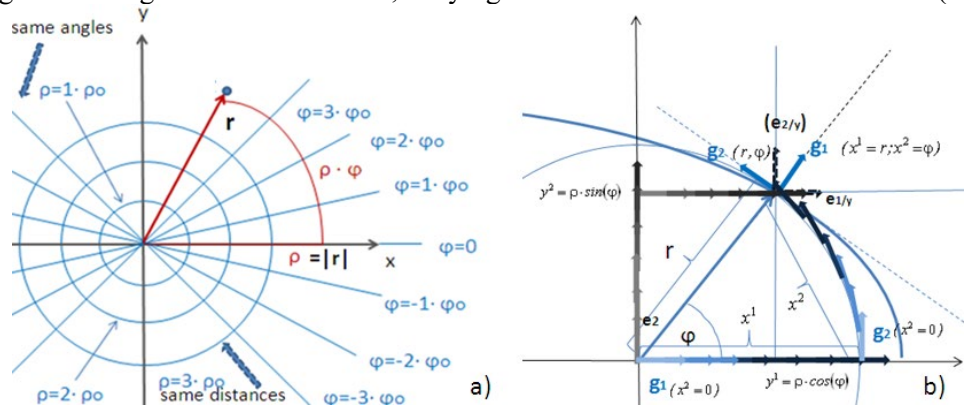

Fig. 2. Illustration of coordinate lines in $S_{x,x}$ & $S_{\rho,\varphi}$ Euclidian space – a), and vector(s) line-integration – b).

With reference to Fig. 2b, the position vector in Cartesian coordinates is produced by line integration of the polar coordinates basis vectors over respective coordinate(s) lines, Fig. 2a, as

$$\mathbf{r} = \int_0^{\rho} \mathbf{g}_1 (for\ \varphi = 0) \cdot d\rho + \int_0^{\varphi} \mathbf{g}_2 (for\ \rho\ constant) \cdot d\varphi$$

$$\mathbf{r} = \int_0^{\rho} cos(0) \cdot \mathbf{e}_1 \cdot d\rho + \int_0^{\rho} sin(0) \cdot \mathbf{e}_2 \cdot d\rho + \int_0^{\varphi} \rho \cdot [-sin(\theta)] \cdot \mathbf{e}_1 \cdot d\varphi + \int_0^{\varphi} \rho \cdot [cos(\theta)] \cdot \mathbf{e}_2 \cdot d\varphi$$

$$\mathbf{r} = \rho \cdot \mathbf{e}_1 - \rho \cdot \left\langle \mathbf{e}_1 \cdot \int_0^{\varphi} [sin(\theta)] \cdot d\varphi - \mathbf{e}_2 \cdot \int_0^{\varphi} [cos(\theta)] \cdot d\varphi \right\rangle = \rho \cdot \mathbf{e}_1 - \rho \cdot \left\langle \mathbf{e}_1 \cdot [-cos(\varphi)]_0^{\varphi} - \mathbf{e}_2 \cdot [sin(\varphi)]_0^{\varphi} \right\rangle$$

$$\mathbf{r} = \rho \cdot \mathbf{e}_1 - \rho \cdot \langle \mathbf{e}_1 \cdot [cos(0) - cos(\varphi)] - \mathbf{e}_2 \cdot [sin(\varphi) - sin(0)] \rangle$$

$$\mathbf{r} = \rho \cdot \mathbf{e}_1 - \rho \cdot \mathbf{e}_1 + \rho \cdot cos(\varphi) \cdot \mathbf{e}_1 + \rho \cdot sin(\varphi) \cdot \mathbf{e}_2 ; \mathbf{r} = \rho \cdot cos(\varphi) \cdot \mathbf{e}_1 + \rho \cdot sin(\varphi) \cdot \mathbf{e}_2 = x \cdot \mathbf{e}_x + y \cdot \mathbf{e}_y ,$$

resulting in the consistent/correct form of the position vector in Cartesian coordinates[6].

While the formulation under 1. above merely restores the Cartesian form of the position vector with the components represented by polar 'coordinates', and can be operationally used to conduct the position vector differentiations, it essentially departs from the form from which the basis vectors are determined, and might be rather restrictive in many respects, in particular when

[5] Which Vujičić at some places, handout at the MI-SANU Mechanics Seminar of February 2015, referred to in the infinitesimal terms (ϕ=0 and ρ→0) as the correspondence $\begin{bmatrix} x \\ y \end{bmatrix} \Leftrightarrow \begin{bmatrix} \rho \\ \rho \cdot \varphi \end{bmatrix}$, along $\mathbf{g}_i(0,0) = \mathbf{e}_i(0,0)$.

[6] In another lecture's handout, at the MI-SANU Seminar for History and Philosophy of Mathematics and Mechanics, February 24, 2015, Vujičić essentially has it in $\mathbf{r} - \mathbf{r}_0 = (y^i - y_0^i) \cdot \mathbf{e}_i = \int_{x_0}^{x_i} d[x^i \cdot \mathbf{g}\ (x)]$.

it comes to representation of the position vector in terms of the trajectorial coordinates basis vectors, representing the main topic of this submission, but likely also for the spatial derivatives.

3. Derivations of velocity and acceleration in the coordinate lines tangential space

While the reliance on the polar coordinates in representation of a point's position vector has traditionally been 'avoided' and/or unjustifiably 'prohibited', they are reserved solely to representation of vectors "at the point" – velocity and acceleration of a point, gradient of a scalar field, etc., whereby it was done in various ways: by direct time-wise differentiation of the one-component position vector form, the intermediate representation of the Cartesian components by the polar radius and the angle, and invariably dealt with as "non-inertial". With exception of [3], the explication of the position vector in the unified form[7] is virtually non-existent in literature

$$\boldsymbol{r} = y^i \cdot \boldsymbol{e}_i = x^i \cdot \boldsymbol{g}_i \ , \tag{1a}$$

and 'overlooked' are the related definitional relation for the respective basis vectors formulations

$$\boldsymbol{g}_i = \frac{\partial \boldsymbol{r}}{\partial x^i} \text{ and } \boldsymbol{e}_i = \frac{\partial \boldsymbol{r}}{\partial y^i} . \tag{1b}$$

As per the Vujičić's coordinates-independent formulation approach [4] "Differential of a vector $\boldsymbol{r} = y^i \cdot \boldsymbol{e}_i = x^i \cdot \boldsymbol{g}_i$ is equal to its absolute derivative $D\boldsymbol{r}$, what in the coordinates' form means that $d\boldsymbol{r} = D\boldsymbol{r} = \boldsymbol{e}_i \cdot Dy^i = \boldsymbol{g}_i \cdot Dx^i$, since $d\boldsymbol{e}_i = D\boldsymbol{e}_i = 0$, $(d\boldsymbol{g}_i) = D\boldsymbol{g}_i = 0$. Further evaluation leads to the invariant form of the velocity vector

$$\mathbf{v} = \frac{d\mathbf{r}}{dt} = \frac{D\mathbf{r}}{dt} = \dot{\rho} \cdot \mathbf{g}_1 + \dot{\varphi} \cdot \mathbf{g}_2 = \dot{\rho} \cdot \mathbf{e}_\rho + \rho \cdot \dot{\varphi} \cdot \mathbf{e}_\varphi \text{ "} \ ^{8} \tag{2}$$

Here, although not explicitly justified[9] the covariant constancy of the Christoffel symbols is used.

Also, instead of covariant derivatives could be used total/absolute differentiation by chain-rule: $\mathbf{v} = \frac{\partial \mathbf{r}}{\partial \rho} \cdot \frac{d\rho}{dt} + \frac{\partial \mathbf{r}}{\partial \varphi} \cdot \frac{d\varphi}{dt} = \mathbf{g}_1 \cdot \dot{\rho} + \mathbf{g}_2 \cdot \dot{\varphi} = \dot{\rho} \cdot \mathbf{e}_\rho + \rho \cdot \dot{\varphi} \cdot \mathbf{e}_\varphi$, fusing space- and time-derivatives. (3)

---

[7] Equation 12 in [4] – '(in)famous' in Serbian academic circles in the field of mechanics and mathematics.

[8] Here and elsewhere in his derivations and argumentations, ever since his early paper "Tranformacija Koordinata Vektora Položaja," Journal TEHNIKA, 1980. No. 6, pp.585-868, Vujičić apparently wrongly adjoins the above (in Section 2. mentioned) 'pseudo-tensorial' transformation of the very position vector coordinates $y^i = \frac{\partial y^i}{\partial x^j} x^j$, which might have partly been contributing to prevailing lack of reception. Yet, by the end of subsection 1.2, there becomes discerned his prevalent intention to treat the very coordinate of vectors at the point as the quantities that get transformed as tensors, i.e. the very vectors to be just rotated!?! In [3] the 'rotational' matrix with the entries $\partial y^i / \partial x^j$, considered tensors, does play quite central a role.

[9] Besides in [12], reference [1] in [4], there apparently are only a few references with the explicit statement on the covariant derivative of (locally rectangular) curvilinear/generalized coordinates, as for example [13]: $(d\mathbf{g}_i) = D\mathbf{g}_i \,] = \mathbf{g}_{i;j} = \frac{\partial \mathbf{g}_i}{\partial x_i} - \Gamma^k_{i;j} \cdot \mathbf{g}_k \equiv \mathbf{0}$. For the polar coordinates that is easily confirmed by accounting for the zero-valued Christoffel symbols except for $\Gamma^1_{22} = -\rho$ and $\Gamma^2_{12} = \Gamma^2_{21} = 1/\rho$, as follows:

for i=1 & j=1 one gets $\mathbf{g}_{1;1} = \frac{\partial \mathbf{g}_1}{\partial \rho} - \Gamma^1_{1;1} \cdot \mathbf{g}_1 - \Gamma^2_{1;1} \cdot \mathbf{g}_2 = \frac{\partial}{\partial \rho}\left[cos(\varphi) \cdot \mathbf{e}_1 + sin(\varphi) \cdot \mathbf{e}_2\right] - 0 \cdot \mathbf{g}_1 - 0 \cdot \mathbf{g}_2 = \mathbf{0}$; for i=2 & j=2 $\mathbf{g}_{2;2} = \frac{\partial \mathbf{g}_2}{\partial \varphi} - \Gamma^1_{2;2} \cdot \mathbf{g}_1 - \Gamma^2_{2;2} \cdot \mathbf{g}_2 = \frac{\partial}{\partial \varphi}\left[\rho(-cos(\varphi) \cdot \mathbf{e}_1 - sin(\varphi) \cdot \mathbf{e}_2)\right] + \rho \cdot \mathbf{g}_1 - 0 \cdot \mathbf{g}_2 = -\rho \cdot \mathbf{g}_1 + \rho \cdot \mathbf{g}_1 = \mathbf{0}$; etc. for $i \neq j$ …

In the startling contrast to these, along the alleged refutation of the coordinates-independent representation of the position vector, in [5] has been attempted a "brute-force" differentiation, equation 9, with the untenable imposition of conditions on the very Christoffel symbols to ensure/enforce the invariance of velocity, equations 10 and 11, in this submission's notations:
$\left\langle \frac{\partial y^j(x^1,x^2)}{\partial x^i} + y^k(x^1,x^2)\cdot\Gamma^j_{ik}(x^1,x^2) \right\rangle = \begin{cases} 1, j=i \\ 0, j\neq i \end{cases}$, that readily can be shown as by far untenable.

To intermediately establish correspondence, that is – sameness between covariantly determined velocity polar components at the point and the velocity components produced by rotating the velocity's Cartesian coordinates by applying the same rotation matrix as used in Fig. 1for relating the position vector's components in (x,y) and (x',y') Cartesian coordinate systems, with $\psi = \varphi$, starting from substitution of variables $x = \rho\cdot cos(\varphi),\quad y = \rho\cdot sin(\varphi)$; $\mathbf{r} = x\cdot\mathbf{e}_x + y\cdot\mathbf{e}_y$, by the time-wise differentiation is produced $\mathbf{v} = \dot{\mathbf{r}} = \dot{x}\cdot\mathbf{e}_x + \dot{y}\cdot\mathbf{e}_y$, and by using chain-rule furthermore $\mathbf{v} = [\dot\rho\cdot cos(\varphi) - \rho\cdot\dot\varphi\cdot sin(\varphi)]\cdot\mathbf{i} + [\dot\rho\cdot sin(\varphi) + \rho\cdot\dot\varphi\cdot cos(\varphi)]\cdot\mathbf{j}$, and with suitable groupings

$$\begin{bmatrix}\dot x\\ \dot y\end{bmatrix} = \begin{bmatrix} cos(\varphi) & -sin(\varphi)\\ sin(\varphi) & cos(\varphi)\end{bmatrix}\cdot\begin{bmatrix}\dot\rho\\ \rho\cdot\dot\varphi\end{bmatrix},\ \text{and}\ \begin{bmatrix}\dot\rho\\ \rho\cdot\dot\varphi\end{bmatrix} = \begin{bmatrix} cos(\varphi) & sin(\varphi)\\ -sin(\varphi) & cos(\varphi)\end{bmatrix}\cdot\begin{bmatrix}\dot x\\ \dot y\end{bmatrix}. \tag{4}$$

And further, to relate the previous two derivations with the tensor calculus/analysis approach, definitional relation for the transformation of a vector at the point formulated in [6], often having been referred to by V. Vujičić, $\xi^i = \left(\frac{\partial y^i}{\partial x^j}\right)_{x^k = x_0^k}\cdot\zeta^j$ is invoked, to the effect that Jacobi's matrix becomes $A = \begin{bmatrix}\frac{\partial y^1}{\partial x^1} & \frac{\partial y^1}{\partial x^2}\\ \frac{\partial y^2}{\partial x^1} & \frac{\partial y^2}{\partial x^2}\end{bmatrix} = \begin{bmatrix} cos(x^2) & -x^1\cdot sin(x^2)\\ sin(x^2) & x^1\cdot cos(x^2)\end{bmatrix} = \begin{bmatrix} cos(\varphi) & -\rho\cdot sin(\varphi)\\ sin(\varphi) & \rho\cdot cos(\varphi)\end{bmatrix}$, and furthermore[10]

$$\begin{bmatrix}v_x^1\\ v_x^2\end{bmatrix} = \begin{bmatrix} cos(\varphi) & -\rho\cdot sin(\varphi)\\ sin(\varphi) & \rho\cdot cos(\varphi)\end{bmatrix}\cdot\begin{bmatrix}\dot r\\ \dot\varphi\end{bmatrix} = \begin{bmatrix} cos(\varphi) & -sin(\varphi)\\ sin(\varphi) & cos(\varphi)\end{bmatrix}\cdot\begin{bmatrix}\dot\rho\\ \rho\cdot\dot\varphi\end{bmatrix}\ \text{i.e.}\ \begin{bmatrix}\dot\rho\\ \rho\cdot\dot\varphi\end{bmatrix} = \begin{bmatrix} cos(\varphi) & sin(\varphi)\\ -sin(\varphi) & cos(\varphi)\end{bmatrix}\cdot\begin{bmatrix}\dot x\\ \dot y\end{bmatrix},$$

establishing the rotationally-invariant relation $\begin{bmatrix}v_x\\ v_y\end{bmatrix} = \begin{bmatrix}\dot x\\ \dot y\end{bmatrix} \xleftrightarrow{rotaciono-transformatorno} \begin{bmatrix}\dot\rho\\ \rho\cdot\dot\varphi\end{bmatrix} = \begin{bmatrix}v_\rho\\ v_\varphi\end{bmatrix}$, so that $\mathbf{v} = \dot x\cdot\mathbf{e}_{1/x} + \dot y\cdot\mathbf{e}_{2/y} = \dot\rho\cdot\mathbf{e}_\rho + \rho\cdot\dot\varphi\cdot\mathbf{e}_\varphi$, reestablishing the physical azimuthal velocity.

For the acceleration, covariantly differentiating velocity[11]. [4][3], $\mathbf{a} = \frac{d\mathbf{r}}{dt} = \frac{D\mathbf{r}}{dt}$ gains form

$$\mathbf{a} = \ddot y^i\cdot\mathbf{e}_i = \left(\ddot x^i + \Gamma^i_{jk}\cdot\dot x^j\cdot\dot x^k\right)\cdot\mathbf{g}_i, \tag{5}$$

or components-wise $a_x = \ddot x$, $a_y = \ddot y$ and (in "physical", normalized polar coordinates[12]) $a_\rho = \ddot\rho - \rho\cdot\dot\varphi^2$, $a_\varphi = \rho\cdot\ddot\varphi + 2\cdot\dot\rho\cdot\dot\varphi$, by applying Christoffel symbols given in Footnote 9. The same results are produced by applying either the essentially tensorial transformation of a vector at the point or the two-times time-wise differentiation of the position vector,

[10] With identifying the velocities as the coordinates' time-derivatives $(\xi^1,\xi^2) = (\dot x,\dot y)$ and $(\zeta^1,\zeta^2) = (\dot\rho,\dot\varphi)$, with respectively adjoined basis vectors $\mathbf{e}_1,\mathbf{e}_2$ and $\mathbf{g}_1,\mathbf{g}_2$, i.e. – invariantly: $\mathbf{v} = \dot x\cdot\mathbf{e}_1 + \dot y\cdot\mathbf{e}_2 = \dot\rho\cdot\mathbf{g}_1 + \dot\varphi\cdot\mathbf{g}_2$.

[11] In [3] the covariant form of acceleration vector is arrived at by augmenting the missing components to essentially ensure the parallel transport "feature"; in [4] the covariant expression has been take as known.
With identifying the velocities as the coordinates' time-derivatives $(\xi^1,\xi^2) = (\dot x,\dot y)$ and $(\zeta^1,\zeta^2) = (\dot\rho,\dot\varphi)$, with respectively adjoined basis vectors $\mathbf{e}_1,\mathbf{e}_2$ and $\mathbf{g}_1,\mathbf{g}_2$, i.e. – invariantly: $\mathbf{v} = \dot x\cdot\mathbf{e}_1 + \dot y\cdot\mathbf{e}_2 = \dot\rho\cdot\mathbf{g}_1 + \dot\varphi\cdot\mathbf{g}_2$.

[12] In [4], besides other mistyping, this azimuthal component is adjoined to the "natural" basis vector ...

$\begin{bmatrix}\ddot{x}\\ \ddot{y}\end{bmatrix}=\begin{bmatrix}cos(\varphi) & -sin(\varphi)\\ sin(\varphi) & cos(\varphi)\end{bmatrix}\cdot\begin{bmatrix}x\ddot{\rho}-\rho\cdot\dot{\varphi}^2\\ \rho\cdot\ddot{\rho}+2\cdot\dot{\rho}\cdot\dot{\varphi}\end{bmatrix}$, that is $\begin{bmatrix}a_x\\ a_y\end{bmatrix}\xleftrightarrow{rotaciono-transformatorno}\begin{bmatrix}a_\rho\\ a_\varphi\end{bmatrix}$, in the context of which may become understandable the Vujičić's discontent with the "present misconception that the coordinates of acceleration vector in curvilinear coordinate systems are not vectors in tensors sense," towards refutation of which the reformulation of (5) was made in form of (15b) in [4].

The "linear transformability" of velocity and acceleration vectors ("physical") coordinates is fully confirmed by numerical integrations of the planetary orbital motion equations using the inverse distance-squared attraction ($a_\rho=-\kappa/\rho^2$) and the constant angular momentum in [7].

4. Derivation of covariant velocity and acceleration in the trajectory's tangential space

When in the open literature and the textbooks the trajectorial (tangential-normal) coordinate systems are introduced, these and the (polar) coordinated tangential ones are treated as unrelated (Table 1.). Although the procedure of determination of the basis vectors are quite similar, the resulting velocity and acceleration components bear no relationships with the polar ones: $\boldsymbol{v}=v\cdot\boldsymbol{e}_t$ and $\boldsymbol{a}=\dot{v}\cdot\boldsymbol{e}_t+v\cdot\dot{\theta}\cdot\boldsymbol{e}_n$, i.e. $\mathbf{a}=\dot{v}\cdot\mathbf{e}_t+v^2/r_c\cdot\mathbf{e}_n=a_t\cdot\mathbf{e}_t+a_n\cdot\mathbf{e}_n$, where r_c is the trajectory's curvature radius at the point, whereas v is expressed as transverse velocity w.r.t. curvature radius, $v=r_c\cdot\dot{\theta}$, w/ angles $\theta=\varphi+\frac{\pi}{2}-\psi$, along $\psi=arctng(\frac{\dot{r}}{r\cdot\dot{\varphi}})$, Fig. 1. As is shown in the Appendix A, complexity of such formulation is extremely high, resulting in presence of all to the third order derivatives of basic polar coordinates $\rho\,\&\,\varphi$.

Feature / Form	Rotationally-Invariant	Classically-Covariant	'Heuristic'/ Ad-Hoc Method
Coordinately-Tangential	√	√	X
Trajectorially-Tangential	√	√	√

Table 1. Overview of curvilinear coordinate systems considered in this submission and their relations: green markings, for the cases elaborated thus far (upper raw), and traditionally the only known (lower raw); blue markings (lower raw, left two columns) – entirely newly introduced, along all their mutual relations.

However, based on the derivations and argumentations thus far, there becomes possible – with referring to Fig. 3, to which all previous derivations pertain, to pursue the covariant alternative.

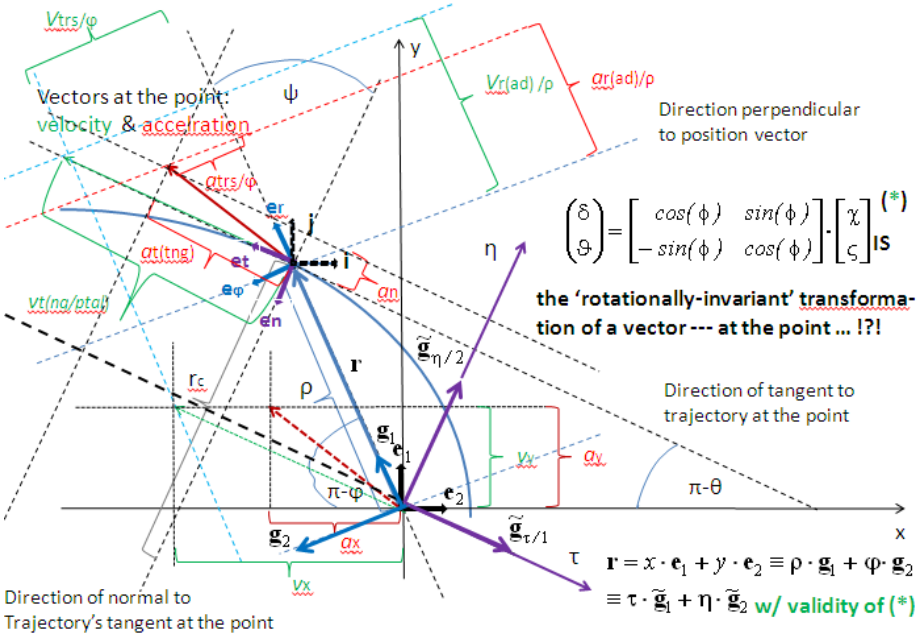

Fig. 3. Coordinate and trajectory lines, their basis vectors and the components of the vectors at the point. It should be noted the sameness, just being mutually translated, of the coordinates/basis-vectors for the point and for the vectors at the point. Besides thus far considered cases, added are the coordinates and basis vectors for the trajectorially tangential "space" only for the coordinates' origin point, to reduce crowding. Inserted is the extended position vector formulation w/ trajectorial coordinates, along the rotation matrix.

Based on the general validity of the position vector representation

$$\mathbf{r} = x\cdot\mathbf{i} + y\cdot\mathbf{j} = x\cdot\mathbf{e}_1 + y\cdot\mathbf{e}_2 = \rho\cdot\mathbf{g}_1 + \varphi\cdot\mathbf{g}_2 = \eta\cdot\tilde{\mathbf{g}}_1 + \tau\cdot\tilde{\mathbf{g}}_2\,, \tag{6}$$

basis vectors for the tangential-normal coordinate system are determined by the partial derivatives $\tilde{\mathbf{g}}_1 = \partial\mathbf{r}/\partial\eta$ and $\tilde{\mathbf{g}}_2 = \partial\mathbf{r}/\partial\tau$, whereby – expressed by chain rule through polar coordinates become[13]

$$\tilde{\mathbf{g}}_1 = \frac{\partial\mathbf{r}}{\partial\eta} = \frac{\partial\mathbf{r}}{\partial\rho}\cdot\frac{\partial\rho}{\partial\eta} + \frac{\partial\mathbf{r}}{\partial\varphi}\cdot\frac{\partial\varphi}{\partial\eta} = \frac{\partial\rho}{\partial\eta}\cdot\mathbf{g}_1 + \frac{\partial\varphi}{\partial\eta}\cdot\mathbf{g}_2 \quad\text{and}\quad \tilde{\mathbf{g}}_2 = \frac{\partial\mathbf{r}}{\partial\tau} = \frac{\partial\mathbf{r}}{\partial\rho}\cdot\frac{\partial\rho}{\partial\tau} + \frac{\partial\mathbf{r}}{\partial\varphi}\cdot\frac{\partial\varphi}{\partial\tau} = \frac{\partial\rho}{\partial\tau}\cdot\mathbf{g}_1 + \frac{\partial\varphi}{\partial\tau}\cdot\mathbf{g}_2\,. \tag{7}$$

By using relationships between the two sets of coordinates ,

$\rho^2 = \eta^2 + \tau^2$ & $\varphi = \pi - arctng(\eta/\tau)$, the above partial derivatives reduce to

$$\partial\rho/\partial\tau = -\left[1/\sqrt{\eta^2+\tau^2}\right]\cdot\tau = -\tau/\rho = -sin(\psi)\,,\quad \partial\rho/\partial\eta = -\left[1/\sqrt{\eta^2+\tau^2}\right]\cdot\eta = -\eta/\rho = -cos(\psi)\,,$$

$$\partial\varphi/\partial\tau = -\left[1/1+(\eta/\tau)^2\right]\cdot\left(-\eta/\tau^2\right) = \eta/\rho^2 = cos(\psi)/\rho\,,\quad \partial\varphi/\partial\eta = -\left[1/\left(1+(\eta/\tau)^2\right)\right]/\tau = \tau/\rho^2 = sin(\psi)/\rho\,,$$

where $\psi = arctng\left(\frac{\dot\rho}{\rho\cdot\dot\varphi}\right)$ and furthermore, with $cos(\psi) = \frac{\rho\cdot\dot\varphi}{\sqrt{(\rho\cdot\dot\varphi)^2+(\dot\rho)^2}}$ and $sin(\psi) = \frac{\dot\rho}{\sqrt{(\rho\cdot\dot\varphi)^2+(\dot\rho)^2}}$, the basis vectors $\tilde{\mathbf{g}}_1$ and $\tilde{\mathbf{g}}_2$ become functions of the polar coordinates and their time-derivatives.

The covariant first and second time-derivatives, essentially the 'true' "absolute" ones (inner product of covariant derivatives and the tangent vector to the *t*-parameterized curve, then are:

$$\tilde{\boldsymbol{\upsilon}} = \dot\eta\cdot\tilde{\mathbf{g}}_1 + \dot\tau\cdot\tilde{\mathbf{g}}_2 = \tilde\upsilon^1\cdot\tilde{\mathbf{g}}_1 + \tilde\upsilon^2\cdot\tilde{\mathbf{g}}_2 \quad\text{and}\quad \tilde{\mathbf{a}} = \tilde a^i\cdot\tilde{\mathbf{g}}_i = \left(\dot{\tilde\upsilon}^i + \tilde\Gamma^i_{jk}\cdot\dot{\tilde\upsilon}^j\cdot\tilde\upsilon^k\right)\cdot\tilde{\mathbf{g}}_i\,, \tag{8}$$

where the related Christoffel symbols are derived from the corresponding metric tensor(s) $\tilde g_{ik} = \tilde{\mathbf{g}}_i\cdot\tilde{\mathbf{g}}_k$ by definitional expression(s): $\tilde\Gamma^i_{jk} = \frac{\tilde g^{il}}{2}\cdot\left(\partial_k\tilde g_{jl} + \partial_j\tilde g_{kl} - \partial_l\tilde g_{jk}\right)$, where $\tilde g^{il}\cdot\tilde g_{lj} = \delta^l_j$. (9)

Rather than pursuing this further[14], by applying the rotational-invariance counterpart for this

[13] They can be determined through basis vectors of the Cartesian coordinate system, through the polar ones.
[14] The full derivation might be available by the time of the Congress taking place.

coordinate system, for the rotation angle w.r.t. the 'polar' by the angle[15] $\pi-\psi$, the rotationally-invariant matrix has form $\begin{bmatrix} -cos(\psi) & sin(\psi) \\ -sin(\psi) & -cos(\psi) \end{bmatrix}=\begin{bmatrix} -\frac{r\cdot\dot{\varphi}}{\sqrt{(r\cdot\dot{\varphi})^2+(\dot{r})^2}} & \frac{\dot{r}}{\sqrt{(r\cdot\dot{\varphi})^2+(\dot{r})^2}} \\ -\frac{\dot{r}}{\sqrt{(r\cdot\dot{\varphi})^2+(\dot{r})^2}} & -\frac{r\cdot\dot{\varphi}}{\sqrt{(r\cdot\dot{\varphi})^2+(\dot{r})^2}} \end{bmatrix}$; rotationally-invariant tangential-normal coordinates become

$$\begin{bmatrix} v_n \\ v_t \end{bmatrix}=\begin{bmatrix} -\frac{r\cdot\dot{\varphi}}{\sqrt{(r\cdot\dot{\varphi})^2+(\dot{r})^2}} & \frac{\dot{r}}{\sqrt{(r\cdot\dot{\varphi})^2+(\dot{r})^2}} \\ -\frac{\dot{r}}{\sqrt{(r\cdot\dot{\varphi})^2+(\dot{r})^2}} & -\frac{r\cdot\dot{\varphi}}{\sqrt{(r\cdot\dot{\varphi})^2+(\dot{r})^2}} \end{bmatrix}\cdot\begin{bmatrix} \dot{r} \\ r\cdot\dot{\varphi} \end{bmatrix}=\begin{bmatrix} \frac{-(r\cdot\dot{r}\cdot\dot{\varphi})^2}{\sqrt{(r\cdot\dot{\varphi})^2+(\dot{r})^2}}+\frac{(\dot{r}\cdot r\cdot\dot{\varphi})^2}{\sqrt{(r\cdot\dot{\varphi})^2+(\dot{r})^2}} \\ -\frac{(\dot{r})^2}{\sqrt{(r\cdot\dot{\varphi})^2+(\dot{r})^2}}-\frac{(r\cdot\dot{\varphi})^2}{\sqrt{(r\cdot\dot{\varphi})^2+(\dot{r})^2}} \end{bmatrix}=\begin{bmatrix} 0 \\ -\sqrt{(r\cdot\dot{\varphi})^2+(\dot{r})^2} \end{bmatrix}, \text{ and} \tag{10}$$

$$\begin{bmatrix} a_n \\ a_t \end{bmatrix}=\begin{bmatrix} -\frac{r\cdot\dot{\varphi}}{\sqrt{(r\cdot\dot{\varphi})^2+(\dot{r})^2}} & +\frac{\dot{r}}{\sqrt{(r\cdot\dot{\varphi})^2+(\dot{r})^2}} \\ -\frac{\dot{r}}{\sqrt{(r\cdot\dot{\varphi})^2+(\dot{r})^2}} & -\frac{r\cdot\dot{\varphi}}{\sqrt{(r\cdot\dot{\varphi})^2+(\dot{r})^2}} \end{bmatrix}\cdot\begin{bmatrix} \ddot{r}-r\cdot\dot{\varphi}^2 \\ r\cdot\ddot{\varphi}+2\cdot\dot{r}\cdot\dot{\varphi} \end{bmatrix}=\begin{bmatrix} -\frac{r\cdot\dot{\varphi}\cdot(\ddot{r}-r\cdot\dot{\varphi}^2)}{\sqrt{(r\cdot\dot{\varphi})^2+(\dot{r})^2}}+\frac{\dot{r}\cdot(r\cdot\ddot{\varphi}+2\cdot\dot{r}\cdot\dot{\varphi})}{\sqrt{(r\cdot\dot{\varphi})^2+(\dot{r})^2}} \\ -\frac{\dot{r}\cdot(\ddot{r}-r\cdot\dot{\varphi}^2)}{\sqrt{(r\cdot\dot{\varphi})^2+(\dot{r})^2}}-\frac{r\cdot\dot{\varphi}\cdot(r\cdot\ddot{\varphi}+2\cdot\dot{r}\cdot\dot{\varphi})}{\sqrt{(r\cdot\dot{\varphi})^2+(\dot{r})^2}} \end{bmatrix}= \tag{9}$$

$$\begin{bmatrix} \frac{-r\cdot\dot{\varphi}\cdot\ddot{r}+r^2\cdot\dot{\varphi}^3}{\sqrt{(r\cdot\dot{\varphi})^2+(\dot{r})^2}}+\frac{r\cdot\dot{r}\cdot\ddot{\varphi}+2\cdot\dot{r}^2\cdot\dot{\varphi}}{\sqrt{(r\cdot\dot{\varphi})^2+(\dot{r})^2}} \\ -\frac{\dot{r}\cdot\ddot{r}\cdot-r\cdot\dot{r}\cdot\dot{\varphi}^2}{\sqrt{(r\cdot\dot{\varphi})^2+(\dot{r})^2}}-\frac{r^2\cdot\dot{\varphi}\cdot\ddot{\varphi}+2\cdot r\cdot\dot{r}\cdot\dot{\varphi}^2}{\sqrt{(r\cdot\dot{\varphi})^2+(\dot{r})^2}} \end{bmatrix}=\begin{bmatrix} \frac{-r\cdot\dot{\varphi}\cdot\ddot{r}+r^2\cdot\dot{\varphi}^3+r\cdot\dot{r}\cdot\ddot{\varphi}+2\cdot\dot{r}^2\cdot\dot{\varphi}}{\sqrt{(r\cdot\dot{\varphi})^2+(\dot{r})^2}} \\ \frac{-\dot{r}\cdot\ddot{r}-\cdot r\cdot\dot{r}\cdot\dot{\varphi}^2-\cdot r^2\cdot\dot{\varphi}\cdot\ddot{\varphi}}{\sqrt{(r\cdot\dot{\varphi})^2+(\dot{r})^2}} \end{bmatrix}$$

In Fig. 4, it is shown evaluation of the tangential part in (10) and the traditional tangential-normal coordinates system components (A.1) for the previously found $\rho(t)$ and $\varphi(t)$.

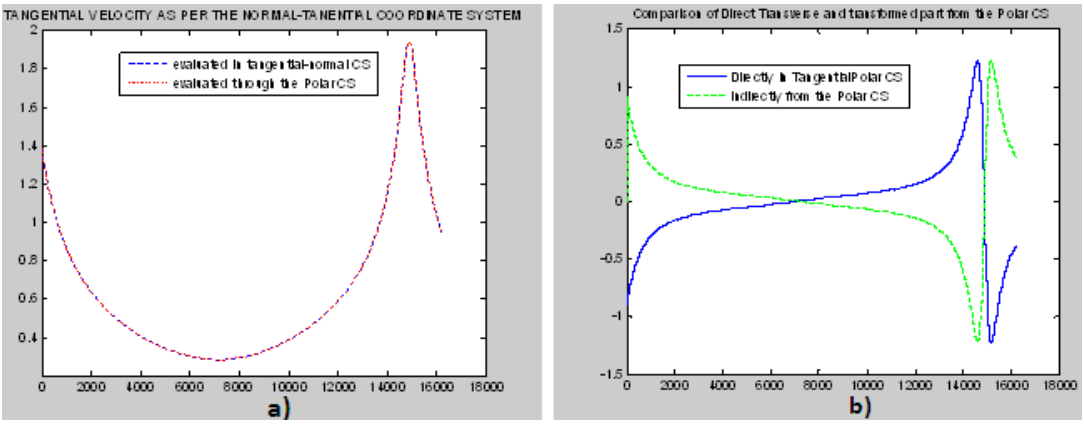

Fig. 4. Comparative evaluations of tangential velocity – a) & acceleration – b) produced by inserting the samples of trajectories polar coordinates produced by the numerical evaluation referred to earlier (p. 6).

Although the numerical integration by using the second-order[16] (10) non-liner differential equations turned out as steadily divergent[17], when the produced elliptic trajectory polar distances and angles are inserted in the two seemingly extremely differing expressions, the results[18] for the

[15] By all means, the selected angle, along the chosen direction of coordinates determines the algebraic sign.
[16] The third order differential equations derived in Appendix A appear hardly tractable.
[17] Likely due to unbalanced single-component central force, its normal component produced by covariantly rotated radial dominating the tangential one; initial velocity was reused from the one in polar coordinates!?!
[18] Apart for reversed sign in the case of acceleration, which - by all means - is related to the axes' orientation. It should be noted that for the evaluations based on (A.1), the numerical differentiation is performed, so that full correctness of the derived cumbersome expressions for the second order derivatives is not ascertained.

(tangential[19]) velocities and accelerations are produced. This establishes the sought-for relationship between the conventional/ad-hoc and the covariant tangential-normal coordinate systems, marked by the red-colored double-arrow in Table 1. By all means, it opens the possibility to approach the modeling of the non-linear dynamical systems in the tangential coordinates space by not restricting it to just their autonomous, not explicitly time-dependent forms. The possibly arising issues of (numerical) integrability should then be only strong indication of the inappropriateness/incompleteness of the very dynamical systems model used[20].

5. Remarks on spatial differentiations and their relations with the time-wise ones

Since in the Cartesian system of coordinates for all the spatial derivatives (Grad, Div, Laplacian Curl) has been formalized the use of the vector-valued Nabla-operator ($\nabla^{(x,y)} = \frac{\partial}{\partial x}\cdot\mathbf{e}_x + \frac{\partial}{\partial x}\cdot\mathbf{e}_y$), consistently with the time-wise derivatives the corresponding operator for polar coordinates should also be formulated as covariantly and/or rotationally-invariant. Indeed, as shown in the Appendix B (Grad, a; Div, b), that truly turns to be the case for the form $\nabla^{(\rho,\varphi)} = \frac{\partial}{\partial\rho}\cdot\mathbf{e}_\rho + \frac{1}{\rho}\cdot\frac{\partial}{\partial\varphi}\cdot\mathbf{e}_\varphi$. However, the expression for the divergence produced traditionally / conventionally differs from this form, in the way that therein appears the additional term - the vector's radial component (u^ρ) divided by ρ.

This appears to be the result of the reliance on essentially radially symmetrical and/or cylindrical configurations, intrinsically related to the 'suppression' or at least lack of full explication of the transverse components of the vector-fields manifested through the components-by-components multiplications and additions of a vector and the transformed Nabla-operator, instead of using the scalar product in Cartesian coordinates – multiplying only the respective vectors' components.

As simple example for the possible issue in this regard[21], including the Div of Grad (Laplacian) and even the Curl), can be the simplest vector field represented by the points position vectors

$$\mathbf{u} = x\cdot\mathbf{e}_x + y\cdot\mathbf{e}_y = \rho\cdot\mathbf{e}_\varphi + \rho\cdot\varphi\cdot\mathbf{e}_\varphi \quad , \tag{10}$$

when the divergence-operators applied in each case by the rotationally-invariant/'covariant' forms produce the result 2, but when transformed form the Cartesian coordinates in the polar ones the traditionally derived/used form(ula) is needed to produce the correct results, which – however – turns out to be the case also with the need for the Cartesian-coordinates divergence-operator when the vector components get transformed from the polar coordinates to the Cartesian ones!?!

As for the relation between the time- and spatial derivatives in the context of the formulation and evaluation of dynamical systems' non-linear differential equations models, it should be attempted to strictly distinguish between and to separate the kinematic and dynamic parts (the

[19] The primary reason for this author's several years long preoccupation with these topics has been the 'retrieval' of the evidently present non-zero tangential acceleration in the Keplerian elliptic orbital trajectories [15], although – due to his second law and the consequent angular momentum constancy – it remains indiscernible in the process of numerical integration either in Cartesian or in the polar coordinates.

[20] In [7] is demonstrated effect of mere relaxation of the angular momentum constancy ad/or its retaining while merely leaving out the transversal acceleration $a_\varphi = 0$ untransformed into $(1/\rho)\cdot L^2$, with $L = \rho^2\cdot\varphi$.

[21] Quite rare dealing with a priory non-zero presumed divergences might have been masking its appearance.

equation's left and right sides)[22], and – since the gradients, divergences (as well as Curls) are essentially related to the external forces' agencies – in particular for the Navier-Stokes equation[23]

$$\partial_t \mathbf{u} + (\mathbf{u} \cdot \nabla)\mathbf{u} = -\rho^{-1} \cdot \nabla p + \mu \nabla^2 \mathbf{u} + \mathbf{F} \qquad (11)$$

on the left-hand side the absolute/covariant time-derivative $D_{(t)}\mathbf{u}$ might be more appropriate than the convective/material derivative - a combination of the time-wise and spatial differentiations[24].

5. Conclusions

In this quite extensive and "in-depth" elaboration, although considering only the 2-D space, the factual validity and valuable effectiveness of the coordinates-independent representation of the position vector have been shown. Along these lines the fully classically-covariant and/or rotationally-invariant formulation of the velocities and accelerations in the trajectorial tangential-normal coordinates/space has been derived, reducing the pertaining non-linear differential equations from the third – for the traditionally derived "natural" tangential-normal coordinates – to the second degree, enabling the tractable integrations as in the Cartesian and polar coordinates.

As possibly most far-reaching repercussion, besides obviating the necessity to in-advance know the trajectories to be able to produce the related tangential-normal base vectors – which has necessitated the reliance on the so-called geodesics-based modeling (featuring the zero-valued tangential acceleration) –, can be hinted the overcoming of the traditional distinguishing between the reference and current configurations in the Continuum Mechanics, in that it becomes possible to work entirely within a particular suitably chosen system of coordinates, whereby the reference configuration can be looked-at/used as mere formulation of the initial conditions, while the need disappears for the deformation tensor to be defined as the coordinates transformation related one.

Acknowledgement: Challenging discussions bordering on a squabble with professors Jovo Jarić and Dragoslav Kuzmanović at the Seminar in Jagićeva 5 have greatly contributed to the author's continued motivation, argumentation and augmentation of both the content and degree of elaboration. I would also like to thank Dr. Zoran Drašković for continual exchange of views on the topics of his earlier interest.

References:[25]

[1] Lützen, J., "*Mechanistic Images in Geometric Form*," Oxford University Press, 2005.
[2] Dell'Aglio, L., "On the genesis of the concept of covariant differentiation," Revue d'histoire Des mathématiques 2, 1996.
[3] Emam, M.H., "*Covariant Physics – From Classical Mehanics to General Relativity and Beyond*." Osford Univeristy Press, 2021.
[4] Vujičić, V. and Nikolić, V., "About nonlinear sciences," Advances in Nonlinear Sciences,Vol. 3, Južnoslovenska ANN, 2011.[5] Hedrih, K., "Linear and on-linear transformation of coordinates and angular velocity and intensity change of basic vectors of tangent space of a position vector of a material system kinetic point," The European Physical Journal, Spec. Topics, Aug 25, '21.[6] Dubrovin, B.A., Novikov, S.P. and Fomenko, A.G., "*Sovremenaya Geometriya*," Nauka,Moscow, 1979 (page 30).

[22] Notorious example of such misconception is the use of "fictitious" centrifugal force (L^2/ρ^3) in Orbital Mechanics (in the absence of the explicit centrifugal force) [14], what might apply to the Coriolis' one too.

[23] Here, ρ - generally spatially and time-wise variable density.

[24] As for the accompanying continuity equation $\partial_t \rho + \nabla \cdot (\rho \cdot \mathbf{u}) = 0$, even in the "stationary" case is $\nabla \cdot \mathbf{u} \neq 0$!!!

[25] For the reviewer' convenience, all the items – with a few referred to in footnotes- are made downloadable from https://www.dropbox.com/home/Files%20of%20the%20Submission%20Articticle's%20References

[7] Nedić, S., "Problematizing Orbital Mechanics Two First Integrals," VIII Congress of the SSM, Uni of Kragujevac, June 2021; transcripted presentation slides are accessible at the author's Webpages on AcadeniaEdu and ReearchGate.
[8] Onikiychuk, V.N., "*Velikaya Tayna Leonarda Eilera*," NPO Profes., Sankt-Petersburg, 2007.
[9] Eisenhart, L.P., "*Riemannian Geometry*," Princeton University Press, 1949.
[10] Anđelić, T., and Stojanovič, R., "*Racionalna Mehanika*," Zavod za Izdavanje Udžbenika SRS, Beograd, 1965.[11] Bakša, A.," *Racionlna Mehanika*", Lectures at the Belgrade University, 2000, with second Edition coauthored by Simić, S., 2016.[12] Sheolevey, B., "Global Covariant Conservation Laws in Riemanian Space," Journal of Mathematical Physics, Vol. 7., No, 1966.
[13] Sochi, T., "*Tensor Calculus*," 2016, University College London, downloadable from arXiv.
[14] Nedić, S. and Gordić, V., "Towards General Theory of Orbital Motion – The Thermo-Gravitational Oscillator," Galilean Electrodynamics Journal, May/June 2017 (Vol. 28, No. 3).
[15] Nedić S., Kepler's Equation and Angular Momentum – Historical Perspective, Critical Analysis and Implications for Developments in Mechanics, Mathematics and Physics, *arXiv 2020*.

Appendix A: Time-dependent velocities and accelerations in tangential-normal coordinates

In he traditionally formulated velocity and aceleration in the tangental-normal coordinates $\mathbf{v} = v_\tau \cdot \mathbf{e}_\tau$ and $\mathbf{a} = \dot{v}_\tau \cdot \mathbf{e}_\tau + v_\tau \cdot \dot{\theta} \cdot \mathbf{e}_n$, i.e. $\mathbf{a} = \dot{v}_\tau \cdot \mathbf{e}_\tau + \left(v_\tau{}^2 / r_c\right) \cdot \mathbf{e}_n = a_\tau \cdot \mathbf{e}_\tau + a_n \cdot \mathbf{e}_n$, (A.1)

r_c - curvature radius at the point, the tangential velocity v is expressed as transverse velocity w.r.t. the curvature radius , i.e. $v_\tau = r_c \cdot \dot{\theta}$, where $\theta = \varphi + \pi/2 - \psi$, along[26] $\psi = arctng\left[\dot{r}/(r \cdot \dot{\varphi})\right]$ and the tangential acceleration as the circular Huygens' centrifugal one. Curvature radius having form

$$r_c = \frac{\left(r^2 + r'^2\right)^{\frac{3}{2}}}{2 \cdot r'^2 + r^2 - r \cdot r''}, \text{ where } r' = \frac{dr}{d\varphi} = \frac{dr/dt}{d\varphi/dt} = \frac{\dot{r}}{\dot{\varphi}} \;\&\; r'' = \frac{d^2 r}{d\varphi_2} = \frac{\ddot{r} \cdot \dot{\varphi} - \dot{r} \cdot \ddot{\varphi}}{\dot{\varphi}^3} \text{ along (Fig. 3),}$$

$$cos(\psi) = \frac{r \cdot \dot{\varphi}}{\sqrt{(r \cdot \dot{\varphi})^2 + (\dot{r})^2}}, sin(\psi) = \frac{\dot{r}}{\sqrt{(r \cdot \dot{\varphi})^2 + (\dot{r})^2}} \;\&\; \dot{\theta} = \dot{\varphi} - \frac{1}{(\dot{r})^2 + (r \cdot \dot{\varphi})^2}\left[\ddot{r} \cdot (r \cdot \dot{\varphi}) - (\dot{r})^2 \cdot \dot{\varphi} - r \cdot \dot{r} \cdot \ddot{\varphi}\right]$$

$$\dot{\theta} = \left(2 \cdot \dot{r}^2 \cdot \dot{\varphi} + r \cdot \dot{\varphi}^3 - r \cdot \ddot{\varphi}^3 - r \cdot \ddot{r} \cdot \dot{\varphi} + r \cdot \dot{r} \cdot \ddot{\varphi}\right) / \left[\dot{r}^2 + \left(r \cdot \dot{\varphi}\right)^2\right];$$

$$v_\tau = r_c \cdot \dot{\theta} = \frac{\left[(\dot{r})^2 + (r \cdot \dot{\varphi})^2\right]^{\frac{3}{2}} \cdot \dot{\varphi}}{2 \cdot \dot{r}^2 \cdot \dot{\varphi} + (r \cdot \dot{\varphi})^2 \cdot \dot{\varphi} - r \cdot \ddot{r} \cdot \dot{\varphi} + r \cdot \dot{r} \cdot \ddot{\varphi}} - \frac{\left[(\dot{r})^2 + (r \cdot \dot{\varphi})^2\right]^{\frac{1}{2}} \cdot \left[\ddot{r} \cdot (r \cdot \dot{\varphi}) - (\dot{r})^2 \cdot \dot{\varphi} - r \cdot \dot{r} \cdot \ddot{\varphi}\right]}{2 \cdot \dot{r}^2 \cdot \dot{\varphi} + (r \cdot \dot{\varphi})^2 \cdot \dot{\varphi} - r \cdot \ddot{r} \cdot \dot{\varphi} + r \cdot \dot{r} \cdot \ddot{\varphi}}.$$

$$a_n = r_c \cdot \dot{\theta}^2 = \frac{\left[(\dot{r})^2 + (r \cdot \dot{\varphi})^2\right]^{\frac{3}{2}}}{2 \cdot \dot{r}^2 \cdot \dot{\varphi} + (r \cdot \dot{\varphi})^2 \cdot \dot{\varphi} - r \cdot \ddot{r} \cdot \dot{\varphi} + r \cdot \dot{r} \cdot \ddot{\varphi}} \left\langle \dot{\varphi} - \frac{\left[\ddot{r} \cdot (r \cdot \dot{\varphi}) - (\dot{r})^2 \cdot \dot{\varphi} - r \cdot \dot{r} \cdot \ddot{\varphi}\right]}{\left[(\dot{r})^2 + (r \cdot \dot{\varphi})^2\right]} \right\rangle^2, \text{ and then}$$

$a_\tau = \dot{v}_\tau = \dot{r}_c \cdot \dot{\theta} + r_c \cdot \ddot{\theta}$, both parts suggestive of rather complex expression to result in the sequel.

$$\dot{\theta} = \dot{\varphi} - \frac{1}{\dot{r}^2 = (r \cdot \dot{\varphi})^2} \cdot \left[\hat{r} \cdot (r \cdot \dot{\varphi}) - \dot{r}^2 \cdot r \cdot \dot{\varphi} - r \cdot \dot{r} \cdot \ddot{\varphi}\right]; \; \dot{r}_c = r_c' \cdot \dot{\varphi};$$

$$\dot{r}_c = \frac{\dot{\varphi}}{2} \cdot \left[r^2 + \left(\frac{\dot{r}}{\dot{\varphi}}\right)^2\right]^{\frac{1}{2}} \cdot \left\langle \frac{2 \cdot r \cdot \frac{\dot{r}}{\dot{\varphi}} + \frac{\dot{r}}{\dot{\varphi}} \cdot \frac{\ddot{r} \cdot \dot{\varphi} - \dot{r} \cdot \ddot{\varphi}}{\dot{\varphi}^3} - \frac{3 \cdot \ddot{r} \cdot \dot{\varphi} - 3 \cdot \dot{r} \cdot \ddot{\varphi} - \dddot{r} \cdot \dot{\varphi}^2 + \dot{r} \cdot \dot{\varphi} \cdot \ddot{\varphi}}{\dot{\varphi}^5}}{2 \cdot \left(\frac{\dot{r}}{\dot{\varphi}}\right)^2 + r^2 - \frac{\dot{r}}{\dot{\varphi}} \cdot \frac{\ddot{r} \cdot \dot{\varphi} - \dot{r} \cdot \ddot{\varphi}}{\dot{\varphi}^3}} \right\rangle;$$

$$\ddot{\theta} = \ddot{\varphi} + \frac{\left\langle 2 \cdot \dot{r} \cdot \ddot{r} + 2 \cdot (r \cdot \dot{\varphi}) \cdot \left[\dot{r} \cdot \dot{\varphi} + \dot{r} \cdot \ddot{\varphi}\right] \right\rangle}{\left[\dot{r}^2 + (r \cdot \dot{\varphi})\right]^2} \cdot \left[r \cdot \ddot{r} \cdot \dot{\varphi} - \dot{r}^2 \cdot \dot{\varphi} - r \cdot \dot{r} \cdot \ddot{\varphi}\right] - \frac{\left\langle r \cdot \dddot{r} \cdot \dot{\varphi} - \dot{r} \cdot \ddot{r} \cdot \dot{\varphi} - 2 \cdot \dot{r}^2 \cdot \ddot{\varphi} - r \cdot \dot{r} \cdot \dddot{\varphi} \right\rangle}{\left[\dot{r}^2 + (r \cdot \dot{\varphi})\right]}$$

[26] https://math.stackexchange.com/questions/175191/normal-to-ellipse-and-angle-at-major-axis

Further settling of these expressions has been attempted to a certain extent, but without 'perceptible' chance for significant simplification. Only in that case, done possibly with the aid of the symbolic (as Mathematica) computing might be feasible to make them amenable for reduction to a system of the first order differential equations towards conducting the numerical integration.

Appendix B: Derivation of roationally-invarinat/'classically'-covariant Grad&Div formulae

For Gradient, a)

$$\begin{bmatrix}\nabla_\rho(f)\\ \nabla_\varphi(f)\end{bmatrix}=\begin{bmatrix}\cos(\varphi) & \sin(\varphi)\\ -\sin(\varphi) & \cos(\varphi)\end{bmatrix}\cdot\begin{bmatrix}\nabla_x\\ \nabla_y\end{bmatrix}=\begin{bmatrix}\cos(\varphi) & \sin(\varphi)\\ -\sin(\varphi) & \cos(\varphi)\end{bmatrix}\cdot\begin{bmatrix}\frac{\partial f}{\partial x}\\ \frac{\partial f}{\partial y}\end{bmatrix};\quad \frac{\partial f}{\partial x}=\frac{\partial f}{\partial \rho}\cdot\frac{\partial \rho}{\partial x}+\frac{\partial f}{\partial \varphi}\cdot\frac{\partial \varphi}{\partial x};\quad \frac{\partial f}{\partial y}=\frac{\partial f}{\partial \rho}\cdot\frac{\partial \rho}{\partial y}+\frac{\partial f}{\partial \varphi}\cdot\frac{\partial \varphi}{\partial y}$$

$$\frac{\partial \rho}{\partial y}=\frac{1}{2}\cdot\frac{2\cdot y}{x^2+y^2}=\frac{y}{\rho}=\sin(\varphi);\quad \frac{\partial \varphi}{\partial y}=\frac{1}{1+(y/x)^2}\cdot\frac{1}{x}=\frac{x}{\rho^2}=\frac{\cos(\varphi)}{\rho}.$$

$$\frac{\partial f}{\partial x}=\frac{\partial f}{\partial \rho}\cdot\cos(\varphi)-\frac{\partial f}{\partial \varphi}\cdot\frac{\sin(\varphi)}{\rho};\quad \frac{\partial f}{\partial y}=\frac{\partial f}{\partial \rho}\cdot\sin(\varphi)+\frac{\partial f}{\partial \varphi}\cdot\frac{\sin(\varphi)}{\rho}$$

$$\nabla_\rho(f)=\cos(\varphi)\cdot\left[\frac{\partial f}{\partial \rho}\cdot\cos(\varphi)-\frac{\partial f}{\partial \varphi}\cdot\frac{\sin(\varphi)}{\rho}\right]+\sin(\varphi)\cdot\left[\frac{\partial f}{\partial \rho}\cdot\sin(\varphi)+\frac{\partial f}{\partial \varphi}\cdot\frac{\cos(\varphi)}{\rho}\right]$$

$$\nabla_\rho(f)=\cos^2(\varphi)\cdot\frac{\partial f}{\partial \rho}-\frac{\partial f}{\partial \varphi}\cdot\cos(\varphi)\cdot\frac{\sin(\varphi)}{\rho}+\sin^2(\varphi)\cdot\frac{\partial f}{\partial \rho}+\frac{\partial f}{\partial \varphi}\cdot\frac{\cos(\varphi)}{\rho}\cdot\sin(\varphi)=\frac{\partial f}{\partial \rho}.\quad \text{Also, } \nabla_\varphi(f)=\frac{1}{\rho}\cdot\frac{\partial f}{\partial \varphi}.$$

For Divergence, b)

$$\begin{bmatrix}w^\rho\\ w^\varphi\end{bmatrix}=\begin{bmatrix}\cos(\varphi) & -\sin(\varphi)\\ \sin(\varphi) & \cos(\varphi)\end{bmatrix}\cdot\begin{bmatrix}w^x\\ w^y\end{bmatrix},\ \text{that is}\ \begin{bmatrix}w^x\\ w^y\end{bmatrix}=\begin{bmatrix}\cos(\varphi) & \sin(\varphi)\\ -\sin(\varphi) & \cos(\varphi)\end{bmatrix}\cdot\begin{bmatrix}w^\rho\\ w^\varphi\end{bmatrix}.$$

$$\left\langle\begin{bmatrix}\frac{\partial}{\partial \rho}\\ \frac{1}{\rho}\cdot\frac{\partial}{\partial \varphi}\end{bmatrix}\right\rangle=\begin{bmatrix}\nabla^\rho\\ \nabla^\varphi\end{bmatrix}=\begin{bmatrix}\cos(\varphi) & -\sin(\varphi)\\ \sin(\varphi) & \cos(\varphi)\end{bmatrix}\cdot\begin{bmatrix}\nabla^x\\ \nabla^y\end{bmatrix},\ \text{that is}\ =\left\langle\begin{bmatrix}\frac{\partial}{\partial x}\\ \frac{\partial}{\partial y}\end{bmatrix}\right\rangle=\begin{bmatrix}\nabla^x\\ \nabla^y\end{bmatrix}=\begin{bmatrix}\cos(\varphi) & \sin(\varphi)\\ -\sin(\varphi) & \cos(\varphi)\end{bmatrix}\cdot\begin{bmatrix}\nabla^\rho\\ \nabla^\varphi\end{bmatrix}.$$

By definitional relation for divergence as scalar product of vector and Grad-vector operator,

$$\begin{bmatrix}\nabla^x\\ \nabla^y\end{bmatrix}^T\cdot\begin{bmatrix}w^x\\ w^y\end{bmatrix}=\begin{bmatrix}\nabla^\rho\\ \nabla^\varphi\end{bmatrix}^T\cdot\begin{bmatrix}\cos(\varphi) & \sin(\varphi)\\ -\sin(\varphi) & \cos(\varphi)\end{bmatrix}^T\cdot\begin{bmatrix}\cos(\varphi) & \sin(\varphi)\\ -\sin(\varphi) & \cos(\varphi)\end{bmatrix}\cdot\begin{bmatrix}w^\rho\\ w^\varphi\end{bmatrix}=\begin{bmatrix}\nabla^\rho\\ \nabla^\varphi\end{bmatrix}^T\cdot\begin{bmatrix}w^\rho\\ w^\varphi\end{bmatrix},\ \text{it follows}$$

$$Div^{xy}(\mathbf{w})=\frac{\partial w^x}{\partial x}+\frac{\partial w^y}{\partial y}=\nabla^x\cdot w^x+\nabla^y\cdot w^y=\nabla^\rho\cdot w^\rho+\nabla^\varphi\cdot w^\varphi=\frac{\partial w^\rho}{\partial \rho}+\frac{1}{\rho}\cdot\frac{\partial w^\varphi}{\partial \varphi}=Div^{\rho\varphi}(\mathbf{w})$$

INFLUENCE OF REFLECTED SHOCKWAVES ON NORMAL FORCE COEFFICIENT OF GRID FINS IN SUPERSONIC FLIGHT REGIME

Ognjen Ristić[1]*

[1]Institute for testing of materials – IMS Institute, Belgrade, Serbia
e-mail: risticognjen94@gmail.com

Abstract

The subject of the presented research is the grid fins that serve for controlling the missiles, used instead of the usual planar fins. This type of fins uses inside surfaces of the frame to create an aerodynamics force that will create a torque around the center of the mass of the rocket. For numerical modelling and research of the characteristics of the grid fins the OpenFOAM software was used. The developed model is designed to enable verifying of the assumed behavior of reflected shockwave that passes through grid fins in supersonic flight regime, as well as its influence on normal force coefficient based on different angles of attack. The obtained numerical results are verified by the available experimental results of normal force coefficient. For Mach's number a value of 2.5 was chosen in order to simulate the shockwaves passing through the gaps of a grid fin. For variation of the angle of attack in a particular values range with a particular step, the optimal mesh density is chosen. In the final modelling step the reducing of the time required for numerical simulation of the turbulence model is obtained.

Key words: grid fins, turbulence model, CFD.

1. Introduction

Grid fins are the surfaces that serve for missile control and are used instead of the planar fins. Grid fins use inside surfaces of their frame to create an aerodynamics force that will create a torque around the center of the mass of the rocket. Grid fins are used on rockets since the 1970's. Russian ballistic rockets were equipped with grid fins in order to stabilize the system. They were also used on some supersonic rockets. The most famous example was the "Vympel R-77" and in this case they were used for control purposes. "Falcon 9", produced by "SpaceX" company, used them as a helper to precisely land on a platform [1].

The use of grid fins has its advantages and disadvantages in several aspects. A projectile with grid fins can achieve greater controllability in low and high supersonic flight regimes [2]. However, transonic and low supersonic speeds are considered problematic due to low efficiency and high resistance. Therefore, to control a projectile in transonic flight mode, the control surfaces need to be carefully designed. The main disadvantage of grid fins is that high resistance occurs at high transonic speeds.

The specificity of the grid fins is the superior packing ability, which makes the launching of these missiles easier from inside the weapon or from the barrel of the launcher. The design of this type of rocket is mainly guided by the volume of the launch station. For that reason, while the

rockets are kept in this limited space before they are launched, it is necessary to place the control surfaces on the body of the rocket.

Missile control and maneuvering is performed in two ways, which are called conventional and unconventional flight control. Unconventional control includes thrust vector control and missile carrier control [1], while conventional aerodynamic control is performed by deflecting control surfaces. Conventional aerodynamic control is highly dependent on the location of the control surfaces. When control is done by using a normal scheme, it is common practice for control surfaces to be designed as wings. The stabilizing control surfaces act as a control element, in addition to their original purpose of providing a stable flight for the aircraft. To achieve this, each fin has the ability to rotate around its hinge axis. The normal scheme aims to create a sufficient amount of torque around the center of mass of the projectile to create a certain buoyancy force.

Control of the use of the rotating wing scheme is achieved by turning them so that they create the buoyancy force with which the projectile maneuver will be performed. Since the creation of force does not require rotation of the body, the control of the rotating wings is usually achieved faster than the control of the duck scheme or the normal scheme. However, the deflection of the large wing requires greater actuator power [1]. The control, using the duck scheme, is achieved by small control surfaces located on the front part of the projectile. This type of projectile also carries stabilizers on the back of the body. Rotating the front control surfaces can create sufficient torque around the center of mass of the rocket, similar to a normal scheme. In this paper, the normal scheme is used as the primary alternative, because it is the most common missile control technique.

The aerodynamic normal force is calculated by estimating the surface integral of static pressure and drag contribution (equation 1).

$$C_n = \frac{N}{\frac{1}{2}\rho U^2 A_{ref}} = \frac{N}{\frac{1}{2}\varkappa p M^2 A_{ref}} \tag{1}$$

where: C_n - coefficient of normal force, N - normal force and A_{ref} = 0.025881m^2- rocket cross-sectional area. The convention of signs taken for these coefficients follows in Figure 1.

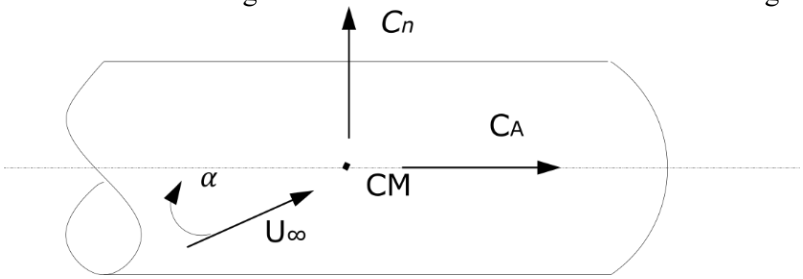

Fig. 1. Convention of signs

Washington and Miller [3] conducted numerous experiments covering different flight modes as well as geometric parameters. Their results are used to compare the results obtained in the research presented in this paper. Burhalter, in order to configure grid fins, developed a theoretical method for calculating grid fins isolated from bodies at subsonic velocity [4] and defined the upward bending effect of flows that must be taken into account at non-zero angles of attack [5].

The performance of grid fins significantly depends on the flight conditions, that is, on the Mach number. It is known that the slope of the buoyancy curve, which shows the efficiency of wing control, is not applied at transient speeds due to the formation of shock waves inside the cells of the fin. At the transient values of the Mach number, Belotserkovsky formulated this phenomenon as a loss of dynamic pressure due to congestion that occurs inside the fin cells [6]. M. Tripathi, M.M. Sucheendran and A. Misra varied geometrical properties of the fins to determine its influence on subsonic aerodynamics of cascade type grid fin, experimentally and numerically [7]. Different approach concerning design of sept back and forward grid fins, was done by G. A. Faza, H. Fadillah, F. Y. Silitonga and Mochamad Agoes Moelyadi in order to obtain numerical results for aerodynamic efficiency of different grid fin designs v/s angle of attack [8].

2. Speed of sound and Mach number

Air consists of a huge number of molecules that move chaotically, at different instantaneous speeds and have different energies at different times. It is almost impossible to track the motion of each of the molecules, so in the kinetic theory of gases, the mean velocity of the motion of molecules is defined by time averaging. For ideal gases, this speed depends only on the temperature. If we take the example of a firecracker explosion, the explosion releases a certain amount of energy absorbed by the surrounding air molecules, which leads to an increase in the speed at which they move. These molecules collide with the surrounding molecules, giving them the energy, they possess. In this way, the energy released by detonation is transmitted through the air by the interaction of molecules. Thus, we can assume that an "energy wave" travels through the surrounding air at a speed that must in some way be related to the mean velocity of the molecule, because the interaction of molecules actually transmits that energy. As it passes through the wave, the increased energy of the molecule is macroscopically manifested by small changes in pressure (and therefore density and temperature). When the wave passes by the observer, this small change in pressure is registered by the eardrum, and this information is transmitted to the brain as sound. Therefore, the speed spreads and small disturbances are called the speed of sound [9]. The speed of sound is an important quantity in the study of compressible flows of fluids, and for ideal gases it is calculated according to the formula:

$$c = \sqrt{\varkappa RT} \tag{2}$$

For air under standard conditions (p = 101325Pa, T = 288K), the speed of sound is c = 340.9 $\frac{m}{s}$.

The Mach number at a point in the current space is defined as the ratio of the local speed of the current and the value of the speed of sound at that point:

$$M = \frac{U}{c} \tag{3}$$

Based on the value of Mach number, flows can be divided into:

- $M < 1$ subsonic flow
- $M = 1$ critical flow regime
- $M > 1$ supersonic flow

Mach number also has a certain physical meaning. Imagine fluid parts moving at some speed U. The kinetic and internal energies per unit mass of the fluid part are: $\frac{U^2}{2}$ and e. The relationship of these two types of energy is:

$$\frac{U^2/2}{\mathrm{e}} = \frac{U^2/2}{c_v T} = \frac{U^2/2}{RT(\varkappa-1)} = \frac{(\varkappa/2)U^2}{C^2/(\varkappa-1)} = \frac{\varkappa(\varkappa-1)}{2} M^2 \tag{4}$$

Thus, the square of Mach number is proportional to the ratio of kinetic and internal energy. It is a measure of the macroscopic movement of gas in relation to the chaotic movement of its molecules. As the speed of sound has a finite value and, in a gas, it depends only on its local temperature, the speed of the source will affect the propagation of the sound wave.

Depending on the position of the shock wave in relation to the direction of flow, the shock waves are divided into straight and oblique. A straight or normal shock wave is normal in relation to the flow direction, and an oblique shock wave is inclined at an angle to the flow direction. When passing through the shock wave, the gas flows from the undisturbed to the disturbed area, and on that occasion, there are final increases in pressure, temperature and density, and final decreases in the flow velocity and Mach number. For practical application, the change of the flow quantities when passing through the shock wave is especially interesting. Sudden changes in flow quantities take place at a very short distance from several free paths of molecules, of the order of 0.2 μm, so the shock wave is considered to be a discontinuity in the flow field [9].

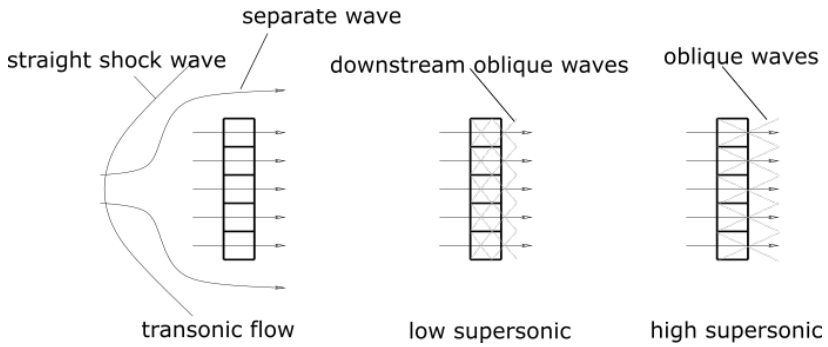

Fig. 2. Possible types of flow in different flight regimes

The flow field around the lattice surface of the wing is determined by Mach number. In the transonic flight mode, the projectile with grid fins has the biggest drawback: increased resistance. The reason for the increased resistance is the field of internal flow within the cube as a wing cell. In the transonic mode, the flow inside the cells is congested, so the flow upstream from the wing slows down. This means that the grid fins act as an obstacle to the flow of air, which increases the resistance [10].

3. Supersonic flight regime

The grid fin in supersonic flight mode is exposed to shock waves to varying degrees, depending on Mach number. For Mach numbers values that are slightly larger than 1, a straight shock wave occurs in front of the water edge of the grid fin [6]. This is also called a separate wave (Figure 2). As Mach's number increases, the location of the impact approaches the edges of the wing. At certain values of Mach number, the shock waves become bound to leading edges. After that, oblique and diluted waves are observed. Oblique waves bounce off the walls of grid fins at relatively low Mach numbers. As the Mach number increases, the angles overlapping the oblique waves become smaller, and are thus converted into non-repulsive waves, Figure 3.

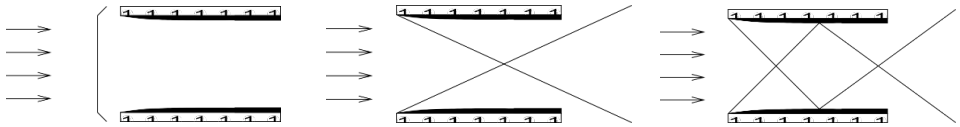

Fig. 3. A phenomenon that occurs inside the wing at different values of Mach number

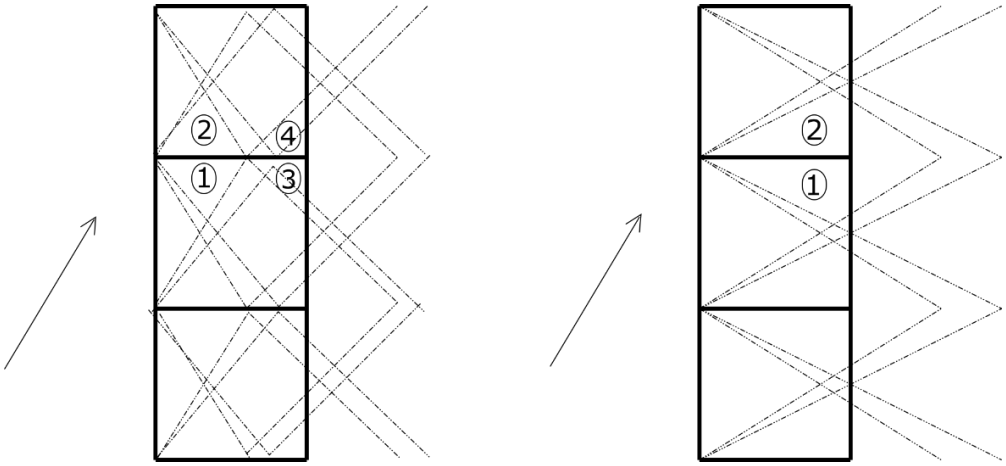

Fig. 4. Areas of characteristic pressure distribution associated with oblique shock waves

The illustration in Figure 4 shows the scheme of the waves that bounce off and the waves that do not bounce off the inside of the fin. It flows at an angle of attack creating force on each surface by creating overpressure in area 1 and under pressure in area 2, in both schemes. However, in the case of wave reflection, area of compressed air, area 3 and area of compressed air, area 4 contribute to the buoyancy forces.

4. Numerical domains

The grid fins are made of the planar surfaces that are repeating according to the pattern. This makes it possible to make calculation process easier with extraction of one part of that pattern and only observing behavior of flow around that part called unit grid fin [2]. This idea reduces computational time and resources required for calculations. Schematic view of the UGF is shown in Figure 5 (left).

The other approach would be to model the entire rocket geometry with all four fins installed (given in Figure 5. right). The entire domain is modeled using the blockMeshDict file, and then imprinting the CAD model in the domain using surfaceFeatureExtractDict application that is implemented in OpenFOAM. Meshing was done by using snappyHexMeshDict file [11].

Geometrical parameters of grid fins, related to the overall dimensions of the grid fins, are called height s, total length b and chord c. Width w and thickness t, are the ones that define dimensions of cells. In addition, thickness of frame t_f, define dimension of external framework, which serves as a bearing element that keeps cells together (Figure 2).

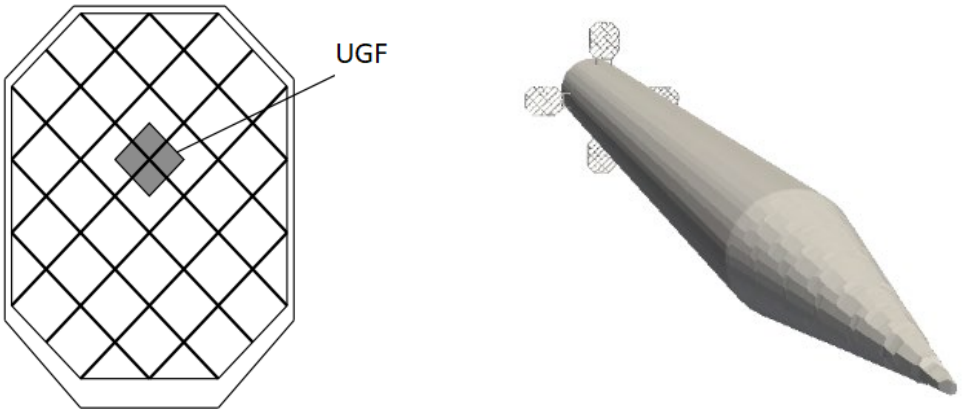

Fig. 5. Unit grid fin approach (left) and CAD model of the rocket with four fins (right)

4.1 Experiments used for results verifying

Wind tunnel tests for various grid fin models have been performed by Washington and Miler [3]. The aerodynamic forces and the torque were measured when fins were mounted on a long projectile with cylindrical body of the caliber 10.4 (Figure 6 (down)). There are four fins in (x) configuration. Aero-scale is located between the body of the rocket and wing 4, in order to measure the aerodynamic load on the tail. Pressure and temperature values were taken as values of standard atmosphere (p = 101325Pa, T = 288K).

It is necessary to know how well UGF concept is representing the actual domain. Idea is to calculate aerodynamic force and torque on UGF and then multiply it with number of repetitions in pattern, n. The components except inside frame, like external frame and rods that connect fins to rocket doesn't take into calculations [4].

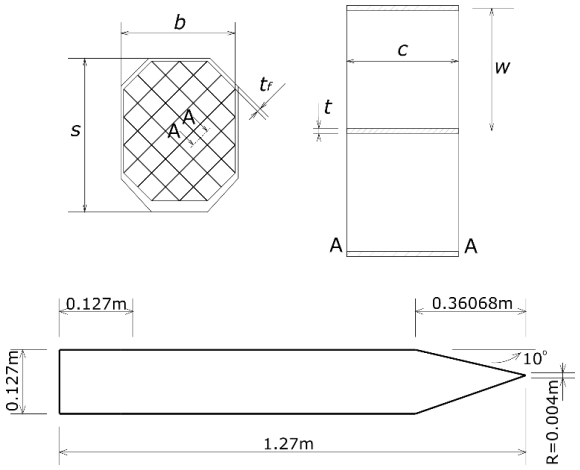

Fig. 6. Geometrical parameters of the fins(up) and sketch of the rocket used in experiments (down)

A large part of the frame is covered by cells of type 1, cells on the side of the frame are different, just like it is shown in Figure 7. They are labelled type 2 and type 3. Type 1 cells seem like a complete UGF, while the cells of the type 2 and type 3 are 3/4 and 1/2 from UGF, respectively. When number of repetitions, n is calculated there are 28 cells of type 1, 4 cells of type 2 and 14 cells of type 3, or 38 cells of UGF in total (Figure 7 left). Consequently, every aerodynamic force obtained in numerical calculations has to be multiplied with 38 to obtain force on whole fin. It is not necessary to do this process if force coefficients are calculated with numerical simulations.

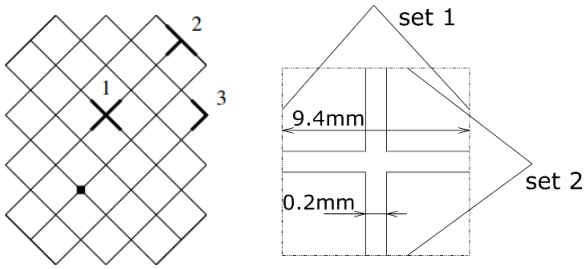

Fig. 7. Types of cells (left) and cyclic conditions scheme (right)

Defining of boundary condition, for boundaries of domain is done using cyclic conditions. That is possible since behavior in domain can be divided in two sets. Behavior of flow is exactly the same one in relation to another (Figure 7 right).

4.2 Turbulence modelling

In this paper, the same cases will be modelled with two different turbulence models, after which a comparison of these results will be performed:

- Standard k - ε turbulence model:

This model uses wall functions that analytically give fluid velocity in a viscous sublayer near the wall. It provides good convergence and does not consume too much computer memory. The expression for calculating the value for k is:

$$k = \frac{3}{2}\left(I\left|u_{ref}\right|\right)^2 \tag{5}$$

where with $I = 0.05$, and u_{ref} is the flow rate. The expression for calculating the value ε is:

$$\varepsilon = \frac{c_\mu^{0.75} k^{1.5}}{L} \tag{6}$$

Where recommended value for c_μ = 0.09, while L = 0.097 m represents the fin length in this case.

- $k - \omega$ SST turbulence model:

The basic k - model can be used for flow calculations and inside viscous sublayer. The SST formulation of the model combines the strengths of the $k - \omega$ and k - ε models, [12]. When using this model, it is necessary to define the value of the dissipation frequency ω. It is determined based on the expression:

$$\omega = c_\mu^{0.25} \frac{\sqrt{k}}{L} \tag{7}$$

Boundary conditions used in this paper will follow in a Table 1:

Mach number	U [m/s]	k [m^2/s^2]	$\mathcal{E}$ [m^2/s^3]
2.5	850.435	2712.1	239265.8438

Table 1. Boundary conditions.

5. Numerical modelling and results

In this paper, two types of meshes were used, a structured mesh obtained using a blockMeshDict file (Figure 8-left) and an unstructured one using a snappyHexMeshDict file (Figure 8-right). The image display of both types of fine mesh follows in the Figure 8. Cross section numerical domain where fluid flow occurs is displayed on Figure 9. The number of elements generated for unstructured mesh in this case is 292313.

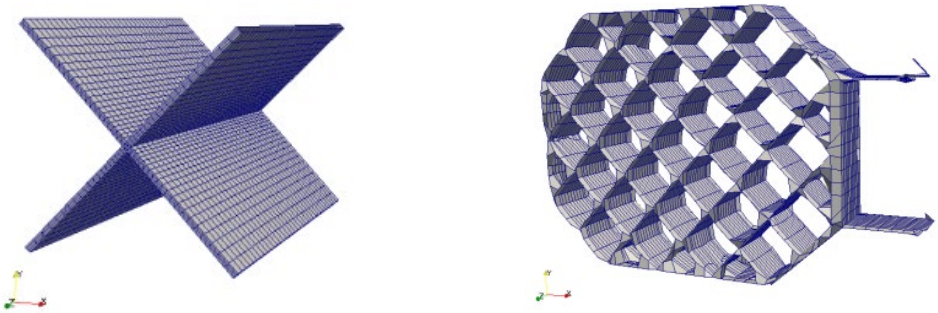

Fig. 8. Structured mesh of UGF (left) and unstructured mesh of cad model (right)

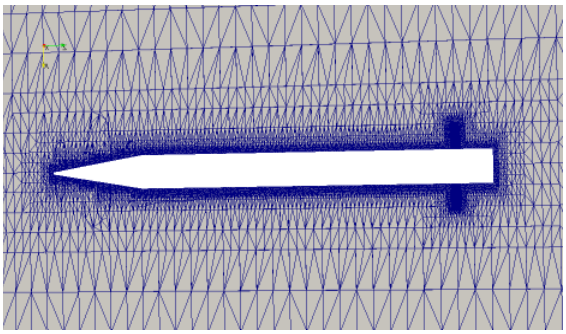

Fig. 9. Cross section of numerical domain (unstructured)

In this part of the paper the results obtained by obstructing the two types of mesh and comparing the results with the experimental results obtained by other researchers are presented. The angle of attack is varied by [0^0; 2.5^0; 5^0; 7.5^0; 10^0; 12.5^0; 15^0]. Also, different models of turbulence were used. This chapter will show the differences between the values obtained by the laminar UGF model, the turbulent UGF model (k - ε and $k-\omega$ SST), the snappyHexMesh approach (also k - ε and $k-\omega$ SST) and the experimental values. The obtained values are shown in Figure 10. The UGF model was found to be too erroneous while the snappyHexMesh approach well describes realistic behavior down to high values of the angle of attack. Figure 11 shows the occurrence of flow congestion through grid fins using both approaches. In this way, the assumption of the formation of separate waves through the fins at the values of Mach number M=2.5 was confirmed.

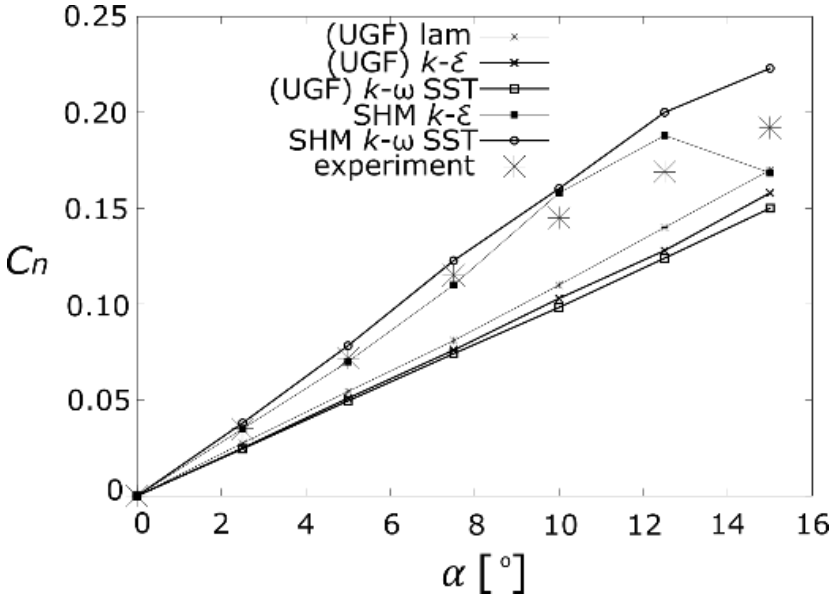

Fig. 10. Comparison of numerical results and experiment

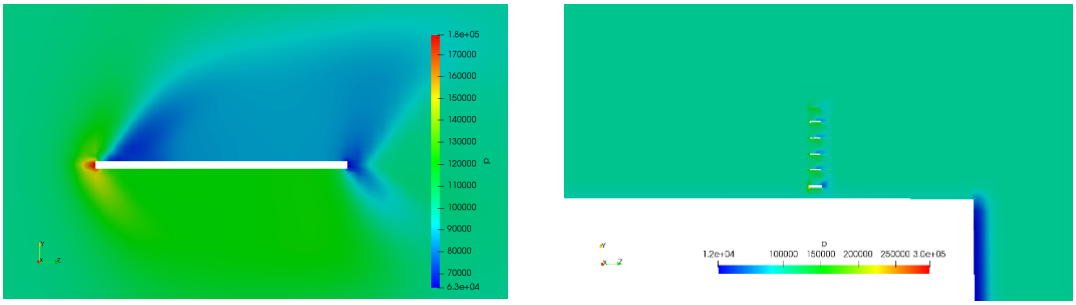

Fig. 11. Pressure distribution example (α = 5^0) of UGF (left) and of cad model (right)

5.1 Analysis of the influence of numerical mesh density on the accuracy of results

The results obtained on a numerical mesh of higher density in the case of its generation by the snappyHexMesh application are presented. The increase in the density of the numerical mesh was done mostly in the zones around the grid fins, because the fins are the ones that make the normal coefficient around the center of mass of the rocket, but also on the body of the rocket. The values for the value of the Mach number $M = 2.5$ will be presented and compared with the values obtained on the previous mesh, as well as the experiment performed by other researchers. The following is an overview of the dense mesh in Figure 12-left and its cross section in Figure 12-right. The number of elements generated for unstructured mesh in this case is 2781225.

α=[^{0}]	Sparse mesh ϵ[%]	Dense mesh ϵ[%]
5	9.15	4.958
10	10.55	5.86
15	16.145	19.109

Table 2. Relative errors of obtained results compared to experimental values published by other researchers, [3]

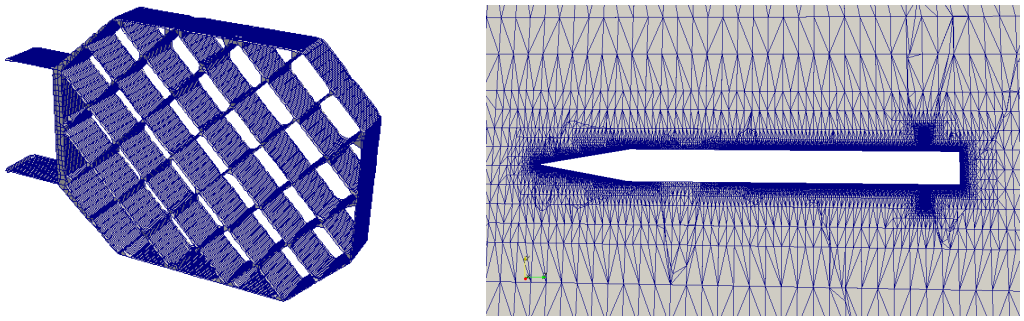

Fig. 12. Unstructured mesh of fin (left) and unstructured mesh of the whole cad model (right)

Meshing was done by modifying the data within the snappyHexMeshDict file. The results obtained by using a denser mesh are presented in Figure 13 and compared with the results obtained in the previous chapter using the $k-\omega$ SST model. The Table 2 gives the relative errors which refers to the relative error in relative to experimental values depending on the mesh density for Mach number M =2.5 and angles of attack α = [5^0, 10^0, 15^0].

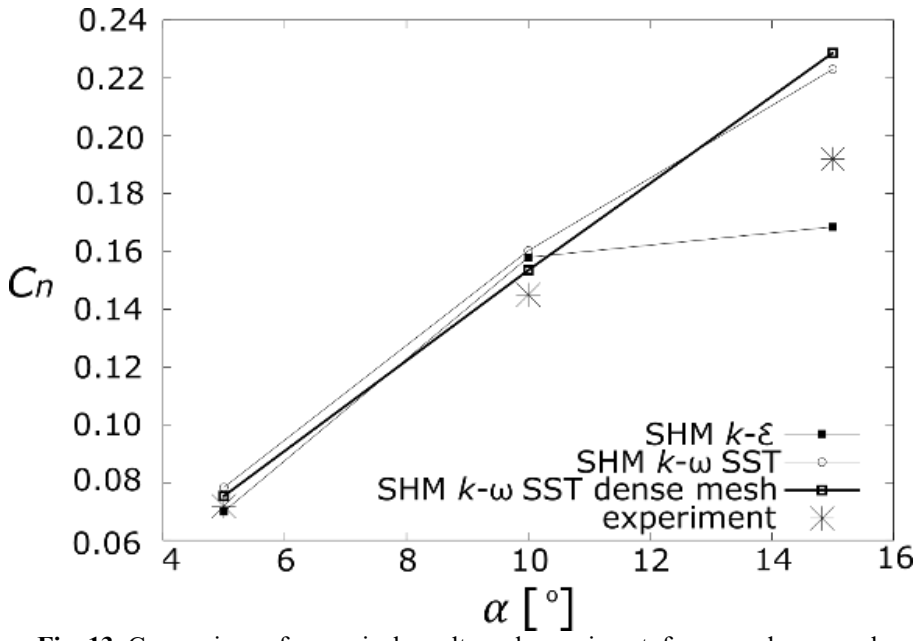

Fig. 13. Comparison of numerical results and experiment, for more dense mesh

6. Conclusion

In this paper, the normal force coefficient Cn, which makes grid fins as control surfaces in the transonic flight regime, was studied by comparing experimental values, which were obtained by other researchers, and computational results. Angle of attack α= [0º, 2.5º, 5º, 7.5º, 10º, 10.5º, 12.5º,

15°] was varied. The most important conclusion is that the simulations within OpenFOAM software follows the experimental values quite faithfully. The concept of unit grid fin (UGF) cannot be used in order to reduce computational costs and to ensure satisfactory accuracy in transonic flight conditions.

The model of the entire rocket gives much more accurate results in the transonic range of Mach numbers than the UGF model. The influence of fluid flow bending due to passing over the nose and body of the rocket is too great, to be ignored using the UGF approach. $k - \varepsilon$ method follows the experimental values a little worse than $k - \omega$ SST. SnappyHexMesh approach and more dense mesh give much more accurate results for small values of the angle of attack, while this is not the case with large angles of attack, the error is even greater than with a sparse mesh.

For some of the further research it is possible to:

- gradually make the mesh with more elements to see how it affects the solutions;
- compare the mesh density and the convergence time required;

Acknowledgements: This article/publication is based upon work from COST Action CA21106 [WG4: Direct WISPs searches, WG 5:Dissemination and Outreach], supported by COST (European Cooperation in Science and Technology).

References:

[1] E. L. Fleeman., Tactical Missile Design, American Institute of Aeronautics and Astronautics, Inc., Reston, VA, 2001.
[2] S. M. Belotserkovsky, L. A. Odnovol, Y. Z. Safin, A. I. Tylenev, V. P. Frolov, and V. A. Shitov, Reshetchatye Krylya (Grid fins), Mashinostroenie, Moscow (in Russian), 1985.
[3] D. Washington and M. S. Miller, In RTO AVT Symposium on Missile Aerodynamics, Sorrento, Italy, 1998.
[4] J. E. Burkhalter and H. J. Frank, Grid fin aerodynamics for missile applications in subsonic flow, Journal of Spacecraft and Rockets, 33(1), January- February 1996.
[5] J. E. Burkhalter, R. J. Hartfield, and T. M. Leleux, Nonlinear aerodynamic analysis of grid fin configurations, Journal of Aircraft, 32(3):547-554, May-June 1995.
[6] E. Dikbas, Master thesis. Desing of a grid fin aerodynamic control device for transonic flight regime, Middle east technical university, 2015.
[7] M. Tripathi, M.M. Sucheendran and A. Misra, Effect of aspect ratio variation on subsonic aerodynamics of cascade type grid fin at different gap-to-chord ratios, THE AERONAUTICAL JOURNAL, Page 1 of 27. c Royal Aeronautical Society 2019, 2019.
[8] G. A. Faza, H. Fadillah, F. Y. Silitonga and Mochamad Agoes Moelyadi, Study of Swept Angle Effects on Grid Fins Aerodynamics Performance, IOP Conf. Series: Journal of Physics: Conf. Series 1005 (2018) 012013, 5th International Seminar of Aerospace Science and Technology, 2018.
[9] C. Crnojević, Mehanika fluida, Mašinski fakultet Univerziteta u Beogradu, 2014.
[10] Y. Zeng, J. Cai, M. Debiasi, and T. L. Chng, Numerical study on drag reduction for grid-fin configurations, In 47th AIAA Aerospace Sciences Meeting Including The New Horizons Forum and Aerospace Exposition, AIAA- 2009-1105, Orlando, FL, USA, January 2009.
[11] Ognjen Ristić, Master thesis, NUMERICAL CALCULATION OF GRID FINS IN SUBSONIC AND TRANSONIC FLIGHT REGIME, Faculty of Mechanical Engineering, University in Belgrade, 2018, 2018.
[12] Florian R. Menter, Improved two-equation k-omega turbulence models for aerodynamic flows, 1992.

IMPROVING AIRFOIL PERFORMANCE BY DESIGNED BLOWING

Jelena Svorcan, Toni Ivanov, and Aleksandar Simonović

[1] Department of Aerospace Engineering, Faculty of Mechanical Engineering
University of Belgrade, Kraljice Marije 16, 11120 Belgrade 35
e-mail: jsvorcan@mas.bg.ac.rs, tivanov@mas.bg.ac.rs, asimonovic@mas.bg.ac.rs

Abstract

Modern trends in the development of urban air vehicles and small-scale unmanned air vehicles require them to be as efficient as possible. One option is to improve their aerodynamic performance by semi-active boundary layer control (BLC) techniques, which are more economic and accessible through 3D printing, such as injection/blowing. Flow control generally serves to reduce BL thickness and friction drag, as well as to delay transition and separation. This computational study investigates and quantifies the change in lift and drag coefficients of NACA 23012 airfoil at the critical angle-of-attack (AoA) at M = 0.18 and Re = 1.8 million. Flow simulations are performed using the finite volume method in ANSYS Fluent. Clean and controlled flows are considered steady, incompressible, and viscous. Equations governing the flow are closed by k-ω SST turbulence model. The adopted numerical set-up is validated by available experimental data. Main observations on the possible improvements of aerodynamic performance at a higher angle-of-attack are presented and discussed.

Keywords: NACA 23012, lift, drag, turbulence, blowing.

1. Introduction

Airfoils, main constituents of lifting surfaces, affect the overall aerodynamic performance of flying vehicles. Resulting flows can be controlled to increase aerodynamic efficiency by reducing BL thickness and friction drag, delaying laminar-turbulent transition and preventing or postponing its separation. Numerous flow control techniques have been tried [1]. A relatively reasonable and economic methods are continuous injection or suction (or their combination) that locally change velocity profile and energize the boundary layer [1, 2]. Nowadays, with the advancement of novel production practices, it is possible to design and incorporate a BLC that is structurally simple, does not require any additional moving parts, only locally influences the flow field, and does not significantly increase the total manufacturing and maintenance costs. This work proposes a BLC appropriate for airfoils at higher AoAs. The idea is to suck in the slower flow from the airfoil pressure side, accelerate it through a variable-area passage and blow it along the rear part of the airfoil suction side. This simple solution should be designed for a particular airfoil and flow regime. A well proven NACA 23012 airfoil is chosen as baseline for its reasonably high maximum lift and low profile drag. This paper describes the initial computational study of flows with and without flow control that can be further improved in the future.

2. Methodology

Computational domains around the airfoils are 3D, cylindrical and stretch 10 in radial, and 0.2 chord lengths in spanwise direction. Grids are unstructured with fine resolution near the airfoil walls numbering 8-9 million control volumes for the cases with and without flow control, respectively. All flow simulations are realized by finite volume method in ANSYS Fluent. The flow is considered spatial (2.5D), steady, incompressible, and viscous. Reynolds-averaged Navier-Stokes equations are closed by k-ω SST turbulence model. Velocity of the undisturbed flow is assigned to the inlet boundaries, two sides form a periodic boundary, while no-slip boundary conditions are assumed along the airfoil walls. Pressure-based solver with SIMPLE coupling schemes for pressure and velocity fields are employed. All spatial derivatives are approximated by 2nd order schemes. Computations were performed until reaching the converged values of aerodynamic coefficients (3000 iterations).

3. Results and Discussion

The adopted computational set-up was first validated on the clean configuration through comparison with available experimental data [3, 4]. Although some discrepancies between the two data sets are observed, the trends of aerodynamic coefficients are well captured. Afterwards, some qualitative results were post-processed. Here, only critical AoA α = 14.4° is considered. Figure 1 illustrates the obtained velocity fields around the airfoil without and with semi-active flow control, respectively. It can be observed that the existence of variable-area channel leads to the enlarged zone of accelerated flow near the leading edge, an obvious reduction of the separated zone near the trailing edge as well as considerably narrowed wake. Quantitatively, the values of lift and drag coefficients computed on the clean airfoil are C_L = 1.36 and C_D = 0.0364, respectively, resulting in lift-to-drag ratio L/D = 37.2. On the other hand, the corresponding values obtained on the modified airfoil are C_L = 1.46 (7.5% increase), C_D = 0.0333 (8.5% decrease) and L/D = 43.7, i.e., an increase of nearly 17.5% in lift-to-drag ratio is achieved.

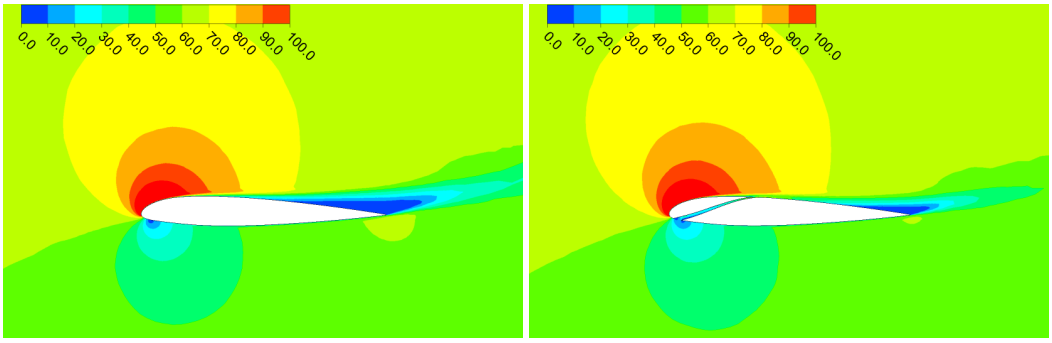

Fig. 1. Velocity contours around airfoils without (left) and with (right) flow control at AoA = 14.4°.

4. Conclusions

Possible changes of airfoil lift and drag coefficients by semi-active boundary layer control are quantified and interesting flow visualizations are presented. Although investigated flow fields are simplified, they provide an insight into the complex flow phenomena occurring in the boundary layer and justify further research studies as well as exploration of different channel geometries.

References:

[1] Svorcan J., Wang J.M., Griffin K.P., *Current state and future trends in boundary layer control on lifting surfaces*, Advances in Mechanical Engineering, Vol. 14(7), 2022.
[2] Lehmkuhl O., Lozano-Durán A., Rodriguez I., *Active flow control for external aerodynamics: From micro air vehicles to a full aircraft in stall*, Journal of Physics: Conference Series, Vol. 1522(1), 012017, 2020.
[3] Monastero M., *Validation of 3-D ice accretion documentation and replication method including pressure-sensitive paint*, MSc thesis, University of Illinois at Urbana-Champaign, 2013.
[4] Broeren A., Addy H. Jr., Lee S., Monastero M., McClain S., *Three-dimensional ice-accretion measurement methodology for experimental aerodynamic simulation*, Journal of Aircraft, Vol. 55(2), 817-828, 2018.

3D PRINTING TECHNOLOGY IN CRANIOPLASTY: CASE STUDY

Tijana Geroski[1,2], Dalibor Nikolić[2,3], Vojin Kovačević[4,5], and Nenad Filipović[1,2]

[1] Faculty of Engineering, University of Kragujevac, Sestre Janjić 6, 34000 Kragujevac, Serbia
[2] Bioengineering Research and Development Centre (BioIRC), Prvoslava Stojanovića 6, 34000 Kragujevac, Serbia
[3] Institute for Information Technologies, Jovana Cvijića bb, 34000 Kragujevac, Serbia
[4] Center for neurosurgery, Clinical Centre Kragujevac, Zmaj Jovina 30, 34000 Kragujevac, Serbia
[5] University of Kragujevac, Faculty of Medical Sciences, Department of Surgery, Svetozara Markovića 69, 34000 Kragujevac, Serbia
e-mails: tijanas@kg.ac.rs, markovac85@kg.ac.rs, vojincnh@gmail.com, fica@kg.ac.rs

Abstract

Cranioplasty is the surgical repair of a bone defect in the skull resulting from a previous operation or injury, which involves lifting the scalp and restoring the contour of the skull with a graft made from material that is reconstructed from scans of the patient's own skull. The paper introduces a 3D printing technology in creating a 4-piece mold, which is filled with polymethyl methacrylate (PMMA) to reconstruct the missing bone part of the skull. The procedure included several steps to create a 3D model in an STL format, conversion into a G-code which is further used to produce the mold itself using a 3D printer. Presented use case surgery showed a good match of the missing bone part and the part created using 3D printed mold, without additional steps in refinement. In such a way, 3D printing technology helps in creating personalized and visually appealing bone replacements, at a low cost of the final product.

Keywords: cranioplasty, 3D printing, mold, personalized medicine.

1. Introduction

Cranioplasty is a frequent neurosurgical procedure used to address cranial vault abnormalities [1]. 3D printing enables the production of patient-specific synthetic cranioplasties for major deformities. While certain medical device firms provide patient-specific implants, cost and manufacture time are significant barriers to their widespread adoption. Individual implants sometimes cost more than CA$10,000, thus neurosurgeons must exercise caution when determining which patients would benefit the most from these implants [2]. Manufacturing time is typically weeks, limiting the use of commercial alternatives in situations of trauma or when rapid rebuilding is necessary. Given these constraints, surgeons frequently choose 'free-hand' repair of cranial abnormalities using polymethyl methacrylate (PMMA), titanium mesh, or a mix of the two. This approach produces less predictable results, frequently resulting in unsatisfactory restoration of cranial vault contour and overall cosmesis [3].

The goal of this study is to share our experience with an innovative, cost-effective approach for cranioplasty that uses desktop 3D printers to create patient-specific molds to help in the intraoperative shaping of polymethyl methacrylate (PMMA) cranioplasty.

2. Materials and methods

A use case of the patient who underwent cranioplasty utilizing 3D printed custom mold was conducted at a Center for Neurosurgery, Clinical Centre Kragujevac in 2022. A four-piece mold was utilized.

The following steps are typical for a prototype: (i) 3D model is created and saved in a format supported by the CAM packets (STL) (ii) any flaws are fixed, and (iii) the format is converted into G-code by the CAM packet. Finally, (iv) the model is produced using a 3D printer.

2.1 Mold creation using 3D printing

Making a patient-specific model is a very complex process and consists of several steps. The creation of a patient-specific 3D model usually begins with the segmentation of DICOM images obtained by CT scanning. Based on the threshold, the segmentation software isolates part of the bone and generates a precise 3D model of part of the patient's skull. Part of the missing bone is clearly visible in this model (Fig. 1).

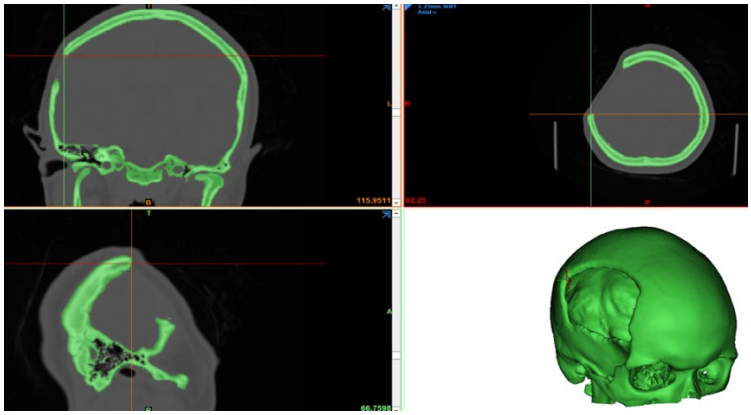

Fig. 1. Segmentation of CT images and generation of a 3D model of skull

The model is then imported into computer design - CAD software, in which a 3D model of the missing part of the skull is manually created (virtual surgery) (Fig. 2).

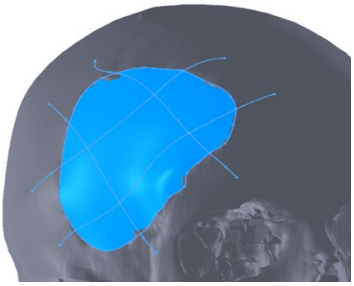

Fig. 2. Created missing part of the skull in CAD software.

The mold-making process, which is the next step, is very complex and requires a detailed analysis of the part being made from the mold in order to position the mold-casting plane in the appropriate place (Fig. 3). This process is mostly done manually and is experience dependent.

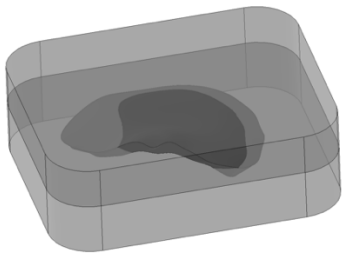

Fig. 3. 3D mold model

After creating the mold in the CAD software, the next step is to create the so-called G-code models for 3d printing. For this purpose, specialized software "Slicing" is used, which generates a series of 2D sections from a 3D model. The thickness of the section for this model is used at 0.16 mm in order to obtain a high precision of the print. Mold was printed on an FDM (Fused Deposition Modeling) printer (Fig. 4 left) with a nozzle diameter of 0.4 mm, and polylactic acid, also known as PLA, was used as the material. This is a thermoplastic monomer obtained from renewable, organic sources such as corn starch or sugar cane and belongs to the group of non-toxic bioplastics. The final product is a four-piece mold as depicted in Fig. 4 right.

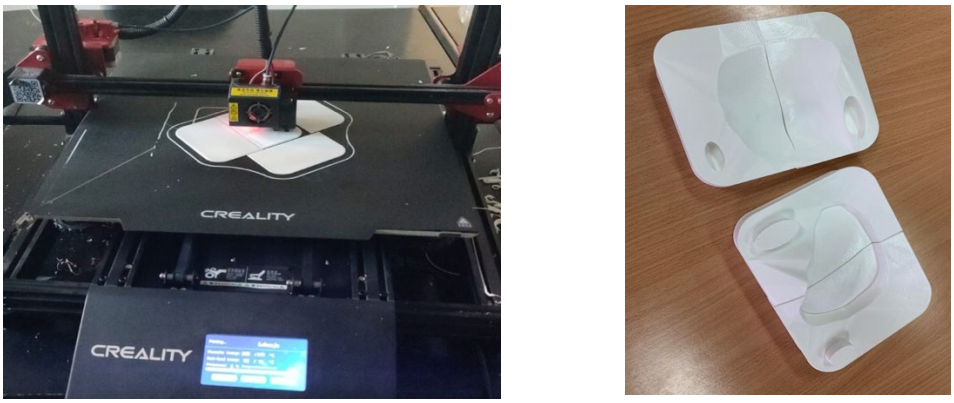

Fig. 4. 3D mold printing process (left), final four-piece mold product (right)

2.1 Cranioplasty

The goal of the surgery are not only cosmetic purposes. Restoring the natural contour and shape of the skull provides a rigid protective structure around the brain which is significant for many neurophysiological processes. In essence, the cranioplasty is performed to replace the rigid bony structure that is missing in the skull. Fig. 5 shows a preoperative CT scan (left), followed by a post-operative CT scan (right). Images show that in this specific patient case, the skull piece created using the 3D printed mold fits very well, with no additional refinement and better aesthetics than using the standard “free-hand” procedure.

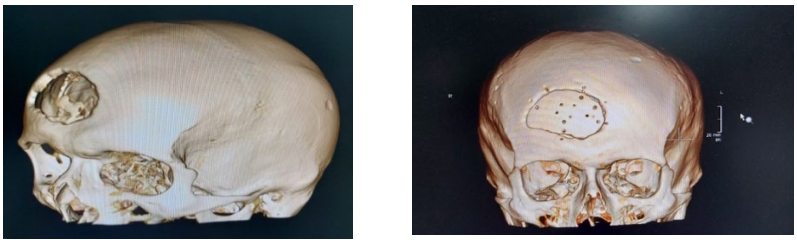

Fig. 5. Preoperative CT scan (left), post-operative CT scan (right)

Fig. 6 shows the process of mold use in creating missing skull part (left), and end result during surgery. No further complications were observed in a patient.

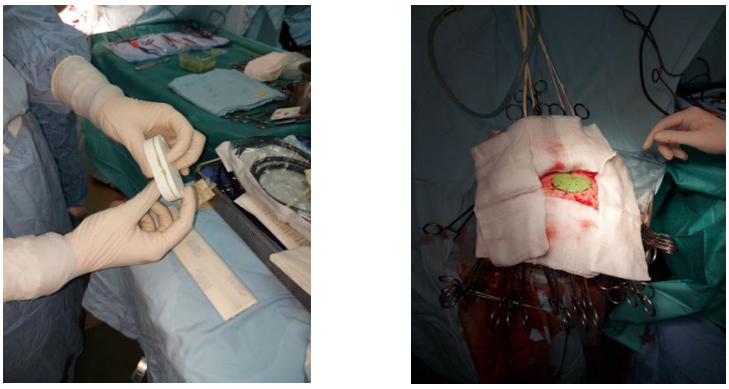

Fig. 6. Creation of missing skull piece using 3D printed mold (left), the end result of attaching the piece during surgery

3. Conclusions

Modern rapid prototyping systems have been built on the basis of established and enhanced technology and may thus be widely employed in the industry. Despite being a relatively new technology in the industry, 3D printed technology plays an important role in meeting some important market targets such as shortening TTM (Time to Market) and lowering the cost of the final product, which made this technology much more interesting to the industry and created a need for skilled engineers in the fields of rapid prototyping. This paper shows that 3D printing may be utilized to give good cranioplasty cosmesis at a low cost. The use of this strategy on a larger scale might result in considerable healthcare cost reductions without affecting patient outcomes.

Acknowledgement: The research was funded by the Ministry of Science, Technological Development and Innovation of the Republic of Serbia, contract number [451-03-47/2023-01/200107 (Faculty of Engineering, University of Kragujevac)]. This research is also supported by the project that has received funding from the European Union's Horizon 2020 research and innovation programmes under grant agreement No 952603 (SGABU project). This article reflects only the author's view. The Commission is not responsible for any use that may be made of the information it contains.

References:

[1] M. Lannon, A. Algird, W. Alsunbul and B. Wang, "Cost-effective cranioplasty utilizing 3D printed molds: a Canadian single-center experience," Canadian Journal of Neurological Sciences, vol. 49, no. 2, pp. 196-202, 2022.
[2] A. Binhammer, J. Jakubowski, O. Antonyshyn and P. Binhammer, "Comparative cost-effectiveness of cranioplasty implants," Plastic Surgery, vol. 28, no. 1, pp. 29-39, 2020.
[3] J. Oliver, J. Banuelos, A. Abu-Ghname, K. Vyas and B. Sharaf, "Alloplastic cranioplasty reconstruction: a systematic review comparing outcomes with titanium mesh, polymethyl methacrylate, polyether ether ketone, and norian implants in 3591 adult patients," Annals of plastic surgery, vol. 82, no. 5S, pp. S289-S294, 2019.

ON DEVIATIONS IN NONLINEAR TIME DOMAIN REGIME OF VIBRATIONS OF THE PARTLY COUPLED STRUCTURES WITH THE CURVATURES

Vladimir Stojanović[1,2], Jian Deng[2], Dunja Milić[1], and Marko D. Petković[3]

[1] Faculty of Mechanical Engineering, University of Niš, Aleksandra Medvedeva 14, 18000 Niš
e-mail:stojanovic.s.vladimir@gmail.com, dunja1994milic@gmail.com,
[2] Faculty of Engineering, Lakehead University, Thunder Bay, Ontario, Canada P7B 5E1
e-mail: jian.deng@lakeheadu.ca,
[3] Faculty of Sciences and Mathematics, University of Niš, Višegradska 33, 18000 Niš
e-mail: dexterofnis@gmail.com

Abstract

Geometrically nonlinear time domain dynamic analysis of a coupled Timoshenko beam-beam or beam-arch mechanical system is investigated in this paper. The coupled structure is modelled with variable discontinuity in an elastic layer as a real case from technical practice when there is no continuous distribution of the elastic layer, or the stiffness of the layer is changed by some other influences at different locations. A p-version finite element method is developed for vibrations of a shear deformable coupled beam system with discontinuity in an elastic layer between. The main contribution of the work is the simultaneous vibration analysis of the coupled effects of varying discontinuity and varying curvature of the new modelled coupled mechanical system, new general mode shapes and the forced vibrations in the time domain determined by the Newmark method.

Keywords: Coupled beam system, Vibrations, Discontinuity, Newmark method.

1. Introduction

Vibrations and dynamic analysis of coupled beams or plates have been of a wide practical interest. In the case when a shear deformable beam considers the geometrically nonlinear effect, and a nonlinear elastic layer possesses a discontinuity, it is efficient to use the improved *p*-version of the finite element method developed for structures with this kind of discontinuity [1]. One of the types of complex coupled beam models is analysed in this paper. The influence of different discontinuities in the elastic layer that connects two beams, or one beam and one arch was considered. The effects of transverse shear (Timoshenko beam), the effects of the different curvature of the lower beam and the different position and size of the discontinuity in the elastic layer that connects them were considered. The principal goal of this work is to present the influence of the discontinuity in an elastic layer on natural frequencies, deviations of mode shapes and nonlinear time domain responses for various sizes and locations of the discontinuity, various curvature effect of the lower beam/arch in the steady state regime under concentrated harmonic excitation. The equations of motion are obtained by the principle of virtual work and solved by the Newmark method. The model is validated by comparing the results with the finite element software ANSYS [2].

2. Instructions

In this paper, rotary inertia and shear effects are taken into consideration for describing the coupled beam-beam or beam-arch system elastically connected with a nonlinear elastic layer that possesses the discontinuity. We consider the viscoelastically connected beam-beam or beam-arch system joined by a nonlinear Winkler layer. Equations of motion of the nonlinearly coupled geometrically nonlinear beam-beam (when the curvature does not exist at the lower beam), or beam-arch system elastically connected with the nonlinear elastic layer with discontinuity are obtained and presented in a more condensed notation as

$$\mathbf{M}\ddot{\mathbf{q}}(t) + \tilde{\alpha}(\mathbf{K}_{\ell})\dot{\mathbf{q}}(t) + \tilde{\beta}(\mathbf{M})\dot{\mathbf{q}}(t) + \left(\mathbf{K}_{\ell} + \mathbf{K}_{\mathrm{n}\ell}\left(\mathbf{q}(t)\right)\right)\mathbf{q}(t) = \mathbf{F}(t), \tag{1}$$

where $\mathbf{M}$, $\mathbf{K}_{\ell}$ and $\mathbf{K}_{\mathrm{n}\ell}$ are the linear mass, linear stiffness, and nonlinear stiffness matrices, respectively.

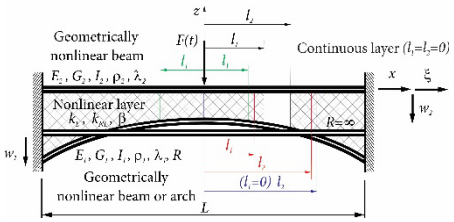

Fig. 1. A Timoshenko coupled beam-arch/beam system by an elastic foundation with variable discontinuity

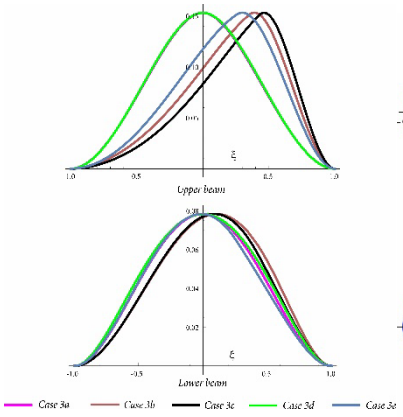

Fig. 2. Deviations of the transverse mode shapes for varying discontinuity with the curvature effect

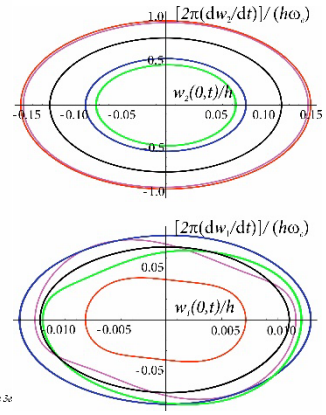

Fig. 3. Phase plots

The present work consists of the comparison of the results with various locations, types (size) of discontinuity in an elastic coupling layer and various curvatures of the lower supported beam. It is explained in which cases of a steady-state regime of vibrations the influence of curvature takes precedence over discontinuity and vice versa.

Acknowledgments: This research was financially supported by the Ministry of Science, Technological Development and Innovation of the Republic of Serbia (Contract No. 451-03-47/2023-01/ 200109) and partly by the Natural Sciences and Engineering Research Council of Canada.

References:

[1] Bardell, N.S., *The application of symbolic computing to the hierarchical finite element method*, International Journal for Numerical Methods in Engineering, Vol.28, 1181-1204, 1989.
[2] Stojanović, V., Ribeioro, P., Stoykov, S., *Non-linear vibration of Timoshenko damaged beams by a new p-version finite element method*, Computers & Structures, Vol.120, 107-119, 2013.
[3] Petyt, M., *Introduction to Finite Element Vibration Analysis*, Cambridge University Press, Cambridge, 1990.

CLOSED-FORM SOLUTIONS AND STABILITY OF SHELLS UNDER THE WHITE NOISE EXCITATION

Vladimir Stojanović[1,2], Jian Deng[2], Dunja Milić[1], and Marko D. Petković[3]

[1] Faculty of Mechanical Engineering, University of Niš, Aleksandra Medvedeva 14, 18000 Niš
e-mail:stojanovic.s.vladimir@gmail.com, dunja1994milic@gmail.com,
[2] Faculty of Engineering,
Lakehead University, Thunder Bay, Ontario, Canada P7B 5E1
e-mail: jian.deng@lakeheadu.ca,
[3] Faculty of Sciences and Mathematics,
University of Niš, Višegradska 33, 18000 Niš
e-mail: dexterofnis@gmail.com

Abstract

The paper investigates the stochastic stability conditions of circular cylindrical shells, compressed by time-dependent stochastic membrane forces. The main contribution of the paper is the determination of the moment Lyapunov exponents of the linear cylindrical shell for the first time. The moment and almost-sure stochastic stability of a three-degree-of-freedom coupled continuous system, under parametric excitation of white noise, are investigated. It is assumed that the system possesses a small damping which can classify the presented mechanical system in the group of gyroscopic stochastic mechanical systems. The system of stochastic differential equations of motion is decoupled by using the contact transformation method with the obtained appropriate symplectic matrix of the system. Then a scheme for determining the moment Lyapunov exponents is presented which contains an analytical procedure. The moment and almost-sure stability boundaries are obtained analytically. These results are important and useful in engineering applications as an example of a procedure for dynamic analysis of mechanical systems with coupled stochastic oscillators.

Keywords: Cylindrical shell, stochastic stability, Moment Lyapunov exponent, perturbation.

1. Introduction

The stochastic instability of plates and shells and their vibrations have an important place in many fields of construction and foundation engineering. All dynamic stability problems that have been considered so far at the level of determining moments of Lyapunov exponents belonged to the class with a maximum of two or three degrees of freedom of vibration. So Kozić et al. [1] investigated the stochastic stability of a double beam system under compressive axial loading, while Stojanović and Petković [2] used the method of regular perturbation to determine moment Lyapunov exponent and stability of a three-dimensional system on elastic foundation. In a group of two-degree-of-freedom dynamical systems, Deng [3] studied the dynamic stochastic stability of gyroscopic systems under bounded noise parametric excitation. The objective of this paper is to study the

moment and almost sure stability of a 3DOF coupled system driven by white noise using the contact transformation method and perturbation approach with application to circular cylindrical shells assuming that the system possesses low damping. A scheme for determining the moment Lyapunov exponents is presented for 3DOF coupled systems.

2. Instructions

We are considering a subcase of the circular conical shell that basically presents an example of an elastic circular cylindrical shell compressed by time-dependent stochastic membrane forces, as it is shown in Fig. 1.

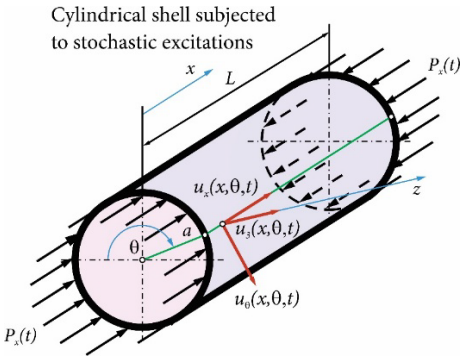

Fig. 1. Geometry of a circular cylindrical shell

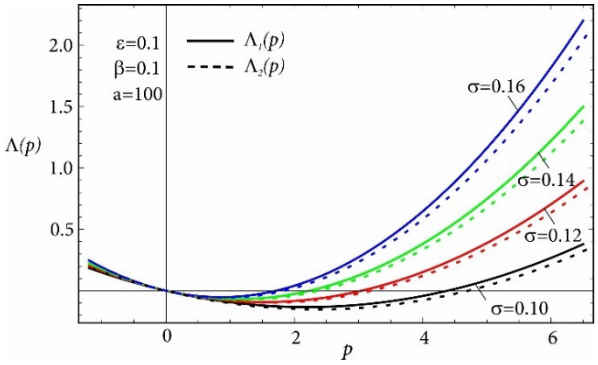

Fig. 2. Moment Lyapunov exponent $\Lambda(p)$ for varying intensity of the random process σ

The stochastic system of the six-dimensional class under white noise excitations is studied analytically through the determination of the moment Lyapunov exponents and the Lyapunov exponents. An eigenvalue problem for the moment Lyapunov exponent is established using the theory of stochastic dynamic systems. For weak noise excitations, the almost-sure and p-th moment stability boundaries in the first and second perturbation with respect to the damping coefficients are determined.

Acknowledgments: This research was financially supported by the Ministry of Science, Technological Development and Innovation of the Republic of Serbia (Contract No. 451-03-47/2023-01/ 200109) and partly by the Natural Sciences and Engineering Research Council of Canada.

References:

[1] Kozić, P., Janevski, G., Pavlović, R., *Moment Lyapunov exponents and stochastic stability of a double-beam system under compressive axial loading*, International Journal of Solids and Structures, Vol.47, 1435-1442, 2010.
[2] Stojanović, V., Petković, M., *Moment Lyapunov Exponents and Stochastic Stability of a Three-Dimensional System on Elastic Foundation Using a Perturbation Approach*, ASME Journal of Applied Mechanics, Vol.80(5), 051009, 2013.
[3] Deng, J., *Stochastic Stability of Gyroscopic Systems Under Bounded Noise Excitation*, International Journal of Structural Stability and Dynamics, Vol.18, 1850022, 2018.

DYNAMICS OF A MULTILINK AERODYNAMIC PENDULUM

Yury D. Selyutskiy and Andrei P. Holub

[1] Institute of Mechanics, Lomonosov Moscow State University, Michurinsky pr. 1, 119192, Moscow, Russia
e-mail: seliutski@imec.msu.ru, holub.imech@gmail.com

Abstract

A multiple link in the wind flow is considered. A wing is installed on the last link of the pendulum, and it is supposed that the aerodynamic forces are applied only to this link. Dynamics of this system as a potential working element of an oscillatory-type wind power harvesting device is studied. Periodical regimes appearing in the system for different flow speeds, different number of pendulum links and different loads applied to the pendulum are numerically investigated. It is shown that the increase in the number of links allows for reducing the critical wind speed when oscillations occur. Besides, it is shown that the maximum power that can be harvested using a two-link pendulum is higher in a wide range of wind speeds than the power harvested with pendulums with a larger number of links. At the same time, pendulums with a larger number of links allow for obtaining high enough power in a larger range of values of the load than the double pendulum.

Keywords: oscillations, stability, wind power harvesting, aeroelasticity.

1. Introduction

In recent decades, a growing interest has been observed to various wind power harvesting systems, including those based on the use of flow-induced oscillations. In [1], a comprehensive review of the potential of such oscillations for the generation of power from wind is provided. In [2], a wind power harvester based on a double aerodynamic pendulum is discussed. This work is dedicated to the consideration of a more general case, when the working element of a wind power generator represents a multiple pendulum.

2. Problem Statement and Discussion of Results

Consider a multiple aerodynamic pendulum (see Fig. 1) which represents a chain of n similar links connected with joints. The first rod can rotate about the fixed vertical axis. In all inter-link joints, there are installed similar spiral springs. A wing with a symmetrical airfoil is fixed to the nth link. The system is placed in a horizontal steady flow. We assume that the flow interacts only with the wing, and the corresponding aerodynamic load can be described with the quasi-steady approach. The viscous friction in the first joint is used to simulate the useful load.

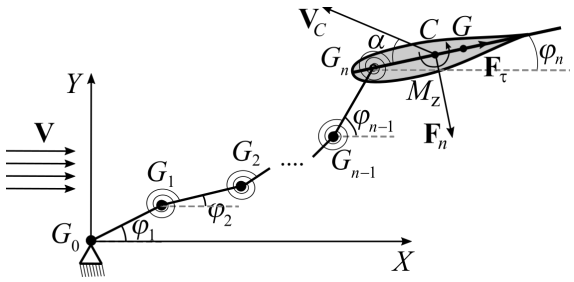

Fig. 1. Scheme of the multilink aerodynamic pendulum (top view)

The system was reduced to dimensionless form, and numerical simulation of its dynamics was performed. Calculations show that the increase in the number of links allows for decreasing the critical speed when self-sustained oscillations appear. In Fig. 2, the power produced by the system during periodic oscillations is demonstrated for different values of the number of links n, dimensionless wind speed V, and dimensionless load χ.

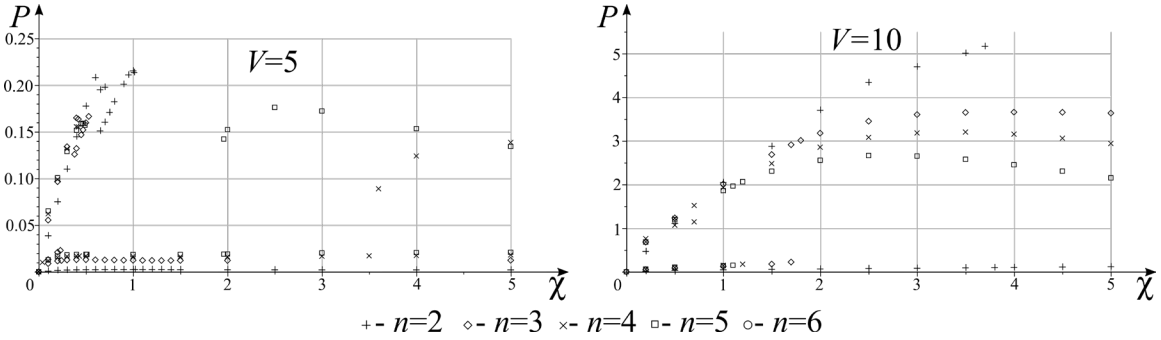

Fig. 2. Output power at periodic regimes depending on the load, number of links, and the wind speed

It should be noted that, in a wide range of wind speeds, the maximum power produced by a pendulum with two links is larger than that produced by pendulums with a larger number of links. However, regimes with high enough power exist for the double pendulum only in a relatively narrow range of loads. At the same time, pendulums with a larger number of links allow for generating somewhat less power, but in a considerably wider range of loads.

3. Conclusions

The analysis of the dynamics of an aerodynamic pendulum with multiple links shows that such a system can be considered as a prospective enough working element of a small oscillatory type of wind power harvester. Such devices could be used to provide power to consumers (such as sensors) at remote locations.

The study is supported by the Russian Science Foundation (project no. 22-29-00472).

References:

[1] Abdelkefi A. *Aeroelastic Energy Harvesting: A Review*, Int. J. Eng. Sci., Vol. 100, 112-135, 2016. Doi: 10.1016/j.ijengsci.2015.10.006.

[2] Selyutskiy Y., Dosaev M., Holub A., Ceccarelli M. *Wind Power Harvester Based on an Aerodynamic Double Pendulum*, Proc. Inst. of Mech. Engineers, P. C: J. Mech. Eng. Sci., Vol. 236 (18), 10025–10032, 2022. Doi: 10.1177/09544062221085.

DYNAMICS OF ASYMMETRIC MECHANICAL OSCILLATOR MOVING ALONG AN INFINITE BEAM-TYPE COMPLEX RAIL SYSTEM

Vladimir Stojanović[1,2], Jian Deng[2], Dunja Milić[1], and Marko D. Petković[3]

[1] Faculty of Mechanical Engineering, University of Niš, Aleksandra Medvedeva 14, 18000 Niš
e-mail: stojanovic.s.vladimir@gmail.com, dunja1994milic@gmail.com
[2] Faculty of Engineering,
Lakehead University, Thunder Bay, Ontario, Canada P7B 5E1
e-mail: jian.deng@lakeheadu.ca
[3] Faculty of Sciences and Mathematics, University of Niš, Višegradska 33, 18000 Niš
e-mail: dexterofnis@gmail.com

Abstract

The paper investigates the dynamic behavior and stability of vibrations of a complexly coupled mechanical oscillator that moves on an endlessly long continuous beam-foundation system. The beam-foundation system comprises three parts. The system can become unstable due to the elastic waves, which are generated by the moving of the complex discrete oscillator. The varying stiffness of the primary suspension and its asymmetricity present the novelty in the model which is deeply analyzed. The study is complemented with parametric analysis. The mathematical description of the present model that represents the complex moving oscillator system contains involved expressions, to handle them the D-decomposition method and the argument principle are used.

Keywords: Instability, varying stiffness, D-decomposition method, principle of argument.

1. Introduction

In order to satisfy the increased mobilization and the greater demand for passenger comfort it is important to study the stability of a moving complex mechanical oscillator that can find application in the railway industry as a model of high-speed trains. In the case where the velocity of a high-speed train exceeds the velocity of elastic waves that are spread out through railway structure, vibration instability due to Doppler waves may occur. The initial study of an infinite beam on an elastic foundation subjected to a concentrated moving force was presented by Timoshenko [1]. His groundwork has been followed and extended by many other researchers. Frýba [2] gives theoretical formulations for the problems of moving loads on continuous beams, beams on elastic foundations, frames, arches, etc., and Verichev and Metrikine [3] studied a rigid body travelling on a Timoshenko beam supported by an elastic foundation. This paper considers the stability of vibrations of a complex moving oscillator that is moving along a continuous and infinite complex three-part viscoelastic beam-foundation system. The model chosen for observation is made of a complexly coupled system that possesses primary and secondary suspension and the interaction between the infinite beam and the uniformly moving complex mechanical oscillator is considered.

2. Instructions

We are considering the complex three-part viscoelastic beam/foundation model presented in Fig. 1. The rail is a supported infinite beam, both the slab and the base are represented as supported free beams, and viscoelastic spring–damping elements represent the connections of the track structure. The slab track system has five parts, and those five parts are the rail, pad, slab, CA mortar, and the base.

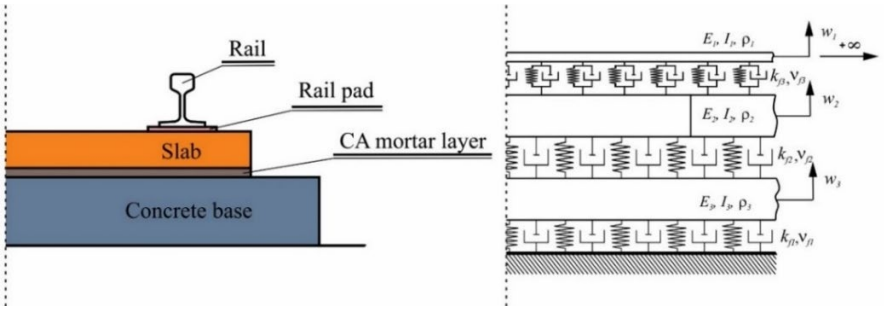

Fig. 1. Complex foundation system

This paper studies the stability of vibrations of presented complex moving oscillator. The peculiarity of the moving oscillator that is examined here is the asymmetric primary suspension system—the suspension supports that make the primary suspension have disparate values of stiffness among each other. It was found that this type of design leads to a significant increase in the span of stable regions. The instability regions are found by applying the principle of argument and the D-decomposition method.

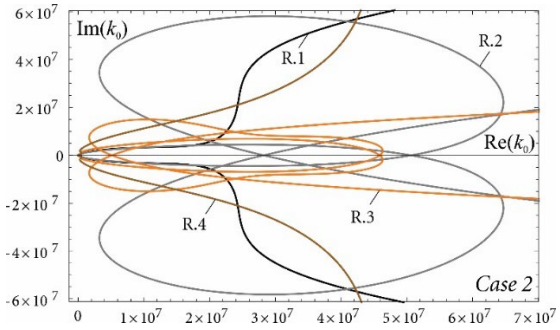

Fig. 2. D-decomposition curves ($v = 1.12\ v_{cr}$) when the first suspension possesses the higher stiffness $\zeta_1 = 8$ and other factors are the same $\zeta_2 = \zeta_3 = \zeta_4 = 1$

Acknowledgments: This research was financially supported by the Ministry of Science, Technological Development and Innovation of the Republic of Serbia (Contract No. 451-03-47/2023-01/ 200109) and partly by the Natural Sciences and Engineering Research Council of Canada.

References:

[1] Timoshenko, S., Roy, R., *Method of analysis of statical and dynamical stresses in rail*, In: Proceedings of the 2nd International Congress for Applied Mechanics, Zürich, Switzerland, 407–418, 1926.
[2] Fryba, L., *Vibration of Solids and Structures under Moving Loads*, Telford, London, 1999.
[3] Verichev, S.N., Metrikine, A.V., *Instability of a bogie moving on a flexibly supported Timoshenko beam*, Journal of Sound and Vibration, Vol.253(3), 653–668, 2002.

THREE-LINK SNAKE ROBOT CONTROLLED BY AN INTERNAL FLYWHEEL

Yury D. Selyutskiy, Liubov A. Klimina and Anna A. Masterova

Institute of Mechanics, Lomonosov Moscow State University, Michurinskiy prosp. 1, 119192 Moscow, Russia
e-mail: klimina@imec.msu.ru, masterovaanya@yandex.ru, seliutski@imec.msu.ru

Abstract

A bio-inspired three-link snake robot with a single control input is studied. The robot moves over a horizontal surface. Links are elastically connected to each other by joints equipped with spiral springs. Each link contacts the supporting plane in a single point. The friction in contact points is assumed dry and anisotropic, the friction coefficient corresponding to the direction transversal to the link being much larger than the one corresponding to the direction along the link. A similar property of friction forces is valid for real snakes. The goal of the control is to ensure a serpentine-style propulsion of the robot in a prescribed direction. For this purpose, an internal flywheel is used installed in the head link. A mathematical model of the robot is constructed. The control law is proposed. Numerical simulation is performed for different sets of parameters. Oscillations of the flywheel result in a wave-type motion of the snake-robot body. The distribution of friction forces during such motion ensures the propulsion of the robot.

Keywords: snake robot, anisotropic friction, control.

1. Introduction

The locomotion of snakes inspires various robotic systems, e.g. [1-3]. Such apparatus can be equipped with supports that ensure anisotropy of friction [2-3]. Special distribution of friction forces during the motion ensures different maneuvers of a robot, in particular the serpentine motion.

Here we consider a snake robot with anisotropic dry friction in support. The main difference from other designs is that no control torque in interlink joints is applied. The robot has passive joints equipped with spiral springs. The control is formed by rotation of the internal flywheel located in the head link (Fig. 1). Thus, the number of control inputs is reduced to one. The control law is constructed that provides serpentine-style propulsion in a given direction.

2. Description of the mechanical system and the control law

The robot consists of three links AK, KL, LC (Fig. 1) and moves in the horizontal plane OXY. An i^{th} $(i=1,2,3)$ link has mass m_i and central moment of inertia J_i. Each link contacts the supporting plane in a single point that coincides with the center of mass of the link: A, B, C

respectively ($AK = KB = BL = LC = r$). The flywheel with the mass m_f and the central moment of inertia J_f is installed at the head link. Point A is the center of mass and the axis of rotation of the flywheel. Spiral springs with stiffness coefficient c are installed in joints K and L. Anisotropic dry friction forces are applied at points A, B, C. The model [4] is used for friction. Principal axes of the friction tensor coincide with directions along the link (the corresponding friction coefficient ε is small) and transversal to the link (with large friction coefficient μ).

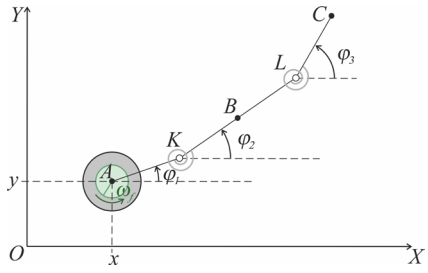

Fig. 1. The scheme of the robot

The control torque U is applied to the inner flywheel and limited by a certain value $U_{\max}$. The goal of the control is to ensure steady motion of the robot with the average speed of the point A directed against the OX axis. The following control is proposed:

$$U = \begin{cases} U_p, & |U_p| \le U_{\max}, \\ U_{\max}\operatorname{sign}(U_p), & |U_p| > U_{\max}, \end{cases} \qquad U_p = -\left(U_{\max}\operatorname{sign}\left(\sin(2\pi w_0 t)\right) + k_0 y - k_1 \varphi_1\right).$$

Here t is time, w_0 is the excitation frequency, k_0, k_1 are feedback coefficients.

Geometrical and mass parameters of the robot, as well as coefficients of the control law were adjusted during numerical simulations. The average speed of steady propulsion is about 0.43 m/s for the following set of parameters: $r = 0.05\text{m}$, $m_1 = 0.2\text{kg}$, $J_1 = 0.002\text{kgm}^2$, $m_2 = 0$, $m_3 = 0.25\text{kg}$, $J_3 = 0$, $m_f = 0.05\text{kg}$, $J_f = 0.0005\text{kgm}^2$, $c = 0.15\text{kgm}^2\text{s}^{-2}$, $\varepsilon = 0.025$, $\mu = 0.9$, $U_{\max} = 0.1\text{Nm}$, $w_0 = 1.2\text{s}^{-1}$, $k_0 = 0.1\text{N}$, $k_1 = 0.1\text{Nm}$.

3. Conclusions

The scheme of the snake robot with a single control input is proposed. The mathematical model is constructed and investigated numerically.

This study was supported by the Russian Science Foundation (project no. 22-21-00303).

References:

[1] Chernousko F.,L., *Locomotion of multibody robotic systems: Dynamics and optimization*, Theor. Appl. Mech., Vol. 45, 17–33, 2018.

[2] Derammelaere S., Copot C., Haemers M., Verbelen F., Vervisch B., Ionescu C., Stockman K., *Realtime locomotion control of a snakeboard robot based on a novel model, enabling better physical insights*, Eur. J. Control, Vol. 45, 57–64, 2019.

[3] Yona T., Or Y., *The wheeled three-link snake model: Singularities in nonholonomic constraints and stickslip hybrid dynamics induced by coulomb friction*, Nonlin. Dyn., Vol. 95, 2307–2324, 2019.

[4] Zmitrowicz A., *Mathematical descriptions of anisotropic friction*, Int. J. Solids Struct., Vol. 25, 837–862, 1989.

WAVE PROPAGATION CHARACTERISTICS OF CURVED HEXAGONAL LATTICE WITH RESONATORS

S. Mukherjee[1], M. Cajić[2], S. Adhikari[3] and S. Marburg[1]

[1] Technical University of Munich, Chair of Vibroacoustics of Vehicles and Machines, 85748 Garching, Germany
e-mail: shuvajit.mukherjee@tum.de, steffen.marburg@tum.de
[2] Mathematical Institute of the Serbian Academy of Sciences and Arts, Kneza Mihaila 36, Belgrade, Serbia
e-mail: mcajic@mi.sanu.ac.rs
[3] James Watt School of Engineering, The University of Glasgow, Glasgow G12 8QQ, UK
e-mail: Sondipon.Adhikari@glasgow.ac.uk

Abstract

Mechanical lattices are complex architectured materials composed of interconnected nodes and beams that exhibit unique physical properties, including band gap. The geometry of the lattice majorly dictates the band gap, which is a range of frequencies that cannot propagate through the lattice. In this work, we present a new hexagonal curved lattice with local resonators and investigated their band gap. Inclusion of local resonating beams at the nodes of the lattice influences the dispersion properties for the curved hexagonal lattice. The new geometry results in lowering and occurrence of new band gaps. Bloch theorem is applied to study in-plane wave propagation and get the unique dispersion properties of the modified lattices. The influence of the curvature along with the length and angle of the resonating beams are explored for the dispersion characteristics and wave directionality through iso-frequency contours of dispersion surfaces. This study can be utilized for the design and optimization of these structures for specific applications.

Keywords: hexagonal lattices, bandgaps, 2D materials, wave propagation, curved beam.

1. Introduction

Lattices are periodic structures which possess the ability to manipulate electromagnetic and acoustic waves in unprecedented ways, including the creation of band gaps [1,2]. Band gaps are ranges of frequencies in which waves cannot propagate through a material, and they are crucial for many applications such as acoustic filters, waveguides, and sensors. Recently, there has been a growing interest in the use of mechanical lattices as metamaterials to achieve tunable and controllable band gaps in the mechanical domain. The band gap characteristics of mechanical lattices are determined by their geometry, topology, and material properties, and can be tuned by adjusting these parameters [3]. In this work, we present the effect of local resonating beam members in the bandgap characteristics of curved hexagonal lattice [4]. The detailed investigation is performed considering Bloch wave analysis. The study showcases structures that shed light on the

possible applications of curved lattices in mechanical filters, sound isolation, tunable acoustics, energy absorption, vibration control, as well as wave propagation control and manipulation.

2. Mathematical modelling, results and discussion

Finite element modelling of the unit cell is employed to discretize the governing equations of a unit cell (Fig. 1a and b). To obtain the dispersion relation harmonic solution is introduced and periodic boundary condition is employed. The dispersion characteristics ($\omega(k_1,k_2)$) is then obtained by solving an eigen value problem mentioned in equation 1 for a set of values for wavenumbers k1 and k2 in the first Brillouin zone.

$$\left(K_r\left(k_1,k_2\right)-\omega^2 M_r\left(k_1,k_2\right)\right)q_r=0 \tag{1}$$

K_r and M_r are the reduced stiffness and mass matrix of the periodic unit cell and q_r is the reduced generalized nodal displacement vector. Figure 1 shows the lattice along with the unit cell, Brillouin zone, and corresponding dispersion diagram for the lattice with cell angle θ = 300, curvature angle ψ = 300, and angle of the resonating beam θ = 450. Figure 1 (d) shows the opening of new band gaps in the both lower and higher frequency regions. The lowering of the band gap is observed in comparison to the curved lattice without the resonating beams. Depending on the orientation angle and length of the resonating beams the band gaps can be manipulated. It is observed that the band gap corresponding to the conventional lattice with cell angle θ = 300 disappeared in the new case and also the iso frequency contours from which the directionality of the wave propagation can be obtained are different.

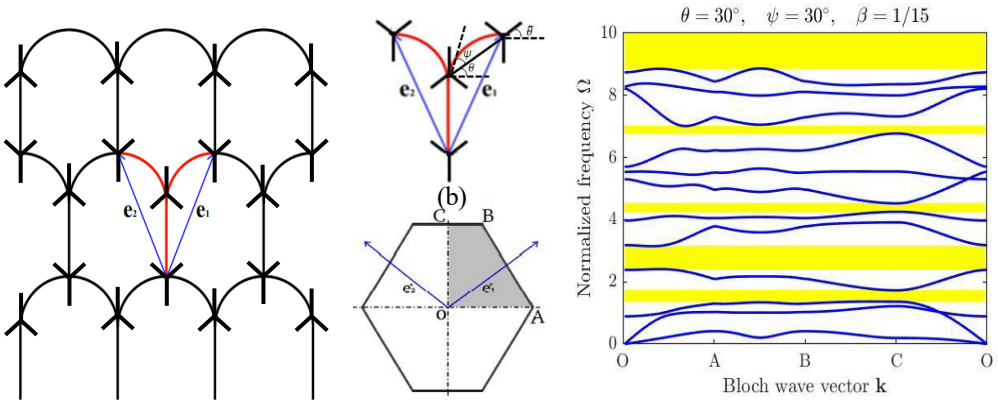

(a) (b) (c)

Fig. 1. Figure showing (a) lattice with unit cell and direct lattice vectors, (b) details of the unit cell, (c) Brillouin zone with reciprocal lattice vectors and (d) frequency band structures for lattice with cell angle θ= 300, curvature angle ψ = 300, angle for resonating beam θ= 450 and slenderness ratio of beam β = 1/15.

3. Conclusions

The degree of curvature in the beam along with resonating members is a critical factor in creating new band-gaps, particularly in the lower frequency range. This type of lattice has the potential to effectively reduce low-frequency vibrations.

References:

[1] Phani A. S., Woodhouse J., Fleck N., Wave propagation in two-dimensional periodic lattices. J Acoust Soc Am, Vol. 119(4), 1995–2005, 2006.
[2] Leamy M. J., Exact wave-based Bloch analysis procedure for investigating wave propagation in two-dimensional periodic lattices. J Sound Vib, Vol. 331(7),1580–96, 2012.
[3] Trainiti G., Rimoli J. J., Ruzzene M., Wave propagation in undulated structural lattices. Int J Solids Struct, Vol. 97, 431–44, 2016.
[4] Mukherjee S., Cajić M., Karličić D., Adhikari S., Enhancement of band-gap characteristics in hexagonal and re-entrant lattices via curved beams. Compos Struct, Vol. 306, 116591, 2023.

PARAMETRIC AMPLIFICATION IN PERIODIC CHAIN SYSTEM

Milan Cajić[1], Nikola Nešić[2] and Danilo Karličić[1]

[1] Mathematical institute SASA, Kneza Mihaila 36, Belgrade, Serbia
e-mail: mcajic@mi.sanu.ac.rs , danilok@mi.sanu.ac.rs
[2] Faculty of Technical Science, University of Priština in Kosovska Mitrovica, Knjaza Miloša 7, 38220 Priština, Serbia
e-mail: nikola.nesic@pr.ac.rs

Abstract

The paper shows periodic chain system exhibiting the topological interface states. The effect of parametric amplification on the interface states is investigated for the case with Mathieu-Duffing type oscillator at the interface.

Keywords: Periodic chains, Interface modes, Mathieu-Duffing oscillator.

1. Introduction

The linear and nonlinear one-dimensional phononic-like systems in their mechanical setup are widely examined in the literature. This often includes investigation of the band structure and unique wave propagation characteristics achieved through different couplings of discrete masses through spring, dashpot or inerter elements. In recent years more attention was devoted to finding special periodic configurations where topologically protected interface/edge states can be achieved [1]. The introduction of nonlinearity in phononic-like periodic systems rises some new questions referring to robustness and stability of existing interface/edge states [2]. The investigation of parametric amplification in a nonlinear Mathieu-Duffing type of oscillator has shown to be beneficial for energy harvesting purposes since it increases the steady state amplitudes and thus can provide higher energy harvesting efficiency [3]. The main objective of this work is to investigate the effect of nonlinearity and parametric amplification onto the periodic chain system and whether it affects topological interface modes. The corresponding motion equations will be derived and harmonic balance method in the state space form will be used to find the periodic solutions and investigate steady state responses of the mass points in the interface mode regime.

2. Problem description and some results

The considered periodic chain system consists of two sub-lattices with periodically repeating and grounded masses mutually connected through two different linear spring elements. Such phonic-like system in its linear configuration generates a unique localized interface mode having a frequency within the band gap region. In linear systems, these types of modes are the result of the band inversion effect and appear within the frequency range of topologically non-trivial band gaps. They emerge at the interface between two sub-lattice types with the same band structure but different topological properties of eigenmodes. At the place of the interface mass, we additionally

introduce the nonlinear springs and periodic excitation in order to investigate the effect of parametric excitation. The motion equations of the masses within the unit cells left and right from the interface and the interface mass itself, respectively are given as

$$m\ddot{u}_a^p + k_i\left(u_a^p - u_{a+1}^p\right) + k_j\left(u_a^p - u_{a+1}^{p-1}\right) + ku_a^p = 0, \tag{1}$$

$$m\ddot{u}_1^0 + k_1(2u_1^0 - u_2^0 - u_2^{-1}) + k_n(u_1^0)^3 + \epsilon(u_1^0)^2 + c\dot{u}_1^0 + (\delta + \alpha\cos\Omega t)u_1^0 = Fh(\Omega t), \tag{2}$$

where $a = 1{,}2$ denotes the first and second mass in the cell, $i = 2$ and $j = 1$ for the cells left from the interface and $i = 1$ and $j = 2$ for the cells right from the interface, while p denotes the repeating unit cell number and is given as $p = [-N, \ldots, 2, 1, 0, 1, 2, \ldots N]$. The general state space form of equations $\dot{\mathbf{x}} = f(\mathbf{x}, t)$ after adopting new time $\Omega t = \tau$ and increments $\mathbf{x} = \mathbf{x}_0 + \Delta\mathbf{x}$ and $\Omega = \Omega_0 + \Delta\Omega$ we will obtain as

$$\Omega_0\Delta\dot{\mathbf{x}} - \Im\Delta\mathbf{x} + \dot{\mathbf{x}}_0\Delta\Omega = \mathbf{r}(\mathbf{x}_0, \dot{\mathbf{x}}_0, \tau), \tag{2}$$

where $\Im$ is the Jacobian matrix $(\partial f(\mathbf{x}, t)/\partial\mathbf{x})$ and $\mathbf{r}$ is the residual vector. Note that the increments are approximated as truncated Fourier series. After forming the above equations, the Newton-Raphson iteration procedure is performed until the norm of $\mathbf{r}$ reaches the preset tolerance and Fourier coefficients are obtained giving the solution of our system at particular excitation frequency.

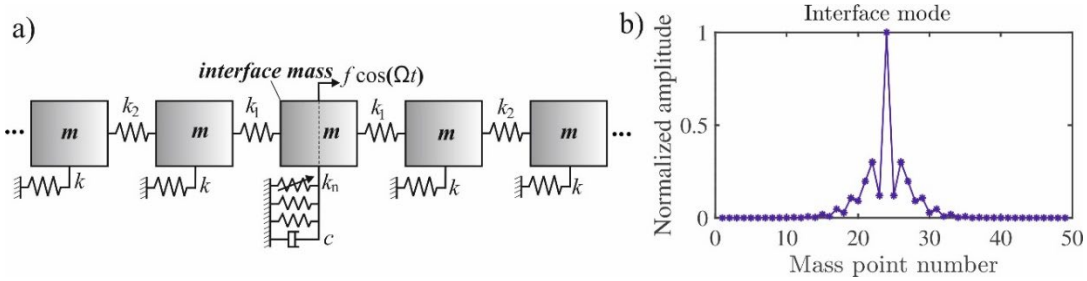

Fig. 1. a) Illustration of periodic chain system, b) Interface mode localization at the interface.

Figure 1b. shows frequency response i.e., steady state amplitudes of the mass points of the periodic chain system. The normalized amplitudes demonstrate their localization at the interface in the case of small excitation amplitudes. The effect of parametric excitation and higher excitation amplitudes on the robustness of topological interface modes will be investigated and demonstrated in detail.

3. Conclusions

Robustness of topological interface modes to defects and disorders in the periodic lattice arrangement is well known. This paper questions weather robustness of such modes is affected by introducing the Mathieu-Duffing type oscillator and how they behave for different excitation amplitudes. The linear stability analysis is performed to investigate the stability of interface states in the presence of strong nonlinearity and whether they can maintain localization over long time periods.

References:

[1] Chatterjee, T., Karličić, D., Cajić, M., Adhikari, S., & Friswell, M. I., *Uncertainty quantification in inerter-based quasiperiodic lattices*, International Journal of Mechanical Sciences, 108258, 2023.

[2] Patil, G. U., & Matlack, K. H., *Review of exploiting nonlinearity in phononic materials to enable nonlinear wave responses*, Acta Mechanica, Vol. 233, 1-46, 2022.

[3] Karličić, D., Chatterjee, T., Cajić, M., & Adhikari, S., *Parametrically amplified Mathieu-Duffing nonlinear energy harvesters*, Journal of Sound and Vibration, 488, 115677, 2020.

MODELING AN INDENTATION OF A HEAD OF VIDEO-TACTILE SENSOR INTO A LINEAR ELASTIC TISSUE

Marat Z. Dosaev and Anfisa S. Rezanova

[1] Institute of Mechanics, Lomonosov Moscow State University, Michurinskiy pr-t, 1, 119192 Moscow, Russia
e-mail: dosayev@imec.msu.ru

Abstract

A video-tactile sensor is being developed to assess the physiological state of the human back muscles. The problem of contact of a linearly elastic spherical head of the sensor with a soft biological tissue is solved. The problem is solved numerically using the finite element method by the ANSYS package. A sample of soft biological tissue was modeled as a round cylinder made of a linearly elastic incompressible material. In addition to the axial force that presses the head against the tissue; additional pressure is applied to the inner surface of the sensor head.

Calculation of the stress state of the contact model of the sensor head with the tissue under study makes it possible to estimate the local stiffness of the tissue based on the results of experiments. An estimate of the error in determining the Young's modulus of tissue from a given measurement error of the contact area is given.

Keywords: Video-tactile sensor, biological soft tissue, silicon head, Young's modulus estimation.

1. Introduction

In [1], a video-tactile sensor was developed to determine the local stiffness of soft tissues and a method for its use was proposed. Preliminary tests of the sensor on porcine liver showed that this device is able to identify samples with an elastic modulus in the range of 1-10 *kPa* (which is close to the characteristics of a healthy porcine liver). In this paper, we consider a scheme of such a sensor for estimating the local stiffness coefficient of the back muscles. The material for the sensor head was chosen polydimethylsiloxane with Young's modulus $E_h = 2.1$ *MPa*. The purpose of the work is to develop an adequate model of contact between the sensor head and soft tissue.

2. Method

The method for estimating the local stiffness E_t of a soft tissue is as follows. First, a finite-dimensional model of the contact between the sensor head and soft elastic tissue is created. The contact characteristics are numerically calculated in a wide range of tissue Young's modulus values. Then, quasi-static experiments are carried out to indent the sensor head into soft tissue. During indentation, several couples of values of the contact area and the magnitude of the axial force are recorded. Then the experimental points are superimposed on the calculated curves, and the most suitable curve for the obtained experimental points is selected from them.

A stationary problem of equilibrium of a stressed system consisting of a stiff sensor chamber, a sensor head, and a tissue under study is being solved. Contacting bodies experience significant deformations. The problem is geometrically non-linear; the solution was obtained numerically using the finite element method using the ANSYS package. An assessment of the influence of the parameters of the mathematical model on the results of calculating the stress-strain state of soft biological tissue was carried out.

The range of indentation of the device into the test sample is limited from above, since at high enough values of the indentation force, a transition to the annular contact area is possible (Fig. 1,b). As an additional control over the compliance of the sensor, the implementation of additional air pressure created inside the head of the sensitive element is proposed. This additional pressure is taken into account in the calculated contact model (Fig. 1,c).

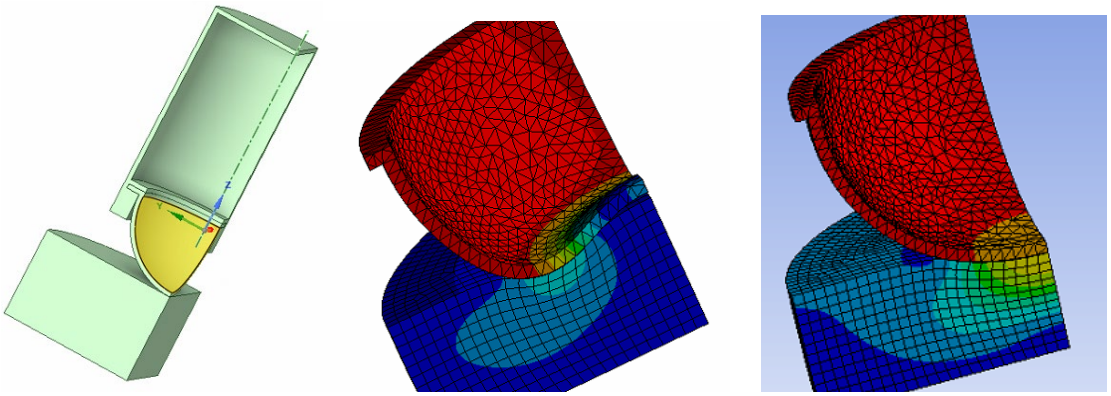

a b c

Fig. 1. Indentation of sensor head to a soft tissue sample: a) The contact scheme; b) Deformations without additional pressure for $E_t = 10$ *kPa*; c) Deformations with an additional pressure of 5 *kPa* for $E_t = 10$ *kPa* .

3. Conclusions

The error in determining the elastic modulus of a tissue depends on its absolute value. Increasing the air pressure in the sensor head chamber can increase the range of approach between the indenter and the sample. Without additional pressure, the greatest accuracy in determining the values of the tissue elasticity modulus was found within 100 kPa - 1 MPa. But the range of possible mutual approach of contacting bodies is not enough for obtaining needed experimental data. When calculating the dependence of the contact area on the axial force taking into account the additional pressure, the error in determining the Young's modulus of the tissue does not exceed 5.5%. Moreover, with an increase in additional pressure, this error only decreases. The proposed method for determining the local stiffness of soft tissue is promising.

This work has been supported by the Interdisciplinary Scientific and Educational School of Moscow University «Fundamental and Applied Space Research»

References:

[1] Dosaev M., Goryacheva I., Martynenko Y., et al, *Application of Video-Assisted Tactile Sensor and Finite Element Simulation for Estimating Young's Modulus of Porcine Liver*, J. Med. Biol. Eng., Vol. 35, 510–516, 2015. https://doi.org/10.1007/s40846-015-0064-1

ELEMENTS OF THE THEORY OF CONSTITUTIVE RELATIONS AND FORMULATIONS OF THE LINEARIZED PROBLEMS ON STABILITY

Dimitri V. Georgievskii

[1] Institute of Mechanics, Mechanical and Mathematical Faculty, Moscow State University, Leninskie Gory 1, 119991 Moscow, Russia
e-mail: georgiev@mech.math.msu.su

Abstract

The report consists of three interconnected parts, one way or another concerning the various aspects of continuum mechanics and the theory of constitutive relations. In the first of them, the basic properties of the operators included in the constitutive relations are described and, on this basis, a certain classification of media is given. In the second part, the apparatus of tensor nonlinear isotropic functions in the theory of constitutive relations in relation to tensor (vector) nonlinear, or quasilinear media, is developed. In the third part, for the environments described in the previous two parts, the formulations of linearized stability boundary-value problems are given in terms of small perturbations of both initial data and material functions.

Keywords: mechanics of solid, constitutive relation, material function, elasticity, plasticity, rheology, tensor function, invariant, stability, perturbation.

1. Elements of the Theory of Constitutive Relations (CR)

1.1. Tangent module and tangent pliability as the inverse tensors of the fourth rank. Bounded above, nonnegative, and positive definite tangent modulus. Soft and hard characteristics of the material.
1.2. Material functions as the quantities that are involved in definitions of the CR-operators and may be determined only in setting experiments.
1.3. Rheonomic and scleronomous media. Aging and ageless materials.
1.4. Homogeneous and nonhomogeneous media. Composites as the media where the CR-operators depend on coordinates in a discontinuous way. Layered (laminated, stratified), fibrous and granular composites. Micro- and nanocomposites.
1.5. Elastic solid as the medium where at any time moment the strain tensor and temperature in this time moment are the only independent state parameters.
1.6. Viscous fluid as the medium where at any time moment the strain rate tensor and temperature in this time moment are the only independent state parameters.
1.7. Media with memory. Viscoelastic solid.
1.8. Non-local media. Strong and weak nonlocality.

2. Isotropic Tensor Functions and Their Invariants in the Theory of Constitutive Relations

1.9. Most general form of the isotropic tensor function in three-dimensional space.
1.10. Media possessing a scalar potential. The conditions of potentiality.
1.11. Incompressible media (fluids). The most general form of the isotropic tensor function in case of incompressibility. Algebraic connection of invariants.
1.12. Nonlinear elastoviscoplastic media in mechanics of continuum and their possible classification. Tensor (vector) CR and scalar CR. Tensor linear (quasilinear) and tensor nonlinear CR.

3. Formulation of the Boundary-Value Problem in Terms of Perturbations

1.13. The closed systems of linearized equations in terms of perturbations.
1.14. Linearization of constitutive relations.
1.15. Linearization of boundary conditions and their transfer from perturbed boundaries to non-perturbed ones.
1.16. Integral measures evaluating initial and current perturbations. Stability by two measures.
1.17. Stability with respect to perturbations of material functions.

References:

[1] Truesdell C. *A First Course of Rational Continuum Mechanics*, Acad. Press, New York – San Francisco – London, 1977.
[2] Ilyushin A.A. *Mechanics of Continuous Media*, Moscow State Univ. Press, Moscow, 1990 (in Russian).
[3] Pobedria B.E. *Numerical Methods in Elasticity and Plasticity*, Moscow State Univ. Press, Moscow, 1995 (in Russian).
[4] Gurtin M.E., Fried E., Anand L. *The Mechanics and Thermodynamics of Continua*, Cambridge Univ. Press, Cambridge, 2010.
[5] Reddy J.N. *Introduction to Continuum Mechanics*, Cambridge Univ. Press, Cambridge, 2013.
[6] Maugin G.A. *Continuum Mechanics Through the Twentieth Century: a Concise Historical Perspectives*, Solid Mechanics and Its Applications, Vol. 196, Springer, Dordrecht, 2013.
[7] Georgievskii D.V. *The Selected Problems in Mechanics of Continuous Media*, LENAND Press, Moscow, 2018 (in Russian).

DEVELOPMENT AND MOULD TECHNOLOGY FOR TESTING OF BIOCOMPOSITE STRUCTURES (APPLICATION FOR THERMOINSULATED BIO PLATES)

Marija Baltić[1], Milica Ivanović[1], Dragoljub Tanović[1] and Miloš Vorkapić[2]

[1] Faculty of Mechanical Engineering, University of Belgrade, Kraljice Marije 16, 11120 Belgrade 35
e-mail: mbaltic@mas.bg.ac.rs,
[2] ICTM - CMT, University of Belgrade, Njegoševa 12, 11000 Belgrade, Republic of Serbia

Abstract

Biocomposite materials are a combination of two or more different biomaterials at the macroscopic level, with competitive mechanical and insulation properties, relatively stable when exposed to high temperatures and tailorable. In this paper, materials are with a vegetative part of fungi (mycelium-mesh structure of hyphae) which are increasingly used to create biocomposites with unique processing technology. The vegetative part of a fungus called mycelium, can serve as a natural binder for products made of biocomposite and acts like a self-assembling adhesive by digesting and adhering to the surface of specific organic matter. This paper presents the development of mould technology to set the biocomposite structure and test its mechanical characteristics. The primary purpose of the mould is to bring the loose natural material into a solid preparation following the standards ASTM D7250 and ASTM D1037, which include testing the technologically prepared and hardened sample for tensile and pressure. Development and moulding of biocomposite are the technological processes of drying after sowing mycelium so a variant of the mould with a perforated upper part was used to harden the samples thoroughly.

Keywords: mycellium biocomposite, mould, 3D printing, testing, thermoinsulation.

1. Introduction

With global carbon emissions of 39% [1], the building industry has a large responsibility to constantly propose new and improved low-carbon solutions. It takes over a million years to decompose standard synthetic thermal insulation materials. The general characteristic of organic materials is that they have a lower coefficient of thermal conductivity and a higher heat capacity compared to most synthetic materials. The thermal conductivity of such materials varies significantly, greatly depending on different characteristics: degree of porosity, the temperature of the material, the moisture content, the direction of fiber propagation, which affects the direction of the temperature gradient. Mycelium-based polymers hold special potential as thermal insulation foams due to their low thermal conductivity and inherent fire safety features. Research that has been done on thermal conductivities refers that mycelium composites based on hemp fibers or wheat straw have low thermal conductivities (0,04 W/(mK)) and can compete with polystyrene (0.03-0.04 W/(mK)) and polyurethane foam (0.006-0.18 W/(mK)) [2].

2. Development and manufacturing of a mould

Manufacturing of biocomposite structure usually proposes the next steps: 1) preparation of mould according to the type of testing and appropriate standards; 2) binding of plies with natural glue in order to prevent the growth of mycelium; 3) forming, sterilization and hardening plies and structure; 4) filling of mould by mycelium biomaterial; 5) drying and prevention growth of mycelium fibres; 6) infusion of natural resin to improve mechanical characteristics [3]. For the first phase - tensile testing, 10 moulds were manufactured for the production of specimens according to standard D1037. The mould was first created and developed in CATIA and by appropriate software printed in the 3D printer (additive technology).

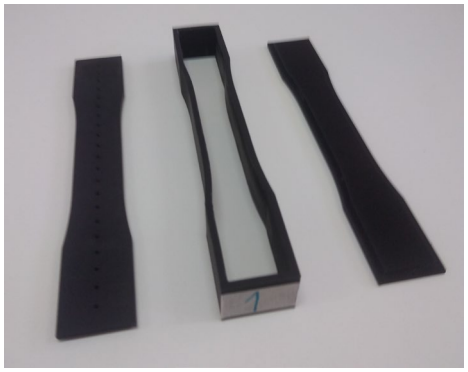

Fig 1. Parts of mould

Fig 2. Moulds for production of testing specimen

3. Conclusion

Moulds for the production of biocomposite mycelium structures (for tensile and pressure testing) were developed, simulated and manufactured. The next phase involves experimental testing and analysis of drying and hardened biocomposite specimens according to appropriate standards and determination of mechanical characteristics.

References:

[1] IEA (2019), Global Status Report for Buildings and Construction 2019, IEA, Paris
[2] Mitchell Jones, Andreas Mautner, Stefano Luenco, Alexander Bismarck, Sabu John, *Engineered mycelium composite construction materials from fungal biorefineries: A critical review*, Materials & Design, Volume 187, 2020, 108397, ISSN 0264-1275
[3] Jiang L., Walczyk D., McIntyre G., Bucinell R., Li B., *Bioresin infused then cured mycelium-based sandwich-structure biocomposites: Resin transfer molding (RTM) process, flexural properties, and simulation*, Journal of Cleaner Production 207 (2019) pp. 123-135, 2018.

LEFT VENTRICLE CARDIAC HYPERTROPHY SIMULATIONS USING SHELL FINITE ELEMENTS

Bogdan Milićević[1,2], Miljan Milošević[2,3,4], Vladimir Simić[2,3], Danijela Trifunović[5], Goran Stanković[5,6], Nenad Filipović[1,2] and Miloš Kojić[2,6,7]

[1] Faculty of Engineering, University of Kragujevac, Kragujevac 34000, Serbia
e-mail: bogdan.milicevic@uni.kg.ac.rs, fica@kg.ac.rs
[2] Bioengineering Research and Development Center (BioIRC), Kragujevac 34000, Serbia
e-mail: miljan.m@kg.ac.rs, vsimic@kg.ac.rs, mkojic42@gmail.com
[3] Institute for Information Technologies, University of Kragujevac, Kragujevac 34000, Serbia
[4] Belgrade Metropolitan University, Belgrade 11000, Serbia
[5] Cardiology Department, University Clinical Center of Serbia, Visegradska 26, 11000 Belgrade, Serbia
e-mail: danijelatrif@gmail.com, gorastan@gmail.com
[6] Serbian Academy of Sciences and Arts, Belgrade 11000, Serbia
[7] Houston Methodist Research Institute, Houston TX 77030, USA

Abstract

Prior to experimental or clinical applications, numerical modeling of the cardiac cycle can be used to assess clinical scenarios. The change in the wall thickness, displacement field, and general cardiac function are all impacted by hypertrophy. In our research, we calculated the effects of eccentric and concentric hypertrophy and monitored alterations in the thickness and shape of the ventricles. Concentric hypertrophy led to the development of a thicker wall, whereas eccentric hypertrophy resulted in a thinner wall. The recently established material modal, which was based on Holzapfel's research, was used to calculate passive stresses. Our modeling approach is based on composite shell finite elements, which enable easier and more efficient modeling compared to traditional 3D finite elements. We used echocardiographic images to generate the left ventricle model. Since our modeling technique is based on accurate patient-specific geometry and realistic Holzapfel's constitutive curves, it can be used as the foundation for real-world applications. Our model can be used to test the medical hypothesis about the evolution of hypertrophy in a healthy and diseased heart under the effect of various situations and factors.

Keywords: composite shell finite elements, echocardiography, left ventricle, cardiac hypertrophy.

1. Introduction

In [1], a close association was found between the macroscopic growth tensor and the factors influencing its temporal evolution and microstructural processes. In reference [2], the authors created a continuum model and computer simulation tool to predict the eccentric and concentric growth that is the inevitable result of the parallel clustering process, due to the stress and strain of newly created sarcomere units. Their main kinetic principle is that each cardiomyocyte deforms

in a similar way to the surrounding myocardial tissue. To model the left ventricle in our study, we systematized the techniques from [1,2] and employed a shell multilayer finite element method developed described in [3]. We developed an echocardiography-based LV model, which is produced by providing the patient's LV dimensions, and contours extracted from echocardiographic images. Once the model has been created, we investigate the impact of hypertrophic growth using various characteristics and attributes to test various hypothesized scenarios and monitor the course of the condition.

2. Results

Contours of the external and internal surfaces, at the end of diastole, are shown in Fig. 1a for a healthy heart and a heart with eccentric hypertrophy, after six months. Only half of the contour is shown since the model is symmetric. It can be seen that eccentric hypertrophy produces heart elongation. In Fig. 1b contours of the LV wall, at the end of systole, are shown for a healthy heart and a heart with concentric hypertrophy after six months. It can be seen that the LV is slightly shorter due to hypertrophy.

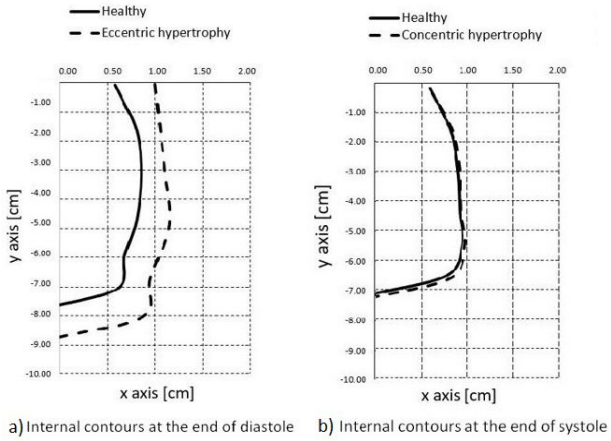

Fig. 1. a) Internal contours at the end of diastole showing the LV extension due to eccentric hypertrophy. b) Internal contours at the end of systole - a slight increase of the LV length do to hypertrophy

3. Conclusions

The echocardiography-based model combined with composite shell finite elements and experimental constitutive curves offers a computational approach that can be implemented in medical practice.

Acknowledgement: This research was supported by the European Union's Horizon 2020 research and innovation programme under grant agreement No 952603 (http://sgabu.eu/). This article reflects only the author's view. The Commission is not responsible for any use that may be made of the information it contains. The research was also funded by the Ministry of Education, Science and Technological Development of the Republic of Serbia, contract numbers [451-03-68/2022-14/200107 and 451-03-68/2022-14/200378].

References:

[1] Serdar Göktepe, Oscar John Abilez, Kevin Kit Parker, Ellen Kuhl, A multiscale model for eccentric and concentric cardiac growth through sarcomerogenesis, Journal of Theoretical Biology, 265, 433–442, 2010.

[2] M. K. Rausch. A. Dam, S. Göktepe, O. J. Abilez, E. Kuhl , Computational modeling of growth: systemic and pulmonary hypertension in the heart ,Biomech Model Mechanobiol, Vol 10, 799–811 (2011) ,DOI 10.1007/s10237-010-0275-x.
[3] M. Kojic, M. Milosevic, A. Ziemys, Computational Models in Biomedical Engineering - Finite Element Models Based on Smeared Physical Fields: Theory, Solutions, and Software, Elsevier, 2022

NONLINEAR CHARACTERIZATION OF A VIBRATION SYSTEM MODEL

Tamara Nestorović, Umaaran Gogilan and Atta Oveisi

Mechanics of Adaptive Systems, Institute of Computational Engineering,
Ruhr-Universität Bochum, Universitätsstr. 150, D-44801 Bochum, Germany
e-mail: tamara.nestorovic@rub.de, umaaran.gogilan@rub.de, atta.oveisi@rub.de

Abstract

Development of reliable system models decisively determines the success of model-based vibration control methods. Although most of well-established control methods mainly rely on model-based techniques which are developed for linear or linearized models, in many applications the linearity assumption is not sufficient for precise modeling of the system behavior. In this paper the nonlinear characterization of a vibrating structure model is performed based on the Acceleration Surface Method (ASM), aiming at improvement of the modelling reliability by identifying nonlinearity and incorporating it into structural model in the form of nonlinear terms of corresponding order. The method is implemented on a benchmark of a clamped-clamped beam consisting of two parts with different geometric properties, with a potential for identification of nonlinear vibration behavior. The nonlinear model is aimed at observer based-controller design for vibration suppression.

Keywords: nonlinear model characterization, Acceleration Surface Method (ASM), clamped-clamped beam.

1. Introduction

The nonlinear characterization is performed for the vibrating system consisting of a clamped-clamped beam with two parts having different lengths and thicknesses. The joint between the two beam parts is realized with screws and the thin part of the beam should provide pronounced nonlinear behavior under increasing excitation amplitudes. The experimental setup with the clamped-clamped beam, vibration exciter – shaker and a set of transducers (accelerometers) that record the system response at different positions along the beam is represented in Figure 1. For the purpose of modelling, the lumped-mass substitute model is set up as shown in Figure 2.

$$\mathbf{M}\ddot{\boldsymbol{x}}(t)+\mathbf{B}\dot{\boldsymbol{x}}(t)+\mathbf{C}\dot{\boldsymbol{x}}(t)+\sum_{i=1}^{n}\mathbf{A}_i\mathbf{y}_i=\boldsymbol{f}(t) \tag{1}$$

A general model represented by Eq. (1) consists of the underlying linear model (first three terms of the left-hand side of the equation) augmented by nonlinear terms, with $\mathbf{y}_i$ being the analytical form of the nonlinearity after the characterization [2] and with constant matrices $\mathbf{A}_i$ that contain the unknown coefficients of the nonlinearity. The term $\boldsymbol{f}(t)$ on the right-hand

side of Eq. (1) represents the vector of external excitation acting on all degrees of freedom, which may be non-fully populated.

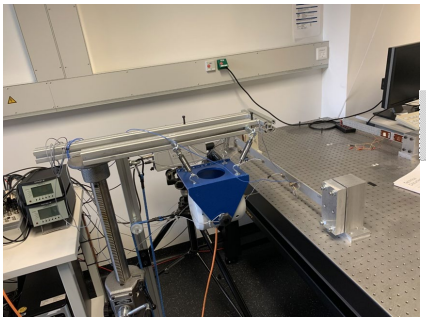

Fig. 1. Experimental setup with the nonlinear clamped-clamped beam

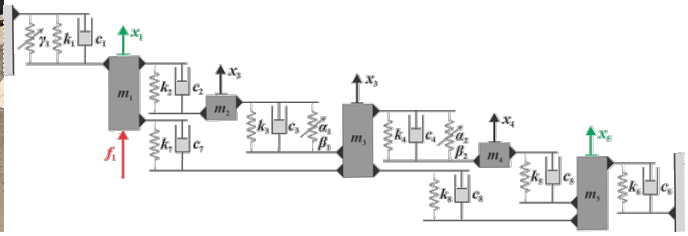

Fig. 2. Substitute lumped-mass model of the nonlinear system

2. Acceleration surface method

The method enables characterization of the nonlinearity from the corresponding functions of the relative displacement vs. acceleration, considering the coupling between the considered lumped masses, in this case placed at opposite sides with respect to the present geometric nonlinearity, Fig. 3*a*) – connection between the thick and the thin part of the beam. Fig. 3*b*) represents determining of the nonlinear coefficients from the acceleration surface projection by polynomial fitting procedure for the lumped masses at positions 4 and 5 of the nonlinear beam.

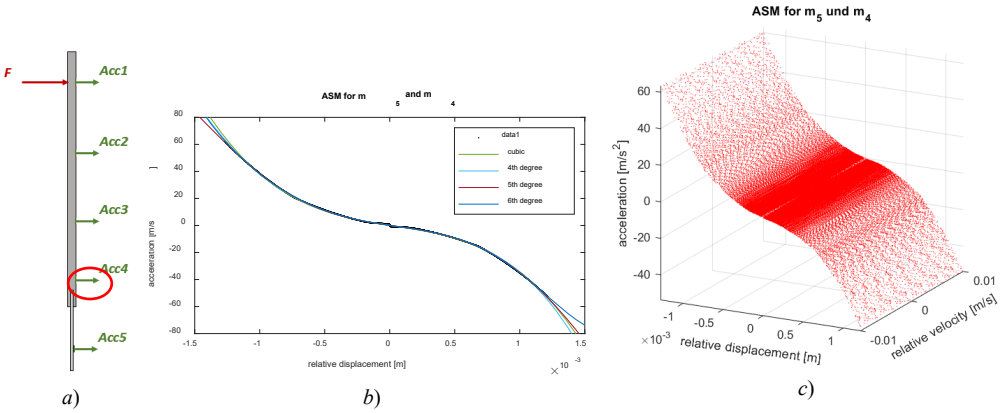

a) *b*) *c*)

Fig. 3. ASM nonlinearity characterization

In connection with the identification of the underlying linear model through grey-box identification procedure and optimization of the frequency responses using genetic algorithm, an overall model which reliably captures nonlinear properties of the system is obtained.

References:

[1] Gogilan U., Oveisi A., Nestorović T., *Implementation of State Observer-Based Conditioned Reverse Path Method to the Identification of a Nonlinear System*, 16th International Conference: Dynamical Systems Theory and Applications, in DSTA-2021 Conference Books – Abstracts (eds. J. Awrejcewicz, M. Kaźmierczak, J. Mrozowski, P. Olejnik), 503-504, Politechnika Łódzka, https://doi.org/10.34658/9788366741201

[2] Noël, J. P., Kerschen, G., *Nonlinear System Identification in Structural Dynamics: 10 More Years of Progress*, Mech. Syst. Signal Process., 83, pp. 2–35, 2017.

AN EXERGAME-INTEGRATED IOT-BASED ERGOMETER SYSTEM FOR PERSONALIZED TRAINING OF THE ELDERLY

Fong-Chin Su[1,2], Chih-Chun Lin[2], Li-Chieh Kuo[3], Yu-Sheng Lin[4], Chia-Ming Chang[5], Fang Wen Hu[6], Yi-Jing Chen[2], Chun-Tse Lin[2]

[1]Department of Biomedical Engineering
[2]Medical Device Innovation Center
[3]Department of Occupational Therapy, National Cheng Kung University, Tainan, Taiwan
[4]Department of Mechanical Engineering, Southern Taiwan University of Science and Technology, Tainan, Taiwan
[5]Department of Internal Medicine, 6Department of Nursing, National Cheng Kung University Hospital, Tainan, Taiwan

Abstract

Reduced physical activity is reported in the elderly, especially in institutional residents. Institutionalized older adults exhibit a high prevalence of frailty. we developed an artificial intelligence of things (AIoT)-based feedback assistive strengthening ergometer (AIFASE), for the physical strengthening of the elderly with intelligent assistance. The AIFASE system allows the clinical staff to record the personal physical performance of the elderly and generates personalized exercise prescriptions accordingly. AIFASE also displays the current usage status of all ergometers and the users' physiological conditions. The algorithms were developed to generate warning alerts when the training workload was too large by personal physiological detection. AIFASE automatically customized the exercise prescription according to the user's exercise performance.

A 12-week intervention in a long-term care facility was conducted. In total, sixteen participants (84.38 ± 6.0 years; 4 males and 12 females) were recruited with 1:1 randomization of exercise to control groups. The muscle strength of the lower extremities, timed up and go test (TUG), and Short-form Physical Performance Battery (SPPB) of the participants were measured. After a 12-week AIFASE intervention, the intervention group exhibited significant improvements in the strength of the hip flexor, Semi-Tandem Stand, and Tandem Stand. In conclusion, we developed an AIoT ergometer that delivered customized physical training prescriptions to improve the physical performance of long-term care facility residents. We believe that the application of AIFASE could help improve the quality of institutional care.

Acknowledgement: Support from the Ministry of Science and Technology of Taiwan (Grant number: MOST 110-2627-M-006 -002) and by the Medical Device Innovation Center, National Cheng Kung University.

L-TYROSINE INFLUENCE ON THE REACTION KINETICS OF IODATE-HYDROGEN PEROXIDE OSCILLATORY REACTION

J. Maksimović[1], A. Ivanović-Šašić[2], S. Maćešić[1], Ž. Čupić[2] and Lj. Kolar-Anić[1,2]

[1]Faculty of Physical Chemistry, University of Belgrade, Serbia
e-mail:jelena.maksimovic@ffh.bg.ac.rs,
stevan.macesic@ffh.bg.ac.rs,ljiljana.kolar.anic@ffh.bg.ac.rs,
[2] Institute of Chemistry, Technology and Metallurgy, University of Belgrade, Serbia
e-mail: zcupic@ihtm.bg.ac.rs, ana.ivanovic.sasic@ihtm.bg.ac.rs

Abstract

The impact of L-tyrosine amino acid on the kinetics of the BL oscillatory reaction was investigated under closed reactor conditions. The study was focused on examining the sensitivity of the BL reaction matrix to tyrosine perturbations. A high sensitivity of the BL matrix to very low tyrosine concentrations was observed.

Keywords: L-tyrosine, Bray-Liebhafsky reaction, oscillatory reactions.

1. Introduction

The Bray-Liebhafsky (BL) reaction is the oldest known oscillating reaction that represents the catalytic decomposition of hydrogen peroxide into oxygen and water, in the presence of iodate (IO_3^-) and hydrogen ions (H^+). [1] It is represented by chemical reaction:

$$2H_2O_2 \xrightarrow{H^+, IO_3^-} 2H_2O + O_2 \quad (1)$$

Although the BL reaction was discovered more than a century ago and appears to be simple because it involves only three reactants, it has a very complex and unexplored mechanism that may include a series of stable and unstable intermediate species, including radical ones: $IO_2^{\bullet}$, $HOO^{\bullet}$, $HO^{\bullet}$, and $I^{\bullet}$.

The Bray–Liebhafsky oscillatory reaction proved to be useful in determining the activity of various analytes under closed and open reactor conditions due to its extreme sensitivity to external stimuli (perturbations). In this study, the impact of L-tyrosine on the BL reaction kinetics under closed reactor conditions was investigated. The amino acid L-tyrosine (4-hydroxyphenylalanine, C9H11NO3) is a precursor for the synthesis of the catecholamines dopamine (DA) and norepinephrine (NE). Under stressful conditions, DA and NE levels drop, which can compromise cognitive function. By increasing catecholamine levels in the brain, L-tyrosine supplementation may be able to reduce the cognitive decline caused by acute stress. Also, it is a precursor for biosynthesis of thyroid hormones through the iodination process. To explain tyrosine activity, numerical simulations were performed using the proposed model of the BL oscillatory reaction.

The response of the BL matrix to a low concentration of tyrosine single pulse perturbations (about 1×10^{-6} M) was investigated both numerically and experimentally. [2]

2. Experimental part

All experiments were carried out in a closed well-stirred reactor (with stirring rate, σ = 900 rpm) and thermostated at T = 54.0 ºC. The reaction volume was 38.8 ml. The initial concentrations of the reactants were: $[KIO_3]_0 = 1.40 \times 10^{-1}$ mol dm^{-3}, $[H_2SO_4]_0 = 4.23 \times 10^{-2}$ mol dm^{-3}, $[H_2O_2]_0 = 2.84 \times 10^{-3}$ mol dm^{-3}. All stock reactants solutions were pro analysis grade and prepared in deionised water. The substances were added to the reaction vessel in the following order: KIO_3, H_2SO_4 and when the temperature and potential were stabilised, H_2O_2 was added. The moment when H_2O_2 was added to the vessel was taken as the beginning of the reaction. Forty minutes after the addition of H_2O_2, 200 μl of commercial L-tyrosine of different concentrations was added. The time evolution of the BL reaction was followed by the platinum electrode as a working electrode and a double junction Ag/AgCl electrode as a reference electrode.

3. Numerical simulation

Numerical simulations were performed in MATLAB, using the ODE15s solver routine based on the Gear algorithm for the integration of stiff differential equations. The proposed model of the BL reaction [3] was used with the original rate constants recalculated to the temperature used in the experiment. The concentrations of all reactants were identical to the experimental values.

4. Conclusions

The impact of l-tyrosine on the kinetics of the BL reaction under closed reactor conditions was investigated because of its importance in the synthesis of the catecholamines dopamine (DA) and norepinephrine (NE). The impact of L-tyrosine was analysed under closed reactor conditions and by numerical simulations. The results show a great potential for the BL matrix in the analysis of L-tyrosine. Numerical simulations indicate several possible pathways of influence.

Acknowledgement: We are grateful to the financial support from Ministry of Science, Technological Development and Innovation of Republic of Serbia (Grant Numbers 172015 and 45001, and Contract numbers 451-03-47/2023-01/200026 and 451-03-47/2023-01/200146. This research was supported by Science Fund of Republic of Serbia #Grant Number. 7743504, NES.

References:

[1] Bray W.C., Liebhafsky HA, *Reactions involving hydrogen peroxide, iodine and iodate ion. I Introduction*. J America Chemical Society, Vol. 53, 38–44, 1931.

[2] Negrojević L., Lončar A., Maksimović J, Anić S., Čupić Ž., Kolar-Anić LJ., *Bray–Liebhafsky oscillatory reaction in a continuous-flow stirred tank reactor as the matrix system for determination of tyrosine,* Reaction Kinetics, Mechanisms and Catalysis, Vol. 135, 1147–1162 2022.

[3] Kolar-Anić Lj., Mišljenović Đ., Anić S., Nicolis G., *The infuence of the reduction of iodate ion by hydrogen peroxide on the model of the Bray-Liebhafsky reaction*. Reaction Kinetics Catalysis Letters, Vol 54, 35–41, 1995.

PSO-OPTIMIZED FRACTIONAL ORDER ITERATIVE LEARNING CONTROLLER FOR 3 DOF UNCERTAIN EXOSKELETON SYSTEM

Živković LJ. Nikola[1] and Lazarević P. Mihailo[2]

[1] Lola institute Ltd., Kneza Višeslava 70a, 11030 Belgrade, Serbia
e-mail: nikola.zivkovic@li.rs
[2] Faculty of Mechanical Engineering, University of Belgrade, Kraljice Marije 16, 11120 Belgrade, Serbia
e-mail: mlazarevic@mas.bg.ac.rs

Abstract

This paper proposes a Fractional-order Iterative Learning Control (FOILC) algorithm combined with feedback linearization for the upper limbs' rehabilitation exoskeleton. The control system is divided into an inner and outer loop, where the feedback linearization controller closes the inner loop linearizing the nominal part of the robot dynamics. The outer loop consists of feedforward action and classical feedback controller with Proportional and Derivative action (PD). Feedforward action is proposed as the FOILC of the PD$^{\alpha}$-type, where α is the fractional derivative order. Since feedback linearization control action can cancel only a nominal part of the model dynamics, uncertainty is introduced as an additive uncertainty. The uncertainty is defined as a change in the mass parameter of each exoskeleton link [1]. The control object is a three-DoF open-chain exoskeleton model. The mathematical model of the exoskeleton is modeled in Simulink using Robotics Toolbox. The feedback linearization controller is the model-based controller, which accounts for the known part of the dynamics leaving the uncertain part uncontrolled. A classical PD feedback controller is introduced alongside FOILC in feedforward to stabilize and improve the tracking performance of the linearized system with uncertainties. The main advantage of FOILC is robustness to uncertainty and disturbances that are non-varying along the iteration axis. In this study, we chose the FOILC controller, a variation of ILC, to improve trajectory tracking with present uncertainties in the exoskeleton system model. The FOILC controller consists of the previous control signal, proportional and fractional order derivative terms. The learning gains and fractional order of the FOILC are optimized using the Particle Swarm Optimization (PSO) method. PSO is a population-based stochastic optimization method inspired by the social behavior of birds flocking or fish schooling. The main idea of PSO is to search for an optimal solution by simulating the social behavior of particles moving in a multi-dimensional search space. PSO is particularly well-suited for this problem since we have nine parameters in total for tuning. This research aims to investigate the behavior of the error convergence over iterations with optimized learning gains and fractional order of the FOILC controller for various percentages of the mass parameter change. The numerical simulation is conducted in Matlab and Simulink with the time step Ts = 0.005s. The desired trajectory is defined in the joint space as a fifth-order polynomial. The infinite norm of the error vector (max norm) for each iteration is used as a measure of the performance of the proposed control system. Figure 1 shows the error norm comparison between different percentages of mass uncertainty, and Fig. 2 shows the difference between PSO-optimized FOILC and non-optimized integer order ILC for mass uncertainty equal to 30 percent of the original mass of the links.

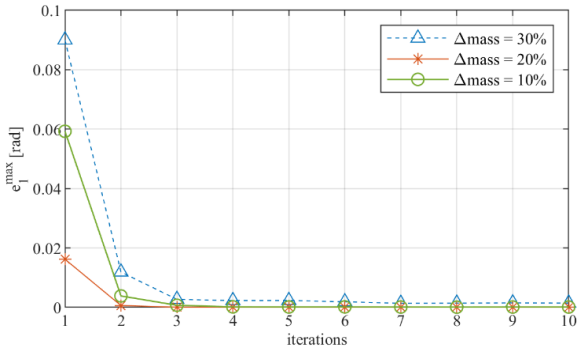

Fig. 1. Error norm of the joint 1 for different mass percentages.

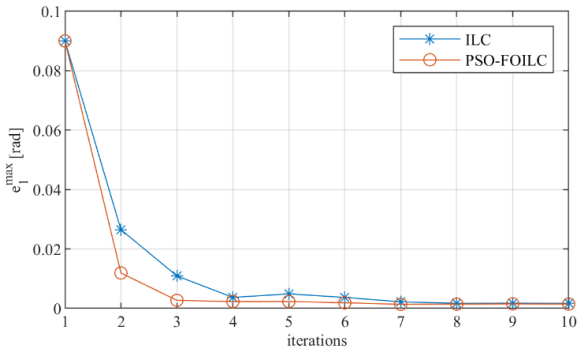

Fig. 2. Error norm of the joint 1 for optimized FOILC and non-optimized ILC.

From previous diagrams, it is clear that PSO optimized FOILC converges faster than its non-optimized integer order counterpart and that PSO optimized FOILC displays satisfactory robustness to different mass uncertainties.

Keywords: iterative learning control, fractional derivative, feedback linearization, particle swarm optimization, uncertainty.

Acknowledgement: This research has been supported by the research grants of the Serbian Ministry of Science, Technological Development and Innovations, grant No. 451-03-68/2023-14/200066 and 451-03-47/2023-01/ 200105 from 03.02.2023.

References:

[1] Lazarevic M., Mandic P., Ostojic S. *Further results on advanced robust iterative learning control and modeling of robotic systems*, Proceedings of the Institution of Mechanical Engineers, Part C: Journal of Mechanical Engineering Science, Vol. 235, No. 20, 4719-4734, 2021.
[2] Slotine J., *Applied nonlinear control,* Prentice Hall, Englewood Cliffs, 1991.
[3] Ahn H. S., Chen Y., Moore K. L. *Iterative Learning Control: Robustness and Monotonic Convergence for Interval Systems,* Springer-Verlag, London, 2007.
[4] Kennedy J., Eberhart R., *Particle swarm optimization*, Proceedings of ICNN'95 – International Conference on Neural Networks, Vol 4, 1942-1948, 1995.

INHIBITORY EFFECT OF 4-HYDROXYCOUMARIN DERIVATIVE ON KRAS PROTEIN

Marko Antonijević[1], Žiko B. Milanović[1], Edina H. Avdović[1], Dušan S. Dimić[2] and Zoran Marković[1]

[1]Institute for Information Technologies, University of Kragujevac, Jovana Cvijića bb, 34000 Kragujevac, Serbia
e-mail: mantonijevic@uni.kg.ac.rs, ziko.milanovic@uni.kg.ac.rs, edina.avdovic@pmf.kg.ac.rs, zmarkovic@uni.kg.ac.rs
[2]Faculty of Physical Chemistry, University of Belgrade, Studentski trg 12-16, 11000 Belgrade, Serbia
e-mail: ddimic@ffh.bg.ac.rs

Abstract

A large number of compounds containing coumarin fragments in their structure have been isolated from the plant world. Some natural derivatives of coumarin are used in the treatment of some diseases. An important feature of both natural and synthetic derivatives is their cytotoxicity. *In vitro* results on the cytotoxic effects of new coumarin compounds clearly showed the potential to significantly reduce cell viability, especially against pancreatic cancer MIA PaCa-2 cell line, mainly by induction of apoptosis [1].

KRAS is one of the most mutated oncogenes in human cancer. These mutations are found in almost 30% of human malignancies, yet the most common and carcinogenic KRAS (G12D) variation remains uninhibited. One major advance in KRAS inhibition has been the discovery of covalent inhibitors of KRAS carrying the G12C driver mutation. In this research, to understand the inhibitor efficacy of 4-hydroxycoumarin derivative 3-(1-((3-hydroxyphenyl)amino)ethylidene)chroman-2,4-dione against KRAS, molecular docking simulations were used. To examine the binding affinity of the investigated compounds, the AutoDock 4.2 software [2] was applied. The AMDock program [3] was employed to determine the receptor's pockets and binding sites. For determination of binding affinity, binding energies were examined. Besides the examination of binding energies, inhibitory constant (K_i) is an important parameter because it resembles the approximate concentration of the compound necessary for protein inhibition. The value of K_i can be compared to experimentally determined IC_{50} values.

Piperazine was used as a standard for comparing the binding affinity of the investigated coumarin towards KRAS. According to the results presented in Table 1 and Fig. 1., the investigated coumarin binds KRAS very well, which indicates a high inhibitory activity of this compound against the KRAS protein. The Gibbs energy of this complex is higher compared to standard piperazine, which indicates a slightly lower binding affinity of the investigated compound, which is to be expected due to fact that the volume of investigated coumarin is slightly higher. Also, inhibitory constants are in direct correlation with binding energies, and confirm the above set trend.

Keywords: coumarin, molecular docking, inhibitory activity, cancer, KRAS.

Protein	Coumarin		Piperazine	
	ΔG_{bind}	$k_i(\mu M)$	ΔG_{bind}	$k_i(\mu M)$
KRAS	-7.39	3.83	-10.94	0.96

Table 1. Thermodynamic parameters ΔG_{bind} (kcal/mol) and ki (μM) obtained from molecular docking simulation for coumarin and piperazine with KRAS.

In addition, coumarin derivative binds to the important amino acids, which means that it expresses high inhibitory potential towards KRAS regardless of the binding energies. The biggest contribution to the stabilization of the protein-coumarin complex comes from the attractive charge and the formation of hydrogen bonds. It was found that amino acid residues such as ASP12, LIS16 and ASP12 form strong hydrogen bonds with the oxygen atoms of lactone and hydroxyl group, while attractive charge comes from the amino acid residues such as ASP12 and GLU37 which form interactions with the nitrogen atom as in the case of piperazine [4]. In addition, a significant contribution to the stabilization of the protein-coumarin complex comes from Pi-anions and Pi-sulfur interactions which are formed between aromatic or aliphatic parts of the investigated compound and amino acid residues of proteins (Fig. 1).

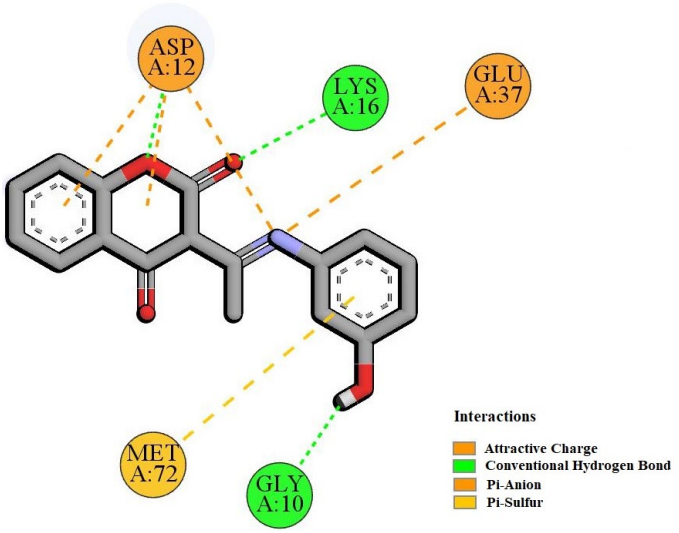

Fig. 1. The most favorable 2D binding confirmation of the coumarin to KRAS obtained after the molecular docking simulation.

Acknowledgment: This work was supported by the Ministry of Science, Technological Development and Innovation of the Republic of Serbia (Contract Nos. 451-03-47/2023-01/200378 and 451-03-47/2023-01/ 200146).

References:

[1] Avdović E.H. et. al., *Synthesis and Biological Screening of New 4-Hydroxycoumarin Derivatives and Their Palladium (II) Complexes*, Oxidative Medicine and Cellular Longevity, Vol. 2021, 18, 2021

[2] Morris, G. M., et. al. *AutoDock4 and AutoDockTools4: Automated docking with selective receptor flexibility,* Journal of computational chemistry, Vol. 30(16), 2785, 2009

[3] Valdés-Tresanco, M. S., et. al. *AMDock: a versatile graphical tool for assisting molecular docking with Autodock Vina and Autodock4*. Biology Direct, Vol. 15, 1, 2020.

[4] Zhongwei M., et. al. *KRAS(G12D) can be targeted by potent inhibitors via formation of salt bridge*, Cell Discovery, Vol 8, 2022.

GALLIC ACID DERIVATIVES AS INHIBITORS OF CARBOXY ANHYDRASES

Marko Antonijević, Dušica Simijonović, Jelena Đorović Jovanović and Zoran Marković

[1]Institute for Information Technologies, University of Kragujevac, Jovana Cvijića bb, 34000 Kragujevac, Serbia

e-mail: mantonijevic@uni.kg.ac.rs, dusica.simijonovic@pmf.kg.ac.rs, jelena.djorovic@uni.kg.ac.rs, zmarkovic@uni.kg.ac.rs

Abstract

Carbonic anhydrase II (CA II) is an enzyme from the family of carbonic anhydrases, which catalyze the reversible hydration of carbon dioxide. CA II is a zinc-containing enzyme found in high concentrations in red blood cells, where it plays an important role in carbon dioxide transport from the tissues to lungs. This enzyme has been linked to several other physiological processes, including acid-base regulation, bone resorption, and fluid secretion, in addition to its role in carbon dioxide transport. CA II has also been identified as a potential drug target for a variety of diseases, including glaucoma, epilepsy, and cancer [1]. Since 1950, CA inhibitors were the subject of extensive research when it comes to the suppression of epilepsy, heart conditions, cancer as well as altitude sickness. Acetazolamide was one of the first and most important medications in the class carboxy anhydrase inhibitors. It is commonly used to treat glaucoma, altitude sickness, epilepsy, and edema, among other medical conditions. It is also used to treat metabolic alkalosis, a condition in which the body has an excess of bicarbonate ions. This medication has been shown to reduce cerebrospinal fluid production, lowering intracranial pressure and providing relief to patients suffering from conditions such as hydrocephalus and pseudotumor cerebri. However, acetazolamide, like all medications, can cause side effects such as nausea, dizziness, and tingling in the extremities [2]. According to the literature, gallic acid and its derivatives are potent inhibitors of the carboxy anhydrases [3]. Three selected compounds from the series of gallic acid derivatives, as well as gallic acid itself will be subjected to the molecular docking simulations to determine their potential application as CA II inhibitors which are less toxic than commercially available drugs. Structures of investigated compounds are given in Fig. 1.

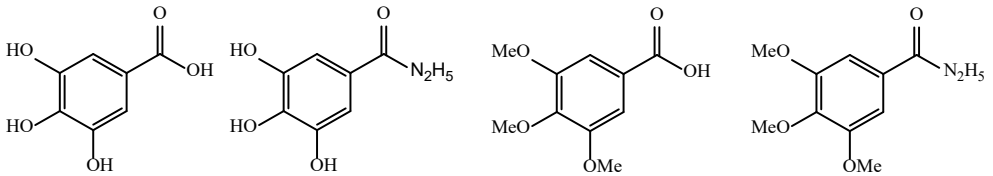

Gallic acid (1a) 3.4.5-trihydroxybenzohydrazide (1b) Eudesmic acid (2a) 3.4.5-trimethoxybenzohydrazide (2b)

Fig. 1. Structures of investigated compounds, natural and synthetic derivatives of gallic acid.

To predict the possible protein/enzyme targets for investigated compounds, they were subjected to SwissTargetPrediction webserver [4]. After the initial prediction, to obtain more precise parameters and binding affinity of investigated compounds towards the selected

protein/enzyme targets, AutoDock4.2 software package was used to perform molecular docking simulations (MD), as described in our previous work [5]. Ligand structures were optimised by implementation of Gaussian 16 software package, with implementation of M062X hybrid model at 6-311++G(d,p) level of theory. Protein structure was obtained from the RCSB Protein Data Bank, with the ID: **2EU2**. Protein preparation, as well as visualization of the obtained results was done by BIOVIA Discovery Studio 2020 [5].

As can be seen from Table 1, binding energies as well as inhibitory constants indicate that Eudesmic acid (2a) and hydrazide analogue (2b) show lower binding potential towards CA II than acetazolamide (STN). However, gallic acid (1a) and its hydrazide analogue (1b) are showing almost the binding potential as STN, which indicates the possible usage of these compounds as CA II inhibitors. Inhibitory constant (K_i) is an important parameter because it corresponds to the approximate concentration of the compound required for protein inhibition. The value of K_i can be compared to experimentally determined IC_{50} values. Also, as can be seen from Fig. 2, compounds 1a and 1b show interactions with same amino acid residues as acetazolamide. This confirms the prediction made by SwissTargetPrediction server that compounds 1a and 1b are potent inhibitors of CA II and should be subjected to further investigations.

Compound	**STN**	**1a**	**1b**	**2a**	**2b**
ΔG_{bind} (kcal/mol)	-6.38	-6.62	-6.34	-5.69	-5.63
K_i (μM)	21.06	14.04	22.53	67.48	74.68

Table 1. Binding energies and inhibitory constants describing inhibitory potential of acetazolamide and investigated compounds towards the CA II.

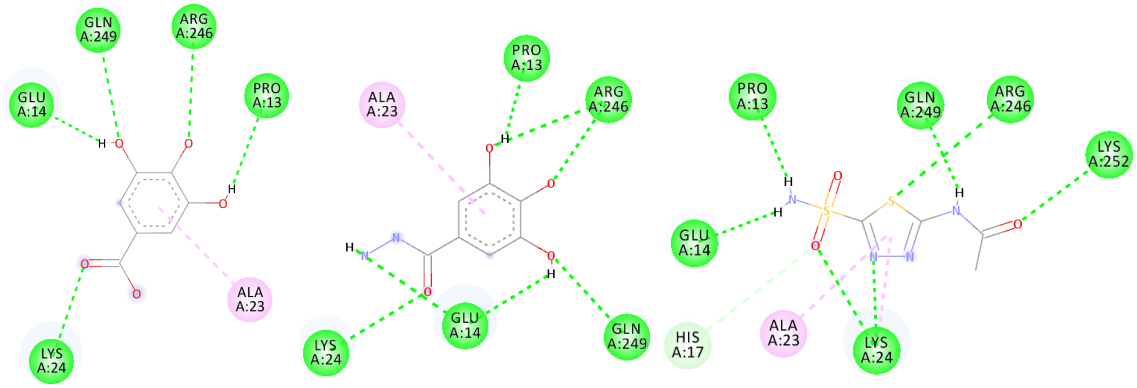

Fig. 2. Interactions between the 1a (left), 1b (center), and STN (right) with CA II, respectively.

Keywords: acetazolamide, gallic acid, eudesmic acid, carbonic anhydrase, molecular docking.

Acknowledgment: This work was supported by the Ministry of Science, Technological Development, and Innovation of the Republic of Serbia (Contract Nos. 451-03-47/2023-01/200378).

References:

[1] Supuran, C. T. *Carbonic anhydrases-an overview*. Current pharmaceutical design, 14(7), 603-614, 2008.

[2] Stokes, M. B., Chan, W. P. A., Worthley, M. I., & Coates, P. T. *Acetazolamide—another tool in the congestion battle?* Kidney International, 103(6), 1012-1014, 2023.

[3] Supuran, C. T. *Emerging role of carbonic anhydrase inhibitors*. Clinical Science, 135(10), 1233-1249, 2021.
[4] Gfeller, D., Grosdidier, A., Wirth, M., Daina, A., Michielin, O., & Zoete, V. *SwissTargetPrediction: a web server for target prediction of bioactive small molecules*. Nucleic acids research, 42(W1), W32-W38, 2014.
[5] Jovanović, J. Đ., Antonijević, M., Vojinović, R., Filipović, N. D., & Marković, Z. *In silico study of inhibitory capacity of sacubitril/valsartan toward neprilysin and angiotensin receptor.* RSC advances, 12(46), 29719-29726, 2022.

DEEP LEARNING IN PIV APPLICATIONS

Jelena T. Ilić[1], Ivana M. Medojević[1]and Novica Z. Janković[1]

[1] Faculty of Mechanical Engineering, University of Belgrade, Kraljice Marije 16, 11120 Belgrade 35, Serbia
e-mail: jilic@mas.bg.ac.rs, imedojevic@mas.bg.ac.rs , njankovic@mas.bg.ac.rs

Abstract

In the last decades, the field of fluid dynamics has significantly evolved thanks to the development of experimental and measurement techniques (hot wire, LDA, PTV, PIV), as well as the increasing computational capabilities and the improvement of available software and methods, such as CFD. All these techniques generate enormous volumes of data. Extracting valuable and useful information from them is often a time-consuming task, that could be aided by Deep Learning (DL). Herein, some of the many possible applications of DL, in particular the YOLO algorithm, in the practice of PIV, are considered and suggested.

Keywords: PIV, deep learning, YOLO algorithm.

1. Introduction

Neural networks (NN) are widely used model of the machine learning process (ML) and aim to deal with large amounts of data. It is, therefore, a useful tool in various fields of science, including fluid dynamics. In the 1990s, there were attempts to use NNs in PTV and PIV [1], but they did not prevail because, simple cross-correlation was much more efficient at that time. Meanwhile, among machine learning methods, DL algorithms have flourished, including Convolutional NNs (CNN) which are especially useful in computer vision. One of these DL algorithms was developed in 2015 – the You Look Only Once (YOLO) algorithm [2]. Although it was developed for real time object recognition and its location detection in autonomous vehicles, it soon found application in many fields such as agriculture [3], medicine [4], environmental research [5], biochemistry [6], etc. Last year, the application of YOLO algorithm in some fluid dynamics related areas was reported [7,8]. In the next section, two potential applications of the YOLO algorithm in Particle Image Velocimetry (PIV) practice are proposed.

2. Potential of YOLO algorithm in PIV image processing

The application of PIV strongly relies on accurate image processing, both in the process of obtaining the values of flow velocities, and in analyzing the final results of PIV measurement.

In an effort to improve the process of determining velocity values in PIV, instead of ordinary cross-correlation, Lee et.al. [9] proposed supervised cascade deep CNN, declaring that it is successful and significantly improves spatial resolution. The study had been done (2017) before the YOLOv2 version was released [2]. Since then, later versions of the YOLO algorithm have

proven to be useful in the measurement of displacement and complex object velocities [5]. It has also been applied in image velocimetry measurement in surface of the flow of an irrigation canal [7], where ripples and naturally floating objects are the counterpart of seeding particles in PIV. The idea of applying YOLO in PIV is to perform segmentation of pair of PIV images, detect images of individual seeding particles and determine their displacements. The hardest part is to create an appropriate training set for a YOLO network.

In PIV experiments, a large number of flow visualization images are acquired. DL might help identify structures, in those images, that are of interest for fluid dynamics researchers. To train certain DL algorithm to recognize elements in various flow visualization diagrams, experts should label images of characteristic objects of a flow image (e.g. vortices). Based on the labeled images, the DL network could be trained to quickly recognize characteristic objects of a flow in all newly obtained distribution images. On the other hand, the distributions of flow parameters (velocity, turbulence level, Reynolds number), obtained by PIV, or other experimental or numerical methods, are different for different tunnel configuration or different fan (shape and number of blades), but the human eye can hardly detect the differences. Hu et al. [8] presented a system that diagnoses the location of air obstructions in the lungs, based on CFD velocity distribution images on a specific cross-section of a trachea, using two open-source algorithms – ResNet50 and YOLOv4. It can be assumed that the trained YOLO or another DL network can identify with high precision which image of the flow parameter distribution is produced by which flow configuration, (the accuracy of YOLO is above 90% in almost all reported studies).

3. Conclusion

According to the aforementioned, fluid researchers might probably benefit from the latest Deep Learning methods, and YOLO algorithms in particular, because they provide a powerful tool for processing of large amount of data as well as image processing.

References:

[1] Brunton S.L., Noack B.R., Koumoutsakos P., *Machine Learning for Fluid Mechanics*, Annual Review of Fluid Mechnics, Vol. 52, 477-508, 2020.
[2] Jiang P., Ergu D., Liu F., Cai Y., Ma B., *A Review of Yolo Algorithm Developments*, Procedia Computer Science, Vol. 199, 1066-1073, 2022.
[3] Medojević I., Veg E., Joksimović A., Ilić J., *Promotion of Color Sorting in Industrial Systems Using Deep Learning Algorithm,* Applied Sciences, Vol. 12, 12817, 2022.
[4] Zhuang Z., Liu G., Ding W., Raj A.N.J., Qui S., Guo J., Yuan Y., *Cardiac VFM visualisation and analysis based on YOLO deep learning model and modified 2D continuity equation*, Computerized Medical Imaging and Graphics, Vol. 82, 101732, 2020.
[5] Xu X., Chen X., Wu B., Wang Z., Zhen J., *Exploiting high-fidelity kinematic information from port surveillance videos via a YOLO-based framework*, Ocean and Coastal Management, Vol. 222, 106117, 2022.
[6] Arjun A., Ajith R.R., Ranjith S.K., *Mixing characterization of binary-coalesced droplets in microchannels using deep neural network*, Biomicrofluidics, Vol. 14, 034111, 2020.
[7] Li S., Liu H., Wang S., Zhou Y., Zhou B., Han Y., *Study on flow distribution of irrigation canal system based on image velocimetry*, Computers and Electronics in Agriculture, Vol. 195, 106828, 2022.
[8] Hu P., Cai C., Yi H., Zhao J., Feng Y., Wang Q., *Aiding Airway Obstruction Diagnosis With Computational Fluid Dynamics and Convolutional Neural Networks: A New Perspective and Numerical Case Study*, Journal of Fluid Engineering, Vol. 144, 081206, 2022.
[9] Lee Y., Yang H., Yin Z., *PIV-DCNN: cascaded deep convolutional neural networks for particle image velocimetry*, Experiments in Fluids, Vol. 58, 171, 2017.

SECONDARY FLOWS OF PRANDTL'S SECOND KIND MECHANISM OF FORMATION AND METHOD OF PREDICTION

N. Nikitin

Institute of Mechanics, Lomonosov Moscow State University. Michurinsky pr. 1, 117192 Moscow, Russia
e-mail: nvnikitin@mail.ru

Abstract

This paper formulates a mechanism that makes it possible to explain and, in some cases, predict the shape of secondary flows of Prandtl's second kind arising in turbulent flows in straight pipes of non-circular cross-section.

Keywords: turbulent flows in straight pipes, secondary flows, Reynolds equations, direct numerical simulations.

1. Introduction

One of the interesting manifestations of turbulence is the occurrence of secondary flows in rectilinear flows. The most famous are the secondary flows in non-circular pipes. The change in the curvature of the wall along the perimeter of the cross-section of the pipe creates a spatial inhomogeneity of the Reynolds stresses and, as a consequence, motion in the plane perpendicular to the flow. L. Prandtl proposed to call such flows caused by Reynolds stresses secondary flows of the second kind, in contrast to secondary flows of the first kind, which arise in curved flows under the action of centrifugal effects in both turbulent and laminar flows. The characteristic velocities of secondary flows of the second kind are not high. They usually do not exceed a few percent of the mean bulk velocity. Nevertheless, their contribution to the transverse transport processes is comparable to the contribution of turbulent effects [1]. This paper formulates a mechanism that makes it possible to explain and, in some cases, predict the shape of secondary flows of Prandtl's second kind arising in turbulent flows in straight pipes of non-circular cross-section [2-4].

2. The mechanism of secondary flows

The secondary flows are consistent with the distribution of mean pressure along the perimeter of the cross section. In the section of the boundary between the neighboring points of the local maximum and minimum pressure, the fluid particles must move along the boundary in the direction from higher pressure to lower. This is because there are no Reynolds stresses on the solid wall, and the pressure force can only be balanced by viscous friction force acting against the direction of the motion. In some cases, the location of local pressure extremes along the perimeter of the pipe cross-section can be determined based on the analysis of the curvature of the

boundary. Fluctuating motion along a curved trajectory along the boundary causes a change in pressure on the wall the greater the greater the curvature of the boundary. There is an increase in pressure on the concave sections of the boundary, and on the convex, on the contrary, there is a decrease. The scheme of the occurrence of secondary flows in turbulent flows along the inner and along the outer corners is shown in Fig. 1. A number of examples known from the literature confirm the effectiveness of the proposed principle. Among them are the flows in a pipe of square cross-section, in a pipe of elliptical cross-section, in pipes with a cross-section in the form of a circular sector with different apex angles, in rectangular pipes with rounded corners, in an eccentric annular pipe. In most cases, an approximate picture of secondary flows can be predicted *a priori*, using only symmetry considerations and analysis of the curvature of the cross-section boundary.

The conditions of the formulated mechanism are violated near free boundaries, where, in addition to the pressure gradient, tangential stresses also act on the fluid particles and the result of their competition is unknown in advance. The paper presents the results of direct numerical simulation of turbulent flows in rectangular channels containing free boundaries, demonstrating and explaining the features of secondary flows in these cases.

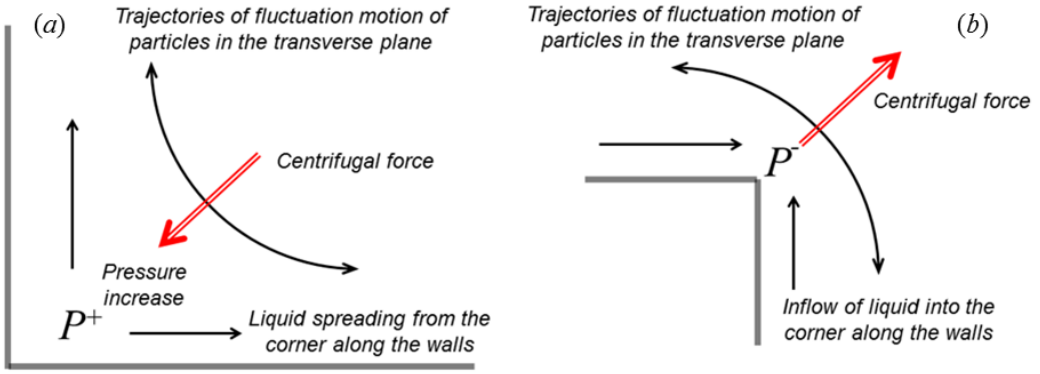

Fig. 1. Mechanism of secondary flow in the vicinity of the internal corner (*a*) and external corner (*b*).

3. Conclusions

The results of this work provide a rational basis for understanding the reasons for the formation and prediction of the shape of secondary flows of Prandtl's second kind arising in straight pipes of non-circular cross-section.

Acknowledgement: The work was carried out with the financial support of the RNF, project No. 22-21-00184.

References:

[1] Nikitin N., Yakhot A., *Direct numerical simulation of turbulent flow in elliptical ducts,* Journal of Fluid Mechanics, Vol. 532, 141-164, 2005.
[2] Nikitin N., *Turbulent secondary flows in channels with no-slip and shear-free boundaries,* Journal of Fluid Mechanics, Vol. 917, A24, 2021.
[3] Nikitin N.V., Popelenskaya N.V., Stroh A., *Prandtl's secondary flows of the second kind. Problems of description, prediction, and simulation,* Fluid Dynamics, Vol. 56, 513-538, 2021.
[4] Nikitin N., Krasnopolsky B., *Turbulent flows along a streamwise external corner,* Journal of Fluid Mechanics, Vol. 940, A16, 2022.

RESEARCH ON HIGH EFFICIENCY AND HIGH RELIABILITY PUMPS IN JIANGSU UNIVERSITY

Ji Pei and Wenjie Wang

National Research Center of Pumps, Jiangsu University, 301 Xuefu Road 212013, Zhenjiang, Jiangsu, China
e-mail: jpei@ujs.edu.cn

Abstract

Rotodynamic pump, the most widely used pump machinery in the world, is a kinetic machine in which energy is continuously imparted to the pumped fluid by means of a rotating impeller. According to the forms of impeller, this kind of pump can be divided into three types: centrifugal, mixed-flow and axial-flow pump. Rotodynamic pumps can be used in almost every social and industrial areas, such as urban drainage, agricultural engineering, water conservancy, energy industry, petrochemical industry, coal industry, metallurgy, aerospace, shipbuilding and marine engineering, et al. Efficiency and reliability are the most important key factors to evaluate the pump overall performance, which need to be considered during design, manufacture and research process. It is involved in several academic fields, such as complex fluid dynamics, bubble dynamics, structure dynamics and optimization algorithm, etc. Therefore, the basic theory and its application for high efficiency and high reliability rotodynamic pumps are the current research focuses, which have very important academic significance. In this presentation, the research work on High Efficiency and High Reliability Pumps by the National Research Center of Pumps in Jiangsu University, China will be briefly introduced. Several key methods and technologies considering hydraulic design and optimization, cavitation suppression as well as monitoring and diagnosis will be included, and the real application cases, such as pumping station, two-phase flow pump, nuclear power pump, chemistry and oil industry pump, and water-saving irrigation equipment, will be involved.

Aiming at solving the problem of low efficiency caused by internal flow turbulence in rotodynamic pumps, an analysis method for unstable flow structure inside the pump based on entropy energy production method and vortex identification method is proposed, which reveals the relationship between flow loss and vortex structure distribution. Combining numerical and experimental studies, it has been shown that the gap in the vaneless zone can significantly control the hydraulic loss, and the relative position of the diffuser has a significant impact on the main frequency and amplitude of pressure fluctuations. The flow control technology of sequential position effectively reduces the flow loss and pressure pulsation. Aiming at the problem of poor cavitation performance of large-capacity pump devices resulting in poor operational stability, a Reynolds time-averaged turbulence model considering the rotation effect was proposed, and a high-precision cavitation prediction calculation method based on large eddy simulation was established. The Kelvin-Helmholtz (K-H) structure of attached cavities and the multi-dimensional flow field characteristics of cavity group evolution are revealed. A fast numerical prediction method for pump performance with modified boundary conditions was proposed. Comparing with the traditional cavitation performance prediction method of gradually reducing the inlet

pressure, the calculation time of new approach is significantly reduced by 44 %, which provides theoretical support for the optimization of pump cavitation performance.

Hydraulic optimization design is the most fundamental way to improve the performance of rotodynamic pumps. It is a core issue that needs to be considered in the process of pump design, manufacturing and technology research and development. Related advanced theories and technologies have become research hotspots in the field of high-end equipment manufacturing and engineering applications of fluid machinery. It is difficult to meet the requirements only by half-empirical and half-theoretical hydraulic design methods. Therefore, it is necessary to explore the theory and technology of hydraulic optimization. A combined surrogate model (ANN-Kriging-RSM) is proposed to improve the prediction accuracy of the approximation function. A modified standard PSO and multi-objective PSO (MOPSO) are proposed to improve the convergence accuracy and search speed. LabVIEW and Python software are used to build a fully automatic optimization design platform. Write the interface program calling Workbench software through Python to realize the real-time unsteady solver of the hybrid particle swarm algorithm in iterative calculation, that is, call the relevant batch files to automatically perform the three-dimensional modeling, mesh division and unsteady numerical calculation of the impeller and guide vane and postprocessing. The problem of difficult multi-interface calling of commercial optimization software in the optimization of rotodynamic pump is solved.

Keywords: rotodynamic pump, unsteady flow, cavitation, optimization.

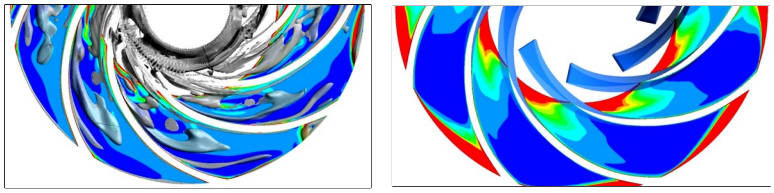

Fig. 1. Analysis of unsteady flow (a) entropy energy production (b) vortex structure distribution.

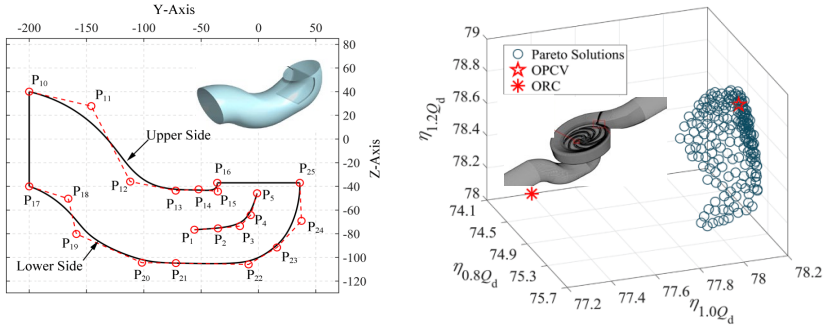

Fig. 2. Multi-objective optimization on inline pump (a) optimized parameter (b) Pareto of three objectives.

References:

[1] Gan X, Pavesi G, Pei J, et al. Parametric investigation and energy efficiency optimization of the curved inlet pipe with induced vane of an inline pump[J]. Energy, 2022, 240: 122824.

[2] Pei J, Osman M K, Wang W, et al. Unsteady flow characteristics and cavitation prediction in the double-suction centrifugal pump using a novel approach[J]. Proceedings of the Institution of Mechanical Engineers, Part A: Journal of Power and Energy, 2020, 234(3): 283-299.

VISCOUS GENERALIZED MAXWELL-STEFAN MODEL OF DIFFUSION

Damir Madjarević[1] and Srboljub Simić[2]

[1] Department of Mechanics, Faculty of Technical Sciences, University of Novi Sad, Trg Dositeja Obradovića 6, Novi Sad, Serbia
e-mail: damirm@uns.ac.rs

[2] Department of Mathematics and Informatics, Faculty of Sciences, University of Novi Sad, Trg Dositeja Obradovića 4, Novi Sad, Serbia
e-mail: ssimic@uns.ac.rs

Abstract:

The paper presents a systematic derivation of the governing equations for diffusion processes in the presence of viscous stresses. They are derived as moment equations of the system of Boltzmann equations for mixtures of gases, and inherit a small parameter due to so-called diffusive scaling. In the asymptotic limit, the classical Maxwell-Stefan diffusion model is derived. To recover the viscous stresses, higher-order model is derived and additional small parameter – the relaxation time – is introduced to take into account their order of magnitude. Generalized Maxwell-Stefan diffusion model with classical viscous stresses is derived by means of asymptotic analysis.

Keywords: mixtures, Maxwell-Stefan diffusion, viscous stresses.

1. Higher-order Maxwell-Stefan diffusion model

Diffusion is a process in which motion of one species relative to another occurs. In a lot of circumstances – like in binary mixtures, motion relative to a background material, or processes close to local equilibrium – classical or generalized Fick's model of diffusion may be appropriate. However, when cross-diffusion of species come into play, like in gaseous mixtures, the Maxwell-Stefan model provides predictions of higher accuracy. Models of this kind are used in various applications, ranging from engineering to medicine.

The Maxwell-Stefan diffusion can be derived starting from the system of Boltzmann equations in diffusive scaling [1,2]:

$$\alpha\partial_t f^i + v_l\partial_{x_l} f^i = \frac{1}{\alpha}\sum_{j=1}^{S} Q^{ij}\left(f^i, f^j\right)(\boldsymbol{v}), \tag{1}$$

where $f^i(t,\boldsymbol{x},\boldsymbol{v})$ is the species velocity distribution function, $\boldsymbol{v}$ is molecular velocity, Q^{ij} are collision operators, and α is a unique small parameter representing the Mach and Knudsen number, at the same time. Starting from (1), macroscopic balance laws of mass, momentum and momentum flux of the species can be derived as moment equations:

$$\alpha\left(\partial_t\rho^i + \partial_{x_k}\left(\rho^i u_k^i\right)\right) = 0, \tag{2}$$

$$\alpha^2\left[\partial_t\left(\rho^i u_l^i\right) + \partial_{x_k}\rho^i u_k^i u_l^i\right] - \partial_{x_k} t_{kl}^i = \sum_{j=1}^{S}\frac{2\pi|b^{ij}|_{L^1}}{m_i+m_j}\rho^i\rho^j\left(u_l^j - u_l^i\right), \tag{3}$$

$$\partial_t\left(\alpha^3\rho^i u_k^i u_l^i - \alpha t_{kl}^i\right) + \partial_{x_k}\left(\alpha^3\rho^i u_k^i u_l^i u_n^i - \alpha\left(u_k^i t_{ln}^i + u_l^i t_{nk}^i + u_n^i t_{kl}^i\right)\right) = P_{kl}^i\left(\rho^i, u_k^i, t_{kl}^i, \alpha\right), \tag{4}$$

where ρ^i are species mass densities, u_k^i are components of species macroscopic velocities, and t_{kl}^i are species partial stress tensors. In equation (3), $|b^{ij}|_{L^1}$ denotes the norm of the collision cross section, and P_{kl}^i is the source term in the momentum flux balance law (4) whose structure is provided in [2].

Standard Maxwell-Stefan model is derived from the balance laws of mass (1) and momentum (2) of the species, in the so-called asymptotic limit when $\alpha \to 0$, and partial stress tensors are diagonal, $t_{kl}^i = -p^i\delta_{kl}$:

$$\partial_t\rho^i + \partial_{x_k}\left(\rho^i u_k^i\right) = 0, \tag{5}$$

$$\partial_{x_l}p^i = \sum_{j=1}^{S}\frac{2\pi|b^{ij}|_{L^1}}{m_i+m_j}\rho^i\rho^j\left(u_l^j - u_l^i\right). \tag{6}$$

2. Viscous stresses in Maxwell-Stefan model

In the Maxwell-Stefan model (2)-(4) stress tensor t_{kl}^i is usually split into a sum of spherical (pressure) part and viscous stresses σ_{kl}^i, which are traceless in the case of monatomic gases, $t_{kl}^i = -p^i\delta_{kl} + \sigma_{kl}^i$. If the model is supposed to be closed at the level of momentum balances, i.e. using (2)-(3) only, the viscous stresses are usually assumed in the form of classical Newtonian stresses, are introduced into diffusion models by assumption [3]. In the higher-order Maxwell-Stefan diffusion model, they are governed by the balance laws of momentum flux of the species. Our aim is to use this model as a starting point, and derive the viscous generalization of the Maxwell-Stefan model through an asymptotic analysis. This amounts to applying the so-called Maxwellian iteration procedure [4]. This method recovers the Newtonian stresses as a limiting case for the 13 moments model of viscous and heat-conducting monatomic gas. However, such a procedure needs another small parameter to be recognized – the relaxation time.

Partial viscous stress tensors σ_{kl}^i will be assumed in the form of power series of relaxation time as a small parameter. This will yield the classical form of the viscous stresses. However, their inclusion into momentum balances of the species will provide a proper insight into the order of magnitude of viscous dissipation. It may be concluded that asymptotic analysis and thermodynamic limit of moment equations through an order of magnitude estimate give better information about the structure and relevance of viscous stresses in Maxwell-Stefan diffusion model than usual ad hoc procedures.

Acknowledgment: This research was supported by the Faculty of Technical Sciences, University of Novi Sad (Project No. 2023-054).

References:

[1] Anwasia B., Simić S., *Maximum entropy principle approach to a non-isothermal Maxwell-Stefan diffusion problem*, Applied Mathematics Letters, 129, 107949, 2022.
[2] Grec B., Simić S., *Higher-order Maxwell-Stefan model of diffusion*, arXiv:2305.08412
[3] Kerkhof P.J.A.M., Geboers M.A.M., *Analysis and extension of the theory of multicomponent fluid diffusion*, Chemical Engineering Science, 60, 3129-3167, 2005.
[4] Ruggeri T., Sugiyama M., *Classical and Relativistic Rational Extended Thermodynamics of Gases*, Springer Nature, Cham, 2021.

COMPUTATIONAL ANALYSIS OF DRUG EFFECTS ON HYPERTROPHIC CARDIOMYOPATHY

Smiljana Tomasevic[1,2], Miljan Milosevic[2,3], Bogdan Milicevic[1,2], Vladimir Simic[2,3], Momcilo Prodanovic[2,3,4], Srboljub M. Mijailovich[4,5]and Nenad Filipovic[1,2]

[1] Faculty of Engineering, University of Kragujevac, Sestre Janjic 6, 34000 Kragujevac, Serbia
e-mails: smiljana@kg.ac.rs, bogdan.milicevic@uni.kg.ac.rs, fica@kg.ac.rs
[2] Bioengineering Research and Development Center (BioIRC), Prvoslava Stojanovica 6, 34000 Kragujevac, Serbia
e-mails: miljan.m@kg.ac.rs, vsimic@kg.ac.rs, momcilo.prodanovic@gmail.com
[3] Institute for Information Technologies, University of Kragujevac, Jovana Cvijica bb, 34000 Kragujevac, Serbia
[4] FilamenTech, Inc., Newton, MA 02458, USA;
e-mail: smijailo@gmail.com
[5] BioCAT, Department of Biology, Illinois Institute of Technology, Chicago, IL 60616, USA

Abstract

In analysis of cardiomyopathy, understanding of disease progression is still limited, as well as the effects of drugs interactions on cardiac tissue. The present provides insight into the model-based simulation of myocardial function under hypertrophic cardiomyopathy (HCM), employing the finite element (FE) PAK software coupled with multi-scale model of muscle contraction. The main advantage and novelty of the study is coupled macro and micro simulations into the integrated Fluid Solid Interaction (FSI) system and its application in the examination of heart behavior and drug interactions. The analysis of myocardial function and changes of pressure and volume within the LV parametric model of HCM are presented at basic condition and after simulated effects of administered drugs. The obtained results provide better insight into the myocardial function in HCM patients as well as into estimated effects of drug therapy.

Keywords: finite element analysis, hypertrophic cardiomyopathy, drug effects.

1. Introduction

Cardiomyopathies are defined as structural and functional abnormalities of the ventricular myocardium [1]. Hypertrophic cardiomyopathy (HCM) is characterized by enlargement of the heart with increased left ventricle (LV) wall thickness, often with asymmetrical hypertrophy of the septum that separates the LV from the right ventricle (RV) and can lead to left ventricular outflow tract obstruction (LVOTO). Although there are clinical improvements in cardiomyopathy risk assessment, patients are still exposed to high risk of severe events. Computational modeling and computer-aided drug design can significantly advance the understanding of cardiac muscle activity in cardiomyopathy, speed up the drug discovery and reduce the risk of severe events.

2. Materials and methods

The present study provides insight into the model-based simulation of myocardial work under HCM, employing the finite element (FE) PAK software coupled with multi-scale model of muscle contraction. FSI algorithm within the PAK software is used for modeling the LV with nonlinear material model, together with stretches integration along muscle fibers. The methods are integrated within the SILICOFCM platform [2]. The FE simulations of HCM LV parametric model using PAK solver enable quantitative assessment of the effect of administered drugs on cardiac output including increase in both systolic and diastolic pressures, and the left ventricle ejection fraction (LVEF). The applied boundary conditions are related to adopted nominal inlet and outlet velocities for mitral and aortic valves of LV, as well as applied calcium concentrations.

3. Results and conclusions

Simulations of the effect of drugs on improving performance of HCM LV parametric model include the drugs that affect calcium transients (Disopyramide) and changes in kinetic parameters (Mavacamten). All simulations are performed using PAK FSI, FE solver and coupled with multi-scale model of muscle contraction. Myocardial function is presented through changes in pressures and volumes (P-V diagrams) for the HCM LV model at basic condition (without administered drug) and with using Disopyramide and Mavacamten. The predicted P-V diagram for HCM at basic condition shows lower volumes and higher ventricular pressures than normal, with reduced LVEF (LVEF=59.33%). The principal effects of drugs on HCM after simulations are decrease in peak pressures and shift of P-V loops toward higher volumes and higher LVEF, which is in accordance with clinical observations [3].

The results provide a quantitative assessment of the effects of different on the cardiac output, including both systolic and diastolic LV pressures and volumes, as well as the LVEF. This approach can give better insight into estimated effects of drug therapy, leading to improved patient monitoring and treatment.

Acknowledgment: This work is supported by the European Union's Horizon 2020 research and innovation pro-grammes SILICOFCM (Grant agreement 777204) and SGABU (Grant agreement 952603). The Commission is not responsible for any use that may be made of the information it contains. The research was also funded by Serbian Ministry of Education, Science, and Technological Development, grants [451-03-9/2022-14/200122 (Institute for Information Technologies, University of Kragujevac)] and [451-03-47/2023-01/200107 (Faculty of Engineering, University of Kragujevac)].

References:

[1] Elliott, P.; Anastasakis, A.; Borger, M.A.; Borggrefe, M.; Cecchi, F.; Charron, P.; Hagege, A.A.; Lafont, A.; Limongelli, G.; Mahrholdt, H.; et al. 2014 ESC Guidelines on Diagnosis and Management of Hypertrophic Cardiomyopathy. Eur. Heart J. 2014, 35, 2733–2779, doi:10.1093/eurheartj/ehu284

[2] SILICOFCM H2020 Project: In Silico Trials for Drug Tracing the Effects of Sarcomeric Protein Mutations Leading to Familial Cardiomyopathy, 777204, 2018-2022, www.silicofcm.eu.

[3] Warriner, D.R.; Brown, A.G.; Varma, S.; Sheridan, P.J.; Lawford, P.; Hose, D.R.; Al-Mohammad, A.; Shi, Y. Closing the Loop: Modelling of Heart Failure Progression from Health to End-Stage Using a Meta-Analysis of Left Ventricular Pressure-Volume Loops. PLoS One 2014, 9, e114153, doi:10.1371/journal.pone.0114153.

OBLIQUE TRANSITION IN HIGH-SPEED SEPARATED BOUNDARY LAYERS

Anubhav Dwivedi[1], G. S. Sidharth[2] and Mihailo R. Jovanović[1]

[1]Ming-Hsieh Department of Electrical and Computer Engineering, University of Southern California, Los Angeles, CA 90089, USA
e-mail: anubhavd91@gmail.com, mihailo@usc.edu
[2] Department of Aerospace Engineering, Iowa State University, Ames, IA 50011, USA

Abstract

We utilize resolvent and weakly nonlinear analyses in combination with direct numerical simulations (DNS) to identify mechanisms for oblique transition in a Mach 5 flow over an adiabatic slender double-wedge. Even though the laminar separated flow is globally stable, resolvent analysis demonstrates significant amplification of unsteady external disturbances. These disturbances are introduced upstream of the separation zone, and they lead to the appearance of oblique waves further downstream. We demonstrate that large amplification of oblique waves arises from interactions of the fluctuation shear stress with streamline curvature of the laminar base flow in the separated shear layer. This is in contrast with the attached boundary layers, where no such mechanism exists. We also use a weakly nonlinear analysis to show that the resolvent operator associated with linearization around the laminar base flow governs the evolution of steady reattachment streaks that arise from quadratic interactions of unsteady oblique waves. These quadratic interactions generate vortical excitations in the reattaching shear layer which lead to the formation of streaks in the recirculation zone and their subsequent amplification, breakdown, and transition to turbulence downstream. Our analysis of the energy budget shows that deceleration of the base flow near reattachment is primarily responsible for amplification of steady streaks. Finally, we employ DNS to examine latter stages of transition and demonstrate the predictive power of input-output framework in uncovering triggering mechanisms for oblique transition in separated high-speed boundary layer flows.

Keywords: hypersonic flow, compressible boundary layers, boundary layer receptivity.

References:

[1] Dwivedi A., Sidharth G., Jovanović M. R., Oblique transition in hypersonic double-wedge flow, J. Fluid Mech., Vol. 948, A37-1 – A37-37, 2022., doi:10.1017/jfm.2022.697

THERMODINAMICAL RESTRICTIONS FOR MOVING POINT LOAD MODEL INVOLVING GENERALIZED VISCOLEASTIC FOUNDATION

Lidija Z. Rehlicki Lukešević[1], Marko B. Janev[2], Branislava B. Novaković[1], and Teodor M. Atanacković[1]

[1] Faculty of Technical Sciences, University of Novi Sad, Trg Dositeja Obradovića 6, Novi Sad, Serbia
e-mail: lidijarl@uns.ac.rs , nbrana@uns.ac.rs , atanackovic@uns.ac.rs
[2] Mathematical Institute of the Serbian Academy of Sciences and Arts, Knez Mihajlova 36, Belgrade, Serbia
e-mail: markojan@mi.sanu.ac.rs

Abstract

The dynamic response of an elastic beam of finite length on a viscoelastic foundation subjected to moving load has begun to draw increasing attention from researchers in recent years. It has numerous applications especially in the areas of railway track, bridge, and pipeline design, where modelling of viscoelastic foundation plays a significant role in the obtained accuracy of the dynamic response.

Moving load resting on a beam on a purely, i.e., Winkler elastic foundation was treated extensively in [1], but it suffers from inaccuracy in modelling of response due to the fact that damping, which is present in all real foundations, has been ignored.

In order to incorporate the damping effect and thus model the time-dependent behavior more accurately and features of real foundations, such as creep or stress-relaxation, researchers introduced an integer order-based viscoelastic foundation.

Since fractional operators do not only depend on time alone, but also on the whole previous time interval, researchers applied fractional derivatives to the modelling of viscoelastic properties of materials used in structures and foundations in order to describe time memory effects in real materials more accurately. It has shown significant improvement, as it can be seen in [2] and [3].

In [4], the question of determining restrictions for the constitutive equation in the finite elasticity theory was first raised by C. Truesdell. In [5], by assuming the isothermal conditions in a material undergoing sinusoidal strain, a simple method for obtaining the thermodynamical restrictions on coefficients of general linear models of viscoelasticity has been presented by Bagley and Torvik and later determined in many special cases (see [6] and [7]). The conclusion was that both loss and storage modulus must be positive for all frequencies. The mathematical analysis connecting the approach applied in [5] with the second law of thermodynamics in the case of constitutive equations with fractional derivatives, has been presented in many papers and books. Nevertheless, a more general approach that delivers the restrictions on coefficients of constitutive relation that involves fractional derivatives for the week form of thermodynamical inequality under isothermal conditions, given by

$$D(x)=\int_0^T \sigma(t,x)\frac{\partial \varepsilon(t,x)}{\partial t}dt \geq 0,\ x\in R,\ T>0 \qquad (1)$$

is presented in [8]. The term $\sigma(t,x)$ is the Cauchy stress while $\varepsilon(t,x)$ is strain given by $\varepsilon = \partial u / \partial x$ where u is displacement at an arbitrary point $x \in R$ of the rod and time t. We mention that inequality (1) holds for any cycle of duration $T > 0$, where cycle denotes $\varepsilon(0,x) = \varepsilon(T,x)$ and that certain regularity of ε is imposed. We also note that a strong form of thermodynamical inequality corresponds to (1) (which implies (1)) is given by $\sigma(t,x)(\partial\varepsilon(t,x)/\partial t) \geq 0$ $x \in R$, $t \in [0,T]$, $T > 0$. The approach presented in [8] is then extended in [9] to the case of constitutive relations involving distributed order of fractional derivatives, generalized Kelvin-Voight model involving symmetrized fractional derivatives of complex order, as well as anti-Zener model.

In this paper, we analyzed the dynamic behavior of Euler-Bernoulli finite length beam resting on a viscoelastic foundation subjected to moving load, where we assume the generalized Kelvin-Voight type foundation, in a sense that the constitutive relation describing the model contains symmetrized Riemann-Liouvile fractional derivatives of complex order type. A mixed initial value-boundary condition problem is formulated, and a close form solution is obtained by using the method of separation of variables. Namely, it is obtained as a form of Fourier series with respect to space variable, where coefficients satisfy certain ordinary linear fractional differential equations of complex fractional order, with respect to time variable. The solutions of the mentioned fractional differential equations are obtained analytically, using the inverse Laplace transform. Moreover, we prove that the thermodynamic restrictions on parameters of generalized Kelvin-Voight type constitutive relation are sufficient for the existence and uniqueness of the solution. We present a numerical example that confirms the applied theory.

Keywords: moving load, Euler-Bernoulli beams, fractional viscoelastic foundation, derivatives of complex fractional order.

References:

[1] Thambiratnam D., Zhuge Y., *Dynamic analysis of beams on an elastic foundation subjected to moving loads*, Journal of Sound and Vibration. Vol. 198, 149-169, 1996.

[2] Eldred L. B., Baker V. P., Palazotto A. N., *Kelvin-Voigt versus fractional derivative model as constitutive relations for viscoelastic materials*, AIAA J. Vol. 33, 547-550, 1995.

[3] Meral F.C., Royston T.J., Magin R., *Fractional calculus in viscoelasticity: An experimental study*, Communications in Nonlinear Science and Numerical Simulation, Vol. 15, 939-945, 2010.

[4] Truesdell C., *Das ungeloste Hauptproblem der endlichen Elastizitats theorie*, Journal of Applied Mathematics and Mechanics Vol. 36, 97-103, 1956.

[5] Bagley R. L., Torvik P.J., *On the fractional calculus model of viscoelastic behavior*, Journal of Rheology, Vol. 30, 133-155, 1986.

[6] Atanackovic T. M., *On a distributed derivative model of a viscoelastic body*, Comptes Rendus Mecanique Vol. 331 (10), 687-692, 2003.

[7] Atanackovic T. M., Konjik S., Oparnica Lj., Zorica D., *Thermodynamical restrictions and wave propagation for a class of fractional order viscoelastic rods*, Abstract and Applied Analysis, http://dx.doi.org/10.1155/2011/975694, 2011.

[8] Atanackovic T. M., Janev M., Pilipovic S., *On the thermodynamical restrictions in isothermal deformations of fractional Burgers model*, Philosophical Transactions of the Royal Society A – Journals, https://doi.org/10.1098/rsta.2019.0278, 2020.

[9] Atanackovic T. M., Janev M., Pilipovic S., Selesi D., *Viscoelasticity of Fractional Order: New Restrictions on Constitutive Equations with Applications*, International Journal of Structural Stability and Dynamics Vol. 20 (13), 2041011, 2020.

FLEXIBLE DEPLOYABLES MADE FROM SOFT KIRIGAMI COMPOSITES

Jan Zavodnik[1*], Mohammad Khalid Jawed[2] and Miha Brojan[1]

[1] Laboratory for Nonlinear Mechanics, University of Ljubljana, Faculty of Mechanical Engineering, Laboratory for Nonlinear Mechanics, Aškerčeva 6, SI-1000, Ljubljana, Slovenia
e-mail: jan.zavodnik@fs.uni-lj.si
[2] Department of Mechanical and Aerospace Engineering, University of California, Los Angeles, 420 Westwood Plaza, Los Angeles, CA, USA.

Abstract

Kirigami structures have been attracting increasing attention in recent years for their ability to create intricate patterns and 3D forms by cutting and folding flat sheets of materials. In this study, we introduce a new class of thin, flexible, fully deployable structures made by attaching a flexible pre-stretched sheet to a kirigami layer. Due to the kirigami's carefully designed pattern, which enables a partial release of the stresses through bending and in-plane deformations, we are able to achieve different desired 3D forms. Perhaps the most desirable deformation is the change of Gaussian curvature (spherical bending) which is usually difficult due to required large in-plane deformations. We demonstrate the feasibility of this approach through experiments enabled by our novel experimental system, purposely developed theory and numerical simulations. These new kirigami structures have potential applications in the design of lightweight structures, deployable structures that can adapt to changing environments in a wide range of fields, including aerospace, robotics, and biomedical engineering.

Keywords: morphing, shell buckling, residual stress, composites.

1. Experimental exploration

We begin our experimental exploration by stretching a circular elastic sheet using our purposely designed device and bonding together two sheets of material to form a composite structure, as shown in Fig. 1. (A). For a small prestretch λ, we obtain a shallow spherical cup, but as our experiments reveal the composite structure loses its stability at larger λ and settles in an n-fold mode, depending on the amount of λ. To prevent the loss of stability, which is caused by additional compressive membrane stresses due to the change in Gaussian curvature, we use kirigami patterns of the unstretched layer to relieve them.

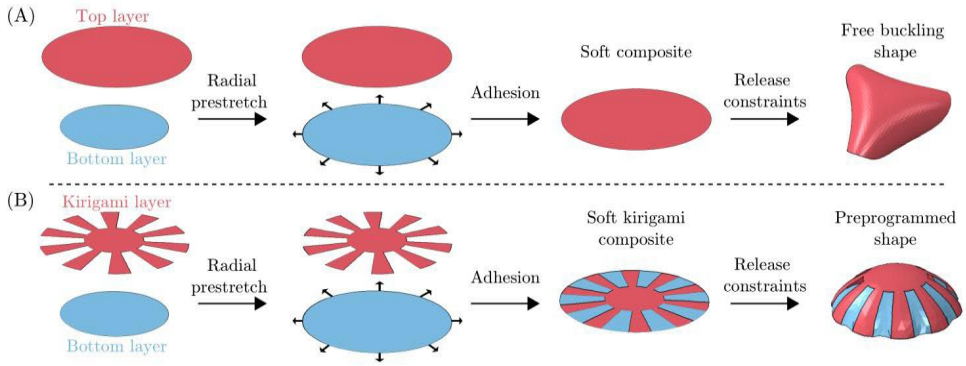

Fig. 1. Overview of the problem. The bottom layer is stretched, attached to the unstretched layer and released to obtain a 3D hemispherical form. (A) Without the kirigami layer. (B) With the kirigami layer.

2. The underlying mechanics

To understand the underlaying mechanics we use the composite plate theory [1], the Föppl-Von Karman plate and Donnel-Mustari-Vlasov shallow shell theory [2]. We find that with the increase of the prestretch the *n*-fold symmetric modes become energetically favorable (see Fig. 2). However, our theory reveals that for a much larger prestretch the cylindrical deformation mode is energetically preferable, because it effectively does not contain any membrane stresses.

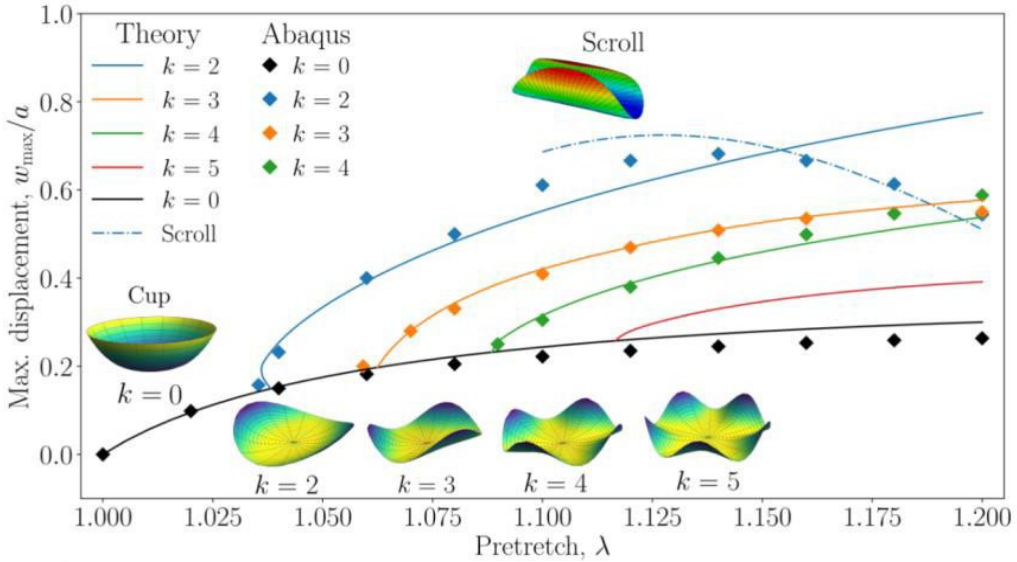

Fig. 2. Deformation modes of the soft composite plate. Normalized maximum vertical displacement w_{max}/a in relation to the pre-stretch λ of the stretched sheet, where a is the radius of the circular plate. The theory is compared to the numerical simulation results from Abaqus.

The theory provides the understanding that through cutting the unstretched layer reduces the membrane stresses and the right cutting parameters might prevent the *n*-fold wrinkling of the outer edge of the initially circular composite to achieve predominantly spherical bending deformation. The presumption is confirmed when our numerical and experimental tests with kirigami layers yield spherical deformation modes, as seen in Fig. 3.

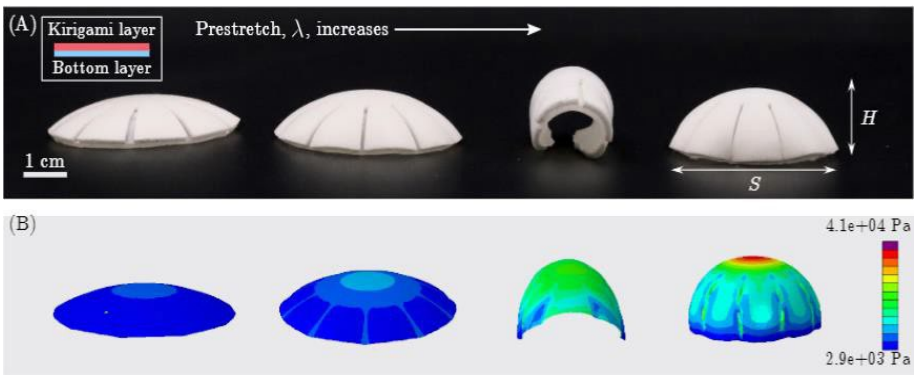

Fig. 3. Comparison of the deformation modes of soft kirigami composites with different prestetches. The kirigami layer stabilizes the strucuture and prevents the loss of stability. (A) Experiments. (B) Numerical results.

3. Conclusions

With our soft kirigami composites we can fabricate self-assembled 3D structures that include all ranges of bending deformations from cylindric to spherical deformations, which cause large membrane deformations due to large Gaussian curvature change. Our theory enables us to understand the underlying mechanics of the soft kirigami composites and therefore the design of various foldable, self-assembling 3D structures that form from 2D sheets.

References:

[1] Robert M. J., *Mechanics of composite materials*, Taylor & Francis, New York, NY, 1999.
[2] Ibrahim K. E., *Non-linear theories of sandwich shells*, International Journal of Non-Linear Mechanics, Vol. 8, 303-311, 1973.

THIN COMPOSITE PLATES WITH STRESS CONCENTRATORS ANALYZED BY THEORY OF CRITICAL DISTANCES

Ivana D. Atanasovska[1] and Dejan B. Momcilovic[2]

[1] Mathematical Institute of the Serbian Academy of Sciences and Arts, Kneza Mihaila 36, Belgrade, Serbia
e-mail: iatanasovska@mi.sanu.ac.rs
[2]The IMS Institute, Bulevar vojvode Misica 43, Belgrade, Serbia
e-mail: dejan.b.momcilovic@gmail.com

Abstract

The increased requirements for mass reduction of lightweight constructions are still very challenging, and cover a wide range of research topics. One of the main problems in this framework is the behaviour of composite structures with stress concentrators, which are usually different holes intended for connection or access to other parts of the structures. In this paper, the composite thin plates with stress concentrators in the form of holes with few different shapes are investigated. The influence of the lay-up at the load capacity under fatigue is analysed for two different lay-ups of carbon/epoxy composite plates. The Theory of Critical Distances (TCD) is used for analysing the results for stress gradients obtained by the Finite Element Analysis (FEA) of the modelled cases. The discussion of the obtained results shows the specific potential and efficiency of the presented approach for analysing composite structures with stress concentrators.

Keywords: thin plate, composites, stress concentrator, Theory of Critical Distances (TCD).

1. Introduction - models and methods

The research of the behaviour of thin plate with stress concentrators under fatigue is the subject of increasing interest due to the new methods and approaches developed in the theoretical and applied mechanics in recent years [1, 2]. Due to the very significant increase in the production of composite lightweight constructions, great attention is being paid to researching the composite plates with different stress concentrators [2]. In this paper, the thin plates with stress concentrators in the form of holes of different shapes are investigated. The analysis of the fatigue behavior of cross-ply and angle-ply carbon/epoxy composites are performed by FEA. The stress analysis is performed for pure tensile loading case (Fig.1 and Fig.2).

2. Results and conclusions

The obtained stress gradients in the case of circular hole are presented in Fig. 3 and analysed in accordance with the main definition of the point TCD method [2, 3]. The value of critical distances for the analysed composite materials, for both modelled lay-ups are calculated in

accordance with the available experimental results for the fatigue strength of standard smooth specimens and the fatigue threshold stress intensity [4].

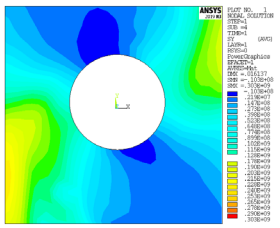

Fig. 1. Tensile stress gradients for circular hole and lay-up case 2 – for first and second layers

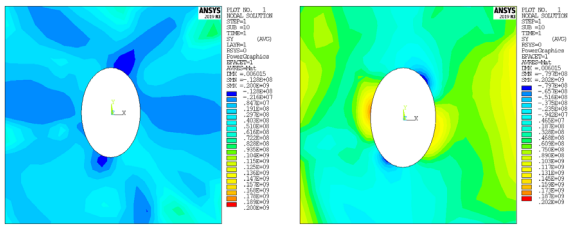

Fig. 2. Tensile stress gradients for elliptical hole and lay-up case 1 – for first and second layers

The obtained values for the critical distance are 0.11 mm for case 1 and 0.66 mm for case 2 lay-up of modelled composites, while the critical stress values are equal to the fatigue strength (418 MPa for case 1 and 90 MPa for case 2). Analysis of the obtained results (Fig. 3) shows that the case 1 lay-up has better behaviour for the analysed case-study.

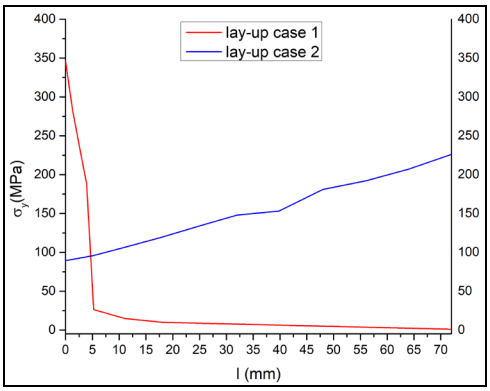

Fig. 3. Comparative stress gradients for circular hole and different lay-ups

Acknowledgment: This research was funded by the Ministry of Science, Technological Development and Innovation, Republic of Serbia, Grant numbers: 451-03-47/2023-01/200029; 451-03-47/2023-02/200012

References:

[1] Jun-Min Seo, Yun-Jae Kim, Masaki Omiya, *Crack growth simulation in thin plate using simplified strain based damage model*, Engineering Fracture Mechanics, Vol. 260, 108188, 2022.

[2] Morgan D., Quinlan S., Taylor D., *Using the theory of critical distances to predict notch effects in fibre composites*, Theoretical and Applied Fracture Mechanics, Vol. 118, 103285, 2022.

[3] Atanasovska I., Momcilovic D., *Theory of Critical Distances in analysis of the influence of tooth profile on gears bending capacity*, 5th Balkan Association on Power Transmission Conference 2016, Ohrid, Macedonia, pp. 63-70, 2016.

[4] Putic S., Uskokovic P.S., Aleksic R., *Analysis of fatigue and crack growth in carbon-fiber epoxy matrix composite laminates*, Strength of Materials, Vol. 35, No. 5, 500-507, 2003.

STEADY STATE SOLUTION FOR DYNAMICS OF A NONIDEAL CRANK-SLIDER MECHANISM WITH AN ACTIVE MASS DAMPER (AMD)

Julijana Simonović[1], Nikola D. Nešić[2], José Manoel Balthazar[3], Maurício Aparecido Ribeiro[4] and Jorge Luis Palacios Felix[5]

[1] Faculty of Mechanical Engineering University of Niš, A. Medvedeva 14, 18104 Niš, Serbia
e-mail: julijana.simonovic@masfak.ni.ac.rs
[2] Faculty of Technical Sciences, University of Priština in Kosovka Mitrovica, Knjaza Miloša 7, 38220 Kosovska Mitrovica, Serbia
e-mail: nikola.nesic@pr.ac.rs
[3] Universidade Tecnológica Federal do Paraná- Campus Ponta Grossa, Ponta Grossa, PR, Brasil, Faculdade de Engenharia de Bauru - FEB/UNESP, Bauru, São Paulo. Brazil
e-mail: jmbaltha@gmail.com
[4] Universidade Tecnológica Federal do Paraná- Campus Ponta Grossa, Ponta Grossa, PR, Brasil
e-mail:mau.ap.ribeiro@gmail.com
[5]Universidade Federal da Fronteira Sul, UFFS, Cerro Largo, Rio Grande do Sul
e-mail: jorge.felix@uffs.edu.br

Abstract

Active mass dampers (AMD) are devices used to control the vibration of structures and machines. Their application in engineering practice increases. The base of the portal frame is excited with a non-ideal motor and the vibrations of the structure are controlled with an AMD cart located at the top of it. This system is mathematically modelled and equations of motion are derived using Lagrange equations of the second kind. Nondimensioned equations of motion are solved by using the perturbation method of multiple time scales and periodic steady-state solutions are explicitly obtained.

Keywords: active mass damper, steady-state, multiple time scales.

1. Introduction

The idea of controlling dynamics and energy harvesting of systems by using AMD and auto-parametric vibration absorbers has been already presented, explored and exploited in engineering practice [1, 2]. Our model consists of a base portal frame that is excited with a non-ideal motor. The vibration of the structure is controlled by the cart located at the top of the frame, Fig. 1. This system is mathematically modeled and equations of motion derived using Lagrange equations of the second kind. Nondimensioned equations of motion are solved by using perturbation method of multiple time scales and periodic steady state solutions are explicitly obtained. The model of an attached damped oscillator with a damped spring pendulum is presented and solved with the same method as in [1].

2. Mathematical modeling

We analyzed full interaction between mechanical and electrical field quantities of the vibration system presented in Fig. 1. The crank-slider mechanism is coupled via rod to the support of a Portal Frame with an Active Mass Damper (AMD). When the electromotor shaft and crank r rotates through an angle φ, the suspension shows a displacement $x_b = r\cos\varphi$.

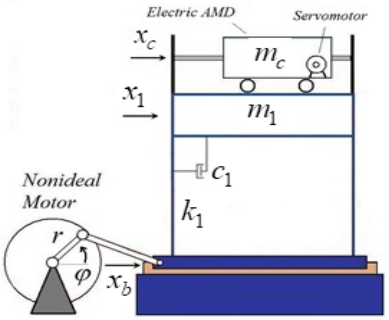

Fig. 1. *Portal Frame with (AMD) on top and non-ideal base excitation.*

The governing equations of motion are derived using Lagrangian formulation $L = T\text{-}V$, where potential energy is $V=1/2\ k_1 x_1^2$ and kinetic energy:

$$T = \frac{1}{2}m_c(\dot{x}_c + \dot{x}_1 - r\dot{\varphi}\sin\varphi)^2 + \frac{1}{2}\frac{J_m k_g^2 \dot{x}_c^2}{r_{mp}^2} + \frac{1}{2}m_1\left(\dot{x}_1 - r\dot{\varphi}\sin\varphi\right)^2 + \frac{1}{2}I\dot{\varphi}^2 \tag{1}$$

By including generalized forces for each of three independent variables and using Lagrange's equations of the second kind, we obtain the system of second order differential equations:

$$\begin{bmatrix} a_c & m_c & -m_c r\sin\varphi \\ m_c & m_c + m_1 & -(m_c+m_1)r\sin\varphi \\ -m_c r\sin\varphi & -(m_c+m_1)r\sin\varphi & I_m \end{bmatrix}\begin{bmatrix} \ddot{x}_c \\ \ddot{x}_1 \\ \ddot{\varphi} \end{bmatrix} = \begin{bmatrix} m_c r\dot{\varphi}^2\cos\varphi - c_{AMD}\dot{x}_c \\ (m_c+m_1)r\dot{\varphi}^2\cos\varphi - k_1 x_1 - c_1\dot{x}_1 \\ -(m_c+m_1)r^2\dot{\varphi}^2\cos\varphi\sin\varphi + \rho - \gamma\dot{\varphi} \end{bmatrix} \tag{2}$$

This system can be easily transformed in 6 state space differential equations of the first order which could be later easily manipulated for designing control system.

After nondimensionalisation in Eq. (2) and using Taylor expansion of trigonometric terms by keeping only two terms in it, the equations of motion become:

$$\begin{aligned} &\ddot{X}_c + \alpha_c\dot{X}_c + \beta_c X_1 - \beta_a\left(\varphi - \tfrac{\varphi^3}{6}\right)\ddot{\varphi} - \beta_a\left(1 - \tfrac{\varphi^2}{2}\right)\dot{\varphi}^2 = 0 \\ &\ddot{X}_1 + \alpha_1\dot{X}_1 + X_1 + \beta_c\ddot{X}_c - \left(\varphi - \tfrac{\varphi^3}{6}\right)\ddot{\varphi} - \left(1 - \tfrac{\varphi^2}{2}\right)\dot{\varphi}^2 = 0 \\ &\ddot{\varphi} + \alpha_2\dot{\varphi} + \delta_1\left(\varphi - \tfrac{2\varphi^3}{3}\right)\dot{\varphi}^2 - \delta_2\left(\varphi - \tfrac{\varphi^3}{6}\right)\ddot{X}_c - \delta_1\left(\varphi - \tfrac{\varphi^3}{6}\right)\ddot{X}_1 - s = 0 \end{aligned} \tag{3}$$

Multiple time scales method is applied to Eq. (3). Three-time scales are introduced with $\tau_n = \varepsilon^n t$ where $n = 0,1,2$ and ε being small book-keeping parameter. Following rescaling of parameters is made: $\beta_a = \varepsilon\tilde{\beta}_a,\ \beta_c = \varepsilon\tilde{\beta}_c,\ \alpha_c = \varepsilon^2\tilde{\alpha}_c,\ \alpha_i = \varepsilon^2\tilde{\alpha}_i,\ \delta_i = \varepsilon\tilde{\delta}_i,\ (i = 1,2)$. First three approximations are obtained using method of multiple time scales.

3. Conclusions

This paper system deals with modeling electromechanical interaction of an active vibration suppression system. Using multiple scales method periodic steady state solutions are obtained for three independent coordinates. The analysis of key role parameters of the steady-state solution gives us insight into the AMD system controlling possibilities.

Acknowledgement: This research was financially supported by the Ministry of Science, Technological Development and Innovation of the Republic of Serbia (Contract No. 451-03-47/2023-01/ 200109).

References:

[1] He, Ji-Huan, et al., *Stability of three degrees-of-freedom auto-parametric system*, Alexandria Engineering Journal, Vol. 61(11), 8393-8415, 2022.
[2] Felix J.L.P., et al., *On vibration mitigation and energy harvesting of a nonideal system with autoparametric vibration absorber system*, Meccanica 53 (13), 3177–3188, 2018.

DESIGN AND OPTIMIZATION OF SPLITTER BLADE OF RETURN CHANNEL FOR THE IMPROVEMENT OF PUMP TURBINE PERFORMANCE

Geyuan Tai[1], Wenjie Wang[1], Ji Pei[1], Giorgio Pavesi[2] and Shouqi Yuan[1]

[1] National Research Center of Pumps, Jiangsu University, 301 Xuefu Road 212013, Zhenjiang, Jiangsu, China
e-mail: taigeyuan@qq.com, wenjiewang@ujs.edu.cn, jpei@ujs.edu.cn, shouqiy@ujs.edu.cn
[2] Department Industrial Engineering, University of Padova, Via Venezia 1 35131, Padova, Italy
e-mail: giorgio.pavesi@unipd.it

Abstract

With the rapid development of industrialization and sharply increasing demand for electricity, pumped storage units are developing towards high head and large capacity. The two-stage pump-turbine cannot only meet the current power demand, but it also has the advantages of low investment cost and stable operation. Therefore, it has great development potential. However, at present, when the unit operates under low flow rate condition, there are usually some terrible phenomena such as rotor-stator interaction in the vaneless space, and severe backflow in the interference region of guide vane and return channel. These phenomena cause serious reduction of efficiency and high amplitude pressure pulsation in the unit. In order to improve these phenomena, an optimal design of the splitter blade for the U-shaped return channel has been carried out. The purpose is to enhance the operating efficiency of the unit under low flow rate condition without losing the efficiency under other operating conditions, and to suppress high amplitude pressure fluctuation in the vaneless space and the interference region of guide vane and return channel.

According to the structural characteristics of the U-shaped return channel, this paper selects the distance al from the leading edge of the splitter blade to the inlet of the return channel, the distance at from the trailing edge of the splitter blade to the outlet of the return channel, the offset distance offset from the splitter blade to the prototype blade, and the number of blades n as the design parameters. Based on the orthogonal experimental design method, this paper selects the orthogonal table of five factors and four levels to design splitter blade of return channel. Further, the numerical calculation method is used to simulate the transient process when the units operate under 0.6Qd, 1.0Qd and 1.1Qd conditions, and the optimal splitter blade model is selected from 16 schemes in combination with direct vision analysis, range analysis, internal flow analysis and pressure fluctuation time-frequency analysis. And the Savitzky-Golay and Wavelet Transform methods are used to complete the time and frequency domain analysis of pressure fluctuation.

When the unit is in low flow rate condition, at the vaneless space, the main components of pressure pulsation include BPF (the blade passing frequency) and the low-frequency below BPF. At the V01 monitoring point in the vaneless space, the pressure amplitude at BPF of the original scheme is as high as 3.2kPa, and the pressure at low-frequency fluctuates violently. However, when the unit adopts the splitter blade design schemes, the pressure pulsation signal at BPF is significantly weakened, especially when the scheme 1 is adopted, the maximum value of the

pressure amplitude at BPF is reduced by 60%. However, at the monitoring point V03 in the vaneless space, the pressure amplitude of the splitter blade schemes and the prototype scheme are both very high and the main frequency amplitude is virtually identical. Under the design flow rate condition, the main frequency of pressure pulsation in the vaneless space is BPF. And the splitter blade significantly reduces the pressure amplitude at BPF of the V01 monitoring point, but has little effect on the pressure pulsation of the V03 monitoring point. And the unit under large flow rate condition also shows similar unsteady characteristics.

The main frequency amplitude analysis of the monitoring points in a whole flow channel shows that, when the unit adopts scheme 1, under low flow rate condition, the total dominant frequency amplitude of four monitoring points in the vaneless space decreased by 1.2 kPa, while it increased by 0.8 kPa in the interference region of guide vane and return channel. Under the design flow rate condition, the total dominant frequency amplitude in the two regions decreased by 0.8 kPa and 1.7 kPa respectively. Under high flow rate condition, the total amplitude of pressure fluctuation increased by 0.3 kPa in the vaneless space and decreased by 0.5 kPa in the interference region of guide vane and return channel.

1) The splitter blade can inhibit the pressure pulsation at V01, but has no significant effect on the pressure pulsation signal at the V03 monitoring point. It shows that the long blade can effectively reduce the pressure pulsation caused by rotor-stator interaction in the vaneless space, while the short blade has little control effect on the pressure pulsation in this area.

2) The splitter blades can improve the rotor-stator interference phenomena in the unit, but are basically unable to control the unstable flow in the vaneless space and the interference region of guide vane and return channel. This is mainly caused by the shorter length of the short blade, the larger space between the guide vane and the return channel, and the weakening control effect of the splitter blade on the streamline under low flow rate condition.

3) The scheme 1 is selected as the optimal model in this paper. This model can improve the unit efficiency by nearly 3% under low flow rate condition without losing the unit efficiency under other conditions, and effectively suppress the high amplitude pressure pulsation caused by the rotor-stator interference in the vaneless space and the interference region of guide vane and return channel.

Keywords: pump turbine, splitter blade of return channel, optimization, pressure fluctuation.

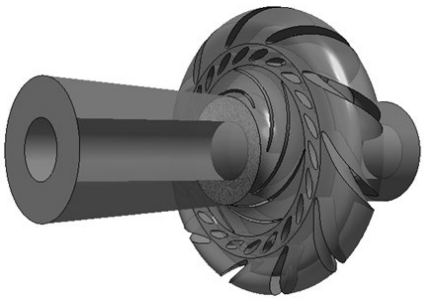

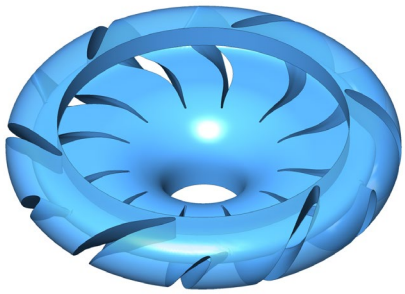

Fig 1. Computational domain of pump turbine Fig 2. Return channel with splitter blade

References:

[1] Yang J, Pavesi G, Yuan S, et al. Experimental characterization of a pump–turbine in pump mode at hump instability region[J]. *Journal of Fluids Engineering*, 2015, 137(5).

[2] Wang W, Tai G, Pei J, et al. Numerical investigation of the effect of the closure law of wicket gates on the transient characteristics of pump-turbine in pump mode[J]. *Renewable Energy*, 2022, 194: 719-733.
[3] Zuo Z, Liu S, Sun Y, et al. Pressure fluctuations in the vaneless space of High-head pump-turbines—A review[J]. *Renewable and Sustainable Energy Reviews*, 2015, 41: 965-974.

AN OVERVIEW: ON NONLINEAR DIFFERENTIAL EQUATIONS AND INTEGRALS OF THE DYNAMICS OF BALL ROLLING ALONG CURVED LINES AND SURFACES

Katica R. (Stevanović) Hedrih[1,2]

[1] Mathematical Institute of Serbian Academy of Sciences and Arts, Belgrade, Serbia
e-mail: katicah@mi.sanu.ac.rs,khedrih@sbb.rs
[2] Faculty of Mechanical Engineering, University of Niš, Niš, Serbia
e-mail: katicahedrih@gmail.com

Abstract

The introduction part of the short lecture presents the basic contents of two doctorates on ball rolling, defended at the beginning of the last century and in the last millennium, at the University of Belgrade. In the main part of this communication, first, a brief overview of the author's previous results is indicated, and then the latest, not yet published, scientific results of the investigation of the rolling, without sliding, of a heavy ball on a stationary circle/sphere from the outside or from the inside are shown, while it is in permanent contact, without sliding, with the moving concentric cicle/sphere from the inside, that is, from the outside. The nonlinear differential equations and integrals of the dynamics of ball rolling along curved lines and surfaces with corresponding Phase trajectory portraits are presented.

Keywords: two doctoral dissertation, rolling ball without slipping, contact points, angular velocities, nonlinear differential equations, cyclic integral.

1. Introduction as a preliminary

At the beginning of the last century and in the last millennium, at the University of Belgrade two doctorates on ball rolling were defended. The topic of the first doctorate was "Rolling without sliding of a gyroscopic ball on a sphere" [4] and was defended in 1924. The author of this doctoral dissertation is Vasilij Demchenko [4]. The topic of the second doctorate is "Rolling of a heavy, rigid ball on an elastic surface" [5], and the doctorate was defended in 1932. The author of this doctoral dissertation is Konstantin Voronec [5], who was later the founder of the Department of Fluid Mechanics at the Faculty of Mechanical Engineering in Belgrade, as well as the first head of the Department of Mechanics of the Mathematical Institute of the Serbian Academy of Sciences and Arts.

The composition of both commissions included the same members, prominent academicians of the Serbian Academy of Sciences and Arts, and individually, famous Serbian scientists: Antin Bilimonič, Mihailo Petrović and Milutin Milanković.

2. The latest scientific results of the dynamics of rolling, without slipping, a heavy ball/disk on a stationary circle/sphere, in which it is in constant contact, without sliding, with a moving circle/sphere

An overview of the author's results of the investigation of the rolling of a heavy ball along stationary and rotating curvilinear trajectories is given and points out the phenomena of bifurcations and triggers of coupled singularities with the presentation of a series of phase portraits [2, 3] . There were also performed nonlinear differential equations of the dynamics of the rolling of a heavy ball on curved surfaces and it was shown that, when dealing with revolving surfaces, there is always one cyclic integral [1].

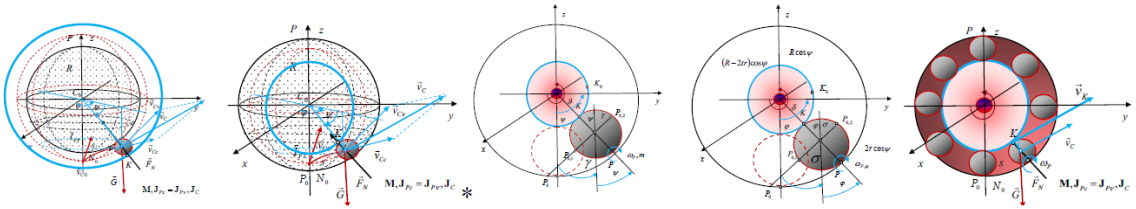

Figure 1. Geometric and kinetic elements of several rolling models, no-slip, heavy ball/disc on circle/sphere inside/outside and in contact, no-slip, on circle/sphere outside/inside

Analytical expressions of kinetic elements, such as angular velocities of rolling and rotation of the dynamics of the system elements with rolling, without sliding of the heavy ball/disc on the stationary circle/sphere outside/inside and in contact with the moving circle/sphere inside/outside, were derived, as well as nonlinear differential equations and their integrals (see Figure 1).

3. Concluding considerations

The rolling of a heavy ball on curvilinear paths and curved surfaces [1-6] is a dynamic system, which is a very attractive task for serious and talent researchers.

References:

[1] Hedrih (Stevanovic) K. R. (2019) *Rolling heavy ball over the sphere in real Rn3 space*. Nonlinear Dynamics, (2019) 97:63–82, https://doi.org/10.1007/s11071-019-04947-1.

[2] Hedrih (Stevanovic) K., Non-linear phenomena in vibro-impact dynamics: Central collision and energy jumps between two rolling bodies. Dedicated to memory of Professor and important scientist Ali Nayfeh (December 21, 1933-March 27, 2017). Nonlinear Dynamics, February 2018, Volume 91, Issue 3, pp 1885–1907. DOI :10.1007/s11071-017-3988-x. https://link.springer.com/article/10.1007/s11071-017-3988-x\

[3] Hedrih (Stevanovic) K., The Latest Theory of Body Collisions in Rolling and the Dynamics of Vibro-Impact Systems through Scientific Projects over Three Decades, Special Issue, Guest Editor: Katica R. (Stevanović) Hedrih, Mathematical Institute SASA, Belgrade, NON-PERIODICAL ISSUES – PROCEEDINGS of Mathematical Institute SASA, Belgrade [Collection of Papers], Zbornik radova 19 (27), 2022, pp. 75-160, Series of thematic collection of papers that is published occasionally, Belgrade, ttp://elib.mi.sanu.ac.rs/files/journals/zr/27/zrn27p75-160.pdf

[4] Dem?3nko, V., *Kotrljanje bez klizanja giroskopske lopte po sferi (Rolling without slipping a gyroscopic ball on a sphere)*, doktorska disertacija, odbranjena pred Komisijom u sastavu (doctoral dissertation defended before the Commission composed of: A. Bilimović, M. Petrović, M. Milanković; University of Belgrade, Novem. 15, 1923, pp. 1-94. http://www.m-hikari.com/atam/atam2017/atam1-2017/index.html..

[5] Voronec K., *Rolling of a solid body on an elastic surface*, doctoral dissertation, October 9, 1930, 1932, Faculty of Philosophy in Belgrade, Commission Anton Bilimović, Milutin Milanković and Mihailo Petrović; the dissertation is in the Fund of the SANU Library and is kept within the Legacy - Special Library of Academician ANTON BILIMOVĆ (1879–1970) - PB 13, signature PB 13; 221..

9th International Congress of the Serbian Society of Mechanics
July 5-7, 2023, Vrnjačka Banja, Serbia

A SIS MODEL WITH A SATURATED INCIDENCE RATE

Marcin Choiński

Institute of Information Technology, Warsaw University of Life Sciences, Str. Nowoursynowska 159, building 34, 02-776 Warsaw, Poland

Abstract

The paper introduces a continuous epidemic model in which an illness transmission function with a saturated incidence rate will be considered. This function is based on the approach presented in [3]. This model is classified as a SIS (*susceptible-infected-susceptible*) type one. The variables are densities of healthy (susceptible) people and infected ones. Basic properties of the system will be presented, including the value of the basic reproduction number and the existence of stationary states appearing in the system. Further local stability of the stationary states will be discussed. It will also be shown that global stability of the system is reached. Later, a discrete version of the analyzed system will be presented. As a discretization method, the strictly positive scheme is chosen. Due to this kind of discretization, positivity of the variables is preserved, what is necessary from the biological point of view. In the analysis of the discrete system, the main results concern local stability of the stationary states. Theoretical results will be complemented with numerical simulations. Results from this paper constitute a continuation of the work presented in [1] and [2].

Keywords: SIS model, local and global stability, discretization.

1. Introduction of a model

We introduce a continuous model of epidemic dynamics which is analyzed in the paper. We assume that a homogeneous population consists of two groups: susceptible (S) and infected people (I). In order to express a term reflecting illness transmission, we used a modified mass–action law with a saturated incidence rate. This approach is applied in [3]. The analyzed system has the form:

$$S' = C - \beta S\frac{I}{1+\varepsilon I} + \gamma I - \mu S,$$
$$I' = \beta S\frac{I}{1+\varepsilon I} - (\gamma + \alpha + \mu)I,$$

where C stands for a constant inflow into the population, β reflects illness transmission, γ stands for a recovery, μ and α are accordingly a natural death and a disease-related death rate. A coefficient ε reflects the crowding effect of the infective individuals [4] – if a number of the

infected people is increasing, then susceptible individuals are trying to avoid the infected ones. Every parameter is positive and fixed. A case when ε=0 was analyzed in [1].

In order to reduce a number of parameters appearing in the system, we make a scaling as it was shown in [1]. We obtain a model:

$$x' = C - x\frac{y}{1+\varepsilon y} + y - \mu x,$$

$$y' = x\frac{y}{1+\varepsilon y} - k y,$$

where k=1+μ+α.

2. Stationary states

The scaled system has two stationary states:

a) a disease–free one $E_0 := \left(\frac{C}{\mu}, 0\right)$ – always existing;

b) an endemic one $E_e := \left(\frac{(C\varepsilon+\alpha+\mu)k}{\alpha+\mu+k\varepsilon\mu}, \frac{C-k\mu}{\alpha+\mu+k\varepsilon\mu}\right)$ – existing if $C > k\mu$.

After the analysis of stability of stationary states, we formulate two theorems:

Theorem: *If E_e does not exist, then E_0 is locally stable. If E_e exists, then it is locally stable and E_0 loses its stability.*

Theorem: *If E_e does not exist, then E_0 is globally stable in R^2_+. If E_e exists, then it is globally stable in R^2_+.*

3. Conclusions

The obtained results related to the stability of the stationary states are the same as those for the model from [1] where ε=0. Hence, in the context of stability it is not needed to consider the saturated incidence rate in the proposed *SIS* model. However, from the epidemiological point, we are often not interested in the asymptotic behavior of the model, but we investigate how the epidemic dynamic is in a determined period. In this approach, the difference between the model presented in this paper and the model from [1] can be significant because of the form of the transmission function – see that the case when ε=0 yields a transmission function which is bilinear.

References:

[1] Bodzioch M., Choiński M., Foryś U., *SIS Criss-Cross Model of Tuberculosis in Heterogeneous Population*, Discrete and Continuous Dynamical Systems - Series B, Vol. 24 (5), 2169–2188, 2019.

[2] Choiński M., Bodzioch M., Foryś U., *A Non-standard Discretized SIS Model of Epidemics,* Mathematical Biosciences and Engineering, Vol. 19 (1), 115–133, 2022.

[3] Suryanto P., *A Dynamically Consistent Nonstandard Numerical Scheme for Epidemic Model with Saturated Incidence Rate*, International Journal of Mathematics and Computation, Vol. 13 (D11), 112–123, 2011.

[4] Xiao D, Ruan S. *Global analysis of an epidemic model with nonmonotone incidence rate)=, incidenrrrraterate*, Mathematical Biosciences, 208, 419–429, 2007.

MODELING OF PENETRATION DEPTH OF A SHAPED CHARGE JET

Predrag M. Elek, Miloš D. Marković, Dejan T. Jevtić and Radovan V. Đurović

Weapon Systems Department, Faculty of Mechanical Engineering University of Belgrade, 16 Kraljice Marije Street, 11120 Belgrade 35
e-mail: pelek@mas.bg.ac.rs, mdmarkovic@mas.bg.ac.rs, djevtic@mas.bg.ac.rs, rdjurovic@mas.bg.ac.rs

Abstract

The shaped charge effect is currently the most powerful target penetration mechanism. It relies on the conversion of explosive charge detonation energy into kinetic energy of a hypervelocity metal penetrator, known as a jet. The first stage of the shaped charge mechanism is the formation of a jet through processes of detonation wave propagation and interaction with a metal liner which accelerates and collapses towards the symmetry axis creating the slug and the jet. Our focus in the present research is on the second stage of the process: the jet interaction with the target material and consequent target penetration/perforation.

There are many approaches to the modeling of shaped charge jet penetration depth into target material. Two major analytical models are: the simple density law and the model with variable jet velocity. However, the most accurate is the approach based on numerical simulations using so-called hydrocodes. Modeling and simulation in Abaqus/Explicit software is presented in detail. The complete process of jet formation and penetration is simulated using the Eulerian approach.

Comprehensive comparison between results obtained using various theoretical models (analytical and numerical) and experimental data has been performed providing useful insights and conclusions.

Keywords: shaped charge, detonation wave, jet penetration, penetration depth, numerical simulation.

References:

[1] Walters WP and Zukas JA, *Fundamentals of shaped charges*, Wiley-Interscience, New York, 1989.
[2] Micković D, Jaramaz S, Elek P, Miloradović N, Jaramaz D. *A Model for Explosive Reactive Armor Interaction with Shaped Charge Jet*, Propellants, Explosives, Pyrotechnics, Vol. 41, No. 1, pp. 53-61, 2016.
[3] Micković D, Jaramaz S, Elek P, Jaramaz D, Micković D: *A model for shaped charge warhead design*, Strojniški vestnik – Journal of Mechanical Engineering, Vol. 58, No. 6, pp. 404-411, 2012.
[4] Ugrčić M, Ugrčić D. *FEM techniques in shaped charge simulation*, Scientific Technical Review, Vol. 59, No. 1, pp. 26-34, 2009.

EFFECT OF SMOOTH MUSCLE ACTIVATION IN THE STATIC AND DYNAMIC MECHANICAL CHARACTERIZATION OF HUMAN AORTAS

Marco Amabili[1], Ivan Breslavsky[1], Francesco Giovanniello[1], Giulio Franchini[1], Ali Kassab[2], Gerhard Holzapfel[3]

[1] Department of Mechanical Engineering, McGill University, Montreal, Canada
e-mail: marco.amabili@mcgill.ca
[2] Research Center, Centre Hospitalier Universitaire de Montréal (CHUM), Université de Montréal, Montreal, Canada
[3] Research Institute of Biomechanics, Graz University of Technology, Austria

Abstract

The rupture of aortic aneurysms causes around 10,000 deaths each year in the USA. Prosthetic tubes for aortic repair present a large mismatch of mechanical properties with the natural aorta, which has negative consequences for perfusion. This motivates research into the mechanical characterization of human aortas to develop a new generation of mechanically compatible aortic grafts.

Experimental data and a suitable material model for human aortas with smooth muscle activation are not available in the literature despite the need for developing advanced grafts; the present study closes this gap. Mechanical characterization of human descending thoracic aortas was performed with and without vascular smooth muscle (VSM) activation. Specimens were taken from 13 heart-beating donors. The aortic segments were cooled in Belzer UW solution during transport and tested within a few hours after explantation. VSM activation was achieved through the use of potassium depolarization and noradrenaline as vasoactive agents. In addition to isometric activation experiments, the quasi-static passive and active stress-strain curves were obtained for circumferential and longitudinal strips of the aortic material. This characterization made it possible to create an original mechanical model of the active aortic material that accurately fits the experimental data. The dynamic mechanical characterization was executed using cyclic strain at different frequencies of physiological interest. An initial pre-stretch, which corresponded to the physiological conditions, was applied before cyclic loading. Dynamic tests made it possible to identify the differences in the viscoelastic behavior of the passive and active tissue. This work illustrates the importance of VSM activation for the static and dynamic mechanical response of human aortas. Most importantly, this study provides material data and a material model for the development of a future generation of active aortic grafts that mimic natural behavior and help regulate blood pressure. The regulation of the vascular tone (i.e. the level of VSM contraction) also plays a key role in hypertension and its treatment. Therefore, the relationship between VSM activation and arterial mechanical properties is also relevant to address hypertension.

PLANE MOTION OF A BODY RESTING ON ONE CYLINDRICAL HINGE AND ONE SLIDING ELASTIC SUPPORT RESTING ON A ROUGH PLANE

Marat Z. Dosaev and Vitaly A. Samsonov

[1] Institute of Mechanics, Lomonosov Moscow State University, Michurinskiy pr-t, 1, 119192 Moscow, Russia
e-mail: dosayev@imec.msu.ru

Abstract

To prevent severe damage in seismically hazardous areas, various sliding joints are added to building structures, such as slipping attachments. A heavy flat body based on a cylindrical hinge and a homogeneous heavy rod is considered as a model of such a design. The rod slides without friction along a guide rigidly connected to the body, while at one end this rod rests on a rough plane, and at the other end it is connected to the body by means of an elastic spring. The presence of dry friction gives the system the properties of a variable structure problem.

The motion of the mechanical system near the vertical equilibrium position is considered. The interaction of an elastic force with dry friction leads to oscillations, which occur qualitatively differently in different regions of the phase plane. The influence of dry friction leads to the formation of an infinite number of damped oscillations performed by the system in an infinite time.

Keywords: slipping attachment, elastic spring, dry friction, variable structure dynamic system.

1. Introduction

In construction practice, often to prevent the destruction of buildings in the event of earthquakes, additional mobility is introduced into structures. For example, slipping attachments are used. The study of the behavior of such structures is of particular interest for recent theoretical and applied research (for example, [1, 2]).

2. Method

Let us consider the problem of motion along a horizontal rough plane of a heavy rectangular (for simplicity) flat body $ABCD$ ($AB = 2a$, $AD = 2b$) of mass m with center of mass G, supported by a weightless rod AA_1 ($AA_1 = l$) rigidly connected to it, on a cylindrical hinge A_1 and on a homogeneous rod B_1B_2 of mass m_1, length l_2 and center mass G_1(Fig.1). The rod B_1B_2 slides without friction along the guide parallel support AA_1, which is rigidly connected to the body. At the same time, at one end, this rod rests on a rough plane, and at the other end it is connected to the body by means of an elastic spring of stiffness k. For definiteness, we assume that the system is in equilibrium with the vertical position of the supports.

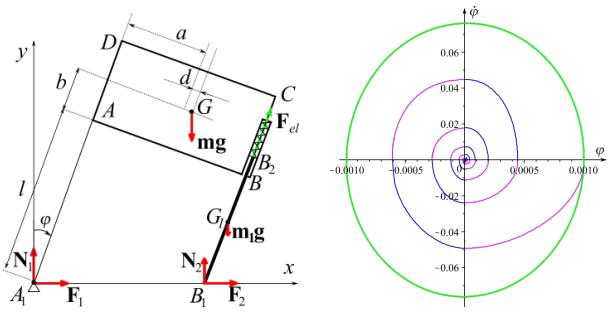

a b

Fig. 1. A planar body on one joint and one elastic support: a) The problem statement; b) Trajectories of damped oscillations on the phase plane.

Let us write the equation for the change in the angular momentum of the system, neglecting the mass m_1 of the supporting rod:

$$J\ddot{\varphi} = gm((l+b)\sin\varphi + (a+d)\cos\varphi) - \frac{(mg(a+d)/a + 4ak\sin\varphi/\cos\varphi)a}{(\cos\varphi - \mu signum(\dot{\varphi}\sin\varphi)\sin\varphi)\cos\varphi} \qquad (1)$$

The equation of motion (1) was numerically integrated for a certain set of parameters. The value of the friction coefficient μ varied over a wide range. The trajectories of motion from the state of rest are calculated, slightly deviating the system from the equilibrium position. Figure 2 shows the calculation of body oscillations for $\mu \gg 1$ (blue and pink curves) and for $\mu = 0$ (green curve).

3. Conclusions

In the absence of friction, the trajectory of motion on the phase plane is an ellipse traditional for an elastic system. Trajectories for non-zero values of the friction coefficient are pieces of different ellipses. Equation (2) retains an integral of the energy integral type on each of these segments. In this case, two regions are distinguished on the phase plane, in which the trajectories behave qualitatively differently. In the region $\varphi\dot{\varphi} < 0$, the system has less stiffness than in the region $\varphi\dot{\varphi} > 0$. Stiffness jumps lead to the fact that the trajectories gradually approach the origin of coordinates. In other words, the variability of the structure of a dynamical system leads to the fact that different trajectories are obtained in different areas of the phase plane, which together form a converging spiral. Thus, in this problem, the influence of dry friction leads to the formation of an infinite number of damped oscillations performed by the system in an infinite time.

The work was supported by the Russian Science Foundation No. 22-21-00303.

References:

[1] Zhao J., et al, *Sliding corner gusset connections in concentrically braced frames using BRBs: Numerical analysis and practical design,* Engineering Structures, Vol. 246, 113055, 2021. https://doi.org/10.1016/j.engstruct.2021.113055.

[2] Atashfaraz B, Taiyari F, Hayati Raad H., Formisano A. *Efficiency investigation of hybrid sliding rocking columns as elevated reservoirs supporting systems*, Soil Dynamics and Earthquake Engineering, Vol. 136, 106222, 2020. https://doi.org/10.1016/j.soildyn.2020.106222.

THE INFLUENCE OF MAGNUS FORCE ON TURBULENT PARTICLE-LADEN FLOWS IN HORIZONTAL NARROW CHANNEL

Darko Radenković[1] and Milan Lečić[1]

[1] Faculty of Mechanical Engineering, University of Belgrade, Kraljice Marije 16, 11120 Belgrade 35
e-mail: dradenkovic@mas.bg.ac.rs, mlecic@mas.bg.ac.rs

Abstract

The Pneumatic conveying of solid particles has great practical importance. However, due to the presence of gas and solid phase and wall confinement, the investigations of these flows have been presenting great challenges for researchers for a long time.

In pneumatic conveying of solid particles, with an increase in particle angular velocity due to the particle-wall collision, there is an increasing effect of Magnus force. The effect of such force in numerical simulations of such flows is often neglected. However, is it justified to neglect this force in numerical simulations of that flow configuration?

To answer this question, Euler-Lagrange simulations of pneumatic conveying in a narrow horizontal channel are performed using OpenFOAM. The length of the channel is 6m, height is 35 mm, and width is 350 mm. The bulk air velocity is 20 m/s and the flow is turbulent with a Reynolds number of around 40000. Numerical simulations are conducted for glass particles of diameter 130 micrometers.

It has been shown in [1] that wall roughness can influence significantly particle-laden flows in horizontal channels, by amplification of particle wall-normal velocity, causing a more uniform particle distribution over the channel cross section. Therefore, the effect of wall roughness in the present numerical simulations is taken into account according to [2]. A model for turbulence of the continuous phase is k-epsilon. The particle equation of motion includes drag force, gravity, and the effect of Magnus force is analyzed. The influence of 1-way and 2-way coupling between air and solid phase has also been analyzed. To account for the rotation of spherical particles, Newton's second law is used, with torque acting on spherical particles calculated according to [3]. The Magnus force along with 2-way coupling reduces fluid velocity in the lower half of the channel, while in the upper half of the channel air velocity is increased, in comparison to pure fluid flow (Fig. 1). On the other hand, Magnus force with 2-way coupling reduces particle velocity in the lower half of the channel (Fig. 2) in comparison to calculations without Magnus force. Fig. 3 shows a drastic effect of Magnus force on particle concentration profiles, causing flow of a significant number of particles in the bottom half of the channel. It is expected that inter-particle collisions redistribute particle momentum, causing a more uniform particle distribution over the channel cross section.

Keywords: particle-laden flows, wall roughness, inter-particle collisions, Magnus force, Euler-Lagrange simulations.

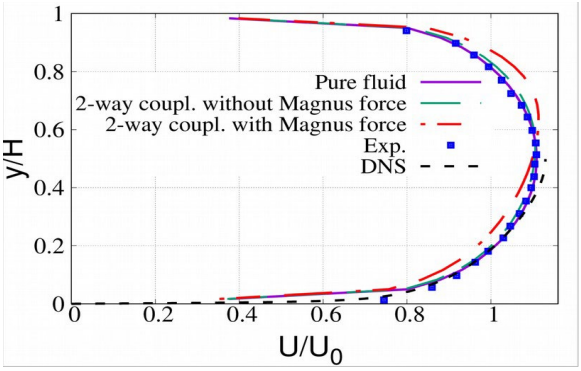

Fig. 1. Nondimensional fluid velocity profiles across channel height. Experiment is from [1] and DNS from [4].

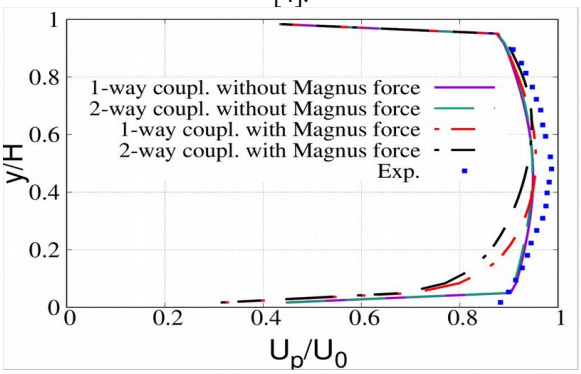

Fig. 2. Nondimensional particle velocity profiles across channel height.

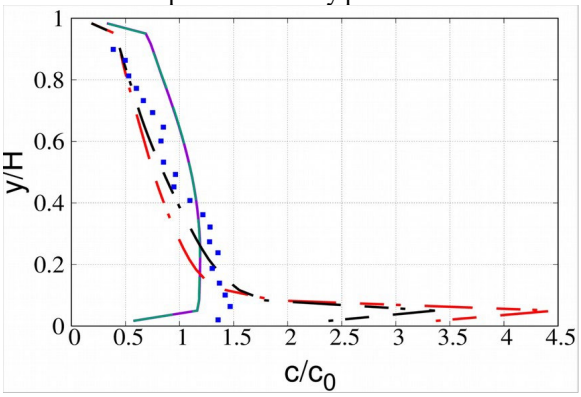

Fig. 3. Nondimensional particle concentration profiles across channel height. Legend is the same as in Fig. 2.

References:

[1] Laín S., Sommerfeld M., Euler/Lagrange computations of pneumatic conveying in a horizontal channel with different wall roughness, Powder Technology, Vol. 184, 76-78, 2008.

[2] Radenkovic D., Simonin O., Modelling of three-dimensional particle rebound from an anisotropic rough wall, Powder Technology, Vol. 393, 165-183, 2021.

[3] Rubinow, S.I., Keller, J.B, The transverse force on a spnning sphere moving in a viscous fluid, J. Fluid Mech., Vol 11, 447-459, 1961.

[4] M. Lee and R. D. Moser, Direct numerical simulation of turbulent channel flow up to Reτ= 5200," Journal of Fluid Mechanics, Vol. 774, 395–415, 2015.

ANALYTICAL AND NUMERICAL ANALYSIS OF COMPRESSIBLE ISOTHERMAL FLOW BETWEEN PARALLEL PLATES

Petar V. Vulićević, Snežana S. Milićev and Nevena D. Stevanović

[1]Faculty of Mechanical Engineering, University of Belgrade, Kraljice Marije 16, 11120 Belgrade 35
e-mail: petar.vulicevic@protonmail.com, smilicev@mas.bg.ac.rs, nstevanovic@mas.bg.ac.rs

Abstract

Analytical solutions of Navier-Stokes equations exist only in special cases, one of them is the flow between parallel plates. In order to solve these equations analytically, we need to reduce them by ruling out unnecessary terms. The flow between parallel plates is an idealized case, as the plates are of infinite width. Therefore, there are no changes of variables in the z direction, $\frac{\partial()}{\partial z}=0$, and velocity component $w=0$. The pressure difference due to body forces can be neglected, so the y component of velocity is $v=0$. The flow is steady, $\frac{\partial()}{\partial t}=0$, and since compressibility effects cannot be neglected, the ideal gas equation of state is included, $p=\rho RT$. After these simplifications [1], the continuity equation and projections of Navier-Stokes equations take the following form:

$$\frac{\partial \rho u}{\partial x}=0 \Rightarrow \rho u=f(x), \tag{1}$$

$$\begin{aligned} x:&\quad u\frac{\partial u}{\partial x}=-\frac{1}{\rho}\frac{\partial p}{\partial x}+v\left(\frac{\partial^2 u}{\partial x^2}+\frac{\partial^2 u}{\partial y^2}\right)+\frac{1}{3}v\frac{\partial^2 u}{\partial x^2},\\ y:&\quad \frac{1}{\rho}\frac{\partial p}{\partial y}=\frac{1}{3}v\frac{\partial^2 u}{\partial y\partial x}. \end{aligned} \tag{2}$$

To further simplify the Navier-Stokes equations, it is necessary to transform it into a non-dimensional form by dividing dimensional variables with corresponding reference values: $\tilde{u}=u/u_r,\ \tilde{x}=x/l,\ \tilde{y}=y/h,\ \tilde{p}=p/p_r,\ \tilde{\rho}=\rho/\rho_r$, where index r stands for reference values at the outlet cross section. Now, the projections of the non-dimensional Navier-Stokes equations in streamwise (x) and crosswise (y) direction take the following form:

$$\begin{aligned} x:&\quad \kappa\, Ma_r^2\frac{h}{l}\tilde{p}\tilde{u}\frac{\partial \tilde{u}}{\partial \tilde{x}}=-\frac{h}{l}\frac{\partial \tilde{p}}{\partial \tilde{x}}+\frac{\kappa Ma_r^2}{Re_r}\left(\frac{h^2}{l^2}\frac{\partial^2 \tilde{u}}{\partial \tilde{x}^2}+\frac{\partial^2 \tilde{u}}{\partial \tilde{y}^2}\right)+\frac{1}{3}\frac{\kappa Ma_r^2}{Re_r}\frac{h^2}{l^2}\frac{\partial^2 \tilde{u}}{\partial \tilde{x}^2},\\ y:&\quad \frac{\partial \tilde{p}}{\partial \tilde{x}}=\frac{1}{3}\frac{\kappa Ma_r^2}{Re_r}\frac{h}{l}\frac{\partial \tilde{u}}{\partial \tilde{x}\partial \tilde{y}}. \end{aligned} \tag{3}$$

Here two characteristic non-dimensional numbers appear, Mach number $Ma=u_r/\sqrt{\kappa p_r/\rho_r}$ and Reynolds number $Re=\rho_r u_r h/\eta$. The ratio between the channel height and the length of the channel is defined by a small parameter $\varepsilon=h/l$. If the flow is subsonic, Mach and Reynolds number can be assumed as: $\kappa Ma^2=\varepsilon^m,\ m>0$ and $\kappa Ma^2/Re=\beta\varepsilon$, where β is of order 1, $\beta=\mathcal{O}(1)$. From those two relations, we obtain correlation between Reynolds number and small parameter ε: $Re=\frac{1}{\beta}\varepsilon^{m-1}$. Thus, the projections of the Navier-Stokes equations are:

$$\begin{aligned} x: \quad & \varepsilon^m \tilde{\rho}\tilde{u}\frac{\partial \tilde{u}}{\partial \tilde{x}} = -\frac{\partial \tilde{p}}{\partial \tilde{x}} + \beta\left(\varepsilon^2\frac{\partial^2 \tilde{u}}{\partial \tilde{x}^2} + \frac{\partial^2 \tilde{u}}{\partial \tilde{y}^2}\right) + \frac{1}{3}\beta\varepsilon^2\frac{\partial^2 \tilde{u}}{\partial \tilde{x}^2}, \\ y: \quad & \frac{\partial \tilde{p}}{\partial \tilde{y}} = \frac{1}{3}\beta\varepsilon^2\frac{\partial^2 \tilde{u}}{\partial \tilde{y}\tilde{x}}. \end{aligned} \tag{4}$$

Assuming that parameter $m \geq 1$, i.e., $Re \leq 1$, all terms of order $\mathcal{O}(\varepsilon)$ or smaller vanish in the above equations. Crosswise projection of Eq. (4) implies that the pressure is constant throughout cross section and depends only on x-coordinate, $p = f(x)$. Under these assumptions streamwise projection of Eq. (4) reduces to:

$$\frac{\mathrm{d}\tilde{p}}{\mathrm{d}\tilde{x}} = \beta\frac{\partial^2 \tilde{u}}{\partial \tilde{y}^2}. \tag{5}$$

By substituting no-slip boundary conditions, $\tilde{y} = 0, \tilde{u} = 0$ and $\tilde{y} = 1, \tilde{u} = 0$, into Eq. (5), dimensionless velocity distribution can be obtained:

$$\tilde{u} = \frac{1}{2\beta}\frac{\mathrm{d}\tilde{p}}{\mathrm{d}\tilde{x}}(\tilde{y}^2 - \tilde{y}) \tag{6}$$

Mass flow rate per unit length in non-dimensional form, given that $\dot{\tilde{m}} = \int_0^1 \tilde{\rho}\tilde{u}\,\mathrm{d}\tilde{y} = 1$, is:

$$-\frac{\tilde{p}}{12\beta}\frac{\mathrm{d}\tilde{p}}{\mathrm{d}\tilde{x}} = 1 \tag{7}$$

After solving Eq. (7), pressure distribution along the channel in non-dimensional form is:

$$\tilde{p} = \sqrt{1 + 24\beta(1 - \tilde{x})} \tag{8}$$

For inlet cross section, $\tilde{x} = 0$, and substituting it to Eq. (8), we obtain:

$$\Pi = \sqrt{1 + 24\beta} \tag{9}$$

where Π is the ratio between inlet and outlet pressure. Eq. (9) implies that for known mass flow rate, Π can be obtained, and conversely, for known Π, mass flow rate can be obtained.

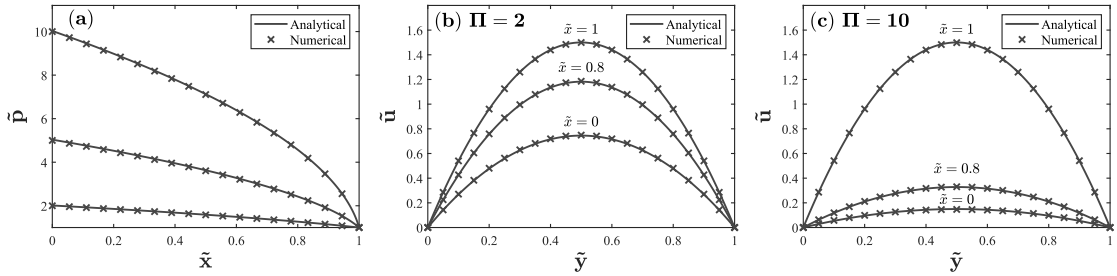

Fig. 1. Comparison of numerical and analytical results. **a** Pressure distribution, **b**, **c** Velocity profile

The analytical results are compared with numerical results obtained with the commercial software Ansys Fluent 19.1 [2]. As shown in Fig. 1, a slight deviation for higher values of ratio Π can be observed. This deviation can be attributed to the absence of the advective term in the Navier-Stokes equations. In conclusion, the numerical and analytical results are in good agreement.

Keywords: compressible, isothermal, numerical simulation, analytical solution, parallel plates.

References:

[1] Nevena Stevanović, *Osnove mikrofluidike i nanofluidike.* Mašinski fakultet, Univerzitet u Beogradu, Beograd, 2014.

[2] *ANSYS Fluent Theory Guide, Release 19.1*; ANSYS, Inc.: Canonsburg, PA, USA, 2019.

FREQUENCY BAND STRUCTURE ANALYSIS OF A PERIODIC BEAM-MASS SYSTEM FOR PIEZOELECTRIC ENERGY HARVESTING

Stepa M. Paunović

[1] Mathematical Institute of the Serbian Academy of Sciences and Arts Kneza Mihaila 36, 11000 Belgrade
e-mail: stepa.paunovic@mi.sanu.ac.rs

Abstract

In this contribution dynamic properties of a periodic system of bimorph cantilevers with attached concentrated masses are analyzed. Governing equations are derived through Hamilton's principle and solved by Galerkin discretization. Results show how these systems can be used as wave filters as well as for energy harvesting purposes, since their frequency band structure can be easily tailored to meet any specific requirement by simply rearranging the attached masses.

Keywords: periodic beams, piezoelectric energy harvesting, frequency band structure design.

1. Problem statement and mathematical model

Periodic systems are often used as wave filters since they can be designed so that the waves of certain frequencies pass, while other frequencies cannot propagate, leaving "band gaps" in frequency domain. Systems of periodically connected bimorph beams combine wave filtering and energy harvesting capabilities [1,2]. In this contribution, dynamic properties of one such system of N_b beams organized into N_c 2-beam cells are analyzed. Beams have N_{m1} or N_{m2} concentrated masses attached and are connected by coupling layers with compliance modulus of either k_1 or k_2. All the beams have same properties (length L, width b, bending stiffness YI, mass per unit length m, piezoelectric constant e_{31}), while the number of attached concentrated masses and/or the connecting layer properties change periodically. All piezo-layers are connected in parallel into an electric circuit with electric resistance R. The system is subjected to a harmonic excitation force F acting at one side of the system, inducing system vibrations and generating electric voltage v. Through Hamilton's principle and Kirchhoff's rules, the following equations for the beam displacements for each beam $w_{(p)}(x,t)$, $p=1,2,\ldots,N_b$, and electric total voltage v are obtained [3]:

$$\left(m+\sum_{a=1}^{N_{m(p)}} M_a\delta(x-x_a)\right)\ddot{w}_{(p)}+YIw''''_{(p)}+k_p(w_{(p)}-w_{(p-1)})+k_{p+1}(w_{(p+1)}-w_{(p)})-V\left(\delta'(x)-\delta'(x-L)\right)v=f \qquad (1)$$

$$C_p\dot{v}+\frac{1}{2R}v+e_{31}bh_{pc}\int_0^L \dot{w}''_{(p)}=0 \qquad (2)$$

These are solved by Galerkin discretisation $w_{(p)}(x,t)=\Sigma_i^n \Phi_i(x)q_i(t)$, with bare beam mode shapes used as trial functions, leading to a system of $n+1$ algebraic equations expressed in matrix form as: $\mathbf{Mu+Ku=f}$, $\mathbf{u}=\{\mathbf{q},v\}^T$. Applying harmonic excitation force $F=F_0\ exp(i\Omega t)$ to the first

beam gives the frequency response functions which are used to analyze system dynamic properties.

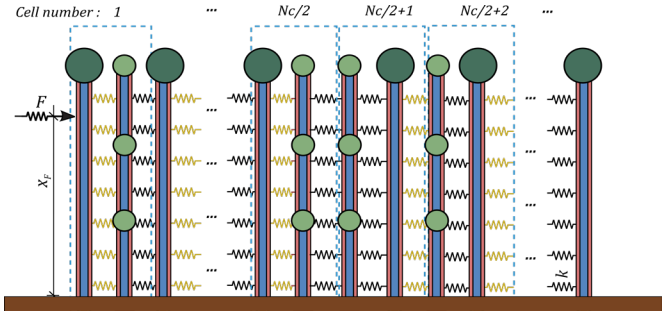

Fig. 1. Periodic system of bimorph piezoelectric cantilever beams with attached concentrated masses. N_c 2-beam cells are connected symmetrically to the middle of the chain, thus producing an interface.

2. Frequency band structure analysis

A system of $N_b=40$ beams with different layouts is analyzed. Layout 1 (blue) is a non-periodic system, where all beams have $N_m=1$ attached masses, and all coupling layers have modulus $k=200N/m$. Layout 2 (green) – masses are constant throughout the system $N_m=1$, while layers' stiffness changes periodically, with $k_1=300$, $k_2=100$. Layout 3 (red) – same as Layout 2, but with a symmetry plane in the middle (Fig.1a), producing an interface beam and corresponding interface modes. Layout 4 (black), 5 (orange) and 6 (purple) – all coupling layers have stiffness $k=200$, while number of attached masses N_m changes periodically, without and with the interface. Results show how periodicity creates bandgaps, bridged only by interface modes, and how these properties can be tailored to meet particular demands by simply rearranging the attached masses.

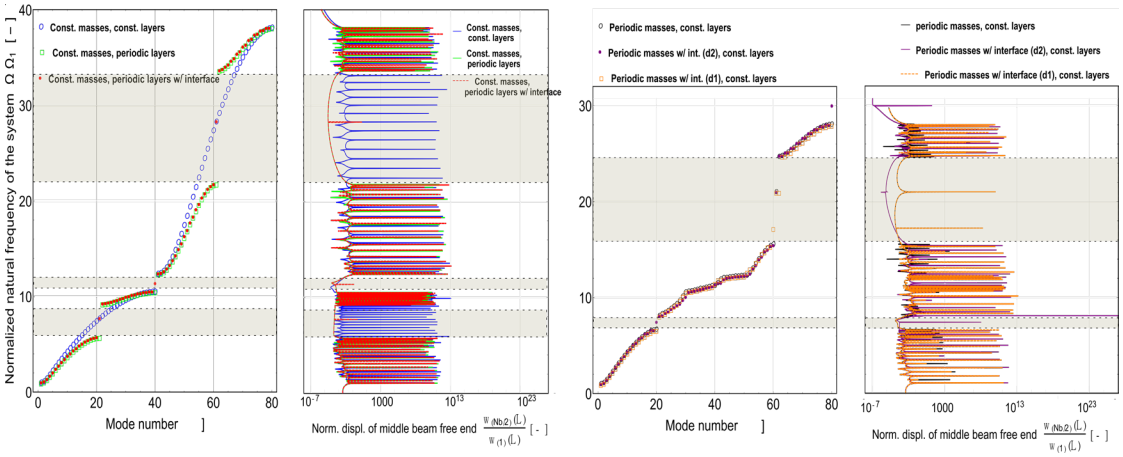

Fig. 2. Frequency band structure for different system layouts, showing band gaps and interface modes

Acknowledgment: This work was supported by the Serbian Ministry of Science, Technological development and Innovations, through the Mathematical Institute of the Serbian Academy of Sciences and Arts.

References:

[1] M He, Lim, K. & Zhang, F. *A novel periodic beam with multilayer acoustic black holes for deep sub-wavelength vibration attenuation*. Acta Mechanica, Vol.1, 2023.

[2] Meruane, V., Pichara, K., *A broadband vibration-based energy harvester using an array of piezoelectric beams connected by springs*. Shock and Vibration, Vol. 1, 1-14, 2016.
[3] Erturk, A., Inman, D., *Piezoelectric energy harvesting*, John Wiley&Sons, UK, 2011.

STABILITY OF PARAMETRIC VIBRATIONS OF THE COUPLED RAYLEIGH BEAMS

Dunja Milić[1], Jian Deng[2], Vladimir Stojanović[1,2], and Marko D. Petković[3]

[1] Faculty of Mechanical Engineering, University of Niš, Aleksandra Medvedeva 14, 18000 Niš
e-mail: stojanovic.s.vladimir@gmail.com, dunja1994milic@gmail.com
[2] Faculty of Engineering, Lakehead University, Thunder Bay, Ontario, Canada P7B 5E1
e-mail: jian.deng@lakeheadu.ca
[3] Faculty of Sciences and Mathematics, University of Niš, Višegradska 33, 18000 Niš
e-mail: dexterofnis@gmail.com

Abstract

This paper discusses stochastic stability of double beam system connected by Kerr-type three-parameter elastic foundation which is subjected to the compressive axial forces. The beams are modeled using the Rayleigh beam theory and the axial forces contain a constant part and a time-dependent stochastic function. The study investigates the almost sure and moment stability of the double beam system under stochastic compressive axial loading by the Lyapunov exponent and moment Lyapunov exponents. For weak noise excitations, a singular perturbation method is used to obtain second-order expansions of the moment Lyapunov exponent and the Lyapunov exponent. Numerical study is conducted for chosen parameters and the almost sure and moment stability in the first and second perturbation is presented graphically.

Keywords: Stochastic stability, Kerr-type elastic layer, Double-beam system.

1. Introduction

Beam-type systems have always attracted the attention of scientists because of their great application in many branches of technology. This study focuses on investigating the stochastic stability of a system of two beams connected by elastic foundation and subjected to the compressive stochastic axial forces. Rayleigh beam model is used, and elastic foundation is presented as Kerr-type three-parameter elastic foundation. In [1] Dutta and Roy discuss various foundation models available in the literature, among others the Kerr foundation is presented, which consists of a shear layer introduced into a Winkler foundation where the spring constants above and under that layer are different. Kozić et al. [2] presents an analytical theory to define the dynamic characteristics of two parallel-beams continuously joined by a Kerr-type three parameter layer. There is already a lot of research on the topic of system stability under the influence of stochastic loads. An approximation for the moment Lyapunov exponents was conducted by Arnold et al. in [3]. Xie [3] studied moment Lyapunov exponents of a two-dimensional system under real-noise excitation. The method of regular perturbation is applied to obtain the weak-noise expansions of the moment Lyapunov exponent, Lyapunov exponent, and stability index in terms of the small fluctuation parameter.

2. Instructions

We consider the system shown in Fig. 1. It consists of two parallel Rayleigh beams of the same length L, joined by Kerr-type elastic layer, which contains two linear elastic spring layers of stiffness moduli K_1 and K_2 mutually connected by a unit shear layer of constant G. It is assumed that double beam system is under the stochastic excitation, where $F_1(t)$ and $F_2(t)$ are stochastically varying static loads.

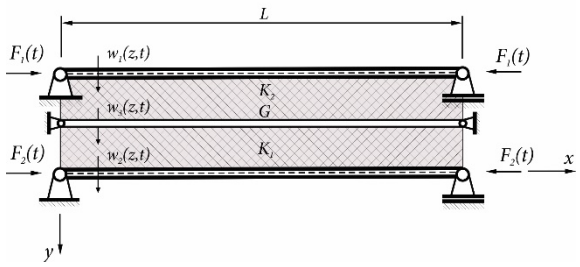

Fig. 1. Double-beam system

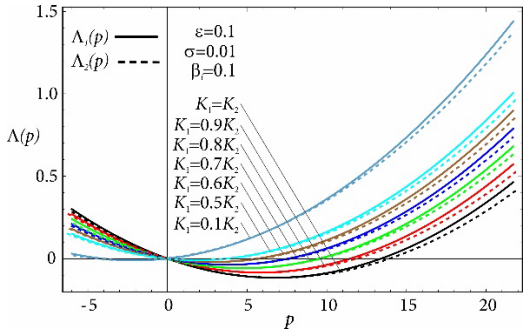

Fig. 2. Moment Lyapunov exponent $\Lambda(p)$ for varying stiffness of the layers

The concept of Lyapunov exponents is used in order to study the stability of the presented model. For weak noise excitations, the second order expansions of the moment Lyapunov exponent is obtained with singular perturbation method, the Lyapunov exponent is then obtained using the relationship between the moment Lyapunov exponent and the Lyapunov exponent. After the numerical analysis, the stability with the change in the stiffness of the layers, shear modulus, the damping coefficients and the intensity of the random process is graphically illustrated.

Acknowledgments: This research was financially supported by the Ministry of Science, Technological Development and Innovation of the Republic of Serbia (Contract No. 451-03-47/2023-01/ 200109) and partly by the Natural Sciences and Engineering Research Council of Canada.

References:

[1] Dutta, S.C., Roy, R., *A critical review on idealization and modeling for interaction among soil–foundation–structure system*, Computers & Structures, Vol.80(20-21), 1579-1594, 2002.

[2] Kozić, P., Pavlović, R., Karličić, D., *The flexural vibration and buckling of the elastically connectedparallel-beams with a Kerr-type layer in between*, Mechanics Research Communications, Vol.56, 83-89, 2013.

[3] Arnold, L., Doyle, M.M., Sri Namachchivaya, N., *Small noise expansion of moment Lyapunov exponents for two-dimensional systems*, Dynamics and Stability of Systems, Vol.12(3), 187-211, 2007.

[4] Xie, W.-C., *Moment Lyapunov exponents of a two-dimensional system under real-noise excitation*, Journal of Sound and Vibration, Vol. 239(1), 139-155, 2001.

The Ninth International Congress
of the Serbian Society of Mechanics
July 5-7, 2023, Vrnjačka Banja, Serbia